

## Scientific Journal for Damietta Faculty of Science

المجلة العلمية لكلية العلوم – جامعة دمياط



Damietta - EGYPT

ISSN (Print) 2314-8594

ISSN (Online) 2314-8616

<https://sjdfs.journals.ekb.eg/>



## The Role of Naringenin in Enhancing Metformin Efficacy in Diabetic Rats

Mayar Akram Shamkh<sup>1</sup>, Abdel-Aziz Fatouh Abdel-Aziz<sup>2</sup> and Rasha Fekry Zahran<sup>\*1</sup>

<sup>1</sup>Chemistry Department, Faculty of Science, Damietta University, 34517 Damietta, New-Damietta, Egypt.

<sup>2</sup>Chemistry Department, Faculty of Science, Mansoura University, Mansoura, Egypt.

Received: 11 July 2025 /Accepted: 25 July 2025

\*Corresponding author's E-mail: [zahran@du.edu.eg](mailto:zahran@du.edu.eg)

### Abstract

**Background:** Diabetes mellitus is linked to hepatic dysfunction, requiring effective therapeutic strategies. Metformin (MET), a standard antidiabetic agent, and naringenin (NAR), a citrus flavonoid, have shown complementary actions in enhancing insulin sensitivity and reducing oxidative damage through activation of AMP-activated protein kinase (AMPK). This study explores the dose-dependent effects of MET and NAR combinations on liver function and antioxidant status in diabetic rats.

**Methods:** Sixty male wistar rats were divided randomly into six groups: G1, normal control; G2 vehicle control (MET 50 mg/kg + NAR 50 mg/kg); G3, diabetic group (injected ip with nicotinamide (230 mg/kg) followed by streptozotocin (65 mg/kg), and three diabetic treated groups G4, G5 and G6 received MET (50 mg/kg) with NAR at 25, 50, or 100 mg/kg, respectively. Treatments were administered orally for five weeks. Body weight and fasting blood glucose (FBG) were recorded weekly, along with biochemical liver function parameters and total antioxidant capacity at the end of the experiment.

**Results:** Diabetic rats showed significant weight loss, elevated FBG, liver enzymes (ALT, AST), and bilirubin, alongside reduced total protein and total antioxidant capacity (TAC). Treatment with MET plus NAR significantly resulted in body weight increase, FBG, liver enzymes and TAC normalized compared to untreated diabetic rats.

**Conclusion:** These findings suggest that the combination of metformin and naringenin exerts synergistic antidiabetic and hepatoprotective effects. At the same time improve the antioxidant status in diabetic rats.

**Keywords:** antidiabetic, hepatoprotective, antioxidant, naringenin, streptozotocin

### Introduction

Diabetes mellitus is a long-term metabolic disorder marked by persistently high blood glucose concentrations. This condition arises either due to insufficient insulin

production by the pancreas or due to impaired cellular responsiveness to insulin. Over time, such dysregulation in glucose homeostasis may result in significant health complications (Saeedi et al., 2019). Among its different types, type 2 diabetes is the most prevalent form.

Type 2 diabetes (T2D) represents the most prevalent form of diabetes, constituting more than 90% of cases worldwide (Rob et al., 2025). It is a chronic metabolic condition marked by sustained hyperglycemia, which stems from both insulin resistance in peripheral tissues and an insufficient insulin secretion by pancreatic beta cells. This dysregulation disrupts normal metabolism of carbohydrates, fats, and proteins. The disease progression involves a decline in beta-cell function which disrupts the body's capacity to regulate blood glucose levels effectively, leading to elevated blood glucose levels and associated metabolic complications (Galicia-Garcia et al., 2020, Reed et al., 2021). According to previous studies which reported that diabetes mellitus induces a significant imbalance in the liver's oxidative status, characterized by elevated reactive oxygen species (ROS) production and diminished activities of key antioxidant enzymes, including superoxide dismutase (SOD), catalase (CAT), and glutathione peroxidase (GPx). This oxidative stress in the liver contributes to cellular damage, lipid peroxidation, and impaired hepatic function, which may underline the development of chronic liver disorders associated with diabetes, such as non-alcoholic fatty liver disease (NAFLD), steatohepatitis, and cirrhosis. The hyperglycemia and insulin resistance in diabetes disrupt normal metabolism of lipids, carbohydrates, and proteins, triggering both oxidative stress and an aberrant inflammatory response that activates pro-apoptotic pathways and damages hepatocytes. Pro-inflammatory mediators such as interleukin-1 beta (IL-1 $\beta$ ), interleukin-6 (IL-6), and tumor necrosis factor alpha (TNF- $\alpha$ ) exacerbate this oxidative damage, further promoting liver injury and progression to severe liver pathology (Lucchesi et al., 2013, Mohamed et al., 2016, Zahran et al., 2024).

As a first-line oral antidiabetic medication, metformin is extensively utilized in treating patients with type 2 diabetes mellitus due to its effective glucose-lowering properties and favorable safety profile (Pernicova and Korbonits, 2014, LaMoia and Shulman, 2021).

Metformin primarily acts by inhibiting gluconeogenesis in the liver, leading to a reduction in hepatic glucose production, thereby lowering blood glucose levels (LaMoia and Shulman, 2021). Metformin is transported into hepatocytes through the organic cation transporter 1 (OCT1), where it inhibits complex I of the mitochondrial respiratory chain. This disruption alters the cellular energy balance, thereby stimulating AMP-activated protein kinase (AMPK), a central regulator of both glucose and lipid metabolism (Rena et al., 2017). This activation suppresses gluconeogenic gene expression and improves insulin sensitivity, contributing to better glycemic control (Pernicova and Korbonits, 2014).

Beyond its glucose-lowering effects, metformin exerts protective effects on the liver. It reduces hepatic lipid accumulation, inflammatory responses, and oxidative stress, which serve as major contributors to the development and progression of hepatic disorders, particularly nonalcoholic fatty liver disease (NAFLD) commonly associated with diabetes (Apostolova et al., 2020). By modulating AMPK activity, metformin improves lipid metabolism and inhibits pathways leading to liver fibrosis and injury, thus offering hepatoprotective benefits in diabetic patients (Rena et al., 2017).

Naringenin is a naturally occurring flavonoid predominantly found in citrus fruits, noted for its multifaceted biological activities, encompassing antioxidant, anti-inflammatory, antifibrogenic, and tumor-suppressive effects. It has attracted attention for its potential therapeutic role in various liver diseases caused by oxidative damage, inflammation, and tissue fibrosis (Hernández-Aquino and Muriel, 2018).

The mechanism of action of naringenin involves inhibition of oxidative stress and various signaling cascades, including transforming growth factor-beta (TGF- $\beta$ ) and the mitogen-activated protein kinase (MAPK) pathway, and toll-like receptor (TLR) pathways. This leads to reduced stimulation of hepatic stellate cells (HSCs) alongside a reduction in extracellular matrix (ECM) production, which are key processes in liver fibrosis (Naeini et al., 2021). Additionally, naringenin enhances the cellular antioxidant defense by upregulating enzymes like superoxide dismutase (SOD), catalase (CAT), and glutathione peroxidase (GPx), thus

protecting liver cells from oxidative damage (Xu et al., 2024).

Naringenin's protective effects on the liver include prevention of lipid peroxidation, reduction of inflammation, and inhibition of fibrogenesis. It has demonstrated efficacy in experimental models of liver injury caused by toxins, alcohol, and metabolic disorders, improving liver function and histology. Furthermore, naringenin modulates lipid metabolism, which helps in managing nonalcoholic fatty liver disease (NAFLD) and prevents progression to more severe liver conditions (Mansour et al., 2023).

Streptozotocin (STZ) is a standard diabetogenic agent extensively utilized in preclinical models to simulate diabetes mellitus due to its selective cytotoxicity on pancreatic  $\beta$ -cells, leading to their necrosis and resulting in hyperglycemia similar to human diabetes (Ghasemi and Jeddi, 2023). At appropriate doses, STZ impairs insulin secretion by destroying  $\beta$ -cells and disrupting glucose metabolism, which can model both type 1 and type 2 diabetes depending on the dose and protocol (Rehman et al., 2023). To induce type 2 diabetes specifically, nicotinamide (NA) is administered prior to STZ. Nicotinamide partially protects  $\beta$ -cells from STZ-induced damage by inhibiting poly(ADP-ribose) polymerase-1 (PARP-1) activity, preventing NAD<sup>+</sup> and ATP depletion, and thus allowing some  $\beta$ -cells to survive and respond to glucose stimulation (Yan, 2022) (Szkudelski, 2012). This combination produces a model of type 2 diabetes characterized by partial  $\beta$ -cell dysfunction and reduced insulin sensitivity, mimicking the pathophysiology of human type 2 diabetes more closely than STZ alone (Alenzi, 2009, Elamin et al., 2018).

The present study aims to evaluate the combined effects of metformin and different concentrations of naringenin on liver function and metabolic parameters in a rat model of type 2 diabetes established by STZ and nicotinamide. This combination therapy is hypothesized to provide synergistic benefits by improving glycemic control and exerting hepatoprotective and antioxidant effects, potentially offering approach for managing diabetes-associated liver complications.

## Methods

### *Chemicals*

Metformin hydrochloride (Tokyo Chemical Industry Co., Ltd., Tokyo, Japan), naringenin were purchased from Glentham Life Sciences Ltd., England. Streptozotocin (Sigma Chemical Co., St Louis, MO, USA). Nicotinamide was purchased from Fluka AG, Switzerland. Sodium citrate dihydrate from Glentham Life Sciences Ltd., England. Portable glucometers and glucose test strips (perfecta Bianca, Italy) were purchased from a local pharmacy. All kits were procured from Biodiagnostic Company, Egypt.

### *Animals*

Sixty adults male wister rats weighing (180–200 g) were obtained from the regional center for mycology and biotechnology, Al-Azhar university, Cairo, Egypt. The rats were housed in steel wire cages with mesh walls, which allowed for temperature control set at ( $22 \pm 3$ ) °C. The cages also had adjustable lighting to create a 12-hour cycle of darkness and light. The relative humidity in the cages was maintained at ( $80 \pm 4$ ) %. The rats were provided with free access to food and water. Prior to the experiments, the rats were placed in a standard laboratory setting for acclimation, two weeks in advance.

### *Experimental induction of diabetes mellitus*

All rats were fasted for six hours prior to diabetes induction. To establish a non-obese type 2 diabetes model with residual  $\beta$ -cell function, nicotinamide was administered intraperitoneally at 230 mg/kg 15 minutes before injecting freshly prepared streptozotocin (STZ) at 65 mg/kg body weight dissolved in citrate buffer (50 mM, pH 4.5). This protocol partially protects pancreatic  $\beta$ -cells from STZ toxicity, allowing for a model of type 2 diabetes characterized by partial  $\beta$ -cell damage. Following diabetes induction, a combination of treatments was applied to the animals.

### *Estimation of blood glucose*

Fasting blood glucose levels were measured 72 hours post-diabetes induction using a portable glucometer. Blood samples were collected by clipping the tip of the rat's tail to collect a drop of blood (Togashi et al., 2016).



Inclusion criteria required blood glucose values greater than 180 mg/dL to confirm diabetic status. Following confirmation of diabetes induction, combined treatment protocols were initiated.

#### *Experimental design*

The rats were randomly assigned into six groups each of ten rats. Following the experimental induction of diabetes, treatments with MET and NAR were administered daily via oral gavage for 5 weeks.

#### *Experimental design*

The present study includes the following six groups:

**Control group:** untreated healthy rats.

**MET + NAR group:** healthy rats were administered with metformin (50 mg/kg) and naringenin (50 mg/kg).

**Diabetic (NICO/STZ) group:** diabetes was induced in rats using nicotinamide (230 mg/kg) and streptozotocin (65 mg/kg), without treatment.

**MET<sub>50</sub> + NAR<sub>25</sub> group:** diabetic rats were treated with metformin (50 mg/kg) and naringenin (25 mg/kg) daily for 5 weeks.

**MET<sub>50</sub> + NAR<sub>50</sub> group:** diabetic rats were treated with metformin (50 mg/kg) and naringenin (50 mg/kg) daily for 5 weeks.

**MET<sub>50</sub> + NAR<sub>100</sub> group:** diabetic rats were treated with metformin (50 mg/kg) and naringenin (100 mg/kg) daily for 5 weeks.

Weekly assessments of body weight and fasting glucose levels were recorded throughout the experiment. At the end of Met and NAR treatments, the rats were subjected to an overnight fast before being euthanized using CO<sub>2</sub> for sample collection.

#### *Blood sampling*

At the end of the experiment, rats were euthanized using CO<sub>2</sub>, followed by careful opening of the peritoneal cavity to collect blood samples from the inferior vena cava. Blood was drawn into vacuum tubes to facilitate serum separation for subsequent biochemical analysis.

#### *Estimation of liver function*

Serum levels of aspartate aminotransferase (AST) and alanine aminotransferase (ALT)

were assessed according to the method of (Reitman and Frankel, 1957). The protein concentration was determined according to the method of (Kemp et al., 1961). The total and direct bilirubin in the sample were determined according to the method of (Walter and Gerade, 1970).

#### *Estimation of total antioxidant capacity (TAC)*

The serum antioxidant capacity is measured by adding a known amount of hydrogen peroxide (H<sub>2</sub>O<sub>2</sub>) to the sample, where antioxidants reduce its concentration. The remaining H<sub>2</sub>O<sub>2</sub> is then quantified colorimetrically through an enzymatic reaction that produces a colored product from 3, 5-dichloro-2-hydroxybenzenesulfonate. The assay involves mixing the serum with diluted H<sub>2</sub>O<sub>2</sub> substrate, incubating, adding a chromogen-enzyme mixture, further incubation, and measuring absorbance at 505 nm. TAC is calculated using the difference in absorbance between a blank and the sample, multiplied by a factor of 3.33. This method described by Koracevic et al (Koracevic et al., 2001)

#### *Statistical analysis*

All data are expressed as mean ± standard error (SE). Statistical evaluation was performed using SPSS version 25. Group comparisons were made through one-way ANOVA, and a p-value less than 0.05 was considered statistically significant.

### **Results**

#### *Effects of treatments on body weight*

Normal rats treated with NAR +MET showed an insignificant change in body weight ( $p = 0.068$ ) versus normal group. Additionally, diabetic rat ...exhibited a significant reduction in body weight. ( $p < 0.001$ , **Figure 1**) compared to normal group. In contrast, diabetic rats treated with (MET<sub>50</sub> + NAR<sub>25</sub>), (MET<sub>50</sub>+NAR<sub>50</sub>) and (MET<sub>50</sub> + NAR<sub>100</sub>)

displayed significant increases in body weight relative to diabetic group ( $p < 0.001$ ).

Table 1: Mean Levels of ALT, AST, Total protein, Total Bilirubin and Direct bilirubin for all groups.

	Control	MET +NAR	NICO/STZ	MET <sub>50</sub> + NAR <sub>25</sub>	MET <sub>50</sub> + NAR <sub>50</sub>	MET <sub>50</sub> + NAR <sub>100</sub>
ALT (U/mL)	49.2 ± 0.9	50.8 ± 3.2	148.7 ± 3.8 <sup>a</sup>	53.1 ± 3.5 <sup>c</sup>	65.7 ± 1.2 <sup>c</sup>	52.7 ± 2.5 <sup>c</sup>
AST (U/mL)	74.1 ± 1.1	86.8 ± 2.3 <sup>a</sup>	146.8 ± 3.3 <sup>a</sup>	77.0 ± 0.6 <sup>c</sup>	111.7 ± 0.5 <sup>c</sup>	113.1 ± 0.9 <sup>c</sup>
Total Protein(g/dL)	15.9 ± 0.4	15.6 ± 0.5	8.8 ± 0.5 <sup>a</sup>	15.5 ± 0.5 <sup>c</sup>	14.7 ± 0.5 <sup>c</sup>	15.5 ± 0.5 <sup>c</sup>
Total Bilirubin (mg/dL)	0.44±0.3	1.07±0.1 <sup>a</sup>	1.14±0.1 <sup>a</sup>	0.46±0.04 <sup>c</sup>	0.43±0.03 <sup>c</sup>	0.45±0.07 <sup>c</sup>
Direct bilirubin(mg/dL)	0.27±0.03	0.28±0.04	0.48±0.03 <sup>a</sup>	0.34±0.02 <sup>c</sup>	0.27±0.01 <sup>c</sup>	0.36±0.01 <sup>c</sup>
TAC(mM/L)	0.25 ± 0.01	0.25 ± 0.01	0.21±0.01 <sup>a</sup>	0.26 ± 0.01 <sup>c</sup>	0.25±0.002 <sup>c</sup>	0.24±0.003 <sup>c</sup>

Data represented as mean ± SE, a =significant when compared with the control rat group, c =significant when compared with nicotinamide/streptozotocin injected rat. NICO: nicotinamide, STZ: streptozotocin, MET: metformin, NAR: naringenin, MET<sub>50</sub>: metformin administered at 50 mg/kg, NAR<sub>25</sub>: naringenin administered at 25 mg/kg, NAR<sub>50</sub>: naringenin administered at 50 mg/kg and NAR<sub>100</sub>: naringenin administered at 100 mg/kg. TAC: total antioxidant capacity.

Table 2. Pearson correlation between laboratory parameters in all studied groups

		body weight	FBG	ALT	AST	T.ptn	T.BIL	D.BIL	TAC
body weight	r		-.993**	-.952**	-.890**	.881**	-.586*	-.783**	.714
	p		0.000	0.000	0.000	0.000	0.035	0.002	0.001**
FBG	r	-.993**		.993**	.881**	-.959**	0.472	.864**	-.819-
	p	0.000		0.000	0.001	0.000	0.168	0.001	0.002**
ALT	r	-.952**	.993**		.889**	-.951**	0.509	.829**	-.747
	p	0.000	0.000		0.000	0.000	0.076	0.000	0.000**
AST	r	-.890**	.881**	.889**		-.745*	0.294	.690*	-.953
	p	0.000	0.001	0.000		0.021	0.330	0.013	0.000**
T.ptn	r	.881**	-.959**	-.951**	-.745*		-0.504	-.813**	.697
	p	0.000	0.000	0.000	0.021		0.166	0.004	0.003**
T.BIL	r	-.586*	0.472	0.509	0.294	-0.504		0.437	-0.334
	p	0.035	0.168	0.076	0.330	0.166		0.080	0.379
D.BIL	r	-.783**	.864**	.829**	.690*	-.813**	0.437		-.809
	p	0.002	0.001	0.000	0.013	0.004	0.080		0.005**
TAC	r	.714**	-.819**	-.747**	-.953**	.697**	-0.334	-.809*	
	p	0.001	0.002	0.000	0.000	0.003	0.379	0.005	

\*\* Correlation is significant at the 0.01 level

\* Correlation is significant at the 0.05 level

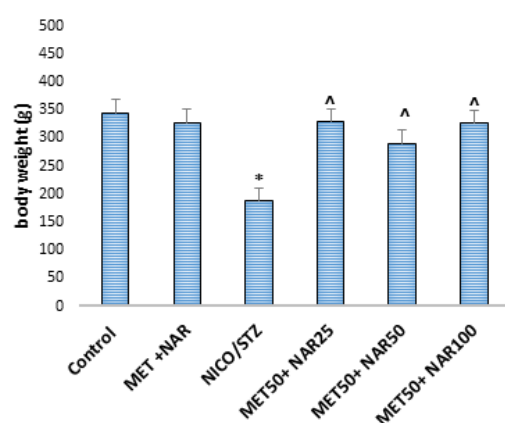


Figure 1. Effect of metformin and Naringenin on body weight. Values are expressed as mean ± SE. \* significant when compared to control group, ^ significant when compared to NICO/STZ group.

### Effects of treatments on fasting blood glucose

Normal treated rats with MET + NAR exhibited insignificant changes in FBG compared to normal group ( $p = 0.78$ , **Table 1** and **Figure 2**). Meanwhile, diabetic group exhibited a significant elevation in fasting blood glucose (FBG) levels relative to the normal group ( $p < 0.001$ ). In contrast, diabetic rats treated with (MET<sub>50</sub> + NAR<sub>25</sub>), (MET<sub>50</sub> + NAR<sub>50</sub>), and (MET<sub>50</sub> + NAR<sub>100</sub>) had a significant reduction in FBG compared to diabetic group ( $p < 0.001$ ).

### Effects of treatments on liver function tests

In **Table 1**, Normal treated rats with MET + NAR showed no significant change in ALT activity compared to normal group ( $p = 0.677$ ). In contrast, ALT and AST activities in diabetic rats were significantly elevated compared to



normal group ( $p < 0.001$ , **Figure 3a and Figure 3b**), whereas Diabetic rats treated with (MET<sub>50</sub> + NAR<sub>25</sub>), (MET<sub>50</sub> + NAR<sub>50</sub>), and (MET<sub>50</sub> + NAR<sub>100</sub>) demonstrated substantial reductions in these enzymes relative to diabetic group ( $p < 0.001$ ).

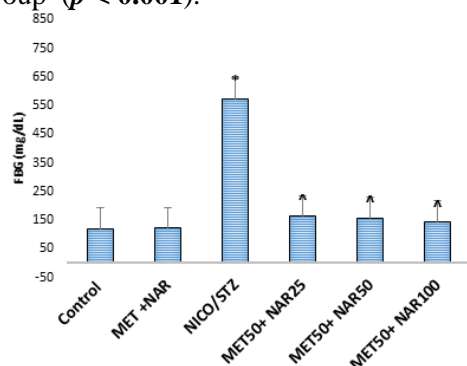


Figure 2. Effects of metformin and Naringenin on FBG. Values are expressed as mean  $\pm$  SE. \* significant when compared to control group, ^ significant when compared to NICO/STZ group.

Similarly, normal rats treated with MET + NAR experienced an insignificant decrease in total protein level compared to normal group ( $p = 0.642$ , **Table 1**). While total protein levels in diabetic group were lower than those in normal group ( $p < 0.001$ ), but whereas diabetic rats treated with (MET<sub>50</sub> + NAR<sub>25</sub>), (MET<sub>50</sub> + NAR<sub>50</sub>), and (MET<sub>50</sub> + NAR<sub>100</sub>) exhibited significant increases in total protein level compared to diabetic group ( $p < 0.001$ , **Figure 3c**). Regarding bilirubin levels, normal rats treated with MET + NAR experienced a significant increase in total bilirubin ( $p < 0.05$ ) with no change in direct bilirubin compared to normal group ( $p = 0.874$ ). Additionally, diabetic rats had a significant rise in total and direct bilirubin compared to normal group ( $p < 0.01$  and  $p < 0.001$ , respectively). Meanwhile, diabetic rats treated with (MET<sub>50</sub> + NAR<sub>25</sub>), (MET<sub>50</sub> + NAR<sub>50</sub>) and (MET<sub>50</sub> + NAR<sub>100</sub>) showed a significant reduction in total bilirubin ( $p < 0.01$ , **Figure 3d**). Notably, Diabetic rats treated with (MET<sub>50</sub> + NAR<sub>25</sub>), (MET<sub>50</sub> + NAR<sub>50</sub>), and (MET<sub>50</sub> + NAR<sub>100</sub>) all displayed significant reductions in direct bilirubin compared to diabetic rats ( $p < 0.01$ ,  $p < 0.001$ , and  $p < 0.05$ , respectively) as shown in **Figure 3e**.

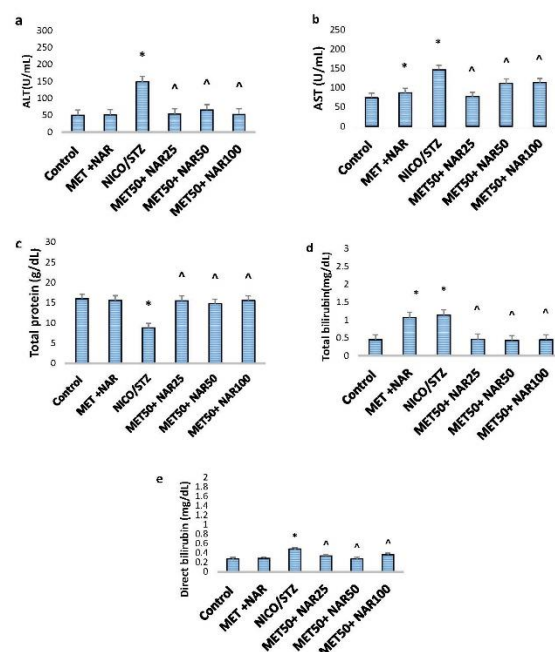


Figure 3. Effects of metformin and naringenin on a) ALT, b) AST, c) Total protein, d) Total bilirubin and e) Direct bilirubin. Values are expressed as mean  $\pm$  SE. \* significant when compared to control group, ^ significant when compared to NICO/STZ group.

#### Effects of treatments on TAC

Normal rats treated with the combination of MET+NAR showed no significant change in total antioxidant capacity (TAC) compared to the normal group ( $p = 0.856$ , **Table 1** and **Figure 4**). In contrast, diabetic rats displayed a significant decrease in TAC ( $p < 0.01$ ) compared to normal rats. Diabetic rats were treated with (MET<sub>50</sub> + NAR<sub>25</sub>), (MET<sub>50</sub> + NAR<sub>50</sub>) and (MET<sub>50</sub> + NAR<sub>100</sub>) significantly increased TAC ( $p < 0.001$ ,  $p = 0.001$ , and  $p = 0.023$ , respectively) compared to untreated diabetic rats.

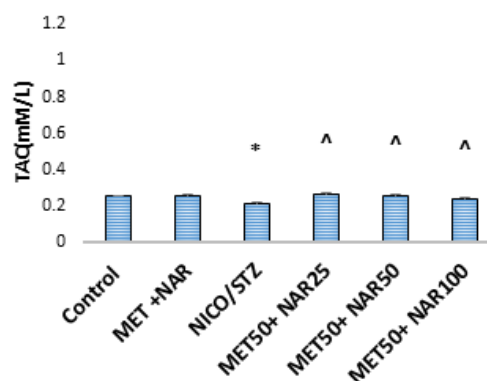


Figure 4. Effects of metformin and naringenin on TAC. Values are expressed as mean  $\pm$  SE. \* significant when compared to control group, ^ significant when compared to NICO/STZ group

## Discussion

Diabetes mellitus is a long-standing metabolic disease marked by elevated blood glucose levels resulting from inadequate insulin secretion, impaired insulin action, or both (Ehsan et al., 2025). Effective diabetes management frequently requires combination therapy, integrating two or more treatments to address the multiple pathways implicated in chronic hyperglycemia and its associated complications. (Nankar et al., 2017). This investigation focused on assessing the effect of naringenin (a citrus flavonoid) and metformin (a standard antidiabetic drug) on STZ-induced diabetic rats by comparing liver function. The findings highlight the therapeutic potential of these compounds, particularly in diabetic conditions, while also revealing dose-dependent variations in efficacy. The results showed a marked increase in serum levels of blood glucose, ALT, AST, total and direct bilirubin, with a concomitant decrease in total protein and body weight secondary to induction of diabetes in rats. These results align with other studies that have observed increased serum levels of blood glucose, ALT, AST, total and direct bilirubin (HJ, 1970, Zulkifle et al., 2024, Kakkar et al., 1998, Kumar et al., 2011).

In this study, the changes that occur in body weight may be a consequence of energy imbalance between intake and expenditure may lead to the utilization of alternative energy sources, primarily through increased lipid metabolism, reduced glucose utilization, and the breakdown of structural proteins (Ojo et al., 2017, Wilson and Islam, 2012). Additionally, an elevation in body weight was observed across all diabetic groups receiving treatment may be due to that naringenin enhances insulin sensitivity, promoting energy expenditure, and improving lipid metabolism thereby reducing weight loss (Coulter et al., 2023).

Notably, the reduction in fasting blood glucose levels in treated groups relative to the diabetic control supports the idea that naringenin improves glucose metabolism by modulating organic cation transporter 1 (OCT1) expression, enhancing metformin's hepatic uptake and subsequent glucose-lowering effects (Mato Mofo et al., 2020).

Diabetes mellitus is often associated with elevated levels of liver enzymes such as alanine aminotransferase (ALT) and aspartate aminotransferase (AST), which serve as

biomarkers of hepatic injury and dysfunction (Targher, 2010). The persistent hyperglycemia characteristic of diabetes induces oxidative stress and inflammation in hepatic tissues, leading to hepatocellular damage and subsequent leakage of these enzymes into the bloodstream (Fang et al., 2019). In this study, all three treatment combinations significantly reduced ALT and AST levels compared to the untreated diabetic group, indicating improved liver function. Metformin's hepatoprotective effect is largely attributed to its activation of AMP-activated protein kinase (AMPK), which suppresses hepatic glucose synthesis and lipid accumulation, thereby mitigating oxidative stress and inflammation (Foretz et al., 2014). Conversely, naringenin exerts its protective role by scavenging free radicals and modulating inflammatory pathways, which helps restore liver integrity and enzyme levels (Assini et al., 2013).

Diabetes-induced reductions in total serum protein reflect underlying hepatic dysfunction caused by persistent hyperglycemia and oxidative injury, which impair the liver's ability to maintain normal protein synthesis (Dharmalingam and Yamasandhi, 2018). In this study, the three treatment combinations significantly increased total protein levels compared to the diabetic group, indicating improved liver function. Metformin acts primarily by activating AMPK, which reduces gluconeogenesis and improves insulin sensitivity, thereby decreasing metabolic burden on the liver and supporting protein synthesis (Nyane et al., 2017). Naringenin enhances hepatic function by promoting AMPK phosphorylation and providing antioxidant protection, which together restore hepatocyte metabolic balance and protein production (He et al., 2022).

Diabetes is often associated with impaired liver function, reflected by increased levels of total and direct bilirubin, which serve as important biomarkers of hepatic injury and cholestasis. The elevated bilirubin levels in diabetic patients arise from oxidative stress and inflammation-induced hepatocyte damage, disrupting bilirubin metabolism and excretion pathways (Ramírez-Mejía et al., 2024). In our study, all three treatment combinations significantly reduced total and direct bilirubin compared to the diabetic group, indicating improved liver function. The hepatoprotective mechanism of metformin is largely dependent



on the upregulation of AMPK activity, which reduces hepatic glucose production and oxidative stress, thereby mitigating liver injury and normalizing bilirubin metabolism (Zhou et al., 2001). Meanwhile, naringenin acts as a potent antioxidant and anti-inflammatory agent, enhancing bilirubin conjugation and excretion by upregulating detoxifying enzymes such as UDP-glucuronosyltransferase (UGT1A1) and improving bile flow (Mulvihill et al., 2016).

In the present study, diabetic rats exhibited markedly lower TAC than the control group. Kawahito, et al, Inoguchi, et al and Nishikawa, et al., illustrated that, hyperglycaemia is known to induce oxidative stress and suppressing endogenous antioxidant defence systems (Kawahito et al., 2009, Inoguchi et al., 2000, Nishikawa et al., 2000). Nevertheless, diabetics treated with all combinations demonstrated substantial improvements in TAC levels compared to diabetic group, with the combination of (MET<sub>50</sub> + NAR<sub>25</sub>) being of significant.

In summary, the co-administration of metformin and naringenin represents a promising therapeutic approach against diabetes-induced metabolic and hepatic dysfunction. This combination effectively reverses weight loss, normalizes fasting blood glucose, and significantly improves liver function markers in diabetic rats. These findings highlight that metformin plus naringenin holds great promise as an adjuvant treatment to mitigate diabetes-related hepatic complications, leveraging their complementary mechanisms to enhance glycemic control. These findings highlight the potential for tailored dosing to address specific diabetic complications.

## Conclusion

This study underscores the efficacy of combining metformin with moderate doses of naringenin for managing diabetic liver dysfunction while providing insights into dose-dependent responses critical for optimizing treatment regimens.

## Competing interests

The authors have no relevant financial or non-financial interests to disclose.

## Ethics approval and consent to participate

All experimental procedures were carried out following the ethical standards and regulations set forth by the Research Ethics Committee of Damietta Faculty of Medicine, Al-Azhar University, Egypt (Permit No. IRB00012367). The study adhered strictly to the institutional guidelines and complied with internationally recognized protocols, including the ARRIVE guidelines, to ensure the humane treatment and welfare of the animals throughout the research.

## References

- Alenzi, F. Q. (2009). Effect of nicotinamide on experimental induced diabetes.
- Apostolova, N., Iannantuoni, F., Gruevska, A., Muntane, J., Rocha, M. & Victor, V. M. (2020). Mechanisms of action of metformin in type 2 diabetes: Effects on mitochondria and leukocyte-endothelium interactions. *Redox biology*, 34, 101517.
- Assini, J. M., Mulvihill, E. E. & Huff, M. W. (2013). Citrus flavonoids and lipid metabolism. *Current opinion in lipidology*, 24, 34-40.
- Coulter, A. A., Greenway, F. L., Zhang, D., Ghosh, S., Coulter, C. R., James, S. L., He, Y., Cusimano, L. A. & Rebello, C. J. (2023). Naringenin and  $\beta$ -carotene convert human white adipocytes to a beige phenotype and elevate hormone-stimulated lipolysis. *Frontiers in Endocrinology*, 14, 1148954.
- Dharmalingam, M. & Yamasandhi, P. G. (2018). Nonalcoholic fatty liver disease and type 2 diabetes mellitus. *Indian journal of endocrinology and metabolism*, 22, 421-428.
- Ehsan, M., Ahmed, S., Majeed, W., Iftikhar, A., Iftikhar, M., Abbas, M. & Mehmood, T. (2025). Rhoifolin improves glycometabolic control in streptozotocin-induced diabetic rats by up-regulating the expression of insulin signaling proteins and down-regulating the mapk/jnk pathway. *Pharmaceuticals*, 18, 361.
- Elamin, N., Fadlalla, I., Omer, S. & Ibrahim, H. (2018). Histopathological alteration in stz-nicotinamide diabetic rats, a complication of diabetes or a toxicity of stz. *Int J Diabetes Clin Res*, 5, 1-8.
- Fang, S., Cai, Y., Li, P., Wu, C., Zou, S., Zhang, Y., Lin, X. & Guan, M. (2019). Exendin-4 alleviates oxidative stress and liver fibrosis by activating nrf2/ho-1 in streptozotocin-induced diabetic mice. *Nan fang yi ke da xue xue bao= Journal of Southern Medical University*, 39, 464-470.

- Foretz, M., Guigas, B., Bertrand, L., Pollak, M. & Viollet, B. (2014). Metformin: From mechanisms of action to therapies. *Cell metabolism*, 20, 953-966.
- Galicia-Garcia, U., Benito-Vicente, A., Jebari, S., Larrea-Sebal, A., Siddiqi, H., Uribe, K. B., Ostolaza, H. & Martín, C. (2020). Pathophysiology of type 2 diabetes mellitus. *International journal of molecular sciences*, 21, 6275.
- Ghasemi, A. & Jeddi, S. (2023). Streptozotocin as a tool for induction of rat models of diabetes: A practical guide. *EXCLI journal*, 22, 274.
- He, W., Wang, Y., Yang, R., Ma, H., Qin, X., Yan, M., Rong, Y., Xie, Y., Li, L. & Si, J. (2022). Molecular mechanism of naringenin against high-glucose-induced vascular smooth muscle cells proliferation and migration based on network pharmacology and transcriptomic analyses. *Frontiers in Pharmacology*, 13, 862709.
- Hernández-Aquino, E. & Muriel, P. (2018). Beneficial effects of naringenin in liver diseases: Molecular mechanisms. *World journal of gastroenterology*, 24, 1679.
- Hj, Z. (1970). Enzymes in hepatic disease. *Diagnostic enzymology*, 24-26.
- Inoguchi, T., Li, P., Umeda, F., Yu, H. Y., Kakimoto, M., Imamura, M., Aoki, T., Etoh, T., Hashimoto, T. & Naruse, M. (2000). High glucose level and free fatty acid stimulate reactive oxygen species production through protein kinase c--dependent activation of nad (p) h oxidase in cultured vascular cells. *Diabetes*, 49, 1939-1945.
- Kakkar, R., Mantha, S. V., Radhi, J., Prasad, K. & Kalra, J. (1998). Increased oxidative stress in rat liver and pancreas during progression of streptozotocin-induced diabetes. *Clinical science*, 94, 623-632.
- Kawahito, S., Kitahata, H. & Oshita, S. (2009). Problems associated with glucose toxicity: Role of hyperglycemia-induced oxidative stress. *World journal of gastroenterology: WJG*, 15, 4137.
- Kemp, P., Hübscher, G. & Hawthorne, J. (1961). Phosphoinositides. 3. Enzymic hydrolysis of inositol-containing phospholipids. *Biochemical Journal*, 79, 193.
- Koracevic, D., Koracevic, G., Djordjevic, V., Andrejevic, S. & Cosic, V. (2001). Method for the measurement of antioxidant activity in human fluids. *Journal of clinical pathology*, 54, 356-361.
- Kumar, D., Kumar, S., Kohli, S., Arya, R. & Gupta, J. (2011). Antidiabetic activity of methanolic bark extract of *albizia odoratissima* benth. In alloxan induced diabetic albino mice. *Asian Pacific Journal of Tropical Medicine*, 4, 900-903.
- Lamoia, T. E. & Shulman, G. I. (2021). Cellular and molecular mechanisms of metformin action. *Endocrine reviews*, 42, 77-96.
- Lucchesi, A. N., Freitas, N. T. d., Cassettari, L. L., Marques, S. F. G. & Spadella, C. T. (2013). Diabetes mellitus triggers oxidative stress in the liver of alloxan-treated rats: A mechanism for diabetic chronic liver disease. *Acta Cirurgica Brasileira*, 28, 502-508.
- Mansour, L. A., Elshopakey, G. E., Abdelhamid, F. M., Albukhari, T. A., Almeahadi, S. J., Refaat, B., El-Boshy, M. & Risha, E. F. (2023). Hepatoprotective and neuroprotective effects of naringenin against lead-induced oxidative stress, inflammation, and apoptosis in rats. *Biomedicines*, 11, 1080.
- Mato Mofo, E. P., Essop, M. F. & Owira, P. M. (2020). Citrus fruit-derived flavonoid naringenin and the expression of hepatic organic cation transporter 1 protein in diabetic rats treated with metformin. *Basic & clinical pharmacology & toxicology*, 127, 211-220.
- Mohamed, J., Nafizah, A. N., Zariyantey, A. & Budin, S. (2016). Mechanisms of diabetes-induced liver damage: The role of oxidative stress and inflammation. *Sultan qaboos university medical journal*, 16, e132.
- Mulvihill, E. E., Burke, A. C. & Huff, M. W. (2016). Citrus flavonoids as regulators of lipoprotein metabolism and atherosclerosis. *Annual review of nutrition*, 36, 275-299.
- Naeini, F., Namkhah, Z., Ostadrahimi, A., Tutunchi, H. & Hosseinzadeh-Attar, M. J. (2021). A comprehensive systematic review of the effects of naringenin, a citrus-derived flavonoid, on risk factors for nonalcoholic fatty liver disease. *Advances in nutrition*, 12, 413-428.
- Nankar, R., Prabhakar, P. & Doble, M. (2017). Hybrid drug combination: Combination of ferulic acid and metformin as anti-diabetic therapy. *Phytomedicine*, 37, 10-13.
- Nishikawa, T., Edelstein, D., Du, X. L., Yamagishi, S.-i., Matsumura, T., Kaneda, Y., Yorek, M. A., Beebe, D., Oates, P. J. & Hammes, H.-P. (2000). Normalizing mitochondrial superoxide production blocks three pathways of hyperglycaemic damage. *Nature*, 404, 787-790.
- Nyane, N. A., Tlaila, T. B., Malefane, T. G., Ndwandwe, D. E. & Owira, P. M. O. (2017). Metformin-like antidiabetic, cardio-protective and non-glycemic effects of naringenin: Molecular and pharmacological insights. *European Journal of Pharmacology*, 803, 103-111.
- Ojo, O. A., Ajiboye, B. O., Ojo, A. B., Oyinloye, B. E., Imiere, O. D. & Adeyonu, O. (2017). Ameliorative potential of *blighia sapida* kd



- koenig bark against pancreatic  $\beta$ -cell dysfunction in alloxan-induced diabetic rats. *Journal of complementary and Integrative medicine*, 14, 20160145.
- Pernicova, I. & Korbonits, M. (2014). Metformin—mode of action and clinical implications for diabetes and cancer. *Nature Reviews Endocrinology*, 10, 143-156.
- Ramírez-Mejía, M. M., Castillo-Castañeda, S. M., Pal, S. C., Qi, X. & Méndez-Sánchez, N. (2024). The multifaceted role of bilirubin in liver disease: A literature review. *Journal of Clinical and Translational Hepatology*, 12, 939.
- Reed, J., Bain, S. & Kanamarlapudi, V. (2021). A review of current trends with type 2 diabetes epidemiology, aetiology, pathogenesis, treatments and future perspectives. *Diabetes, Metabolic Syndrome and Obesity*, 3567-3602.
- Rehman, H. u., Ullah, K., Rasool, A., Manzoor, R., Yuan, Y., Tareen, A. M., Kaleem, I., Riaz, N., Hameed, S. & Bashir, S. (2023). Comparative impact of streptozotocin on altering normal glucose homeostasis in diabetic rats compared to normoglycemic rats. *Scientific reports*, 13, 7921.
- Reitman, S. & Frankel, S. (1957). A colorimetric method for the determination of serum glutamic oxalacetic and glutamic pyruvic transaminases. *American journal of clinical pathology*, 28, 56-63.
- Rena, G., Hardie, D. G. & Pearson, E. R. (2017). The mechanisms of action of metformin. *Diabetologia*, 60, 1577-1585.
- Rob, A., Hoque, A., Asaduzzaman, M. M., Khatoon, M. A. A., Khalil, R., Thomas, D., Ilyas, M., Mahmood, H. & Chowdhury, T. A. (2025). The global challenges of type 2 diabetes. *Bangladesh Journal of Medicine*, 36, 92-98.
- Saeedi, P., Petersohn, I., Salpea, P., Malanda, B., Karuranga, S., Unwin, N., Colagiuri, S., Guariguata, L., Motala, A. A. & Ogurtsova, K. (2019). Global and regional diabetes prevalence estimates for 2019 and projections for 2030 and 2045: Results from the international diabetes federation diabetes atlas. *Diabetes research and clinical practice*, 157, 107843.
- Szkudelski, T. (2012). Streptozotocin–nicotinamide-induced diabetes in the rat. Characteristics of the experimental model. *Experimental biology and medicine*, 237, 481-490.
- Targher, G. (2010). Elevated serum  $\gamma$ -glutamyltransferase activity is associated with increased risk of mortality, incident type 2 diabetes, cardiovascular events, chronic kidney disease and cancer—a narrative review. *Clinical Chemistry and Laboratory Medicine*, 48, 147-157.
- Togashi, Y., Shirakawa, J., Okuyama, T., Yamazaki, S., Kyohara, M., Miyazawa, A., Suzuki, T., Hamada, M. & Terauchi, Y. (2016). Evaluation of the appropriateness of using glucometers for measuring the blood glucose levels in mice. *Scientific reports*, 6, 25465.
- Walter, M. & Gerade, R. (1970). Bilirubin direct/total. *Microchem J*, 15, 231-233.
- Wilson, R. D. & Islam, M. S. (2012). Fructose-fed streptozotocin-injected rat: An alternative model for type 2 diabetes. *Pharmacological reports*, 64, 129-139.
- Xu, J., Chen, J., Deng, J., Chen, X., Du, R., Yu, Z., Gao, S., Chen, B., Wang, Y. & Cai, X. (2024). Naringenin inhibits apap-induced acute liver injury through activating ppara-dependent signaling pathway. *Experimental Cell Research*, 437, 114028.
- Yan, L.-J. (2022). The nicotinamide/streptozotocin rodent model of type 2 diabetes: Renal pathophysiology and redox imbalance features. *Biomolecules*, 12, 1225.
- Zahran, R. F., Rady, G. M. & El-Sonbati, A. Z. (2024). Evaluation of antioxidant and anti-inflammatory activities of 4-((quinolin-2-yl)methyleneamino)-1, 2-dihydro-2, 3-dimethyl-1-phenylpyrazol-5-one on ehrlich ascites carcinoma bearing mice. *Scientific Journal for Damietta Faculty of Science*, 14, 1-12.
- Zhou, G., Myers, R., Li, Y., Chen, Y., Shen, X., Fenyk-Melody, J., Wu, M., Ventre, J., Doeber, T. & Fujii, N. (2001). Role of amp-activated protein kinase in mechanism of metformin action. *The Journal of clinical investigation*, 108, 1167-1174.
- Zulkifle, N., Shaari, M., Omar, N. & Tajuddin, S. (2024). The effects of aquilaria malaccensis leaf extracts on blood glucose level, kidney profile and liver function in streptozotocin induced diabetic rats. *J. Trop. Agric. and Fd. Sc*, 52, 105-111.

## الملخص العربي

**عنوان البحث:** دور النارينجين في تعزيز فعالية الميتفورمين لدى الفئران المصابة بداء السكري.

ميّار أكرم شامخ<sup>١</sup>، عبد العزيز فتوح عبد العزيز<sup>٢</sup>، رشا فكري زهران<sup>١\*</sup>

<sup>١</sup>قسم الكيمياء، كلية العلوم، جامعة دمياط، دمياط، مصر  
<sup>٢</sup>قسم الكيمياء، كلية العلوم، جامعة المنصورة، المنصورة، مصر

يرتبط داء السكري بحدوث خلل في وظائف الكبد وزيادة الإجهاد التأكسدي، مما يستدعي البحث عن استراتيجيات علاجية فعالة للحد من هذه التأثيرات. تهدف هذه الدراسة إلى تقييم التأثير المشترك لكل من الميتفورمين (دواء خافض لسكر الدم من الخط الأول) والنارينجين (مركب فلافونويدي موجود في الحمضيات) على مؤشرات وظائف الكبد والحالة المضادة للأكسدة وذلك من خلال آلية تنشيط إنزيم AMPK. تم إجراء التجربة على ٦٠ جرذا من نوع ويستستر، قُسموا عشوائياً إلى ست مجموعات تشمل مجموعة تحكم سلبية، وتحكم مركبة، ومجموعة سكري غير معالجة، وثلاث مجموعات سكري عولجت بالميتفورمين (٥٠ ملغم/كغ) مدموجاً بجرعات مختلفة من النارينجين (٢٥، ٥٠، ١٠٠ ملغم/كغ) على التوالي. تم تخفيف السكري باستخدام مادة النيكوتيناميد و الستربتوزوتوسين، وأعطى العلاج يومياً عبر التناول الفموي لمدة خمسة أسابيع. شملت التقييمات قياس مستوى الجلوكوز الصائم والوزن أسبوعياً، بالإضافة إلى تحاليل كيميائية لوظائف الكبد وقياس السعة الكلية المضادة للأكسدة. أظهرت النتائج أن الجرذان المصابة بالسكري عانت من انخفاض في الوزن وارتفاع في الجلوكوز الصائم، وإنزيمات الكبد (ALT، AST)، والبيليروبين، مع انخفاض في البروتين الكلي والسعة الكلية المضادة للأكسدة. بينما أدى العلاج المشترك بالميتفورمين والنارينجين إلى تحسّن واضح في هذه المؤشرات، حيث سُجّل تحسّن في الوزن، وانخفاض في الجلوكوز، واستعادة وظائف الكبد والسعة الكلية المضادة للأكسدة. تشير هذه النتائج إلى أن الدمج بين الميتفورمين والنارينجين يُحدث تأثيراً تآزرياً مضاداً للسكري ومحسناً لوظائف الكبد، والسعة الكلية المضادة للأكسدة مما يساهم في تحسين التحكم في سكر الدم والحد من الضرر التأكسدي ويدعم دور النارينجين في تعزيز فعالية الميتفورمين من خلال تعديل تعبير ناقلات الكبد.

## Chinese Cinnamon Essential Oil as a Potential Dental Additive: Antimicrobial Efficacy and Biocompatibility Assessment

Rana R. El Sadda<sup>1</sup>, Rahma A.M. Abobakr<sup>1</sup>, Reham M. Abdallah<sup>1</sup>, Elhossein A. Moawed<sup>1</sup> and Mohamed M. El-Zahed<sup>\*2</sup>

<sup>1</sup>Chemistry Department, Faculty of Science, Damietta University, Egypt.

<sup>2</sup>Botany and Microbiology Department, Faculty of Science, Damietta University, Egypt.

Received: 10 April 2025 /Accepted: 25 May 2025

\*Corresponding author's E-mail: Mohamed.marzouq91@du.edu.eg

### Abstract

The objective of this study was to assess the antimicrobial potential and biosafe dose of Chinese cassia essential oil (CCEO) to be biocompatible for dental applications. CCEO extract was obtained by soaking Chinese cassia sticks in 3 solvents: petroleum ether, chloroform, and methyl alcohol. FTIR and GC-MS spectrometry investigations were used to study the chemical composition of CCEO extract. FTIR showed the presence of O-H functional group that is related to phenols and alcohols, C-H stretching for alkane, C=O bond for aldehyde of saturated fatty acids, C=C bond for alkenes, C-OH bending vibration of alcohols, and C-O-C for aromatic acid esters. The GC-MS results indicated the presence of 36 diverse compounds. Amongst these, E-cinnamaldehyde (38.08%), (7.99%) of carbohydrates (D-Talofuranose, D-Talopyranose, D-Mannopyranose and D-Glucopyranose), p-Coumaric alcohol (7.44%), Cinnamyl alcohol (6.15%) and Cinnamic acid (6.11%) were the most plentiful compounds. The antimicrobial action of the CCEO was tested against *Candida albicans*, methicillin-resistant *S. aureus* (MRSA), and *Enterobacter aerogenes* which displayed memorable antimicrobial activity against all tested microorganisms. CCEO revealed minimum inhibition concentration values of 15 µl/ml, 5 µl/ml, and 25 µl/ml against *C. albicans*, MRSA, and *E. aerogenes*, respectively. In addition, the biocompatibility of CCEO was evaluated on the oral cells. Biosafe dose analysis highlighted the necessity of carefully evaluating oil biocompatibility for dental applications, as excessive concentrations may compromise cell membrane integrity, induce oxidative stress, and trigger inflammatory responses. CCEO displayed to be a highly promising supplementary additive to improving antimicrobial and biosafe properties.

**Keywords:** Chinese cassia, antimicrobial, biocompatibility, dental, inflammatory, oral

### Introduction

Antimicrobial resistance (AMR) refers to the defense mechanisms that microorganisms have developed to fend against the effects of antibiotics or medications (Amaratunga *et al.*,



2016). Numerous microorganisms, including bacteria and yeasts, are capable of becoming so resistant to antimicrobial treatments that they lose their effectiveness. The various strategies by which microbes resist the available antibiotics include ribosome recycling and splitting, inactivating a drug, altering a drug target type, restricting drug uptake, and active drug efflux (Seely *et al.*, 2024). AMR was responsible for about 3.57 million of the 4.95 million deaths that took place worldwide (Michael *et al.*, 2014). AMR is estimated by the UN and WHO to have a far greater global impact than the 700,000 deaths per year that would lead to 10 million deaths per year by 2050 (WHO, 2023).

One of the most frequent infectious agent-related causes of morbidity and mortality in the globe is *Staphylococcus aureus*. These sphere-shaped, Gram-positive bacteria are the most dangerous of the many common staphylococcal bacteria. They can cause nosocomial bacteremia, cardiovascular infections, prosthetic joints, surgical sites, and acute skin infections that are the main cause of pneumonia and other respiratory tract infections (Gordon *et al.*, 2021). It was estimated that 20,000 people died from *S. aureus* bacteremia each year in the United States. Because methicillin-resistant *S. aureus* (MRSA) is the most significant clinically, *S. aureus* infections are particularly worrisome because *S. aureus* isolates frequently exhibit drug resistance. (Fayed *et al.*, 2024; Nicholas *et al.*, 2019). *S. aureus* has acquired determinants by horizontal gene transfer of mobile genetic elements, which has led to the evolution of resistance to many drugs. Antibiotic manufacturers may have developed these determinants to protect themselves against potentially inhibiting compounds or their competitors. Mutations that alter the locations of drug binding on molecular targets and an increase in the production of endogenous efflux pumps can also result in resistance. In principle, a set of inhibitors that target different locations can reduce the development of resistance by mutation, or two or more mutations can be wanted for resistance to pass the MIC breakpoint (Timothy, 2017).

*Enterobacter aerogenes* belongs to the Enterobacteriaceae family which were originally divided into three genera: *Escherichia*, *Enterobacter*, and *Klebsiella*, where the *Enterobacter* genus included *E. aerogenes* and *E. cloacae* (Wesevich *et al.*,

2020). *E. aerogenes* is a Gram-negative, electively anaerobic, rod-shaped bacillus, and it is motile by peritrichous flagella (Anne *et al.*, 2019). It is found in the human gastrointestinal tract and does not cause disease in healthy people, but it hits neonates, immunocompromised patients, individuals that received antibiotic therapy, and old people (Abou-Dobara *et al.*, 2024).

Another serious infection known as invasive candidiasis affects the eyes, heart, blood, bones, brain, and/or other bodily components and is brought on by the yeast, a type of fungus, *Candida* (El-Zahed *et al.*, 2023). *Candida albicans* is a commensal fungus that colonizes the surface of the oral mucosa and that is normally harmless in healthy persons. Under particular conditions, this opportunistic microorganism can cause a superficial infection called candidiasis (Mohamed & El-Zahed, 2024). *C. albicans* have well-documented pathogenic features, involving its ability to adhere to epithelial cells, and the hyphae formation that infiltrates epithelial cells (O'Donnell *et al.*, 2015). The most popular oral infection is denture candidiasis, which mainly derived from *C. albicans* in patients that wear polymethylmethacrylate (PMMA) dentures (Yeon *et al.*, 2020). Oral candidiasis is characterized by pain when eating or swallowing and by the emergence of white plaques on red, inflamed mucosa (throat, inner cheeks, and tongue) (O'Donnell *et al.*, 2015).

Recently, researchers have focused their research on discovering and developing alternative medicines from medicinal plants in order to prevent the serious side effects that are frequently connected to traditional pharmaceuticals (El Sadda *et al.*, 2025; Fayed *et al.*, 2025). One of these alternative medicines that has an important consideration is cinnamon, a frequently used cooking spice with a safety profile and remarkable features related to the regulations of blood sugar and its antimicrobial potential (El-Gohary *et al.*, 2024; El Sadda *et al.* 2024). The dried bark of several species of the *Cinnamomum* genus, such as *C. zeylanicum*, *C. verum*, and *C. cassia*, is used to make cinnamon. Because different species of cinnamon in the genus *Cinnamomum* are produced under varied geographical and environmental conditions, there are notable differences in their chemical composition. These differences are mostly represented in the composition of the primary bioactive

components. The plant's branches, bark, and leaves are among the parts from which cinnamon oil can be produced; each part contributes a somewhat distinct chemical composition (Jiageng *et al.*, 2024).

Mojtaba *et al.*, (2022) documented that CCEO have powerful antibacterial and antifungal activity due to their major component cinnamaldehyde. The study documented their bactericidal action against *S. aureus* and *Escherichia coli*. Roberto *et al.* (2023) reported that *C. cassia*, called Chinese cassia or Chinese cinnamon, essential oil (CCEO) has displayed potent antimicrobial activity against *Candida* species. In addition, Chen *et al.*, (2019) explained that CCEO shows anti-inflammatory properties by preventing the formation of inflammatory mediators. It has been shown that CCEO can decrease pro-inflammatory cytokine expression and thereby relieve inflammatory responses, suggesting that CCEO holds promise as a natural anti-inflammatory agent. Hesham *et al.*, (2022) displayed the biocompatibility of, antibacterial formulations based on cinnamon oil that were efficient against *Culex pipiens* adults and pupae. Warunya *et al.* (2020) showed that cinnamon essential oil at each potent concentration did not display any toxicity when examined on normal human fibroblast cells. So, this essential oil could be a potential candidate for pharmaceutical and cosmetic and product. Thus, this study was aimed at extracting of CCEO, assessing its antimicrobial effect against three organisms (*C. albicans*, MRSA and *E. aerogenes*), and investigating its biocompatibility behavior on oral human cells.

## Materials and methods

### Sample collection

Chinese cassia sticks (*C. cassia*, 100% organic, origin: India, Organic Way LLC, USA) were purchased from the market that in Damietta city, Damietta, Egypt, and taken to the Analytical Laboratory at the Faculty of Science, Damietta University, for extraction. They were oblong, rolled shapes, rough and thick sticks, 8-15 cm long, and had a dark brown-red color (Figure 1). The sticks

were washed to eliminate any dirt, and any damaged sticks were discarded.



**Figure 1.** Chinese cassia sticks.

### Extraction of CCEO

200 grams of Chinese cassia sticks were soaked for 3 weeks in the dark bottles at room temperature (25°C) with 330 ml of solvents (petroleum ether, chloroform, or methyl alcohol). Then, the extracted oils were placed in a rotary evaporator for an hour at a temperature of 55°C until the solvents evaporated from the extracted essential oils (EOs) (Singh *et al.*, 2007).

### Chemical profile and constituents' identification of the extracted EOs

GC–MS spectrometry (TSQ 9000 triple quadrupole mass spectrometer, Thermo Scientific™ TRACE™ 1310 Gas Chromatograph, Center for Excellence in Research of Advanced Agricultural Sciences (CERAAS), Damietta University, Egypt, and FTIR (FT/IR-4100type A, Central Laboratory, Faculty of Science, Damietta University, Egypt) were used to identify the phytochemicals in the extracted EOs.

### Biosafety assessment of CCEO on oral epithelial cells

The oral epithelial cells (OECs, Nawah Scientific Inc., Mokattam, Egypt) and were used during the biosafety assessment of CCEO according to the method provided by Diao *et al.* (2025). DMEM, which was enhanced with 10% heat-inactivated fetal bovine serum, 100 mg/ml streptomycin, and 100 units/ml penicillin, was used, and the incubation occurred in an incubator with 5% (v/v) CO<sub>2</sub> at 37°C. The

sulforhodamine B (SRB) test was used to assess cell viability.

#### *Antimicrobial activity of CCEO using agar well diffusion method*

The CCEO's antimicrobial activity was investigated based on the Clinical and Laboratory Standards Institute (CLSI) protocol (CLSI, 2017). 0.5 MacFarland ( $1-2 \times 10^8$  CFU/ml) from *C. albicans* ATCC10231, MRSA ATCC 43300, and *E. aerogenes* ATCC13048 were kindly provided from the Microbiology Lab, Botany and Microbiology Department, Faculty of Science, Damietta University, prepared and added separately under aseptic conditions on the surface of Muller-Hinton agar (MHA) plates. CCEO and standard drugs (penicillin G and miconazole) were added into 5 mm wells. Plates were incubated at 37°C for 48 hours for bacterial strains or at 28°C for 48 hours for yeast. After the incubation, inhibition zone diameters (IZD) were recorded in millimeters.

#### *Minimum inhibitory concentration (MIC)*

The MICs of CCEO, penicillin, and miconazole were studied according to the broth microdilution method (CLSI, 2000; 2012). Serial dilutions (0–100  $\mu$ l/ml) of the antimicrobial agents were prepared and tested against 0.5 McFarland standard of each microbial strain that was sub-cultured in Mueller-Hinton broth medium (MHB). After the incubation at 37°C for 48 hours for bacterial strains or at 28°C for 48 hours for yeast, microbial growth was assessed spectrophotometrically at 600 nm.

#### *Statistical analysis*

Statistical analysis of the data was administered using SPSS version 18 software. Experimental values are demonstrated as the mean  $\pm$  standard deviation (SD) for each outcome were given (O'Connor, 2000). The ANOVA test was used for the analysis at a significance threshold of 0.05. Three iterations of the experiments were conducted.

## Results

FTIR spectra (Figure 2) were employed

to identify the obvious functional groups of the CCEO samples (crude and fractions A & B). Consecutive absorption bands at 3389.28  $\text{cm}^{-1}$ , 3406.64  $\text{cm}^{-1}$  and 3416.28  $\text{cm}^{-1}$  assigned to (O-H), H-bonded for phenol and alcohol. Peaks at 2941.88  $\text{cm}^{-1}$ , 2957.3  $\text{cm}^{-1}$ , 2835.81  $\text{cm}^{-1}$ , 2840.63  $\text{cm}^{-1}$  and 2841.6  $\text{cm}^{-1}$  assigned to (C-H) vibration for alkane. 1719.23  $\text{cm}^{-1}$  is due to (C=O) bond for aldehyde of saturated fatty acids. Absorption bands at 1670.05  $\text{cm}^{-1}$ , 1656.55  $\text{cm}^{-1}$  and 1630.52  $\text{cm}^{-1}$  are implies stretching of alkenes (C=C). Bands at 1455.99  $\text{cm}^{-1}$ –1400.7  $\text{cm}^{-1}$  are corresponds to bending vibration of alcohol (C-OH). 1302.68  $\text{cm}^{-1}$  is attributed to bending (=C-H) and (CH<sub>2</sub>) alkanes. Absorption bands at 1266.04  $\text{cm}^{-1}$ , 1259.29  $\text{cm}^{-1}$  and 1250.61  $\text{cm}^{-1}$  indicated to the stretching vibration of phenols (C-OH) and symmetric expansion of the aromatic acid ester (C-O-C). Other peaks at 975.804  $\text{cm}^{-1}$ –679.785  $\text{cm}^{-1}$  showed the existence of aromatic (C=C) (Lixourgioiti *et al.*, 2022).

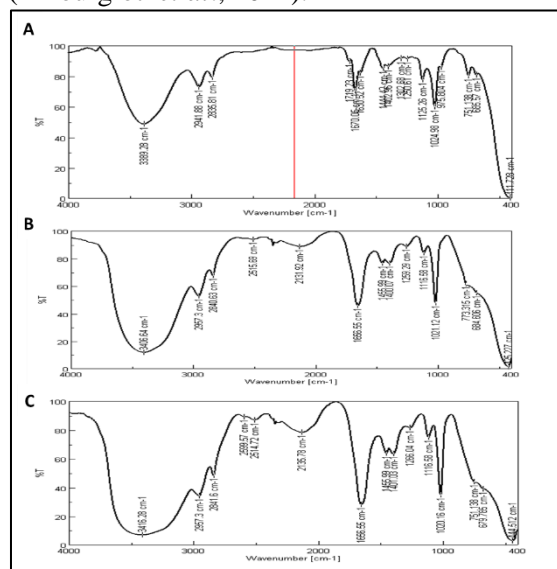


Figure 2. FTIR spectra of CCEO crude; (A), fraction A; (B), and fraction B; (C).

#### *Chemical composition of CCEO using GC-MS analysis*

Table 1 and Figure 3 show 36 different compounds, including E-cinnamaldehyde (38.08%), 7.99% of carbohydrates (D-talofuranose, D-talopyranose, D-mannopyranose, and D-glucopyranose), p-coumaric alcohol (7.44%), cinnamyl alcohol (6.15%) and cinnamic acid (6.11%)

were the main constituents of the cinnamon EOs.

#### *Biosafety dose of CCEO for oral cells*

Figure 4 illustrates the impact of CCEO on normal oral epithelial cells. In the control group (no oil), cells appear intact and densely packed, indicating healthy growth without any signs of cytotoxicity. At a low oil concentration (0.01  $\mu\text{l/ml}$ ), a slight reduction in cell density is

observed, though the cells remain largely intact, suggesting minimal effects on viability. However, at a higher concentration (100  $\mu\text{l/ml}$ ), clear changes happen, such as cells getting smaller, coming off their surfaces, and showing less color when stained, which means they are being harmed significantly. This suggests that higher oil concentrations may have a more detrimental effect compared to lower concentrations. Figure 5 presents the  $\text{IC}_{50}$  value of CCEO, which was determined to be 87.7  $\mu\text{l/ml}$ .

**Table 1.** Chemical composition of CCEO using GC-MS.

Peak	Retention time	Components	Contents (%)	Molecular formula	Molecular weight
1	8.773	Glycerol, 3TMS derivative	0.42	$\text{C}_{12}\text{H}_{32}\text{O}_3\text{Si}_3$	308.64
2	9.100	E-Cinnamaldehyde	34.53	$\text{C}_9\text{H}_8\text{O}$	132
3	9.557	Copaene	2.97	$\text{C}_{15}\text{H}_{24}$	204
4	9.649	E-Cinnamaldehyde	3.55	$\text{C}_9\text{H}_8\text{O}$	132
5	9.929	Cinnamyl alcohol, TMS derivative	6.15	$\text{C}_9\text{H}_{10}\text{O}$	134
6	10.399	$\alpha$ - Muurolene	5.21	$\text{C}_{15}\text{H}_{24}$	204
7	10.536	Naphthalene, 1,2,3,5,6,8a-hexahydro-4,7-dimethyl-1-(1-methylethyl)-, (1S-cis)-	4.01	$\text{C}_{15}\text{H}_{24}$	204
8	10.708	Cinnamic acid, (E)-, TMS derivative	6.11	$\text{C}_{12}\text{H}_{16}\text{O}_2\text{Si}$	220
9	11.085	p-Coumaric alcohol, 2TMS derivative	7.44	$\text{C}_{15}\text{H}_{24}\text{O}_3\text{Si}_2$	308.5
10	11.491	Coumarin	1.76	$\text{C}_9\text{H}_6\text{O}_2$	146
11	11.715	Coumarin	0.79	$\text{C}_9\text{H}_6\text{O}_2$	146
12	11.789	Epizonarene	1.27	$\text{C}_9\text{H}_{13}\text{NO}_3$	183
13	12.046	D-(-)-Tagatofuranose, pentakis(trimethylsilyl) ether (isomer 1)	2.08	$\text{C}_{21}\text{H}_{52}\text{O}_6\text{Si}_5$	541
14	12.241	D-(+)-Talofuranose, pentakis(trimethylsilyl) ether (isomer 2)	0.82	$\text{C}_{21}\text{H}_{52}\text{O}_6\text{Si}_5$	541
15	12.498	$\alpha$ -D-(+)-Talopyranose, 5TMS derivative	1.33	$\text{C}_{21}\text{H}_{52}\text{O}_6\text{Si}_5$	541
16	12.773	1H-Inden-1-one, 2,3-dihydro-3-methyl	0.60	$\text{C}_{10}\text{H}_{10}\text{O}$	146
17	12.928	$\alpha$ -D-Mannopyranose, 5TMS derivative	0.88	$\text{C}_{21}\text{H}_{52}\text{O}_6\text{Si}_5$	541
18	13.157	Palmitic Acid, TMS derivative	1.15	$\text{C}_{19}\text{H}_{40}\text{O}_2\text{Si}$	328.6
19	13.483	Ferulic acid, 2TMS derivative	0.28	$\text{C}_{16}\text{H}_{26}\text{O}_4\text{Si}_2$	338.5
20	13.923	9,12-Octadecadienoic acid (Z,Z)-, TMS derivative	1.74	$\text{C}_{21}\text{H}_{40}\text{O}_2\text{Si}$	352.6
21	14.232	1H-Inden-1-one, 2,3-dihydro-2-methyl	0.09	$\text{C}_{10}\text{H}_{12}\text{O}$	148
22	15.016	Silane, diethylnonyloxypentadecyloxy	2.96	$\text{H}_4\text{Si}$	32
23	15.285	Succinic acid, butyl 3,4-dimethylphenyl ester	1.70	$\text{C}_{17}\text{H}_{24}\text{O}_4$	292
24	15.640	1-Ethyl-4-phosphorinanone thiosemicarbazone	3.40	$\text{C}_8\text{H}_{16}\text{N}_3\text{PS}$	217.27
25	15.840	$\alpha$ -D-Glucopyranose, 5TMS derivative	1.14	$\text{C}_{21}\text{H}_{52}\text{O}_6\text{Si}_5$	541
26	15.995	1-Monooleoylglycerol, 2TMS derivative	1.40	$\text{C}_{27}\text{H}_{56}\text{O}_4\text{Si}_2$	500.9
27	16.349	3-Chloro-4-methylphenol	1.53	$\text{C}_7\text{H}_7\text{ClO}$	142.5
28	16.515	6-Hydroxynicotinic acid, 2TBDMS derivative	1.59	$\text{C}_{18}\text{H}_{33}\text{NO}_3\text{Si}_2$	367.6
29	17.007	Imidazole, 2-bromo-4-methyl-5-nitro-	0.28	$\text{C}_4\text{H}_4\text{BRN}_3\text{O}_2$	206
30	17.128	Fenoprop, TMS derivative	0.29	$\text{C}_{12}\text{H}_{15}\text{Cl}_3\text{O}_3\text{Si}$	154
31	17.585	Erythritol, 4TMS derivative	0.32	$\text{C}_{16}\text{H}_{42}\text{O}_4\text{Si}_4$	410.8
32	18.415	Cholesterol, TMS derivative	0.20	$\text{C}_{30}\text{H}_{54}\text{OSi}$	458.8
33	18.587	1-Monolinolein, 2TMS derivative	0.12	$\text{C}_{27}\text{H}_{54}\text{O}_4\text{Si}_2$	498.9
34	18.970	Stigmast-5-ene, 3.beta.-(trimethylsiloxy)-, (24S)-	1.35	$\text{C}_{32}\text{H}_{58}\text{OSi}$	486.8
35	21.104	1-Monooleoylglycerol, 2TMS derivative	0.38	$\text{C}_{27}\text{H}_{56}\text{O}_4\text{Si}_2$	500.9
36	21.482	Triethylenemelamine	0.15	$\text{C}_9\text{H}_{12}\text{N}_6$	204



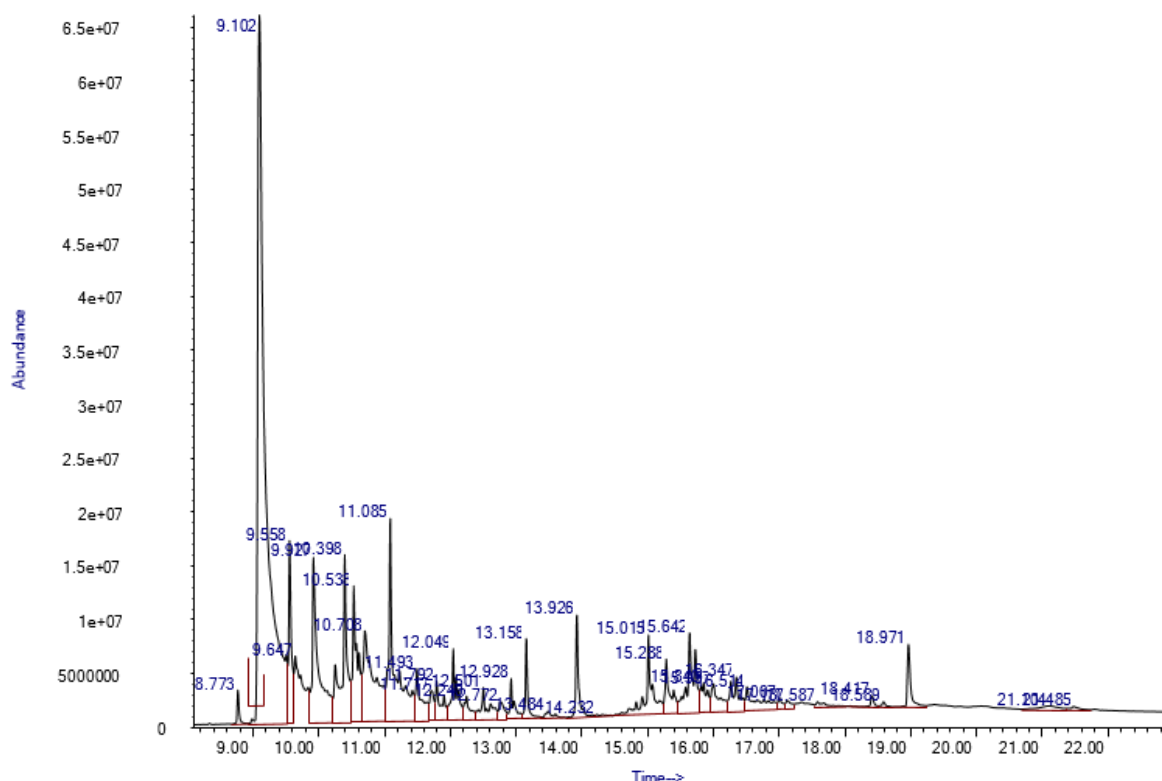


**Figure 3.** Compounds and their % ratios determined using GCMS analysis of the CCEO.

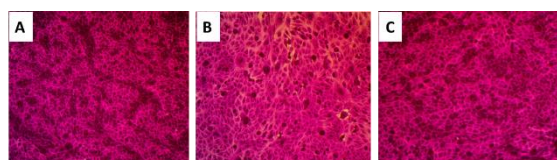


**Figure 4.** Effect of CCEO on normal dental oral cells. Morphological changes at different concentrations (low concentration (0.1 µl/ml); (A), and high concentration (100 µl/ml); (B)) using SRB stain compared to the oral epithelial cells control; (C).

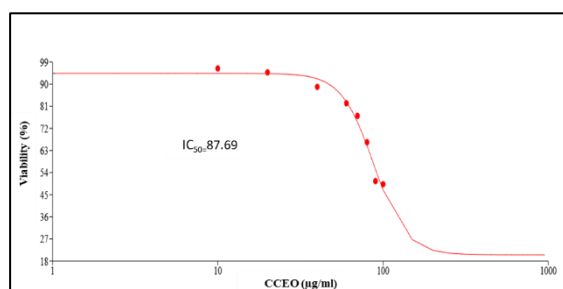


**Figure 5.** Dose response curve for CCEO on normal dental oral cells viability.

### Antimicrobial activity of CCEO

The antimicrobial activity of the CCEO

was evaluated against various organisms (*C. albicans*, MRSA, and *E. aerogenes*), as shown in Figure 6 and Table 2. CCEO demonstrated greater antifungal activity against *C. albicans*, exhibiting an IZD of 50 mm compared with miconazole with an IZD of 18 mm. Also, CCEO showed strong antibacterial action against MRSA and *E. aerogenes* with an IZD of 20 mm for both compared with penicillin G, which showed no inhibition against MRSA, and an IZD of 15 mm for *E. aerogenes*.

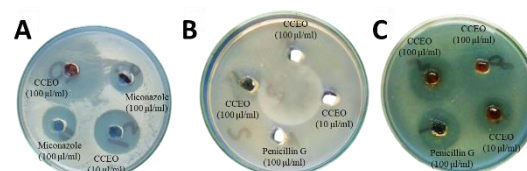


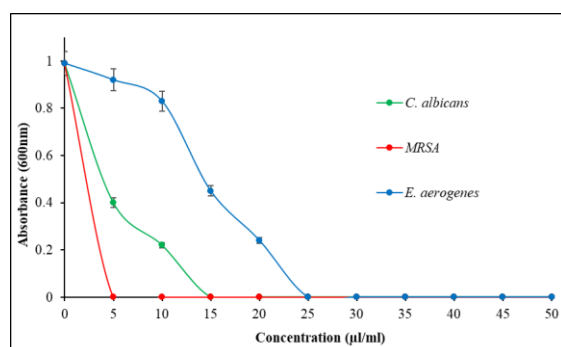
**Figure 6.** Agar well diffusion test of CCEO against *C. albicans*; (A), MRSA; (B), and *E. aerogenes*; (C).

The MIC of CCEO extract against *C. albicans*, MRSA, and *E. aerogenes* was determined (Figure 7). CCEO completely inhibited *C. albicans* at 15 µl/ml, MRSA at 5 µl/ml, and *E. aerogenes* at 25 µl/ml.

**Table 2.** Inhibition zone in mm of CCEO against the tested microorganisms.

Antimicrobial agent (100 $\mu$ l/ml)	Inhibition zones (mm $\pm$ SD)		
	<i>C. albicans</i>	MRSA	<i>E. aerogenes</i>
CCEO	50 $\pm$ 0 <sup>c*</sup>	20 $\pm$ 0 <sup>b</sup>	20 $\pm$ 0 <sup>b</sup>
Penicillin G	-	-ve	16 $\pm$ 0.14 <sup>a</sup>
Miconazole	18 $\pm$ 0.03 <sup>a</sup>	-	-

\*Means with common letters are not significantly different according to Duncan's multiple range test ( $P < 0.05$ ,  $n = 3$ ).

Figure 7. The MIC of CCEO against *C. albicans*, MRSA and *E. aerogenes*.

## Discussion

Cinnamon oil is an aromatic liquid acquired from the bark, leaves, and twigs of *C. zeylanicum* (Melyssa *et al.*, 2014). The obtained results showed that CCEO contains various bioactive compounds that share in antimicrobial activity. Similarly, several bioactive compounds such as cinnamaldehyde, coumarin and coumaric alcohol, cinnamyl alcohol, and cinnamic acid were previously documented (Raluca *et al.*, 2024). The main identified components in GC-MS analysis are E-cinnamaldehyde (CA) (38.08%), which is in agreement with (Katarzyna *et al.*, 2016). The chemical formula for CA, an aromatic aldehyde, is  $C_9H_8O$ . A benzene ring ( $C_6H_5$ ) connected to a propenyl group ( $-CH=CH_2$ ) and an aldehyde functional group ( $-CHO$ ) at the alpha position make up this compound. CA has powerful antioxidant action, making it helpful for medicinal objectives, and is also known for its capability to inhibit bacteria and fungi growth (Jiageng *et al.*, 2024).

Numerous pharmacological studies have also documented the anti-inflammatory, hypoglycemic, antitumor, antibacterial, and other pharmacological properties of CA (Saifudin *et al.*, 2013). Since cinnamon oil contains cinnamaldehyde, coumaric alcohol,

cinnamyl alcohol, and cinnamic acid, numerous studies have documented its anti-inflammatory and antibacterial qualities. These attributes demonstrate that cinnamon oil exerts immunomodulatory activity by inhibiting the generation of important inflammatory mediators (Aftab *et al.* 2023; Yi *et al.* 2024). Low concentrations of CCEO have little effect on normal oral cells; higher concentrations may cause irritation and inflammation. This is consistent with prior research on the biocompatibility and cytotoxic effects of various oils on oral cells. Numerous studies have investigated the role of oils in dental applications, such as medicated mouth rinses and essential oil-based formulations. Some plant-derived oils, including coconut oil and tea tree oil, have shown antimicrobial activity while remaining biocompatible at lower concentrations (Shekar *et al.*, 2015). However, at elevated concentrations, certain oils may compromise cell membrane stability, trigger oxidative stress, and interfere with metabolic functions, ultimately reducing cell viability (Ali *et al.*, 2023). The cytotoxic effects seen at higher oil concentrations may be linked to disturbances in cell membrane integrity and mitochondrial activity. Lipid-based compounds present in oils can interact with cellular lipids, altering membrane permeability, increasing the production of reactive oxygen species (ROS), and eventually leading to apoptosis or necrosis. Additionally, cytotoxicity may arise from bioactive components within the oil that provoke inflammatory responses or inhibit critical cellular enzymes (Ali *et al.*, 2023).

Under ordinary immune function, *C. albicans* exists safely with the host, but with weakness in the immune system, it can become pathogenic, causing grave systemic infections when it enters the bloodstream (Baka *et al.*, 2024a; Clarissa & Alexander, 2015). The anti-candidal activity of CCEO oil against planktonic and biofilm cultures of *C. albicans* has been documented by Yaru *et al.* (2014). The current study displayed a good antifungal action of the CCEO against *C. albicans*, achieving a 50 mm inhibition zone with MIC at 15  $\mu$ l/ml. The result of the present study agrees with Tran *et al.* (2020) who showed that IZD of bark CCEO against two strains of *C. albicans* were 53 mm and 56.68 mm, and MICs for both strains were below 0.03% (v/v). In addition, the current result is in agreement with Rym *et al.* (2017), who reported that CCEO inhibits

ergosterol biosynthesis in *Candida* species and influence fungal membrane integrity by permeabilizing the cell. According to Wijesinghe *et al.* (2021), CCEO inhibits fungal growth by disrupting the cell wall, which results in intracellular leakage. The MIC of CCEO was determined to be 1.0 mg/ml. According to a different study, CCEO may cause *C. albicans* to accumulate reactive oxygen species (ROS), which would ultimately lead to cell death. Chen and associates (2019). Additionally, the antifungal properties of cinnamon bark essential oil were described by Marie & Daniel (2019), who also found that the oil's MIC values ranged from 0.039% to 0.078% (v/v). It was also shown that CCEO permeabilized the cell membrane of *C. albicans*, which resulted in increased uptake of SYTOX Green dye and ultimately cell death. Additionally, CCEO demonstrated anti-inflammatory qualities by lowering the release of pro-inflammatory cytokines IL-6 and IL-8 from human oral epithelial cells stimulated with TNF- $\alpha$ . The secretion of IL-6 and IL-8 was reduced by 29% and 57%, respectively, by CCEO at a concentration of 62.5  $\mu$ l/ml.

The current findings are explained by the high concentration of CA, which has inherent antimicrobial qualities and a special antifungal effect. It might inhibit microbial growth through the cell wall that can harm the fungal cell walls' structural and functional integrity. The hydrophilic aldehyde group in CA's structure makes it easy for hydrophilic radicals on the fungal surface to absorb it, which breaks down the polysaccharide structure of the wall to enter the cell wall, affecting cell biosynthesis and preventing growth and reproduction (Fugo *et al.*, 2014). Furthermore, Jie *et al.* (2022) noted that by CA, the cell wall's surface was minus, the hyphae and external layer of the cell wall of *C. albicans* disintegrated and dropped off, and the cell wall barely deteriorated. The CA caused necrosis, disintegration, denaturation, and cell edema by directly penetrating the cell membrane and harming the nucleus and organelles, ultimately resulting in cell death. With its potent fungicidal action, CA can eradicate harmful fungi, improve the recovery rate from invasive *Candida* infections, and lower mortality rates. In another work, Mohd *et al.* (2013) found that CA decreased  $\beta$ -1-glucan synthase, which in turn caused *C. albicans* cell walls to thicken. CA has been shown to have antibacterial

efficacy against a range of fungi in another study (Hongbo *et al.*, 2015).

The current study showed good antibacterial action of the CCEO against *E. aerogenes*, achieving a 20 mm with MIC at 25  $\mu$ l/ml, and displayed good antibacterial activity of the CCEO against MRSA, achieving 20 mm with MIC at 5  $\mu$ l/ml. Current results are in agreement with Rana & Jayashankar (2022), as they concluded that the inhibition zone of the cinnamon oil was 23 mm for *E. aerogenes* and 27 mm for MRSA. According to Chengjie *et al.* (2024), cinnamon oil and its constituents have varying degrees of antibacterial activity against both Gram-negative bacteria, including *Salmonella* sp., *E. coli*, and *Pseudomonas aeruginosa*, and Gram-positive bacteria like *S. aureus*, as well as yeast such as *C. albicans*.

Positive findings have also been found in studies on the antifungal properties of plant extracts, particularly against *Candida* species and other harmful fungus, including *Aspergillus niger* and *A. fumigatus* (Baka *et al.*, 2024b; Elazab *et al.*, 2024). The major reason for inhibition attributed to the growth of bacteria is the active component in cinnamon oil, which contains CA as the main component responsible for its antibacterial, anti-inflammatory, and anti-cancer properties (Raluca *et al.* 2024). The MIC results in the current study demonstrated that MRSA (Gram-positive bacterium) 5  $\mu$ l/ml was more sensitive to CCEO than *E. aerogenes* (Gram-negative bacterium) 25  $\mu$ l/ml. This result agreed with Shareef (2001), who reported that CCEO gave MIC against some pathogenic bacteria such as (*S. aureus*, *K. pneumonia*, *E. coli*, *P. aeruginosa*, *Proteus* spp., and *Brucella* spp.), and showed that Gram-positive bacteria were more sensitive than Gram-negative to CCEO. The obtained study that evaluated the antibacterial properties of cinnamon oil, particularly from Chinese cassia, against *S. aureus* was also supported by Yunbin *et al.* (2016). They specified a MIC of 1.0 mg/ml and an inhibition zone of 28.7 mm. The bacteria were immediately cultured in a culture medium that was identical to a progression concentration of cinnamon oil. In addition, the current study agreed with Mahfuzul *et al.* (2008), who recorded that CCEO displayed high antibacterial activity against *S. aureus*. Furthermore, Lidaiane *et al.* (2022) examined the antibacterial action of cinnamon oil against *S. aureus*, which showed antibacterial potential with an MIC of 1.6 mg/ml. Also, Vinicius &

Edeltrudes (2009) evaluated the antimicrobial activity of 11 essential oils, including cinnamon, against 10 strains of Gram-positive and Gram-negative bacteria; the results concluded that CCEO showed a greater inhibitory effect. Antibacterial activity of CCEO occurred by cell membrane degeneration by damaging the force of protons, flowing of electrons, active transport, and cell component coagulation. The active components in the CCEO, such as cinnamaldehyde, are responsible for the bacterial cell wall destruction and have the ability to interfere with the bacterial enzymes' synthesis (Matan *et al.*, 2006). Using the disk diffusion method, Shinta *et al.* (2021) examined the antibacterial activity of cinnamon oil that was steam-distilled from *C. burmannii* against MRSA. Cinnamon oil was made in 1%, 2%, 4%, and 8% concentrations for the study, and its efficacy against five MRSA isolates that were obtained from cow's milk was evaluated. The results showed that 4% cinnamon oil effectively inhibited all tested MRSA strains, with inhibition zones exceeding 8 mm, while 8% cinnamon oil produced an average inhibition zone diameter of 20 mm. The potent antimicrobial action of CCEO might be due to the presence of E-cinnamaldehyde (38.08%) and cinnamic acid (6.11%), with a total existence ratio reaching to 44.19%, as recorded by the GC-MS results compared to previous studies (Katarzyna *et al.*, 2016; Raluca *et al.*, 2024). In an effort to clarify the mechanism of action, numerous studies and reviews have been conducted. The findings indicate that CCEO breaks down bacterial cell membranes, increasing membrane permeability and ultimately causing cell death because of the presence of the aforementioned bioactive compounds. Bacterial cell enlargement and laceration are two major morphological alterations that might result from high CCEO concentrations. Furthermore, intracellular potassium ion (K<sup>+</sup>) release signifies membrane damage, and CCEO's lipophilicity makes it easier for it to penetrate bacterial membranes, altering their characteristics and enhancing permeability (Vasconcelos *et al.*, 2018).

## Conclusions

CCEO displayed no harmful action on human cells, proposing its potential as a good alternative for treating microbial infections. A

thorough evaluation of oil biocompatibility is essential, especially for dental applications. The detected cytotoxic effects could stem from membrane damage, oxidative stress, or inflammatory reactions. Understanding the safety profile and mechanisms of oil-induced cytotoxicity is key to ensuring its effective and safe use in oral applications. CCEO showed anti-candidal properties due to the presence of CA that might help in the prevention of its biofilm formation and damage the structure of the cell wall of the fungal cell. Also, CCEO showed antibacterial action against MRSA and *E. aerogenes*. Future work is required to study the antimicrobial mechanisms of CCEO against different microbes.

## References

- Abou-Dobara MI, Kamel MA, El-Sayed AK, & El-Zahed MM. (2024). Antibacterial activity of extracellular biosynthesized iron oxide nanoparticles against locally isolated  $\beta$ -lactamase-producing *Escherichia coli* from Egypt. *Discover Appl. Sci.* 6(3), 113.
- Aftab A, Mohammad JA, Mohammed HA, Mohammad AS, & Mohammad R. (2023). Antioxidant, antibacterial, and anticancer activity of ultrasonic nanoemulsion of *Cinnamomum cassia* L. essential oil. *Plants*12(4): 834. doi: 10.3390/plants12040834.
- Ali M, Simran S, Hhuynh N, Dong HS, Michelle P, Hayuong P, Michael J, Antonio C, & Nicolas C. (2023). Assessment of oxidative stress-induced oral epithelial toxicity. *Biomolecules*, 13(8):1239.
- Amaratunga K, Tarasuk J, Tsegaye L, Archibald CP, & Group A. (2016). Antimicrobial Resistance (AMR): Advancing surveillance of antimicrobial resistance: Summary of the 2015 CIDSC Report. *Canada Communicable Disease Report*, 42(11), 232.
- Anne DRA, Lavigne JP, & Pagès JM. (2019). *Enterobacter* spp. "update on taxonomy, clinical aspects, and emerging antimicrobial resistance", *Clin. Microbiol. Rev.* 32:e00002-19.
- Baka ZA, Fayed RM, & El-Zahed MM. (2024a). A simple green synthesis and characterization of selenium nanoparticles and evaluation of their *in vitro* anticandidal activity. *JDFS*. 14(3), 102-111.
- Baka ZA, El-Sharkawy AM, & El-Zahed MM. (2024b). Anti-*Aspergillus niger* action of biosynthesized silicon dioxide nanoparticles alone or combined with *Matricaria chamomilla* L. extract. *J. microbiol. biotechnol. food sci.* 13(5), e10816-e10816.



- Chen L, Wang Z, Liu L, Qu S, Mao Y, Peng X, & Tian J. (2019). Cinnamaldehyde inhibits *Candida albicans* growth by causing apoptosis and its treatment on vulvovaginal candidiasis and oropharyngeal candidiasis. *Appl. Microbiol. Biotechnol.* 103, 9037-9055.
- Chengjie S, Ling G, Zhuohang L, Bin C, Shengliang L, Lu L, Qinlin W, Xinyi J, Yuhua A, Zongde W, & Man Q. (2014). Antibacterial activity of cinnamon essential oil and its main component of cinnamaldehyde and the underlying mechanism. *Front. Pharmacol.* 15, 1378434.
- Clarissa JN, & Alexander DJ. (2015). *Candida albicans* biofilms and human disease. *Annu. Rev. Microbiol.* 69: 71–92.
- CLSI (Clinical and Laboratory Standards Institute) (2000). Methods for dilution antimicrobial susceptibility test for bacteria that grow aerobically (document M45). Clinical and Laboratory Standards Institute, Wayne, Pennsylvania, USA.
- CLSI (2017). Performance standards for antimicrobial susceptibility testing. In: Performance standards for antimicrobial susceptibility testing: approved standard, 27<sup>th</sup> Edition. Clinical and Laboratory Standards Institute, Wayne, Pennsylvania, USA.
- Diaa TAY, Mohamed MA, Bushra MB, Lamiaa AS, & Torki AA. (2025). Latrunculin U: A potent actin-disrupter from the Red Sea marine sponge *Negombata magnifica*. *Nat. Prod. Res.* 1-9.
- El Sadda RR, El-Shobaky AR, El Sharawy HO, Moawed EA, Gohar OH, El-Zahed MM, & El-Tohamy WS. (2024). Evaluation of biological potential of red onion skin extract for anticancer and antimicrobial activities. *Process Biochem.* 147, 587-599.
- El Sadda, R. R., Abobakr, R. A. M., Abdallah, R. M., Moawed, E. A., & El-Zahed, M. M. (2025). *In vitro* study of polymethyl methacrylate combined with seed oil of *Nigella sativa* L. as an antimicrobial bio-based polymer for dental applications. *J. microbiol. biotechnol. food sci.* 14(5), *In press*.
- Elazab NT, Baka ZA, Saleh HH, & El-Zahed MM. (2024). Green synthesis of silver nanoparticles using *Cakile maritima* seed extract: Molecular, antifungal and physiological studies. *PMPP*, 129, 102183.
- El-Gohary, H., Azab, M., Abdelrahman, A., Fayyad, D., El-Kholy, M., Mohamed, D., & El-Zahed, M. M. (2024). *In vitro* antibacterial action of *Zingiber officinale* roscoe crude extract irrigation against *Staphylococcus aureus* isolated from infected human root canals. *J. microbiol. biotechnol. food sci.* 14(3), e11691-e11691.
- El-Zahed, M. M., Kiwaan, H. A., Farhat, A. A., Moawed, E. A., & El-Sonbati, M. A. (2023). Anticandidal action of polyurethane foam: A new modifier with functionalized isothiuronium group. *Iran. Polym. J.* 32(1), 71-79. doi: 10.1007/s13726-022-01112-1.
- Fayed RM, Baka ZA, & El-Zahed MM. (2024). Antibacterial activity of green synthesized zinc oxide nanoparticles using *Washingtonia robusta* H. Wendl fruit extract. *Scientific JDFS.* 14(3), 90-101.
- Fayed RM, Baka ZAM, Farouk BH, & El-Zahed MM. (2025). Antibacterial and cytotoxic activities of a newly green synthesized ZnO/Se nanocomposite combined with *Washingtonia robusta* H. Wendl fruit extract. *ISBAB.* 64, 103500.
- Fugo X, Huijuan H, Jonathan NS, & Yueju Z. (2014) Growth inhibition and morphological alterations of *Fusarium verticillioides* by cinnamon oil and CA. *Food Control.* 46:343–350.
- Gordon YCC, Justine SB, & Michael O. (2021). Pathogenicity and virulence of *Staphylococcus aureus*. *Virulence* 12(1): 547–569.
- Hesham AM, Shawky MA, Saad SA, & Mohamed ZSA. (2022). Cell cytotoxicity, antimicrobial, and mosquitocidal activity of prepared cinnamon oil formulations. *Adv. Anim. Vet.* 11(3): 355-516.
- Hongbo L, Qingshan S, Wei Z, Haizhen M, & Daodong P. (2015). Nanocapsular dispersion of CA for enhanced inhibitory activity against aflatoxin production by *Aspergillus flavus*. *Molecules.* 20(4):6022–32.
- Jiageng G, Xinya J, Yu T, Shidu Y, Jiaojiao L, Jinling X, Fan Z, Chun Y, & Erwei H. (2024). Therapeutic potential of cinnamon oil: Chemical composition, pharmacological actions, and applications. *Pharmaceuticals* 17, 1700.
- Jie HD, XiaoGZ, Gang SW, Jing NL, Jia W, Xiao MQ, & Yan LL. (2022). Effect of cinnamaldehyde on *C. albicans* cell wall and (1,3)-  $\beta$  - D-glucans *in vivo*. *BMC complement. med. ther.* 22:32.
- Katarzyna MB, Agnieszka JB, Krzysztof Ś, & Elżbieta Ł-C. (2016). Antioxidant profile of essential oils and extracts of cinnamon bark (*Cinnamomum cassia*). *Eur. J. Biol. Res.* 6(4): 310-316.
- Lidaiane MSSF, Karina HS, Otávio AS, Elina BC, CésarACL, Celso VN, Elisângela AA, & Cristiane MFM. (2022). Antimicrobial activity of cinnamon (*Cinnamomum verum*) essential oil and cinnamaldehyde against *Staphylococcus aureus*. *Res., Soc. Dev.* 11(13):e560111335844.
- Lixourgioti, P, Goggin KA., Koria ZX., Murphy DJ, van RS, & Koidis A. (2022). Authentication of cinnamon spice samples using FT-IR spectroscopy and chemometric classification. *JFST.* 154 (4):112760.

- Mahfuzul H, Vijay KJ, & Shinichi K. (2008). Antimicrobial activity of clove and cinnamon extract against food borne pathogens and spoilage bacteria, and inactivation of *Listeria monocytogenes* in ground chicken meat with their essential oils. Rep. Nat'l. Food Res. Inst. 72:9-21.
- Marie PV, & Daniel G. (2019). Determination of the effects of cinnamon bark fractions on *Candida albicans* and oral epithelial cells. BMC complement. med. ther. 19(1):303.
- Matan N, Rimkeeree H, Mawson AJ, Chompreeda P, Haruthaithanasan V, & Parker M. (2006). Antimicrobial activity of cinnamon and clove oils under modified atmosphere conditions. Int. J. Food Microbiol. 107(2):180-5.
- Melyssa N, Tânia PS, Cristiane SSM, Isis RGC, Terezinha IES, & Erika SK. (2014). Early state research on antifungal natural products. Molecules. 19(3):2925–56.
- Mohamed EA, & El-Zahed MM. (2024). Anticandidal applications of selenium nanoparticles biosynthesized with *Limosilactobacillus fermentum* (OR553490). Discover Nano. 19(1), 115.
- Mohd SAK, Iqbal A, & Swaranjit SC. (2013). Phenyl aldehyde and propanoids exert multiple sites of action towards cell membrane and cell wall targeting ergosterol in *Candida albicans*. AMB Express. 3(1):54.
- Mojtaba D, Zahra C, Siedamir PT, Shabnam R, Aref S. (2022). *Cinnamomum*: The new therapeutic agents for inhibition of bacterial and fungal biofilm-associated infection. Front. Cell Infect. Microbiol. 8:12:930624.
- Michael CA, Dominey-Howes D, & Labbate M. (2014). The antimicrobial resistance crisis: Causes, consequences, and management. Public Health Front., 2, 145.
- Nicholas AT, Batu KSK, Stacey AM, Emily ME, Patrik PS, Manuela C, Thomas LH, & Vance GFJR. (2019). Methicillin-resistant *Staphylococcus aureus*: An overview of basic and clinical research. Nat. Rev. Microbiol. 17(4):203-218.
- Raluca AGI, Dana T, Paul RT, Oana MG, Laurent,iu T, Manuella M. (2024). Spicing Up Meat Preservation: *Cinnamomum zeylanicum* essential oil in meat-based functional foods-A five-year review. Foods. 13(16):2479.
- Rana THA, & Jayashankar M. (2022). Antibacterial effect of cinnamon oil against uropathogenic multidrug resistant bacteria. J. Pharm. Res. Int. 34(33A): 6-15.
- Rym E, Majdi H, Dorra G, Ines K, Thouraya BH, Salem E, Ferid L, & Olfa T. (2017). Antifungal mechanism of the combination of *Cinnamomum verum* and *Pelargonium graveolens* essential oils with fluconazole against *Candida strains*. Appl. Microbiol. Biotechnol. 10(18):6993–7006.
- Saifudin A, Kadota S, & Tezuka Y. (2013). Protein tyrosine phosphatase 1B inhibitory activity of Indonesian herbal medicines and constituents of *Cinnamomum burmannii* and *Zingiber aromaticum*. J. Nat. Med., 67, 264-270.
- Seely SM, Basu RS, & Gagnon MG. (2024). Mechanistic insights into the alternative ribosome recycling by HflXr. Nucleic Acids Res., 52(7), 4053–4066.
- Shareef AA. (2001). Evaluation of antibacterial activity of essential oils of *Cinnamomum* sp. and *Boswellia* sp. JBRS. 37(5):60-71.
- Shekar BRC, Nagarajappa R, Suma S, & Thakur R. (2015). Herbal extracts in oral health care-A review of the current scenario and its future needs. Phcog. Rev., 9(18), 87.
- Shinta LNF, Mustofa HE, Wiwik T, & Lucia S. (2021). Antibacterial of cinnamon Bark (*Cinnamomum burmannii*) essential oil against methicillin-resistant *Staphylococcus aureus*. J. Med. Vet. 4(1): 56.
- Singh, G., Maurya, S., de Lampasona, M.P., & Catalan, C.A.N. (2007). A comparison of chemical, antioxidant and antimicrobial studies of cinnamon leaf and bark volatile oils, oleoresins and their constituents. Food and Chemical Toxicology, 45(9), 1650–1661.
- Timothy JF. (2017). Antibiotic resistance in *Staphylococcus aureus*. Current status and future prospects. FEMS Microbiol. Rev. 1;41(3):430-449.
- Tran HN, Graham L, & Adukwu EC. (2020). *In vitro* antifungal activity of *Cinnamomum zeylanicum* bark and leaf essential oils against *Candida albicans* and *Candida auris*. Appl. Microbiol. Biotechnol. 104, 8911-8924.
- Vasconcelos NG, Croda J, & Simionatto S. (2018). Antibacterial mechanisms of cinnamon and its constituents: A review. Microb. Pathog. 120:198-203.
- Vinicius NT, & Edeltrudes OL. (2009). Antibacterial property of spice essential oils on food contaminating bacteria. JFST. 29(3):542–545.
- Warunya B, Acharawan T, Patamaporn S, & Oraphan W. (2020). Determination of antioxidant, anti-aging and cytotoxicity activity of the essential oils from *Cinnamomum zeylanicum*. J. Microbiol. Biotech. Food Sciences 10(3):436-440.
- Wesevich A, Sutton G, Ruffin F, Park LP, Fouts DE, Fowler Jr VG, & Thaden JT. (2020). Newly named *Klebsiella aerogenes* (formerly *Enterobacter aerogenes*) is associated with poor clinical outcomes relative to other *Enterobacter*

- species in patients with bloodstream infection. J. Clin. Microbiol. 58(9), 10-1128.
- WHO (World Health Organization) (2023). Antimicrobial resistance. WHO (November 21). Available online at: <https://www.who.int/news-room/factsheets/detail/antimicrobial-resistance>.
- Yaru L, Ying N, Linyan Z, Shurong L, Xuanming T, Yang D, & Shuying L. (2014). The possible mechanism of antifungal activity of cinnamon oil against *Rhizopus nigricans*. J. Chem. Pharmaceut. Res. 6(5):12–20.
- Yeon-JY A, Reum K, Hiran P, Seung HH, & Kee-YK. (2020). *Candida albicans* virulence factors and pathogenicity for endodontic infections. Microorganisms. 26; 8(9): 1300.
- Yi TL, Wei CT, Hsueh YL, Shih YF, Hsiang WC, Chung HH. (2024). Enhancing therapeutic efficacy of cinnamon essential oil by nanoemulsification for intravaginal treatment of *Candida vaginitis*. Int. J. Nanomed.19, 4941–4956.
- Yunbin Z, Xiao YL, & Quek S. (2016). Antibacterial activity and mechanism of cinnamon essential oil against *Escherichia coli* and *Staphylococcus aureus*. Food Control. 59, 282-289.

## الملخص العربي

**عنوان البحث:** زيت القرفة الصينية العطري كمكون إضافي قوي لمواد الأسنان: دراسات التوافق الحيوي والتقييم الفعال له كمضاد للميكروبات

رنا الصدة<sup>١</sup>، رحمة أبو بكر<sup>١</sup>، ريهام عبدالله<sup>١</sup>، الحسيني معوض<sup>١</sup>، محمد مرزوق الزاهد<sup>٢</sup>

<sup>١</sup>قسم الكيمياء، كلية العلوم، جامعة دمياط، دمياط، مصر  
<sup>٢</sup>قسم النبات والميكروبيولوجي، كلية العلوم، جامعة دمياط، دمياط، مصر

هدفت هذه الدراسة إلى تقييم النشاط المضاد للميكروبات والجرعة الآمنة بيولوجيًا لزيت القرفة العطري لضمان توافقه الحيوي مع تطبيقات طب الأسنان. تم الحصول على مستخلص زيت القرفة العطري عن طريق نقع أعواد القرفة في ثلاث مذيبات: بتروليوم إيثر، والكلوروفورم، والكحول الميثانولي. استُخدمت دراسات طيف الأشعة تحت الحمراء، وكروماتوغرافيا الغاز المزود بمطياف الكتلة لدراسة التركيب الكيميائي لمستخلص زيت القرفة العطري. أظهر طيف الأشعة تحت الحمراء وجود المجموعة الوظيفية O-H المرتبطة بالفينولات والكحولات، وتمدد C-H للألكانات، ورابطة C=O للألدهيدات في الأحماض الدهنية المشبعة، ورابطة C=C للألكينات، وكذلك انحناء C-OH للكحولات، و C-O-C لإستر الأحماض العطرية. أشارت نتائج كروماتوغرافيا الغاز المزود بمطياف الكتلة إلى وجود ٣٦ مركبًا متنوعًا. من بين هذه المركبات، كانت E-cinnamaldehyde (٣٨,٠٨%)، و D- و D-Mannopyranose، و D-Talopyranose، و D-Talofuranose (٧,٩٩%) من الكربوهيدرات، والكحول p-Coumaric (٧,٤٤%)، وكحول Cinnamyl (٦,١٥%)، وحمض Cinnamic (٦,١١%) (Glucopyranose)، والكحول p-Coumaric (٧,٤٤%)، والكحول Cinnamyl (٦,١٥%)، وحمض Cinnamic (٦,١١%) هي المركبات الأكثر شيوعًا. تم اختبار التأثير المضاد للميكروبات لمستخلص زيت القرفة العطري ضد كانديدا أليكانس، وبكتيريا مارسا، والإنتروباكتري إيريوجينيس، والتي أظهرت نشاطًا مضادًا للميكروبات ملحوظًا ضد جميع الكائنات الدقيقة المختبرة. أظهر مستخلص زيت القرفة العطري قيم تركيز تثبيط أدنى تبلغ ١٥ ميكرو لتر/مل، و ٥ ميكرو لتر/مل، و ٢٥ ميكرو لتر/مل ضد كانديدا أليكانس، وبكتيريا مارسا، والإنتروباكتري إيريوجينيس، على التوالي. بالإضافة إلى ذلك، تم تقييم التوافق الحيوي لمستخلص زيت القرفة العطري على الخلايا الفموية. أبرز تحليل الجرعة الآمنة بيولوجيًا ضرورة التقييم الدقيق للتوافق الحيوي للزيوت في تطبيقات طب الأسنان، إذ قد تُضعف التركيزات الزائدة سلامة غشاء الخلية، وتُسبب الإجهاد التأكسدي، وتُحفز الاستجابات الالتهابية. وقد ثبت أن مستخلص زيت القرفة العطري مادة تكميلية واعدة للغاية لتحسين خصائصها المضادة للميكروبات والسلامة بيولوجيًا.

## Quantum Chemical Molecular Dynamics and Experimental Studies of Corrosion Inhibition Effect of Allyl Rhodanine Azodye Derivatives on C-Steel in 2 M HCl

A.A. El-Sonbaty<sup>\*1</sup>, M. Mossad<sup>2</sup> and M.H. Mahmoud<sup>1</sup>

<sup>1</sup>Mathematical and Physical Engineering Department, Faculty of Engineering, Mansoura University, El-Mansoura, Egypt.

<sup>2</sup>Public Works Engineering Department, Faculty of Engineering, Mansoura University, Mansoura 35516, Egypt.

Received: 12 April 2025 /Accepted: 25 May 2025

\*Corresponding author's E-mail: aaelsonbaty@hotmail.com

### Abstract

The inhibition impact of freshly created allyl rhodanine azodye derivatives inhibitors (**1-3**) on C-steel and their adsorption patterns in 2 M HCl were investigated using weight reduction strategy, potentiodynamic polarization, electrochemical impedance spectroscopy (EIS), electrochemical frequency modulation (EFM) techniques, and scanning electron microscopy (SEM). The total resistance of the carbon corrosion process and inhibition efficiency of compounds (**1-3**) was increased with the increase of the inhibitor concentration. The corrosion rate reduced as the percentage of the compounds in the HCl solution increased, according to Tafel polarisation curves..

**Keywords:** Corrosion prevention, Tafel polarization, Quantum chemical molecular dynamics parameters, C-steel

### Introduction

Owing to its superior mechanical attributes and affordable price, carbon steel (CS) is utilised in a large variety of usage in industry. It is typically utilized in construction and metal processing equipment, chemical processing, drums, heat exchangers, tanks, and maritime applications. In pickling, manufacturing scrubbing, and oil-well acidizing, rust is typically removed with acid solutions, which causes corrosion process on C-steel. Oxidation

inhibitors are thus used to reduce or avoid corrosion as well as to defend against sudden metal breakdown and acid consumption, mainly in acidic conditions (**Morgan et al., 2017**).

Chemical oxidation inhibitors with molecules of S, N<sub>2</sub> and O<sub>2</sub> and heterocyclic structures can significantly decrease the likelihood of corrosion when only extremely little amounts are added and consider more efficient inhibitors.<sup>1,2</sup> The mechanism of inhibition based on that the hetero atoms such as N, O or S atoms on the metal's surface reduced the flow of corrosion products to the



metal surface by limiting the active sites and creating a physical border (Abou-Dobara *et al.*, 2019a; Diab *et al.*, 2019a; Eldesoky *et al.*, 2015; El-Sonbati *et al.*, 2019a; El-Sonbati *et al.*, 2022a).

The research the prevention of corrosion and the weight reduction technique, tafel polarisation, electrochemical impedance spectroscopy and electrochemistry frequency modulation methods were used to investigate the electrochemical performance of allyl rhodanine azodye derivatives inhibitors for C-steel in 2 M HCl solvent. The test coupon upper layer was examined using scanning electronic microscopy, which reported that these compounds avoided oxidation of C-steel in 2 M HCl by forming a shielding layer on its surface. That serves as a defence against corrosive environments.

## Experimental

### Molecular structure

Software called (Material Studio Version 4.4) has been used to do quantum chemical computations (Abou-Dobara *et al.*, 2019b; Diab *et al.*, 2018; El-Sonbati *et al.*, 2018a; Mohamed *et al.*, 2016; Refaat *et al.*, 2016).

### Composition of metal coupons and medium

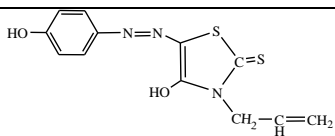
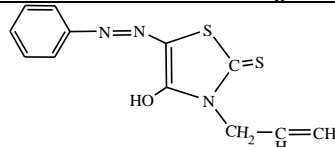
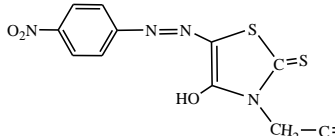
C-steel, was employed for the oxidation examinations. Its weight percentage is 0.20 C, 0.30 Si, 0.53 Mn, 0.055S, 0.045 P, Fe balance. In order to create the test sample, which contains 2 M of HCl, HCl (BDH grade, 37%) was diluted with dual bidistilled water.

### Inhibitor preparation and characterization

The inhibitors (Table 1) used for this study were derived from the reaction of N-allylrhodanine and p-aniline extracts bonding (Abou-Dobara *et al.*, 2019b; Diab *et al.*, 2018; El-Sonbati *et al.*, 2018a). The resulting s inhibitors were characterized and it was found that, compound (1): brown solid, m.p.  $185 \pm 1$  °C, IR (KBr,  $\nu$  cm<sup>-1</sup>): 3444 (O-H), 1415 (N=N), 1727 (C=O), compound (2): yellow solid, m.p.  $178 \pm 1$  °C, IR (KBr,  $\nu$  cm<sup>-1</sup>) 1490 (N=N), 1724 (C=O), and compound (3): greenish yellow solid, m.p.  $171 \pm 1$  °C, IR (KBr,  $\nu$  cm<sup>-1</sup>) 1334

(O-N=O)<sub>sy</sub>, 1496 (O-N=O)<sub>Asy</sub>, 1554 (N=N), 1700 (C=O).

**Table 1.** Investigated inhibitors (1-3).

Compound No.	
(1)	
(2)	
(3)	

### Measuring Methodologies

#### Weight reduction technique

Specimens of C-steel coupons as rectangular with dimensions 20.0 × 20.0 × 2 mm were rubbed with emery paper of varying grades; Triplicate Coupons were carried out for same behaviors with various temperatures. The corrosion proportion ( $\nu$ ) was estimated utilizing the formula (1):

$$\nu = W/St \quad (1)$$

where W represents the three adjacent carbon steel coupons' approximate amount reduction, S is the amount of carbon steel coupons' surface and t is the exposure period. The evaluated chemicals' IE<sub>w</sub>% protective effectiveness on the carbon steel oxidation was computed by equation (1):

$$IE_w \% = (\nu_o - \nu)/\nu_o \times 100 \quad (1)$$

where  $\nu_o$  and  $\nu$  are the corrosion percentage readings before and after adding the inhibitor.

#### Tafel polarization technique

The electrochemical procedure was carried out (Morgan *et al.*, 2017).

#### Frequency Modulation by Electrochemistry procedure

The use of electrochemical modulation technique can be a nondestructive experiment and fast technique for measure the rate of corrosion.

### Electrochemical impedance spectroscopy

The comparable electric connection modeling within the system uses  $R_{ct}$  to describe the charge transfer,  $R$  to indicate the resistor,  $R_s$  to reflect the solution resistance, and  $C_{dl}$  to represent the capacity of the dual layer.

### Surface morphology

With and without the recommended dose of the examined inhibitors, the steel's analysis was submerged in one molar hydrochloric acid for 12 hours.

## Results and discussion

### Mass diminution method

As illustrated in Figure 1, the degradation of C-steel masses in 2 M HCl decreases approximately linearly as time without and with varying doses of compound (1) at  $30 \pm 1$  °C. Comparing the rate of corrosion to that without inhibitors  $IE_w$  % is computed using equation (2) (Morgan *et al.*, 2017):

$$IE_w \% = 100 \times [1 - (C.R_{\text{Corr}}/C.R_{\text{Corr}}^{\circ})] \quad (2)$$

where  $C.R_{\text{Corr}}^{\circ}$  and  $C.R_{\text{Corr}}$  are the corrosion rates without and with inhibitor, respectively. The (%  $IE_w$ ) of the organic inhibitor derivatives listed in Table 1 obeyed the sequence: compound (1) > compound (2) > compound (3). Straight line was obtained by plotting % IE against Hammett's substituent coefficients ( $\sigma^R$ ) (Figure 2).

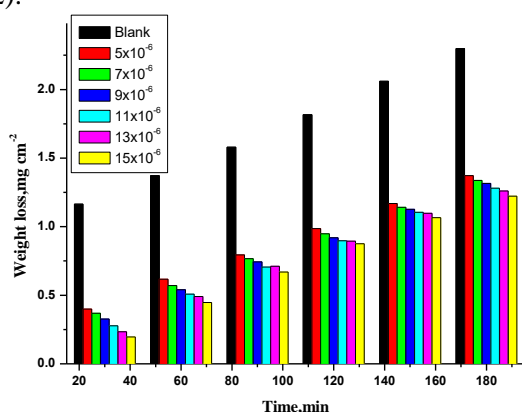


**Figure 1.** Charts demonstrating the mass-reduction of inhibitor (1).

**Table 2.** Variation of indicators of losing the weight at 60 minutes.

Conc. (M)	Inhibition efficiency (%IE)		
	(1)	(2)	(3)
$1 \times 10^{-6}$	55.0	49.0	37.7
$3 \times 10^{-6}$	58.4	51.2	42.2
$5 \times 10^{-6}$	60.7	54.3	45.0
$7 \times 10^{-6}$	62.9	57.9	47.9
$9 \times 10^{-6}$	64.2	59.8	51.7
$11 \times 10^{-6}$	67.43	62.47	54.52

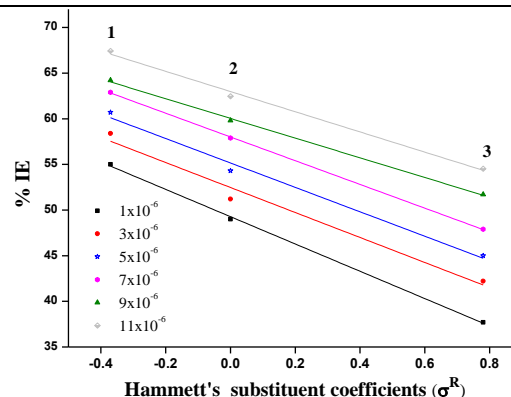


**Figure 2.** % IE against  $\sigma^R$  of the compounds.

### Kinetic results

Using the formula: one can determine the Arrhenius activation energy ( $E_a^*$ ) value (Figure 3).

$$C.R = A \exp(-E_a^*/RT) \quad (3)$$

where  $A$  is the Arrhenius constant,  $T$  is the absolute temperature,  $k$  is the corrosion rate and  $R$  is the universal gas constant. According to Figure 3, the activation energy for carbon steel corrosion in 2 M HCl was determined to be 32 kJ mol<sup>-1</sup>, which is consistent with the information obtained by other researchers (Eldesoky *et al.*, 2015; El-Sonbati *et al.*, 2019a; El-Sonbati *et al.*, 2022a). Applying the transition condition theory using equation (4):

$$C.R = RT/Nh e^{(\Delta S^*/R)} e^{(-\Delta H^*/RT)} \quad (4)$$

Straight lines result from the draw of  $1/T$  versus  $\log k/T$ ; since its interrupt and slope,  $\Delta S^*$  and  $\Delta H^*$  be able to be estimated, one-to-one (Figure 4 & Table 3). Equations were made to determine the activation enthalpy and entropy ( $\Delta H^*$  and  $\Delta S^*$ ) of the corrosion process. Given that there is less disordering occurring as reactants go from the reactants to the activated compound, the -ve  $\Delta S^*$  signals point to an attachment stage rather than a dissociate stage being represented by the active site in the rate-determining stage. The endothermic nature of the metal dissolving process is shown in the +ve

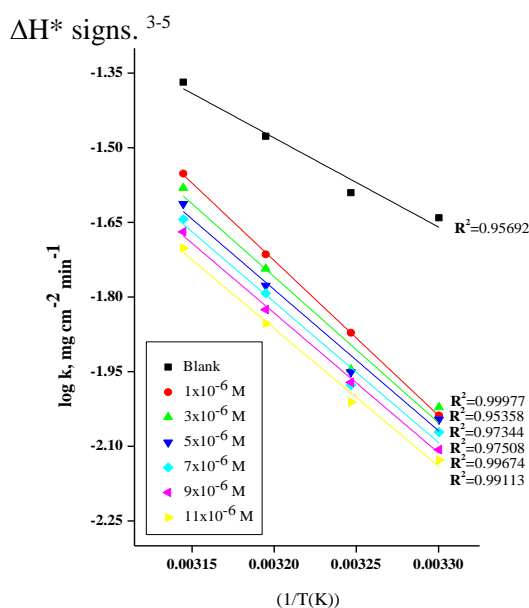


**Figure 3.** log k vs. 1/T curves for C-steel of inhibitor (1).

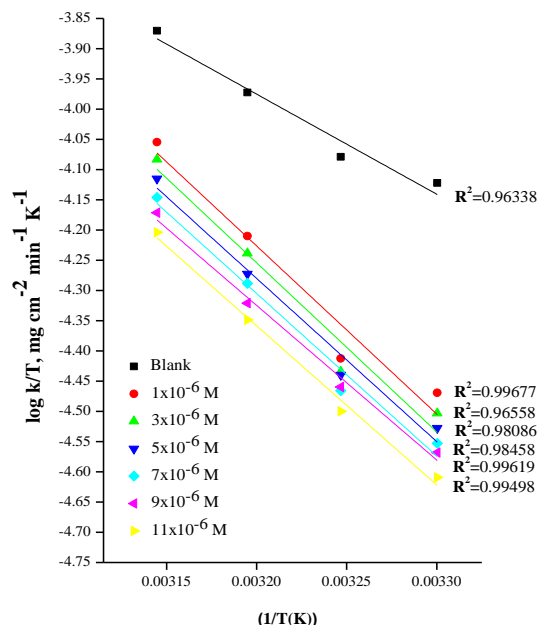


**Figure 4.** log (k / T) vs. 1/T curves for C-steel dissolution of inhibitor (1).

Obviously, the activation energy ( $E_a$ ) data using higher than when there are no inhibitors. Physical adsorption results from the increased  $E_a$  measurements when organic inhibitors are present among the surface of C-steel and inhibitors molecules. As a result, the  $E_a$  increment statistics result in a decreased corrosion rate.

**Table 3.** The dissolution Kinetic factors.

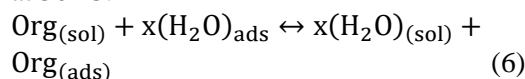
Comp.	Conc. (M)	$E_a^*$ (kJ mol <sup>-1</sup> )	$\Delta H^*$ (kJ mol <sup>-1</sup> )	$-\Delta S^*$ (J mol <sup>-1</sup> K <sup>-1</sup> )
(1)	Blank	34.285	30.572	175.81
	$1 \times 10^{-6}$	59.628	54.704	103.36
	$3 \times 10^{-6}$	56.161	51.718	113.53
	$5 \times 10^{-6}$	54.307	49.819	120.10
	$7 \times 10^{-6}$	54.088	49.641	121.15
	$9 \times 10^{-6}$	53.777	49.138	123.18
(2)	$11 \times 10^{-6}$	52.983	48.456	125.96
	$1 \times 10^{-6}$	48.365	43.922	137.06
	$3 \times 10^{-6}$	49.020	44.551	135.35
	$5 \times 10^{-6}$	51.294	46.737	128.71
	$7 \times 10^{-6}$	54.061	49.386	120.65
	$9 \times 10^{-6}$	53.943	52.033	112.63
(3)	$11 \times 10^{-6}$	57.863	53.014	110.52
	$1 \times 10^{-6}$	24.701	21.184	211.44
	$3 \times 10^{-6}$	26.840	23.230	205.29
	$5 \times 10^{-6}$	27.970	24.339	202.09
	$7 \times 10^{-6}$	28.022	24.347	202.48
	$9 \times 10^{-6}$	30.402	26.633	195.54
	$11 \times 10^{-6}$	31.513	27.716	192.51

### Theory for adsorption

The following equation (5) was used to calculate the various concentrations of the inhibitors of the carbon steel electrode.

$$\theta = [1 - (R_{\text{corr}}/R_{\text{corr}}^0)] \quad (5)$$

where R and  $R^0$  were used to illustrate the appropriate isotherm to evaluate the process adsorption. R and  $R^0$  were the rate of corrosion in hydrochloric acid as defined before and after at 30 °C: <sup>4</sup>



Where x is the amount of water molecules that an inhibitor molecule replaces. Fitting ( $\theta$ ) data to various isotherms has been attempted. According to the following equation (7), Temkin isotherm provided the best results for the adsorption data in the current study:

$$2a\theta = \ln(CK_{\text{ads}}) \quad (7)$$

Where a is the heterogeneous factor of the carbon steel surface, C is the dose of inhibitors and  $K_{\text{ads}}$  is the equilibrium constant for adsorption.

With the use of  $K_{\text{ads}}$ , the Gibbs free adsorption energies ( $\Delta G_{\text{ads}}^0$ ) might be estimated as follows:

$$\Delta G_{\text{ads}}^0 = -RT \ln(55.5 K_{\text{ads}}) \quad (8)$$

where 55.5 is the concentration of 1L of water in solution (M/L).

If C is the bulk concentration of the inhibitor and 1/y is the number of surface- one inhibitor molecule's participation in the

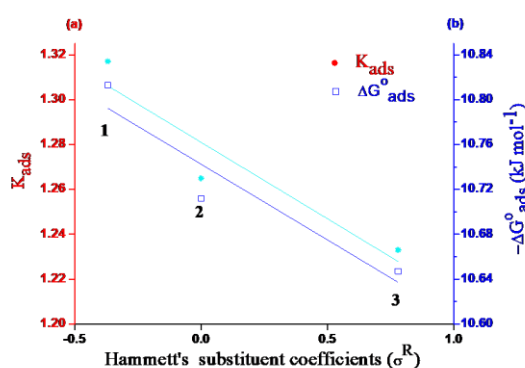
effective spots, then  $K = K' (1/y)$  as following:  
 $\log (\theta/(1 - \theta)) = \log K' + y \log C$  (9)

Table 4 contains the calculated values for  $K_{\text{ads}}$  and  $\Delta G^{\circ}_{\text{ads}}$ .

**Table 4.** The kinetic adsorption isotherm parameter after 60 minutes.

Inhibitors	$K_{\text{ads}} (\text{M}^{-1})$	$-\Delta G^{\circ}_{\text{ads}} (\text{kJ mol}^{-1})$
(1)	1.317	10.813
(2)	1.265	10.712
(3)	1.233	10.647

According to the data in Table 4, the greater-efficiency inhibitor has higher -ve  $\Delta G^{\circ}_{\text{ads}}$  data, and the adsorption spontaneity for method and surface stabilization on the exterior of carbon steel. As a result, the following is the order of protective effectiveness: compound (1) follows compound (2), and so on (3). The data of  $K_{\text{ads}}$  were obtained to run in parallel to the IE [ $K (1) > K (2) > K (3)$ ], and are affected by the substituent inductive or mesmeric effects. Figure 5 illustrates a straight line that results from charting the relationship between Hammett's substituent coefficients vs.  $K_{\text{ads}}$  and  $-\Delta G^{\circ}_{\text{ads}}$  values.



**Figure 5.** Hammett's substituent coefficients vs.  $K_{\text{ads}}$  and  $-\Delta G^{\circ}_{\text{ads}}$

#### Tafel polarization measurements

By using the polarisation method, the impact of inhibitors on the corrosion of carbon steel was examined (El-Sonbati *et al.*, 2019a; El-Sonbati *et al.*, 2022a). The Tafel polarization charts for carbon steel for different doses of chemical (1) at 25 °C are shown in Figure 6.

1. A reduction in the rate of corrosion, which causes a reduction in the current intensity ( $i_{\text{corr}}$ )
2. An growth in the proportion of  $\text{IE}_p$  as a result of better covering surface

The corrosion potential values did not differ noticeably from the blank. Equation (10) was used to calculate the effectiveness of the inhibition:

$$\% \text{IE}_p = [(i_{\text{corr}}^{\circ} - i_{\text{corr}})/i_{\text{corr}}^{\circ}] \times 100 \quad (10)$$

where  $i_{\text{corr}}^{\circ}$  and  $i_{\text{corr}}$  are, respectively, current corrosion flows without and with different amounts of compound (1).

Table 5 shows that after the addition of the organic derivatives. The order of the effectiveness of inhibitors is: (1) > (2) > (3).

**Table 5.** Kinetic characteristics.

Comp.	Conc., M.	$-E_{\text{corr}}$ (mV vs. SCE)	$\beta_a \times 10^{-3}$ (mV dec <sup>-1</sup> )	$\beta_c \times 10^{-3}$ (mV dec <sup>-1</sup> )	% IE
	Blank	439	81.60	234.0	-----
(1)	$1 \times 10^{-6}$	477	88.90	166.8	80.5
	$3 \times 10^{-6}$	467	91.70	214.5	80.6
	$5 \times 10^{-6}$	478	100.20	158.1	81.1
	$7 \times 10^{-6}$	489	83.60	188.1	81.3
	$9 \times 10^{-6}$	482	49.40	91.7	93.7
(2)	$11 \times 10^{-6}$	466	36.70	63.9	96.0
	$1 \times 10^{-6}$	479	81.90	166.8	77.9
	$3 \times 10^{-6}$	454	71.80	147.7	78.1
	$5 \times 10^{-6}$	466	79.80	152.5	78.4
	$7 \times 10^{-6}$	467	96.50	237.4	79.1
(3)	$9 \times 10^{-6}$	468	91.20	175.2	79.7
	$11 \times 10^{-6}$	466	88.00	204.8	79.9
	$1 \times 10^{-6}$	439	78.10	215.4	5.7
	$3 \times 10^{-6}$	467	113.50	232.2	50.3
	$5 \times 10^{-6}$	453	74.30	158.2	61.5
(3)	$7 \times 10^{-6}$	479	89.00	152.7	75.7
	$9 \times 10^{-6}$	467	79.70	147.1	76.3
	$11 \times 10^{-6}$	480	106.40	155.4	76.8

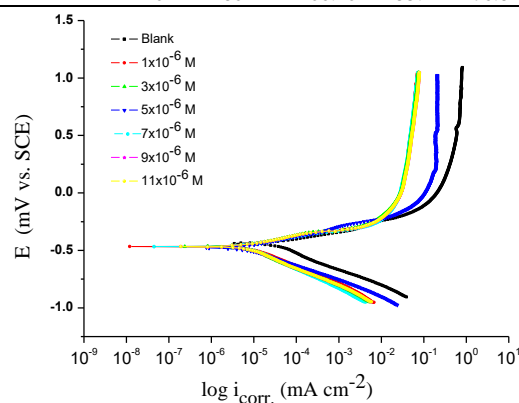


**Figure 6.** Potentiodynamic polarisation of inhibitor (1).

#### EFM methods

The optimum solution for online corrosion monitoring is provided by the EFM method. The EFM spectra for carbon steel containing and without distinct chemical (1) doses are shown in Figure 7. Table 6 includes the kinetic characteristics obtained



from EFM together with the causality variables (CF-2 and CF-3), corrosion density current ( $i_{\text{corr}}$ ), cathodic and anodic Tafel lines (a and c), and corrosion density current ( $i_{\text{corr}}$ ). The correlation factors CF-2 and CF-3, which are quite close to their theoretical values, show the high quality of the estimated values. Using equation 11, the inhibition efficiencies % IE<sub>EFM</sub> were determined.

% IE<sub>EFM</sub> =  $\left[1 - (i_{\text{corr}}/i_{\text{corr}}^0)\right] \times 100$  (11)  
where the terms  $i_{\text{corr}}^0$  and  $i_{\text{corr}}$  refer to the corrosion densities of both with and without them. This experiment's determination of protective efficiency is as follows:

(1) > (2) > (3).

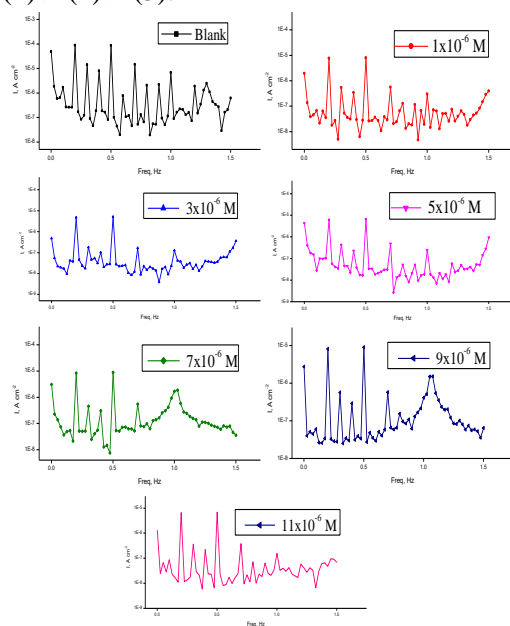


Figure 7. EFM spectra of compound (1).

### EIS evaluation

EIS is a potent and well-proven technology in the corrosion process. Impedance curves can be used to study kinetics of electrodes, surface properties, and mechanistic information. Figure 8 displays the (a) Nyquist and (b) Bode graphs minus and incorporating different dosages of inhibitors from open-circuit potential. This instruction was followed by the loop capacities increasing size (Figure 8a) in relation to a constant inhibitor dose: Compounds (1) through (3) demonstrate the higher inhibitory impact of compound (1). Given the addition of the impedance increase caused by the addition of dosages of inhibitors, Bode curves (Figure 8b). This circuit, that depicts one electron transport reaction, is entirely according to the results of our

experiments. For a circuit with a CPE variable ( $Y_0$  and  $n$ ),  $C_{dl}$  was determined by applying equation (12) (Eldesoky *et al.*, 2015; Morgan *et al.*, 2017):

$$C_{dl} = Y_0 \omega^{n-1} / \sin \left[ n \left( \frac{\pi}{2} \right) \right] \quad (12)$$

where  $Y_0$  = magnitude of the CPE,  $\omega = 2\pi f_{\text{max}}$ , at  $f_{\text{max}}$ , the imagined component of the impedance oscillates at its highest frequency. According to the results of the trials, charged transfer was mostly responsible for influencing the Nyquist charts for the corrosion reaction (El-Sonbati *et al.*, 2019a; Morgan *et al.*, 2017).

Table 6. Electrochemical kinetic characteristics by the EFM

Com p.	Conc., M.	$i_{\text{corr}}$ ( $\mu\text{A cm}^{-2}$ )	$\beta_a \times 10^{-3}$ (mV dec <sup>-1</sup> )	$\beta_c \times 10^{-3}$ (mV dec <sup>-1</sup> )	CF-2	CF-3	%IE
	Blank	141.5	68.40	219.0	1.93	2.81	----
(1)	$1 \times 10^{-6}$	16.11	172.2	272.6	2.05	3.02	88.6
	$3 \times 10^{-6}$	15.78	116.5	236.6	1.92	3.21	88.8
	$5 \times 10^{-6}$	14.53	90.94	134.3	2.03	2.98	89.7
	$7 \times 10^{-6}$	13.62	85.48	131.8	1.82	2.54	90.3
	$9 \times 10^{-6}$	13.50	90.68	149.1	1.69	2.95	90.4
(2)	$11 \times 10^{-6}$	12.62	99.56	150.5	1.97	2.83	91.0
	$1 \times 10^{-6}$	19.72	90.63	191.2	1.89	3.00	86.0
	$3 \times 10^{-6}$	18.45	112.70	189.1	1.96	2.89	86.9
	$5 \times 10^{-6}$	18.27	80.63	133.0	1.85	3.29	87.0
	$7 \times 10^{-6}$	18.00	109.70	180.7	2.00	3.04	87.2
(3)	$9 \times 10^{-6}$	17.74	112.30	212.5	1.89	3.07	87.4
	$11 \times 10^{-6}$	16.79	61.56	97.89	1.57	2.78	88.1
	$1 \times 10^{-6}$	49.38	80.64	194.7	1.90	2.91	65.1
	$3 \times 10^{-6}$	31.64	88.90	180.7	1.89	3.40	77.6
	$5 \times 10^{-6}$	25.46	76.70	135.0	1.93	2.90	82.0
	$7 \times 10^{-6}$	24.01	115.50	242.2	1.95	2.88	83.0
	$9 \times 10^{-6}$	22.28	87.63	167.6	1.88	3.04	84.2
	$11 \times 10^{-6}$	21.92	138.20	211.7	1.99	2.69	84.5

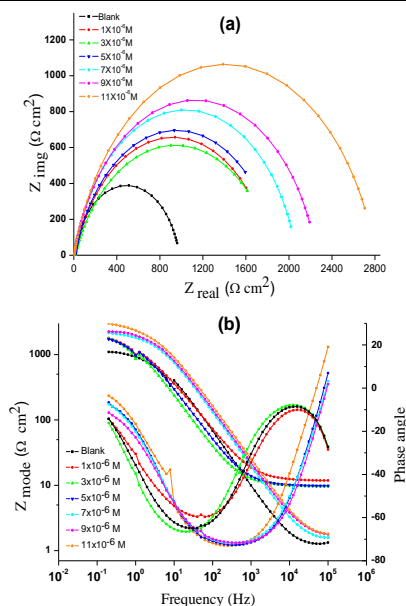
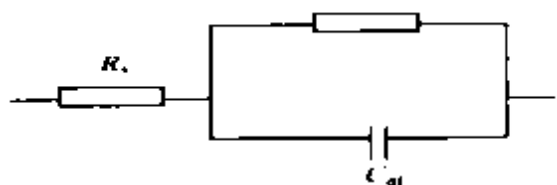


Figure 8. The Nyquist and Bode curves (a) and (b), respectively of compound (1).



**Figure 9.** A model of an equivalent circuit is.

According to the EIS data in Table 7, when the concentrations of inhibitors increased, the  $R_{ct}$  data increased and as a result of the inhibitors sticking to the carbon steel's surface and the amount of the dissolving reaction was reduced, the  $C_{dl}$  data decreased. In general, an increase in  $R_{ct}$  data is accompanied by a decrease in corrosion. A decrease in  $C_{dl}$  could be caused by a rise in the thickness of electrical double layers or a fall in the local dielectric constant (Moretti *et al.*, 1994).

$$\% E = \theta \times 100 = \left[ 1 - \left( R_{ct}^0 / R_{ct} \right) \right] \quad (13)$$

where  $R_{ct}^0$  and  $R_{ct}$  refer for, respectively, the resistance to charge transfer with and without an inhibitor. Tafel polarization fits the percent %E order of the studied compounds ( $1 > 2 > 3$ ).

**Table 7.** Data on the EIS.

Comp.	Conc., M.	$R_s$ ( $\Omega \text{ cm}^2$ )	$R_{ct}$ ( $\Omega \text{ cm}^2$ )	$C_{dl} \times 10^{-4}$ ( $\mu\text{F cm}^{-2}$ )	% IE
	Blank	1.19	980	9.07	---
(1)	$1 \times 10^{-6}$	9.44	1825	1.76	46.3
	$3 \times 10^{-6}$	11.01	1862	1.73	47.3
	$5 \times 10^{-6}$	9.50	1892	1.52	48.2
	$7 \times 10^{-6}$	1.47	2070	1.37	52.6
	$9 \times 10^{-6}$	1.67	2258	1.02	56.5
	$11 \times 10^{-6}$	1.62	2803	1.01	65.0
(2)	$1 \times 10^{-6}$	10.35	1635	2.64	40.0
	$3 \times 10^{-6}$	9.96	1694	2.60	42.1
	$5 \times 10^{-6}$	9.89	1739	2.52	43.6
	$7 \times 10^{-6}$	1.36	1777	2.07	44.7
	$9 \times 10^{-6}$	10.15	1778	1.81	44.8
	$11 \times 10^{-6}$	1.34	1779	1.77	44.9
(3)	$1 \times 10^{-6}$	11.81	1013	7.72	3.2
	$3 \times 10^{-6}$	11.08	1253	3.48	21.7
	$5 \times 10^{-6}$	1.11	1375	3.47	28.7
	$7 \times 10^{-6}$	9.87	1455	2.97	32.6
	$9 \times 10^{-6}$	14.11	1495	2.88	34.4
	$11 \times 10^{-6}$	9.92	1580	2.73	37.9

### SEM investigation and EDX analysis

The surfaces of carbon steel were examined using SEM prior to and after corrosion in 2 M HCl in the absence and existence of  $11 \times 10^{-6}$  M inhibitors as shown in Figure 10.

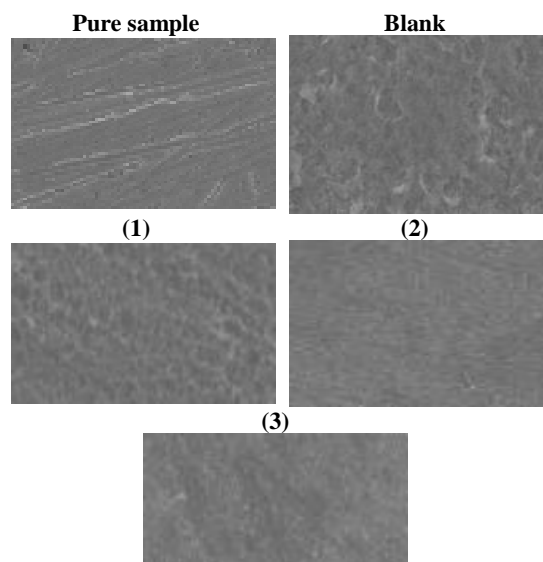


**Figure 10.** Carbon steel SEM micrographs

When carbon steel was exposed to  $11 \times 10^{-6}$  M of the examined inhibitors for three days, Figure 11 depicts the EDX spectrum of a surface made of carbon steel. A comparable distribution elemental is given in Table 8.

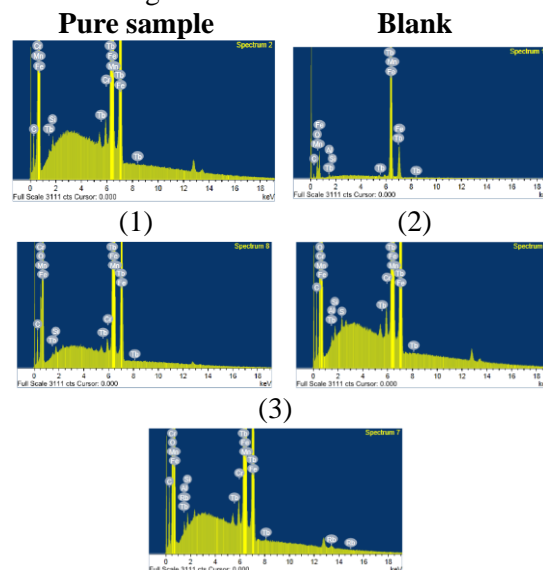


**Figure 11.** EDX study for CS containing.

**Table 8.** Composition of the surface.

Mass %	C	O	Al	Mn	Fe	S
Pure sample	6.78	---	0.29	0.47	87.53	---
Blank	10.58	14.84	0.70	0.40	69.75	---
(1)	10.83	12.02	0.31	0.45	71.51	---
(2)	11.14	9.15	0.19	0.47	74.40	0.17
(3)	11.45	7.41	---	0.43	76.47	---

### Quantum chemical

Table 9 represents the calculation of a few quantum properties of the substances under

consideration in its keto form. Optimal geometries, HOMO distribution, and Figure 12 display the non-protonated LUMO distribution derivatives (**Diab et al., 2019b; El-Ghamaz et al., 2012; El-Sonbati et al., 2018b; El-Sonbati et al., 2018c; El-Sonbati et al., 2022b; Morgan et al., 2018; Salama et al., 2023**). As a result, inhibitor molecules can receive electrons from the metal more readily the lesser the LUMO potential. As a result, the energy band gap value,  $\Delta E = E_{\text{LUMO}} - E_{\text{HOMO}}$ , reflects the inhibitor's ability to stop reactions; the smaller its value, the greater the effectiveness of the inhibition (**Diab et al., 2019c; Diab et al., 2022; El-Sonbati et al., 2018d; El-Sonbati et al., 2019b; El-Sonbati et al., 2020; El-**

**Sonbati et al., 2021**). Compound **1** has the most  $E_{\text{HOMO}}$ , followed by compound **(2)** and compound **(3)**, due to the presence existence of an electron-donating group (OH) in its molecular structure.

**Table 9.** The estimated quantum chemical characteristics.

	(1)	(2)	(3)
$E_{\text{HOMO}}$ (eV)	-3.363	-3.333	-5.832
$E_{\text{LUMO}}$ (eV)	-2.948	-2.352	-3.303
$\Delta E$ (eV)	0.415	0.981	2.529
$\eta$ (eV)	3.156	2.843	4.568
$\sigma$ (eV <sup>-1</sup> )	0.208	0.491	1.265
$\Pi$ (eV)	-4.819	-2.039	-0.791
$S$ (eV <sup>-1</sup> )	2.409	1.0194	0.395
$\omega$ (eV)	23.993	8.236	8.249

$\Delta N_{\text{max}}$	15.207	5.795	3.612
-------------------------	--------	-------	-------

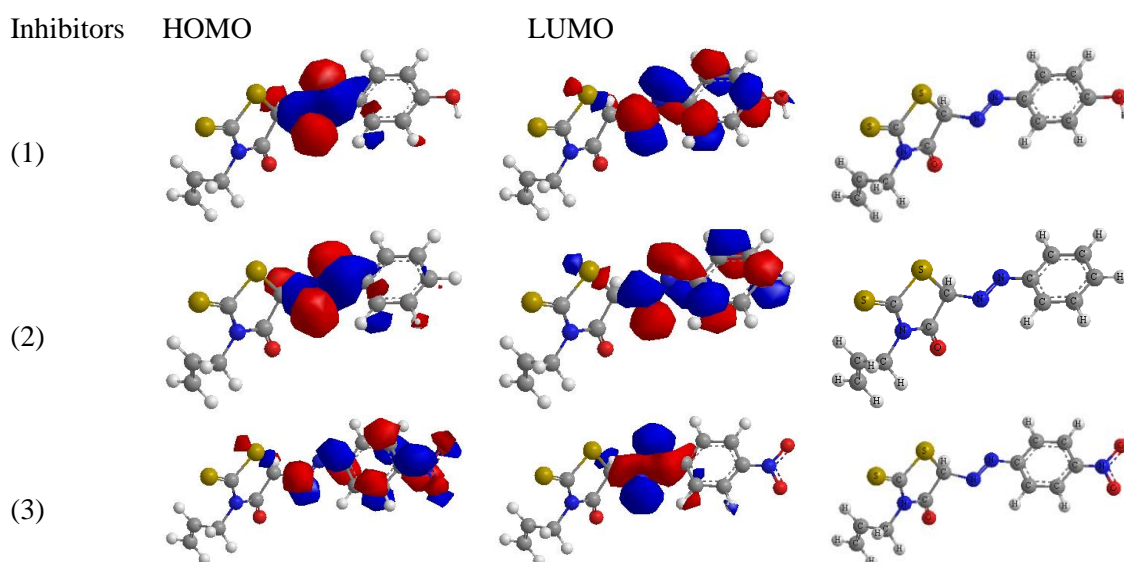


**Figure 12.** Molecular orbital plots.

Compound **(1)** has a strong tendency to donate electrons. Additionally, compound **(1)** has a lesser  $E_{\text{LUMO}}$  value, which confirms compound stronger corrosion behavior **(1)**. Another evidence for compound **(1)** stronger propensity to adsorb onto the surface of carbon steel comes from the fact that it has a lower  $\Delta E$  value.

## Conclusions

1. All of the studied chemicals are found to be effective carbon steel corrosion inhibitors in 2 M HCl solution.
2. The kind and variety of substituents found in the inhibitor molecule

determine the various levels of inhibitive activity.

3. EFM was utilized as a quick and non-destructive method to measure corrosion. Adding the inhibitor increased the resistance to charge transfer and decreased the double layer capacitances, raising the IE percentage, according to the EIS data.
4. Allyl rhodanine azodye compounds are mixed-type inhibitors, according to the results of potentiodynamic polarization.
5. SEM-EDX pictures and analysis showed that a thin layer had formed on the carbon steel. The results of the electrochemical and chemical

investigations were in good agreement.

6. The active sites of the derivatives of allyl rhodanine and azodye were determined by quantum chemistry calculations to be hetero atoms of both oxygen and nitrogen (**1-3**).

### Highlights:

The inhibition impact of freshly created allyl rhodanine azodye derivatives (**1-3**) on C-steel (CS) and their adsorption patterns in 2M HCl were investigated.

The corrosion rate reduced as the percentage of the compounds in the HCl solution increased, according to Tafel polarisation curves. On corrosion inhibition process, the temperature effect has been studied.

### References

- Abou-Dobara MI, Omar NF, Diab, MA, El-Sonbati AZ, Morgan ShM, Salem OL, Eldesoky AM. 2019a. Polymer complexes. LXXV. Characterization of quinoline polymer complexes as potential bio-active and anti-corrosion agents. *Mater. Sci. Eng. C.*, 103, 109727. <https://doi.org/10.1016/j.msec.2019.05.012>
- Abou-Dobara MI, Omar NF, Diab MA, El-Sonbati AZ, Morgan ShM, El-Mogazy MA. 2019b. Allyl rhodanine azo dye derivatives: Potential antimicrobials target d-alanyl carrier protein ligase and nucleoside diphosphate kinase. *J. Cell. Biochem.*, 120(2), 1667-1678. <https://doi.org/10.1002/jcb.27473>
- Diab MA, El-Sonbati AZ, Morgan ShM, El-Mogazy MA. 2018. Polymer complexes. LXXI. Spectroscopic studies, thermal properties, DNA binding and antimicrobial activity of polymer complexes. *Appl. Organomet. Chem.*, 32(8), e4378. <https://doi.org/10.1002/aoc.4378>
- Diab MA, Nozha SG, El-Sonbati AZ, El-Mogazy MA, Morgan ShM. 2019a. Polymer complexes. LXXVIII. Synthesis and characterization of supramolecular uranyl polymer complexes: Determination of the bond lengths of uranyl ion in polymer complexes. *Appl. Organomet. Chem.*, 33(10), e5153. <https://doi.org/10.1002/aoc.5153>
- Diab MA, El-Sonbati AZ, El-Ghamaz NA, Morgan ShM, El-Shahat O. 2019b. Conducting polymers X: Dielectric constant, conduction mechanism and correlation between theoretical parameters and electrical conductivity of poly (N, N'-bis-sulphanyl p-phenylenediamine-2, 6-diaminopyridine) and poly (N, N'-bis-sulphanyl p-phenylenediamine-3, 5-diamine-1, 2, 4-trizole). *Eur. Polym. J.*, 115, 268-281. <https://doi.org/10.1016/j.eurpolymj.2019.03.036>
- Diab MA, Mohamed GG, Mahmoud WH, El-Sonbati AZ, Morgan ShM, Abbas SY. 2019c. Inner metal complexes of tetradentate Schiff base: Synthesis, characterization, biological activity and molecular docking studies. *Appl. Organomet. Chem.*, 33(7), e4945. <https://doi.org/10.1002/aoc.4945>
- Diab MA, El-Sonbati AZ, Gomaa EA, El-Mogazy MA, Morgan ShM, Abou-Dobara MI, Osman MA. 2022. Polymer complexes: LXXIX—synthesis, characterization, geometrical structures, biological activity and molecular docking studies of azo dye complexes. *J. Iran. Chem. Soc.*, 19(7), 3079-3102. <https://doi.org/10.1007/s13738-022-02516-9>
- Eldesoky AM, El-Bindary MA, El-Sonbati AZ, Morgan ShM. 2015. New eco-friendly corrosion inhibitors based on azo rhodanine derivatives for protection copper corrosion. *J. Mater. Environ. Sci.*, 6, 2260-76. <https://ksascholar.dri.sa/en/publications/new-eco-friendly-corrosion-inhibitors-based-on-azo-rhodanine-deri>
- El-Ghamaz NA, El-Sonbati AZ, Morgan ShM. 2012. Optical properties of some synthesized azo thin films. *J. Mol. Struct.*, 1027, 92-98. <https://doi.org/10.1016/j.molstruc.2012.06.004>
- El-Sonbati AZ, Diab MA, Morgan ShM, El-Mogazy MA. 2018a. Polymer complexes. LXXIII. Synthesis, characterization, thermal properties, electron spin resonance study and antimicrobial activity of Cu (II) polymer complexes: Relation between representative Pascal constants and thermal activation energy of decomposition. *Appl. Organomet. Chem.*, 32(11), e4530. <https://doi.org/10.1002/aoc.4530>
- El-Sonbati AZ, Diab MA, Morgan ShM, Eldesoky AM, Balboula MZ. 2018b. Polymer complexes. LXIX. Some divalent metal (II) polymer complexes of potentially bidentate monomer N-[4-(5-methyl-isoxazol-3-ylsulfamoyl)-phenyl]-acrylamide: synthesis, spectroscopic characterization, thermal properties, antimicrobial agents and DNA studies. *Appl. Organomet. Chem.*, 32(3), e4207. <https://doi.org/10.1002/aoc.4207>
- El-Sonbati AZ, Diab MA, Morgan ShM, Balboula MZ. 2018c. Polymer complexes. LXVIII. Spectroscopic studies of supramolecular copper (II) polymeric complexes of biologically active monomer derived from novel sulfa drug. *Appl. Organomet. Chem.*, 32(2), e4059. <https://doi.org/10.1002/aoc.4059>

- El-Sonbati AZ, Diab MA, Morgan ShM, Seyam HA. 2018d. Supramolecular structures for determination and identification of the bond lengths in novel uranyl complexes from their infrared spectra. *J. Mol. Struct.*, 1154, 354-365. <https://doi.org/10.1016/j.molstruc.2017.10.020>
- El-Sonbati AZ, Diab MA, Eldesoky AM, Morgan ShM, Salem OL. 2019a. Polymer complexes. LXXVI. Synthesis, characterization, CT-DNA binding, molecular docking and thermal studies of sulfoxine polymer complexes. *Appl. Organomet. Chem.*, 33(5), e4839. <https://doi.org/10.1002/aoc.4839>
- El-Sonbati AZ, Mahmoud WH, Mohamed GG, Diab MA, Morgan ShM, Abbas SY. 2019b. Synthesis, characterization of Schiff base metal complexes and their biological investigation. *Appl. Organomet. Chem.*, 33(9), e5048. <https://doi.org/10.1002/aoc.5048>
- El-Sonbati AZ, Diab MA, Morgan ShM, Abou-Dobara MI, El-Ghettany AA. 2020. Synthesis, characterization, theoretical and molecular docking studies of mixed-ligand complexes of Cu (II), Ni (II), Co (II), Mn (II), Cr (III), UO<sub>2</sub> (II) and Cd (II). *J. Mol. Struct.*, 1200, 127065. <https://doi.org/10.1016/j.molstruc.2019.127065>
- El-Sonbati AZ, Omar NF, Abou-Dobara MI, Diab MA, El-Mogazy MA, Morgan ShM, El-Ghettany AA. 2021. Structural, molecular docking computational studies and in-vitro evidence for antibacterial activity of mixed ligand complexes. *J. Mol. Struct.*, 1239, 130481. <https://doi.org/10.1016/j.molstruc.2021.130481>
- El-Sonbati AZ, El-Mogazy MA, Nozha SG, Diab MA, Abou-Dobara MI, Eldesoky AM, Morgan ShM. 2022a. Mixed ligand transition metal (II) complexes: Characterization, spectral, electrochemical studies, molecular docking and bacteriological application. *J. Mol. Struct.*, 1248, 131498. <https://doi.org/10.1016/j.molstruc.2021.131498>
- El-Sonbati AZ, Diab MA, Morgan ShM, Abbas SY, Mohamed GG. 2022b. Synthesis, theoretical study, molecular docking and biological activity of nano tridentate (E)-2-((3-hydroxyphenyl) methyl) phenol metal complexes. *Inorg. Chem. Commun.*, 137, 109193. <https://doi.org/10.1016/j.inoche.2022.109193>
- Mohamed GG, El-Sherif AA, Saad MA, El-Sawy SE, Morgan ShM. 2016. Mixed-ligand complex formation of tenoxicam drug with some transition metal ions in presence of valine: Synthesis, characterization, molecular docking, potentiometric and evaluation of the humeral immune response of calves. *J. Mol. Liq.*, 223, 1311-1332. <https://doi.org/10.1016/j.molliq.2016.09.065>
- Moretti G, Quartanone G, Tassan A, Zingales A. 1994. Inhibition of mild steel corrosion in 1N sulphuric acid through indole. *Werkst. Korros.*, 45(12), 641-647. <https://doi.org/10.1002/maco.19940451203>
- Morgan ShM, El-Sonbati AZ, Eissa HR. 2017. Geometrical structures, thermal properties and spectroscopic studies of Schiff base complexes: Correlation between ionic radius of metal complexes and DNA binding. *Mol. Liq.*, 240, 752-776. <http://dx.doi.org/10.1016/j.molliq.2017.05.114>
- Morgan ShM, Diab MA, El-Sonbati AZ. 2018. Supramolecular assembly of hydrogen bonding, ESR studies and theoretical calculations of Cu (II) complexes. *Appl. Organomet. Chem.*, 32(10), e4504. <https://doi.org/10.1002/aoc.4504>
- Salama HM, Diab MA, El-Sonbati AZ, El-Mogazy MA, Eldesoky AM, Amin BH, El-Zahed MM. 2023. New potential Mn (II) mixed ligand complexes: synthesis, structural characterization, molecular docking, antibacterial activity and electrochemical studies. *JICS*, 20(12), 2977-3007. <https://doi.org/10.1007/s13738-023-02892-w>
- Refaat HM, El-Badway HA, Morgan ShM. 2016. Molecular docking, geometrical structure, potentiometric and thermodynamic studies of moxifloxacin and its metal complexes. *J. Mol. Liq.*, 220, 802-812. <https://doi.org/10.1016/j.molliq.2016.04.124>

## المخلص العربي

**عنوان البحث:** الديناميكيات الجزيئية الكيميائية الكمية والدراسات التجريبية لتأثير تثبيط التآكل لمشتقات أزوداي الأليل رودانين على الفولاذ الكربوني في ٢ مولر حمض الهيدروكلوريك

أحمد السنباطي<sup>١</sup>، محمد مسعد<sup>٢</sup>، محمد حنفي محمود<sup>١</sup>

<sup>١</sup>قسم الهندسة الرياضية والفيزيائية، كلية الهندسة، جامعة المنصورة، المنصورة، مصر



## ٢ قسم هندسة الأشغال العامة، كلية الهندسة، جامعة المنصورة، المنصورة، مصر

يشتمل البحث علي دراسة تآكل الصلب الكربوني في محلول ٢ مولر من حمض الهيدروكلوريك في عدم وجود وفي وجود لمشتقات أزوداي الأليل رودانين باستخدام طرق الفقد في الوزن والاستقطاب المهبطي والمصعدى وتقنيات المعاوقة الكهروكيميائية الطيفية (EIS) والتردد الكهروكيميائي المعدل (EFM) حيث وجد أن هذه المركبات تقلل من تآكل الصلب الكربوني. كذلك وجد أن معدل التآكل يزداد بزيادة درجة الحرارة وأن التنشيط يحدث عن طريق ادمصاص فيزيائي. وظهرت النتائج تطابقا تاما في جميع التقنيات المستخدمة. ووجد أن كفاءة التنشيط للمركبات كانت كالتالى:

$$(1) > (2) > (3)$$

## Environmental Concentration of Paint Particulate Matters and Dust Metals in the Paint Furniture Workshops

Maie. I. El-Gammal<sup>1</sup>, Mahmoud. S. Ibrahim<sup>1</sup>, Alia A. Shakour<sup>2</sup>, Neven M. El-Galad<sup>3</sup> and Reham Sh. El-Henawy<sup>\*1</sup>

<sup>1</sup>Environmental Sciences Department, Faculty of Science, Damietta University, Egypt.

<sup>2</sup>Air Pollution Department, National Research Centre, Cairo, Egypt.

<sup>3</sup>Environmental Affairs Department, Damietta Governorate, Egypt.

Received: 11 April 2025 /Accepted: 07 May 2025

\*Corresponding author's E-mail: reham\_henawy@yahoo.com

### Abstract

The present study employed six paint furniture workshops; A, B, C, D, E and F, which have small and different size and types of painting, in close to carpenter workshops at El-Shoaraa in Damietta city. The particulate matter of PM<sub>10</sub> and PM<sub>2.5</sub> were measured, using Casella device for dust detective (Casella Cel-712 Microdust Pro Real-Time Dust Monitor). On the other hand, total suspended particulate (TSP) samples were collected using sampling air pump connected an open face holder on Whatman glass fiber filter. Metallic constituents of TSP were determined, using Atomic Absorption Spectrophotometer (A.A.S). The study results indicated that the mean concentrations of PM<sub>10</sub> ranged from 26.85 to 44.41 µg/m<sup>3</sup>, whereas, the mean concentrations of PM<sub>2.5</sub> ranged from 39.5 to 125 µg/m<sup>3</sup>. The TSP concentrations ranged from 359 to 410 µg/m<sup>3</sup>. The most paint particulate matters (PM) detected have unacceptable concentrations.

The mean heavy metals concentration of Pb, Cd and Zn in paint furniture workshops was (14.59, 7.59, 10.82) µg/m<sup>3</sup>, respectively. Thus, the present study evaluated concentrations of dust that might generate in the indoor air of workshops involving spray painting and varnishing. Therefore, to protect air quality and painter's safety, and health concerns, occupational health and safety regulations, its implementation and enforcement within spray-painting furniture workshops must be improved and to ensure greater attention mitigations and management is given.

**Keywords:** TSP, PM<sub>10</sub> and PM<sub>2.5</sub>, Heavy Metals, Paint, Furniture Workshops

### Introduction

The paints are used as a related activity in a variety of industries include motor vehicles, buildings, furniture, white goods, machinery,

ships and aircraft. Spray painting in furniture finishing processes is one of the major activities of painting. Paint is a mixture of various chemicals that work together to provide color, protection, and durability to surfaces. The composition of paint can vary depending on the type (latex, oil-based, epoxy, etc.) and brand,

but some common components are pigments, binder, solvents, additives, extenders, retarders, driers, fragrances and preservatives (**Hussain, 2024**). Spray painting is usually a mixture of resins or polymers which cure or harden to produce a durable coating on the application surface, coloured pigments and fillers, and solvents or water acting as carriers for the resins that evaporate during application and drying (**Ifjen et al., 2022**).

Paint is used to decorate, protect buildings and other objects, and industrial coatings, which are applied as finish-manufactured goods such as cars, vehicle restoration, wood and furniture, and prolong the life of natural and synthetic materials, which acts as a barrier against environmental conditions (**Veleva, 2012**). Spraying is a painting technique that employs a spraying device, by using a valve to release chemicals and paintings coupled with compressed gas, air, allows for easy and even application over various surfaces, with a choice of applying coating material to produce the required thickness film of a liquid material release in mod of aerosol or vapour. Coatings can differ between paint, ink, varnish, and various other materials. Spray painting is one of the primary methods of painting besides using a brush or a roller, because it is quicker, cleaner, and easier to achieve a uniform coat. Application may be manual or automatic, but the majority of spray operate by using manual finishing techniques. The most of them is inserted with dry filters to control particulate; paint droplets, which is generated by overspray (**Sefiane, 2014**). A furniture spray painting is a tool that has gained popularity for many years with a professional, to complete the proses faster with less effort, and with a smooth and professional finish. (**Thorud et al., 2005 and Veleva, 2012**). Varnish as a homogeneous, Transparency or semitransparent liquid that is converted to a

solid, after being applied as a thin layer (**Schurr and Allison, 1981**). However, Lacquer is a coating, dries by evaporation much rather oxidation or polymerization, so dry very rapidly (**Lu et al., 2004**). Alkyd is a prevailing product in the coating painting surface, since the 1930s. Therefore, they contend the water-based coatings such as acrylics and latex, and still make them a more preferable coating for architectural, machinery, wood and industrial applications, cause impedance to environmental factors and almost, the strong adhesion to all surface (**Stoye and Freitag, 1998; Chong, 2020**).

In the wood-furniture industry, emissions from spray painting comprise many sources, including operations such as finishing; spray booths, flash-off areas, ovens, mixing, touch-up and repair, gluing, and cleaning. The potential emissions to atmosphere from spray painting operations are sanding and blasting dust arising from surface preparation in some activities, such as smash repairing or timber painting (**Ratnasingam et al., 2009**). Most of the dust is generated, so fine that literally find its way out into the work area (**NOHSC, 1999; SafeWork, 2022**).

There are various types of paints are based on synthetic paints, with a mixture of volatile organic solvents such as semi bright and matt lacquer "varnish", lacquer polyesters, polyurethane lacquer, acrylate, synthetic resins that give colour and appearance, used for surface coating of wood and furniture (**Thorud et al., 2005**).

Furniture spray painting is aerosol a solvent-intensive process, which, forming a mist of fine liquid paint droplets (10-50  $\mu\text{m}$ ). During the process, painter is exposed to the chemicals which are atomized, which can be absorbed through skin and mucous

membranes, inhalation route (**McKeown, 2011**).

Anthropogenic particulate matter (PM) originates from human activities, such as construction, agricultural and industrial emissions (**Liu et al., 2021**). Addition to airborne particulate matter (PMs), exposure to spray paint PMs (SPPMs) may also be associated with human health and pulmonary dysfunction (**Lai et al. 2017; Chen et al., 2019**).

In the indoor environment, exposure to pollutants has increased with reduced ventilation that making many indoor environments act as concentrators of emissions from plastics, paints, and other building materials. Poor ventilation always increases the indoor pollutant when outdoor does not go through to dilute emission from paints and others (**Ruan and Rim, 2019**).

The paints contain pigments for opacity as coloring materials and a variety of additives as drying materials (tenner) to accelerate solidification and formation, and organic solvents to regulate viscosity. Within wood manufacturing industry, exposure may occur to solvents, wood preservatives in glues and surface coating and to engine exhausts. Furniture painting workers are artisan that could be occupationally at risk hazardous attributed to the chemical composition of paints (**El Gammal, 2008; Ratnasingam et al., 2009, 2010**). Inorganic pigments are anti-corrosion coloring components of paint that can influence and control the corrosion of metal substrates, known as "inhibitors." These coating components are usually introduced into the primer layer. A variety of metals such as aluminum, chromium, lead, iron, and zinc are known as effective anti-corrosive pigments, and they are introduced into the coating formulation as finely ground metal or powdered metal oxide (**Veleva, 2012**).

Spray painting workers in furniture workshops are occupationally exposed to intense painting vapors the inhaled airborne metal particles, beside other constituents. Data revealed that occupational exposure to paintings spray induce several health hazards related to blood components, as well as liver, kidney and brain functions (**El-Gammal, 2008; Abdel maksoud et al., 2018; Abdrabouh et al., 2023**).

The toxic metals; lead, cadmium,

mercury and zinc are known to promote adverse health effects, such as carcinogenicity, nephrotoxicity, neurotoxicity and cardiotoxicity. Human exposure to these toxicants is predominantly secondary to anthropogenic activities (**IARC, 1989; ATSDR, 2012; Lai et al., 2018; Garaga, 2024**). Lead, a heavy metal, has been proven to influence the ecosystem negatively. Exposure to lead heavy metal may cause diverse health problems. It will be absorbed, bound to red blood cells, and distributed to the main compartments, bones and soft tissues, liver, kidneys, bone marrow, and brain (**Abdel maksoud et al., 2018; Abdrabouh et al., 2023; Halmo and Nappe, 2024**). The major sources of lead are, lead (Pb) smelters, automobile emissions and pigments and paints (**Dara, 1993; Chuitha et al., 2014**).

The higher risk priority number in the furniture painting process, which required reducing by implementing of the defects and then improve the painting process quality. Numerous studies evaluated the exposure of human to dust in occupational environments by combining adverse health effects (**El Gammal, 2008; Vergara-Murillo et al., 2022; Abdrabouh et al., 2023; Garaga, 2024**). The characterization of human exposure is a critical component of occupational epidemiological studies and environmental (**Berglund, 2001**) and it is an essential step in regulatory processes (**NRC (National Research Council), 1991**).

Environmental concerns have led to changes in the ingredients in spray paint, moving away from harmful ones to environmentally friendly options. Moreover, many studies have been made to produce eco-friendly exceptional resin compounds from natural renewable resources, vegetable oils obtained from various seeds are considered the best natural sources (**Ifjen et al., 2022**).

This study monitored the dust concentrations and metal dust in the most common work environment; the spray paint and varnish workshops where the workers exposed to the adverse health effects due to the exposure to these compounds.

## Materials and Methods:

*Physical characteristics and activities in the workshops.*

The studied environments are carpentry, varnishing and painting workplaces and found in a residential area, Al-Shoaraa which located at the northern direction of Damietta city, with high population density (46348 population) (**Damietta Governorate, 2023**). The study was conducted in six of spray painting and varnishing furniture workshops (A, B, C, D, E and F), which are located on the ground floor of building in very narrow streets. The selected workshops have a small size; the areas of the investigated workshops were limited; varies from 25m<sup>2</sup> to about 80m<sup>2</sup>. The most painting workshops have poor natural ventilation through small windows. Almost, there is no exhaust ventilation in the most of

workshops. The equipment has no fitted extraction ventilation or was frequently not working.

It occupies about 4-8 workers per a workshop, with lack of dust control, or personal protection. It was noted that the personal protection was not used appropriately, and filter respirators were saturated of dust and paint, and incorrect procedures are adopted. Each painting workshop different in premises and size of shop, and a unique environment that work practices, workload, and in chemical structure and type and toxicity of the solvent which is used (**Table 1**).

Table (1): Characteristics and Activities performed in Paint Furniture Workshops Evaluated.

Workshop	Characteristics	Products	Activities	No. of Painters
Varnishing (A)	Area: 60 m <sup>2</sup> No of windows: 3 Height: 4 m	Varnish, alcohol, turpentine, solvent, wax and paraffin	furniture surface finishing, such as varnishing, lacquering, waxing and coloring.	6
Varnishing (B)	Area: 75 m <sup>2</sup> No of windows: 2 Height: 4 m	Turpentine, solvent, Poly vinyl alcohol (PVA) paint, synthetic paint, lacquer and spackling	Paint wood, polish and touch up painted surfaces and dry surfaces	5
Varnishing (C)	Area: 45 m <sup>2</sup> No of windows: 2 Height: 4 m	Varnish, alcohol, turpentine, solvent, wax and paraffin	Wood and furniture surface finishing, such as varnishing, lacquering, waxing and coloring.	4
Spray Painting (D)	Area: 25 m <sup>2</sup> No of windows: 2 Height: 4 m	Varnish, alcohol, gasoline, turpentine, solvent, wax and paraffin	Wood and furniture surface finishing, such as varnishing, lacquering, waxing and coloring.	4
Spray Painting (E)	Area: 80 m <sup>2</sup> No of windows: 3 Height: 5 m	Turpentine, solvent, Poly vinyl alcohol paint, lacquer and spackling	Paint wood, Polish, touch up and dry painted surfaces prepare painting equipment.	8
Spray Painting (F)	Area: 55 m <sup>2</sup> No of windows: 2 Height: 5 m	Turpentine, lacquer and spackling, solvent, PVA Poly vinyl alcohol and synthetic paint.	Polishing and painting wood and touch up painted surfaces and dry surfaces preparing equipment.	3

#### *Painting Furniture Particulate Concentration Measurements:*

##### *Sampling*

A total of 360 samples were collected twice a week, from each of the six painting workshops; Varnishing workshops (A, B, C,) and Spray paint workshops (D, E and F), along

the months of March 2021 and June 2021, through 9 AM and 5 PM, along the period of day work in paint workshops. One hundred and ninety-two samples were collected inside each of the six paint workshops evaluated, and 72 samples were collected in the outside of workshops, at a distance of approximately 260 m and away from the influence of the paint workshop activities (**Martins et al., 2019**).



### *Determination of Paint Furniture Dust; TSP, PM<sub>10</sub> and PM<sub>2.5</sub>*

Total dust (TSP), particles of less than 10 µm in diameter (PM<sub>10</sub>) and particulate matter of less than 2.5 µm in diameter (PM<sub>2.5</sub>) were measured for each of the six workshops.

#### *PM<sub>10</sub> and PM<sub>2.5</sub> Measurements:*

Particles of (PM<sub>10</sub>) and (PM<sub>2.5</sub>) were measured for each workshop using the Casella device for dust detective (Casella CEL-712 Microdust Pro Real-Time Dust Monitor) operated at 1.0 L/min ± 5% constant, along the sampling period. The time measuring ranged from 0.25 to 32 mm in 31 channel sizes, each unit being certified with NIST (National Institute of Standards and Technology) monodisperse latex on the size of calibrated channels. The sampling monitor was mounted 1.5 m high for indoor measurements in the painting furniture workshops (Ruiz-Jimenez et al., 2019).

#### *Total Suspended Particulates (TSP) Measurement:*

A total of 192 (TSP) suspended particulate samples were collected from painting workshops (A, B, C, D, E and F) between the months of March 2021 and June 2021, using sampling air pump connected an open face holder on Whatman glass fiber filter (pore size 0.45µ, diameter 47mm), operated at 1.5 L/min for a period of 8h at a height of 1.5 m above the ground level during workday.

#### *Determination of Metallic dust particles in paint workshops:*

In the present study, heavy metals lead (Pb), cadmium (Cd), Zinc (Zn), were measured in the particulate matter in the paint furniture workshops, for a period of 30 days. Particulate matter was collected using the filtration technique. The filters were then extracted using concentrated HNO<sub>3</sub> (86 to 71 %) and the metallic constituents of TSP were determined by using Atomic Absorption Spectrophotometer (A.A.S). (Perkin-Elmer double beam 2380 atomic absorption spectrometer was used with adapted Perkin-Elmer hollow-cathode lamps and conventional 10-cm slot burner head for an air-acetylene

flame).

#### *Statistical analysis:*

The results were statistically evaluated using SPSS (version 22) (Core Team, 2025). On the other hand, Bray-Curtis cluster analysis based on general characters, of the workshops evaluated was performed.

## **Results and Discussion**

Tables (2 and 3) show the results to represent the monthly concentrations of PM<sub>10</sub> and PM<sub>2.5</sub> inside the six paint workshops evaluated. The mean concentrations of PM<sub>10</sub> in painting furniture workshops (B < A < C < D < F < E) was 26.85 µg/m<sup>3</sup>, 32.85 µg/m<sup>3</sup>, 33.83 µg/m<sup>3</sup>, 34.74 µg/m<sup>3</sup>, 41.55 µg/m<sup>3</sup> and 44.41 µg/m<sup>3</sup>, respectively, (Fig. 1). The highest concentration of PM<sub>10</sub> is observed in Spray paint workshop (D) is 61 µg/m<sup>3</sup>, whereas the lowermost of PM<sub>10</sub> was 14.7 µg/m<sup>3</sup> in Varnishing paint workshop (B), (Fig. 2).

Whereas, the monthly mean amounts of particulate matter < 2.5 microns (PM<sub>2.5</sub>) inside the paint furniture workshop, PM<sub>2.5</sub> was 39.5 µg/m<sup>3</sup>, 43.75 µg/m<sup>3</sup>, 70 µg/m<sup>3</sup>, 72 µg/m<sup>3</sup>, 119.25 µg/m<sup>3</sup> and 125 µg/m<sup>3</sup>, respectively (B < C < A < D < E < F) (Fig. 3). The highest concentration of PM<sub>2.5</sub> was observed in Spray paint workshop (F) was 134 µg/m<sup>3</sup>, whereas the lowermost of PM<sub>2.5</sub> was 32 µg/m<sup>3</sup> in varnishing paint workshop (B), (Fig. 4).

As can be observed, the mean concentrations of PM<sub>2.5</sub> and PM<sub>10</sub> were considerably higher than the World Health Organization's 24-hour mean PM<sub>10</sub> limits (50 µg/m<sup>3</sup>), which resulted in more severe adverse pulmonary effects. One significant risk factor for pulmonary epithelial barrier failure was exposure to PM<sub>2.5</sub>. Chen et al. (2019) provided evidence that exposure to SPPMs, particularly SPPM1, may raise the chance of developing pulmonary dysfunction. Additionally, Yi-Chun et al. (2019) showed that pulmonary dysfunction in human normal bronchial epithelial cells is caused by ambient concentrations of spray paint particle matter.

Table (4) shows the monthly mean concentrations of TSP inside the paint workshops (A < C < B < D < E < F) was 359 µg/m<sup>3</sup>, 359.41 µg/m<sup>3</sup>, 362.84 µg/m<sup>3</sup>, 370.31 µg/m<sup>3</sup>, 384.88 µg/m<sup>3</sup> and 410 µg/m<sup>3</sup>,

respectively, (**Fig 5**). The highest concentration of TSP was observed in Spray paint workshop (**F**) was  $489 \mu\text{g}/\text{m}^3$ , whereas the lowermost concentration of TSP was  $229 \mu\text{g}/\text{m}^3$  in varnishing paint workshop (**B**), (**Fig 6**). Because the coarsest fractions are removed by gravity, the finest dust size was found when the compressor was not running, whereas the coarsest dust size is created during emery operations (**Black, 2015**).

The concentrations of suspended particulates measured for paint furniture workshops exceed the maximum concentrations recorded at many cities in the world, and also exceed the ambient air quality standards of the Egyptian and U.S.A ambient air quality standard ( $230 \mu\text{g}/\text{m}^3$ ) (**EEAA, 1994**) the U.S.A standard ( $260 \mu\text{g}/\text{m}^3$  for 24 h.) (**Dara, 1993; Chuitha et al., 2014**), and exceed the WHO Air Quality guideline ( $120 \mu\text{g}/\text{m}^3$  for 24 h.) (**WHO, 2024**). PM spray painting particles exposure enters the human body via respiration, able to enter the lungs are extremely small, their incredibly huge surface area makes it easier for them to interface with the respiratory epithelium's mucosa (**Zhao et al., 2015**). This PM may react with proteins, nucleic acids, and cell membranes, resulting in more severe pathogenic alterations and a loss of respiratory function epithelia. Lung cancer, chronic obstructive pulmonary disease (COPD), acute respiratory tract infections, and a host of cardiovascular disorders can result from this. Because they cause significant oxidative stress and inflammatory reactions, ultra-fine particles are particularly harmful (**Gao et al., 2015**).

For outside samples, the mean concentrations obtained for each of particulates;  $\text{PM}_{10}$  and  $\text{PM}_{2.5}$  and TSP samples outside the paint furniture workshop were (39.5, 43.75, 70, 72, 119.25 and 125)  $\mu\text{g}/\text{m}^3$ , respectively, (**B < C < A < D < E < F**) (**Fig.7**). These outcomes indicate that the source, which is likely vehicular emission and population activities. These results were confirmed by **Martins et al. (2019)** by documenting that it would be better to spray outside because painting requires enough ventilation. The painting inside, however, requires that a well-ventilated location be selected, that any objects or areas be taped and covered, and that the following safety equipment be worn: respirator mask, gloves, coveralls, eye protection, or at least long sleeves and pants.

Table (2): Monthly Mean Concentrations of  $\text{PM}_{10}$  ( $\mu\text{g}/\text{m}^3$ ) in the Paint Workshops Evaluated during the Study Period.

Workshops	A	B	C	D	E	F
Monthly Mean						
1 <sup>st</sup> Month	29.15	26.83	33.41	32.97	45.15	42.63
2 <sup>nd</sup> Month	36.53	24.86	34.63	39.52	46.92	36.13
3 <sup>rd</sup> Month	32.88	28.88	33.45	31.73	41.16	45.91
Mean	32.85	26.85	33.83	34.74	44.41	41.55
S. D.	8.43	6.83	4.90	7.93	7.78	10.24
Max. Conc.	51.1	37.1	42.1	44.1	61	56.8
Min. Conc.	19.8	14.7	25.4	20.9	27.7	19.6

Table (3): Monthly Mean Concentrations of  $\text{PM}_{2.5}$  ( $\mu\text{g}/\text{m}^3$ ) in the Paint Workshops Evaluated during the Study Period.

Workshops	A	B	C	D	E	F
Monthly Mean						
1 <sup>st</sup> Month	64	32	35	67	123	134
2 <sup>nd</sup> Month	79	35	36	78	113	129
3 <sup>rd</sup> Month	68	37	45	68	124	110
4 <sup>th</sup> Month	69	54	59	75	117	127
Mean	70	39.5	43.75	72	119.25	125
S. D.	6.92	9.18	10.58	6.19	8.81	11.99
Max. Conc.	79	54	59	78	124	134
Min. Conc.	64	32	35	67	113	110

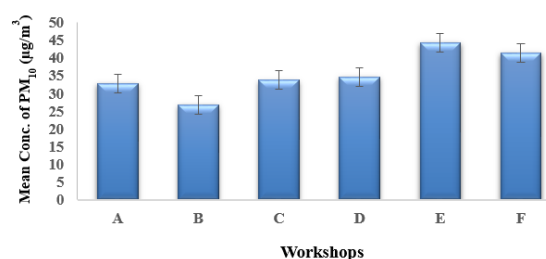


Fig. (1): Mean of  $\text{PM}_{10}$  Concentrations  $\pm$  standard deviation in the Paint Workshops Evaluated

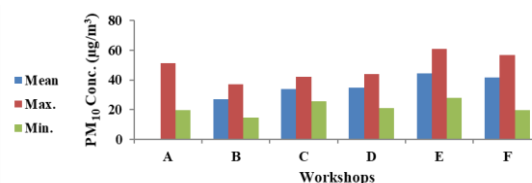


Fig. (2): Mean, Maximum and Minimum Concentrations of  $\text{PM}_{10}$  in the Paint Workshops Evaluated

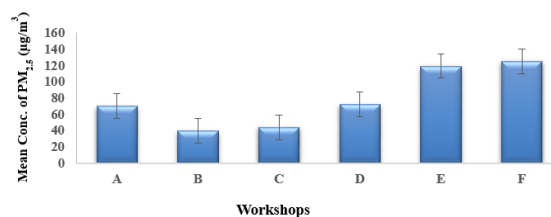


Fig. (3): Mean of  $\text{PM}_{2.5}$  concentrations  $\pm$  standard deviation in the Paint Workshops Evaluated

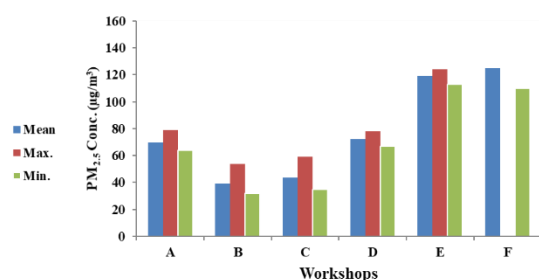


Fig. (4): Mean, Maximum and Minimum Concentrations of PM<sub>2.5</sub> in the Paint Workshops Evaluated.

Table (4): Monthly Mean Concentrations of TSP (µg/m<sup>3</sup>) in the Paint Workshops Evaluated during the Study Period.

Workshops	A	B	C	D	E	F
<b>Monthly Mean</b>						
<b>1<sup>st</sup> Month</b>	294.125	334.125	352.875	412.375	365	434.25
<b>2<sup>nd</sup> Month</b>	341.25	363.375	342.375	397.625	404.75	405.625
<b>3<sup>rd</sup> Month</b>	404.875	390.875	363.125	338.875	389.25	385.375
<b>4<sup>th</sup> Month</b>	395.75	363	379.25	332.375	380.5	414.75
<b>Mean</b>	359.00	362.84	359.41	370.31	384.88	410.00
<b>S. D.</b>	65.78	70.74	53.84	46.44	35.60	46.47
<b>Max. Conc.</b>	477	476	482	455	465	489
<b>Min. Conc.</b>	243	229	232	286	320	328

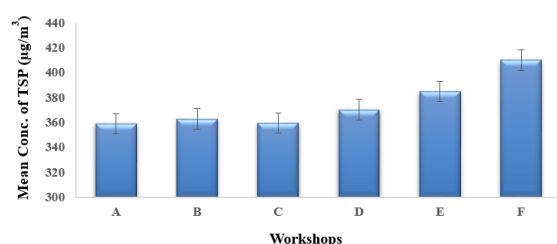


Fig (5): Mean of TSP concentrations± standard deviation in the Paint Workshops Evaluated

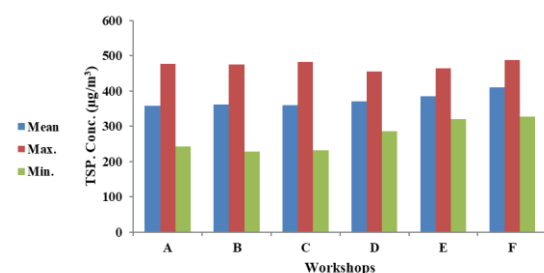


Fig. (6): Mean, Maximum and Minimum Concentrations of (TSP) in the Paint Workshops Evaluated.

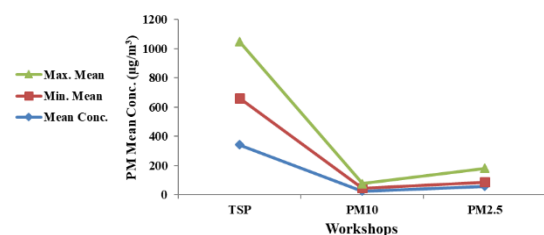


Fig. (7): PM Concentrations of TSP, PM<sub>10</sub> and PM<sub>2.5</sub> Outside of Paint Workshops Evaluated during the Study Period

The high variation is explained by the different activities, and the way that each employee utilized the products, that every paint shop is a distinctive setting with varying shop sizes, locations, and chemical types and structures (Table 1). It is noticed, the high mean particulate concentration in spray paint workshops (E and F) is due to the high density of painting furniture works, lack of ventilation and non-using dust control and exhaust ventilation systems. Whereas, the low mean particulate concentration which recorded in varnishing paint workshops (A and B) is due to good ventilation, also the low density of works plays a role in the minimizing the concentration from other workshops (Fig. 8), (El-Gammal and Niazy, 2000; Hafez, 2017 and Hagraas et al., 2017).

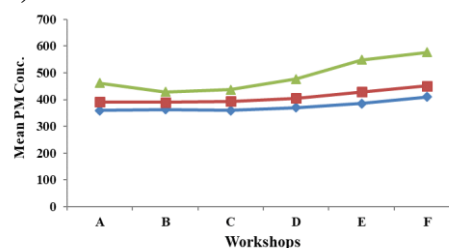


Fig. (8): Mean Concentrations of TSP, PM<sub>10</sub> and PM<sub>2.5</sub> inside the Paint Workshops Evaluated During the Study Period.

Table (5) and Figure (9) summarize the results of the mean, maximum, and minimum concentrations of TSP, PM<sub>10</sub> and

PM<sub>2.5</sub> was  $374.40 \pm 19.95$ ,  $35.71 \pm 6.34$  and  $78.25 \pm 36.51 \mu\text{g}/\text{m}^3$ , in paint workshops evaluated (A, B, C, D, E, F), during study period.

Table (5): Comparing Mean Concentration of TSP, PM<sub>10</sub> and PM<sub>2.5</sub> ( $\mu\text{g}/\text{m}^3$ ) during the Study Period in in the Paint Workshops Evaluated.

Workshop	TSP	PM <sub>10</sub>	PM <sub>2.5</sub>
A	359.00	32.85	70.00
B	362.84	26.85	39.50
C	359.40	33.83	43.75
D	370.31	34.74	72.00
E	384.87	44.41	119.25
F	410.00	41.55	125.00
Max. Mean	410.00	44.41	125.00
Min. Mean	359.00	26.85	39.50
Mean Conc.	374.40	35.71	78.25
S. D.	19.95	6.34	36.51

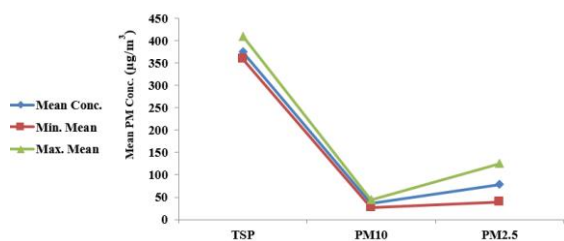


Fig. (9): Mean, Maximum, Minimum Concentrations of TSP, PM<sub>10</sub> and PM<sub>2.5</sub> during the Study Period.

The application of cluster analysis based on the different particulates for different pain furniture workshops (A, B, C, D, E and F). The results indicated that the paint workshops (D and F) form two separate groups left the other Varnishing paint workshops Varnishing A, B, C and Spry paint (E) as similar group in evaluated (Fig.10). These workshops have similar characters, which may be the reason to form a group.

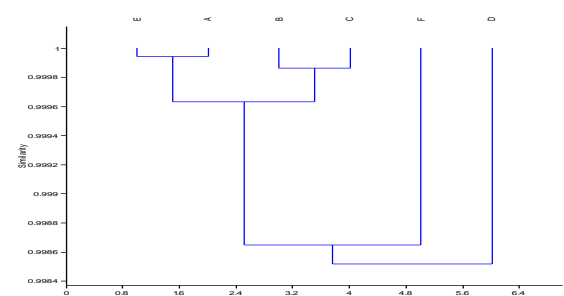


Fig. (10): Bray-Curtis Cluster Analysis Based on General Characters of Paint Workshops Evaluated (A, B, C, D, E and F) in a Residential Area, Al-Shoaraa at Damietta City, Egypt.

### Metallic Constituents of Particulate Matter:

Table (6) provides heavy metals dust of (Pb), (Cd), and (Zn), inside paint workshops evaluated (A, C and E) for a period of 30 days. The results show that the daily mean concentrations of (Pb) ranged from (19.16  $\mu\text{g}/\text{m}^3$  to 10.89, 13.03 to 7.88, 22.45 to 14.53)  $\mu\text{g}/\text{m}^3$ , respectively, in the workshop evaluated, during the study period. The highest daily concentrations of Pb was  $22.45 \mu\text{g}/\text{m}^3$ , recorded in workshop (E) at a highly working day density, whereas the lowermost amounts of Pb was  $10.23 \mu\text{g}/\text{m}^3$  in varnishing paint workshop (C). (Pb) is a heavy metal commonly found in the environment and main component of paints. It is probably the most serious atmospheric heavy metal pollutant (Martins et al., 2019; Vergara-Murillo et al. 2022; Abdrabouh et al, 2023; Simatupang et al. 2024). It is clear that the levels of lead particulates in painting furniture workshops in Damietta City were higher than the recommended air quality standards of ( $1 \mu\text{g}/\text{m}^3$  for 1 yr) recommended by Egypt (EEAA, 1994).

For the results of cadmium (Cd), concentrations show the daily mean ranged from (5.35 to 11.92  $\mu\text{g}/\text{m}^3$ ), (4.10 to 7.13  $\mu\text{g}/\text{m}^3$ ), and (6.88 to 12.6  $\mu\text{g}/\text{m}^3$ ) in workshops evaluated (A, C and E), respectively, during the study period. The highest daily concentration of Cd was  $12.6 \mu\text{g}/\text{m}^3$ , found in workshop (E), while the lowest concentration of Cd was  $4.10 \mu\text{g}/\text{m}^3$ , recorded in workshop (C). For the results of Zinc (Zn), concentrations show the daily mean ranged from (13.54 to 6.79  $\mu\text{g}/\text{m}^3$ , 8.91 to 5.46  $\mu\text{g}/\text{m}^3$  and 18.66 to 9.90  $\mu\text{g}/\text{m}^3$ ), respectively, at workshops evaluated, during the study period. The highest daily concentration of Zn was  $18.66 \mu\text{g}/\text{m}^3$ , found at workshop (E), while the lowest concentration of Zn was  $6.46 \mu\text{g}/\text{m}^3$ , recorded at workshop (C). Zinc chromate or zinc yellow is used widely in the metal and painting industries (Flyvholm, 1991). As the likelihood of industrial sources for Zn is not found, so the high Zn concentration detected at painting furniture workshops, which emitted Zn from using chemicals in painting processes. Zinc is one of the metals whose oxides can result in acute and reversible syndrome (Plum et al., 2010; Akafuah et al., 2016).

Table (6): Mean Concentrations of Heavy Metals, Pb, Cd and Zn in SPM in Paint Furniture Workshops Evaluated (A, C and E) in ( $\mu\text{g}/\text{m}^3$ )

Workshops	A			C			E		
Element	Pb	Cd	Zn	Pb	Cd	Zn	Pb	Cd	Zn
Sample No.									
2	10.89	5.35	6.79	7.88	4.10	5.46	14.53	6.88	9.90
4	13.83	5.87	8.67	9.81	4.84	7.68	16.77	8.61	12.54
7	17.58	7.98	11.98	10.21	6.88	8.78	18.98	8.88	16.87
9	19.16	11.92	13.54	13.03	7.13	8.91	22.45	12.6	18.66
Mean	15.37	7.78	10.25	10.23	5.74	7.71	18.18	9.24	14.49
S. D.	3.73	2.99	3.07	2.12	1.50	1.60	3.38	2.41	4.00

The metal elements in particles (SPM) on all sampling days of Pb, Cd, Zn in the workshop evaluated (A) were  $15.37 \pm 3.73$ ,  $7.78 \pm 2.99$ ,  $10.25 \pm 3.07 \mu\text{g}/\text{m}^3$ , for workshop (C) was  $10.23 \pm 2.12$ ,  $5.74 \pm 1.50$ ,  $7.71 \pm 1.60 \mu\text{g}/\text{m}^3$ , whereas, for workshop (E) was  $18.18 \pm 3.38$ ,  $9.24 \pm 2.41$ ,  $14.49 \pm 4.00 \mu\text{g}/\text{m}^3$ , respectively (**Table 7**). In comparing of dust heavy metal; Pb, Cd, Zn Pb concentration for paint workshop evaluated (A, C, E). The highest concentrations of Pb were ( $18.18 \mu\text{g}/\text{m}^3$ ) recorded at workshop (E). However, the lowest concentrations of Pb were ( $10.23 \mu\text{g}/\text{m}^3$ ), recorded at workshop (C). The highest concentrations of Cd were ( $9.24 \mu\text{g}/\text{m}^3$ ) recorded at workshop (E). However, the lowest concentrations of Cd were ( $5.74 \mu\text{g}/\text{m}^3$ ), recorded at workshop (C). The highest concentrations of Zn were ( $14.49 \mu\text{g}/\text{m}^3$ ) recorded at workshop (E). However, the lowest concentrations of Zn were ( $1.60 \mu\text{g}/\text{m}^3$ ), recorded at workshop (C). These results were according to work intensity in painting furniture workshops. This is confirmed by **Pandey et al. (1998)** and **Khan et al. (2021)**. Furthermore, **El-Gammal (2008)** who documented, as the primary source of lead pollution in the Damietta City area does not appear to be heavy industry or lead smelters.

Table (7): Mean Concentration of Heavy Metals; Pb, Cd and Zn ( $\mu\text{g}/\text{m}^3$ ) in SPM in the Paint Workshops Evaluated (A, C and E)

Workshop	Pb	Cd	Zn
A	15.36	7.78	10.24
C	10.23	5.73	7.70
E	18.18	9.24	14.49
Max. Mean	18.18	9.24	14.49
Min. Mean	10.23	5.73	7.70
Mean Conc.	14.59	7.59	10.82
S. D.	4.03	1.76	3.43

#### *Distribution of the Heavy Metals (%) in SPM in the Painting Workshops Evaluated (A, C and E):*

The distribution of the mean percentage amounts of (Pb, Cd and Zn) in the sampling sites (painting furniture workshops) was evaluated for (A, C and E), as shown in **fig. (11)**. Results showed that the exposure to spray paintings in furniture workshops could participate in significant elevation of Cd and Pb concentrations in samples obtained from workshops evaluated. Pb% constituted of SPM increased by 46%, 43% and 43% for painting workshops (A, C and E), respectively, however, Cd % was 23%, 24% and 22 %, respectively. However, the percent of Zn mean concentrations was 31%, 33% and 35 %, respectively.

It was clearly noticed that the Pb percent was the highest percent between the evaluated metals (Pb, Cd, Zn) at the paint workshops (A, C and E). This is due to the fact that paints are one of the most notable environmental sources of lead, with the main source of lead in paints being the usage of lead-based compounds throughout the manufacturing process (**Yusuf, 2017**). The high occurrence of the three metals (Pb, Cd, Zn) in the particulates samples due to exposure to intense painting vapors, consequently, they represented an integral part of components in several paints, where Pb has anticorrosive properties, help in fast drying and increase durability with fresh appearance, additionally, pigments containing Cd are characterized by bright colors (**Flora et al., 2012**). The percentage diversity of Pb, Cd, and Zn concentrations in particulate measurement in the workshops is associated with differences in the work environment, including shop size and location, work practices, workload, and chemical structure; solvent type and toxicity;



and the amount, duration, and route of exposure, all of which are unfortunately undetectable due to technical limitations.

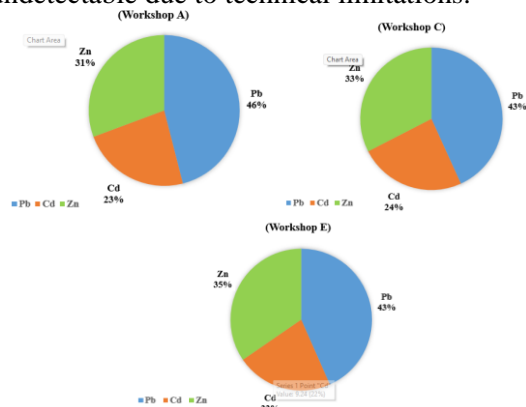


Fig. (11): Distribution of the Heavy Metals, (Pb, Cd, Zn) % in SPM in the Paint Workshops Evaluated (A, C and E).

Because of the risks that pollutants pose to human health and the environment, many countries have implemented regulations to control their emissions. These regulations usually set pollution limits for particular industries, such as painting (Gupta et al., 2018).

### Conclusion and Recommendation:

The present study focuses on the evaluated the workshops involving spray paint and varnishing based on the concentrations of dust that might generate in paint workshops' indoor air and the metal elements in particles. Data revealed the high variation related to the exposure of spray paintings in furniture workshops could participate in significant elevation of Cd and Pb concentrations in samples obtained from workshops evaluated was explained by the different activities, and the method that each worker utilized the products that every paint workshop is a different setting with varying sizes, locations, and types of chemicals used.

To improve air quality and reduce health impacts in paint workshops, we then recommend increasing local ventilation, replacing solvent-based products with water-based ones, and establishing procedures for keeping the containers closed after use. Spray paint's ingredients must be changed from hazardous to ecologically benign due to environmental concerns

### References

- Abdel Maksoud, N., Abdel Aal, K., Ghandour, N., EL-baz, M and Shaltout, E. (2018). Assessment of hematotoxicity and genotoxicity among paint workers in Assiut Governorate: a case control study. *Egypt. J. Foren.Sci.*, 8 (6), 1-11.
- Abdrabouh, A. E., Hagra, A. E., Essam, N. M., El-Gammal, M. I. (2023). Related health hazards with occupational exposure to cadmium and lead during spray painting in car and furniture workshops. *Journal of Environmental Sciences*, 52(3), 1-8.
- Agency for Toxic Substances and Disease Registry (ATSDR). (2012). Toxicological profile for Manganese. U. S. Department of Health and Human sciences, Atlanta, GA.
- Akafuah, N. K., Poozesh, S., Salaimah, A., Patrick, G., Lawler, K. and Saito, K. (2016). Evolution of the automotive body coating process-A review. *Coating*, 6(2), 24.
- Black, J. B. (2015). Toxicity value1000 workshop processes practices and materials, 5th ed., 9781138784727. Published by Taylor & Francis.
- Chen, Y. C., Lin, C. H., Lung, S. C., Ku-F, C., Wang, W. V., Chou, Cheng-Tai, Lai, C. H. (2019). Environmental concentration of spray paint particulate matters causes pulmonary dysfunction in human normal bronchial epithelial BEAS-2B cell. *Process Safety and Environmental Protection*, 126, 250-258.
- Chong, C. (2020). Comparing Solvent-Based and Water-Based Coatings. 12-16.
- Chuhitha, S., Viswa Kumar, R., Chandra Mohan, V., Madhavi, K. and Prabhakar Rao, P. (2014). The study of hepato- renal profile associated with lead toxicity in spray painters. *J. Evol. Med. Dent. Sci.*, 3(31), 8697-8703.
- Core Team R. (2025). A language and environment for statistical computing. R. Foundation for Statistical Computing, Vienna, Austria. <https://www.R-project.org/> for Statistical Computing, Vienna, Austria., Version 4.4.3 (2025-02-28), 11-95.
- Damietta Governorate (PAISDT). (2023). Public Damietta Governorate Diwan.
- Dara, S. S. (1993). "A text-book of environmental chemistry and pollution control". S. Chand & Company LTD, 1st ed., Ram Nagar, New Delhi, India, pp.1-57.
- Egyptian Environmental Affairs Agency (EEAA). (1994): Law No. 4, 1994 which was amended by Law No. 9 of 2009 for the Protection of the Environment: Promulgating the environmental law and its executive regulation. Egypt, pp. 53.
- EL-Gammal, M. I. (2008). Assessment of formaldehyde, ammonia and wood dust effects

- on the workers' health during wood working processing. *J. Soc. Zool.*, 56, 261-280.
- El-Gammal, M. I. and Niazy, A. S. (2000). A study of health hazards on painters in spray painting furniture workshops in Damietta city, Egypt. *J. Environ. Sci.*, 20, 107-124.
- Flora, G., Gupta, D. and Tiwari, A. (2012). Toxicity of lead: A review with recent updates. *Interdiscip. Toxicol.*, 5 (2), 47-58.
- Flyvholm, M. A. (1991). Contact allergens in registered chemical products. *Contact Dermatitis*, 25, 49-56.
- Gao, X., Yawen, W., Shiqi, P., Bin, Y., Caimei, F., Weiyi, C. and Xiaona, L. i. (2015). Comparative toxicities of bismuth oxybromide and titanium dioxide exposure on human skin keratinocyte cells. *Chemosphere*, 135, 83-93.
- Garaga, R. (2024). Health Risk Assessment of Different Sources of Metals in PM10 and PM2.5 in the Largest City in Northeast India, *Journal Article. Journal of Hazardous, Toxic, and Radioactive Waste*, 28 (2).
- Gupta, G., Chellappan, D. K., de Jesus Andreoli Pinto, T., Hansbro, P. M., Bebawy, M. and Dua, K. (2018). Tumor suppressor role of miR-503. *Panminerva Med.*, 60, 17-24.
- Hafez, N. M. (2017). Environmental hazards arising from the painting processes. Ph. D. Thesis, Faculty of Science, Mansoura University, pp. 65-90.
- Hagras, A. E., El-Gammal, M. I., Abdrabouh, A. E. and Essam, N. M. (2017). Exposure to Airborne Particles and Organic Solvents Among Painting Workers. *J. Env. Sci., Toxicology and Food Technology*, 10, 26-38.
- Halmo, L and Nappe, T. M. (2024). Lead Toxicity. Pennsylvania: StatPearls Publication, Treasure Island, chapter 5, Bookshelf ID: NBK541097.
- Huang, C. L., Bao, L. J., Luo, P., Wang, Z. Y., Li, S. M., Zeng, E. Y. (2016). Potential health risk for residents around a typical e-waste recycling zone via inhalation of size-fractionated particle-bound heavy metals. *J Hazard Mater*, 317, 449-456.
- Hussain, M. Sh. (2024). Chemistry of Paint (1), Experiment Findings. *Catalent Cell&Gene Therapy J.* DOI: 10.13140/RG.2.2.30304.08963 I 10.1007/s11356-018-2669-8.
- Ifjen, I. H., Maliki, M., Odi, H. D., Odiachi, I. J., Aghedo, O. N., Ohiocheoya, E. B. (2022). Review on Solvents Based Alkyd Resins and Water Borne Alkyd Resins: Impacts of Modification on Their Coating Properties. *Chemistry Africa. The Tunisian Chemical Society and Springer Nature Switzerland AG*, 5 (3).
- International Agency for Research on cancer (IARC). (1989). Some organic solvents, resin monomers and related compounds, pigments and occupational exposures in paint manufacture and painting. *IARC Monogr. Eval. Carcing. Risks chem. Hum.*, 47.
- Khan, M. R., Ahmad, N., Ouladsmame, M. and Azam, M. (2021). Heavy metals in acrylic color paints intended for the school children use: A potential threat to the children of early age. *Molecules*, 26, 2375.
- Lai, C. H. and Yan, T. Y. (2016). Characteristics and aerosol size distributions of metal-containing paint particles at a spray-painting workplace *RSC Advances*, 114 (6), 113754-113761.
- Lai, C. H., Lin, C. H., Liao, C. C. (2017). Respiratory deposition and health risk of inhalation of particle-bound heavy metals in the carbon black feeding area of a tire manufacture. *Air Qual Atmos. Health*, 10, 1281-1289.
- Lai, C. H., Lin, C. H., Liao, C.C., Chuang, K. Y., Peng, Y. P. (2018). Effects of heavy metals on health risk and characteristic in surrounding atmosphere of tire manufacturing plant, Taiwan. *RSC Adv.*, 8, 3041-3050
- Lin, C. H., Lai, C. H., Peng, Y. P, Wu, P. C., Chuang, K. Y, Yan, T. Y., Xiang, Y. K. (2018). Comparative health risk of inhaled exposure to organic solvents, toxic metals, and hexavalent chromium from the use of spray paints in Taiwan. *Environmental Science and Pollution Research*, 33, 33906-33916.
- Liu, X., Song, H., Lei, T., Liu, P., Xu, C., Wang, D., Yang, Z., Xia, H., Wang, T., and Zhao, H. (2021). Effects of natural and anthropogenic factors and their interactions on dust events in Northern China. *Catena*, 196, 104919.
- Lu, R., Harigaya, S., Ishimura, T., Nagase, K. Miyakoshi, T. Ishimura, T. (2004). Development of a fast drying lacquer based on raw lacquer sap. *Progress in Organic Coatings*. 51 (3), 238-243.
- Martins, M. E., Priscia, F. B., Neemias, E. S., Paula, T. R., Renata, S. S., Isreal, F., Elisa, R. F., Andreia, S. F., Ronald, S. M., Izabela, B. M. and Sergio, M. C. (2019). BTEX in an occupational environment. *Int. J. Environ. Impacts*, 2 (2), 174-191.
- McKeown, N. J. ( 2011). *Medscape Reference. www.emedicine.com.*, volume 40, 1193-1205.
- National Occupational Health and Safety Commission (NOHSC). (1999). National Guidance Material for Spray Painting, Spray painting and surface coating. Australian workplaces free from injury and disease, Annual Report, 1999-2000, Commonwealth of Australia 2000 ISSN 0818-3627, [www.nohsc.gov.au](http://www.nohsc.gov.au).
- National Research Council (NRC). (1991). Public Health and Hazardous Wastes Environmental

- Epidemiology. Volume; 1, Research Council (US) Committee on Environmental Epidemiology. Washington (DC): National Academies Press (US).
- Pandey, P. K., Patel, K. S. and Šubrt, P. (1998). Trace elemental composition of atmospheric particulate at Bhilai in central-east India. *Sci. Total Environ.*, 215, 123-134.
- Plum, L. M., Rink, L. and Haase, H. (2010). The Essential Toxin: Impact of Zinc on Human Health. *International Journal of Environmental Research and Public Health (IJERPH)*, 7 (4), 1342-65.
- Ratnasingam, J., Ioras, F., Hunm, O. C., Manikam, M. and Farrokhpayam, S. R. (2009). Dust-emission from abrasive sanding processes in the Malaysian wooden furniture industry. *J. Applied Sci.*, 9, 3770-3774.
- Ratnasingam, J., Natthondan, V., Ioras, F. and McNulty, T.(2010). Dust, Noise and Chemical Solvents Exposure of Workers in the Wooden Furniture Industry in South East Asia. *J. Appl. Sci.*, 10 (14), 1413-1420.
- Ruan, T. and Rim, D. (2019). Indoor air pollution in office buildings in megacities: effects of filtration efficiency and outdoor air ventilation rates. *Sustain Cities Soc.*, 49, 101609.
- SafeWork (NSW). (2022). Spray painting and powder coating. code of practice, 5-54. Website [www.safework.nsw.gov.au](http://www.safework.nsw.gov.au) © Copyright SafeWork NSW 2022.
- Schurr, J. M. and Allison, S. A. (1981). Polyelectrolyte contribution to the persistence length of DNA. *Journal of Biopolymers*, 20, (2), 251-268.
- Sefiane, K. (2014). Patterns from drying drops. *Journal of Advances in colloid and interface sciences*. 206, 372-381.
- Simatupang, M. M., Veronika, E., Irfandi, A., Azteria, V. (2024). Potential Impacts of Lead On Health: A Review of Environmental Exposure, Population at Risk, And Toxic Effects. *Journal of Environmental Health*. 16 (3), 277-288.
- Stoye, D. and Freitag, W. (1998). (eds) In: *Paints, coatings and solvents*. 45-46.
- Thorud, S., Merete, G., Ellingsena, Dag G. and Molanderab, P. (2005). Air formaldehyde and solvent concentrations during surface coating with acid-curing lacquers and paints in the woodworking and furniture industry. *J. Environ. Monit.*, 7, 586-591.
- Veleva, L. (2012). *Protective Coatings and Inorganic Anti-Corrosive Pigments*, (Chapter 28), n book: *Paint and Coatings Testing Manual Book*, MNL 17 (pp.282-299), 2nd ed., Publisher: ASTM International, OH, USA. <https://www.researchgate.net/publication/261176552>.
- Vergara-Murillo, F., Martinez-Yanez, K., Fortich-Revollo, A., Paternina-Cacedo, A., and Johnson-Restrepo, B. (2022). Biochemical and Hematological Markers in Workers with Chronical Exposure to Lead and Cadmium in Colombia. *Toxics*, 10, 524.
- World Health Organization (WHO). (2024). *Environment, Climate Change and Health department, Air quality, energy and Health Unit*, Geneva, 6th ed. (6.1).
- Yi-Chun, C., Chia-Hua, L., Shih-Chun, C. L., Ku-Fan, C., Wen-Cheng, V. W., Cheng-Tai, C. and Chia-Hsiang, L. (2019). Environmental concentration of spray paint particulate matters causes pulmonary dysfunction in human normal bronchial epithelial BEAS-2B cell. *Process Safety and Environmental Protection*, 126, 250-258.
- Yusuf, A. (2017). Assessment of Levels of Heavy Metals in Paints from Interior Walls and Indoor Dust from Residential Houses in Nairobi City County, Kenya. *Ch. Sci. Int. J.*, 21 (1), 1-7.
- Zhao, F., Huan, M., Liang, Y., Bing, W. and Yuliang, Z. (2015). Nanosurface chemistry and dose govern the bioaccumulation and toxicity of carbon nanotubes, metal nanomaterials and quantum dots in vivo. *Science Bulletin*, 60 (1), 3-20.

## الملخص العربي

### عنوان البحث: التركيز البيئي لجسيمات الطلاء وغبار المعادن في ورش طلاء الأثاث

مي إبراهيم الجمال<sup>١</sup>، محمود سالم إبراهيم<sup>١</sup>، عليّة عبد الشكور<sup>٢</sup>، نيفين الجمال<sup>٣</sup>، رهام شريف الحناوي<sup>١</sup>

<sup>١</sup>قسم علوم البيئة، كلية العلوم، جامعة دمياط، دمياط، مصر  
<sup>٢</sup>قسم تلوث الهواء، المركز القومي للبحوث، القاهرة، مصر  
<sup>٣</sup>قسم شئون البيئة، محافظة دمياط، مصر

اهتمت هذه الدراسة بالقياسات البيئية للجسيمات الناتجة عن أعمال الدهانات بورش طلاء الأثاث ، وكذلك قياس العناصر الثقيلة حيث يعتبر غبار الدهانات المتطاير الناتج عن الرش من أهم المخاطر البيئية الناتجة عن ورش دهانات الخشب نظرا لما تحتويه من مذبذبات عضوية وعناصر ثقيلة وبالتالي وضع التوصيات والاقتراحات للحد من هذه المخاطر الصحية.

وقد تمت الدراسة والقياسات في ست ورش لدهانات الأثاث (A, B, C, D, E and F) بمدينة دمياط - قرية الشعراء وهي تنتم بورش عمل صغيرة الحجم في اماكن ذات كثافة سكانية عالية والشوارع بينها ضيقة، وقد تمت قياسات جسيمات  $PM_{10}$  ،  $PM_{2.5}$  باستخدام جهاز قياس الأثرية (كاسيلا). وكذلك تم تجميع عينات من الجسيمات العالقة الكلية (TSP) باستخدام مضخة هواء لأخذ العينات وتم قياس المعادن الثقيلة (الرصاص ، الكاديوم ، الزنك) بالجسيمات العالقة (TSP) باستخدام مطياف الامتصاص الذري (A.A.S). أشارت نتائج الدراسة إلى أن متوسط تركيزات  $PM_{10}$  تراوحت بين ٢٦,٨٥ ، ٤٤,٤١ ميكروجرام/م<sup>٣</sup>، على التوالي. بينما تراوحت متوسط تركيزات  $PM_{2.5}$  بين ٣٩,٥ ، ١٢٥ ميكروجرام/م<sup>٣</sup>، على التوالي. وأوضحت النتائج أن متوسط تركيزات TSP يتراوح بين ٣٥٩ و ٤١٠ ميكروجرام/م<sup>٣</sup>. ورُصدت معظم جسيمات الطلاء (PM) بتركيزات غير مسموح بها. بينما أظهرت النتائج أن متوسط قياس تركيزات المعادن الثقيلة (الرصاص، والكاديوم، والزنك) في ورش طلاء الأثاث فكان (١٠,٨٢، ٧,٥٩، ١٤,٥٩) ميكروجرام/م<sup>٣</sup>، على التوالي.

وبذلك أوضحت الدراسة بعض التأثيرات البيئية في ورش طلاء الأثاث من خلال التعرض للملوثات منها الجسيمات والعناصر الثقيلة مما يعرض العمال وسكان المناطق المحيطة بالورش لمخاطر التعرض لتلك الملوثات. وبناء على ذلك تم وضع الاقتراحات والتوصيات اللازمة من قبل الدراسة الحالية في محاولة للتقليل من هذا الأثر السلبي حفاظا على بيئة العمل وجودة الهواء والاقبال من الانبعاثات للحد من الآثار البيئية والصحية على العمال وسكان المنطقة الناتجة عن عمليات دهانات الاثاث في بعض الورش بمدينة دمياط.

## Land Use- Land Cover Utilization by Egyptian Fruit Bats at Nile Valley and Delta, Egypt

Reem El-Gamal<sup>\*1</sup>, Alaa El-Din Sallam<sup>2</sup>, Rana O. Khayat<sup>3</sup> and Basma M. Sheta<sup>1</sup>

<sup>1</sup>Zoology Department, Faculty of Science, Damietta University, Damietta, Egypt

<sup>2</sup>Zoology Department, Faculty of Science, Suez Canal University, Ismailia, Egypt

<sup>3</sup>Biology Department, Faculty of Science, Umm Al-Qura University, Makkah, Saudi Arabia

Received: 22 April 2025 /Accepted: 20 June 2025

\*Corresponding author's E-mail: reemibrahem\_pg@science.suez.edu.eg

### Abstract

This study investigates the spatial distribution and land cover utilization patterns of the Egyptian fruit bat (*Rousettus aegyptiacus*) across six governorates in the Nile Valley and Delta, Egypt. Using 15 km<sup>2</sup> buffer zones to represent the average nightly foraging range of breeding colonies, we analyzed land use/land cover (LULC) composition derived from ESRI 2020 Global Land Cover Data. Results revealed significant variability in LULC composition among governorates, with cropland dominating Menoufia and Ismailia, built-up areas prevalent in Giza, and water bodies most abundant in Damietta. A strong positive correlation ( $r = 0.995$ ) was observed between mean bat body mass and the percentage of water bodies, highlighting the importance of water availability for this species. While the study is primarily descriptive due to limitations such as a single LULC observation per governorate and a small sample size for body mass analysis ( $n=6$ ), it provides valuable insights into the adaptability of *R. aegyptiacus* to diverse landscapes, mainly agricultural and urban environments. These findings underscore the potential influence of water resources on body mass and suggest that cropland and urban areas may serve as important foraging habitats. Future research should focus on larger sample sizes and multi-year data collection to better understand the ecological drivers influencing *R. aegyptiacus* distribution and body condition, ultimately informing conservation strategies for this ecologically significant species.

**Keywords:** LULC (Land Use/Land Cover), *Rousettus aegyptiacus*, Habitat Selection, Buffer Zones, Foraging Range

### Introduction

The Egyptian fruit bat (*Rousettus aegyptiacus*) is a large, widely distributed bat species native to Africa and the Middle East, renowned for its

ecological significance as a primary seed disperser and pollinator (Ramírez-Francel et al., 2022). This species exhibits remarkable dietary flexibility, feeding on a wide range of fruits, including cultivated species like figs, dates, and guavas, as well as nectar and pollen. Consequently, *R. aegyptiacus* plays a vital role



in maintaining ecosystem health, contributing to forest regeneration and the pollination of numerous plant species (Del Vaglio et al. 2011; Lučan et al. 2016).

*R. aegyptiacus* is known for its adaptability to diverse habitats, ranging from natural environments such as woodlands, savannahs, and forests to anthropogenic landscapes including agricultural lands, orchards, and even urban parks (Hulva et al. 2012; Kafash et al. 2022; Majumdar et al. 2016; Roberts et al. 2016). These bats often form large, stable colonies, roosting in caves, rock crevices, buildings, and occasionally in dense foliage (Shehata et al. 2015). Their nightly foraging flights can extend up to 15 km, representing the average nightly foraging range and a significant area of influence on the surrounding ecosystem (Del Vaglio et al. 2011; Dechmann et al. 2010). The ability to utilize a variety of habitats and food sources has contributed to the widespread distribution of *R. aegyptiacus*, but it also exposes the species to a range of environmental pressures (Ramírez-Fráncel et al. 2022).

Despite their adaptability, *R. aegyptiacus* faces increasing threats from habitat loss and fragmentation caused by human activities such as agricultural expansion, urbanization, and persecution (Aziz et al. 2021; Frick et al. 2020). The conversion of natural habitats to monoculture farming reduces foraging opportunities and disrupts natural ecosystem processes. Urbanization, with its associated habitat destruction and light pollution, can fragment bat populations and alter their foraging behavior. Additionally, persecution due to perceived agricultural damage further threatens local populations (Aziz et al. 2021; Frick et al. 2020). Understanding the ecological factors influencing *R. aegyptiacus* habitat selection within their normal flight range is crucial for developing effective conservation strategies.

Land cover composition is a key determinant of habitat suitability for many wildlife species, including bats. The availability and spatial distribution of different land cover types, such as forests, agricultural lands, and urban areas, can directly impact bat foraging behavior, roosting site selection, and overall population dynamics (Meyer et al. 2015). For *R. aegyptiacus*, which exhibits a wide dietary range and adaptability to various landscapes, the relationship between land cover and habitat use within their normal flight range is

particularly complex. While previous studies have documented the presence of *R. aegyptiacus* in diverse habitats (Fleming and Racey 2010; Hutson et al. 1992), the specific land cover characteristics influencing their distribution and habitat selection in Egypt remain poorly understood.

The Nile Valley and Delta, the study's focal region, is one of Egypt's most agriculturally productive and densely populated areas. The region supports diverse land cover types, including croplands, urban areas, water bodies, and fragmented natural vegetation. However, rapid urbanization and agricultural expansion have led to habitat fragmentation, posing significant challenges for wildlife dependent on these ecosystems. This study aims to fill this gap by analyzing the land cover composition within the average nightly foraging range of *R. aegyptiacus* breeding colonies and examining potential factors influencing their body mass. By doing so, it contributes to a better understanding of the ecological requirements of *R. aegyptiacus* and informs conservation efforts for this important species in Egypt.

## Material and method

### Data Preparation

**Morphometric and Roost Size Data:** Data about mean body mass, forearm length, and tibia length were collected from a sample size of 10 bats per colony at each of the six study sites. Roost size estimates were also recorded.

### Occurrence Point Data:

The precise geographical locations of *R. aegyptiacus* breeding colonies were determined using data obtained from previous field surveys, as detailed in (El-Gamal et al. 2025) from November 2022 to March 2024. These surveys, which covered six governorates across the Nile Valley and Delta, provided the occurrence records used in both the present study and our previous MaxEnt modeling effort. These colony locations were formatted as a shapefile, with each point representing a colony and containing accurate latitude and longitude coordinates. The occurrence point data was added to ArcGIS version 10.8.

### *Land Use/Land Cover (LULC) Data:*

Land use/land cover data were acquired from the ESRI 2020 Global Land Cover Data. This dataset provided a classified representation of the land surface, categorizing land cover into six distinct classes: Bare ground, Built areas, Crops, Rangeland, Trees, and Water. The spatial resolution of the LULC data was 10 meters. The LULC data was added to ArcGIS version 10.8 for subsequent analysis.

### *Create Buffers*

To assess the land cover composition within the average nightly foraging range of *R. aegyptiacus*, 15 km<sup>2</sup> circular buffer zones were generated around each documented breeding colony location. This buffer size was selected to represent the approximate average nightly foraging range of *R. aegyptiacus* (Del Vaglio *et al.*, 2011; Dechmann *et al.*, 2010). The "Buffer" tool within the Analysis toolbox of ArcGIS version 10.8 was used. The occurrence point layer was selected as the input feature, and a new polygon layer representing the buffer zones was created. The buffer distance was set to a fixed radius of 15 km<sup>2</sup>.

### *Overlay Analysis*

To determine the land cover composition within each buffer zone, the "Spatial Join" tool within the Analysis toolbox of ArcGIS version 10.8 was used. The buffer zone polygon layer was selected as the target feature, and the LULC data layer was selected as the join feature. The "Spatial Join" tool was used to add information about the LULC contained within each buffer polygon to the buffer layer's attribute table, ensuring all original buffer polygons were retained.

### *Analysis and Interpretation*

#### *Calculating Area:*

A new field, "Area\_sqkm" was added to the attribute table of the output buffer layer. The field calculator within ArcGIS version 10.8 was used to calculate the area of each polygon in square kilometers.

#### *Summarize by LULC:*

The "Summarize" tool within ArcGIS version 10.8 was used to calculate the total area (km<sup>2</sup>) of each land cover class within each buffer zone and across all buffer zones. The percentage of each land cover class within each buffer zone was calculated by dividing the area of each class by the total area of the buffer zone (15 km<sup>2</sup>) and multiplying by 100. The total area and percentage of each land cover class across all six governorates were also calculated. Mean percentages and standard deviations of land cover classes were calculated across the six governorates.

### *Data Analysis and Visualization:*

The calculated area (km<sup>2</sup>) and percentage of each land cover class were tabulated for each governorate (Table 1). The total area and percentage of each land cover class across all six governorates were calculated (Table 2). Mean percentages and standard deviations of land cover classes were calculated across the six governorates (Table 3). The mean morphometric measurements ( $\pm$  SEM) of *R. aegyptiacus* and associated land cover percentages at six colony sites across Egypt (Table 4). The spatial distribution of land cover classes was visualized using a land use/land cover map (Figure 1). A pie chart was created to visualize the percentage of each land cover class within each governorate (Figure 2), facilitating a comparative analysis of land cover distribution across the study area.

In R studio, correlation analysis was conducted to examine relationships between mean body mass, forearm length, tibia length, roost size, and land cover percentages using the `cor()` function. Linear regression models were constructed to assess the predictive power of morphometric and land cover variables on mean body mass and forearm length using the `lm()` function. Analysis of variance (ANOVA) and the Kruskal-Wallis test were performed to test differences in morphometric measures across governorates. Data was visualized using a pie chart generated in R using the `ggplot2` package.

## **Results**

The spatial distribution and composition of land cover types within 15 km<sup>2</sup> buffer zones surrounding *R. aegyptiacus* breeding colonies were investigated across six Egyptian

governorates: Aswan, Damietta, Fayoum, Giza, Ismailia, and Menoufia. The geographical locations of these governorates within Egypt are presented in **Figure 1**, providing a fundamental

spatial framework for the study. The overall land use/land cover (LULC) patterns for the study region are depicted in **Figure 1**, providing a spatial context for the subsequent analyses.

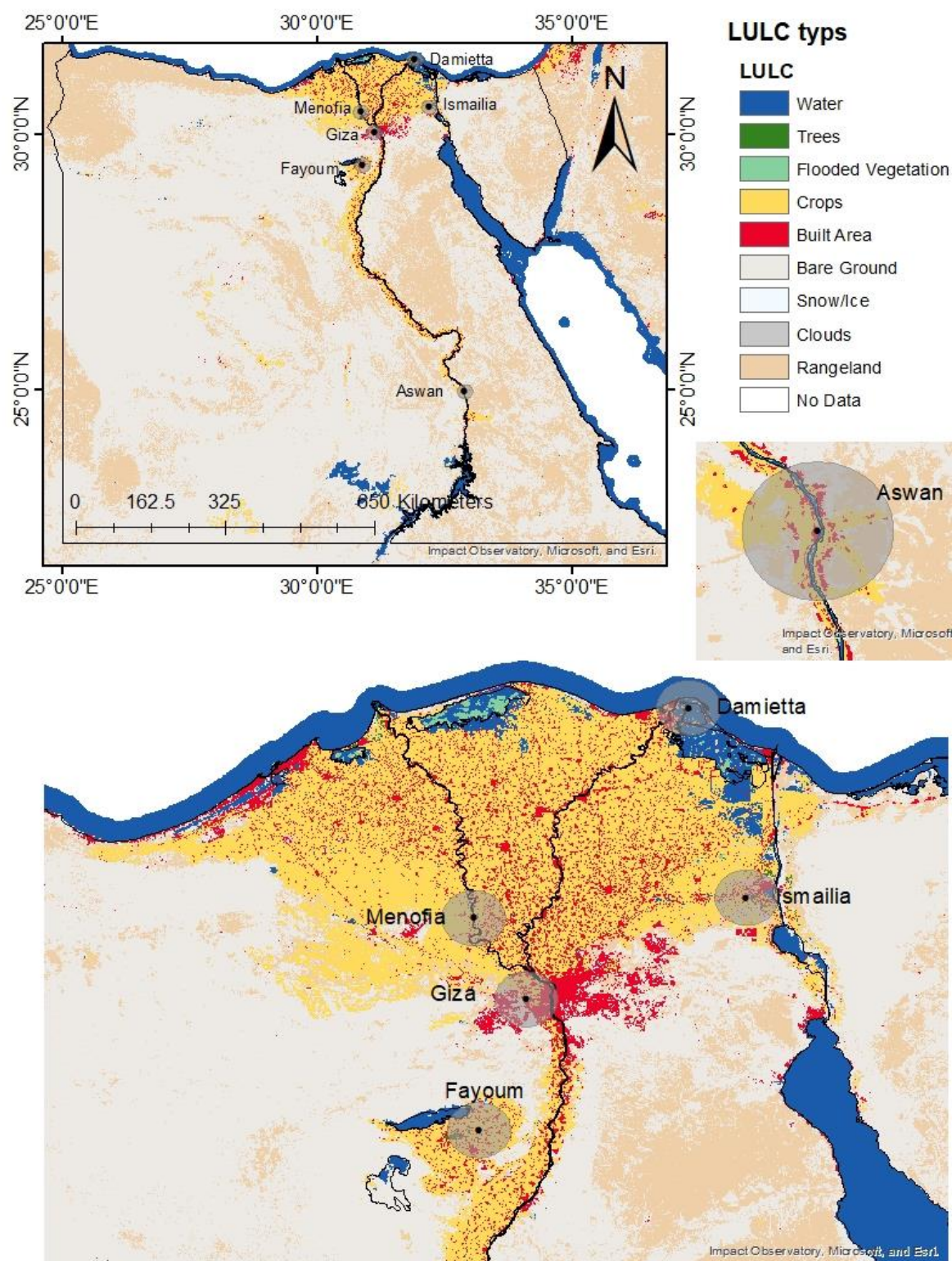


Figure 1: Distribution of land use/land cover types within 15 km<sup>2</sup> buffers around Egyptian fruit bat (*Rousettus aegyptiacus*) maternity roost, illustrating the landscape context of reproductive sites.

**Table 2** presents the total area (km<sup>2</sup>) and percentage of each land cover type within the

combined buffer zones across all six governorates. Cropland emerged as the dominant land cover, constituting 65.50% of the total buffered area (2029.61 km<sup>2</sup>). Build areas accounted for 24.70% (766.67 km<sup>2</sup>), followed by bare ground at 15.40% (477.30 km<sup>2</sup>). Rangeland, water, and trees represented smaller proportions of the total land cover, at 8.50%, 5.00%, and 0.60%, respectively.

Table 1: Land Cover Composition within 15 km<sup>2</sup> Buffer Zones by Governorate

Governorate	Water (%)	Trees (%)	Crops (%)	Built-up (%)	Bare Ground (%)	Rangeland (%)
Menoufia	1.76	0.10	85.62	11.21	0.21	1.09
Giza	1.80	0.00	22.97	51.57	20.06	3.58
Ismailia	1.79	1.26	55.74	17.12	10.73	13.36
Fayoum	5.68	1.04	76.44	12.88	3.52	0.44
Damietta	8.13	0.00	6.55	8.57	1.14	0.85
Aswan	2.69	0.16	39.96	7.16	31.90	18.10

A detailed breakdown of land cover composition within each governorate is presented in **Table 1**. This table provides the area (km<sup>2</sup>) and percentage of each land cover type within the 15 km<sup>2</sup> buffer zone for each governorate. **Figure 2** visually represents the percentage of each land cover type within each governorate, allowing for a direct comparison of land cover distribution among locations.

**Figure 2** and **Table 1** reveal distinct patterns of land cover distribution. Menoufia exhibited the highest percentage of cropland (85.62%), followed by Ismailia (55.74%). Giza was dominated by building areas, constituting 51.57% of the buffered area. Aswan showed a significant proportion of bare ground (31.90%) and the highest percentage of rangeland (18.10%). Damietta had the highest percentage of water bodies (8.13%). Fayoum showed a moderate percentage of crops (76.44%). The spatial distribution of these land cover types, as shown in **Figure 1**, aligns with the patterns observed in **Table 1**.

The overall mean percentage and standard deviation ( $\pm$  SD) of land cover types across the six governorates are presented in **Table 3**. Cropland had the highest mean percentage (28.11%) but also exhibited the greatest variability (SD = 35.46%). This high variability corresponds to the distinct differences in cropland percentages observed across the governorates in **Figure 2** and **Table 1**, with Menoufia and Ismailia showing significantly higher proportions. The mean percentage of built-up areas (20.10%) in **Table 3** reflects the

dominance of built-up areas in Giza, as observed in **Figure 2** and **Table 1**. The relatively low mean percentages of rangeland and trees in **Table 3** align with the low proportions observed in most governorates in **Figure 2** and **Table 1**.

Table 2: Total land cover composition within 15 km<sup>2</sup> buffer zones surrounding study sites, showing the total area (km<sup>2</sup>) and percentage of each land cover type. Cropland is the dominant land cover.

Type of Landcover	total area of each Landcover type within buffer zones km2	Percentage of Total Area
crops	2029.61211	65.50%
build areas	766.66714	24.70%
bare ground	477.298427	15.40%
rangeland	264.221532	8.50%
Water	154.444258	5.00%
Trees	18.079252	0.60%
Total	3100.32	100.00%

The dominance of cropland, as shown in **Table 2**, is further illustrated in **Figure 1** and **Figure 2**, where Ismailia and Menoufia exhibited particularly high percentages. The spatial distribution of build areas, as shown in **Figure 1**, corresponds to the high percentages observed in Giza, Ismailia, and Menoufia and the overall percentage in **Table 2**.

Table 3: Descriptive statistics showing the mean percentage and standard deviation for each land cover type across the six study governorates.

landcover	Mean Percentage (%)	Standard Deviation (%)
Bare ground	13.78	12.301738
building	20.104	18.880758
crops	28.106	35.458607
Rangeland	4.94	5.494834
trees	3.2338	3.33817
water	19.104	19.172588

Due to the inherent limitation of having a single percentage observation per land cover type within each governorate, further inferential statistical analyses were not feasible. Therefore, the results presented herein are primarily descriptive, focusing on the observed trends in land cover composition as visually represented in **Figure 1**, and **Figure 2**, and quantitatively summarized in **Table 1**, **Table 2**, and **Table 3**. **Table 4** presents the mean morphometric measurements ( $\pm$  SEM) of *R. aegyptiacus* and associated land cover percentages at six colony sites across Egypt. The data reveals variations in body mass, forearm length, head, body length and tibia length among the different governorates. Notably, Damietta exhibited the highest mean body mass ( $152.93 \pm 3.99$  g),

while Menoufia had the lowest ( $103.75 \pm 4.89$  g).

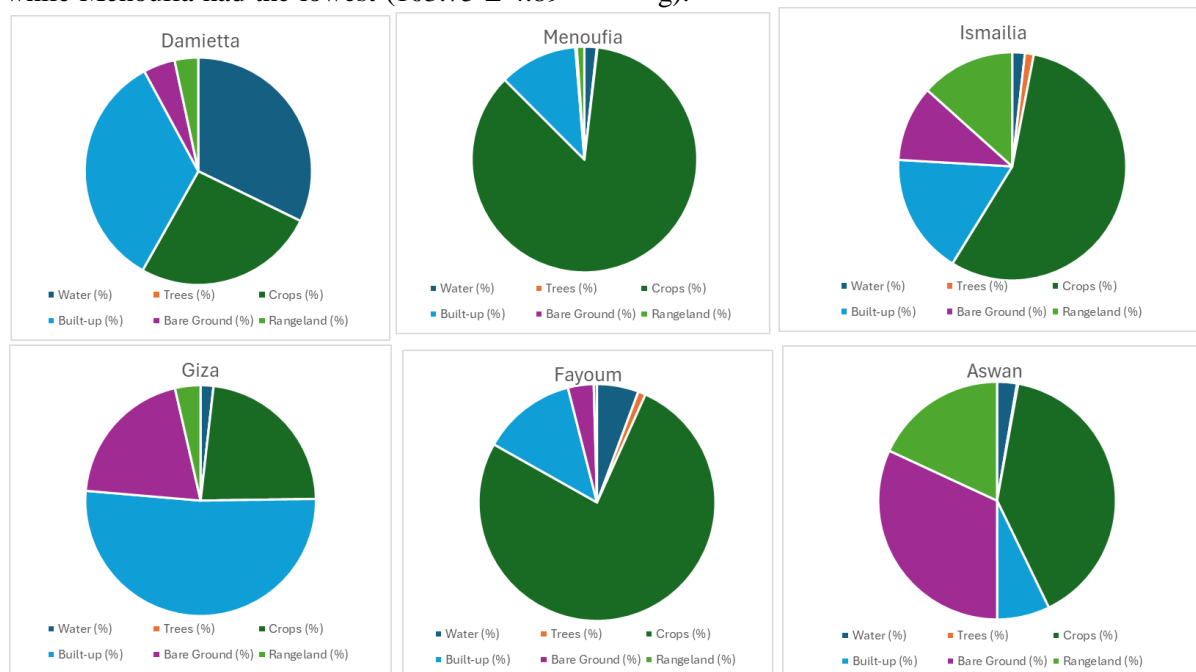


Figure 2 :Percentage of land cover types within 15 km² buffer zones surrounding Egyptian fruit bat (*Rousettus aegyptiacus*) breeding colonies.

Table 4: Mean Morphometric Measurements ( $\pm$  SEM) of *Rousettus aegyptiacus* and Associated Land Cover Percentages at Six Colony Sites Across Egypt. Symbol '\*' indicates that at least one pairwise comparison for that variable was significant ( $p < 0.05$ ) based on the post-hoc Tukey's HSD test. Sample size ten individuals at each site.

Governorate	Mean body size/mass (gm)	Forearm Length (mm)	Head (mm)	Body Length (mm)	Tibia Length (mm)	Roost size	Percentage Cropland	Percentage Building	Percentage Water
Damietta	$152.93 \pm 3.99^*$	$96.07 \pm 0.8^*$	$47.02 \pm 0.4^*$	$171.2 \pm 3.17^*$	$28.16 \pm 3.08^*$	2500	6.55	8.57	8.13
Menoufia	$103.75 \pm 4.89$	$79.62 \pm 1.36$	$42.23 \pm 0.53$	$152.88 \pm 1.89$	$33.8 \pm 1.95$	400	85.62	11.21	1.76
Ismailia	$106.3 \pm 11.95$	$89.78 \pm 3.24^*$	$42.85 \pm 1.43$	$149.3 \pm 5.87$	$39.66 \pm 1.73$	3000	55.74	17.12	1.79
Giza	$106.11 \pm 13.37$	$89.92 \pm 1.66^*$	$43.33 \pm 0.71$	$147 \pm 3.46$	$40.54 \pm 1.17$	1200	22.97	51.57	1.8
Faiyum	$135.64 \pm 4.04$	$95.01 \pm 0.61^*$	$45.9 \pm 0.39^*$	$155 \pm 2.22$	$42.84 \pm 0.56^*$	1400	76.44	12.88	5.68
Aswan	$107.75 \pm 4.6^*$	$95.04 \pm 1^*$	$46.67 \pm 0.43^*$	$162.08 \pm 2.97^*$	$19.76 \pm 0.76^*$	640	39.96	7.16	2.69

Statistical analyses, employing both ANOVA and Kruskal-Wallis tests, demonstrated a statistically significant difference in mean body mass among the governorates ( $p < 0.05$ ; Table 4). Subsequent post-hoc Tukey's HSD tests indicated that the mean body mass in Damietta was significantly greater than that observed in Menoufia, Ismailia, Giza, and Aswan. Furthermore, Faiyum also presented significant differences in mean body mass when compared to other governorates.

Contrary to initial hypotheses, morphometric analyses also revealed statistically significant differences in forearm length, body length, and tibia length across the governorates ( $p < 0.05$ ; Table 4). Post-hoc Tukey's HSD tests identified significant pairwise differences for forearm

length in Damietta, Ismailia, Giza, Faiyum, and Aswan. Similarly, significant differences in body length were detected in Damietta and Aswan, and for tibia length in Damietta, Faiyum, and Aswan, based on the post-hoc analysis.

Correlation analysis revealed a strong positive correlation ( $r = 0.995$ ) between mean body mass and the percentage of water bodies. A moderate positive correlation ( $r = 0.62$ ) was observed between mean body mass and forearm length. Weaker correlations were observed between body mass and other variables, including cropland percentage and roost size.

Due to the limited sample size, governorate roost sites ( $n=6$ ), linear regression models encountered singularities and zero degrees of freedom, rendering them unreliable. Therefore,



regression analysis did not yield meaningful results in this study.

## Discussion

This study investigates the land cover utilization patterns of *R. aegyptiacus* across six governorates in the Nile Valley and Delta, Egypt, focusing on the relationship between land cover composition and body mass. The findings reveal significant variability in land cover types, with cropland dominating in Menoufia and Ismailia, built-up areas prevalent in Giza, and water bodies most abundant in Damietta. A strong positive correlation ( $r = 0.995$ ) between mean body mass and the percentage of water bodies underscores the importance of water availability for this species (Adams and Hayes 2021). However, the lack of a clear relationship between cropland percentage and body mass suggests that other factors, beyond land cover composition, influence body condition.

### *Cropland and Body Mass*

The absence of a correlation between cropland percentage and body mass may in bat populations, particularly for frugivorous species such as *R. aegyptiacus*, can be attributed to a confluence of interacting ecological and anthropogenic factors. First, the suitability and quality of cultivated crops as a food source for fruit bats are highly variable. Not all crops are metabolically beneficial or palatable to these species, and even preferred fruits demonstrate significant regional variation in nutritional value. Furthermore, the widespread application of pesticides in agricultural systems introduces contaminants into the bats' diet, potentially leading to direct toxicological effects, bioaccumulation, and subsequent impairment of physiological functions and energy reserves, thereby negatively impacting body condition. The designation of *R. aegyptiacus* as an agricultural pest in some regions also leads to direct human-induced mortality and disturbance, further complicating the relationship. Second, seasonal variability in fruit availability may influence foraging success, as crops may not be equally productive year-round. Third, competition among bats or other frugivorous species in high-cropland areas could reduce individual access to

resources (Bachorec et al. 2020; Palmeirim et al. 1989). Finally, environmental stressors, such as human disturbance or light pollution, may offset the benefits of abundant cropland. These factors highlight the complexity of the relationship between agricultural landscapes and bat ecology, warranting further investigation (Lučan et al. 2016).

### *Adaptability to Urban and Agricultural Landscapes*

The prevalence of built-up areas in Giza demonstrates the adaptability of *R. aegyptiacus* to urban environments. This adaptability likely stems from the availability of artificial roosting sites and alternative food sources in anthropogenic landscapes. Similarly, the dominance of cropland in Menoufia and Ismailia suggests that agricultural areas provide critical foraging habitats. However, the high variability in cropland percentages across governorates indicates that *R. aegyptiacus* can thrive in diverse environmental conditions, further emphasizing its ecological flexibility (Hulva et al. 2012; Kafash et al. 2022; Majumdar et al. 2016; Roberts et al. 2016).

### *Role of Water Bodies*

The strong correlation between water body percentage and *R. aegyptiacus* body mass suggests a critical role for water resources. While direct evidence linking water bodies to specific life cycle stages of this species in Egypt is limited, several hypotheses can explain this relationship. Firstly, water bodies provide essential drinking sources, particularly crucial in arid and semi-arid regions. Maintaining proper hydration directly influences physiological condition and thus body mass. Secondly, water bodies often support riparian vegetation, which can serve as foraging sites or corridors for bat movement. Thirdly, the presence of water may enhance insect abundance, providing an additional food source for *R. aegyptiacus* or attracting fruit bearing vegetation (Barclay et al. 2006). Furthermore, water bodies may influence bat behavior. For example, bats may concentrate on foraging activities near water sources to maximize resource availability. Proximity to water could also reduce foraging energy expenditure, allowing for better body condition. It is important to note that further targeted research



is needed to definitively establish the specific mechanisms through which water bodies influence *R. aegyptiacus* ecology in Egypt. However, the strong correlation observed aligns with broader ecological principles emphasizing the importance of water resources for bat populations, particularly in dry regions (Lučan et al. 2016). There are studies that have investigated methods of controlling populations of Egyptian fruit bats, due to them being considered a pest to fruit crops (Korine et al. 1999). These studies have investigated using water-based baits for population control (Taha and Soliman 2019). This highlights that these bats do utilize open water sources. This also highlights that their presence near water sources can bring them into conflict with humans, due to the proximity of farms and orchards to those water sources. Water bodies provide essential drinking sources, which are crucial for survival in arid and semi-arid regions like Egypt. Maintaining proper hydration directly impacts physiological condition and thus supports healthy body mass. This need is particularly acute for lactating females, who have significantly increased water requirements to produce milk (Adams and Hayes 2008; Korine et al. 2004).

### Conservation Implications

The findings underscore the importance of maintaining agricultural and urban habitats for *R. aegyptiacus*, particularly in regions where natural habitats are scarce. Protecting water bodies and mitigating human-wildlife conflicts, such as reducing persecution due to perceived agricultural damage, are critical for the species' long-term survival. Conservation strategies should focus on enhancing habitat quality and ensuring the availability of key resources, such as water and diverse food sources (Voigt and Kingston 2016).

### Conclusion

In conclusion, this study provides valuable insights into the land cover utilization patterns of *R. aegyptiacus* in the Nile Valley and Delta, Egypt. The findings underscore the species' adaptability to diverse landscapes, particularly agricultural and urban environments, and highlight the importance of water availability for body condition. While the study is primarily

descriptive due to limitations in sample size and data replication, it lays the groundwork for future research on the ecological drivers influencing *R. aegyptiacus* distribution and habitat selection. These findings have important implications for conservation strategies, particularly in regions experiencing rapid land cover change due to urbanization and agricultural expansion.

### References:

- Adams R A, Hayes MA (2008). Water availability and successful lactation by bats as related to climate change in arid regions of western North America. *Journal of Animal Ecology*, 77(6), 1115–1121. <https://doi.org/10.1111/J.1365-2656.2008.01447>.
- Adams R A, Hayes MA (2021). The Importance of Water Availability to Bats: Climate Warming and Increasing Global Aridity. 105–120. [https://doi.org/10.1007/978-3-030-54727-1\\_7](https://doi.org/10.1007/978-3-030-54727-1_7)
- Del Vaglio M A, Nicolau H, Bosso L. (2011). Feeding habits of the Egyptian fruit bat *Rousettus aegyptiacus* on Cyprus island: a first assessment, 22(2), 281–289. <https://doi.org/10.4404/Hystrix-22.2-4587>
- Aziz S A, McConkey K R, Tanalgo K, Sritongchuay T, Low M R., Yong J Y, Mildenstein T L, Nuevo-Diego C E, Lim V C, Racey P A (2021). The Critical Importance of Old-World Fruit Bats for Healthy Ecosystems and Economies. *Frontiers in Ecology and Evolution*, 9, 641411. <https://doi.org/10.3389/FEVO.2021.641411/BI-BTEX>
- Bachorec E, Horáček I, Hulva P, Konečný A, Lučan R K, Jedlička P, Shohdi W M, Řeřucha Š, Abi-Said M, Bartonička T (2020). Spatial networks differ when food supply changes: Foraging strategy of Egyptian fruit bats. *PLoS ONE*, 15(2), e0229110. <https://doi.org/10.1371/JOURNAL.PONE.0229110>
- Barclay R M, Barclay L E, Jacobs D S (2006). Deliberate insectivory by the fruit bat *Rousettus aegyptiacus*. *Acta Chiropterologica*, 8(2), 549–553. [https://doi.org/10.3161/1733-5329\(2006\)8\[549: DIBTFB\]2.0.CO;2](https://doi.org/10.3161/1733-5329(2006)8[549: DIBTFB]2.0.CO;2)
- Dechmann D K N, Kranstauber B, Gibbs D, Wikelski M (2010). Group Hunting-A Reason for Sociality in Molossid Bats? *PLOS one*, 5(2), e9012. <https://doi.org/10.1371/JOURNAL.PONE.0009012>
- El-Gamal R, El-Din Sallam A, Sheta B M (2025). Modeling The Spatial Distribution and Habitat

- Suitability of The Egyptian Fruit Bat (*Rousettus Aegyptiacus*) In Egypt. *Egyptian Journal of Zoology*.  
<https://doi.org/10.21608/EJZ.2025.349759.1128>
- Fleming T H, Racey P A (Eds.). (2010). *Island bats: evolution, ecology, and conservation*. University of Chicago Press.
- Frick W F, Kingston T, Flanders J (2020). A review of the major threats and challenges to global bat conservation. *Annals of the New York Academy of Sciences*, 1469(1), 5–25.  
<https://doi.org/10.1111/NYAS.14045>
- Hulva P, Marešová T, Dundarova H, Bilgin R, Benda P, Bartonička T, Horáček I (2012). Environmental margin and island evolution in Middle Eastern populations of the Egyptian fruit bat. *Molecular Ecology*, 21(24), 6104–6116.  
<https://doi.org/10.1111/mec.12078>
- Hutson A M, Mickleburgh S P, Racey P A (1992). Old world fruit bats: an action plan for their conservation. *Old World Fruit Bats: An Action Plan for Their Conservation*.  
<https://doi.org/10.2305/IUCN.CH.1992.SSC-AP.6.EN>
- Kafash A, Ashrafi S, Yousefi M (2022). Modeling habitat suitability of bats to identify high priority areas for field monitoring and conservation. *Environmental Science and Pollution Research*, 29(17), 25881–25891.  
<https://doi.org/10.1007/S11356-021-17412-7/FIGURES/6>
- Korine C, Izhaki I, Arad Z (1999). Is the Egyptian fruit-bat *Rousettus aegyptiacus* a pest in Israel? An analysis of the bat's diet and implications for its conservation. *Biological Conservation*, 88(3), 301–306.  
[https://doi.org/10.1016/S0006-3207\(98\)00126-8](https://doi.org/10.1016/S0006-3207(98)00126-8)
- Korine C, Speakman J, Arad Z (2004). Reproductive energetics of captive and free-ranging Egyptian fruit bats (*Rousettus aegyptiacus*). *Ecology*, 85(1), 220–230. <https://doi.org/10.1890/02-0632>
- Lučan R K, Bartonička T, Jedlička P, Rerucha Š, Šálek M, Čížek M, Nicolaou H, Horáček I (2016). Spatial activity and feeding ecology of the endangered northern population of the Egyptian fruit bat (*Rousettus aegyptiacus*). *Journal of Mammalogy*, 97(3), 815–822.  
<https://doi.org/10.1093/JMAMMAL/GYW014>
- Majumdar K, Majumder J, Datta B K (2016). Vegetation composition, structure and distribution status of trees used by two tropical fruit bat species in degraded habitats of Northeast India. *Zoology and Ecology*, 26(2), 63–76.  
<https://doi.org/10.1080/21658005.2016.1148978>
- Meyer C F J, Struebig M J, Willig M R, Meyer C F J, Struebig M J, Willig M R (2015). Responses of Tropical Bats to Habitat Fragmentation, Logging, and Deforestation. *Bats in the Anthropocene: Conservation of Bats in a Changing World*, 63.  
[https://doi.org/10.1007/978-3-319-25220-9\\_4](https://doi.org/10.1007/978-3-319-25220-9_4)
- Palmeirim J M, Gorchoy D L, Stoleson S (1989). Trophic structure of a neotropical frugivore community: is there competition between birds and bats? *Oecologia*, 79(3), 403–411.  
<https://doi.org/10.1007/BF00384321/METRICS>
- Ramírez-Fráncel L A, García-Herrera L V, Losada-Prado S, Reinoso-Flórez, G, Sánchez-Hernández A, Estrada-Villegas S, Lim B K, Guevara G (2022). Bats and their vital ecosystem services: a global review. *Integrative Zoology*, 17(1), 2–23.  
<https://doi.org/10.1111/1749-4877.12552>
- Roberts S H, Jacobs M D, Clark R M, Daly C M, Tsimijaly L H, Rossizela R J, Prettyman S T (2016). A review of the *Pteropus rufus* (É. Geoffroy, 1803) colonies within the Tolagnaro region of southeast Madagascar – an assessment of neoteric threats and conservation condition. *Madagascar Conservation & Development*, 11(1). <https://doi.org/10.4314/MCD.V11I1.7>
- Shehata M M, Chu D K, Gomaa M R, AbiSaid M, El Shesheny R, Kandeil A, Bagato O, Chan S M, Barbour E K, Shaib H S, McKenzie P P, Webby R J, Ali M A, Peiris M, Kayali G (2015). Surveillance for Coronaviruses in Bats, Lebanon and Egypt, 2013-2015. *Int J Infect Dis*, 39, 7–9.  
<https://doi.org/10.1016/j.ijheh.2007.10.003>
- Taha A, Soliman S (2019). Effect of  $\alpha$ -Chlorohydrin water-bait on the fertility of captive males of the Egyptian fruit-bat (*Rousettus aegyptiacus*) and the proper time for controlling its free-ranging populations in Egypt. *Egyptian Journal of Aquatic Biology and Fisheries*, 23(4), 227–237.  
<https://doi.org/10.21608/EJABF.2019.53599>
- Voigt C, Kingston T (2016). Bats in the Anthropocene: conservation of bats in a changing world. <https://doi.org/10.1007/978-3-319-25220-9>.

## الملخص العربي

عنوان البحث: استخدام الأراضي و الغطاء الأرضي بواسطة خفافيش الفاكهة المصرية في وادي النيل والدلتا، مصر

ريم الجمل\*<sup>١</sup>، علاء الدين سلام<sup>٢</sup>، رنا الخياط<sup>٣</sup>، بسمة شتا<sup>١</sup><sup>١</sup>قسم علم حيوان-كلية العلوم-جامعة دمياط-مصر.<sup>٢</sup>قسم علم حيوان-كلية العلوم-جامعة قناة السويس-مصر.<sup>٣</sup>قسم البيولوجي-كلية العلوم-جامعة ام القرى -السعودية.

تبحث هذه الدراسة في التوزيع المكاني وأنماط استخدام الغطاء الأرضي لخفاش الفاكهة المصري (*Rousettus aegyptiacus*) عبر ست محافظات في وادي النيل والدلتا، مصر. باستخدام مناطق عازلة بمساحة ١٥ كيلومترًا مربعًا لتمثيل متوسط نطاق البحث عن الطعام ليلاً لمستعمرات التكاثر، قمنا بتحليل تركيبة استخدام الأراضي/الغطاء الأرضي (LULC) المشتقة من بيانات الغطاء الأرضي العالمي لـ ESRI لعام ٢٠٢٠. كشفت النتائج عن تباين كبير في تركيبة استخدام الأراضي/الغطاء الأرضي بين المحافظات، حيث تهيمن الأراضي الزراعية على المنوفية والإسماعيلية، وتسود المناطق المبنية في الجيزة، بينما تكثر المسطحات المائية في دمياط. لوحظ وجود ارتباط إيجابي قوي ( $r = 0.995$ ) بين متوسط كتلة جسم الخفاش ونسبة المسطحات المائية، مما يسلط الضوء على أهمية توافر المياه لهذا النوع. رغم أن الدراسة وصفية في المقام الأول نظرًا لقيود مثل رصد واحد لتأثيرات استخدام الأراضي على مستوى المحافظة، وصغر حجم العينة المستخدمة في تحليل كتلة الجسم ( $n=6$ )، إلا أنها تقدم رؤية قيمة حول قدرة خفاش الفاكهة المصري على التكيف مع بيئات متنوعة، لا سيما البيئات الزراعية والحضرية. تُبرز هذه النتائج التأثير المحتمل لموارد المياه على كتلة الجسم، وتشير إلى أن الأراضي الزراعية والمناطق الحضرية قد تُشكل موائيل مهمة للبحث عن الطعام. ينبغي أن تُركز الأبحاث المستقبلية على عينات أكبر حجمًا وجمع بيانات على مدى سنوات متعددة لفهم العوامل البيئية المؤثرة على توزيع خفاش الفاكهة المصري وحالة جسمه بشكل أفضل، مما يُسهم في نهاية المطاف في وضع استراتيجيات للحفاظ على هذا النوع المهم بيئيًا.

## Heavy Metals in the Bottom Sediments of El Manzala Lagoon, Egypt: Assessment and Correlation with other Mediterranean Aquatic Ecosystems

Sherif M. El Baz<sup>1</sup>, M. M. Khalil<sup>1</sup>, A. H. El-Afandy<sup>3</sup>, A. Y. Nabet<sup>4</sup>, T.M. El-Katony<sup>2</sup>, Hoda R. Saad<sup>\*1</sup> and Mona A. El Harairey<sup>1</sup>

<sup>1</sup>Geology Department, Faculty of Science, Damietta University, New Damietta, Egypt.

<sup>2</sup>Botany and Microbiology Department, Faculty of Science, Damietta University, New Damietta, Egypt.

<sup>3</sup>Egyptian Nuclear Materials Authority, Cairo, Egypt.

<sup>4</sup>EIA Department Manager at Ghulaf Environmental Trading Est, Saudi Arabia.

Received: 14 April 2025 /Accepted: 29 April 2025

\*Corresponding author's E-mail: hodaragab@hotmail.com

### Abstract

Recently, an accurate monitoring for coastal lagoons becomes an urgent need to protect them from severe effects of pollution. The present study objects to evaluate the heavy metal pollution in one of the most important coastal lagoons in Egypt, called Manzala Lagoon (ML). The measured concentrations of heavy metals (HMs) reflect that  $Fe > Zn > Pb > Ni > Cu > Co > Cd$ . To evaluate the levels of contamination in the studied Lagoon, seven contamination indices are calculated, including contamination factor (Cf), Degree of contamination (Dc), Geo-accumulation index (Igeo), Pollution Load Index (PLI), enrichment factor (Ef), Ecological risk factor (Er) and Potential ecological risk factor (Ri). According to the Cf, the sediments are lowly polluted with Zn, Ni, Co, Cu and Fe, moderately polluted with Pb, and very highly polluted with Cd. The average value of Dc (15.96), indicating a considerable level of contamination. Furthermore, the average values of Ef point to minor enrichment for Ni and Cu, moderate enrichment for Zn and Co, severe enrichment for Pb, and extremely severe enrichment for Cd. The average value of Ri reaches 676.3, suggesting that the sediments have very high risk. Consequently, Cd and Pb are the principal contributors for the ecological risk in ML. Finally, the comparison between the concentrations of heavy metals in the Manzala Lagoon and other Mediterranean is done.

**Keywords:** Contamination indices; Heavy metals; Manzala Lagoon; Egypt; Mediterranean

### Introduction

Because of the harmful consequences on the

aquatic environment, pollution of coastal habitats is a global concern. Urbanisation, agricultural waste, industrial sewage, and other human activities can all contribute to pollution (e.g., Zenina, 2009; Tan et al., 2021; El Ouaty

et al., 2024). In this context, the northern coastal lagoons of Egypt (El Mariout, Edku, El Burullus, El Manzala, El Bardawil), were exposed to these stresses (e.g., El Nemr, 2003; Masoud et al., 2011; Shalaby et al., 2017; El Baz and Khalil, 2018; El-Amier et al., 2023). Heavy metals like Cd, Hg, Pb, Zn, As, Ni, and Cr are the most dangerous pollutants (e.g., Forstner and Wittmann, 1983; Selvaraj et al., 2004). Temperature, organic matter, pH, salinity, and bottom sediment types are some of the most important determinants of HM levels (e.g., Galanopoulou et al., 2009; Mallick et al., 2016).

It is well known that, the concentrations of metals in sediments are greater than those in water (Singer, 1977).

In relation to the assessment of pollution, many investigations pointed to the importance of evaluating the degree of contamination in different aquatic ecosystems in Africa (e.g., Ennouri et al., 2010; Masoud et al. 2011; Belabed et al., 2013; Abdul et al., 2019), Asia (e.g., Tan et al., 2021), Northern America (Alvarez Zarikian, 2000), Europe (e.g., Ruiz et al., 2004), and Australia (e.g., Roy and Crawford, 1984).

The current development project, that have been carried by the Egyptian government, led to the re-formation of the northern coastal lagoons, where many island, fish farms and aquatic macrophytes were removed. So, the total surface area and the depths of the lagoon increased (e.g., Abd Ellah, 2022). Thus, there is an urgent need to make a continuous assessment for the health of these lagoons during the different stages of the promising Egyptian project. The present study concentrates on assessing the heavy metal pollution in the ML. This investigation may act as a base for future comparative studies on ML after and before the development project. Accordingly, the present study objects (1) to estimate the concentrations of heavy metal in the bottom sediments of ML, (2) to compare these results with those previously recorded from ML and other aquatic ecosystems in the Mediterranean region, and (3) to assess the contamination levels in the studied sites.

## Study area

El Manzala Lagoon (ML) represents one of the most largest coastal lagoon in Egypt, locating in

the north-eastern part of the Nile Delta. It is placed between latitudes  $31^{\circ}07'N$  and  $31^{\circ}30'N$  and longitudes  $32^{\circ}17'E$  and  $31^{\circ}48'E$ . In addition, it is surrounded by four governorates; Port Said, Damietta, Al Dakahlia and Al Sharkia (Fig. 1). The northern sector of the lagoon is separated from the Mediterranean Sea by a sandbar, which permits the connection to the sea through artificial inlets. Furthermore, the entrance of freshwater to the lagoon is related to three canals (Ratma, Souffra, and Inaniya) in the western side and five drains (Hadous, Faraskour, Bahr El-Bakar, Ramsis and El-Serw) in the southern side. Accordingly, ML becomes a brackish lagoon due to the mixing of freshwater with marine water. Economically, it plays a vital role in the production of high amounts of fish.



Fig.1 location map of El Manzala Lagoon shows sample locations

Many studies the have been done on the pollution in ML (e.g., Badawy and Wahaab, 1997; Abdel-Satar and Genid, 2009; Shalaby et al., 2017; El Baz, 2017; Abdel Gawad, 2018; Redwan and Elhaddad, 2022). In this context, the study of Badawy and Wahaab (1997) concluded that, the level of Cr in the sediments recorded the highest concentration, followed by Zn, Cu, Ni, Pb and Cd. Moreover, Abdel-Satar and Genid (2009) arranged the order of heavy metals as follows; Fe (4460  $\mu g/g$ ), Mn (1334  $\mu g/g$ ), Pb (379.4  $\mu g/g$ ), Zn (207.8  $\mu g/g$ ), Ni (108.14  $\mu g/g$ ), Cu (90.99  $\mu g/g$ ), Co (38.8  $\mu g/g$ ), and Cd (10.61  $\mu g/g$ ). In addition, EL-Bady (2016) established that Fe has the highest concentration (1074.55 $\mu g/g$ ), followed by Zn (39.53 $\mu g/g$ ), Cu (31.21 $\mu g/g$ ), Ni (30.83 $\mu g/g$ ), Pb (0.077 $\mu g/g$ ) and Cd (1.67  $\mu g/g$ ). Goher et al. (2017) concluded that the sediments of ML were moderately polluted with Pb, Zn, Cd and Cu in most stations, but they are lowly contaminated with Fe and Mn. Abdel Gawad (2018) indicated that the concentrations of Fe have the highest concentrations (8342.47  $\mu g/g$ ), followed by Ni (40.73  $\mu g/g$ ), Zn (30.32  $\mu g/g$ ),

Cu (26.34  $\mu\text{g/g}$ ), Pb (0.244  $\mu\text{g/g}$ ) and Cd (0.0264  $\mu\text{g/g}$ ). Redwan and Elhaddad (2022) concluded that Fe has the highest concentration (14130  $\mu\text{g/g}$ ), followed by Cu, Zn (110  $\mu\text{g/g}$ ), Ni (60  $\mu\text{g/g}$ ), Pb (20  $\mu\text{g/g}$ ) and Cd (1.8  $\mu\text{g/g}$ ).

## Materials and methods

The current study was done on twenty six sites from ML, Egypt. These sites were chosen based on the degree of proximity to the drains or the Mediterranean Sea. Twenty six samples were collected, in December 2022, using a grab sampler from the bottom sediments of ML. At each site, sample was subdivided into two groups, one for the analysis of grain size and the second for heavy metals (HMs). These samples were saved in ice box and transported to the

laboratory. Some ecological parameters (salinity, depth and pH) were recorded during sampling. The environmental and geographical data for each station are shown in Table 1. To investigate the size of the bottom sediments, the standard method of Folk (1974) was applied on 26 sites. According to Liao et al. (2014), the digestion of sediment was done to measure the concentrations of seven metals (Fe, Cu, Zn, Co, Cd, Pb and Ni) in 20 sediment samples. The results of the environmental parameters of the lagoon and the concentrations of HMs were displayed on the distribution maps, using Arc Map. To assess the concentrations of HMs, some pollution indices, such as Cf, Dc, PLI,  $I_{\text{geo}}$ , Ef, Er, and Ri were calculated. Pearson's correlation coefficient was applied to determine the relationships between the measured metals.

Table 1. Coordinates of the studied sites and their measured environmental parameters.

Site no.	Lat. (N)	Long. (E)	Water depth (cm)	pH	Salinity (g/l)	Sand %	Silt %	Clay %
1	31° 21' 41"	31° 56' 11"	400	8.80	10.7	46	45	9
2	31° 21' 19"	31° 58' 01"	300	8.75	10.2	45	47	8
3	31° 21' 15"	31° 59' 20"	250	8.86	11.1	48	45	6
4	31° 21' 15"	32° 1' 09"	125	8.70	11.7	47	46	7
5	31° 20'	32° 2'	90	8.88	10.5	53	38	9
6	31° 18'	32° 6'	85	8.80	10.8	40	43	17
7	31° 17'	32° 6'	150	8.73	7.2	38	42	20
8	31° 17'	32° 2'	410	8.74	10.4	25	45	30
9	31° 19'	32° 1' 09"	450	8.75	10.1	26	43	31
10	31° 20'	31° 58' 01"	500	8.82	9.6	25	43	32
11	31° 20' 5"	31° 56' 11"	210	8.98	9.4	22	44	34
12	31° 18' 46"	31° 55' 56"	200	9.00	7.5	23	42	35
13	31° 19'	31° 57' 27"	250	8.81	9.2	25	45	30
14	31° 17'	32° 2' 29"	300	8.79	10.8	23	44	33
15	31° 16'	32° 7'	200	8.51	4.6	25	35	40
16	31° 13'	32° 7'	160	8.65	5.4	22	33	45
17	31° 14' 30"	32° 5'	100	8.52	5.3	12	38	50
18	31° 14'	32° 3'	150	8.41	4.3	1	39	50
19	31° 14' 42"	32° 2'	175	8.86	7.1	10	36	51
20	31° 15' 10"	32° 1' 36"	200	8.76	6.9	9	37	54
21	31° 15' 59"	32° 0' 56"	220	8.78	6.9	11	37	52
22	31° 15' 59"	31° 59' 13"	70	8.72	7	9	44	47
23	31° 16'	31° 58' 11"	250	8.88	8.6	10	42	48
24	31° 17'	31° 57' 09"	350	8.84	7.9	12	43	45
25	31° 17'	31° 55' 35"	150	9.00	5	10	44	46
26	31° 18'	31° 54' 10"	170	9.04	5.4	11	46	43

## Results

### Environmental parameters

The values of depth vary between the different sites, where the maximum depth reaches 5 m at site 10, and the minimum reaches 0.7 m at site 12, with an average of 2.27 m. It is clear that the central and north western parts of the lagoon

have the greatest depths (Table 1 and Fig. 2.a). The studied sites display different values of salinity, where the lowest value is 4.3 g/l at site 18 in the southern part, while the highest value is 11.7 g/l at site 4 in the northern part (Table 1), with an average of 8.21 g/l, indicating that the ML is brackish water and increased toward the Mediterranean Sea. In general, the northern sector has higher salinities than the southern sector (Fig. 2.b). Relatively small variations in the values of pH between sites are recorded,



where the highest value is 9.04 at site 26 in the western part, and the lowest is 8.51 at site 15 in the eastern part (Table 1 and Fig. 2.c), with an average of 8.78 reflecting that the lagoon is alkaline.

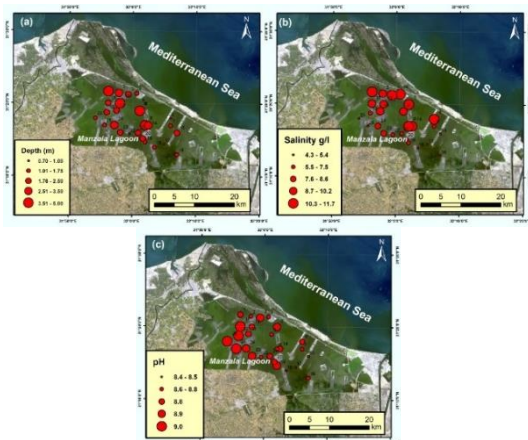


Fig. 2a shows the depth value of different sites at study area. a); fig.2b) shows salinity of different sites at study area; fig.2c) shows pH of different sites at study area.

The substrate of ML consists of a combination of sand, silt and clay (Table 1). The highest portions of sand covered the northern part due to entrance of sea water through the inlets (Fig. 3.a). The percentage of sand changes from 53% (site 5) to 9 % (sites 20 and 22). Also, the percentage of silt increases in the northern and western parts (Fig. 3.b). Generally, the invasion of drains, especially in the southern part, supplies the lagoon with higher portions of clay (Fig. 3.c). The lowest percentage of clay is 6 % (at site 3), while the highest is 52 % (at site 21).

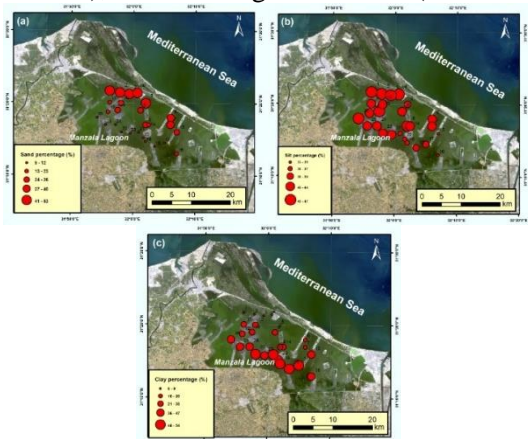


Fig.3a) shows the percentage of sand at different sites of study area.; fig.3b) shows the percentage of silt at different sites of study area; fig.3c) shows the percentage of clay at different sites of study area

### Concentrations of HMs in the sediments

Concentrations of Fe, Cu, Zn, Co, Cd, Pb and Ni are clarified in Table 2. For Fe, the maximum value is 43375.81  $\mu\text{g/g}$  at site 12, while the minimum is 1395.58  $\mu\text{g/g}$  at site 22 (Fig. 4.a), with an average of 15223.39  $\mu\text{g/g}$ . For Cu, the highest level is 48.01  $\mu\text{g/g}$  at site 12, while the lowest is 1.07  $\mu\text{g/g}$  at site 25 (Fig. 4.b), with an average of 16.94  $\mu\text{g/g}$ .

For Zn, the maximum level is 188.5  $\mu\text{g/g}$  at site 15, while the minimum is 6.43  $\mu\text{g/g}$  at site 25 (Fig. 4.c), with an average of 67.15  $\mu\text{g/g}$ . For Co, the maximum is 13.64  $\mu\text{g/g}$  at site 17, while the minimum is 2.37  $\mu\text{g/g}$  at site 25, with an average of 8.89  $\mu\text{g/g}$  as shown in Figure 5.a. For Cd, the maximum level is 9.71  $\mu\text{g/g}$  at site 1, while the minimum is 0.19  $\mu\text{g/g}$  at site 2, with an average of 3.88  $\mu\text{g/g}$  (Fig. 5.b). For Pb, the maximum is 117.15  $\mu\text{g/g}$  at site 5, while the minimum is 12.48  $\mu\text{g/g}$  at site 11 (Fig. 5.c), with an average of 20  $\mu\text{g/g}$ . For Ni, the maximum level is 94.51  $\mu\text{g/g}$  at site 23, while the minimum is 10.67  $\mu\text{g/g}$  at site 6 (Fig. 5.d), with an average of 45.6  $\mu\text{g/g}$ .

### Contamination indices

To estimate the degree of pollution in the lagoon, some indices could be calculated such as Cf, Dc,  $I_{\text{geo}}$ , Ef, Er and Ri (Table 3). Average shale (World geochemical background concentration) of Turekian and Wedepohl (1961) is used here.

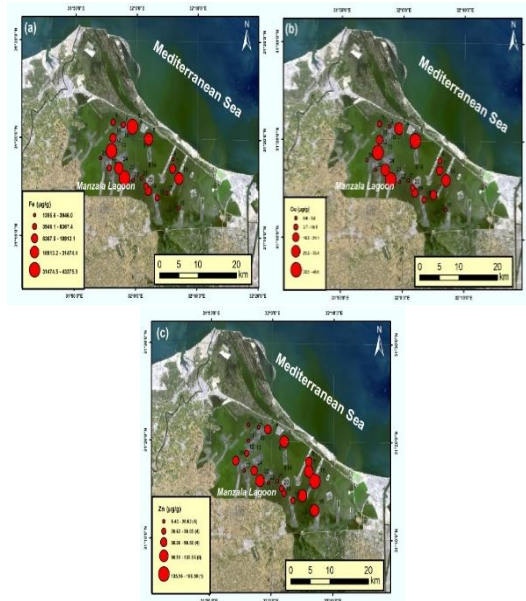


Fig. 4a) concentration of Fe in the studied sites.; fig.4b)concentration of Cu in the studied sites; fig.c) concentration of Zn in the studied sites

Table2. Measured heavy metals ( $\mu\text{g/g}$ ) in the studied site

Site No.	Fe	Cu	Zn	Co	Cd	Pb	Ni
1	8367.42	10.05	13.69	ND	9.71	58.75	30.5
2	6669.16	ND	10.09	ND	0.19	25.05	ND
3	38620.69	23.84	77.04	ND	1.97	33.1	80
5	25519.93	37.81	124.37	10.94	2.22	117.15	62.47
6	3946	5.83	90.5	ND	ND	45.83	10.67
7	13309.98	14.36	135.55	ND	1.05	45.01	21.19
11	18913.1	21.1	18.14	2.41	0.83	12.48	39.66
12	43375.81	48.01	41.92	9.97	2.22	34.9	93.63
15	26181.82	33.4	188.5	7.98	1.11	62.89	57.51
16	1994.27	2.67	101.24	ND	ND	45.46	ND
17	3382.34	13.34	108.85	13.64	7.65	69.87	35.53
18	5544	7.2	46.4	10.4	7.6	87.2	27.4
19	15106.86	13.88	45.77	11.96	4.63	57.1	45.61
20	7266.73	6.78	50.05	ND	0.92	41.98	12.65
21	2505.95	3.17	20.62	13.01	8.56	58.21	27.12
22	1395.58	1.15	15.4	ND	ND	34.37	ND
23	42290.2	43.33	103.14	6.27	3.33	52.94	94.51
24	31474.45	31.39	76.82	2.37	2.92	42.88	68.61
25	5371.43	1.07	6.43	ND	ND	22.23	ND
26	3232.09	3.63	68.58	ND	7.26	64.57	22.54
Max	43375.81	48.01	188.5	13.64	9.71	117.15	94.51
Min	1395.58	1.07	6.43	2.37	0.19	12.48	10.67
Average	15223.39	16.94	67.15	8.89	3.88	50.59	45.6
Back ground Shale *	47200	45	95	19	0.3	20	68

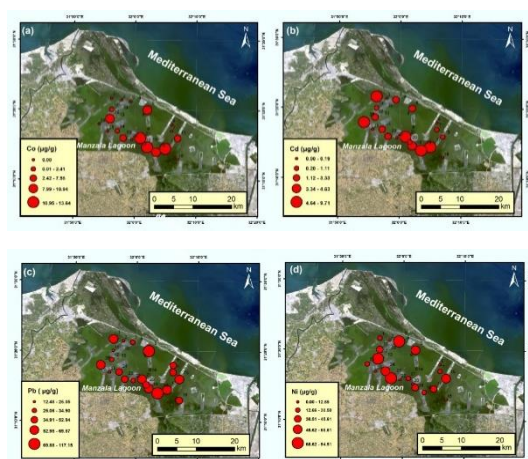


Fig.5a) shows concentration of Co in the studied sites; fig.5b) shows the concentration of Cd in the studied sites; fig 5c) shows concentration of Pb in the studied sites; Fig 5d) shows concentration of Ni in the studied sites.

### Contamination factor ( $C_f$ )

The levels of contamination is categorized by Hökanson (1980) into the following classes; low  $C_f$  ( $<1$ ), moderate ( $1 \leq C_f < 3$ ), considerable ( $3 \leq C_f < 6$ ), and very high ( $6 \leq C_f$ ). According to the values of  $C_f$ , it is clear that the examined bottom sediments of ML, are lowly

contaminated with Fe (0.02-0.91) and Co (0.12-0.71) as shown in Table 4. Also, the sediments are lowly contamination with Cu, except for site 12, that is moderately contaminated (1.98). Also, most sites are lowly contamination with Zn, with the exception of sites 5, 7, 15, 16, 17 and 23 that are moderately contaminated. Similarly, most sites are lowly contaminated with Ni, with the exception of sites 3, 12, 23 and 24 that are moderately contaminated. On the contrary, variable values were calculated for Pb, where site 11 is lowly contaminated, sites 1, 2, 3, 6, 7, 12, 16, 19, 20, 21, 22, 23, 24 and 25 are moderately contaminated, whereas sites 5, 15, 17, 26 are considerably contaminated. For Cd, most sites are very highly contaminated; sites 11, 15 and 20 are considerably contaminated, while site 2 is lowly contaminated.

### Degree of contamination ( $D_c$ )

According to the  $D_c$ , values range between 1.31 (site 25) and 48.73 (site 1), with an average of 15.98. Therefore, low degrees are recorded at sites 6, 11, 16, 20, 22 and 25, moderate values at sites 2, 3, 12, and 15, considerable degrees at sites 5, 19, 23, and 24, and very high values at sites 1, 17, 18, 21, and 26 (Table 4 and Fig. 6.a).

Table 3. Contamination indices applied for the evaluation of metals in ML.

Contamination indices	Classes
<b>Contamination factor (Cf)</b> $CF = C_{\text{metal}} / C_{\text{background value}}$ Where $C_{\text{metal}}$ = metal concentration in polluted sediments $C_{\text{background value}}$ = background value of the metal.	The contamination factors were divided into four classes by Hakanson (1980): $Cf < 1$ (low Cf), $1 \leq Cf < 3$ (moderate Cf), $3 \leq Cf < 6$ (significant Cf), and $6 \leq Cf$ (extremely high Cf).
<b>Degree of contamination (Dc)</b> The sum of all values of contamination factors.	Four classes of contamination were distinguished by Hakanson (1980): $Dc < 7$ (low), $7 < Dc < 28$ (extremely high).
<b>Pollution Load Index (PLI)</b> $PLI = (Cf_1 * Cf_2 * Cf_3 * \dots * Cf_n)^{1/n}$ Where n is the number of metals and Cf is the Contamination factor.	Tomlinson et al. (1980) distinguished two groups: $PLI < 1$ (unpolluted); $PLI = 1$ (minimum pollution); $PLI > 1$ (polluted).
<b>Geo-accumulation index (Igeo)</b> $I_{\text{geo}} = \log_2 (C_n / (1.5 * B_n))$ Where $C_n$ is the concentration of the element in sediment sample and $B_n$ is the background concentration of the element.	$I_{\text{geo}} < 0$ (unpolluted), $I_{\text{geo}} = 0-1$ (unpolluted-moderately polluted), $I_{\text{geo}} = 1-2$ (moderately polluted), $I_{\text{geo}} = 2-3$ (moderately-strongly polluted), $I_{\text{geo}} = 3-4$ (strongly polluted), $I_{\text{geo}} = 4-5$ (strong to very strongly polluted), and $I_{\text{geo}} > 5$ (very strong polluted) are the seven grades Müller (1969) made of the geo-accumulation index.
<b>Enrichment factor (Ef)</b> $EF = (M/Fe)_{\text{sample}} / (M/Fe)_{\text{crust}}$ Where $(M/Fe)_{\text{sample}}$ is the ratio of metal and Fe concentrations in the sample, and $(M/Fe)_{\text{crust}}$ is the ratio of metal and Fe concentrations in the earth's crust.	$EF < 1$ (no enrichment), $EF < 3$ (little enrichment), $EF = 3-5$ (moderate enrichment), $EF = 5-10$ (moderately severe enrichment), $EF = 10-25$ (severe enrichment), $EF = 25-50$ (very severe enrichment), and $EF > 50$ (very severe enrichment) are the seven classifications that Birch (2003) identified.
<b>Risk factor (Er)</b> $Er = Tr * Cf$ Where Tr is the toxic-response factor for a given substance, and Cf is the contamination factor.	Hakanson (1980) distinguished the following classes: $Er < 40$ (low), $40 \leq Er < 80$ (moderate), $80 \leq Er < 160$ (considerable), $160 \leq Er < 320$ (high), $Er \geq 320$ (very high).
<b>Potential ecological risk index (Ri)</b> The sum of all values of risk factors.	Hakanson (1980) distinguished the following classes: $Ri < 150$ (low), $150 < Ri < 300$ (moderate), $300 < Ri < 600$ (considerable), $Ri > 600$ (very high).

Table 4. Calculated Cf, Dc and PLI for the measured metals.

Site	Contamination factor (Cf)							Dc	PLI
	Fe	Cu	Zn	Co	Cd	Pb	Ni		
1	0.17	0.22	0.14	-	32.36	2.93	0.44	48.73	0.79
2	0.14	ND	0.10	-	0.63	1.25	-	12.43	0.33
3	0.81	0.52	0.81	-	6.56	1.65	1.17	11.55	1.28
5	0.54	0.84	1.30	0.57	7.4	5.85	0.91	17.44	1.45
6	0.08	0.12	0.95	-	-	2.29	0.15	3.61	0.32
7	0.28	0.31	1.42	-	3.5	2.25	0.31	8.09	0.82
11	0.40	0.46	0.19	0.12	2.76	0.62	0.58	5.16	0.46
12	0.91	1.06	0.44	0.52	7.4	1.74	1.37	13.47	1.22
15	0.55	0.74	1.98	0.42	3.7	3.14	0.84	11.39	1.18
16	0.04	0.05	1.06	-	-	2.27	-	3.44	0.27
17	0.07	0.29	1.14	0.71	25.5	3.49	0.52	31.02	0.97
18	0.11	0.16	0.48	0.54	25.33	4.36	0.40	31.00	0.80
19	0.32	0.30	0.48	0.62	15.43	2.85	0.67	17.84	0.98
20	0.15	0.15	0.52	-	3.06	2.09	0.18	6.18	0.49
21	0.05	0.07	0.21	0.68	28.53	2.91	0.39	32.86	0.56
22	0.02	0.02	0.16	-	-	1.71	-	1.93	0.12
23	0.89	0.96	1.08	0.33	11.1	2.64	1.38	18.41	1.43
24	0.66	0.69	0.80	0.12	9.73	2.14	1.00	15.18	0.99
25	0.11	0.02	0.06	-	-	1.11	-	1.31	0.29
26	0.06	0.08	0.72	-	24.2	3.22	0.33	28.63	0.68

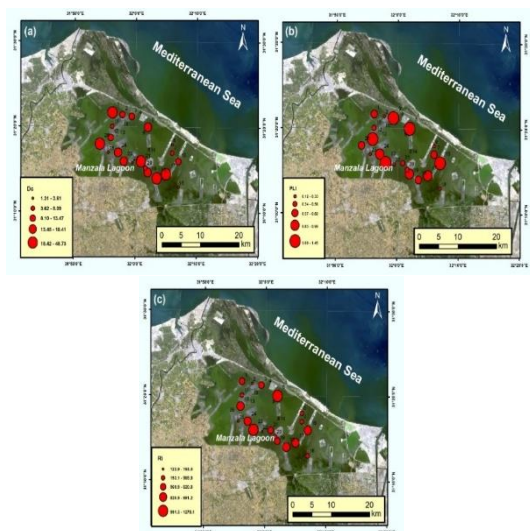


Fig.6a) show Dc for the measured metals, Fig.6b) shows PLI for the measured metals Fig.6c) shows RI for the measured metals .

### Pollution Load Index (PLI)

According to Tomlinson et al. (1980), PLI reflects the pollution levels in every sites. The Table 5.  $I_{geo}$  for the measured metals.

Site	Geoaccumulation index ( $I_{geo}$ )						
	Fe	Cu	Zn	Co	Cd	Pb	Ni
1	-0.92744	-0.82714	-1.01741	-	1.33407	1.958333	-0.5243
2	-1.02596	-	-1.14992	-	-0.37446	0.835	-
3	-0.26321	-0.452	-0.2671	-	0.64124	1.103333	-0.10551
5	-0.44315	-0.2517	-0.0591	-0.41583	0.69314	3.905	-0.21293
6	-1.25388	-1.06364	-0.19717	-	-	1.527667	-0.98044
7	-0.72586	-0.67215	-0.02172	-	0.36797	1.500333	-0.68247
11	-0.57327	-0.50502	-0.89518	-1.07283	0.26586	0.416	-0.41025
12	-0.21279	-0.14797	-0.53139	-0.45615	0.69314	1.163333	-0.03719
15	-0.43203	-0.30556	0.121496	-0.55284	0.39211	2.096333	-0.24886
16	-1.55025	-1.40279	-0.14846	-	-	1.515333	-
17	-1.32082	-0.70415	-0.11699	-0.32003	1.23049	2.329	-0.458
18	-1.10621	-0.97197	-0.4873	-0.43781	1.22761	2.906667	-0.57085
19	-0.67086	-0.68691	-0.49323	-0.37711	1.01238	1.903333	-0.34954
20	-0.98869	-0.99807	-0.45441	-	0.31055	1.399333	-0.90651
21	-1.45106	-1.32824	-0.83953	-0.34057	1.27921	1.940333	-0.57531
22	-1.70528	-1.76861	-0.96629	-	-	1.145667	-
23	-0.22379	-0.19252	-0.14039	-0.65758	0.86922	1.764667	-0.03312
24	-0.35208	-0.33251	-0.26834	-1.0801	0.81217	1.429333	-0.17221
25	-1.11994	-1.79992	-1.3456	-	-	0.741	-
26	-1.34055	-1.2694	-0.31762	-	1.20774	2.152333	-0.65565

### Enrichment factor (Ef)

To detect the anthropogenic origin of metals, Ef was as introduced by Birch (2003). For Cu, site 17 is moderately enriched, sites 3, 19, 20, 22, and 25 have no enrichment; while the other sites have minor enrichment (Table 6). For Zn, sites 1, 2, 3, 11, 12, and 25 have no enrichment, sites 5, 19, 23, and 24 have minor enrichment, sites 15, 18, and 21 have moderate Ef, sites 7

calculated values of PLI range between 0.12 (site 22) and 1.45 (site 5), with an average of 0.77. Most sites are unpolluted ( $< 1$ ), whereas sites 3, 5, 12, 15 and 23 are polluted ( $> 1$ ) as shown in (Table 4 and Fig. 6b).

### Geo-accumulation index ( $I_{geo}$ )

The geo-accumulation index of Müller (1969) is followed here. The outputs of  $I_{geo}$ , reflect that the bottom sediments of ML are unpolluted with Fe, Cu, Co and Ni, where all values are less than 0. For Cd, site 2 is unpolluted ( $I_{geo} = -0.374$ ); sites 3, 5, 7, 11, 12, 15, 20, 23 and 24 are unpolluted-moderately polluted (0.26-0.86); while sites 1, 17, 18, 19, 21 and 26 are moderately polluted (1.01-1.33). It is noted that site 1 is the most polluted with Cd. For Pb, sites 2, 11 and 25 are unpolluted-moderately polluted (0.41-0.83), sites 1, 3, 6, 7, 12, 16, 19, 20, 21, 22, 23, and 24 are moderately polluted (1.10-1.95), sites 15, 17, 18, and 26 are moderately to strongly polluted (2.09-2.90), while site 5 is strongly polluted (3.9) as displayed in Table 5.

and 22 are moderately severe enrichment, while sites 6, 17, and 26 have severe Ef. For Co, sites 11, 12, 15, 23, and 24 have no enrichment, sites 5 and 19 have minor Ef, site 18 had moderate Ef, while sites 17 and 21 have severe Ef. For Cd, sites 1, 17, 18, 21, and 26 have extremely severe enrichment, site 19 has very severe enrichment, sites 5, 7, 20, 23, and 24 have severe Ef, sites 2, 3, 11, 12, and 15 have moderately severe Ef. For Pb, sites 3, 11, 12, 23 have minor enrichment, site 24 has moderate Ef, sites 2, 7,



15, 19, 25 have moderately severe Ef, sites 1, 5, and 20 has severe Ef, sites 6, 17, 18, and 26 has very severe Ef, while sites 16 and 22 have extremely severe Ef. For Ni, sites 1, 3, 5, 6, 7, 11, 12, 15, 19, 20, 23, and 24 have minor Ef, sites 18 and 26 have moderate Ef, while sites 17 and 21 have moderately severe Ef.

Table 6. Calculated Ef for the measured metals.

Site	Enrichment factor (Ef)					
	Cu	Zn	Co	Cd	Pb	Ni
1	1.25	0.81	-	182.57	16.57	2.53
2	-	0.75	-	4.48	8.86	-
3	0.64	0.99	-	8.02	2.02	1.43
5	1.55	2.42	1.06	13.68	10.83	1.69
6	1.54	11.39	-	-	27.40	1.87
7	1.13	5.059	-	12.41	7.98	1.10
11	1.17	0.47	0.31	6.90	1.55	1.45
12	1.16	0.48	0.57	8.05	1.89	1.49
15	1.33	3.57	0.75	6.67	5.66	1.52
16	1.40	25.22	-	-	53.79	-
17	4.13	15.98	10.01	355.84	48.75	7.29
18	1.36	4.158	4.66	215.68	37.11	3.43
19	0.96	1.50	1.96	48.22	8.92	2.09
20	0.97	3.42	-	19.91	13.63	1.20
21	1.32	4.08	12.89	537.43	54.81	7.51
22	0.86	5.48	-	-	58.1215	-
23	1.07	1.21	0.36	12.38	2.95	1.55
24	1.04	1.21	0.18	14.59	3.21	1.51
25	0.20	0.59	-	-	9.76	-
26	1.17	10.54	-	353.40	47.14	4.84

### *Ecological risk factor (Er) and Potential ecological risk factor (Ri)*

To detect the toxicity of the studied HMs, Er is calculated based on Hakanson (1980). The toxic response factors of Cd, Ni, Pb, Cu, and Zn are 30, 5, 5, 5, and 1 respectively (Hakanson, 1980). For Cu, sites 6, 16, 18, 21, 22, 25 and 26 have low levels of toxicity, sites 1, 7, 17 and 19 have moderate levels, sites 3, 11 and 24 have considerable levels, sites 5, 12, 15 and 23 have high levels (Table 7). For Zn, sites 1, 11, 22, and 25 have low levels, sites 3, 12, 18, 19, 20, 24, and 26 have moderate levels, sites 5, 7, 16, 17, and 23 have considerable levels, while site 15 have high level. For Cd, sites 2, 7, 11, 15, and 20 have low levels, sites 3, 5 and 12 have moderate levels, sites 19, 23 24 have considerable levels, while sites 1, 17, 18, 21, and 26 have high levels. For Pb, site 11 has moderate levels, sites 2 and 25 has considerable levels, sites 1, 3, 6, 7, 12, 15, 16, 19, 20, 21, 22, 23, and 24 have high levels, while sites 5, 17, 18, and 26 have very high levels. It is noted that site 5 was the highest value of Er. According to Hakanson (1980), Ri is identified as the sum of all of risk factors. These values range between 122.93 (site 25) and 1278.12 (site 5), with an average of 676.30. Sites 2 and 25 have low Ri, site 22 has moderate Ri, sites 6, 7, 11, 16, and 20 have considerable Ri, while sites 1, 3, 5, 12, 15, 17, 18, 19, 21, 23, 24, and 26 have very high Ri (Fig. 6 c).

Table 7. Calculated Er and Ri for the measured metals.

Site	Ecological risk factor (ER)					Potential ecological risk index (Ri)
	Cu	Zn	Cd	Pb	Ni	
1	50.25	13.69	291.3	293.75	152.5	801.49
2	-	10.09	5.7	125.25	-	141.04
3	119.2	77.04	59.1	165.5	400	820.84
5	189.05	124.37	66.6	585.75	312.35	1278.12
6	29.15	90.5	-	229.15	53.35	402.15
7	71.8	135.55	31.5	225.05	105.95	569.85
11	105.5	18.14	24.9	62.4	198.3	409.24
12	240.05	41.92	66.6	174.5	468.15	991.22
15	167	188.5	33.3	314.45	287.55	990.8
16	13.35	101.24	-	227.3	-	341.89
17	66.7	108.85	229.5	349.35	177.65	932.05
18	36	46.4	228	436	137	883.4
19	69.4	45.77	138.9	285.5	228.05	767.62
20	33.9	50.05	27.6	209.9	63.25	384.7
21	15.85	20.62	256.8	291.05	135.6	719.92
22	5.75	15.4	-	171.85	-	193
23	216.65	103.14	99.9	264.7	472.55	1156.94
24	156.95	76.82	87.6	214.4	343.05	878.82
25	5.35	6.43	-	111.15	-	122.93
26	18.15	68.58	217.8	322.85	112.7	740.08

## Discussion

This investigation tries to assess the levels of pollution in the bottom sediments of ML after the dredging process that carried out by the Egyptian government. Moreover, the detection of the ecological risks that resulted from the contaminated sediments is another target. Furthermore, the measurements of some ecological parameters are essential to realize the quality of any aquatic environment.

The measured concentrations of HMs indicate that the average levels of the metals are arranged as:  $\text{Fe} > \text{Zn} > \text{Pb} > \text{Ni} > \text{Cu} > \text{Co} > \text{Cd}$ . It is noted that, Fe fluctuates in a wide range in the sediments of ML, representing the highest concentration than any other metal. Similarly, Zn, Pb and Ni have wide range of variations between different sites. Pb, Zn and Cd are toxic elements and they have dangerous effects on marine fauna (Zahrán et al., 2015). Pb possesses higher concentrations due to different sources, including phosphate fertilizers, paint factories, and gas factories (e.g., Hamed et al., 2013; Redwan and Elhaddad, 2022). The excessive usage of phosphate fertilizers and pesticides in agriculture may be the reason for increasing the levels of Cd (Redwan and Elhaddad, 2022). Moreover, the sources of Cu and Ni may be related to the discharges of agricultural drains in the southern side and industrial wastes in the eastern side (industrial region in Port Said).

The comparison between the concentrations of the measured HMs and those of the back ground Shale (Turekian and Wedepohl, 1961) is discussed here as follows. The measured concentrations of Fe and Co in all the studied sites are lower than those of the back ground Shale. For Cu, all sites have lower values, except site 12 (in the south-western part) has higher value. For Zn, most sites have lower values, with the exception of sites 5, 7, 15, 16, 17 and 23 that have higher values. For Cd, most sites have higher values. For Pb, all sites have higher values, with the exception of site 11 (western part) has lower value. For Ni, most sites have lower values, with the exception of sites 3, 12, 23 and 24 have higher values.

The present distribution patterns of the HMs in the lagoon are disturbed, due to the dredging processes that led to the accumulation of polluted sediments in many sites in the lagoon. Therefore, these polluted sediment may

be easily transported to different uncontaminated parts, resulting in high levels of pollution. Consequently, the concentrations of the examined metals have no significant trends.

To detect the relationship between the heavy metals, Pearson's correlation was applied on heavy metals. The resulting correlation matrix is shown in (Table 8). The values are considered significant if  $p\text{-value} \leq 0.05$ , moderate significant  $\leq 0.01$ , and highly significant  $\leq 0.001$ . According to Suresh et al. (2011), the significant positive correlation between heavy metals reflects their common sources, and the same behavior during the transport. It is noted that, Fe has strong positive correlation with Cu (0.92) and Ni (0.93), indicating the same geochemical behavior (Figs. 7.a, 7.b). Also Cu has a strong positive correlation with Ni (0.93) as shown in Figure 7.c. Also, Pb has a moderate positive correlation with Co (0.58) and a significant positive correlation with Cd (0.49) as presented in Figure 7.d. Moreover, Cd has a significant positive correlation with Co (0.49). Pb is signified as an indicator of anthropogenic source. Consequently, Cd, Co and Zn may have the same origin. On the other side, Fe and Cu have no significant relationship with Cd and Pb.

It is necessary to compare the current results with the former results on ML (Table 9), to determine the state of the lagoon after the development processes that carried out by the Egyptian government. The previous studies reflected that the southern side is more polluted than the northern side (e.g., Abdel-Satar and Genid, 2009; El Baz, 2017; Elmorsi et al., 2017; Abdel Gawad, 2018; Redwan and Elhaddad, 2022).

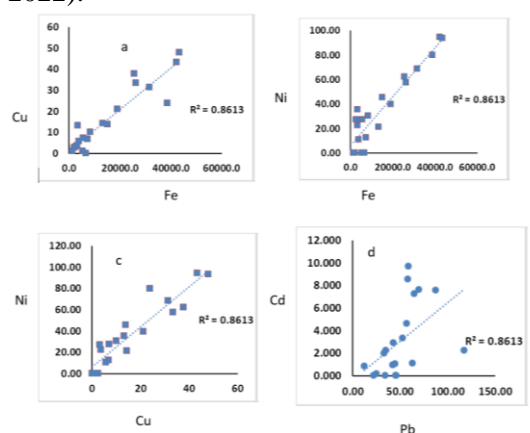


Fig 7 shows Pearson's correlation on heavy metals; (Figs. 7.a, 7.b) Fe has strong positive correlation with Cu (0.92) and Ni (0.93); Figure 7.c) Cu has a strong positive correlation with Ni (0.93); Figure 7.d) Pb has a moderate



positive correlation with Co (0.58) and a significant

In this context, the current concentration of Fe (15223.39) is higher than those of the previous studies of Abdel-Satar and Genid (2009), El Baz (2017) and Elmorsi et al., (2017). For Zn (67.15 µg/g), it is lower than that of Redwan and Elhaddad (2022), but it is higher than those of EL-Bady (2016) and Abdel Gawad (2018). For Cu (16.94 µg/g), it is lower than those of the above-mentioned studies. For

positive correlation with Cd (0.49).

Pb (50.59) and Cd (3.88), they are higher than those of Abdel Gawad (2018) and Redwan and Elhaddad (2022), but they are lower than those of Abdel-Satar & Genid (2009). Also, the unexpected lower concentrations of HMs in some southern sites of the lagoon may be due to the removal of huge amounts of bottom sediments.

Table 8. Pearson's correlation coefficients (r) between the measured heavy metals in in bottom sediments of ML.

	Fe	Cu	Zn	Co	Cd	Pb	Ni
Fe	1						
Cu	0.92***	1					
Zn	0.30	0.45*	1				
Co	0.18	0.38	0.19	1			
Cd	-0.17	-0.08	-0.15	0.47*	1		
Pb	-0.03	0.19	0.45*	0.58**	0.49*	1	
Ni	0.93***	0.93***	0.33	0.43	0.13	0.19	1

\*, \*\*, \*\*\* significant correlation at  $P \leq 0.05$ , moderate significant  $\leq 0.01$ , and highly significant  $\leq 0.001$

Table 9. Comparison between the analyzed heavy metals (µg/g) in Manzala Lagoon and those measured in other localities.

Locality	Mn	Fe	Cu	Zn	Cd	Ni	Pb	Cr	Reference
Manzala Lagoon, Egypt	1334	4460	90.99	207.8	10.61	108.14	379.4	-	Abdel-Satar and Genid, 2009
	725.55	1074.55	31.21	39.53	1.67	30.83	0.077	40.95	EL-Bady, 2016
	38.1488	8342.47	26.34	30.32	0.0264	40.73	0.244	-	Abdel Gawad, 2018
	880	14130	110	110	1.8	60	20	-	Redwan and Elhaddad, 2022
	-	15223.39	16.94	67.15	3.88	45.6	50.59	-	Present study
Burullus Lagoon, Egypt	948	17550	30	50	0.2	40	30	-	Melegy et al., 2019
Bardawil, Lagoon, Egypt	352.57	2092.7	46.01	52.93	15.79	30.29	29.8	42.09	EL-Bady, 2016
Mariout Lagoon, Egypt	585	19340	91	139	0.7	40	59	-	EL-Bady, 2020
Mediterranean Coast, Egypt	381	13256	8.46	22.19	0.22	25.93	13.17	82.74	Soliman et al., 2015a
Red Sea Coast, Egypt	136.3	7094.4	25.4	24	1.05	11.5	8.55	18.3	El-Kahawy et al., 2021
Mediterranean Coast, Libya	28.6	571.4	15.4	20.1	8.3	22.2	36.6	18.7	Soliman et al., 2015b
Tarut Island, Arabian Gulf, Saudi Arabia	75.2	3447	5.8	17.6	0.7	-	58.7	27.1	Youssef et al., 2015
Homa Lagoon, Turkey		16500-28300	9-24	38-88	0.5-0.8	-	6-30	92-220	Tas and Sunlu, 2013
Gulf of Izmir, Turkey	522.43	-	22.38	99.87	0.03	108.12	48.37	109.56	Bergin et al., 2006
Sidi Moussa lagoon, Morocco		-	30.4	49.8	-	29.1	-	96.9	Maanan et al., 2004
Oubeira Lagoon, Algeria		13436.25	23.51	89.95	0.038	101.75	21.21	102.75	Belabed et al., 2011
Tunis Lagoon, Tunisia		41727.19	27.28	148.52	1.51	71.81	102.22	99.84	Abidi et al., 2022

### Risk assessment of HMs

The average values of Cf are arranged as follows: Cd (12.95208) > Pb (2.529925) > Zn (0.706895) > Ni (0.680461) > Co (0.468158) > Cu (0.37662) > Fe (0.322529). These values

indicate that the sediments are lowly polluted with Zn, Ni, Co, Cu and Fe; moderately polluted with Pb; while they are very highly polluted with Cd. The average value of Dc reaches 15.96, indicating a considerable level of contamination. According to PLI, most sites are unpolluted, whereas sites 3, 5, 12, 15, and 23 are

polluted. Concerning the values of  $I_{geo}$ , the bottom sediments of ML are unpolluted with Fe, Cu, Co and Ni. On the contrary, all sites are polluted with Pb. For Cd, most sites are polluted and the highest value reaches 1.33 in site 1. The average values of Er are arranged as follows: Pb (252.99) > Ni (228) > Cd (116.56) > Cu (84.73) > Zn (67.15). Furthermore, the average values of enrichment factor indicate minor enrichment for Cu (1.28); moderate enrichment for Zn (4.96) and Co (3.28); extremely severe enrichment for Cd (112.51); a moderate Ef for Pb (21.05) and minor Ef for Ni (2.66). Consequently, Cd and Pb are the principal contributors for the ecological risk in ML. According to Ungureanu et al. (2016), Pb and Cd originate chiefly from anthropogenic activities. These results indicate a high Er for Pb and Ni; a considerable Er for Cd and Cu; whereas Zn has a moderate Er. Moreover, the average value of Ri (676.30), suggesting that the bottom sediments of ML have very high risk, due to the higher levels of Cd and Pb.

#### *Comparison between the measured HMs and those from other aquatic ecosystems*

The concentrations of the measured HMs are correlated with those documented from other sites inside Egypt (Table 9 and Fig. 8) and outside Egypt (Figure 9), including Libya, Tunisia, Algeria, Morocco, Saudi Arabia and Turkey (Table 9).

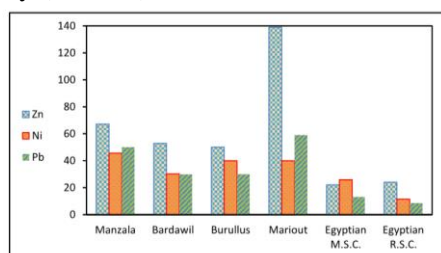


Fig 8 shows the concentrations of the measured HMs which correlated with those documented from other sites inside Egypt

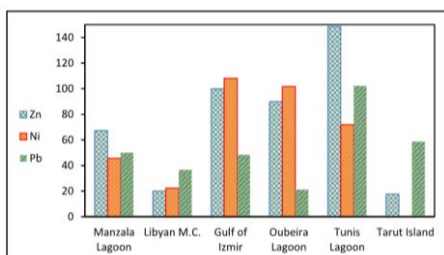


Fig 9 shows the concentrations of the measured HMs which correlated with those documented from other sites outside Egypt

#### *Egypt*

Many studies have been carried out on the evaluation of HMs in the surface sediments of the Egyptian lagoons and coasts, including Burullus Lagoon (e.g., Masoud et al., 2011; El Baz and Khalil, 2018; Melegy et al., 2019), Bardawil, Lagoon, Mariout Lagoon (e.g., EL-Bady, 2016), Edku Lagoon (e.g., Badr-ElDin et al., 2022), the Mediterranean Coast (Soliman et al., 2015a), and the Red Sea Coast (El-Kahawy et al., 2021). In Burullus Lagoon, Masoud et al. (2011) and El Baz and Khalil (2018) pointed to the higher concentrations of Cd. In Edku Lagoon, the investigation of Badr-ElDin et al. (2022) suggested that, Cd and Pb have severe effects on the aquatic biota. According to El-Bady (2016), the highest degrees of contamination were recorded in the Bardawil Lagoon, whereas the Burullus Lagoon had the lowest values. The study of Soliman et al. (2015a) on the surface sediments of the Egyptian Mediterranean coast, indicated that Fe has the greatest concentration followed by Mn, Cr, Ni, Zn, Pb, Cu and Cd. Moreover, El-Kahawy et al. (2021) examine the concentrations of metals in the sediments of the Red Sea Coast, and concluded that the order of metals were Fe > Mn > Cu > Zn > Cr > Ni > Pb > Cd.

#### *Libya*

Also, Soliman et al. (2015b) recorded higher levels of Pb (36.6 µg/g), Ni (22.2 µg/g), Cr (18.7) and Cd (8.3 µg/g) from the sediments of the Mediterranean Coast of Libya. They concluded that, the sediments were polluted with Cd. Also, Omar et al. (2021) investigated the metal pollution in the surface sediments along the northeastern coast of Libya and indicated that the metals were arranged as Al > Fe > Mn > Zn > Cu > Pb > Cd. They concluded that the concentrations of metals have lower values than those of the background, with the exception of Cd, that has higher values in some sites.

#### *Tunisia*

Fe has the highest content (41727.19 µg/g), followed by Zn (148.52 µg/g), Pb (102.22 µg/g), Cr (99.84 µg/g), Ni (71.81 µg/g), Cu (27.28 µg/g), and Cd (1.51 µg/g), according to a study by Abidi et al. (2022) in the bottom

sediments of the South Lagoon of Tunis.

#### *Algeria*

Belabed et al. (2011) showed that the sediments of Oubeira lagoon display the following levels HMS: Fe (13436.25 µg/g), Cr (102.75 µg/g), Ni (101.75 µg/g), Zn (89.95 µg/g), Pb (21.21 µg/g) and Cd (0.038 µg/g).

#### *Morocco*

Also, many investigations have been carried out on the assessment of HMs in the bottom sediments of different Moroccan ecosystems (Maanan et al., 2004; Ben bouih et al., 2005; Tnoumi et al., 2022). The study of Tnoumi et al. (2022), on the sediments of Khnifiss Lagoon recorded minor enrichments with Ni and Cd.

#### *Saudi Arabia*

In the Arabian Gulf, Saudi Arabia, Youssef et al. (2015) recorded higher values of Pb (58.7 µg/g) from the surface sediments of Tarut Island.

#### *Turkey*

The geochemical analysis of Bergin et al. (2006) for the HMs in the surface sediments of the Gulf of Izmir, reflected that Mn had the highest levels followed by Cr, Ni, Zn, Pb, Cu, Cd. They observed high values for Cr (109.56 µg/g), Ni (108.12 µg/g), Zn (99.87 µg/g) and Pb (48.37 µg/g). Moreover, Tas and Sunlu (2013), indicated that the concentrations of Fe in the Homa lagoon ranged from 16500-28300 µg/g, Cr (92-220 µg/g), Zn (38-88 µg/g), Cu (9-24 µg/g), Pb (6-30 µg/g) and Cd (0.5-0.8 µg/g).

From the above-mentioned studies, it is clear that the current levels of Fe in ML is higher than those recorded in Burullus (Melegy et al., 2019), Egyptian Mediterranean Coast (Soliman et al., 2015a), Egyptian Red Sea (El-Kahawy et al., 2021), Libyan Mediterranean Coast (Soliman et al., 2015b), Oubeira Lagoon, Algeria (Belabed et al., 2011); Tarut Island, Arabian Gulf, Saudi Arabia (Youssef et al., 2015) and Gulf of Izmir, Turkey (Bergin et al., 2006), but it is lower than those recorded in Mariout (EL-Bady, 2016) and the South Lagoon of Tunis, Tunisia (Abidi et al., 2022).

For Cu, It is lower than those recorded in the Burullus (Melegy et al., 2019), Bardawil

(EL-Bady, 2016), Egyptian Red Sea (El-Kahawy et al., 2021), Gulf of Izmir, Turkey (Bergin et al., 2006), Sidi Moussa lagoon, Morocco (Maanan et al., 2004), Oubeira lagoon, Algeria (Belabed et al., 2011), Tunis Lagoon, Tunisia (Abidi et al., 2022), but it is higher than those of the Egyptian Mediterranean Coast (Soliman et al., 2015a), Libyan Mediterranean Coast (Soliman et al., 2015b), Tarut Island, Arabian Gulf, Saudi Arabia (Youssef et al., 2015) and Homa Lagoon, Turkey (Tas & Sunlu, 2013).

For Zn, It is lower than those recorded in Mariout (EL-Bady, 2016), Gulf of Izmir, Turkey (Bergin et al., 2006), Oubeira lagoon, Algeria (Belabed et al., 2011) and Tunis Lagoon, Tunisia (Abidi et al., 2022), but it is higher than those in Burullus (Melegy et al., 2019), Egyptian Red Sea (El-Kahawy et al., 2021), Sidi Moussa lagoon, Morocco (Maanan et al., 2004), Egyptian Mediterranean Coast (Soliman et al., 2015a); Libyan Mediterranean Coast (Soliman et al., 2015b), Tarut Island, Arabian Gulf, Saudi Arabia (Youssef et al., 2015) and Homa Lagoon, Turkey (Tas and Sunlu, 2013).

For Cd, it is higher than those recorded in all the above sites, with the exception of Bardawil (EL-Bady, 2016) and Libyan Mediterranean Coast (Soliman et al., 2015b). For Ni, it is higher than those recorded in all the above environments, with the exception of Gulf of Izmir, Turkey (Bergin et al., 2006) and Oubeira lagoon, Algeria (Belabed et al., 2011). For Pb, it is higher than those recorded in all the above ecosystems, with the exception of Mariout Lagoon (EL-Bady, 2016).

#### **Conclusions**

The continuous monitoring for pollution is very essential for saving the health of ML. Based on the geochemical analysis of HMs in the bottom sediments of ML, the metals are arranged as: Fe > Zn > Pb > Ni > Cu > Co > Cd. Compared with many other aquatic ecosystems in Egypt, ML possesses higher concentrations of Fe, Pb, Cd, Zn and Ni. On the contrary, it displays lower levels of HMs compared with north African Lagoons. This study tries to assess the levels of pollution depending on the contamination indices. The findings of Cf reflect that the sediments have high contamination with Cd, moderate contamination with Pb, and lowly

contamination with Zn, Ni, Co, Cu and Fe. The values of  $I_{geo}$  indicated that the sediments are unpolluted with Fe, Cu, Co and Ni; unpolluted-moderately polluted with Cd; and moderately to strongly polluted with Pb. Moreover, the average values of enrichment factor indicate minor enrichment for Ni, Cu, moderate enrichment for Zn, Co, severe enrichment for Pb and extremely severe enrichment for Cd. The results of risk factors reflect a higher risk for Pb and Ni; a considerable risk for Cd and Cu; whereas Zn displays a moderate risk. The average value of  $R_i$  (676.30) suggest that sediments have very high risk. Thus, Cd and Pb are the principal contributors for the ecological risk in ML.

### Data availability

All data generated or analyzed during this study are included in this published article.

### Declarations

The authors declare no competing interests.

### References

- Abd Ellah, R.G., 2022. Using single beam bathymetric data technique to estimate dredging: a case study in Lake Manzala (Egypt). *Arabian Journal of Geosciences*, 15, 1-9.
- Abdel Gawad, S.S., 2018. Concentrations of heavy metals in water, sediment and mollusk gastropod, *Lanistes carinatus* from Lake Manzala, Egypt. *Egyptian Journal of Aquatic Research*, 44, 77-82.
- Abdel-Satar, A., Geneid, Y.A., 2009. Evaluation of Heavy metal status in ecosystem of Lake Manzalah, Egypt. *Global Journal of Environmental Research*, 3 (3), 194-204.
- Abdul, W.O, Oguntuase, K.E., Omoniyi, I.T, Bbada, S.B., Adekoya, E.O. Bashir, A. O., Ibebuike, L.C., Opajobi, G.A., 2019. Dynamics of Heavy Metal Pollution in Tropical lagoon of Gulf of Guinea, West Africa. *J. Appl. Sci. Environ. Manage.* 23 (5), 985-993.
- Abidi, M., Yahyaoui, A., Ben Amor R., Chouba, L., Gueddari, M., 2022. Evaluation of heavy metal pollution risk in surface sediment of the South Lagoon of Tunis by a sequential extraction procedure. *Sci. Mar.* 86 (1), e028. <https://doi.org/10.3989/scimar.05172.028>
- Alvarez Zarikian, C.A., Blackwelder, P.L, Hood, T., Nelsen, T.A., Featherstone, C., 2000. Ostracods as indicators of natural and anthropogenically-induced changes in coastal marine environments. In: *Coasts Millennium*, Proc. 17th Int. Conf. Coast. Soc. July 9-12. Portland, 896-905.
- Badawy, M.I., Wahaab, R.A., 1997. Environmental impact of some chemical pollutants on Lake Manzala. *International Journal of Environmental Health Research*, 7 (2), 161-170.
- Badr-ElDin, A. M., Badr, N. B. E., Hallock, P.M., 2022. Evaluation of trace-metal pollution in sediment cores from Lake Edku, Egypt. *Regional Studies in Marine Science* 53, 1-12.
- Belabed, Bendjema, A., Boudjelida, H., Djabri, L., Bensouilah, M., 2011. Evaluation of the metal contaminations in the surface sediments of the Oubeira lagoon, National park of El Kala, Algeria. *Archives of Applied Science Research* 3 (4), 51-62.
- Ben Bouih, H., Nassali, H., Leblans, M., Srhiri, A., 2005. Contamination en Métaux Traces des Sédiments du lac Fouarat (Maroc). *Afrique Science*, 1 (1), 109-125.
- Bergin, F., Kucuksezgin, F., Uluturhan, E, Barut, I. F., Meric, E., Avsar, N., Nazik, A. (2006). The response of benthic foraminifera and ostracoda to heavy metal pollution in Gulf of Izmir (Eastern Aegean Sea). *Estuarine, Coastal and Shelf Science*, 66, 368-386.
- El-Amier, Y.A., El-Halawany, E.F., El Aiatt, A.A., Kotb, W.K., 2023. Sediment concentrations of heavy metals in the Bardawil Lagoon (Eastern Mediterranean Sea): Assessment of contamination and ecological risks. *Egyptian Journal of Chemistry* 67 (2), 543-553.
- El Baz, S.M., 2017. Recent Benthic Foraminifera as ecological indicators in Manzala Lagoon, Egypt. *Revue de micropaléontologie*, 60, 435-447.
- El Baz, S.M., Khalil, M.M., 2018. Benthic foraminifera and trace metal distribution: a case study from the Burullus Lagoon, Egypt. *Revue de micropaléontologie*, 6, 97-109.
- EL-Bady, M.S.M., 2016. Potential Ecological Risk Index of the Northern Egyptian Lagoons, South of Mediterranean Sea, Egypt. *International Journal of ChemTech Research*, 9 (3), 172-190.
- El-Kahawy, R., El-Shafeiy, M., Helal, S., Aboul-Ela, N., Abd El-Wahab, M., 2021. Benthic ostracods (crustacean) as a nearshore pollution bio-monitor: examples from the Red Sea Coast of Egypt. *Environmental Science and Pollution Research*, 1-19. <https://doi.org/10.1007/s11356-020-12266-x>
- El-Kholy, R., El-Saadi, A., Abdin, A., 2012. Pollution and measures towards de-pollution of the Mediterranean Sea. In R. Choukr-Allah, R. Ragab, R. Rodriguez-Clemente (Eds.),

- Integrated water resources management in the Mediterranean region: Dialogue towards new strategy, 175-194.
- El Morsi, D. A., Gaballah, G., Mahmoud, W., & Tawfik, A. I. (2017). Sex Determination in Egyptian Population from Scapula by Computed Tomography. *Journal of Forensic Research*, 8(3), 376.
- El Nemr, A., 2003. Assessment of heavy metal pollution in surface muddy sediments of Lake Burulus southeastern Mediterranean, Egypt. *Egyptian Journal Aquatic Biology and Fishing*, 7 (4), 67-90.
- El Ouaty, O., El Mrini, A., Nachite, D., Marrocchino, E., Rodella, I., 2024. Sediment Quality Indices for the Assessment of Heavy Metal Risk in Nador Lagoon Sediments (Morocco) Using Multistatistical Approaches. *Sustainability*, 16, 1-32. <https://doi.org/10.3390/su16051921>
- Ennouri, R., Chouba, L., Magni, P., Kraiem, M.M., 2010. Spatial distribution of trace metals (Cd, Pb, Hg, Cu, Zn, Fe and Mn) and oligo-elements (Mg, Ca, Na and K) in surface sediments of the Gulf of Tunis (Northern Tunisia). *Environ. Monit. Assess.*, 163, 229-239. <https://doi.org/10.1007/s10661-009-0829-5>
- Folk, R. L., 1974. *Petrology of Sedimentary Rocks*. Hemphill Publishing Co, Austin, 170 p.
- Forstner, U., Wittmann, G.T.W., 1983. *Metal Pollution in the Aquatic Environment*. Springer-Verlag, Berlin, 30-61.
- Galanopoulou, A. S., Kokaia, M., Loeb, J. A., Nehlig, A., Pitkänen, A., Rogawski, M. A., Staley, K. J., Whittemore, V. H., & Dudek, F. E. (2009). *Epilepsy Therapy Development: Technical and Methodological Issues in Studies with Animal Models*.
- Goher, M.E., Abdo, M.H., Bayoumy, W.A., El-Ashkar, M.T.Y., 2017. Some heavy metal contents in surface water and sediment as a pollution index of El-Manzala Lake, Egypt. *Journal of Basic and Environmental Sciences*, 4, 210-225.
- Hamed, Y. A., Abdelmoneim, T. S., ElKiki, M. H., Hassan, M. A., & Berndtsson, R. (2013). Assessment of Heavy Metals Pollution and Microbial Contamination in Water, Sediments and Fish of Lake Manzala, Egypt. *Life Science Journal*, 10(1), 86-99.
- Hegazy, W.H., Hamed, M.A., Toufeek, M.E.S., Mabrouk, B.K.A., 2016. Determination of some heavy metals in water of the southern region of Lake Manzala. *Egypt. Egyptian Journal of Aquatic Biology and Fisheries*, 20 (4), 69-81.
- Hökanson, L., 1980. Ecological Risk Index for Aquatic Pollution Control. A sedimentological approach. *Water Research* 14, 975-1001.
- Liao, Y., Min, X., Yang, Z., Chai, L., Zhang, S., Wang, Y., 2014. Physicochemical and biological quality of soil in hexavalent chromium-contaminated soils as affected by chemical and microbial remediation. *Environ. Sci. Pollut. Res.* 21, 379-388.
- Mallick, D., Shafiqul, I. M., Talukder, A., Mandol, S., Al Imran, M., Biswas, S., 2016. Seasonal variability in water chemistry and sediment characteristics of intertidal zone at Karnafully estuary, Bangladesh. *Pollution*, 2 (4), 411-423.
- Maanan, M., Zourarah, B., Carruesco, C., Aajjane, A., Naud, J., 2004. The distribution of heavy metals in the Sidi Moussa lagoon sediments (Atlantic Moroccan Coast). *Journal of African Earth Sciences*, 39, 473-483.
- Masoud, M. S., Fahmy, M.A., Ali, A.E., Mohamed, E.A., 2011. Heavy metal speciation and their accumulation in sediments of Lake Burullus, Egypt. *African Journal of Environmental Science and Technology*, 5 (4), 280-298.
- Melegy, A.A., El-Bady, M.S., Metwally, H.I., 2019. Monitoring of the changes in potential environmental risk of some heavy metals in water and sediments of Burullus Lake. *Egypt. Bulletin of the National Research Centre*, 43, 143. <https://doi.org/10.1186/s42269-019-0182-y>.
- Müller, G., 1969. Index of geo-accumulation in sediments of the Rhine river. *Geol. J.*, 2 (3), 108-118.
- Omar, W.A., Busaadia, M. A., Saleh, Y. S., Almalki, A. S. A., Marie, M-A.S., 2021. Characterization of metal pollution in surface sediments along the northeastern coast of Libya. *Applied ecology and environmental research*, 20 (2), 1399-1412.
- Redwan, M., Elhaddad, E., 2022. Heavy metal pollution in Manzala Lake sediments, Egypt: sources, variability, and assessment. *Environ. Monit. Assess.*, 194, 1-16. <https://doi.org/10.1007/s10661-022-10081-0>
- Roy, P.S., Crawford, E.A., 1984. Heavy Metals in a Contaminated Australian Estuary-Dispersion and Accumulation Trend. *Estuarine, Coastal and Shelf Science*, 19, 341-358.
- Ruiz, F., Gonzalez-Regalado M.L., Borrego J., Abad, M., Pendón, J.G., 2004. Ostracoda and foraminifera as short-term tracers of environmental changes in very polluted areas: the Odiel Estuary (SW Spain). *Environ. Pollution*, 129, 49-61.
- Selvaraj, K., Moha, V.R., Szefer, P., 2004. Evaluation of metal contamination in coastal sediments of the Bay of Bengal, India: geochemical and statistical approaches. *Mar. Pollut. Bull.*, 49, 174-185.
- Shalaby, B.N., Samy, Y.M., Mashaly, A.O., El Hefnawi, M.A., 2017. Comparative geochemical

- assessment of heavy metal pollutants among the Mediterranean deltaic lakes sediments (Edku, Burullus and Manzala), Egypt. Egypt. J. Chem. 60 (3), 361-378.
- Singer, P. C., 1977. Influence of dissolved organics on the distribution, transport and fate of heavy metals in aquatic system. In: Suffet, I.H. (Ed.), Fate of Pollutants in the Air and Water Environment, Part-1, 155-182. New York.
- Soliman, N. F., Nasr, S.M., Okbah, M.A., 2015a. Potential ecological risk of trace metals in sediments from the Mediterranean coast, Egypt. J. Environ. Health Sci. Eng., 13-70.
- Soliman, N.F., Nasr, S.M., Okbah, M.A., El Haddad, H.S., 2015b. Assessment of metals contamination in sediments from the Mediterranean Sea (Libya) using pollution indices and multivariate statistical techniques. Global Journal of Advanced Research 2, 120-136.
- Tan, C.W.J., Gouramanis, C.b., Pham T.D., Hoang, D.Q., Switzer, A.D., 2021. Ostracods as pollution indicators in Lap An Lagoon, central Vietnam. Environmental Pollution, 278, 1-10.
- Tas, E. Ç., Sunlu, U., 2013. Distribution of some heavy metals in surface sediments from the Homa Lagoon, Izmir Bay, Turkey. Rapp. Comm. int. Mer Médit., 40, 275.
- Tnoui, A., Angelone, M., Armiento, G., Caprioli, R., Crovato, C., De Cassan, M., Montereali, M. R., Nardi, E., Parrella, L., Proposito, M., Schirone, A., Spaziani, F., Zourarah, B., 2022. Heavy metal content and potential ecological risk assessment of sediments from Khnifiss Lagoon National Park (Morocco). Environ. Monit. Assess., 194, 1-17.
- Turekian, K. K., & Wedepohl, K. H. (1961). 1 Distribution of the elements in some major units of the earth's crust. 1 Geological Society of America 2 Bulletin, 72(2), 175-192. 1
- Youssef, M., El-Sorogy, A. S., Al-Kahtany, K. H., Al-Otaibi, N., 2015. Environmental assessment of coastal surface sediments Tarut Island. Arabian Gulf (Saudi Arabia). Mar Poll Bull. doi:10.1016/j.marpolbul.2015.05.010
- Zenina, M. A., 2009. Influence of anthropogenic pollution on ostracod assemblages of Amurskii Bay, Sea of Japan. Russ. J. Mar. Biol. 35 (4), 305-312.  
<https://doi.org/10.1134/S1063074009040051>

## الملخص العربي

### عنوان البحث: المعادن الثقيلة في الرواسب السفلية لبحيرة المنزلة، مصر: تقييم وربط مع النظم البيئية المائية الأخرى في البحر الأبيض المتوسط

شريف الباز<sup>١</sup>، مجدي محمود خليل<sup>١</sup>، عادل حسن الأفندي<sup>٢</sup>، أحمد يسري نابت<sup>٣</sup>، طه القاطوني<sup>٤</sup>، هدى رجب سعد<sup>١</sup>، منى عبد المحسن الحرايري<sup>١</sup>

<sup>١</sup> قسم الجيولوجيا، كلية العلوم، جامعة دمياط، دمياط، مصر

<sup>٢</sup> قسم النبات والميكروبيولوجي، كلية العلوم، جامعة دمياط، دمياط، مصر

<sup>٣</sup> هيئة المواد النووية، القاهرة، مصر

<sup>٤</sup> قسم تقييم الأثر البيئي في مؤسسة الخليج للتجارة البيئية، المملكة العربية السعودية

في الآونة الأخيرة، أصبح الرصد الدقيق للبحيرات الساحلية ضرورة ملحة لحمايتها من الآثار الخطيرة للتلوث. تهدف هذه الدراسة إلى تقييم تلوث المعادن الثقيلة في إحدى أهم البحيرات الساحلية في مصر، وهي بحيرة المنزلة (ML). تُظهر تراكيزات المعادن الثقيلة المقاسة أن  $Fe > Zn > Pb > Ni > Cu > Co > Cd$ . لتقييم مستويات التلوث في البحيرة المدروسة، تم حساب سبعة مؤشرات تلوث، تشمل عامل التلوث (Cf)، ودرجة التلوث (Dc)، ومؤشر التراكم الجغرافي (Igeo)، ومؤشر حمل التلوث (PLI)، وعامل الإثراء (Ef)، وعامل الخطر البيئي (Er)، وعامل الخطر البيئي المحتمل (Ri). وفقاً لـ Cf، فإن الرواسب ملوثة بدرجة منخفضة بالزنك والنيكل والكوبالت والنحاس والحديد، وملوثة بدرجة متوسطة بالرصاص، وملوثة بدرجة عالية جداً بالكاديوم. يبلغ متوسط قيمة Dc (١٥,٩٦)، مما يشير إلى مستوى تلوث كبير. علاوة على ذلك، تشير متوسط قيم Ef إلى إثراء طفيف للنيكل والنحاس، وإثراء متوسط للزنك والكوبالت، وإثراء شديد للرصاص، وإثراء شديد للغاية للكاديوم. يصل متوسط قيمة Ri إلى ٦٧٦,٣، مما يشير إلى أن الرواسب ذات مخاطر عالية جداً. وبالتالي، فإن الكاديوم والرصاص هما المساهمان الرئيسيان في المخاطر البيئية في ML. وأخيراً، تمت مقارنة تراكيزات المعادن الثقيلة في بحيرة المنزلة وغيرها من بحيرات البحر الأبيض المتوسط.



## Advancing Aquifer Monitoring: TDEM's Application in Seawater Intrusion Detection within Heterogeneous Coastal Aquifers of the Nile Delta

Reem A. ElNaggar<sup>\*1</sup>, Ayman I. Taha<sup>2</sup>, Hany M. Shaaban<sup>2</sup>, Eman R. Nofal<sup>3</sup> and Hatem M. Aboelkhair<sup>1</sup>

<sup>1</sup>Faculty of Science Damietta University, 34517, Damietta, Egypt.

<sup>2</sup>National Research Institution for astronomy and geophysics, 11722, Helwan, Cairo, Egypt.

<sup>3</sup>Research Institute for Groundwater, National Water Research Center, 13621, El-Kanater El-Khairiya, Egypt.

Received: 23 May 2025 /Accepted: 21 June 2025

\*Corresponding author's E-mail: reem.elnaggar@du.edu.eg

### Abstract

Coastal aquifers are vital freshwater sources worldwide, yet they are increasingly threatened by seawater intrusion due to over-extraction and climate change. The Nile Delta aquifer, one of the largest coastal groundwater reserves in the world, is particularly vulnerable to salinization, posing significant risks to agriculture, industry, and drinking water supplies. This exacerbates land salinization, infrastructure corrosion, and stresses the local economy. This study aims to explore the efficiency of the Time Domain Electromagnetic (TDEM) method in delineating seawater intrusion within coastal aquifers. The time domain electromagnetic method was used to collect 50 data points along a 50km profile perpendicular to the shoreline towards Mansoura City. Appropriate data processing techniques were applied to increase the signal-to-noise ratio and enhance the readability of data as the area has high cultural noise. Geophysical data inversion and interpretation showed the salt-fresh water boundary. Lithological data from the monitoring well allowed for the calibration of the geophysical model to ensure better results. TDEM data closely matched well data with an average error margin of 5%, showing seawater intrusion extending more than 40 km inland with a gradient nature. Intrusion depth varied between 10 and 20 meters. This confirms TDEM's effectiveness as a fast, cost-effective tool in mapping the salt-fresh water interface in the Nile Delta aquifer. While TDEM has been employed in various coastal settings, it hasn't been employed in the heterogenic nature of the Nile Delta aquifer. This research suggests integrating TDEM with the current monitoring network for tracking changes in aquifer parameters, challenging the complex nature of the area to provide successful results. This approach offers a foundation for improving groundwater management susceptibility and updating water policy.

**Keywords:** Groundwater salinization, Environmental Monitoring, Water Resource Management, Aquifer characterization, Hydrological hazards

## Introduction

Population growth represents increased stress on water availability. This resulted in a continuous decrease in the individual share of water since 1990, placing Egypt with the lowest individual share of water per person in the world (Abd Ellah, 2020). Renewable water resources are limited in Egypt due to the defined share of Nile water as the main source of water. According to the FAO AQUASTAT database SDG 6.4.2 parameter, the level of water stress in Egypt is 141.17%, meaning freshwater withdrawals exceed renewable water resources, causing unsustainable utilization. This creates a high risk of resource depletion, environmental degradation, and long-term water scarcity, urging better water management practices. This makes the groundwater a precious resource that acts as a safety net for Egypt (Negm et al., 2019). The Nile Delta Aquifer is in direct contact with the Mediterranean Sea, which makes it subject to contamination with saltwater (Sefelnasr & Sherif, 2014)

Seawater intrusion is a widespread issue affecting coastal aquifers all over the world, as its progression is affected by external factors as groundwater pumping, irrigation and recharge operations, land use, and sea level rise, where the Egyptian coast is most vulnerable (Bear, 1999; El Raey et al., 1999). Groundwater salinity is affected by seawater intrusion, increasing seaward and depth-wise due to the increased density of more saline water naturally sinking due to gravity. (Sefelnasr & Sherif, 2014). This growing need for water is compensated by the unsystematic pumping of underground water by the villagers, which exceeds the replenishment rate of the aquifer. (Sherif, 1999). This process decreases the pressure in the freshwater zone and allows for saltwater to invade the aquifer. (Abd-Elaty & Polemio, 2023). In addition, the saltwater creates spikes of saltwater (Figure 1). With more surface area being mixed with salt water, the speed at which the saltwater diffuses into the aquifer increases (Zeidan, 2017).

The United States Environmental Protection Agency points out that chloride-rich water may present several issues, such as high blood pressure, a salty taste, the corrosion of piping, fixtures, and appliances, with potential blackening and pitting of stainless steel. (Wiltse

& Dellarco, 1996). Agricultural land salinization caused by seawater intrusion poses a significant threat to food production. Salt can degrade buildings, roads, and water supply systems, increasing operational costs and reducing efficiency. This means saltwater intrusion places immense stress on the economic system, food chain and health system and thus should be considered as a major threat to our country (Mohamed, 2016). The Nile Delta represents 40% of crops, 50% of fish wealth and contributes 60% of industrial yield, which makes it a major contributor to the Egyptian economy (El Raey et al., 1999).

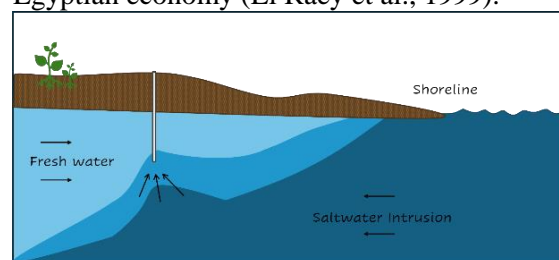


Figure 1 Illustration of saltwater intrusion in a coastal aquifer due to over-pumping of groundwater, altering the subsurface hydrodynamics and water quality. The fresh-saltwater interface is in a dynamic balance governed by hydrogeological conditions and human activities.

Previous studies aimed to determine the effect and extent of seawater intrusion on the Nile Delta aquifer using the time domain electromagnetic method as an efficient, cost-effective tool. The effect of seawater intrusion in the area was proven by (Ahmed et al., 2013) using chemical analysis of water samples obtained from several wells in the area. (Nofal et al., 2015) suggested the presence of a complex wedge system of four saline wedges intruding into the aquifer. The freshwater only exists in the top two wedges, with the rest of the reserve in the aquifer being saline and brackish. Later studies depended mostly on soil samples represented by Elsaid Saeed (2021) due to limited accessibility to well data. (Ding et al., 2020) introduced the possibility of using remote sensing data to predict seawater intrusion. More advanced remote sensing techniques combined with multivariate statistical analysis introduced by Abd El-Hamid et al. (2023) provided promising results in the area. These results can be limited by the capabilities of remote sensing data, low resolution and inaccessibility to detailed subsurface data, depending on indirect indications of seawater intrusion.

This study aims to determine whether the

time domain electromagnetic method (TDEM) can be used to determine the seawater intrusion in this area. The approach is expected to provide the lateral and depth extent of seawater encroachment into freshwater based on previous work conducted in comparable settings (El-Kaliouby & Abdalla, 2015). The objective is to realize the efficiency of TDEM in providing models of the groundwater system at a site where seawater intrusion has occurred with accurate results. The results will contribute to the better management of coastal aquifers with changing saltwater extent and help and protect the essential water supplies and local economy.

### Geologic settings

The Nile Delta aquifer is considered one of the largest groundwater reserves in the world. It is a coastal aquifer that lies under the delta region of Egypt, with a thickness ranging from 200 meters in the south to 900 meters along the shoreline (Sefelnasr & Sherif, 2014). Refilled by irrigation activities, it is a source of water in Egypt and a vast storage facility providing flexibility of management (Elbeih, 2016). The aquifer occupies the Quaternary and Late Tertiary deposits with a water table less than 1 meter below the surface, subjecting the water to various surface contaminants (Sharaky et al., 2016). Groundwater movement follows the general topography, moving from south to north, aquifer recharge sources include the Damietta Branch, flood irrigation water, and rainfall (Gamal et al., 2023).

The study area is located in the northeastern Nile Delta, covering a 50 km profile from the northwest border of New Mansoura City towards Mansoura (Figure 2). This region is composed of fluvial-deltaic deposits represented in thick sand Bilqas Formation deposited with Holocene age, topped with silty Bilqas Formation as valley deposits (Pennington et al., 2017). Based on this model, the Nile Delta aquifer has been defined by a simplified model, treating it as a homogeneous sand-gravel aquifer capped by a clay layer. This model divided the aquifer into a three-layered structure: an upper Holocene aquitard, a primary gravel-sand aquifer with

intermittent clay lenses, and a lower Pliocene clay aquiclude that serves as the base (Negm et al., 2019). This representation suggested a continuous, uniform aquifer, with a gradual southward homogeneity, dipping at an average slope of 4 meters per kilometre. However, recent studies challenge this simplicity. The updated model reveals a more complex, "finger-like" configuration, with sand and clay layers alterations, varying both laterally and vertically (Nofal et al., 2015). This complexity in lithology arises from the dendritic drainage pattern system creating a multilayer aquifer, allowing the saltwater to invade some wedges more than others and creating lenses of salt and fresh water at various depths. (Nofal et al., 2015; Pennington et al., 2017).



Figure 2 Satellite image of a part of Egypt including The Nile Delta valley and River. The study area is located in the northern part of the east and middle delta within the jurisdiction of Damietta and Dakahlia Governorates.

The fluvial-deltaic origin of these deposits means that sedimentation patterns vary significantly across the profile. Near the shoreline, deposits are thicker, with sands and gravels providing primary pathways for groundwater flow, while inland, the clay content increases, reducing permeability (Coutellier & Stanley, 1987). This variability influences the rate and extent of seawater intrusion, as the saline front moves more readily through high-permeability sandy layers and is



hindered by low-permeability clay zones (Stanley Andrew G., 1993).

This complex layering and variable lithology make it challenging to accurately predict the movement of seawater intrusion, as saline water can bypass certain layers through

sand channels or be restricted by clay barriers (Zeidan, 2017). The aquifer's structure not only limits the predictability of traditional models but also calls for more sophisticated techniques to assess the freshwater-saltwater boundary accurately (Dawoud, 2004).



Figure 3 A satellite image of The Nile Delta showing the locations of RIGW National monitoring network modified after (Dawoud, 2004)

### National Monitoring Efforts and Limitations

Egypt established the National Groundwater Quality Monitoring Program (NGQM) in 1998 to monitor both seawater intrusion and point pollution through wells (Figure 3). The design of this program faced a challenge to cover both problems with limited data and budget, adding stress on the model design.

Due to factors like geographical distribution, hydrogeological variability, population density, groundwater usage, and projected pollution loads, a relatively small number of wells were assigned to cover broad regions (Dawoud, 2004). Since the monitoring network was established, measurements have largely depended on the project's available budget. That, combined with the natural

heterogeneity of the aquifer, made the model less reliable. Over time, funding declined. The network degraded. In many areas, testing stopped in most wells. We relied on data from three nearby wells that still provide recent readings. However, this information was clearly insufficient. As a results, we relied on water samples collected during recent construction activities in the area. The data show total dissolved salts (TDS) ranging from 2,650 ppm to 24,500 ppm. High salinity values were observed near the coast and at greater depths. For instance, Point 1 (15 m) recorded the highest salinity at 24,500 ppm. Deeper wells such as Point 7 (250 m) also showed elevated TDS (20,000 ppm), while inland and shallower points like Point 8 (30 m) had much lower concentrations (2,650 ppm). This pattern points toward both lateral and vertical salinity gradients across the region.

Table 1: TDS values of water sample and monitoring well data showing depth and TDS variation across the study area. Coastal and deeper points tend to show higher salinity

Point	Type	Depth	TDS	Latitude	Longitude
1	Water sampling	15	24500	31.478699	31.426046
2	Water sampling	35	6780	31.404750	31.499383
3	Water sampling	40	16200	31.421825	31.423809
4	Monitoring wells	250	7650	31.419531	31.363739
5	Water sampling	25	4710	31.407972	31.364450
6	Water sampling	25	7770	31.369006	31.475753
7	Monitoring wells	250	20000	31.363056	31.421667
8	Water sampling	30	2650	31.279604	31.298451
9	Water sampling	35	7560	31.201812	31.438938
10	Monitoring wells	200	11000	31.127372	31.363687

## Methods

### Time Domain Electromagnetic Method

This approach is a non-invasive, cost-effective method that does not need direct contact with the ground, which gives it the advantage of application in different terrain settings (Spichak, 2015). It can be used to detect the fresh and saltwater interface (Yang et al., 1999). The depth of investigation is controlled by the physical conditions of the area; a 25 m<sup>2</sup> square of wire was expected to reach a depth of 75 m (Zhdanov, 2009). Another set of data, represented in chemical analysis data from both deep and shallow wells in the area, was collected to draw a TDS profile. This profile aimed to investigate the trend in water salinity in the area shown in Figure 4.

### Survey Design and Acquisition

Considering the extent of the saltwater intrusion, the TDEM stations were spaced at nearly 1km, avoiding possible obstacles as fish farms and inaccessible land. The stations were set to be perpendicular to the shoreline to guarantee that they cut through the fresh-salt water boundary. This resulted in 50 stations at a 50km distance from the northwest side of New Mansoura city to the northern boundaries of Mansoura city (Figure 5). The device used is a direct current transmitter and a receiver, both connected to a wire spread on the ground as a square with 25m side length that was expected to reach up to 75m, which may decrease due to soil salinity. The device used was an AIE-2 Measuring System (TDEM), comprising the TDEM-200 transmitter, TEM-IP receiver, and a control unit. This allowed us to record the decay

curve at 0.1, 1 and 10 voltages (Figure 6).

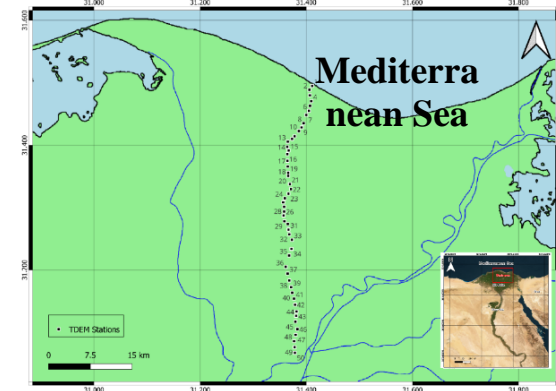


Figure 4 TDEM stations starting at the shoreline at western New Mansoura (Station 1), extending perpendicular to the shoreline ending at Mansoura city borders (Station 2).

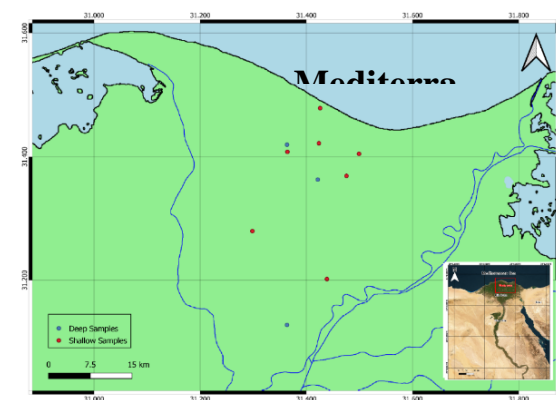


Figure 5 Shallow water samples collected from architectural projects in the area with an average depth of 35m and the deep samples collected from existing monitoring wells with an average depth of 250m.



Figure 6 . Field setup for Time-Domain Electromagnetic (TDEM) data acquisition. (Top) Configuring the receiver and connecting the loop. (Bottom) AIE-2 Measuring System, including a power source connected to the transmitter, and loop connections for signal generation. A phone-like unit controls the survey parameters and operation.

### Data Processing and Inversion

One challenge encountered was cultural noise due to municipal infrastructure, which interfered with the recorded decay curves. Noise distortion was particularly noticeable in the deep sections at some stations, necessitating the removal of these segments. A summation of the three decay curves at different voltages was calculated at each station, resulting in a higher signal-to-noise ratio. Some readings had to be manually adjusted to guarantee less ambiguities during the inversion process (Figure 7). According to the initial investigation of the data, a smooth inversion algorithm was applied to the processed data, utilizing a smoothing factor of 0.01 and a depth smoothing factor of 2, and an initial 4-layer model, which was edited whenever necessary. A fitted model

with an average 5% error margin, which was supervised to ensure a reasonable geological fitting model. The resulting inverted pseudo-section figure (8) showed a wedge of decreased resistivity that has maximum thickness at the shore and decreases gradually as we proceed to the south with increasing depth. The data represented in Table 2 shows variation in resistivity in ohm.m ( $\Omega.m$ ) against layer thickness in meters. Station (1) is the first station on the seashore towards the north and Station (50) is the last station towards the south at Mansoura city. The values show a general decrease in resistivity with depth, suggesting increased salinity and increasing towards the south as fresh water prograde invading the saltwater zone into the more brackish layer.

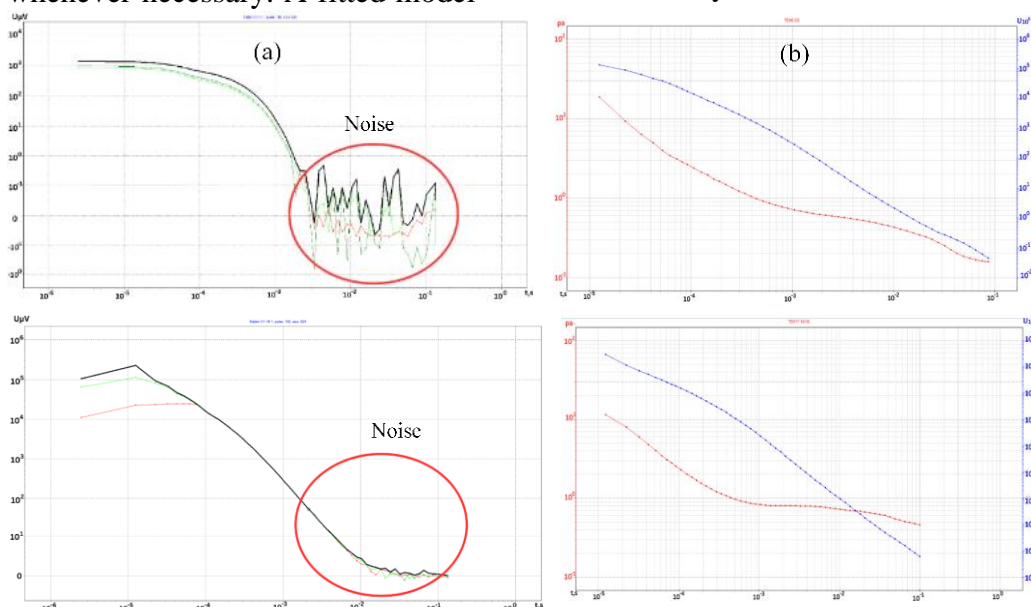


Figure 7 The TDEM decay curve at different voltages reading showing two station readings of the raw preprocessed data with cultural noise at (a) and the processed curves at (b). processing techniques includes removing highly distorted data at the end of profile

Table 2: Variation of resistivity ( $\Omega.m$ ) with depth across stations from the seashore to Mansoura city, illustrating the transition from saline to freshwater conditions.

	Station (1)		Station (10)		Station (20)		Station (30)		Station (40)		Station (50)	
	$\Omega.m$	H	$\Omega.m$	H	$\Omega.m$	H	$\Omega.m$	H	$\Omega.m$	H	$\Omega.m$	H
Layer 1	35.506	1.195	6.024	2.529	4.286	4.574	8.078	12.195	49.46	2.82	52.029	6.634
Layer 2	1.224	0.78	1.014	2.978	1.16	3.447	4.972	5.655	3.77	2.44	13.193	19.162
Layer 3	0.36	1.989	0.339	4.997	0.427	34.658	2.062	13.433	1.3	46.63	5.377	40.122
Layer 4	0.467	40.859	0.478	33.567	0.0496	17.245	1.357	22.653	0.24	20.22	2.693	55.842

To further enhance the reliability of the TDEM data, the results were cross-validated with well data obtained from the monitoring network established by the RIGWA institute. This

integration included comparing both lithological and chemical analysis for the calibration of the TDEM model to assess the reliability of the model.



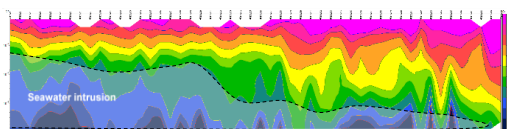


Figure 8: Inverted pseudo-section of TDEM data illustrating resistivity data in ohm.m on y-axis against distance starting at station (1) to the right towards the north at shoreline to station (50) southward to the left. Seawater intrusion shown as a descending wedge represented with resistivity less than 1 ohm and colors ranging from dark green to blue

## Results

Based on TDEM data, the observed depth of penetration varied significantly across the study area, influenced by local salinity levels. In more saline areas, the penetration is restricted to about 60 meters; in less saline zones, this goes up to 80 meters.

The inverted section (Figure 9) showed three distinctive layers according to their resistivity, which was cross-validated with a geologic section obtained from a nearby well. The surface sand layer showed high resistivity, which was either dry or irrigated with fresh water. This layer increase in thickness towards the south corresponds to the increase of the water table depth.

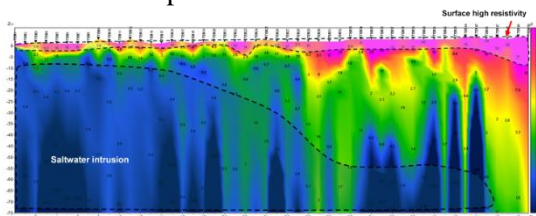


Figure 4: Inverted resistivity section along the profile, displaying resistivity values ( $\Omega \cdot m$ ) with depth. The X-axis represent the stations from 1 to 50 and the Y-axis represent depth in (m). Warmer colours indicate higher resistivity zones, while cooler colours represent lower resistivity regions

Beneath, alternating sand and mud layers displayed moderate resistivity variations, with sand-dominant sections showing higher resistivity compared to clay-rich areas. The saltwater intrusion was revealed as a very low resistive zone with resistivity values between 0.1 and 3 ohm-m, extending inland from the coastline.

Moving southward from station 29, about 24 km inland, resistivity started to increase, which showed that the groundwater transitioned

into the brackish zone, which could potentially be a water resource. Further to the south, the apparent decrease in the value of resistivity would seem to be related to decreased salinity rather than changes in sediment type, since this trend was observed from both sandy and clay-rich sections.

The TDEM profile was compared with lithological data from wells provided by the Research Institute of Groundwater (RIGW) to assess the influence of saline and freshwater on resistivity measurements. The obtained section supported the predictions of the TDEM data of layer stratigraphy, eliminating the possibility that the resistivity difference is caused by lithological differences rather than fluid salinity.

To check this observation, we compared the TDEM profiles with the lithological data of the wells of RIGW. The results were quite consistent, meaning the variation in resistivity is controlled by the salinity of the fluids rather than by lithology. This was further supported by the TDS determinations shown in Figure 10, giving very high concentrations in the northern parts of the profile, topping 20000 ppm, while southward it gradually decreased to about 3000 ppm. This pattern no doubt has shown the extent of seawater intrusion in the study area.

TDEM profile length, along with insufficient well control, restricted resistivity-salinity calibration in the studied locations. As a result, determining the extent of the fresh-saline water interface is still debatable due to the gradual nature of the intrusion, resulting in a wide area of brackish water.

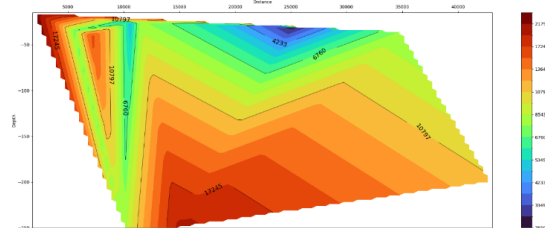


Figure 10: Total dissolved salts profile along the study area from the North (right) to the south (left) perpendicular to the shoreline

## Discussion

This paper focuses on the dynamics of seawater intrusion in the Nile Delta aquifer and demonstrates the effectiveness of TDEM in mapping the salt-freshwater boundary. Saltwater intrusion is inferred inland,

transitioning to brackish water and eventually freshwater further south. The resistivity variations observed are controlled by salinity differences rather than lithological complexity, which has been validated using well data. The identified brackish zone could support irrigation or industrial use, reducing freshwater demand.

While TDEM was successful in defining these limits, poor conditions such as cultural noise, sparse well data and insufficient funding prevented the determination of the freshwater boundary with enough accuracy. The transitional nature of the saline-brackish zones makes it difficult to define a more precise salt-freshwater interface. Although we managed to collect data from local wells and some soil samples, the regulation on water data and the scarce recent well data made it challenging to validate the model with the expected certainty. This data could have been enough to conclude a reliable model, but the area has a high heterogenic lithology that controls aquifer parameters and seawater intrusion in the area which makes it challenging to interpolate data and calls for further research for specific sites or projects. The complex lithology of the area, high power line network and scattered urban residential complexes created a simple electromagnetic noise enough to disturb the data in some stations and prevented readings in others altogether.

Despite these limitations, TDEM showed a promising and economically viable non-invasive technique for coastal aquifer monitoring, while the characterized brackish zone provides possible use for non-potable purposes. This issue is not unique—many coastal aquifers in Mediterranean countries experience similar challenges. The outcomes here could likely be adapted in those regions with relatively low effort and cost. And beyond that, the tool helps guide decision-makers as it offers a practical way to set up a basic, cost-effective monitoring network—especially in areas where data is scarce—by mapping the region and identifying both hazard zones and preliminary salinity levels.

## Conclusion

This study proves that the time domain electromagnetic method is a cost-effective tool for delineating seawater intrusion to guarantee

the continuity of the monitoring process in the Nile Delta aquifer. We managed to map seawater intrusion with proximity to what was determined by well data, showing intrusion extending landward up to 24km. This survey extended to 50km and reached a depth of 60m, which can be increased by increasing loop size, time and power. These changes to survey configuration have a small effect on cost but yield better results. Processing cultural noise from the data was deemed to be challenging using traditional software and inversion techniques, but showed promising potential for more advanced techniques, such as deep learning-based noise filtering (e.g., convolutional neural networks, CNNs) and unsupervised clustering algorithms (e.g., K-means, DBSCAN) for noise identification, which could enhance signal extraction. Additionally, Bayesian inversion and physics-informed neural networks (PINNs) implemented in Python offer promising alternatives for improving resistivity inversion accuracy in complex environments. However, due to the limitations in computational expertise at the time of this study, traditional processing methods were employed. Accordingly, we recommend the integration of available well data and TDEM surveys to manage seawater intrusion with the sustainability of groundwater resources and using more advanced processing techniques. based on TDEM survey data, protected areas where groundwater use is restricted can be set to protect against further intrusion.

## Data Availability Statement

Well data that was used in this research is a combination of published data in research and new updated data that can be requested from the Research Institute of Groundwater (RIGW) in Egypt. Time domain electromagnetic data is the property of the authors acquired through field surveys. The datasets generated during and/or analyzed during the current study are available from the corresponding author upon reasonable request.

## References:

Abd El-Hamid, H. T., Alshehri, F., El-Zeiny, A. M., & Nour-Eldin, H. (2023). Remote sensing and

- statistical analyses for exploration and prediction of soil salinity in a vulnerable area to seawater intrusion. *Marine Pollution Bulletin*, 187. <https://doi.org/10.1016/j.marpolbul.2022.114555>
- Abd Ellah, R. G. (2020). Water resources in Egypt and their challenges, Lake Nasser case study. In *Egyptian Journal of Aquatic Research* (Vol. 46, Issue 1, pp. 1–12). National Institute of Oceanography and Fisheries. <https://doi.org/10.1016/j.ejar.2020.03.001>
- Abd-Elaty, I., & Polemio, M. (2023). Saltwater intrusion management at different coastal aquifers bed slopes considering sea level rise and reduction in fresh groundwater storage. *Stochastic Environmental Research and Risk Assessment*, 37(6), 2083–2098. <https://doi.org/10.1007/S00477-023-02381-9/TABLES/4>
- Ahmed, M. A., Abdel Samie, S. G., & Badawy, H. A. (2013). Factors controlling mechanisms of groundwater salinization and hydrogeochemical processes in the Quaternary aquifer of the Eastern Nile Delta, Egypt. *Environmental Earth Sciences*, 68(2), 369–394. <https://doi.org/10.1007/s12665-012-1744-6>
- Bear, J. (1999). Seawater Intrusion in Coastal Aquifers — Concepts, Methods and Practices - Seawater intrusion in coastal aquifers : concepts, methods, and practices. In *Theory and Applications of Transport in Porous Media: Vol. NA* (Issue NA). <https://doi.org/10.1007/978-94-017-2969-7>
- Coutellier, V., & Stanley, D. J. (1987). LATE QUATERNARY STRATIGRAPHY AND PALEOGEOGRAPHY OF THE EASTERN NILE DELTA, EGYPT. In *Marine Geology* (Vol. 77).
- Dawoud, M. A. (2004). DESIGN OF NATIONAL GROUNDWATER QUALITY MONITORING NETWORK IN EGYPT.
- Ding, Z., Koriem, M. A., Ibrahim, S. M., Antar, A. S., Ewis, M. A., He, Z., & Kheir, A. M. S. (2020). Seawater intrusion impacts on groundwater and soil quality in the northern part of the Nile Delta, Egypt. *Environmental Earth Sciences*, 79(13). <https://doi.org/10.1007/s12665-020-09069-1>
- El Raey, M., Frihy, O., Nasr, S., & Dewidar, K. (1999). Vulnerability Assessment of Sea Level Rise Over Port Said Governorate, Egypt. *Environmental Monitoring and Assessment - ENVIRON MONIT ASSESS*, 56. <https://doi.org/10.1023/A:1005946819600>
- Elbeih, S. F. (2016). Mapping of Groundwater in Egypt Using RS/GIS: Case Studies, Areas Surrounding Nile Valley and Its Delta (pp. 63–88). [https://doi.org/10.1007/698\\_2016\\_52](https://doi.org/10.1007/698_2016_52)
- El-Kaliouby, H., & Abdalla, O. (2015). Application of time-domain electromagnetic method in mapping saltwater intrusion of a coastal alluvial aquifer, North Oman. *Journal of Applied Geophysics*, 115, 59–64. <https://doi.org/10.1016/j.jappgeo.2015.02.003>
- Elsaid Saeed, M. (2021). MONITORING OF LAND DEGRADATION AND SOIL PRODUCTIVITY IN BILQAS DISTRICT, DAKAHLIA GOVERNORATE, EGYPT. *Egyptian Journal of Soil Science*, 0(0), 0–0. <https://doi.org/10.21608/ejss.2021.82334.1456>
- Gamal, G., Hassan, T. M., Gaber, A., & Abdelfattah, M. (2023). Groundwater quality assessment along the West of New Damietta Coastal City of Egypt using an integrated geophysical and hydrochemical approaches. *Environmental Earth Sciences*, 82(4). <https://doi.org/10.1007/s12665-023-10762-0>
- Mohamed, N. N. (2016). Management of Salt-Affected Soils in the Nile Delta (pp. 265–295). [https://doi.org/10.1007/698\\_2016\\_102](https://doi.org/10.1007/698_2016_102)
- Negm, A. M., Sakr, S., Abd-Elaty, I., & Abd-Elhamid, H. F. (2019). An overview of groundwater resources in Nile Delta aquifer. In *Handbook of Environmental Chemistry* (Vol. 73, pp. 3–44). Springer Verlag. [https://doi.org/10.1007/698\\_2017\\_193](https://doi.org/10.1007/698_2017_193)
- Nofal, E., A, A. M., M, E.-D. S., Fekry, A. M., & El-Khairiya-Egypt, E.-K. (2015). Sea Water Intrusion in Nile Delta in Perspective of New Configuration of the Aquifer Heterogeneity Using the Recent Stratigraphy Data. In *Journal of American Science* (Vol. 11, Issue 6). <http://www.jofamericanscience.orghttp://www.jofamericanscience.org.33>
- Pennington, B. T., Sturt, F., Wilson, P., Rowland, J., & Brown, A. G. (2017). The fluvial evolution of the Holocene Nile Delta. *Quaternary Science Reviews*, 170, 212–231. <https://doi.org/10.1016/j.quascirev.2017.06.017>
- Sefelnasr, A., & Sherif, M. (2014). Impacts of Seawater Rise on Seawater Intrusion in the Nile Delta Aquifer, Egypt. *Groundwater*, 52(2), 264–276. <https://doi.org/10.1111/gwat.12058>
- Sharaky, A. M., El Hasanein, A. S., Atta, S. A., & Khallaf, K. M. (2016). Nile and Groundwater Interaction in the Western Nile Delta, Egypt (pp. 33–62). [https://doi.org/10.1007/698\\_2016\\_127](https://doi.org/10.1007/698_2016_127)
- Sherif, M. (1999). SEAWATER INTRUSION IN THE NILE DELTA AQUIFER: AN OVERVIEW.
- Spichak, V. V. (2015). *Electromagnetic sounding of the Earth's interior* (2nd ed.). Elsevier.
- Stanley Andrew G., D. J. W. (1993). NILE DELTA : RECENT GEOLOGICAL EVOLUTION AND HUMAN IMPACT. *Science* (New York, N.Y.), 260(5108), 628–634. <https://doi.org/10.1126/science.260.5108.628>

- Wiltse, J., & Dellarco, V. L. (1996). Reviews in Genetic Toxicology Environmental Protection Agency guidelines for carcinogen risk assessment: Past and future 1. In Mutation Research (Vol. 365). ELSEVIER. www.epa.gov/ORD
- Yang, C. H., Tong, L. T., & Huang, C. F. (1999). Combined application of dc and TEM to sea-water intrusion mapping. Geophysics, 64(2), 417–425. <https://doi.org/10.1190/1.1444546>
- Zeidan, B. A. (2017). Groundwater degradation and remediation in the Nile Delta aquifer. In Handbook of Environmental Chemistry (Vol. 55, pp. 159–232). Springer Verlag. [https://doi.org/10.1007/698\\_2016\\_128](https://doi.org/10.1007/698_2016_128)
- Zhdanov, M. S. (2009). Geophysical Electromagnetic Theory and Methods. In METHODS IN GEOCHEMISTRY AND GEOPHYSICS. <http://elsevier.com/locate/permissions>,

## الملخص العربي

**عنوان البحث:** تطوير مراقبة الطبقات المائية الجوفية: تطبيق طريقة الزمن-المجال الكهرومغناطيسي (TDEM) في كشف تسرب مياه البحر ضمن الطبقات الساحلية غير المتجانسة في دلتا النيل

ريم علي النجار<sup>١\*</sup>، أيمن طه<sup>٢</sup>، هاني شعبان<sup>٢</sup>، إيمان نوفل<sup>٣</sup>، حاتم أبو الخير<sup>١</sup>

<sup>١</sup>كلية العلوم، جامعة دمياط، ٣٤٥١٧، دمياط، مصر

<sup>٢</sup>المعهد القومي للبحوث الفلكية والجيوفيزيقية، ١١٧٢٢، حلوان، القاهرة، مصر

<sup>٣</sup>معهد بحوث المياه الجوفية، المركز القومي لبحوث المياه، ١٣٦٢١، القناطر الخيرية، مصر

تُعد الطبقات الجوفية الساحلية مصدرًا حيويًا للمياه العذبة على مستوى العالم، إلا أنها تواجه تهديدًا متزايدًا بتداخل مياه البحر نتيجة الإفراط في سحب المياه وتغير المناخ. ويُعد خزان دلتا النيل أحد أكبر الخزانات الساحلية للمياه الجوفية في العالم، وهو عرضة بشكل خاص لتداخل مياه البحر، مما يشكل تهديدًا كبيرًا للزراعة والصناعة ومصادر مياه الشرب، ويزيد من تملح التربة وتآكل البنية التحتية، مما يفاقم الضغوط على الاقتصاد المحلي. تهدف هذه الدراسة إلى استكشاف كفاءة طريقة المجال الكهرومغناطيسي (TDEM) في تتبع تسلل مياه البحر داخل الطبقات الجوفية الساحلية. تم استخدام هذه الطريقة لجمع خمسين نقطة بيانات على امتداد مسار طوله ٥٠ كيلومترًا عموديًا على خط الساحل باتجاه مدينة المنصورة. وقد طُبِّقَت تقنيات معالجة مناسبة لزيادة نسبة البيانات إلى الضوضاء وتحسين وضوحها نظرًا لارتفاع الضوضاء في المنطقة. وأظهرت عملية إقلاّب البيانات الجيوفيزيائية وتفسيرها الحدود الفاصلة بين المياه المالحة والعذبة، كما أتاح توفر بيانات الطبقات من آبار المراقبة، معايرة النموذج الجيوفيزيائي للحصول على نتائج أكثر دقة. وأظهرت البيانات تطابقًا وثيقًا مع بيانات الآبار بهامش خطأ متوسط قدره ٥%، مما يكشف عن تداخل مياه البحر لأكثر من ٤٠ كيلومترًا إلى الخزان تدريجيًا، وقد تراوح عمق التداخل بين ١٠ إلى ٢٠ مترًا. وتؤكد هذه النتائج فعالية TDEM كأداة سريعة ومنخفضة التكلفة في رسم حدود تداخل المياه المالحة والعذبة في خزان دلتا النيل. وتُقدّم هذه الدراسة دمج TDEM مع شبكة المراقبة الحالية لتتبع التغيرات في خصائص الخزان الجوفي، مما يوفر أساسًا لتحسين استراتيجيات إدارة المياه الجوفية.

## Characterization and Antimicrobial Potential of *Enterococcus Faecium* Isolates from Raw Bovine Milk and Yoghurt

Hussam H. Arafat<sup>\*1</sup>, M.A. Shoulkamy<sup>1</sup>, M. M. Imam<sup>1</sup> and Amany M. A. Ali<sup>1</sup>

<sup>1</sup>Department of Botany & Microbiology, Faculty of Science, Minia University, Minia City- 61519, Egypt.

Received: 18 February 2025 /Accepted: 19 April 2025

\*Corresponding author's E-mail: hussamhassan77@mu.edu.eg

### Abstract

This study focuses on the isolation of enterococci, a subset of lactic acid bacteria (LAB). The study involves the identification of these isolates through morphological, biochemical, as well as molecular identification using 16S rRNA gene sequencing methods, alongside an exploration of their antimicrobial efficacy. Three isolates were obtained from milk and yoghurt samples, identified as *Enterococcus faecium*. Tolerance of the isolates to bile salts (up to 40%) and mild acidity (pH=4.5), makes them survive in guts and thus applicable as probiotics. The cell-free supernatants (CFSs) derived from these isolates exhibited significant antibacterial activity where inhibition zones reached 9.3-10.33 mm against *Proteus vulgaris*, *Staphylococcus aureus* and *Staphylococcus albus*; while zones recorded against *Pseudomonas aeruginosa*, *Serratia marcescens*, *Klebsiella pneumoniae* and *Escherichia coli*, reached 3-8.3 mm. By contrast, they showed no efficacy against fungi. Notably, the antimicrobial activity of CFSs was maintained at various temperatures, including autoclaving conditions (121 °C). The isolates displayed tolerance across a wide pH range (2.5-9.5), with enhanced activity observed at acidic pH levels compared to basic ones. Heat and pH stability of supernatants encourage their use as bio-preservatives.

**Keywords:** *Enterococcus faecium*, Biochemical characterization, 16S rRNA, Antimicrobial activity

### Introduction

Various genera of cocci lactic acid bacteria, encompassing *Pediococcus*, *Leuconostoc*, *Weissella*, *Lactococcus*, *Enterococcus*, and *Streptococcus* (Whitman *et al.*, 2015), exhibit distinctive characteristics. Lactic acid bacteria (LAB) are Gram-positive, non-motile, catalase-negative, and non-spore-

forming microorganisms with the ability to produce lactic acid. This bacterial group holds significant technological relevance, showcasing features such as proteolytic activity, polysaccharide production, and remarkable resistance to freezing and freeze-drying. Additionally, LAB exhibit probiotic properties, including adhesion and colonization in the digestive mucosa, vitamin production, and the synthesis of antimicrobial compounds (Ananou *et al.*, 2007; LeBlanc *et al.*, 2011; Oliveira *et al.*,

2008). Notably, LAB demonstrate the inhibition of various bacteria, such as *Escherichia*, *Staphylococcus*, *Salmonella*, *Shigella*, and *Bacillus*, along with antifungal activity against *Candida* sp. (Adikari *et al.*, 2021; Islam *et al.*, 2020).

The use of probiotic strains in treatments is considered both safe and stable, avoiding an increase in the risk of multi-drug resistance among pathogens (Rohmann & McGrail, 2006). The antagonistic mechanism between LAB and harmful genera relies on the production of metabolites, including organic acids (such as lactic and acetic acid, leading to a pH decrease that is unfavorable to some pathogens and spoilage microorganisms), bacteriocins, hydrogen peroxide, antifungal peptides, and competition for nutrients (Vasiljevic & Shah, 2008; Rahmeh *et al.*, 2019). LAB coatings present a viable alternative to chemical compounds, enhancing the shelf life and safety of fresh-cut fruits, such as pineapple (Lee *et al.*, 2020 ; Tenea *et al.*, 2020 ; Yang & Moon, 2021).

*Enterococcus faecium* emerges as a potential bio-preservative in dairy and meat products to control *Listeria monocytogenes*, capable of growth at refrigeration temperatures (4 °C) (Lee *et al.*, 2020). Lactic acid bacteria find applications in diverse sectors, including ruminants like cattle, poultry, and beekeeping, contributing to health, growth, reproductive success, and protection against diseases (Yang & Moon, 2021). The supplementation of milk with probiotic lactic acid bacteria, such as *E. faecium*, *L. plantarum*, and *L. acidophilus*, has been linked to increased weight in young calves (Frizzo *et al.*, 2011). In the production of artisanal cheeses, numerous enterococci (e.g., *E. avium*, *E. durans*, *E. faecalis*, *E. faecium*, *E. hirae*, *E. lactis*, among others) play a vital role in imparting unique flavors (Dapkevicius *et al.*, 2021).

Nisin, the widely used bacteriocin as a food bio-preservative, shows decreased stability and a narrow pH range (5.0 - 7.0), with only slight effects on gram-negative bacteria. This prompts the exploration of new antimicrobial components with a broad spectrum (Hécharde & Sahl, 2002). The safety and efficiency of antimicrobial compounds from lactic acid bacteria, have garnered considerable attention in recent research as potential natural alternatives to antibiotics and chemical preservatives in the food industry

(Bhakta *et al.*, 2023).

Thus, this study aims to investigate and characterize the antimicrobial components of lactic acid bacteria, with a specific focus on enterococci, to explore their potential as natural alternatives to antibiotics and chemical preservatives in the food industry.

## Materials and Methods:

### *Isolation of Lactic Acid Bacteria (LAB):*

A 10<sup>-1</sup> dilution of selected food samples (bovine milk, yoghurt) was prepared in approximately 10 ml sterile distilled water (SDW). Each diluted sample (0.5 ml) was plated on de Man, Rogosa, and Sharpe (MRS) agar plates (de Man *et al.*, 1960) and incubated under aerobic conditions at 37 °C for 3 days.

### *Morphological Characterization:*

Colonies with white, convex or raised, smooth surfaces and diameters ( $\leq 2$  mm) were selected for purification (on MRS agar) and Gram staining (Grange & Lyne, 2004). Gram-positive cocci isolates were purified through repeated streaking on MRS agar plates, with strains isolated from milk and yoghurt denoted by the letters (M) and (Y), respectively.

### *Preservation of Isolates:*

Short-term storage (for 1 month at 4 °C) involved three methods: agar slant, stab inoculation using semi-solid MRS medium (with 0.3% CaCl<sub>2</sub> as pH neutralizer) as described by Björkroth and Holzapfel, 2006), and inoculation of MRS broth with young bacterial culture. For long-term storage, isolates were maintained as glycerol stocks at -20 °C (Spencer & de Spencer, 2008). One isolate were deposited in the Culture Collection Ain Shams University (CCASU) of the World Data Centre for Microorganisms (WDCM) under specific codes (*Enterococcus faecium*, CCASU-2023-62) (<https://doi.org/10.12210/ccinfo.1186>) (Table 5).

### *Motility Test:*

Stab inoculation in tubes of semi-solid MRS medium was performed as described by MacFaddin (2000), and motility was assessed



after incubation at 37 °C for 48 hrs.

### Biochemical Characterization:

Various biochemical tests were conducted in MRS broth (Somasegaran & Hoben, 2012), including gas (CO<sub>2</sub>) production (Schillinger & Lücke, 1987), catalase production (Kozaki *et al.*, 1992), gelatin hydrolysis (Aneja, 2007), starch hydrolysis (Evans *et al.*, 2004), tryptophanase activity (Kovacs, 1928), nitrate reduction (Reddy *et al.*, 2007), citrate utilization (Mithun *et al.*, 2015), hydrolysis of arginine (Samelis *et al.*, 1994), NaCl tolerance (Ni *et al.*, 2015), growth at acidic and alkaline pH (Ni *et al.*, 2015), growth at different temperatures (Samelis *et al.*, 1994), Voges-Proskauer test (Barritt, 1936), production of dextran (slime) from sucrose (Hitchener *et al.*, 1982), production of hydrogen sulfide (H<sub>2</sub>S) (Shay & Egan, 1981), methylene blue reduction (Abanoz & Kunduhoglu, 2018), carbon source utilization (Abanoz & Kunduhoglu, 2018), urease test (Steadham, 1979) and bile salts tolerance (Menconi *et al.*, 2014).

### Amplification of 16S rRNA Gene:

Genomic DNA was extracted as described by Spencer and de Spencer (2008), and PCR amplification of the 16S rRNA gene was performed using universal primers 27 F (5'-AGAGTTTGATCCTGGCTCAG- 3') and the reverse primer 1492 R (5'-GGTTACCTTGTACGACTT- 3'). The PCR product was sequenced, and BLAST analysis was conducted to determine sequence similarities.

### Sequence Analysis:

Obtained sequences were edited and analyzed using Lasergene 7.1.0. A phylogenetic tree was constructed to assess evolutionary relationships with sequences from GenBank.

### Antimicrobial Activity Test:

Isolates were grown in MRS broth, and cell-free supernatants (CFSs) were obtained. The well diffusion method (Sonbol *et al.*, 2020) was employed to test antimicrobial activity against various indicator organisms, for example: *Staphylococcus aureus*, *S. albus*, *Pseudomonas aeruginosa*, *Serratia marcescens*, *Klebsiella pneumoniae*, *Escherichia coli*, *Aspergillus niger*, *Aspergillus flavus* and *Candida albicans*.

### Thermal and pH Stability of CFS:

CFSs were subjected to different temperatures and autoclaving, as well as varying pH levels. *Staphylococcus albus* was chosen as an indicator to assess supernatant activity (Oliveira *et al.*, 2008 ; Abanoz & Kunduhoglu, 2018).

### Data statistical analysis:

Data are presented as mean ± SE by applying the SAS program (version 9.4, 2013). Duncan's test was used to determine the significance of the mean differences. The probability was considered significant at p < 0.05.

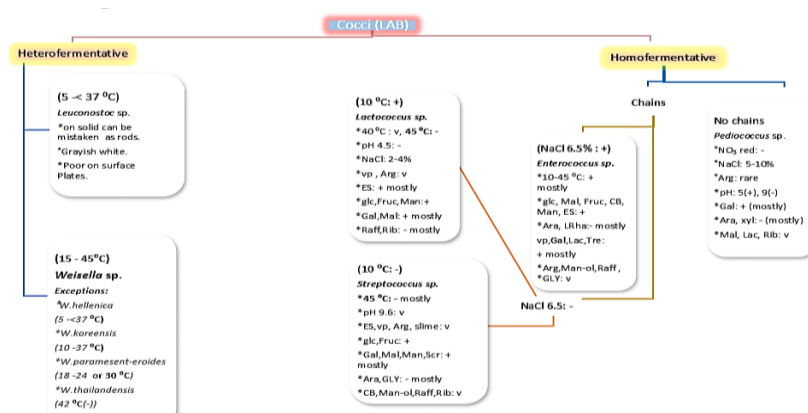


**Fig.1:** Schematic representation for differentiation between cocci Lactic Acid bacteria (LAB).

\*+ = Growth observed, - = No growth, v = variable, Gal=galactose, Fruc=fructose, Glc=glucose, GLY=glycerol, Man=D-mannose, Ara=D-arabinose, Rib=ribose, LRha=L-rhamnose, Man-ol= mannitol, Lac=lactose, Mal=maltose, CB=cellobiose, Raff= raffinose, Scr=sucrose, ES=esculin, Arg= arginine hydrolysis, Xyl=xylose, Tre=trehalose, VP= acetoin production

## Results:

### Isolation and Identification of *Enterococci*:

Three isolates of cocci LAB were successfully obtained, with two originating from milk (4M and 7M) and one from yoghurt (6Y). Colonies exhibited circular, convex morphology, ranging from translucent to opaque, with off-white to pale-white color, smooth surfaces, and entire margins. Under microscopic examination, the strains appeared oval, Gram-positive, and non-spore formers (Table 1).

All isolates exhibited catalase negativity and acid production from glucose without gas formation. Negative results were observed for motility, indole, nitrate reduction, urease, starch and gelatin hydrolysis, and H<sub>2</sub>S production. Positive outcomes were recorded for acetoin production, slime formation, methylene blue reduction, milk coagulation,

arginine hydrolysis, and growth in bile salts up to 40% (Table 2).

Positive carbon source utilization was observed for lactose, mannose, fructose, galactose, cellobiose, mannitol, ribose, raffinose, glycerol, and maltose. Negative results were noted for citrate and arabinose; while only one isolate utilized rhamnose (7M) (Table 3). Isolates demonstrated growth at temperatures ranging from 5 to 45 °C, with tolerance to salinity up to 6.5 % and pH levels between 4.5 and 9.5. None of the isolates grew at pH 3 (Table 4).

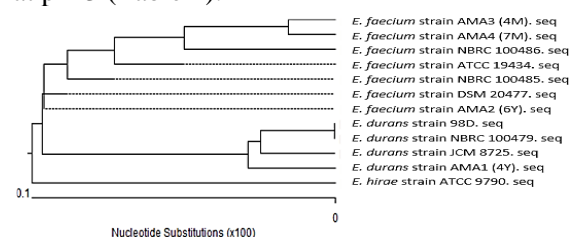


**Fig. 2:** Phylogenetic tree indicating relationship between our isolates and enterococci strains based on 16S rRNA gene sequence.

**Table 1:** Colony morphology and microscopic examination of *Enterococcus faecium* isolates.

Isolate	Shape	Transparency	Color	Margin	Surface	Diameter	Elevation	Cell shape
6Y	Circular	Translucent	Off white	Entire	Smooth	0.5 mm	Convex	Oval in chains
4M	Circular	Opaque with translucent margin	Pale white	Entire	Smooth	1.5 mm	Convex	Oval in chains
7M	Circular	Opaque	Off white	Entire	Smooth	1 mm	Convex	Oval in chains

**Table 2:** Biochemical properties of *Enterococcus faecium* isolates.

Isolate	Acid/gas	Ct	Mot	Ind	NO <sub>3</sub> red	U	St	Gel	H <sub>2</sub> S	Vp	Slime	MB red	Milk coag	Arg	Bile 3 %	Bile 40 %
6Y	+/-	-	-	-	-	-	-	-	-	+	+	+	+	+	+	+
4M	+/-	-	-	-	-	-	-	-	-	+	+	+	+	+	+	+
7M	+/-	-	-	-	-	-	-	-	-	+	+	+	+	+	+	+

\* + = Growth observed, - = No growth, Ct=catalase, Mot=motility, Ind=indole production, NO<sub>3</sub> red= nitrate reduction, U = urease, St = starch hydrolysis, Gel = gelatinase, H<sub>2</sub>S= H<sub>2</sub>S production, Vp= acetoin production, MB red= methylene blue reduction, milk coag= coagulation, Arg= arginine hydrolysis

**Table 3:** Carbon sources utilization of *Enterococcus faecium* [U1] isolates

Isolate	Lac	Man	Fruc	Gal	CB	Man-ol	Rib	Raff	Mal	GLY	Ara	Cit	LRha
6Y	+	+	+	+	+	+	+	+	+	+	-	-	-
4M	+	+	+	+	+	+	+	+	+	+	-	-	-
7M	+	+	+	+	+	+	+	+	+	+	-	-	+

\* + = Growth observed, - = No growth, Lac=lactose, Man=D-mannose, Fruc=fructose, Gal=galactose, CB=cellobiose, Man-ol= mannitol, Rib=ribose, Raff= D-raffinose, Mal=maltose, GLY=glycerol, Ara=D-arabinose, Cit= citrate, LRha=L-rhamnose

**Table 4:** Effect of temperature, NaCl and pH on growth of *Enterococcus faecium* isolates

Isolate	Temperature				NaCl						pH				
	5 °C	37 °C	40 °C	45 °C	3 %	4%	5%	6.5%	8%	9%	3	4.5	7.2	8.7	9.5
6Y	+	+	+	+	+	+	+	+	-	-	-	+	+	+	+
4M	+	+	+	+	+	+	+	W	-	-	-	+	+	+	+
7M	+	+	+	+	+	+	+	+	-	-	-	+	+	+	+

\* + = Growth observed, - = No growth, W= Weak growth.

The amplified 16S rRNA gene, visualized by agarose gel electrophoresis, exhibited a size of approximately 1.5 kbp. Sequences were deposited in GenBank with accession numbers provided (Table 5). The three isolates were identified as *Enterococcus faecium*. A phylogenetic tree illustrating the relationship with other enterococci strains in GenBank is presented in Figure (2).

#### Antibacterial and Antifungal Activity of *Enterococcus* sp.:

The isolated bacterial strains did not exhibit antagonistic effects against each other but demonstrated significant antimicrobial activity against other bacteria, particularly Gram-positive strains (Fig. 3, Table 6).

**Table 5:** Isolates' identification (using Bergey's Manual of Systematics of Archaea and Bacteria; and 16S rRNA similarity).

Isolate	Homology	Accession Number	Identity	Expected species	Accession Number	Deposition Code
6Y	<i>Enterococcus faecium</i> strain DSM 20477	NR_114742.1	100 %	<i>Enterococcus faecium</i> strain AMA2	OP648140	<i>Enterococcus faecium</i> , CCASU-2023-62
4M	<i>Enterococcus faecium</i> strain NBRC100485	NR_113903.1	99.82 %	<i>Enterococcus faecium</i> strain AMA3	OP648141	Not deposited
7M	<i>Enterococcus faecium</i> strain ATCC 19434	NR_115764.1	99.85 %	<i>Enterococcus faecium</i> strain AMA4	OP648142	Not deposited

**Table 6:** Antagonistic test of *Enterococcus faecium* against bacteria and fungi.

Indicators	Gram Positive Bacteria			Gram Negative Bacteria				Fungi		
	<i>P. vulgaris</i>	<i>S. aureus</i>	<i>S. albus</i>	<i>P. aeruginosa</i>	<i>S. marcescens</i>	<i>k. pneumoniae</i>	<i>E. coli</i>	<i>A. niger</i>	<i>A. flavus</i>	<i>C. albicans</i>
Isolate										
6Y	9.30 <sup>a</sup>	10.33 <sup>a</sup>	9.60 <sup>a</sup>	3.00 <sup>b</sup>	4.60 <sup>b</sup>	3.30 <sup>ab</sup>	3.00 <sup>b</sup>	-	-	-
4M	10.03 <sup>a</sup>	10.36 <sup>a</sup>	9.30 <sup>a</sup>	3.60 <sup>ab</sup>	8.30 <sup>a</sup>	4.30 <sup>ab</sup>	3.00 <sup>b</sup>	-	-	-
7M	10.03 <sup>a</sup>	10.06 <sup>b</sup>	9.60 <sup>a</sup>	4.60 <sup>a</sup>	3.00 <sup>bc</sup>	5.30 <sup>a</sup>	4.30 <sup>a</sup>	-	-	-
SE	0.50	0.72	0.344	0.37	0.57	0.60	0.37			
p-value	<.0001	0.0290	0.9826	0.4442	0.0003	0.0372	0.0539			

\*Diameter of inhibition zone measured in (mm).

#### Thermal and pH Stability of CFS:

Figures 4, 5 & 6 illustrate the impact of temperatures and pH on the cell-free supernatant (CFS) of our cultures. Supernatants remained active at temperatures ranging from 50 °C to 100 °C, and even after autoclaving (121 °C for 15 min); they produced an inhibition zone of approximately 10 mm. Though heating didn't cause notable decrease of inhibition zone, statistical analysis showed that inhibitory effects of supernatants significantly decreased by increasing temperature with *p*-value = 0.0004 (6Y), 0.0002(4M) and 0.0085(7M). The final pH of supernatants for *Enterococcus*

Inhibition zones were prominent, reaching 9.3 mm or more in the case of *Proteus vulgaris*, *Staphylococcus aureus*, and *Staphylococcus albus*, while the remaining indicators (*Klebsiella pneumoniae*, *Escherichia coli*, and *Pseudomonas aeruginosa*) had zone < 5.3. A similar pattern was observed against *Serratia marcescens* (with 4M displaying a 8.3 mm inhibition zone). However, the tested fungi (*Candida albicans*, *Aspergillus niger*, and *Aspergillus flavus*) resisted the effects of cell-free supernatants from the isolates (Fig. 3, Table 6). Statistical analysis revealed that supernatants of these isolates weren't significantly different against *S. albus*, *P. aeruginosa* and *E. coli*, but had significant variance against *P. vulgaris*, *S. aureus*, *S. marcescens* and *k. pneumoniae*.

cultures stabilized at 4.5 after 3 days of incubation. Following pH adjustment to different values, supernatants retained activity within a pH range of 2.5-9.5. Notably, the cultures exhibited higher activity at acidic pH levels (2.5, 3.5, and 5.5), with inhibition zones reaching about 10 mm, compared to alkaline pH levels (8.5 and 9.5), where the diameter of the inhibition zone was nearly 5 mm (Fig. 6). These observations were confirmed by statistical analysis of data, as increasing pH level of supernatants significantly decreased their activity (*p*-value=<.0001).

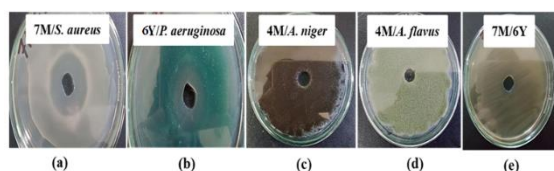


**Fig. 3:** Antagonistic effect of *E. faecium*

\*The indicator organisms are:

- (a) *S. aureus* (b) *P. aeruginosa* (c) *A. niger*  
(d) *A. flavus* (e) *Enterococcus* isolates used in this study.

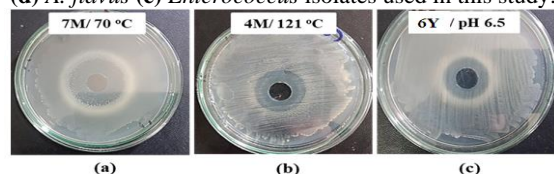


**Fig. 4:** Effect of heat and pH on activity of Cell-Free Supernatant (CFS) of *E. faecium*

(a) At 70 °C, (b) at 121 °C, (c) After exposure to pH 6.5 for 1 h.

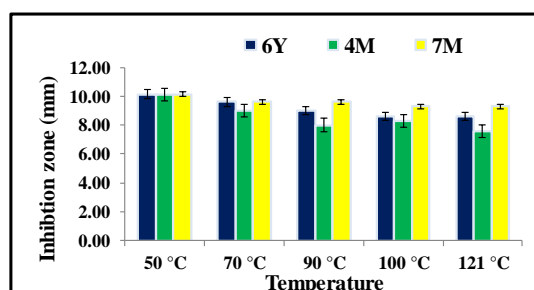
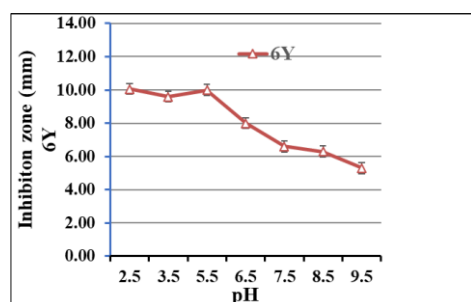
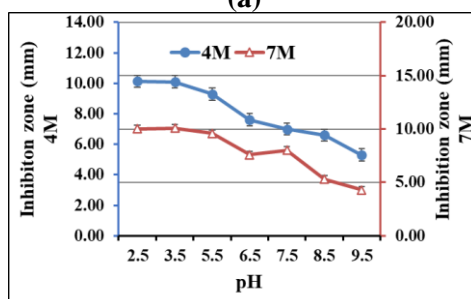


**Fig. 5:** Thermal stability for Cell-Free Supernatant (CFS) of *E. faecium*



(a)



(b)

**Fig. 6:** pH stability for Cell-Free Supernatant (CFS) of *E. faecium*

\*(a): Yoghurt isolate = 6Y, (b): Milk isolates = 4M & 7M

## Discussion:

### Isolation and Identification of Enterococci:

Lactic acid bacteria (LAB) are a well-defined group of Gram-positive, non-spore-forming, and catalase-negative bacteria known for their ability to produce acids from glucose. The identification of enterococci, a subset of LAB, was crucial in our study. Our isolates displayed characteristics consistent with *Enterococcus*, such as Gram-positive cocci arranged in chains, catalase negativity, and growth under homofermentative conditions (Abanoz & Kunduhoglu, 2018; Andrighetto *et al.*, 2001). The absence of gas production ruled out membership in heterofermentative genera like *Leuconostoc* or *Weissella*.

Sequencing the 16S rRNA gene validated the identification of all isolates as *Enterococcus*. A schematic representation based on Bergey's Manual of Systematics of Archaea and Bacteria provided an insightful summary of the features distinguishing various genera of cocci LAB (Fig. 1). Within the genus *Enterococcus*, our isolates were identified at the species level, as *E. faecium*. The biochemical characteristics, such as growth conditions, Voges-Proskauer and arginine dehydrolase tests, helped differentiate *E. faecium* strains. The versatility of *E. faecium* was evident in its isolation from diverse sources, including milk, clinical materials, food, and the environment (Morandi *et al.*, 2012 ; Yerlikaya & Akbulut, 2020). Other *Enterococcus* species, such as *E. lactis*, *E. durans*, and *E. hirae*, were also discussed, highlighting the variations in their acidification abilities for different substrates. The genomic identification through 16S rRNA sequencing aligned with the biochemical characterization. The deposition of isolates in GenBank further enhances the reliability of our findings. The phylogenetic tree illustrated the relationship between our isolates and other members of the *Enterococcus* genus (Fig. 2).

### Antibacterial and Antifungal Activity of *Enterococcus* sp.:

Our isolates demonstrated significant antimicrobial activity, particularly against Gram-positive bacteria like *Proteus vulgaris*, *Staphylococcus aureus*, and *Staphylococcus albus*. This finding aligns with previous research indicating the antimicrobial potential

of LAB against various pathogens, showcasing their role as probiotics and bio-preservatives (Abanoz & Kunduhoglu, 2018; Abesinghe *et al.*, 2020; Gaaloul *et al.*, 2015). Similarly, bacteriocins from *E. faecium* strain exhibited antimicrobial activity against *L. monocytogenes*, *S. aureus* and *Bacillus cereus* (Aspri *et al.*, 2017).

*Enterococcus faecium* LCW 44 also exhibited antibacterial activity against *Clostridium*, *Listeria*, *Staphylococcus*, and *Lactobacillus* but not against Gram-negative bacteria (Vimont *et al.*, 2017). *E. faecalis* KT11 showed antimicrobial activity against Gram-negative indicator bacteria, namely, *Pseudomonas aeruginosa*, *Klebsiella pneumoniae*, *Serratia marcescens* and *Enterobacter aerogenes*, with inhibition zones ranging from 14 to 18 mm (Abanoz & Kunduhoglu, 2018).

Bacteriocins from LAB have been broadly used as biopreservatives (e.g: Nisin), to control pathogenic bacteria in food products including cheese (Khelissa *et al.*, 2021). Several strains of *Enterococcus* are applied as starter cultures (Moreno *et al.*, 2006), and some are used as probiotics (Holzapfel *et al.*, 2018). The mode of action often involves the production of bacteriocins, proteinaceous substances with broad-spectrum antibacterial properties. The stability of these bacteriocins in a wide range of pH and temperature conditions, as observed in our isolates, adds to their appeal for potential applications in food preservation.

While our isolates did not exhibit antagonistic effects against fungi, this aligns with existing literature (Roy *et al.*, 2009; Roy *et al.*, 1996), emphasizing the selectivity of LAB's antifungal activity. Understanding the mechanisms behind these interactions, including the leakage of DNA and proteins from microbial cells contributes to the broader understanding of LAB's antimicrobial activity. The cell-free supernatant (CFS) of the cultures showed important inhibition zones against *Candida pelliculosa* (18.2–24.85 mm) (Abouloifa *et al.*, 2020). This antifungal activity was noticed against *Candida krusei* and *Candida tropicalis* (Oliveira *et al.*, 2008). Nevertheless, none of our isolates gave antagonistic effect against *Aspergillus* or *Candida*. This is in accordance with results of (Qiao *et al.*, 2020), who mentioned that the enterocin TJUQ1 did not have inhibitory ability

against fungi such as *Moniliella pollinis* BH010, *Saccharomyces cerevisiae*, *Botrytis cinerea*, *Fusarium oxysporum* and *Fusarium graminearum* while it could inhibit only the growth of *Zygosaccharomyces rouxii* (Qiao *et al.*, 2020; Liu *et al.*, 2011).

#### *Thermal and pH Stability of CFS:*

The cell-free supernatants (CFS) from our isolates demonstrated remarkable stability across a wide pH range (2.5-9.5) and even after autoclaving. This robust stability is consistent with previous studies on LAB-derived bacteriocins, supporting their potential application as natural preservatives (Lü *et al.*, 2014). The ability of our isolates to maintain antimicrobial activity under extreme conditions enhances their appeal for various industrial applications. Enterocins from *E. faecium* (Kumar *et al.*, 2010), *E. hirae* (Gupta *et al.*, 2016) and *E. faecalis* (Khalkhali & Mojgani, 2017) were reported to be stable for 10–20 min at 121°C.

Bacteriocin KT11 was stable at pH (2 - 11) for 24 h and showed antimicrobial activity against the indicator *S. aureus* ATCC 25923 strain. Maximum bacteriocin activity was recorded at pH 2–5 that is similar to our findings (Abanoz & Kunduhoglu, 2018). It has also been reported that bacteriocins of *E. faecium* (Kumar *et al.*, 2010), and *E. hirae* (Gupta *et al.*, 2016) were stable in the acidic pH levels. The anti-listerial activity of a bacteriocin from *E. durans* was completely retained in the pH range of 2–8 (Du *et al.*, 2017). Bacteriocins stable over a wide pH range have a significant advantage and a potential use as bio-preservatives in food products and fermented foods (Franz *et al.*, 1996).

**In conclusion**, our study unveils three *Enterococcus faecium* strains with promising features, including tolerance to bile salts and acidity, potent antibacterial activity and exceptional thermal stability of cell free supernatants (CFSs). Exopolysaccharides noticed on medium with high concentration of sugar, are applied in fermented milks to improve their texture and manufacture of low-fat cheeses (mozzarella). The application of both traditional biochemical tests and molecular tools, such as 16S rRNA sequencing, ensured accurate identification. These *Enterococcus* strains hold potential as natural preservatives, contributing to the quest for safer and more



sustainable alternatives to chemical preservatives in the food industry.

## List of abbreviations

(LAB): Lactic acid bacteria  
(MRS): de Man, Rogosa and Sharpe culture medium  
(CFSs): Cell free supernatants  
(SDW): Sterile distilled water  
(GRAS): Generally Recognized as Safe  
(EPS): Exopolysaccharides

## Declarations

*Ethics approval and consent to participate:*

This article does not contain any studies with human participants or animals performed by any of the authors.

## Availability of data and material:

The datasets utilized and/or examined in the present study can be obtained by contacting the corresponding author. Additionally, the genetic sequence of the strains analyzed has been submitted to the GenBank nucleotide sequence database at the National Library of Medicine, National Center for Biotechnology Information (NCBI). The assigned accession numbers for the sequences are OP648140, OP648141 and OP648142; and are available at the following URLs (respectively).

<https://www.ncbi.nlm.nih.gov/nuccore/OP648140.1?report=GenBank>

<https://www.ncbi.nlm.nih.gov/nuccore/OP648141.2?report=GenBank>

<https://www.ncbi.nlm.nih.gov/nuccore/OP648142.1?report=GenBank>

## Author contributions:

**HHa:** Supervision, Conceptualization, Software, Investigation, Methodology, Writing – original draft, Writing – review & editing, **MAS:** Supervision, Writing – original draft, Resources, Writing – review & editing, **MMI:** Supervision, Conceptualization, Data curation, Resources, Writing – original draft, Writing – review & editing, **AMAA:** Investigation,

Methodology, Writing – original draft, Writing – review & editing. All authors read and approved the manuscript.

## Acknowledgements

We would like to thank Dr. Magda M. Mehanni (A Lecturer of Microbiology, Department of Botany & Microbiology, Faculty of Science, Minia University) for reviewing this work.

## References:

- Abanoz HS & Kunduhoglu B (2018) Antimicrobial activity of a bacteriocin produced by *Enterococcus faecalis* KT11 against some pathogens and antibiotic-resistant bacteria. *Korean journal for food science of animal resources* **38**: 1064.
- Abesinghe A, Priyashantha H, Prasanna P, Kurukulasuriya MS, Ranadheera C & Vidanarachchi J (2020) Inclusion of probiotics into fermented buffalo (*Bubalus bubalis*) milk: an overview of challenges and opportunities. *Fermentation* **6**: 121.
- Abouloifa H, Rokni Y, Bellaouchi R, Ghabbour N, Karboune S, Brasca M, Ben Salah R, Chihib NE, Saaloui E & Asehrou A (2020) Characterization of probiotic properties of antifungal *Lactobacillus* strains isolated from traditional fermenting green olives. *Probiotics and antimicrobial proteins* **12**: 683-696.
- Adikari A, Priyashantha H, Disanayaka J, Jayatileka D, Kodithuwakku S, Jayatilake J & Vidanarachchi J (2021) Isolation, identification and characterization of *Lactobacillus* species diversity from Meekiri: traditional fermented buffalo milk gels in Sri Lanka. *Heliyon* **7**.
- Ananou S, Maqueda M, Martínez-Bueno M & Valdivia E (2007) Biopreservation, an ecological approach to improve the safety and shelf-life of foods. *Communicating current research and educational topics and trends in applied microbiology* **1**: 475-487.
- Andrighetto C, Knijff E, LOMBARDI A, Torriani S, Vancanneyt M, Kersters K, Swings J & Dellaglio F (2001) Phenotypic and genetic diversity of enterococci isolated from Italian cheeses. *Journal of Dairy Research* **68**: 303-316.
- Aneja K (2007) Experiments in microbiology, plant pathology and biotechnology. New Age International.
- Aspri M, O'Connor PM, Field D, Cotter PD, Ross P, Hill C & Papademas P (2017) Application of bacteriocin-producing *Enterococcus faecium*



- isolated from donkey milk, in the bio-control of *Listeria monocytogenes* in fresh whey cheese. *International Dairy Journal* **73**: 1-9.
- Barritt MM (1936) The intensification of the Voges-Proskauer reaction by the addition of  $\alpha$ -naphthol.
- Bhakta JN, Bhattacharya S, Lahiri S & Panigrahi AK (2023) Probiotic characterization of arsenic-resistant lactic acid bacteria for possible application as arsenic bioremediation tool in fish for safe fish food production. *Probiotics and antimicrobial proteins* **15**: 889-902.
- Björkroth J & Holzapfel W (2006) Genera *Leuconostoc*, *Oenococcus* and *Weissella*. *The prokaryotes* **4**: 267-319.
- Dapkevicius MdLE, Sgardioli B, Câmara SP, Poeta P & Malcata FX (2021) Current trends of enterococci in dairy products: A comprehensive review of their multiple roles. *Foods* **10**: 821.
- de Man Jd, Rogosa d & Sharpe ME (1960) A medium for the cultivation of lactobacilli. *Journal of applied microbiology* **23**: 130-135.
- Du L, Liu F, Zhao P, Zhao T & Doyle MP (2017) Characterization of *Enterococcus durans* 152 bacteriocins and their inhibition of *Listeria monocytogenes* in ham. *Food Microbiology* **68**: 97-103.
- Evans J, Klesius P & Shoemaker C (2004) Starch hydrolysis testing of multiple isolates for rapid differentiation of *Streptococcus iniae*. *Bulletin-European Association of Fish Pathologists* **24**: 231-239.
- Franz C, Schillinger U & Holzapfel W (1996) Production and characterization of enterocin 900, a bacteriocin produced by *Enterococcus faecium* BFE 900 from black olives. *International Journal of Food Microbiology* **29**: 255-270.
- Frizzo LS, Zbrun MV, Soto LP & Signorini M (2011) Effects of probiotics on growth performance in young calves: A meta-analysis of randomized controlled trials. *Animal Feed Science and Technology* **169**: 147-156.
- Gaaloul N, Ben Braiek O, Hani K, Volski A, Chikindas M & Ghrairi T (2015) Isolation and characterization of large spectrum and multiple bacteriocin-producing *Enterococcus faecium* strain from raw bovine milk. *Journal of applied microbiology* **118**: 343-355.
- Grange J & Lyne P (2004) Collins and Lyne's Microbiological Methods. Hodder Education.
- Gupta A, Tiwari SK, Natrebov V & Chikindas ML (2016) Biochemical properties and mechanism of action of enterocin LD3 purified from *Enterococcus hirae* LD3. *Probiotics and antimicrobial proteins* **8**: 161-169.
- Hécharde Y & Sahl H-G (2002) Mode of action of modified and unmodified bacteriocins from Gram-positive bacteria. *Biochimie* **84**: 545-557.
- Hitchener BJ, Egan A & Rogers P (1982) Characteristics of lactic acid bacteria isolated from vacuum-packaged beef. *Journal of Applied Bacteriology* **52**: 31-37.
- Holzapfel W, Arini A, Aeschbacher M, Coppolecchia R & Pot B (2018) *Enterococcus faecium* SF68 as a model for efficacy and safety evaluation of pharmaceutical probiotics. *Beneficial microbes* **9**: 375-388.
- Islam R, Hossain MN, Alam MK, Uddin ME, Rony MH, Imran MAS & Alam MF (2020) Antibacterial activity of lactic acid bacteria and extraction of bacteriocin protein. *Advances in Bioscience and Biotechnology* **11**: 49-59.
- Khalkhali S & Mojangi N (2017) Bacteriocinogenic potential and virulence traits of *Enterococcus faecium* and *E. faecalis* isolated from human milk. *Iranian Journal of Microbiology* **9**: 224.
- Khelissa S, Chihib N-E & Gharsallaoui A (2021) Conditions of nisin production by *Lactococcus lactis* subsp. *lactis* and its main uses as a food preservative. *Archives of Microbiology* **203**: 465-480.
- Kovacs N (1928) Eine vereinfachte methode zum nachweis der indolbildung durch bakterien. *Z Immunitätsforsch* **55**: 311-315.
- Kozaki M, Uchimura T & Okada S (1992) Experimental manual of lactic acid bacteria. Asakurasyoten, Tokyo, Japan 34-37.
- Kumar M, Tiwari SK & Srivastava S (2010) Purification and characterization of enterocin LR/6, a bacteriocin from *Enterococcus faecium* LR/6. *Applied biochemistry and biotechnology* **160**: 40-49.
- LeBlanc J, Laiño JE, Del Valle MJ, Vannini V, van Sinderen D, Taranto MP, de Valdez GF, de Giori GS & Sesma F (2011) B-Group vitamin production by lactic acid bacteria—current knowledge and potential applications. *Journal of applied microbiology* **111**: 1297-1309.
- Lee J, Seo Y, Ha J, Kim S, Choi Y, Oh H, Lee Y, Kim Y, Kang J & Park E (2020) Influence of milk microbiota on *Listeria monocytogenes* survival during cheese ripening. *Food Science & Nutrition* **8**: 5071-5076.
- Liu G, Griffiths MW, Wu P, Wang H, Zhang X & Li P (2011) *Enterococcus faecium* LM-2, a multi-bacteriocinogenic strain naturally occurring in “Byaslag”, a traditional cheese of Inner Mongolia in China. *Food Control* **22**: 283-289.
- Lü X, Yi L, Dang J, Dang Y & Liu B (2014) Purification of novel bacteriocin produced by *Lactobacillus coryniformis* MXJ 32 for inhibiting bacterial foodborne pathogens including antibiotic-resistant microorganisms. *Food Control* **46**: 264-271.

- MacFaddin JF (2000) Biochemical tests for identification of medical bacteria. Lippincott, Williams & Williams, Baltimore.
- Menconi A, Kallapura G, Latorre JD, Morgan MJ, Pumford NR, Hargis BM & Tellez G (2014) Identification and characterization of lactic acid bacteria in a commercial probiotic culture. *Bioscience of Microbiota, Food and Health* **33**: 25-30.
- Mithun S, Dipak V & Sheela S (2015) Isolation and Identification of lactobacilli from raw milk samples obtained from Aarey Milk Colony. *International Journal of Scientific and Research Publications* **5**: 1-5.
- Morandi S, Cremonesi P, Povolo M & Brasca M (2012) *Enterococcus lactis* sp. nov., from Italian raw milk cheeses. *International Journal of Systematic and Evolutionary Microbiology* **62**: 1992-1996.
- Moreno MF, Sarantinopoulos P, Tsakalidou E & De Vuyst L (2006) The role and application of enterococci in food and health. *International journal of food microbiology* **106**: 1-24.
- Ni K, Wang Y, Li D, Cai Y & Pang H (2015) Characterization, identification and application of lactic acid bacteria isolated from forage paddy rice silage. *PloS one* **10**: e0121967.
- Oliveira RB, Oliveira AdL & Glória MBA (2008) Screening of lactic acid bacteria from vacuum packaged beef for antimicrobial activity. *Brazilian Journal of Microbiology* **39**: 368-374.
- Qiao X, Du R, Wang Y, Han Y & Zhou Z (2020) Purification, characterization and mode of action of enterocin, a novel bacteriocin produced by *Enterococcus faecium* TJUQ1. *International Journal of Biological Macromolecules* **144**: 151-159.
- Rahmeh R, Akbar A, Kishk M, Al-Onaizi T, Al-Azmi A, Al-Shatti A, Shajan A, Al-Mutairi S & Akbar B (2019) Distribution and antimicrobial activity of lactic acid bacteria from raw camel milk. *New Microbes and New Infections* **30**: 100560.
- Reddy C, Beveridge TJ, Breznak JA & Marzluf G (2007) Methods for general and molecular microbiology. American Society for Microbiology Press.
- Roghamann M-C & McGrail L (2006) Novel ways of preventing antibiotic-resistant infections: what might the future hold? *American journal of infection control* **34**: 469-475.
- Roy U, Batish V, Grover S & Neelakantan S (1996) Production of antifungal substance by *Lactococcus lactis* subsp. *lactis* CHD-28.3. *International journal of food microbiology* **32**: 27-34.
- Roy U, Jai K K, Sunita G & Virender K B (2009) Partial purification of an antifungal protein produced by *Enterococcus faecalis* CHD 28.3. *Annals of microbiology* **59**: 279-284.
- Samelis J, Maurogenakis F & Metaxopoulos J (1994) Characterisation of lactic acid bacteria isolated from naturally fermented Greek dry salami. *International Journal of Food Microbiology* **23**: 179-196.
- Schillinger U & Lücke F-K (1987) Identification of lactobacilli from meat and meat products. *Food microbiology* **4**: 199-208.
- Shay B & Egan A (1981) Hydrogen sulphide production and spoilage of vacuum-packaged beef by a *Lactobacillus*. Psychrotrophic microorganisms in spoilage and pathogenicity/edited by TA Roberts[et al].
- Somasegaran P & Hoben HJ (2012) Handbook for rhizobia: methods in legume-*Rhizobium* technology. Springer Science & Business Media.
- Sonbol FI, Abdel Aziz AA, El-Banna TE & Al-Fakhrany OM (2020) Antimicrobial activity of bacteriocins produced by *Enterococcus* isolates recovered from Egyptian homemade dairy products against some foodborne pathogens. *International Microbiology* **23**: 533-547.
- Spencer JF & de Spencer ALR (2008) Food microbiology protocols. Springer Science & Business Media.
- Steadham JE (1979) Reliable urease test for identification of mycobacteria. *Journal of clinical microbiology* **10**: 134-137.
- Tenea GN, Olmedo D & Ortega C (2020) Peptide-based formulation from lactic acid bacteria Impairs the pathogen growth in *Ananas comosus* (Pineapple). *Coatings* **10**: 457.
- Vasiljevic T & Shah NP (2008) Probiotics—from Metchnikoff to bioactives. *International dairy journal* **18**: 714-728.
- Vimont A, Fernandez B, Hammami R, Ababsa A, Daba H & Fliss I (2017) Bacteriocin-producing *Enterococcus faecium* LCW 44: a high potential probiotic candidate from raw camel milk. *Frontiers in microbiology* **8**: 865.
- Whitman WB, Rainey F, Kämpfer P, Trujillo M, Chun J, DeVos P, Hedlund B & Dedysh S (2015) Bergey's manual of systematics of archaea and bacteria. Wiley Online Library.
- Yang J-M & Moon G-S (2021) Partial characterization of an anti-listerial bacteriocin from *Enterococcus faecium* CJNU 2524. *Food Science of Animal Resources* **41**: 164.
- Yerlikaya O & Akbulut N (2020) In vitro characterisation of probiotic properties of *Enterococcus faecium* and *Enterococcus durans* strains isolated from raw milk and traditional dairy products. *International Journal of Dairy Technology* **73**: 98-107.

## الملخص العربي

عنوان البحث: توصيف ودراسة النشاط المضاد للميكروبات لعزلات *Enterococcus Faecium* المعزولة من حليب البقر الخام والزباديحسام حسن عرفات<sup>١\*</sup>، محمود على شلقامى<sup>١</sup>، محمد مصطفى امام<sup>١</sup>، أمانى محمد أحمد على<sup>١</sup><sup>١</sup> قسم النبات والميكروبيولوجي، كلية العلوم، جامعة المنيا، مدينة المنيا، مصر

تركز هذه الدراسة على عزل enterococci، وهي مجموعة فرعية من بكتيريا حمض اللاكتيك (LAB). تتضمن الدراسة تعريف هذه العزلات من خلال التعريف المورفولوجي والتجارب الحيوية والجزئية باستخدام طرق تسلسل جينات 16S rRNA، إلى جانب استكشاف فعاليتها المضادة للميكروبات. تم الحصول على ثلاث عزلات من عينات الحليب والزبادي، تم تحديدها باسم *Enterococcus faecium*. إن تحمل هذه العزلات لأملح الصفراء (حتى 40٪) والحموضة المعتدلة (درجة الحموضة = 4,5)، يجعلها تبقى على قيد الحياة في الأمعاء وبالتالي قابلة للتطبيق كبروبيوتيك. أظهرت المستخلصات الخالية من الخلايا (CFSs) المشتقة من هذه العزلات نشاطاً مضاداً للبكتيريا بشكل كبير حيث وصلت مناطق التثبيط إلى (9,3-10,3 مم) ضد *Proteus vulgaris* و *Staphylococcus aureus* و *Staphylococcus albus*. بينما تراوحت مناطق تثبيط النمو ضد *Escherichia coli* و *Serratia marcescens* و *Klebsiella pneumoniae* و *Pseudomonas aeruginosa* (بين 3-8,3 مم). في المقابل لم تُظهر هذه المناطق أي فعالية ضد الفطريات. والجدير بالذكر أن النشاط المضاد للميكروبات لـ CFSs ظل ثابتاً في درجات حرارة مختلفة، بما في ذلك ظروف التعقيم البخار (121 درجة مئوية). وأظهرت العزلات تحملاً واسعاً لدرجات الأس الهيدروجيني (2.5-9.5 pH)، مع ملاحظة زيادة في النشاط عند مستويات الأس الهيدروجيني الحمضية مقارنةً بالمستويات القاعدية. ويحفز استقرار درجة الحموضة والحرارة للمستخلصات على استخدامها كمادة حافظة حيوية.

## Antimicrobial Activity of Biosynthesized Selenium Nanoparticles using *Pseudomonas Aeruginosa*

Laila A. Elshikiby<sup>1</sup>, Zakaria A.M. Baka<sup>1</sup> and Mohamed M. El-Zahed<sup>\*1</sup>

<sup>1</sup>Department of Botany and Microbiology, Faculty of Science, Damietta University, New Damietta city, Egypt.

Received: 20 May 2025 /Accepted: 20 June 2025

\*Corresponding author's E-mail: Mohamed.marzouq91@du.edu.eg

### Abstract

The current study used *Pseudomonas aeruginosa* isolated from clinical specimens to provide a simple and cost-effective approach for biosynthesizing selenium nanoparticles (SeNPs). Vitek 2 was used to confirm the species-level identification of the chosen bacterial isolate after it was recognized traditionally. The biosynthesized SeNPs were verified and described using a variety of tests, including TEM, FT-IR, zeta analyses, and UV-Vis spectroscopy. At 330-370 nm, the adsorption peaks for SeNPs were recorded. The presence of proteins acting as binding and supporting components during synthesis was verified by the FT-IR spectra. The substantial negative surface charge of -17.6 mV contributes to its stability. TEM shows the diameters of SeNPs in the 83-91 nm range. SeNPs had strong antimicrobial activity against *Bacillus cereus*, *Staphylococcus aureus*, *Proteus mirabilis*, *Pseudomonas aeruginosa*, and *Candida albicans* in a dose-dependent manner. The MICs of SeNPs against *B. cereus*, *S. aureus*, *P. aeruginosa*, *P. mirabilis*, and *C. albicans* were 40, 70, 110, 150, and 150 µg/mL, respectively. This study offers safe, effective, and promising nanoparticles as an alternative for treating some pathogenic microbes in both humans and animals.

**Keywords:** *Pseudomonas aeruginosa*, selenium nanoparticles, characterization, antimicrobial activity

### Introduction

Antimicrobial resistance (AMR) poses a significant risk to public health worldwide; in 2019; bacterial AMR was linked to about 5 million deaths (Murray et al., 2022). Combating AMR necessitates a comprehensive and integrated strategy that includes improved infection prevention and control measures, enhanced global policies and funding, AMR

surveillance, improved understanding of mechanisms and drivers at the individual and population levels, and the development of innovative antimicrobial therapeutic strategies. Extreme poverty is made worse in low- and middle-income countries (LMICs) by the effects of AMR-related illness or mortality. If the issue is not resolved, LMICs are predicted to lose more than 5% of their economy by 2050 as a result of lost revenue from indirect healthcare costs (O'Neill, 2016). The effectiveness of almost all known

antibiotics is impacted by a variety of bacterial resistance mechanisms, such as decreased membrane permeability, the use of efflux pumps, enzyme modification or antibiotic degradation, alteration of antibiotic targets, and adaptive mechanisms like biofilm formation. The majority of AMR usually happens 0–6 months after antibiotic exposure (Poku et al., 2023), highlighting the enormous issue of AMR, even if the timing of resistance development may range across various antibiotic-bacteria combinations.

*Escherichia coli*, *Staphylococcus aureus*, *Klebsiella pneumoniae*, *Streptococcus pneumoniae*, *Acinetobacter baumannii*, and *P. aeruginosa* were the six main causes (73%) of AMR-associated mortality in 2019, according to the 2022 Global Burden of Disease research (Miller & Arias, 2024). One separate group of pathogens, ESKAPEE, which includes *Enterococcus* species, *S. aureus*, *K. pneumoniae*, *A. baumannii*, *P. aeruginosa*, *Enterobacter* species, and *E. coli* is known to cause drug-resistant infections in hospital settings. These infections have a wide range of intrinsic or acquired resistance mechanisms that allow them to live or flourish in healthcare settings.

*Pseudomonas* is a genus of Gram-negative bacteria. It is a member of the class Gammaproteobacteria and the family Pseudomonadaceae. While not all strains of this bacterial species are known to cause infections (Xiao et al., 2024), some species, such as *Pseudomonas aeruginosa*, *P. stutzeri*, and *P. putida*, are known to do so. The bacterium can usually survive in a healthy body, and since it doesn't damage anyone, healthy people frequently carry the bacteria without realizing it. Sometimes, mild infections might develop, resulting in problems like hot tub rash or swimmer's ear. *Pseudomonas* infections can be severe or even fatal for people with compromised immune systems or those who are already unwell. There are more than 300 *Pseudomonas* species (Parte et al., 2020). Opportunistic infections—infections that arise in persons with compromised immune systems because of medical illnesses or drugs that weaken the immune system—are caused by the majority of organisms that cause disease in humans. Some strains linked to opportunistic infections are *P. aeruginosa*, *P. putida*, *P. fluorescens*, and *P. stutzeri*. Although the entire body can be impacted by *pseudomonas*, the

infection and its symptoms are more likely to occur in specific organs and parts of the body. These include the urinary tract, ear canal, skin injuries, and lungs. Studies have shown that up to 10% of *Pseudomonas* infections are resistant to antibiotics. They are hard to cure since they may avoid drugs and survive. Resistance mechanisms can be acquired through horizontal gene transfer (acquiring aminoglycoside-modifying enzymes and  $\beta$ -lactamases) or mutations that overexpress efflux pumps or  $\beta$ -lactamases or decrease expression or change target sites and porins. External stimuli, such as antibiotic exposure, activate adaptive resistance mechanisms, which then become inactive when the stimulus is removed (Kunz Coyne et al., 2022).

Currently, improvements in technology, such as nanotechnology, and nanomaterials are often utilized separately or in combination with antibiotics as promising, effective antimicrobial agents for solving AMR concerns. Nanotechnology is a modern science subject that studies and affects the properties of matter at the nanoscale. Nanoparticles (NPs) range in size from 1 to 100 nm and exhibit chemical stability, antifungal properties, low toxicity, and low pathogen resistance (Manimaran et al., 2023). NPs, including Ag, Cu, Au, Fe, and Se, play important roles in agriculture, food, the environment, and nanomedicine (Saqib et al., 2022). NPs can be manufactured in a variety of ways, including physical, chemical, and biological techniques. The increasing cost and toxicity of physical and chemical techniques has led to an increase in green synthesis of NPs. It employs biological substances like plant extracts, fungus, and bacteria. This environmentally benign technology provides a long-term alternative to existing chemical and physical synthesis methods by decreasing the usage of harmful chemicals and boosting the biocompatibility of NPs (Khan et al., 2022). Green synthesis methods can be divided into two categories: top-down and bottom-up approaches. These approaches differ in terms of nanoparticle formation and control over size, shape, and characteristics.

Bacteria are recommended for NPs syntheses because they require minimal conditions, are easy to purify, and produce high yield. As a result, bacteria have become the most studied microorganism, earning the label of "the factory of nanomaterials. Bacteria can operate as a biocatalyst for inorganic material synthesis, a



bio-scaffold for mineralization, or an active component in nanoparticle formation (Iqtedar et al., 2019). Bacteria can produce nanomaterials in broth media during an incubation period, either as extracellular or intracellular. This characteristic makes the biosynthesis of NPs using bacteria a feasible, versatile, and acceptable method for large-scale manufacturing.

Inorganic NPs of metals such as Ag, Au, Ce, Fe, Se, Ti, and Zn hold an important place among NPs due to their distinct bioactivities in nanoforms. Se is a necessary trace element. It is integrated into selenoproteins as selenocysteine, which forms the majority of the active core of their enzymatic activity. Many seleno proteins function as oxidoreductases, regulating the physiological redox balance. Se has a restricted therapeutic window and extremely fragile toxicity margins, but Se nanoparticles (SeNPs) have far lower toxicity. SeNPs have been studied in a variety of oxidative stress and inflammation-mediated illnesses, including arthritis, cancer, diabetes, and nephropathy, for possible therapeutic benefits. SeNPs make an appealing carrier platform for transporting diverse medicines to the site of action (Khurana et al., 2019). NPs' antimicrobial mechanisms include membrane and bacterial cell wall destruction, protein and internal component damage, ion release, DNA damage, and oxidative stress (Besinis et al., 2014).

NPs have a wide range of antibacterial actions, which means that bacteria are unlikely to develop resistance to them (Huh & Kwon, 2011). Thus, the current study aimed to biosynthesize SeNPs using *Pseudomonas aeruginosa* isolate and evaluate their antimicrobial action.

## Materials and methods

### *Sample collection*

In April and May 2024, 22 samples (12 females and 10 males) were obtained from various private clinics and medical analytical laboratories in New Damietta City, Kafr Elbattikh, and Faraskour (Damietta Governorate, Egypt, 31.4°N 31.72°E). These samples included urine, stool, and surface swab samples. The samples were processed using the previously outlined procedures by Santiago-

Rodriguez et al. (2015) and Zboromyrska & Vila (2016).

### *Isolation and identification of bacterial isolates*

The spread plate method was used to isolate drug-resistant pathogenic bacteria on a blood agar basis (Oxoid Ltd., England) supplemented with 2 mg/l ceftazidime (MCKC) and 5% (wt/v) defibrinated, sterile sheep blood (Youri et al., 2007). At 37°C, each plate was incubated for 24 hours. The hemolytic reaction caused by microorganisms was then noted. For 48 hours, each bacterial colony from a different bacterial isolate was transferred and subcultured on Cystine Lactose Electrolyte Deficient (CLED, Oxoid Ltd., England) agar plates. Then, colonial morphological characteristics and color change of colonies and media were recorded. The bacterial isolates were characterized and identified according to Bergey's Manual of Systematic Bacteriology (Yahr & Parsek, 2006). The morphological and cultural characteristics included colony shape, Gram staining, and endospore staining, and the identification was done in a systematic manner as follows: Colonial characters (size, form, pigment production, elevation, surface, edge, color, and opacity) were recorded. Microscopic examination included shape, size, Gram stain, acid fast stain, and endospore formation. The species-level was identified using the Vitek 2 (BioMerieux, Marcy-l'Étoile, France) (Moore et al., 1981).

### *Antibiotic sensitivity test (AST)*

The AST of bacterial isolates was evaluated using the disc diffusion technique (CLSI, 2000a). 50 µL of each bacterial suspension (0.5 MacFarland Standard,  $1.5 \times 10^8$  CFU/mL) was separately added to Mueller-Hinton agar (MHA, Oxoid Ltd., England) flasks, which were then placed into sterile Petri dishes. Vanomycin (30 µg/mL), amoxicillin/clavulanate (20/10 µg/mL), ampicillin (30 µg/mL), cefotaxime (30 µg/mL), ceftazidime (30 µg/mL), chloramphenicol (30 µg/mL), doxycycline (30 µg/mL), levofloxacin (5 µg/mL), nalidixic acid (30 µg/mL) and amoxycillin/clavulanate (20/10 µg/mL) were among the antibiotic discs from different classes that were aseptically applied after solidification. The diameter of the zones of

inhibition (ZOI) was measured and recorded in millimeters after a 24-hour incubation period at 37°C.

#### *Biosynthesis of selenium nanoparticles*

The selected bacterial isolate was grown in nutrient broth medium overnight at 37°C. After the incubation, the bacterial cells were discarded and the bacterial metabolites were collected using centrifugation of bacterial cultures at 4000 rpm for 20 minutes. The obtained bacterial supernatant was filtered using a 0.22 µm syringe filter (Millex GV, Millipore). Sodium selenite solution (1 mM) was prepared, mixed with the selected bacterial isolate supernatant at a ratio of 1:1 (v/v%), and shaken well (150 rpm) at 37°C for 24 hours (Mohamed & El-Zahed, 2024).

#### *Characterization of selenium nanoparticles*

A double-beam spectrum UV–Vis spectrophotometer V-760 (JASCO, UK) and Fourier transform infrared spectroscopy (FT-IR, FT/IR-4100 type A) were two of the methods used to examine the biosynthesized SeNPs. Transmission electron microscopy (TEM, JEOL JEM-2100, Japan) and zeta potential measurements (Malvern Zetasizer Nano-ZS90, Malvern, UK) were used for additional analysis.

#### *Antimicrobial activity of selenium nanoparticles using agar well diffusion method*

Different concentrations (50, 150, and 300 µg/mL) of SeNPs were evaluated for their antibacterial and anticandidal activities against *Bacillus cereus*, *Staphylococcus aureus*, *Proteus mirabilis*, *P. aeruginosa*, and *Candida albicans* using the agar well diffusion method, in accordance with the Clinical and Laboratory Standards Institute (CLSI, 2017). Nutrient agar and yeast extract peptone agar media were prepared and inoculated with 0.5 MacFarland standard ( $1-2 \times 10^8$  CFU/mL) from the microbial strains. Ampicillin and miconazole were used as control antibiotics. 100 µL from each antibacterial agent was added to wells, and the inoculated plates were incubated at 37°C or 30°C for bacteria or yeast, respectively. Zones of inhibition were measured in mm.

#### *Minimal inhibitory concentration (MIC)*

The MICs of SeNPs were assessed using the broth microdilution method in compliance with CLSI guidelines (CLSI, 2000b; 2008). Standard antibiotics and serial solutions (0-150 µg/mL) from SeNPs were made and examined. The test microorganisms were cultivated for 24 hours at 37°C for yeast and 30°C for bacteria. Following the incubation period, a spectrophotometer was used to measure the turbidity of the microbial growth at 600 nm in relation to the growth control.

#### *Minimum microbicidal concentration (MMC)*

Using the pour plate approach, each MIC microbiological flask was inoculated into Mueller-Hinton agar plates, and the bacteria or yeast were then incubated at 37°C or 30°C, respectively. The total number of microbial colonies was expressed in colony-forming units per milliliter (CFU/mL) (Owuama, 2017).

#### *Antioxidant activity of selenium nanoparticles*

According to Turan et al. (2025), the antioxidant activities of SeNPs were examined using the in vitro DPPH radical scavenging technique. At 517 nm, the maximum absorbance of DPPH radical solutions takes place. Ethanol was used to reduce the absorbance of the control sample to  $1.5 \pm 0.5$  after a 1 mM DPPH radical solution was prepared. The results were compared using the established antioxidant ascorbic acid (vitamin C). Different dosages of the DPPH radical solution (10–110 µg/mL) were given to the samples and standards separately. After the samples were incubated for 30 minutes at 25°C, the absorbance values were calculated. Absorbance at 517 nm decreases when a sample is able to scavenge DPPH free radicals. The percentage (%) of inhibition of DPPH was determined using the formula  $\% = (A_{\text{control}} - A_{\text{compound}} / A_{\text{control}}) \times 100$ , where  $A_{\text{control}}$  represents the absorbance in the absence of the compound and  $A_{\text{compound}}$  represents the absorbance in the presence of the compound.

#### *Statistical analysis*

SPSS version 18 software was used to perform statistical analysis of the data. The analysis was conducted using one-way analysis of variance (ANOVA), and each experimental value is displayed as the mean  $\pm$  standard deviation

(SD). A significance threshold of  $p < 0.05$  was set. Every experiment was run in triplicate.

## Results

### *Isolation, purification, and characterization of P. aeruginosa isolates*

Sixteen Gram-negative, rod-shaped, positive citrate and glucose-fermenting bacteria that did not ferment lactose or form spores were identified from the 24-hour-developed resistant bacterial colonies and chosen for subculturing on CLED agar plates. When these bacteria were separated on CLED agar plates, eight of the isolates showed a yellow hue, five showed no color, and three showed a pale pink tint. On CLED agar plates, colonies that were smooth, pale, or colorless were chosen and allowed to grow (Atlas & Synder, 2011). Translucent blue colonies were chosen and purified after 48 hours, and the Vitek 2 was used to identify the species. This revealed the existence of two *P. aeruginosa* isolates encoded with BSF2 and BSF6 (Table 1, Figure 1). The two isolates of *P. aeruginosa* were examined for SeNPs production.

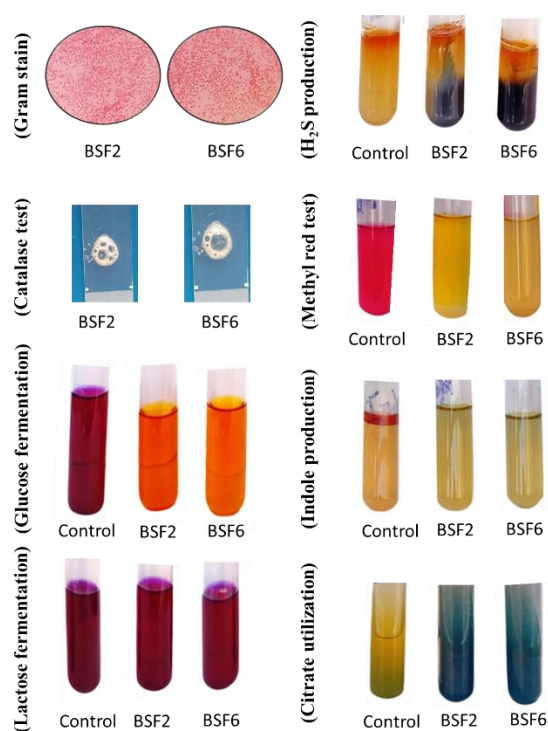


**Figure 1.** Some representative biochemical tests of the bacterial isolates.

**Table 1.** Biochemical tests for *P. aeruginosa* isolates.

Biochemical test	BSF2	BSF6
Citrate utilization	+	+
Catalase	+	+
Oxidase	+	+
Indole production	-	-
Methyl red	-	-
Voges-Proskauer	-	+
Urease	+	+
Nitrate reduction	+	-
H <sub>2</sub> S production	+	+
Lactose fermentation	-	-
Glucose fermentation	±	±

\*+ = Positive; - = Negative; ± = Intermediate reaction.

### *AST investigations*

Table 2 shows that the BSF6 strain is more resistant to all tested antibiotics than the BSF2 strain. According to the findings, the isolates of *P. aeruginosa* have a 100% resistance rate to ampicillin, cefotaxime, ceftazidime, doxycycline, and vancomycin. Amoxicillin/clavulanate, chloramphenicol, levofloxacin, and nalidixic acid revealed antibacterial action against *P. aeruginosa* BSF2. The outcomes showed that the *P. aeruginosa* isolates exhibited multidrug resistance.

**Table 2.** Patterns of antibiotic resistance and sensitivity in *P. aeruginosa* isolates.

Antibiotic	Concentration (µg/ml)	Antibiotics susceptibility	
		BSF	BSF6
Amoxicillin/clavulanate	20/10	+	-
Ampicillin	30	-	-
Cefotaxime	30	-	-
Ceftazidime	30	-	-
Chloramphenicol	30	+	-
Doxycycline	30	-	-
Levofloxacin	5	+	-
Nalidixic acid	30	+	-
Vancomycin	30	-	-

### *Biosynthesis and characterization of SeNPs*

The color of the reaction mixture varies from pale yellow at the beginning of the experiment to red at the end of the incubation time, which is used to evaluate the production of SeNPs by the *P. aeruginosa* isolates (Figure 2). In the control studies, the color of the sample remained unchanged. *P. aeruginosa* BSF6 isolate showed the highest production rate within 24 hours when compared to the other isolate, BSF2, according to the UV-Vis spectrometric assay used to confirm the

formation of SeNPs. When SeNPs were produced utilizing the cell-free metabolites of various isolates of *P. aeruginosa*, absorbance maxima between 330 and 370 nm were found.

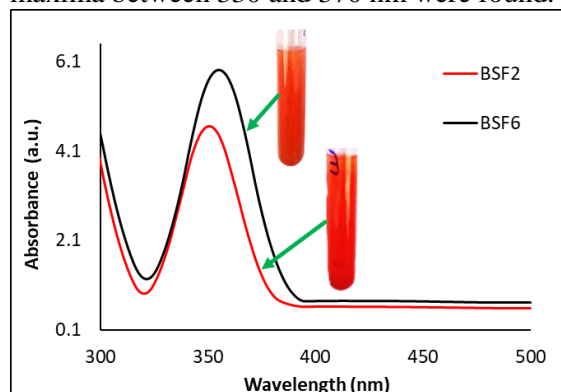


**Figure 2.** Color change and UV-Vis spectroscopy analysis of the biosynthesized SeNPs using *P. aeruginosa* isolates; BSF2 and BSF6.

FT-IR, TEM, and zeta potential studies were used to analyze the biosynthesized SeNPs that *P. aeruginosa* BSF6 generated. The FT-IR spectra of the bacterial crude protein and the protein attached to the surface of SeNPs showed distinct changes in peak location and shape (Figure 3), suggesting that the secondary structure of the protein underwent changes after NPs formation. FT-IR data have shown that contact with SeNPs has affected the secondary structure of proteins. It is possible to attribute the broad peak at  $3633.23\text{ cm}^{-1}$  to the hydroxyl (-OH) group. The C-H vibration is credited with the peak at  $1700.91\text{ cm}^{-1}$ . The bands at  $1447.31\text{ cm}^{-1}$  might be caused by the C-O stretching mode. The amide II band, which appears at bands  $3116.4\text{--}2498.33\text{ cm}^{-1}$ , is a combination of N-H in-plane bending and C-N stretching, while the amide I band is mostly a C=O stretching mode. Se vibration (C-Se) is responsible for  $549.61\text{ cm}^{-1}$  emergence.

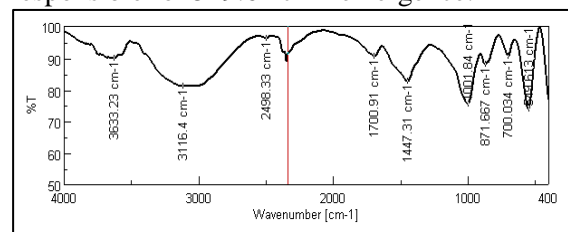


**Figure 3.** FT-IR of the biosynthesized SeNPs.

One crucial measure of the stability of the NPs' colloidal dispersion is still the zeta potential. The measurement of an effective electric charge on NPs' surface is called the zeta potential. Higher electrostatic repulsion between NPs causes the NPs with a larger zeta potential to be

more stable. The biosynthesized SeNPs' negative charge ( $-17.6\text{ mV}$ ) was shown by the Zeta potential measurements, as illustrated in Figure 4.

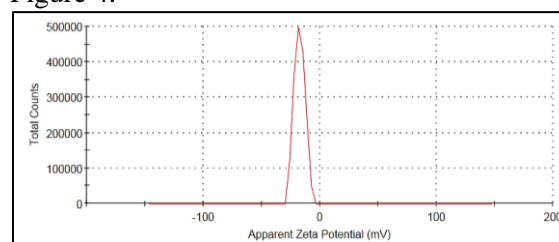


**Figure 4.** Zeta potential analysis of SeNPs.

An essential tool for assessing and studying the size and shape of NPs is the TEM investigation. The TEM micrograph of SeNPs demonstrated their uniform distribution, spherical shape, and absence of aggregation (Figure 5). The size of SeNPs ranged from 83.45 to 91.64 nm.

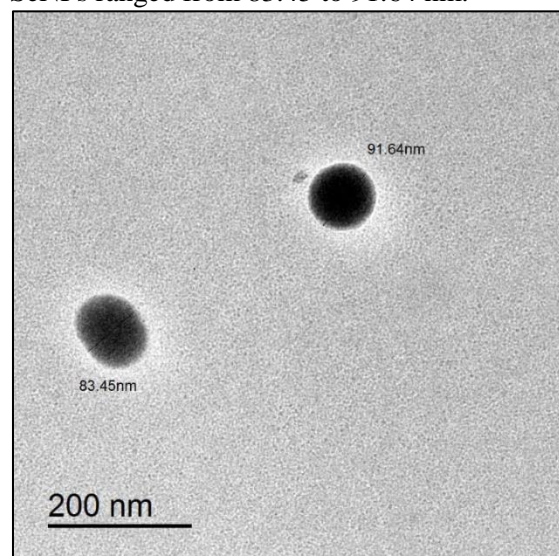


**Figure 5.** TEM of SeNPs with scale bar = 200 nm.

#### *Antimicrobial activity of the biosynthesized SeNPs*

SeNPs were bio-produced utilizing *P. aeruginosa* BSF6, and their antibacterial efficacy against several Gram-positive and Gram-negative bacteria as well as yeast was examined. SeNPs' antibacterial activity was evaluated using the agar well diffusion technique, MIC, and MBC assays, in contrast to the conventional antibiotics ampicillin and miconazole. The inhibition zones formed by the  $150\text{ }\mu\text{g/ml}$  SeNPs were  $20\pm0.06$  and  $12\pm0.03\text{ mm}$  against Gram-positive *B. cereus* and *S. aureus*, and  $10\pm0.18$  and  $9\pm0.16\text{ mm}$  against Gram-negative *P. aeruginosa* and *P. mirabilis*, respectively (Table 2). SeNPs demonstrated

better antibacterial and anticandidal properties than the medical standards miconazole and ampicillin. Additionally, it was mentioned that

**Table 2.** Agar well diffusion of SeNPs against the tested microbes.

Antimicrobial agents	Concentration, $\mu\text{g/mL}$	Inhibition zone in mm (mean $\pm$ SD)				
		Gram-negative bacteria		Gram-positive bacteria		Yeast
		<i>P. aeruginosa</i>	<i>P. mirabilis</i>	<i>B. cereus</i>	<i>S. aureus</i>	<i>C. albicans</i>
SeNPs	50	-ve	-ve	13 $\pm$ 0.21	8 $\pm$ 0.06	10 $\pm$ 0.14
	100	7 $\pm$ 0.14	6 $\pm$ 0.23	17 $\pm$ 0.14	10 $\pm$ 0.06	12 $\pm$ 0.06
	150	10 $\pm$ 0.16	9 $\pm$ 0.18	20 $\pm$ 0.06	12 $\pm$ 0.03	14 $\pm$ 0.14
Ampicillin	50	-ve	-ve	15 $\pm$ 0	-ve	-
	100	-ve	-ve	20 $\pm$ 0	-ve	-
	150	-ve	-ve	22 $\pm$ 0	6 $\pm$ 0	-
Miconazole	50	-	-	-	-	8 $\pm$ 0
	100	-	-	-	-	10 $\pm$ 0
	150	-	-	-	-	12 $\pm$ 0

The antimicrobial properties of the synthesized SeNPs were also evaluated using MIC and MBC (Figure 6). The MICs of SeNPs against *B. cereus*, *S. aureus*, *P. aeruginosa*, *P. mirabilis*, and *C. albicans* were 50, 70, 120, 150, and 50  $\mu\text{g/mL}$ , respectively. The MBC values were 60, 80, 120, and 150  $\mu\text{g/mL}$  against *B. cereus*, *S. aureus*, *P. aeruginosa*, and *P. mirabilis*, respectively. This indicated that the biosynthesized SeNPs were more effective against Gram-positive than Gram-negative bacteria. SeNPs showed dose-dependent antimicrobial activity against all test microbes, which increased by increasing their concentration. *P. mirabilis* followed by *P. aeruginosa* showed low sensitive behavior to SeNPs. To demonstrate a complete bacterial inhibition, high concentrations of SeNPs (150  $\mu\text{g/mL}$ ) were needed.

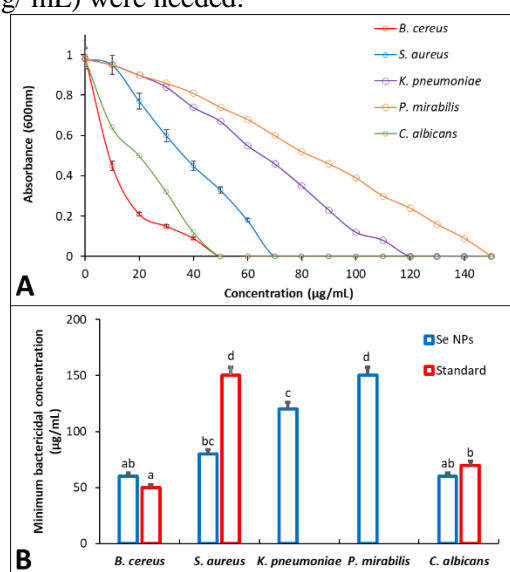


**Figure 6.** The minimum inhibition concentrations and minimum microbicidal concentrations of SeNPs compared to standards; miconazole and ampicillin.

SeNPs work better against bacteria that are Gram-positive than those that are Gram-negative.

### Antioxidant activity

The antioxidant qualities of the biosynthesized SeNPs were evaluated using the in vitro DPPH radical scavenging approach (Figure 7). The experiment's results showed that the radical scavenging ratio increased as the concentrations in the measured range increased and that SeNPs had a concentration-dependent scavenging effect. SeNPs have a 68.2% DPPH radical scavenging activity. At all doses, ascorbic acid, a common antioxidant, outperformed the SeNPs in this investigation.

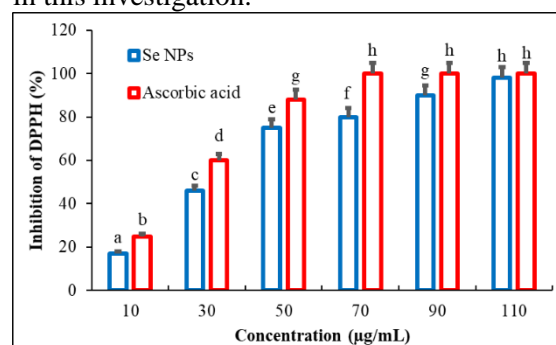


**Figure 7.** DPPH scavenging activity of SeNPs.

### Discussion

An international health emergency is the rise in antibiotic resistance. The battle against microbes was believed to be won. Through a variety of processes, either inherent to the organism or acquired from another, microorganisms can become resistant to novel antimicrobials (Reygaert, 2018). *Pseudomonas* bacteria is one of the most serious bacterial infections due to causing several diseases for the whole part of the body, and the most



dangerous problem is the resistance to antibacterial agents. Although certain types of antibacterial medications, such as ampicillin and ciprofloxacin, are extreme irritants and potentially bactericidal, many studies have found antibacterial resistance in *Pseudomonas* bacteria (Garg et al., 1999). This study seeks to identify an alternative green strategy to bacterial infection concerns, namely *Pseudomonas* resistance to current commercial medications. According to several studies, *P. aeruginosa* cases of  $\beta$ -lactam antibiotic resistance have been discovered (Gniadkowski, 2001; Subedi et al., 2018). Using common biochemical methods, two strains of *P. aeruginosa* that are resistant to drugs were successfully isolated and identified in the current study. The CLSI criteria and an *in vitro* method were employed to assess these bacteria's resistance to different antimicrobial medications. This project also aims to find a different green way to address the issue of bacterial resistance, notably *P. aeruginosa* resistance to the commercial drugs that are currently on the market.

Certain nano-metals and nano-oxides, including Fe, ZnO, Cu, Ag, Mn, Se, Au, and Al, have been found to exhibit antibacterial properties. Nano-metals are primarily synthesized using several physical and chemical techniques. However, as well as toxicity, high reactivity, and instability, drawbacks have been established, including the usage of expensive precursors and the creation of hazardous wastes (Baka et al., 2019; El-Zahed et al., 2023; Fayed et al., 2023). The biological synthesis of nanomaterials is therefore becoming more and more necessary. Bacteria are good instruments for nano-metal manufacturing because they are diverse and adaptable to harsh environmental conditions (Wang et al., 2017). For example, *P. aeruginosa* was found to synthesize AuNPs (Husseiny et al., 2007) and *K. pneumoniae* was also reported for SeNPs biosynthesis (Fesharaki et al., 2010).

To validate the synthesis of NPs, first, qualitatively change the color of the culture media from yellow to red brick color, which is caused by the conversion of selenite to selenium as an element; over time, the sodium selenite in the culture medium changes color to red (Abbas et al., 2021). This implies that selenite has been reduced to elemental Se, and the characteristic red hue produced indicates the resonance of the surface Plasmon of SeNPs.

The SeNPs biosynthesis was confirmed by an absorbance peak that ranged from 330 to 370 nm. Several research studies observed various absorbance peaks for SeNPs. For example, the maximum light absorption was at 294 nm for SeNPs, as reported by Tabibi et al. (2020). In a different study, a team of researchers used microorganisms isolated from several regions of Saudi Arabia to create SeNPs; the chosen strain had an absorption peak at 290 nm (El-Deeb et al., 2018). The manufacture of SeNPs using the bacteria *Ralstonia eutropha* was the subject of another investigation in 2015. This artificial NPs's absorption peak is visible at 270 nm (Srivastava & Mukhopadhyay, 2015). Numerous investigations demonstrate that synthesized SeNPs have a resonance peak at 200–300 nm. Nevertheless, this absorption peak is also influenced by a number of variables, including the isolated environment of the desired strain, material composition, particle size, and shape (Joshi et al., 2008). Furthermore, a lot of study has been done on the creation of SeNPs, which shows that the presence of SeNPs is indicated by distinct absorption peaks (Hemalatha et al., 2014).

Furthermore, studies show that several biomolecules or macromolecules, including proteins and polysaccharides, cover SeNPs produced by bacteria (Abou-Dobara et al., 2024; El-Dein et al., 2021; El-Zahed et al., 2021). Indeed, proteins and carbohydrates have the ability to reduce metal salts to metal NPs. Through the vibration of the functional groups (proteins and carbohydrates) of the nanoparticles, there are certain frequent issues with nanoparticle stability. Accumulation and aggregation of NPs are major issues that limit their utilization in various applications. Capping agents have a significant role in limiting NP aggregation. FT-IR analysis might yield valuable semiquantitative information regarding the existence of biological components in the coating layers of the nanoparticles and their related contents (Tugarova & Kamnev, 2017). The FT-IR study verified the presence of proteins as capping agents around the NPs. Some investigations confirm that protein capping compounds increase the stability of NPs via cysteine and amine residues, preventing NPs accumulation and aggregation (Escobar-Ramírez et al., 2021). In addition, the amide III band of proteins was discovered when using *pseudomonas sp* in the production of SeNPs. This capping agent may

contain negative or positive charges, which play a crucial role in NP stability and colloidal dispersion. SeNPs biosynthesized by *Penicillium* sp. were shown to have a negative charge of -11.8mV, creating a repulsion force between NP grains and increasing their stability. Laslo et al., (2022) found that *L. casei* produced SeNPs with a maximum zeta potential of -23 mV. It is worth noting that the zeta potential surface charge of NPs plays a significant role in antibacterial activity via electrostatic adhesion interactions with microbial cell membranes (Hnain et al., 2013). Our antibacterial activity data showed that SeNPs were effective against both Gram-positive and Gram-negative bacteria. Because Gram-positive and Gram-negative bacteria have different cell wall compositions. It was revealed that SeNPs showed a higher antibacterial activity against Gram-positive bacteria than Gram-negative. Thick walls and substantial levels of peptidoglycan discovered in Gram-positive bacteria's cell walls reduced the harmful impacts of these NPs when compared to Gram-negative bacteria. Several investigations have demonstrated SeNPs' bactericidal effects, which include the generation of reactive oxygen species, changes in cell wall permeability, and cell wall disintegration. SeNPs may interact with microbes' cell walls, triggering cell bursts, among other plausible explanations for their putative antimicrobial properties (Escobar-Ramírez et al., 2021).

The current work biosynthesized SeNPs using *P. aeruginosa* and investigated their antimicrobial activity. The antibacterial activity of SeNPs was tested against different Gram-positive bacteria, Gram-negative bacteria, and yeast in comparison to the standard antimicrobials ampicillin and miconazole using the agar well diffusion method, MIC, and MBC tests. Bacteria cannot multiply when an inhibition zone appears, proving that a treatment is working against them. Compared to SeNPs, *P. aeruginosa* and *P. mirabilis* displayed a complete resistance towards ampicillin. It was shown that SeNPs are more effective against bacteria that are Gram-positive than those that are Gram-negative. This is explained by a substantial change in the makeup of the bacterial walls. Numerous holes were discovered in the cell walls of Gram-positive bacteria, which facilitate the entry of NPs into the bacterial cells. This increases the NPs'

reactivity with bacterial components and fortifies their antibacterial action (Pasquina-Lemonche et al., 2020). In a similar way, biosynthesized SeNPs utilizing *Pseudomonas* sp. demonstrated greater biocidal effect against *C. albicans* with MIC and MFC values of 25 µg/ml than the conventional medication miconazole (40 µg/ml). El-Saadony et al. (2021) found an MIC and MFC of 55 and 80 µg/ml for SeNPs against *C. albicans*. Shakibaie et al. (2015) generated SeNPs using *Bacillus* species Msh1 and found a MIC of 70 µg/mL against *C. albicans*. Aside from the low MIC value of the biosynthesized SeNPs, the cytotoxic effect on normal keratinocyte cells was determined using the trypan blue method. SeNPs have a low hazardous effect, with an IC<sub>50</sub> of around 41.5 µg/mL.

Well-known antimicrobials, SeNPs mainly use oxidative stress to target bacteria. Reactive oxygen species (ROS) are produced, which causes the bacterial cell wall to break and release proteins and nucleic acids. ROS also causes significant respiratory enzymes to malfunction and oxidize important proteins like glutathione, which kills germs (Sahoo et al., 2023). The main mechanism by which Se NPs attack bacteria is oxidative stress. Proteins and nucleic acids are released when the bacterial cell wall breaks down due to the production of ROS. According to Sahoo et al. (2023), ROS also oxidizes important proteins like glutathione and causes critical respiratory enzymes to malfunction, killing bacteria. According to the acquired data, Se NPs demonstrated a concentration-dependent scavenging effect: the radical scavenging ratio rose as the concentrations in the tested range increased. Se NPs have a 68.2% DPPH radical scavenging activity. In this study, the conventional antioxidant ascorbic acid worked better than the Se NPs at all doses. Se NPs, which are efficient nanometallic compounds, improve cell permeability to NPs by destabilizing bacterial membranes and enhancing the biocidal action against the tested bacteria. SeNPs, which are effective nanometallic compounds, increase cell permeability to NPs by making bacterial membranes unstable. They have demonstrated a great deal of potential as a multipurpose antibiotic. The prospective use of SeNPs as promising single or combination antibacterial treatments in a range of environmental, industrial, and medical applications was

validated by these results.

## Conclusions

The cell-free supernatant of the clinical isolate *P. aeruginosa* is used in this work to biosynthesize SeNPs in an easy and environmentally friendly manner. FT-IR was used to determine the presence of the bacterial proteins, which may serve as a reducing and stabilizing agent. FT-IR, zeta analysis, TEM, and UV-Vis spectroscopy were used to confirm the synthesis of SeNPs. The SeNPs' long-term stability was shown by their zeta potential and FT-IR measurement. With MIC values ranging from 45 to 150 µg/ml, the biosynthesized SeNPs demonstrated strong antibacterial and anticandidal properties against yeast and both Gram-positive and Gram-negative bacteria. Gram-positive bacteria were found to be more susceptible to SeNPs than Gram-negative bacteria, which may have uses in many pharmaceutical and medical applications, according to the results of the agar well diffusion assay, MIC, and MBC.

## References:

- Abbas, H. S., Abou Baker, D. H., & Ahmed, E. A. (2021). Cytotoxicity and antimicrobial efficiency of selenium nanoparticles biosynthesized by *Spirulina platensis*. *Archives of Microbiology*, 203(2), 523–532. <https://doi.org/10.1007/s00203-020-02042-3>
- Abou-Dobara, M. I., Kamel, M. A., El-Sayed, A. K. A., & El-Zahed, M. M. (2024). Antibacterial activity of extracellular biosynthesized iron oxide nanoparticles against locally isolated  $\beta$ -lactamase-producing *Escherichia coli* from Egypt. *Discover Applied Sciences*, 6(3), 113. <https://doi.org/10.1007/s42452-024-05770-z>
- Atlas, R. M., & Snyder, J. W. (2011). Reagents, Stains, and Media: Bacteriology. In *Manual of Clinical Microbiology* (pp. 272–303). <https://doi.org/https://doi.org/10.1128/9781555816728.ch17>
- Baka, Z. A., El-sayed, A. K. A., & El-Zahed, M. M. (2019). Synthesis, characterization and antimicrobial activity of chitosan / Ag nanocomposite using *Escherichia coli* D8. *Scientific Journal for Damietta Faculty of Science*, 9(1), 1–6. <https://doi.org/10.21608/sjdfs.2019.194816>
- Besinis, A., Tracy, D. P., & and Handy, R. D. (2014). The antibacterial effects of silver, titanium dioxide and silica dioxide nanoparticles compared to the dental disinfectant chlorhexidine on *Streptococcus mutans* using a suite of bioassays. *Nanotoxicology*, 8(1), 1–16. <https://doi.org/10.3109/17435390.2012.742935>
- Clinical and Laboratory Standards (CLSI). (2000a). Performance standards for antimicrobial disk susceptibility tests, 7th ed. Approved standard M2–A7. National Committee for Clinical Laboratory Standards Wayne, Pa.
- CLSI. (2000b). Methods for dilution antimicrobial susceptibility test for bacteria that grow aerobically. Wayne, PA: *Clinical and Laboratory Standards Institute*.
- CLSI. (2008). Reference method for broth dilution antifungal susceptibility testing of yeasts; approved standard M27-A3. Wayne, PA: *Clinical and Laboratory Standards Institute*.
- CLSI. (2017). *Performance standards for antimicrobial susceptibility testing: Approved standard-twenty-seven edition* (Vols. M100-S26). Clinical and Laboratory Standards Institute, Wayne, Pennsylvania, USA.
- El-Deeb, B., Al-Talhi, A., Mostafa, N., & Abou-Assy, R. (2018). Biological synthesis and structural characterization of selenium nanoparticles and assessment of their antimicrobial properties. *American Scientific Research Journal for Engineering, Technology, and Sciences*, 45(1), 135–170.
- El-Dein, M. M. N., Baka, Z. A. M., Abou-Dobara, M. I., El-Sayed, A. K. A., & El-Zahed, M. M. (2021). Extracellular biosynthesis, optimization, characterization and antimicrobial potential of *Escherichia coli* D8 silver nanoparticles. *Journal of Microbiology, Biotechnology and Food Sciences*, 10(4), 648–656. <https://doi.org/10.15414/jmbfs.2021.10.4.648-656>
- El-Saadony, M. T., Saad, A. M., Taha, T. F., Najjar, A. A., Zabermawi, N. M., Nader, M. M., AbuQamar, S. F., El-Tarabily, K. A., & Salama, A. (2021). Selenium nanoparticles from *Lactobacillus paracasei* HM1 capable of antagonizing animal pathogenic fungi as a new source from human breast milk. *Saudi Journal of Biological Sciences*, 28(12), 6782–6794.
- El-Zahed, A. A. Z., Khalifa, M. E., El-Zahed, M. M., & Baka, Z. A. (2023). Biological synthesis and characterization of antibacterial manganese oxide nanoparticles using *Bacillus subtilis* ATCC6633. *Scientific Journal for Damietta Faculty of Science*, 13(3), 79–87. <https://doi.org/10.21608/sjdfs.2023.242279.1136>
- El-Zahed, M. M., Baka, Z., Abou-Dobara, M. I., & El-Sayed, A. (2021). *In vitro* biosynthesis and antimicrobial potential of biologically reduced

- graphene oxide/ag nanocomposite at room temperature. *Journal of Microbiology, Biotechnology and Food Sciences*, 10(6), e3956–e3956. <https://doi.org/10.15414/jmbfs.3956>
- Escobar-Ramírez, M. C., Castañeda-Ovando, A., Pérez-Escalante, E., Rodríguez-Serrano, G. M., Ramírez-Moreno, E., Quintero-Lira, A., Contreras-López, E., Añorve-Morga, J., Jaimez-Ordaz, J., & González-Olivares, L. G. (2021). Antimicrobial activity of Se-nanoparticles from bacterial biotransformation. *Fermentation*, 7(3), 130. <https://doi.org/https://doi.org/10.3390/fermentation7030130>
- Fayed, R., Elnemr, A.-M., & El-Zahed, M. M. (2023). Synthesis, characterization, antimicrobial and electrochemical studies of biosynthesized zinc oxide nanoparticles using the probiotic *Bacillus coagulans* (ATCC 7050). *Journal of Microbiology, Biotechnology and Food Sciences*, 13(3), e9962. <https://doi.org/10.55251/jmbfs.9962>
- Fesharaki, P. J., Nazari, P., Shakibaie, M., Rezaie, S., Banoe, M., Abdollahi, M., & Shahverdi, A. R. (2010). Biosynthesis of selenium nanoparticles using *Klebsiella pneumoniae* and their recovery by a simple sterilization process. *Brazilian Journal of Microbiology*, 41, 461–466. <https://doi.org/https://doi.org/10.1590/S1517-83822010000200028>
- Garg, P., Sharma, S., & Rao, G. N. (1999). Ciprofloxacin-resistant pseudomonas keratitis. The authors have no proprietary interest in any of the products mentioned in this article. *Ophthalmology*, 106(7), 1319–1323. [https://doi.org/https://doi.org/10.1016/S0161-6420\(99\)00717-4](https://doi.org/https://doi.org/10.1016/S0161-6420(99)00717-4)
- Gniadkowski, M. (2001). Evolution and epidemiology of extended-spectrum  $\beta$ -lactamases (ESBLs) and ESBL-producing microorganisms. *Clinical Microbiology and Infection*, 7(11), 597–608. <https://doi.org/https://doi.org/10.1046/j.1198-743x.2001.00330.x>
- Hemalatha, T., Krithiga, G., Santhosh Kumar, B., & Sastry, T. P. (2014). Preparation and characterization of hydroxyapatite-coated selenium nanoparticles and their interaction with osteosarcoma (SaOS-2) cells. *Acta Metallurgica Sinica (English Letters)*, 27, 1152–1158.
- Hnain, A., Brooks, J., & Lefebvre, D. D. (2013). The synthesis of elemental selenium particles by *Synechococcus leopoliensis*. *Applied Microbiology and Biotechnology*, 97(24), 10511–10519. <https://doi.org/10.1007/s00253-013-5304-0>
- Huh, A. J., & Kwon, Y. J. (2011). “Nanoantibiotics”: a new paradigm for treating infectious diseases using nanomaterials in the antibiotics resistant era. *Journal of Controlled Release*, 156(2), 128–145. <https://doi.org/https://doi.org/10.1016/j.jconrel.2011.07.002>
- Husseiny, M. I., Abd El-Aziz, M., Badr, Y., & Mahmoud, M. A. (2007). Biosynthesis of gold nanoparticles using *Pseudomonas aeruginosa*. *Spectrochimica Acta Part A: Molecular and Biomolecular Spectroscopy*, 67(3–4), 1003–1006. <https://doi.org/https://doi.org/10.1016/j.saa.2006.09.028>
- Iqtedar, M., Mehral, A., Muhammad, A., Asma, S., Roheena, A., & Kaleem, A. (2019). Extracellular biosynthesis, characterization, optimization of silver nanoparticles (AgNPs) using *Bacillus mojavensis* BTCB15 and its antimicrobial activity against multidrug resistant pathogens. *Preparative Biochemistry & Biotechnology*, 49(2), 136–142. <https://doi.org/10.1080/10826068.2018.1550654>
- Joshi, M., Bhattacharyya, A., & Ali, S. W. (2008). Characterization techniques for nanotechnology applications in textiles. *Indian Journal of Fibre & Textile Research*, 33, 304–317. <https://www.scirp.org/reference/referencespapers?referenceid=1237990>
- Khan, Y., Sadia, H., Ali Shah, S. Z., Khan, M. N., Shah, A. A., Ullah, N., Ullah, M. F., Bibi, H., Bafakeeh, O. T., & Khedher, N. Ben. (2022). Classification, synthetic, and characterization approaches to nanoparticles, and their applications in various fields of nanotechnology: a review. *Catalysts*, 12(11), 1386. <https://doi.org/https://doi.org/10.3390/catal12111386>
- Khurana, A., Tekula, S., Saifi, M. A., Venkatesh, P., & Godugu, C. (2019). Therapeutic applications of selenium nanoparticles. *Biomedicine & Pharmacotherapy*, 111, 802–812. <https://doi.org/https://doi.org/10.1016/j.biopha.2018.12.146>
- Kunz Coyne, A. J., El Ghali, A., Holger, D., Rebold, N., & Rybak, M. J. (2022). Therapeutic strategies for emerging multidrug-resistant *Pseudomonas aeruginosa*. *Infectious Diseases and Therapy*, 11(2), 661–682. <https://doi.org/10.1007/s40121-022-00591-2>
- Laslo, V., Pinzaru, S. C., Zagula, G., Kluz, M., Vicas, S. I., & Cavalu, S. (2022). Synergic effect of selenium nanoparticles and lactic acid bacteria in reduction cadmium toxicity. *Journal of Molecular Structure*, 1247, 131325. <http://dx.doi.org/10.1016/j.molstruc.2021.131325>
- Manimaran, M., Muthuvel, A., & Said, N. M. (2023). Microwave-assisted green synthesis of

- SnO<sub>2</sub> nanoparticles and their photocatalytic degradation and antibacterial activities. *Nanotechnology for Environmental Engineering*, 8(2), 413–423. <https://doi.org/10.1007/s41204-022-00297-3>
- Miller, W. R., & Arias, C. A. (2024). ESKAPE pathogens: Antimicrobial resistance, epidemiology, clinical impact and therapeutics. *Nature Reviews Microbiology*, 22(10), 598–616. <https://doi.org/10.1038/s41579-024-01054-w>
- Mohamed, E. A., & El-Zahed, M. M. (2024). Anticandidal applications of selenium nanoparticles biosynthesized with *Limosilactobacillus fermentum* (OR553490). *Discover Nano*, 19(1), 115. <https://doi.org/10.1186/s11671-024-04055-z>
- Moore, D. F., Hamada, S. S., Marso, E., & Martin, W. J. (1981). Rapid identification and antimicrobial susceptibility testing of Gram-negative bacilli from blood cultures by the AutoMicrobic system. *Journal of Clinical Microbiology*, 13(5), 934–939. <https://doi.org/10.1128/jcm.13.5.934-939.1981>
- Murray, C. J. L., Ikuta, K. S., Sharara, F., Swetschinski, L., Aguilar, G. R., Gray, A., Han, C., Bisignano, C., Rao, P., & Wool, E. (2022). Global burden of bacterial antimicrobial resistance in 2019: A systematic analysis. *The Lancet*, 399(10325), 629–655. [https://doi.org/10.1016/S0140-6736\(21\)02724-0](https://doi.org/10.1016/S0140-6736(21)02724-0)
- O'Neill, J. (2016). *Tackling drug-resistant infections globally: final report and recommendations*. Available online at: <https://www.cabidigitallibrary.org/doi/full/10.5555/20173071720>
- Owuama, C. I. (2017). Determination of minimum inhibitory concentration (MIC) and minimum bactericidal concentration (MBC) using a novel dilution tube method. *African Journal of Microbiology Research*, 11(23), 977–980. <https://doi.org/10.5897/AJMR2017.8545>
- Parte, A. C., Sardà Carbasse, J., Meier-Kolthoff, J. P., Reimer, L. C., & Göker, M. (2020). List of prokaryotic names with standing in nomenclature (LPSN) moves to the DSMZ. *International Journal of Systematic and Evolutionary Microbiology*, 70(11), 5607–5612. <https://doi.org/https://doi.org/10.1099/ijsem.0.004332>
- Poku, E., Cooper, K., Cantrell, A., Harnan, S., Sin, M. A., Zanzudana, A., & Hoffmann, A. (2023). Systematic review of time lag between antibiotic use and rise of resistant pathogens among hospitalized adults in Europe. *JAC-Antimicrobial Resistance*, 5(1), dlad001. <https://doi.org/https://doi.org/10.1093/jacamr/dlad001>
- Reygaert, W. C. (2018). An overview of the antimicrobial resistance mechanisms of bacteria. *AIMS Microbiology*, 4(3), 482. <https://doi.org/10.3934/microbiol.2018.3.482>
- Sahoo, B., Leena Panigrahi, L., Jena, S., Jha, S., & Arakha, M. (2023). Oxidative stress generated due to photocatalytic activity of biosynthesized selenium nanoparticles triggers cytoplasmic leakage leading to bacterial cell death. *RSC Advances*, 13(17), 11406–11414. <https://doi.org/10.1039/D2RA07827A>
- Santiago-Rodriguez, T. M., Ly, M., Bonilla, N., & Pride, D. T. (2015). The human urine virome in association with urinary tract infections. *Frontiers in Microbiology*, 6, 14. <https://www.frontiersin.org/journals/microbiology/articles/10.3389/fmicb.2015.00014>
- Saqib, S., Nazeer, A., Ali, M., Zaman, W., Younas, M., Shahzad, A., Sunera, & Nisar, M. (2022). Catalytic potential of endophytes facilitates synthesis of biometallic zinc oxide nanoparticles for agricultural application. *BioMetals*, 35(5), 967–985. <https://doi.org/10.1007/s10534-022-00417-1>
- Shakibaie, M., Mohazab, N. S., & Mousavi, S. A. A. (2015). Antifungal activity of selenium nanoparticles synthesized by *Bacillus* species Msh-1 against *Aspergillus fumigatus* and *Candida albicans*. *Jundishapur Journal of Microbiology*, 8(9), e26381. <https://doi.org/10.5812/jjm.26381>
- Srivastava, N., & Mukhopadhyay, M. (2015). Green synthesis and structural characterization of selenium nanoparticles and assessment of their antimicrobial property. *Bioprocess and Biosystems Engineering*, 38(9), 1723–1730. <https://doi.org/10.1007/s00449-015-1413-8>
- Subedi, D., Ajay Kumar, V., & Willcox, M. (2018). Overview of mechanisms of antibiotic resistance in *Pseudomonas aeruginosa*: An ocular perspective. *Clinical and Experimental Optometry*, 101(2), 162–171. <https://doi.org/10.1111/cxo.12621>
- Tabibi, M., Agaei, S. S., Amoozegar, M. A., Nazari, R., & Zolfaghari, M. R. (2020). Antibacterial, antioxidant, and anticancer activities of biosynthesized selenium nanoparticles using two indigenous halophilic bacteria. *Archives of Hygiene Sciences*, 9(4), 275–286. <http://dx.doi.org/10.52547/ArchHygSci.9.4.275>
- Tugarova, A. V., & Kamnev, A. A. (2017). Proteins in microbial synthesis of selenium nanoparticles. *Talanta*, 174, 539–547. <https://doi.org/https://doi.org/10.1016/j.talanta.2017.06.013>
- Turan, N., Kızılkaya, S., Buldurun, K., Çolak, N., Akdeniz, A., & Bursal, E. (2025). Synthesis, enzyme inhibitory and antioxidant activities, and molecular docking studies of metal complexes of



- a Schiff base ligand bearing pyridine moiety. *Journal of Molecular Structure*, 1338, 142167. <https://doi.org/https://doi.org/10.1016/j.molstruc.2025.142167>
- Wang, L., Chen, H., & and Shao, L. (2017). The antimicrobial activity of nanoparticles: present situation and prospects for the future. *International Journal of Nanomedicine*, 12(null), 1227–1249. <https://doi.org/10.2147/IJN.S121956>
- Xiao, D., Chao, X., Chunyan, Y., Peiyi, Y., Hongjian, Y., Qunying, G., Fengxian, H., Yao-Zhong, K., & Xiao, Y. (2024). Clinical characteristics and antibiotic treatment of peritoneal dialysis-associated peritonitis caused by *Pseudomonas* species: a review of 15 years' experience from southern China. *Microbiology Spectrum*, 12(6), e00096-24. <https://doi.org/10.1128/spectrum.00096-24>
- Yahr, T. L., & Parsek, M. R. (2006). *Pseudomonas aeruginosa*. In M. Dworkin, S. Falkow, E. Rosenberg, K.-H. Schleifer, & E. Stackebrandt (Eds.), *The Prokaryotes: A Handbook on the Biology of Bacteria Volume 6: Proteobacteria: Gamma Subclass* (pp. 704–713). Springer New York. [https://doi.org/10.1007/0-387-30746-X\\_22](https://doi.org/10.1007/0-387-30746-X_22)
- Youri, G., Catherine, B., Caroline, B., & Pierre, B. (2007). Evaluation of a new selective chromogenic agar medium for detection of extended-spectrum  $\beta$ -lactamase-producing Enterobacteriaceae. *Journal of Clinical Microbiology*, 45(2), 501–505. <https://doi.org/10.1128/jcm.02221-06>
- Zboromyrska, Y., & Vila, J. (2016). Advanced PCR-based molecular diagnosis of gastrointestinal infections: Challenges and opportunities. *Expert Review of Molecular Diagnostics*, 16(6), 631–640. <https://doi.org/10.1586/14737159.2016.1167599>

## الملخص العربي

### عنوان البحث: النشاط المضاد ميكروبي لجسيمات السيلينيوم النانومترية المصنعة حيويًا باستخدام عزلة سيدوموناس إيروجينوزا

ليلى عبد السميع الشخبي<sup>١</sup>، زكريا عوض محمد بقا<sup>١</sup>، محمد مرزوق الزاهد<sup>١\*</sup>

<sup>١</sup> قسم النبات والميكروبيولوجي، كلية العلوم، جامعة دمياط، دمياط الجديدة، مصر

استخدمت الدراسة الحالية بكتيريا سيدوموناس إيروجينوزا المعزولة من بعض العينات الطبية في التصنيع الحيوي لتصنيع جسيمات السيلينيوم النانومترية باستخدام نهج بسيط وفعال وقليل التكلفة. وقد استخدم جهاز Vitek 2 لتأكيد تحديد مستوى النوع للعزلة البكتيرية المختارة بعد التعرف عليها بالطرق التقليدية. تم التحقق من إنتاج جسيمات السيلينيوم النانومترية المصنعة حيويًا ووصفها باستخدام مجموعة متنوعة من الاختبارات، بما في ذلك المجهر الإلكتروني النافذ، وتحليل الأشعة تحت الحمراء، وتحليل زيتا، والتحليل الطيفي للأشعة فوق البنفسجية المرئية. وقد سُجِّلت قمم الامتصاص لجسيمات السيلينيوم النانومترية عند موجة طولها ٣٣٠-٣٧٠ نانومتر، كما تم التحقق من وجود بروتينات بواسطة أطيف الأشعة تحت الحمراء والتي قد تعمل كمكونات رابطة وداعمة أثناء التصنيع الحيوي. وقد تم رصد شحنة سطحية سالبة كبيرة على أسطح الجسيمات والتي تصل إلى -١٧.٦ مللي فولت مما قد تساهم أيضًا في استقرارها. وقد أظهر المجهر الإلكتروني النافذ أقطار جسيمات السيلينيوم النانومترية في نطاق تراوح بين ٨٣-٩١ نانومتر. كما أظهرت جسيمات السيلينيوم النانومترية نشاطًا قويًا ضد بكتيريا باسيلس سيريس، وستافيلوكوكس أوريوس، وسيدوموناس إيروجينوزا، وبروتئوس ميرابيليس، بالإضافة إلى خميرة كانديدا البيكانس، وذلك وفقًا للجرعة. وبلغت التركيزات المثبطة الدنيا لجسيمات السيلينيوم النانومترية ضد باسيلس سيريس، وستافيلوكوكس أوريوس، وسيدوموناس إيروجينوزا، وبروتئوس ميرابيليس، وخميرة كانديدا البيكانس ٤٠، و٧٠، و١١٠، و١٥٠، و١٥٠ ميكروجرام/مل، على التوالي. تقدم هذه الدراسة جسيمات نانومترية آمنة وفعالة واعدة كبديل لعلاج بعض الميكروبات المسببة للأمراض لدى البشر والحيوانات.

## Synthesis, Characterization and Biological Applications of Green Synthesized Se NPs using Locally Isolated Multidrug-Resistant *Escherichia Coli*

Zakaria A.M. Baka<sup>1</sup>, Laila A. Elshikiby<sup>1</sup> and Mohamed M. El-Zahed<sup>\*1</sup>

<sup>1</sup>Department of Botany and Microbiology, Faculty of Science, Damietta University, New Damietta city, Egypt.

Received: 21 May 2025 /Accepted: 20 June 2025

\*Corresponding author's E-mail: Mohamed.marzouq91@du.edu.eg

### Abstract

Multidrug-resistant *Escherichia coli* is a leading cause of nosocomial infections globally. The current study aimed to isolate and detect multidrug-resistant *E. coli* for use in the extracellular biosynthesis of selenium nanoparticles (Se NPs) as well as investigate their roles in antibacterial and antioxidant applications. We used Vitek 2 to confirm the species-level identification of the selected bacterial isolate, which had previously undergone classical identification. Different spectroscopy and microscopy analyses were used to characterize the biosynthesized nanoparticles (NPs), such as UV-visible spectroscopy, FTIR, TEM and Zeta analysis. The adsorption peak for Se NPs was observed at 348 nm, which confirmed the successful biogenesis of Se NPs. The presence of proteins linked to NPs that serve as capping and stabilizing agents is indicated by the FTIR spectra. NPs were spherically shaped, negatively charged particles (+48.2 mV) that had an average size of  $\approx 100$  nm, assisted in their stability. Se NPs demonstrated strong antibacterial activity against Gram-positive bacteria (*Bacillus cereus*, *Staphylococcus aureus*) and Gram-negative bacteria (*Proteus mirabilis*, *E. coli*) in a dose-dependent way. The antioxidant potential of Se NPs was also evaluated compared to ascorbic acid, which indicated their distinguished behavior as antioxidants. This study proposes Se NPs as a safe, effective, and feasible substitute for treating some pathogenic bacterial strains as well as good antioxidants, suggesting that this green synthesis of Se NPs could provide promising medical applications.

**Keywords:** Green synthesis, *Escherichia coli*, selenium, nanoparticles, antibacterial, antioxidant

### Introduction

*Escherichia coli* is a Gram-negative, facultative anaerobic, rod-shaped, coliform bacterium that dwells in the gut (gastrointestinal tract) of

healthy humans and animals (Martinson & Walk, 2020) and avoids dangerous pathogenic microorganisms from colonizing the intestines. However, in some conditions, various strains (types) of *E. coli* can cause illness. Many of the types that cause illness can attach (stick) to your cells and cause watery diarrhea, stomach pain,

and other digestive symptoms (gastroenteritis). Some of them have been reported to survive and develop at high antibiotic concentrations (Haefeli et al., 1984). Three primary methods of antibacterial resistance are (1) blocking access to the target, (2) altering the target of the antibiotic, or (3) directly altering the antibiotic. *E. coli* resistance can easily arise from either single point mutations of antibiotic target genes, of which fluoroquinolone resistance is a classic example, or from the transfer of mobile genetic elements, as has been the case with resistance to third-generation cephalosporins and broad-spectrum penicillin (such as ampicillin or amoxicillin) (Ochoa & Gómez-Duarte, 2016). Several global health agencies and governments have acted to combat AMR. Several studies reported the potential antibacterial action of different nanoparticles (NPs) to combat the bacterial resistance problems (El-Zahed et al., 2023; Hasanin et al., 2021; Nandana et al., 2021). Nanotechnology is defined as technology performed at the nanoscale with real-world applications. Controlling or modifying matter at the atomic and molecular levels can affect its size. The range is around 1 to 100 nm (Dubey & Dubey, 2021). The underlying science is known as nanoscience. Nanoscale attributes differ from those at larger scales. Their distinctive physicochemical features, including an extraordinarily large surface area, improved reactivity, and higher mechanical strength, distinguish them from bulk materials and contribute to their wide variety of applications (Bera, 2024). These properties enable nanoparticles (NPs) to give novel answers to some of the world's most urgent issues, such as disease treatment, pollution management, and energy efficiency. As a result, NPs are expected to play a critical role in determining the future of technology. The synthesis of NPs is influenced by factors such as temperature, pressure, time, particle size, shape, preparation cost, and pore size (Demazeau, 2010; Ma et al., 2008). Two approaches that describe the many alternatives for producing nanostructures have been developed. These manufacturing approaches are divided into two categories: top-down and bottom-up. The top-down technique is expensive and unsuitable for soft samples. The top-down method is not ideal for large-scale production but can be used for laboratory experiments. The bottom-up method follows the notion of molecular recognition. Bottom-up

approaches synthesize nanostructures by manipulating atoms, molecules, or clusters individually (Patil et al., 2021). These NPs can be manufactured using chemical, physical, and biological means; the biological production of NPs has gained popularity as a sustainable and environmentally benign alternative to standard chemical and physical processes. Chemical and physical methods are less preferable than biological ways because of high temperature conditions, dangerous substances, acidic pH, and highly poisonous and unsafe methods (Salem & Fouda, 2021a). These biological systems play an important role in nanoparticle synthesis by converting metal ions into NPs, frequently producing products with distinct characteristics that differ from those created using conventional methods (Jafir et al., 2023). However, while biological synthesis processes are environmentally favorable, they have hurdles, notably in terms of scalability and speed. The synthesis process usually takes longer, and temperature, pH, the concentration of biological agents, and the presence of other substances can all influence the size, shape, and yield of the NPs generated (Wang et al., 2023). Furthermore, managing the homogeneity of NPs produced by biological processes is a substantial problem, as the complexity of the biological systems involved might result in variances in particle properties (Sharma et al., 2023). Biological synthesis is widely divided into intracellular and extracellular techniques, such as intracellular synthesis, which is the process of creating NPs within living microorganisms or plants' cells. The intracellular process enables the production of NPs in a regulated environment, as the biological system governs particle growth, resulting in NPs that are frequently uniform in size and shape. Extracellular synthesis, on the other hand, occurs outside of live cells, most commonly in the surrounding media. This approach involves mixing biological extracts, such as plant leaves or fungus, with metal salt solutions (Bhatti et al., 2023). This method uses natural agents such as bacteria, fungi, plant extracts, and enzymes to create NPs (Shafqat et al., 2023). Microbial cells are naturally able to thrive in a variety of environments, and they grow quickly and are simple to maintain. Bacteria can be cultured in artificial environments with an optimal growth rate, making them a more viable candidate for NP synthesis than other microbes.

Bacteria have a remarkable ability to decrease heavy metal ions, making them excellent candidates for NPs production. For example, some bacterial species have evolved the ability to use specialized defensive mechanisms to resist stresses such as the toxicity of heavy metal ions or metals. Bacteria are regarded as a possible biofactory for the production of NPs such as Au, Ag, Pt, TiO<sub>2</sub>, Se, and so forth. On the other hand, selenium NPs (Se NPs) offer distinct advantages because of their dual function as critical micronutrient carriers and redox homeostasis modulators. When compared to traditional selenium treatments, Se NPs provide a more efficient and environmentally friendly alternative for improving plant resistance while limiting toxicity, especially at low concentrations. Se NPs have received worldwide interest due to their high degree of absorption, biological activity, minimal toxicity, and significant efficacy in inhibiting oxidative damage when compared to their Se-based counterparts (Mal et al., 2017; Zhang et al., 2008).

Se NPs may play a favorable function in biomedicine because of their antioxidant (Bai et al., 2017; Jin et al., 2021), anticancer (Liao et al., 2020; Varlamova et al., 2021), antibacterial, and immune regulatory characteristics. Se NPs have been widely recognized to exhibit a wide range of antibacterial and antifungal action (Lin et al., 2021). Their antibacterial properties may be linked to the overproduction of reactive oxygen species (ROS), which causes cell membrane damage, inhibits amino acid synthesis, and prevents DNA replication (Qin et al., 2025). Se can be found in both crystalline and amorphous polymorphic configurations, and each plays a unique purpose. Se, in its organic form found in selenoproteins, is required in animals for enzyme activity, immunological response, reproduction, and pro- and anti-oxidative characteristics (Constantinescu-Aruxandei et al., 2018; Zhang et al., 2004). These essential characteristics have motivated researchers to assess the potential of Se NPs as a strategy for combating multidrug-resistant bacteria and other microbial diseases.

The current study aimed to isolate a multidrug-resistant *E. coli* and use it to biosynthesize Se NPs, in addition to evaluating their antibacterial and antioxidant properties.

## Materials and methods

### *Sample collection*

Under aseptic conditions, 15 samples (10 females and 5 males) were taken in April and May 2024 from private clinics and medical analytical labs in New Damietta City, Kafr Elbattikh, and Faraskour (Damietta Governorate, Egypt, 31.4°N 31.72°E). Urine, stool, and surface exchanges were among the samples. The procedures previously outlined by Santiago-Rodriguez et al. (2015) and Zboromyrska & Vila (2016) were followed while processing the samples.

### *Isolation and identification of bacterial isolates*

Serial dilutions of samples ( $10^{-2}$ - $10^{-8}$ ) were made and infected using the pour plate method in MacConkey agar plates (Oxoid, Basingstoke, United Kingdom) with 2 mg/l ceftazidime (MCKC). All plates were incubated at 37°C and evaluated after 18, 24, or 48 hours. For 48 hours, each bacterial colony from a distinct bacterial isolate was transferred and subcultured on MacConkey and cystine lactose electrolyte deficient (CLED) agar plates from Oxoid Ltd. in England. The morphological properties of colonies and media, as well as color changes, were then recorded. The bacterial isolates were described and identified using Bergey's Manual of Systematic Bacteriology (Yahr & Parsek, 2006). The morphological and cultural criteria included colony structure, Gram staining, and endospore staining, and the identification was done in a systematic fashion as follows: The following colonial characteristics were recorded: size, form, pigment production, elevation, surface, edge, color, and opacity. Microscopic investigation includes shape, size, Gram stain, acid-fast stain, and endospore production. *E. coli* isolates were chosen, purified, and species-level identification was carried out in accordance with standard recommended standards (Koneman et al., 1997). To confirm the identification results, isolates were subcultured on blood agar plates and analyzed with the Vitek 2 (BioMerieux, Marcy-l'Étoile, France) (Moore et al., 1981). Bacterial isolates were preserved in agar slants for additional research (Glupczynski et al., 2007).

### *Antibiotic sensitivity test (AST)*

The disc diffusion technique was used to assess the AST of bacterial isolates (CLSI, 2000a). Mueller-Hinton agar (MHA, Oxoid Ltd., England) flasks were inoculated with 50 µl of each bacterial suspension ( $0.5$  MacFarland Standard,  $1.5 \times 10^8$  CFU/ml) independently, and the flasks were subsequently transferred into sterile Petri dishes. Following solidification, various antibiotic discs from various classes were aseptically applied (vanomycin; 30 µg/ml, amoxicillin/clavulanate; 20/10, ampicillin; 30, cefotaxime; 30, ceftazidime; 30, chloramphenicol; 30, doxycycline; 30, levofloxacin; 5, nalidixic acid; 30, and amoxycillin/clavulanate; 20/10). Following a 24-hour incubation period at 37°C, the diameter of the zones of inhibition (ZOI) was measured and recorded in millimeters.

### *Biosynthesis of selenium nanoparticles*

In 100 mL nutrient broth flasks, a 0.5 McFarland standard ( $1 \times 10^8$  cells/mL) from a chosen bacterial isolate was produced for 24 hours at 37 °C. The inoculation flasks were incubated at 37°C and 150 rpm for the entire night. A 0.22 µm syringe filter (Millex GV, Millipore) was used to filter the bacterial metabolites, and the cells were collected using centrifugation at 5000 rpm for 15 minutes after the incubation period. The bacterial metabolites were then transferred into another clean flask. After making 1 mM of Na<sub>2</sub>SeO<sub>3</sub> solution and adding it to the bacterial metabolite flasks in a 1:1 (v/v) ratio, the flasks were shaken at 150 rpm at 37°C until the color turned red. The generated Se NPs utilizing selected bacterial isolates were recovered by centrifugation at 30,000 rpm for 20 minutes and lyophilized after being washed four times with distilled water (Mohamed & El-Zahed, 2024).

### *Characterization of selenium nanoparticles*

The biosynthesized Se NPs were examined using two methods: a double beam spectrum UV-Vis spectrophotometer V-760 (JASCO, UK) and Fourier transform infrared spectroscopy (FTIR, FT/IR-4100 type A). Various microscopic approaches are used to characterize the morphology of NPs. Transmission electron microscopy (TEM) is the most widely used technique. TEM and zeta

potential measurements (Malvern Zetasizer Nano-ZS90, Malvern, UK) were employed for supplementary analysis.

### *Antibacterial activity of selenium nanoparticles using the agar well diffusion method*

The biosynthesized Se NPs were examined for antibacterial activity against Gram- positive bacteria (*Bacillus cereus*, *Staphylococcus aureus*) and Gram-negative bacteria (*Proteus mirabilis*, *E. coli*) in comparison to the standard antibiotic, ampicillin, using the Clinical and Laboratory Standards Institute agar well diffusion method (CLSI, 2017). A 0.5 McFarland of the tested bacteria was made and inoculated into sterile, cooled, molted MHA, which was then put into sterile Petri dishes. Se NPs and ampicillin were applied to 5 mm wells in inoculated agar plates at doses of 50, 100, and 150 µg/mL, respectively. Plates were incubated at 37°C for 24 hours before measuring ZOI in millimeters.

### *Minimal inhibitory concentration (MIC) and minimum bactericidal concentration (MBC)*

The broth dilution method was used to estimate the MIC values of Se NPs and ampicillin (CLSI, 2000). Se NPs and ampicillin at varying doses (0-75 µg/mL) were introduced to sterilized Muller-Hinton broth conical flasks inoculated with 0.5 McFarland of tested bacterial strains. The flasks were incubated at 37 °C for 24 hours. The growth rate of the bacteria was evaluated using a UV-Vis spectrophotometer at 600 nm against an uninoculated broth medium as a blank.

MIC flasks were inoculated into sterile cooled molten MHA media, which was then placed into a sterile petri plate. The inoculated agar plates were kept at 37°C for 24 hours. After incubation, bacterial colonies were counted in colony-forming units per mL (CFU/mL) to determine MBC values (Owuama, 2017).

### *Antioxidant activity of selenium nanoparticles*

Using the *in vitro* DPPH radical scavenging technique, the antioxidant properties of Se NPs were investigated (Turan et al., 2025). The greatest absorbance of DPPH radical solutions occurs at 517 nm. To achieve this, a 1 mM DPPH radical solution was made, and ethanol

was used to bring the control sample's absorbance down to  $1.5 \pm 0.5$ . Standard antioxidant ascorbic acid (vitamin C) was used to compare the outcomes. The DPPH radical solution was administered separately to the samples and standards at varying doses (10–110  $\mu\text{g/ml}$ ). Following a 30-min incubation period at  $25^\circ\text{C}$ , the samples' absorbance values were determined. A sample's ability to scavenge DPPH free radicals is shown by its lowering absorbance at 517 nm. Inhibition of DPPH in percent (I %) was calculated according to  $\% = (A_{\text{control}} - A_{\text{compound}}/A_{\text{control}}) \times 100$ , where  $A_{\text{control}}$  is the absorbance when the compound is not present, and  $A_{\text{compound}}$  is the absorbance when the compound is present.

### Statistical analysis

The data were statistically analyzed using SPSS version 18. All experiment results were provided as mean  $\pm$  SD using one-way analysis of variance (ANOVA). A substantial threshold of  $p < 0.05$  was used (O'Connor, 2000). Every experiment was done three times.

## Results

### Isolation, purification, and characterization of *E. coli*

The procedure successfully isolated 16 Gram-negative, lactose-fermenting, negative citrate, and non-spore-forming bacterial isolates. Two bacterial isolates were identified as *E. coli* strains using conventional recommendations and a Vitek 2 system test. This revealed the presence of two *E. coli* isolates encoded with AUF2 and CUF1 (Table 1; Figure 1). The two *E. coli* isolates were tested for Se NPs production.

**Table 1.** Biochemical tests for *E. coli* isolates.

Biochemical test	AUF2	CUF1
Citrate utilization	-	-
Catalase	+	+
Oxidase	-	-
Indole production	+	-
Methyl red	+	+
Voges-Proskauer	-	-
Urease	+	-
Nitrate reduction	+	+
H <sub>2</sub> S production	-	-
Lactose fermentation	+	+

\*+ = Present; - = Absent

### AST investigations

Table 2 demonstrates the AUF2 strain's resistance to every antibiotic that has been tested compared to the CUF1 strain. The results show that *E. coli* isolates have a resistance percentage of 100 to ampicillin, cefotaxime, ceftazidime, doxycycline, and vancomycin. The *E. coli* AUF2 isolate has a resistance action against amoxicillin/clavulanate, chloramphenicol, levofloxacin, and nalidixic acid. The obtained results indicated the multidrug resistance behavior for the *E. coli* isolates.

**Table 2.** Patterns of antibiotic resistance and sensitivity in *E. coli* isolates.

Antibiotic	Concentration ( $\mu\text{g/ml}$ )	Antibiotics susceptibility	
		AUF2	CUF1
Amoxicillin/clavulanate	20/10	+	-
Ampicillin	30	+	+
Cefotaxime	30	+	+
Ceftazidime	30	+	+
Chloramphenicol	30	+	-
Doxycycline	30	+	+
Levofloxacin	5	+	-
Nalidixic acid	30	+	-
Vancomycin	30	+	+

### Biosynthesis and characterization of Se NPs

The color of the culture media changes from pale yellow at the start of the experiment to brick red at the end of the incubation period. This is utilized to analyze the generation of Se NPs by *E. coli* isolates (Figure 1). The sample's color did not alter in the control studies. According to spectroscopic study outcomes, AUF2 produced Se NPs at larger concentrations and faster rates than the other isolate, CUF1 within 48 hours. The UV-Vis spectrum of AUF2- and CUF1-Se NPs revealed an adsorption peak ranging from 340 to 350 nm, consistent with the characteristics of colloidal Se NPs (Shah et al., 2010).

Se NPs generated by *E. coli* AUF2 were studied using FTIR, zeta, and TEM potential measurements. The capping agent composition of biosynthesized Se NPs was characterized by FTIR spectra, and their shape, size, distribution, and potential were studied by TEM and Zeta studies. Figure 2 shows the FTIR results. The peak at  $429.08\text{ cm}^{-1}$  attributed to the successful formation of Se NPs. C-O is represented by the third peak at  $863.95\text{ cm}^{-1}$ . The peak with a wavelength at  $1012.45\text{ cm}^{-1}$ , and the other peak



with a wavelength  $\text{cm}^{-1}$  is 1396.21 due to the presence of a C-H bond. The peak at  $1629.55 \text{ cm}^{-1}$  wavelength corresponds to the protein carbonyl amide bonds. The peak, at  $2975.96 \text{ cm}^{-1}$  indicates asymmetric tensile vibrations in the C-H groups. The peak at  $3449.06 \text{ cm}^{-1}$  corresponds to the O-H groups. These moieties hinder Se NP aggregation and increase their stability.

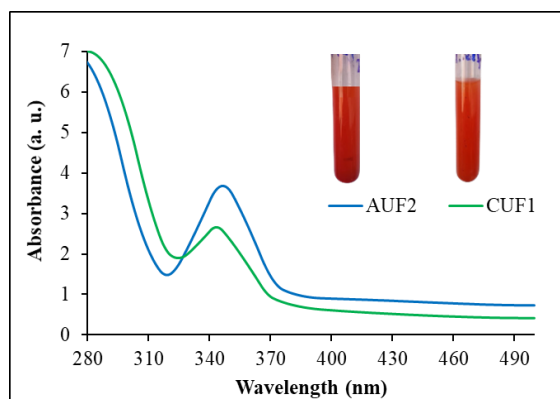


**Figure 1.** UV-vis spectroscopy and color change investigations were performed during the production of Se NPs using *E. coli* isolates; AUF2 and CUF1.

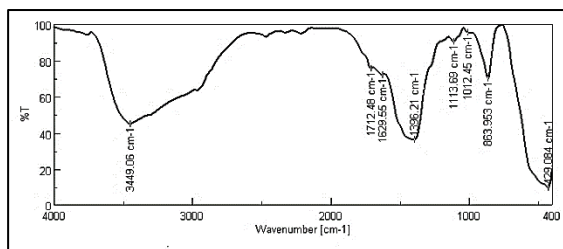


**Figure 2.** FTIR of the biosynthesized Se NPs.

The zeta potential remains a key indicator of the stability of the NPs' colloidal dispersion. The zeta potential is the measurement of an effective electric charge on the surface of NPs. The NPs with a bigger zeta potential are more stable due to higher electrostatic repulsion between them. The zeta potential measurements revealed the positive charge (+48.2 mV) of the biosynthesized Se NPs, as shown in Figure 3.

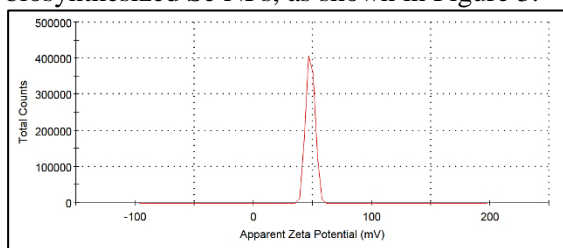


**Figure 3.** Zeta potential analysis of Se NPs.

The TEM studies are a crucial technique for evaluating and researching the size and shape of NPs. SeNPs' homogeneous distribution, spherical shape, and lack of aggregation were all visible in the TEM micrograph (Figure 4). Se NPs were between 94.15 and 108.43 nm in size.

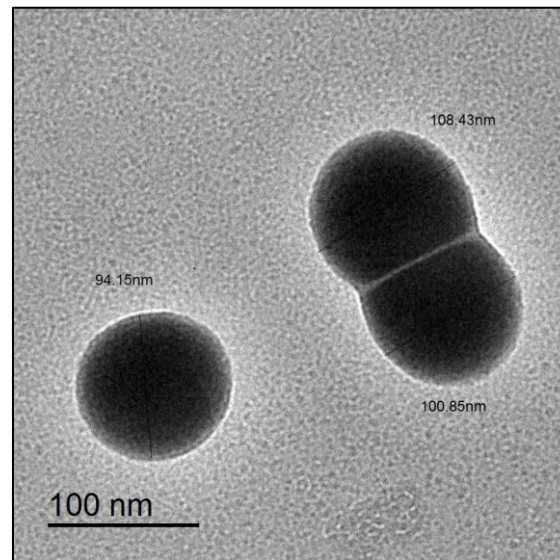


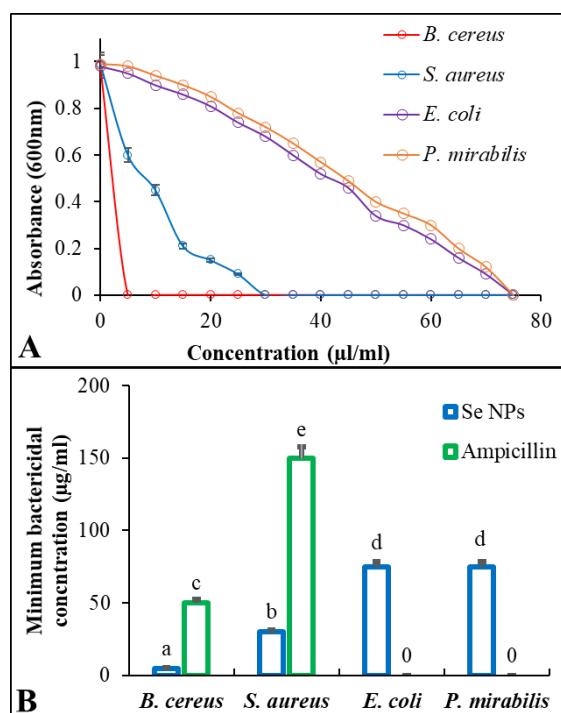
**Figure 4.** TEM of Se NPs. Scale bar = 100 nm.

### *The antibacterial action of selenium nanoparticles*

Se NPs were bio-produced using *E. coli* AUF2, and their antibacterial activity against different Gram-positive and Gram-negative bacteria was investigated. The antibacterial activity of Se NPs was assessed utilizing the agar well diffusion technique, MIC, and MBC assays, as opposed to traditional antibiotics like ampicillin. *In vitro* testing revealed that biosynthesized Se NPs had a higher antibacterial impact against Gram-negative bacteria than ampicillin (Table 3). The MIC test for Se NPs and ampicillin against Gram-positive bacteria ranged from 5 to 30  $\mu\text{g/mL}$ , while against Gram-negative bacteria ranged from 20 to 70  $\mu\text{g/mL}$  (Figure 5A). The MBC results were consistent with MIC concentrations, confirming the enhanced biocidal effect of the biosynthesized Se NPs against the tested bacteria (Figure 5B).

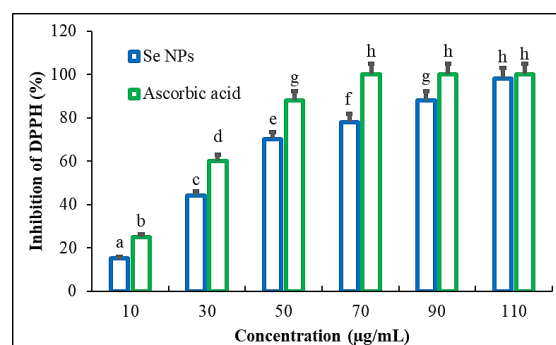
**Table 3.** Agar well diffusion of Se NPs against the tested bacteria.

Antimicrobial agents	Concentration, $\mu\text{g/ml}$	Inhibition zone in mm (mean $\pm$ SD)			
		Gram-negative bacteria		Gram-positive bacteria	
		<i>E. coli</i>	<i>P. mirabilis</i>	<i>B. cereus</i>	<i>S. aureus</i>
Se NPs	50	$7 \pm 0.14$	$6 \pm 0.18$	$17 \pm 0.06$	$16 \pm 0.14$
	100	$10 \pm 0.16$	$8 \pm 0.21$	$20 \pm 0.03$	$18 \pm 0.14$
	150	$12 \pm 0.06$	$10 \pm 0.14$	$23 \pm 0$	$20 \pm 0.06$
Ampicillin	50	-ve	-ve	$16 \pm 0$	-ve
	100	-ve	-ve	$20 \pm 0$	-ve
	150	-ve	-ve	$22 \pm 0$	$7 \pm 0$

**Figure 5.** The minimum inhibition concentrations; (A), and minimum bactericidal concentrations; (B), of Se NPs compared to standard; ampicillin.

#### Antioxidant activity

Using the *in vitro* DPPH radical scavenging technique, the antioxidant properties of the biosynthesized Se NPs were assessed (Figure 6). The findings of the experiment demonstrated that Se NPs had a concentration-dependent scavenging effect and that the radical scavenging ratio rose as the concentrations in the tested range increased. The DPPH radical scavenging activities were 67.5% for Se NPs. In this study, ascorbic acid as a standard antioxidant showed higher antioxidant action than the Se NPs at all concentrations.

**Figure 6.** DPPH scavenging activity of Se NPs.

#### Discussion

Multidrug-resistant *E. coli* is one of the most serious pathogenic bacteria since it causes multiple disorders throughout the body, and the most critical problem is resistance to antibacterial medications. Many *E. coli* strains cause mild illnesses. However, some strains release Shiga toxin, which can cause significant sickness and kidney damage. *E. coli* infections are most commonly found in the gastrointestinal and urinary tracts. Other forms of *E. coli* infections are Bloodstream infections, prostatitis (a prostate infection), pelvic inflammatory disease, or PID, a gallbladder infection (cholecystitis), infections from wounds, pneumonia (infrequent), and meningitis (rare). Symptoms of *E. coli* gastroenteritis are Diarrhea. This is frequently watery and occasionally bloody, stomachaches and cramps, loss of appetite, and a low fever. Watery diarrhea is typically the initial symptom of an *E. coli* infection in the gastrointestinal tract. Symptoms may vary based on the location of infection in your body (İncir & Kaplan, 2025). Although certain types of antibacterial medicines, such as amikacin, gentamicin, ciprofloxacin, amoxicillin/clavulanic acid, imipenem, ampicillin, cefotaxime, cefepime, and ceftazidime.

Numerous investigations have found that  $\beta$ -lactam antibacterial resistance cases of *E. coli* (Gniadkowski, 2001; Katsanis et al., 1994; Nepal et al., 2017). The current work effectively isolated and identified two multidrug-resistant *E. coli* strains using standard biochemical techniques. An *in vitro* technique and the CLSI criteria were used to determine these bacteria's resistance to various antimicrobial medicines. In addition, this study attempts to identify an alternative green method to combat bacterial resistance concerns, specifically *E. coli* resistance to current commercial medications. Recently, researchers have tended to synthesize novel active compounds using an environmentally benign approach. Nanomaterials are among the most active substances in agriculture, health, and industry (Sharma et al., 2018). To avoid the detrimental effects of chemical and physical techniques, these materials should be synthesized using green approaches (Salem & Fouda, 2021). Endophytic microorganisms such as fungi, bacteria, and actinomycetes are thought to be attractive sources for the green synthesis of nanomaterials because they secrete large amounts of active metabolites that can be employed as reducing and capping agents (Meena et al., 2021). Green NPs production utilizing bacteria has received more attention than other microorganisms. This is mostly owing to the remarkable secretion of extracellular metabolites, which increases NPs yield and provides great stability to the produced NPs. Bacteria are also known for their ease of handling, high metal tolerance, biomass production, and scalability. The current study looked at the effectiveness of endophytic bacterial strains for Se-NP synthesis. After adding the metal precursor ( $\text{Na}_2\text{SO}_3$ ) to the bacterial biomass filtrate, the color changed from colorless to red, progressively increasing, suggesting the creation of  $\text{Se}^0$  due to the reduction of  $\text{SeO}_3^{2-}$ . The prior combination was kept in the dark for 24 hours to ensure that the metal had been completely reduced and there was no further color change. Recently,  $\text{Na}_2\text{SO}_3$  was completely reduced by the action of metabolites released by the endophytic bacterial strain, *E. coli*, whereas the  $\text{Se}^0$  form was finished after 24 hours of incubation (Fouda et al., 2022). Furthermore, after 24 hours, Se-NPs were produced by reducing  $\text{Na}_2\text{SO}_3$  with metabolites released by *E. coli*, with no additional color change observed.

The ability of *E. coli* strains to biosynthesize Se NPs was investigated using cell-free supernatants. In comparison to the CUF1 strain, *E. coli* AUF2 showed the highest rate of Se NP synthesis. Se NPs were characterized by UV-visible spectroscopy, FTIR, TEM, and zeta analysis. Se NP biosynthesis was confirmed by an absorbance peak at  $\approx 348$  nm. Several research studies have reported distinct absorbance peaks for Se NPs. For example, Hemalatha et al. (2014) analyzed Se NPs with an absorbance peak of 290 nm, but El-Saadony et al. (2021) reported findings at 263 nm and 300 nm, respectively. The absorbance peak shifts to longer wavelengths as particle size rises (Shah et al., 2010). Se NPs only exhibit a continuous absorption peak in the wavelength range above 300 nm when the particle size is 100 nm or bigger. The absorption peak often shifts towards red, with peak intensity decreasing as nanoparticle size rises (Kaur & Bakshi, 2010).

FTIR spectroscopy was utilized to confirm the existence of functional groups that were primarily engaged in the Se NPs bioreduction process. The FTIR spectrum pattern of Se NPs revealed distinct functional groups on the surface, which may be responsible for the reduction of sodium selenite (inorganic form) to organic form Se NPs (Ashengroph & Hosseini, 2021). Stretching and bending bands of various groups (OH, NH, CO, and CN) validated the range of biogenic Se NPs generated by *E. coli* AUF2. The broad absorption bands correlate to the reducing groups (C-O, NH, and C-C) found in bacterial proteins that were responsible for the reduction of sodium selenite into Se NPs. The overall FTIR spectral fingerprint pattern corresponded to the outline of Se NPs synthesized by Alvi et al. (2021), Mehta et al. (2021), and Ramya et al. (2015) using a green synthesis technique. According to prior research, the presence of particular biomolecules may reduce the ability to produce NPs. Polysaccharides have a variety of functions, including hydroxyl groups and a hemiacetal reducing end that can reduce precursor salts. The conversion of polysaccharide hydroxyl groups to carbonyl groups is crucial in the reduction of selenium salts (Mata et al., 2009).

The reducing end of polysaccharides can also be exploited to provide an amino functionality capable of complexing with and stabilizing metallic NPs (Nadkarni et al., 1994).

Carbohydrates with such amino groups bond strongly to the surface of SeNPs, resulting in a hydrophilic surface (Kemp et al., 2009; Park et al., 2011). These protein-loaded Se NPs have a high antibacterial potential and also exhibit antioxidant activity. They play a key function in medications and are widely thought to have significant health advantages (Chen & Dou, 2008; Lamoral-Theys et al., 2010). During the current study, spherical particles of an average size of  $\approx 100$  nm were observed. It was a consensus from earlier research (Eszenyi et al., 2011; W. Zhang et al., 2011). These particles are charged species, and their charge is assessed using zeta potential. NPs can survive in colloidal systems with zeta potential values reaching +48 mV, depending on their charge. A low zeta potential, on the other hand, might cause particle aggregation and flocculation as a result of van der Waals attractive forces acting on them (Tso et al., 2010; Ye et al., 2020). The size and shape of the Se NPs were validated using a TEM. Spherical-shaped Se NPs were prepared using the *E. coli* AUF2.

Biosynthesized Se NPs made with *E. coli* AUF2 show better biocidal activity against Gram-positive bacteria with MIC and MBC values of 5-30  $\mu\text{g/mL}$  compared to the traditional drug ampicillin (50-150  $\mu\text{g/mL}$ ). El-Saadony et al. (2021) found that LAB-Se NPs had MIC values of 55  $\mu\text{g/mL}$ . Shakibaie et al. (2015) produced Se NPs with *Bacillus* Msh1, which had an MIC of 70  $\mu\text{g/mL}$  against tested microbes.

It was shown that Se NPs are more effective against bacteria that are Gram-positive than those that are Gram-negative. This is explained by a substantial change in the makeup of the bacterial walls. Numerous holes were discovered in the cell walls of Gram-positive bacteria, which facilitate the entry of NPs into the bacterial cells. This increases the NPs' reactivity with bacterial components and fortifies their antibacterial action (Pasquina-Lemonche et al., 2020).

Se NPs primarily exploit oxidative stress to target microorganisms. ROS are created, causing the bacterial cell wall to degrade and release proteins and nucleic acids. ROS also causes crucial respiratory enzymes to malfunction and oxidize key proteins such as glutathione, which kills germs (Sahoo et al., 2023). The obtained results showed that the radical scavenging ratio increased as the concentrations in the measured range increased, indicating that Se NPs exhibited a

concentration-dependent scavenging effect. For Se NPs, the DPPH radical scavenging activity was 67.5%. At all doses, ascorbic acid, a common antioxidant, outperformed the Se NPs in this investigation. Se NPs, which are efficient nanometallic compounds, improve cell permeability to NPs by destabilizing bacterial membranes and enhancing the biocidal action against the tested bacteria.

## Conclusions

An increasing demand for sustainability initiatives in nanotechnology has resulted in the development of biogenic techniques for the synthesis of Se NPs, which are rapidly replacing traditional chemical syntheses. The current study succeeding in isolating two multidrug-resistant *E. coli* strains that tested for the extracellular biosynthesis of Se NPs. The characterization and bioactivities of Se NPs demonstrated their appropriate composition, survivability against bacterial infections, and antioxidant activity. The findings of this study could have a significant impact because of *E. coli* AUF2's easy culture requirements and the inexpensive manufacturing cost of biologically relevant Se NPs. Given these possible biological effects, the investigated Se NPs have enormous potential for use in the pharmaceutical, biomedical, and food industries, particularly as antibacterial and antioxidant agents.

## References:

- Alvi, G. B., Iqbal, M. S., Ghaith, M. M. S., Haseeb, A., Ahmed, B., & Qadir, M. I. (2021). Biogenic selenium nanoparticles (SeNPs) from citrus fruit have anti-bacterial activities. *Scientific Reports*, 11(1), 4811.
- Ashengroph, M., & Hosseini, S.-R. (2021). A newly isolated *Bacillus amyloliquefaciens* SRB04 for the synthesis of selenium nanoparticles with potential antibacterial properties. *International Microbiology*, 24(1), 103–114. <https://doi.org/10.1007/s10123-020-00147-9>
- Bai, K., Bihong, H., Jianlin, H., Zhuan, H., & Tan, R. (2017). Preparation and antioxidant properties of selenium nanoparticles-loaded chitosan microspheres. *International Journal of Nanomedicine*, 12(null), 4527–4539. <https://doi.org/10.2147/IJN.S129958>
- Bera, R. K. (2024). Scientific Theories Are

- Intellectual Constructs. In *The Evolution of Knowledge: Scientific Theories for a Sustainable Society* (pp. 33–72). Springer. [https://doi.org/10.1007/978-981-99-9346-8\\_2](https://doi.org/10.1007/978-981-99-9346-8_2)
- Bhatti, M. M., Vafai, K., & Abdelsalam, S. I. (2023). The role of nanofluids in renewable energy engineering. *Nanomaterials*, 13(19), 2671. <https://doi.org/10.3390/nano13192671>
- Chen, D. I., & Dou, Q. P. (2008). Tea polyphenols and their roles in cancer prevention and chemotherapy. *International Journal of Molecular Sciences*, 9(7), 1196–1206.
- Clinical and Laboratory Standards (CLSI). (2000). Methods for dilution antimicrobial susceptibility test for bacteria that grow aerobically. Wayne, PA: Clinical and Laboratory Standards Institute.
- CLSI. (2000). Performance standards for antimicrobial disk susceptibility tests, 7th ed. Approved standard M2–A7. National Committee for Clinical Laboratory Standards Wayne, Pa.
- Constantinescu-Aruxandei, D., Frîncu, R. M., Capră, L., & Oancea, F. (2018). Selenium analysis and speciation in dietary supplements based on next-generation selenium ingredients. *Nutrients*, 10(10), 1466. <https://doi.org/10.3390/nu10101466>
- Demazeau, G. (2010). Solvothermal processes: definition, key factors governing the involved chemical reactions and new trends. *Zeitschrift Für Naturforschung B*, 65(8), 999–1006. <https://doi.org/10.1515/znB-2010-0805>
- Dubey, N., & Dubey, N. (2021). Current regulatory framework in nanotechnology and medicine. *Nanotechnology in Medicine: Toxicity and Safety*, 373–406. <https://doi.org/10.1002/9781119769897.ch17>
- El-Saadony, M. T., Saad, A. M., Najjar, A. A., Alzahrani, S. O., Alkhatib, F. M., Shafi, M. E., Selem, E., Desoky, E.-S. M., Fouda, S. E. E., & El-Tahan, A. M. (2021). The use of biological selenium nanoparticles to suppress *Triticum aestivum* L. crown and root rot diseases induced by *Fusarium* species and improve yield under drought and heat stress. *Saudi Journal of Biological Sciences*, 28(8), 4461–4471.
- El-Saadony, M. T., Saad, A. M., Taha, T. F., Najjar, A. A., Zabermaawi, N. M., Nader, M. M., AbuQamar, S. F., El-Tarabily, K. A., & Salama, A. (2021). Selenium nanoparticles from *Lactobacillus paracasei* HM1 capable of antagonizing animal pathogenic fungi as a new source from human breast milk. *Saudi Journal of Biological Sciences*, 28(12), 6782–6794.
- El-Zahed, A. A. Z., Khalifa, M. E., El-Zahed, M. M., & Baka, Z. A. (2023). Biological synthesis and characterization of antibacterial manganese oxide nanoparticles using *Bacillus subtilis* ATCC6633. *Scientific Journal for Damietta Faculty of Science*, 13(3), 79–87. <https://doi.org/10.21608/sjdfs.2023.242279.1136>
- Eszenyi, P., Sztrik, A., Babka, B., & Prokisch, J. (2011). Elemental, nano-sized (100–500 nm) selenium production by probiotic lactic acid bacteria. *International Journal of Bioscience, Biochemistry and Bioinformatics*, 1(2), 148.
- Fouda, A., Hassan, S. E.-D., Eid, A. M., Abdel-Rahman, M. A., & Hamza, M. F. (2022). Light enhanced the antimicrobial, anticancer, and catalytic activities of selenium nanoparticles fabricated by endophytic fungal strain, *Penicillium crustosum* EP-1. *Scientific Reports*, 12(1), 11834. <https://doi.org/10.1038/s41598-022-15903-2>
- Glupczynski, Y., Berhin, C., Bauraing, C., & Bogaerts, P. (2007). Evaluation of a new selective chromogenic agar medium for detection of extended-spectrum  $\beta$ -lactamase-producing Enterobacteriaceae. *Journal of Clinical Microbiology*, 45(2), 501–505. <https://doi.org/10.1128/jcm.02221-06>
- Gniadkowski, M. (2001). Evolution and epidemiology of extended-spectrum  $\beta$ -lactamases (ESBLs) and ESBL-producing microorganisms. *Clinical Microbiology and Infection*, 7(11), 597–608. <https://doi.org/10.1046/j.1198-743x.2001.00330.x>
- Haefeli, C., Franklin, C., & Hardy, K. (1984). Plasmid-determined silver resistance in *Pseudomonas stutzeri* isolated from a silver mine. *Journal of Bacteriology*, 158(1), 389–392. <https://doi.org/10.3390/nano15040301>
- Hasanin, M., Elbahnasawy, M. A., Shehabeldine, A. M., & Hashem, A. H. (2021). Ecofriendly preparation of silver nanoparticles-based nanocomposite stabilized by polysaccharides with antibacterial, antifungal and antiviral activities. *BioMetals*, 34, 1313–1328.
- Hemalatha, T., Krithiga, G., Santhosh Kumar, B., & Sastry, T. P. (2014). Preparation and characterization of hydroxyapatite-coated selenium nanoparticles and their interaction with osteosarcoma (SaOS-2) cells. *Acta Metallurgica Sinica (English Letters)*, 27, 1152–1158.
- İncir, İ., & Kaplan, Ö. (2025). Escherichia coli in the production of biopharmaceuticals. *Biotechnology and Applied Biochemistry*, 72(2), 528–541. <https://doi.org/10.1002/bab.2664>

- Jafir, M., Irfan, M., Zia-ur-Rehman, M., Hafeez, F., Ahmad, J. N., Sabir, M. A., Zulfikar, U., Iqbal, R., Zulfikar, F., & Moosa, A. (2023). The global trend of nanomaterial usage to control the important agricultural arthropod pests: A comprehensive review. *Plant Stress*, 10, 100208.
- Jin, Y., He, Y., Liu, L., Tao, W., Wang, G., Sun, W., Pei, X., Xiao, Z., Wang, H., & Wang, M. (2021). Effects of supranutritional selenium nanoparticles on immune and antioxidant capacity in sprague-dawley rats. *Biological Trace Element Research*, 199(12), 4666–4674. <https://doi.org/10.1007/s12011-021-02601-9>
- Katsanis, G. P., Spargo, J., Ferraro, M. J., Sutton, L., & Jacoby, G. A. (1994). Detection of *Klebsiella pneumoniae* and *Escherichia coli* strains producing extended-spectrum beta-lactamases. *Journal of Clinical Microbiology*, 32(3), 691–696. <https://doi.org/10.1128/jcm.32.3.691-696.1994>
- Kaur, G., & Bakshi, M. S. (2010). Nonideal mixing of Se–Te in aqueous micellar phase for nanoalloys over the whole mole mixing range with morphology control from nanoparticles to nanoribbons. *The Journal of Physical Chemistry C*, 114(1), 143–154.
- Kemp, M. M., Kumar, A., Mousa, S., Dyskin, E., Yalcin, M., Ajayan, P., Linhardt, R. J., & Mousa, S. A. (2009). Gold and silver nanoparticles conjugated with heparin derivative possess anti-angiogenesis properties. *Nanotechnology*, 20(45), 455104.
- Koneman, E., Allen, S. D., Janda, W. M., & Schreckenberger, P. C. (1997). Chapter 6: the enterobacteriaceae. *Color Atlas and Textbook of Diagnostic Microbiology*, 5th Edn. Lippincott-Raven Publishers, Philadelphia, 231–315.
- Lamoral-Theys, D., Pottier, L., Dufrasne, F., Neve, J., Dubois, J., Kornienko, A., Kiss, R., & Ingrassia, L. (2010). Natural polyphenols that display anticancer properties through inhibition of kinase activity. *Current Medicinal Chemistry*, 17(9), 812–825. <https://doi.org/10.2174/092986710790712183>
- Liao, G., Tang, J., Wang, D., Zuo, H., Zhang, Q., Liu, Y., & Xiong, H. (2020). Selenium nanoparticles (SeNPs) have potent antitumor activity against prostate cancer cells through the upregulation of miR-16. *World Journal of Surgical Oncology*, 18(1), 81. <https://doi.org/10.1186/s12957-020-01850-7>
- Lin, W., Zhang, J., Xu, J.-F., & Pi, J. (2021). The advancing of selenium nanoparticles against infectious diseases. *Frontiers in Pharmacology*, 12, 682284. <https://doi.org/https://doi.org/10.3389/fphar.2021.682284>
- Ma, J., Liu, X., Wu, L., & Zheng, W. (2008). A solvothermal route to tellurium based thin films. *Crystal Research and Technology: Journal of Experimental and Industrial Crystallography*, 43(12), 1297–1299. <https://doi.org/https://doi.org/10.1002/crat.200800185>
- Mal, J., Wouter J., V., Y. V., N., Eric D., van H., Willie J. G. M., P., Martina G., V., & Lens, P. N. L. (2017). A comparison of fate and toxicity of selenite, biogenically, and chemically synthesized selenium nanoparticles to zebrafish (*Danio rerio*) embryogenesis. *Nanotoxicology*, 11(1), 87–97. <https://doi.org/10.1080/17435390.2016.1275866>
- Martinson, J. N. V., & Walk, S. T. (2020). *Escherichia coli* residency in the gut of healthy human adults. *EcoSal Plus*, 9(1), 10–1128. <https://doi.org/https://doi.org/10.1128/ecosalplus.esp-0003-202090>
- Mata, Y. N., Torres, E., Blazquez, M. L., Ballester, A., González, F., & Munoz, J. A. (2009). Gold (III) biosorption and bioreduction with the brown alga *Fucus vesiculosus*. *Journal of Hazardous Materials*, 166(2–3), 612–618.
- Meena, M., Zehra, A., Swapnil, P., Harish, Marwal, A., Yadav, G., & Sonigra, P. (2021). Endophytic nanotechnology: An approach to study scope and potential applications. *Frontiers in Chemistry*, 9, 613343.
- Mehta, H., Gupta, M., Kaur, P., Kaur, J., & Kaushal, N. (2021). Redox modulatory anti-inflammatory potential of hempseed (*Cannabis sativa*) based green selenium nanoparticles. *Applied Science and Convergence Technology*, 30(3), 81–86.
- Moore, D. F., Hamada, S. S., Marso, E., & Martin, W. J. (1981). Rapid identification and antimicrobial susceptibility testing of Gram-negative bacilli from blood cultures by the AutoMicrobic system. *Journal of Clinical Microbiology*, 13(5), 934–939. <https://doi.org/https://doi.org/10.1128/jcm.13.5.934-939.1981>
- Nadkarni, V. D., Pervin, A., & Linhardt, R. J. (1994). Directional immobilization of heparin onto beaded supports. *Analytical Biochemistry*, 222(1), 59–67.
- Nandana, C. N., Christeena, M., & Bharathi, D. (2021). Synthesis and characterization of chitosan/silver nanocomposite using rutin for antibacterial, antioxidant and photocatalytic applications. *Journal of Cluster Science*. 33, 269–279. <https://doi.org/10.1007/s10876-020-01947-9>
- Nepal, K., Pant, N. D., Neupane, B., Belbase, A., Baidhya, R., Shrestha, R. K., Lekhak, B., Bhatta, D. R., & Jha, B. (2017). Extended spectrum beta-lactamase and metallo beta-lactamase production among *Escherichia coli* and *Klebsiella*



- pneumoniae* isolated from different clinical samples in a tertiary care hospital in Kathmandu, Nepal. *Annals of Clinical Microbiology and Antimicrobials*, 16(1), 62. <https://doi.org/10.1186/s12941-017-0236-7>
- Ochoa, T. J., & Gómez-Duarte, O. G. (2016). Antibiotic resistance in *Escherichia coli*. *Escherichia coli in the Americas*, 301–322.
- O'Connor, B. P. (2000). SPSS and SAS programs for determining the number of components using parallel analysis and Velicer's MAP test. *Behavior Research Methods, Instruments, & Computers*, 32(3), 396–402.
- Owuama, C. I. (2017). Determination of minimum inhibitory concentration (MIC) and minimum bactericidal concentration (MBC) using a novel dilution tube method. *African Journal of Microbiology Research*, 11(23), 977–980. <https://doi.org/10.5897/AJMR2017.8545>
- Park, Y., Hong, Y. N., Weyers, A., Kim, Y. S., & Linhardt, R. J. (2011). Polysaccharides and phytochemicals: A natural reservoir for the green synthesis of gold and silver nanoparticles. *IET Nanobiotechnology*, 5(3), 69–78.
- Pasquina-Lemonche, L., Burns, J., Turner, R. D., Kumar, S., Tank, R., Mullin, N., Wilson, J. S., Chakrabarti, B., Bullough, P. A., Foster, S. J., & Hobbs, J. K. (2020). The architecture of the Gram-positive bacterial cell wall. *Nature*, 582(7811), 294–297. <https://doi.org/10.1038/s41586-020-2236-6>
- Patil, N., Bhaskar, R., Vyavhare, V., Dhadge, R., Khaire, V., & Patil, Y. (2021). Overview on methods of synthesis of nanoparticles. *International Journal of Current Pharmaceutical Research*, 13(2), 11–16.
- Qin, X., Wang, Z., Lai, J., Liang, Y., & Qian, K. (2025). The synthesis of selenium nanoparticles and their applications in enhancing plant stress resistance: A review. *Nanomaterials*, 15(4), 301.
- Mohamed, E. A., & El-Zahed, M. M. (2024). Anticandidal applications of selenium nanoparticles biosynthesized with *Limosilactobacillus fermentum* (OR553490). *Discover Nano*, 19(1), 115. <https://doi.org/10.1186/s11671-024-04055-z>
- Ramya, S., Shanmugasundaram, T., & Balagurunathan, R. (2015). Biomedical potential of actinobacterially synthesized selenium nanoparticles with special reference to anti-biofilm, anti-oxidant, wound healing, cytotoxic and anti-viral activities. *Journal of Trace Elements in Medicine and Biology*, 32, 30–39.
- Rex, J. H. (2009). Method for antifungal disk diffusion susceptibility testing of yeasts: approved guideline. (No Title).
- Sahoo, B., Leena Panigrahi, L., Jena, S., Jha, S., & Arakha, M. (2023). Oxidative stress generated due to photocatalytic activity of biosynthesized selenium nanoparticles triggers cytoplasmic leakage leading to bacterial cell death. *RSC Advances*, 13(17), 11406–11414. <https://doi.org/10.1039/D2RA07827A>
- Salem, S. S., & Fouda, A. (2021a). Green synthesis of metallic nanoparticles and their prospective biotechnological applications: An overview. *Biological Trace Element Research*, 199(1), 344–370. <https://doi.org/10.1007/s12011-020-02138-3>
- Salem, S. S., & Fouda, A. (2021b). Green synthesis of metallic nanoparticles and their prospective biotechnological applications: an overview. *Biological Trace Element Research*, 199(1), 344–370.
- Santiago-Rodriguez, T. M., Ly, M., Bonilla, N., & Pride, D. T. (2015). The human urine virome in association with urinary tract infections. *Frontiers in Microbiology*, 6, 14. <https://www.frontiersin.org/journals/microbiology/articles/10.3389/fmicb.2015.00014>
- Shafqat, U., Maqsood, A., Ishfaq, A., Mustafa, S., Rasheed, Y., Mahmood, F., Hassan, M. U., Al-Khayri, J. M., Aldaej, M. I., & Sattar, M. N. (2023). Green nanotechnology for plant bacterial diseases management in cereal crops: A review on metal-based nanoparticles. *Notulae Botanicae Horti Agrobotanici Cluj-Napoca*, 51(3), 13333.
- Shah, C. P., Dwivedi, C., Singh, K. K., Kumar, M., & Bajaj, P. N. (2010). Riley oxidation: A forgotten name reaction for synthesis of selenium nanoparticles. *Materials Research Bulletin*, 45(9), 1213–1217.
- Shakibaie, M., Mohazab, N. S., & Mousavi, S. A. A. (2015). Antifungal activity of selenium nanoparticles synthesized by *Bacillus* species Msh-1 against *Aspergillus fumigatus* and *Candida albicans*. *Jundishapur Journal of Microbiology*, 8(9), e26381.
- Sharma, A., Agarwal, P., Sebgatollahi, Z., & Mahato, N. (2023). Functional nanostructured materials in the cosmetics industry: A review. *ChemEngineering*, 7(4), 66. <https://doi.org/10.3390/chemeng7040066>
- Sharma, V. P., Sharma, U., Chattopadhyay, M., & Shukla, V. N. (2018). Advance applications of nanomaterials: A review. *Materials Today: Proceedings*, 5(2), 6376–6380.
- Tso, C., Zhung, C., Shih, Y., Tseng, Y.-M., Wu, S., & Doong, R. (2010). Stability of metal oxide nanoparticles in aqueous solutions. *Water Science and Technology*, 61(1), 127–133.
- Turan, N., Kızılkaya, S., Buldurun, K., Çolak, N., Akdeniz, A., & Bursal, E. (2025). Synthesis, enzyme inhibitory and antioxidant activities, and molecular docking studies of metal complexes of

- a Schiff base ligand bearing pyridine moiety. *Journal of Molecular Structure*, 1338, 142167. <https://doi.org/https://doi.org/10.1016/j.molstruc.2025.142167>
- Varlamova, E. G., Goltyaev, M. V., Mal'tseva, V. N., Turovsky, E. A., Sarimov, R. M., Simakin, A. V., & Gudkov, S. V. (2021). Mechanisms of the cytotoxic effect of selenium nanoparticles in different human cancer cell lines. *International Journal of Molecular Sciences*, 22(15), 7798. <https://doi.org/https://doi.org/10.3390/ijms22157798>
- Wang, Q., Chen, N., Li, M., Yao, S., Sun, X., Feng, X., & Chen, Y. (2023). Light-related activities of metal-based nanoparticles and their implications on dermatological treatment. *Drug Delivery and Translational Research*, 13(2), 386–399. <https://doi.org/10.1007/s13346-022-01216-4>
- Yahr, T. L., & Parsek, M. R. (2006). *Pseudomonas aeruginosa*. In M. Dworkin, S. Falkow, E. Rosenberg, K.-H. Schleifer, & E. Stackebrandt (Eds.), *The Prokaryotes: A Handbook on the Biology of Bacteria Volume 6: Proteobacteria: Gamma Subclass* (pp. 704–713). Springer New York. [https://doi.org/10.1007/0-387-30746-X\\_22](https://doi.org/10.1007/0-387-30746-X_22)
- Ye, X., Chen, Z., Zhang, Y., Mu, J., Chen, L., Li, B., & Lin, X. (2020). Construction, characterization, and bioactive evaluation of nano-selenium stabilized by green tea nano-aggregates. *LWT*, 129, 109475.
- Zboromyrska, Y., & Vila, J. (2016). Advanced PCR-based molecular diagnosis of gastrointestinal infections: Challenges and opportunities. *Expert Review of Molecular Diagnostics*, 16(6), 631–640. <https://doi.org/10.1586/14737159.2016.1167599>
- Zhang, J., Wang, X., & Xu, T. (2008). Elemental selenium at nano size (Nano-Se) as a potential chemopreventive agent with reduced risk of selenium toxicity: comparison with selenomethylselenocysteine in mice. *Toxicological Sciences*, 101(1), 22–31. <https://doi.org/https://doi.org/10.1093/toxsci/kf m221>
- Zhang, J., Zhang, S. Y., Xu, J. J., & Chen, H. Y. (2004). A new method for the synthesis of selenium nanoparticles and the application to construction of H<sub>2</sub>O<sub>2</sub> biosensor. *Chinese Chemical Letters*, 15(11), 1345–1348.
- Zhang, W., Chen, Z., Liu, H., Zhang, L., Gao, P., & Li, D. (2011). Biosynthesis and structural characteristics of selenium nanoparticles by *Pseudomonas alcaliphila*. *Colloids and Surfaces B: Biointerfaces*, 88(1), 196–201.

## الملخص العربي

**عنوان البحث:** التصنيع والتوصيف والتطبيقات البيولوجية لجسيمات السيلينيوم النانومترية المصنعة بطريقة خضراء باستخدام بكتيريا اشريشيا كولاي المعزولة محلياً وذات المقاومة المتعددة للعقاقير

زكريا عوض محمد بقا<sup>١</sup>، ليلي عبد السميع الشخبي<sup>١</sup>، محمد مرزوق الزاهد<sup>١\*</sup>

<sup>١</sup> قسم النبات والميكروبيولوجي، كلية العلوم، جامعة دمياط، دمياط الجديدة، مصر

تُعد بكتيريا اشريشيا كولاي ذات المقاومة المتعددة للعقاقير سبباً رئيسياً لانتشار عدوى المستشفيات. تهدف الدراسة الحالية إلى عزل وتعريف بكتيريا اشريشيا كولاي ذات مقاومة متعددة للعقاقير المختلفة لاستخدامها في التصنيع الحيوي الخارجي لجسيمات السيلينيوم النانومترية، بالإضافة إلى دراسة أدوارها في التطبيقات ضد بكتيرية وكمضادات أكسدة. استُخدم جهاز فاينك ٢ لتأكيد تحديد مستوى الأنواع للعزلة البكتيرية المختارة بعد تحديدها بشكل كلاسيكي. استُخدمت تحليلات طيفية ومجهرية مختلفة لتوصيف الجسيمات النانومترية المصنعة حيويًا، مثل التحليل الطيفي للأشعة فوق البنفسجية والمرئية، وتحليل الأشعة تحت الحمراء، والمجهر الإلكتروني النافذ، وتحليل زيتا. لوحظت قمة امتصاص لجسيمات السيلينيوم النانومترية عند ٣٤٨ نانومتر، مما أكد التكوين الحيوي الناجح لجسيمات السيلينيوم النانومترية. يُشير طيف الأشعة تحت الحمراء إلى وجود بروتينات مرتبطة بجسيمات السيلينيوم النانومترية والتي تعمل كعوامل تغطية وتثبيت للجسيمات. ظهرت الجسيمات النانومترية بشكل كروي واضح، واحتوت شحنة سالبة وصلت إلى +٤٨،٢ ملي فولت، كما ظهرت بمتوسط حجم  $\approx 100$  نانومتر. أظهرت جسيمات السيلينيوم النانومترية نشاطاً مضاداً للبكتيريا قوياً ضد البكتيريا موجبة الجرام (باسيلس سيريس، وستافيلوكوكس أوريوس)، والبكتيريا سالبة الجرام (اشريشيا كولاي، وبروتوبس ميرابيلس) بطريقة تعتمد على الجرعة. كما تم تقييم القدرة المضادة للأكسدة لجسيمات السيلينيوم النانومترية مقارنةً بحمض الأسكوربيك، مما أشار إلى سلوكها المتميز كمضادات للأكسدة. تقترح هذه الدراسة أن جسيمات السيلينيوم النانومترية كبديل آمن وفعال ومجدٍ لعلاج بعض السلالات البكتيرية المسببة للأمراض، بالإضافة إلى كونها مضادات أكسدة جيدة، مما يشير إلى أن هذا التصنيع الأخضر لجسيمات السيلينيوم النانومترية يمكن أن يوفر تطبيقات طبية واعدة.

## Assessment of Serum Glial Cell Line-Derived Neurotrophic Factor as a Diagnostic Marker for Patients with Liver Cirrhosis

Mohamed M, Abdel-aziz<sup>1</sup>, Amina M. R. El-Sayed<sup>1</sup>, Lamiaa E. M. Deef<sup>2</sup>, Lotfy Z, Habbak<sup>2</sup> and Ihssin A. Faraj<sup>2</sup>

<sup>1</sup>Gastrointestinal Surgery Center, Faculty of Medicine, Mansoura University.

<sup>2</sup>Zoology, Department, Faculty of science, Damietta University, Damietta, Egypt.

Received: 01 June 2025 /Accepted: 23 July 2025

\*Corresponding author's E-mail: ihssin89@students.du.edu.eg

### Abstract

Background: Cirrhosis is often irreversible and progressive phase of chronic liver disease recognized by loss of liver function and fibrotic remodeling. The aim of this study is to evaluate the diagnostic utility of glial cell line-derived neurotrophic factor (GDNF) in distinguishing cirrhosis patients from healthy individuals. Methods: A total of 61 participants were enrolled, consisting of 42 cirrhotic patients and 19 healthy controls. Serum GDNF, standard liver enzymes, kidney function parameters, and complete blood count indices were assessed. Results: Significant alterations were observed in liver profile markers such as decreased albumin and elevated bilirubin, aspartate aminotransferase (AST), gamma glutamyl transferase (GGT), and international normalized ration (INR) in cirrhotic patients ( $P<0.001$ ). Hematological analysis revealed anemia, thrombocytopenia, and elevated red cell distribution width (RDW), along with increased neutrophil-to-lymphocyte ratio (NLR), indicative of systemic inflammation. GDNF levels were significantly elevated in cirrhosis cases, with a median of 2.3 ng/mL compared to 1.75 ng/mL in controls ( $P=0.001$ ). GDNF demonstrated moderate diagnostic ability with an area under the ROC curve (AUC) of 0.699, sensitivity of 69%, and specificity of 73.7%, suggesting its potential as a non-invasive biomarker. RDW and NLR exhibited the highest diagnostic performance, with AUCs of 0.863 and 0.829, respectively. Conclusion: This result supports the integration of GDNF and other novel biomarkers to improve the early detection and clinical assessment of cirrhotic patients.

**Keywords:** Cirrhosis, Glial cell line derived neurotrophic factor (GDNF), Liver Enzymes.

### Introduction

Liver cirrhosis is a chronic, progressive liver disease characterized by tissue-based development of renewing nodules bordered by

fibrous strips as a result of persistent dysfunction of liver, leading to portal hypertension and end-stage liver dysfunction. It represents the advanced stage of fibrosis, where excessive extracellular matrix (ECM) deposition disrupts hepatic architecture, impairing liver function and blood flow. The

pathogenesis involves activation of hepatic stellate cells (HSCs), which transform into myofibroblasts under inflammatory certain conditions, leading to collagen deposition and sinusoidal capillarization, a process where liver sinusoidal endothelial cells lose their fenestrations, further exacerbating fibrosis. Portal hypertension, a major consequence of cirrhosis, arises from elevated intrahepatic vascular resistance and splanchnic vasodilation, contributing to adverse outcomes including ascites, variceal hemorrhage, and hepatic encephalopathy (**Xie and Benmassoud, 2025**).

Cirrhosis remains a significant public health burden, with an estimated 112 million cases, reflecting a rising prevalence compared to previous decades. The leading etiologies vary by area. HBV and HCV are prevalent in Asia and Africa, while NAFLD are common in Western countries. Notably, advancements in antiviral therapies for HBV and HCV have reduced viral-related cirrhosis, but metabolic and alcohol-related cases are increasing, partly due to rising obesity and alcohol consumption rates (**Wong and Huang, 2018**).

From clinical side, cirrhosis progresses from a compensated phase (often asymptomatic) to decompensation, marked by life-threatening problems. Common presentations include jaundice, ascites, coagulopathy, and hepatic encephalopathy, with diagnostic tools including liver biopsy and elastography. Management focuses on treating the underlying cause (antivirals for HBV/HCV, alcohol cessation), preventing complications such as diuretics for ascites and in advanced cases, liver transplantation (**Sterling et al., 2025**). Emerging evidence suggests that early fibrosis and even cirrhosis may be reversible with effective treatment, highlighting the importance of timely intervention. Despite therapeutic advances, cirrhosis remains a leading reason for mortality, accounting for 1.48 million deaths globally in 2019. Ongoing research into innovative therapeutic approaches and enhanced diagnostic tools offers hope for improving the care of individuals affected by cirrhosis (**Younossi et al., 2024**).

## Patients and Methods:

### *Ethical Approval:*

The Research and Ethical Committees of Al-

Azhar Faculty of Medicine, Damietta, Egypt, approved this study IRB 00012367-2502-006.

### *Participants:*

This study enrolled 61 participants, including 41 patients with cirrhosis and 19 healthy controls. Cirrhosis diagnosis was based on clinical, biochemical, and imaging findings.

### *Biochemical Analysis:*

Serum samples were collected from all participants one day prior to any surgical intervention (where applicable). The following biochemical parameters were measured using standardized assays and methods at the Gastroenterology Surgery Center, Mansoura, Egypt: aspartate transaminase (AST), alanine transaminase (ALT), alkaline phosphatase (ALP), albumin, total bilirubin (Tbili), direct bilirubin (Dbili), gamma-glutamyl transferase (GGT), international normalized ratio (INR), red blood cell (RBC) indices, white blood cell (WBC) indices and platelet indices. Serum GDNF levels were also determined using a validated assay.

### *Statistical Analysis:*

SPSS statistics software version 26.0 (Statistical package for social science Inc., Chicago, IL, USA) was used to perform the statistical analysis. Continuous variables were expressed as mean  $\pm$  standard deviation for normally distributed data or median (interquartile range) for non-normally distributed data. Differences in continuous variables between the control and cirrhosis groups were assessed using an independent samples t-test for normally distributed data or a Mann-Whitney U test for non-normally distributed data. The diagnostic accuracy of GDNF and other relevant indices in distinguishing cirrhosis patients from healthy controls was assessed by calculating the area under the Receiver Operating Characteristic (ROC) curve (AUC), sensitivity, and specificity. Statistical significance was set at  $p < 0.05$ .

## Results:

### *Clinical features of cirrhosis and control*

group.

Median age of the control group was 26 years (IQR: 24–34), while the cirrhosis group had a significantly higher median age of 51 years (IQR: 34–60) with a p-value of 0.001. The gender distribution was similar between the groups. In the control cohort, 73.7% of the participant were male and 73.8% of the cirrhosis patients ( $P=0.978$ ). HBsAg positivity was observed in 7.1% of the cirrhosis group, while none of the controls were positive. HCVAb positivity was markedly higher in the cirrhosis group (61.9%) versus controls (0%), with a P-value of 0.001.

Regarding liver disease severity, Child-Pugh classification showed that 41% of the cirrhosis group were classified as Child C, while all control subjects were classified as Child A. APRI scores revealed that 50% of the cirrhosis group had a score of 3, compared to none in the control group ( $P=0.001$ ). FIB-4 scores were also significantly different ( $P=0.001$ ), with 60% of cirrhosis patients scoring 3, whereas all individuals in the control group had a score of 1. These findings summarize the distribution of key clinical parameters among the study groups (Table.1).

Table (1) Clinical characteristics of cirrhosis and control group.

Variable	Control Median (IQR)	Cirrhosis group N=42	P- value
Age (yr)	26 (24-34)	51 (34-60)	0.001
Gender			
Male n (%)	14 (73.7)	31 (73.8)	0.978
Female n (%)	5 (26.3)	11 (26.2)	
HBsAg n (%)			
+ve	0 (0)	3 (7.1)	0.603
-ve	19 (100)	38 (90.5)	
HCVAb n (%)			
+ve	0 (0)	3 (7.1)	0.001
-ve	19 (100)	26 (61.9)	
Child n (%)			
A	19 (100)	7 (17.9)	0.001
B	0 (0)	16 (41)	
C	0 (0)	16 (41)	
APRI n (%)			
1	18 (94.7)	7 (19.4)	0.001
2	1 (5.3)	11 (30.6)	
3	0 (0)	18 (50)	
FIB4 n (%)			
1	19 (100)	4 (11.4)	0.001
2	0 (0)	10 (28.6)	
3	0 (0)	21 (60)	

HBsAg - Hepatitis B surface antigen, HCVAb - Hepatitis C virus antibody, Child - Child-Pugh score, APRI - Aspartate Aminotransferase to Platelet Ratio Index, FIB4

- Fibrosis-4 Index.

*Serum level of glial cell line derived neurotrophic factor for cirrhosis and the control group.*

Median GDNF levels were significantly higher in the cirrhosis group (2.3 ng/ml,  $P=0.019$ ) compared to the control group (1.75 ng/ml).

Table (2) Serum level of glial cell line derived neurotrophic factor for cirrhosis and control group.

Variable	Control Group N= (19)	Cirrhosis group N= (42)	P value
GDNF (ng/ml)	1.75 (1.20 – 2.04)	2.3(1.6- 2.)	0.001

GDNF - Glial Cell Line-Derived Neurotrophic Factor.

*Serum levels of kidney profile for the studied groups.*

The median serum creatinine level was 0.80 mg/dL (IQR 0.70-0.90) in the control group and 0.70 mg/dL (IQR 0.60-0.90) in the cirrhosis group, with a P-value of 0.693. The mean serum potassium level was  $4.30 \pm 0.449$  mmol/L in the control group and  $4.04 \pm 0.60$  mmol/L in the cirrhosis group, yielding a P-value of 0.332. For uric acid, the mean serum level was  $5.02 \pm 1.93$  mg/dL in the control group and  $4.75 \pm 1.75$  mg/dL in the cirrhosis group, with a corresponding p-value of 0.509. These results indicate that there were no statistically significant differences in the serum levels of creatinine, potassium, and uric acid between the control and cirrhosis groups (Table.3).

Table (3) Serum levels of kidney profile for the studied groups.

Variables	control group N= (19)	Cirrhosis group N= (42)	P - Value
Cr(mg/dL)	0.80	0.70	0.693
Median (IQR)	(.70-.90)	(0.60-0.90)	
K(mmol/l)	$4.30 \pm .449$	$4.04 \pm .60$	0.332
Mean $\pm$ SD			
UA (mg/dL)	$5.02 \pm .93$	$4.75 \pm 1.75$	0.509
Mean $\pm$ SD			

Cr – Creatinine, K – Potassium, UA - Uric Acid

*Serum levels of different liver profile for the studied groups.*

The serum levels of different liver function parameters in the control group (N=19)

and the cirrhosis group (N=42). Levels of serum albumin were significantly lower in the cirrhosis group (median 3.3 g/dL, IQR 2.70–3.77) versus the control group (median 4.50 g/dL, IQR 4.40–4.80), with a p-value of <0.001. Total bilirubin and direct bilirubin levels were also significantly higher in cirrhosis patients, with medians of 1.6 mg/dL and 1 mg/dL, respectively, compared to 0.60 mg/dL and 0.15 mg/dL in controls (P<0.001 for both). Liver enzymes showed marked differences between the groups. ALP was higher in the cirrhosis group (median 65 U/L) than in controls (median 5 U/L), while AST was also increased in the cirrhosis group (median 41.5 U/L) compared to controls (median 21 U/L), with both showing statistical significance (P<0.001). ALT levels were higher in cirrhotic patients than in controls (P<0.001). GGT was notably elevated in cirrhosis patients (median 46 U/L) compared to the control group (median 17 U/L), and INR was higher in cirrhosis (median 1.4) than in controls (median 1.0), both with P-values <0.001 (Table.4).

Table (4) Serum levels of different liver profile for the studied groups.

Variables Median (IQR)	Control Group N= (19)	Cirrhosis group N= (42)	P - Value
Alb(g/dL)	4.50 (4.40 – 4.80)	3.3 (2.70-3.77)	<0.001
T.bili(mg/dL)	0.60 (.50- .70)	1.6(1-4.6)	<0.001
D.bili(mg/dL)	0.15 (0.10- 0.25)	1(.47-2.4)	<0.001
ALP(U/L)	5(5-5)	6(5-7)	<0.001
AST(U/L)	21 (20 – 21)	41.5 (26.7-72.2)	<0.001
ALT(U/L)	23 (21 – 27)	27.5 (21-44.5)	<0.001
GGT(U/L)	17 (12 – 27)	46(30-94)	<0.001
INR	1 (1 – 1.10)	1.4(1.2-1.6)	<0.001

Alb – Albumin, T.bili - Total Bilirubin, D.bili - Direct Bilirubin, ALP - Alkaline Phosphatase, AST - Aspartate Aminotransferase, ALT - Alanine Aminotransferase, GGT - Gamma-Glutamyl Transferase, INR - International Normalized Ratio.

#### Red blood cells and their indices for the studied groups.

Red blood cells and their indices for the control group (n=19) and the cirrhosis group (n=42). The table displays median values with interquartile ranges (IQR) for red blood cell count (RBCs), mean corpuscular volume

(MCV), mean corpuscular hemoglobin (MCH), mean corpuscular hemoglobin concentration (MCHC), and red cell distribution width (RDW). Additionally, mean values with standard deviations (SD) are provided for hemoglobin (HG) and hematocrit (HCT). An overall P-value is included for each variable to indicate the statistical significance of the difference between the two categories. The results demonstrate markedly significant differences (P<0.001) between the control and cirrhosis groups for RBCs ( $3.8 \times 10^6/\text{cell}/\mu\text{L}$ , IQR 3.1-4.2 vs.  $5.20 \times 10^6/\text{cell}/\mu\text{L}$ , IQR 4.60-5.40), HG ( $10.5 \pm 2.2$  g/dL vs.  $14.26 \pm 1.51$  g/dL), HCT ( $31.4 \pm 6.7$  % vs.  $41.79 \pm 5.38$  %), and RDW (15.1 %, IQR 13.1-16.9 versus 12.30 %, IQR 11.50-13.05). In contrast, no statistically significant differences were found in MCV (P=0.099), MCH (p=0.094), and MCHC (P=0.529) between the two groups (Table.5).

Table (5) Red blood cells and their indices for the studied groups.

Variable	Control group N= (19)	Cirrhosis group N= (42)	P - Value
RBCs $\times 10^6$ (Cell/ $\mu\text{L}$ ) Median (IQR)	5.20 (4.60 – 5.40)	3.8 (3.1-4.2)	<0.001
HG (g/dL) Mean $\pm$ SD	$14.26 \pm 1.51$	$10.5 \pm 2.2$	<0.001
HCT (%) Mean $\pm$ SD	$41.79 \pm 5.38$	$31.4 \pm 6.7$	<0.001
MCV (fL) Median (IQR)	82.46(80.16 – 86.20)	87 (80.4-90.9)	0.099
MCH (pg) Median (IQR)	28.50 (27.8 – 29.25)	29.2 (26.5-31.8)	0.094
MCHC(g/dL) Mean $\pm$ SD	$34.30 \pm 1.72$	$33.38 \pm 3.03$	0.529
RDW (%) Median (IQR)	12.30(11.50 – 13.05)	15.1 (13.1-16.9)	<0.001

RBCs - Blood Cell Count, HG – Hemoglobin, HCT – Hematocrit, MCV - Mean Corpuscular Volume, MCH - Mean Corpuscular Hemoglobin, MCHC - Mean Corpuscular Hemoglobin Concentration, RDW - Red Cell Distribution Width.

#### Platelets and their indices for the studied groups:

The cirrhosis group demonstrated significantly lower platelet count (P=0.002) and Pct (<0.001), along with a significantly higher platelet distribution width (P=0.040) and PLCR (P=0.011) versus the controls. No statistically significant differences were found in MPV (P=0.115) and PLR ratio (P=0.942) between the



two categories (Table.6).

Table (6) Platelets and their indices for the studied groups.

Variable	Control group N= (19)	Cirrhosis group N= (42)	P - Value
PLT×10 <sup>3</sup> (cell/μL) Median (IQR)	209(191.9 – 252.9)	89.3(55- 148.8)	0.002
PDW (fL) Median (IQR)	13(11.60 – 10.20)	17.9(12.6- 20.1)	0.170
MPV (fL) Median (IQR)	9.30(6.50 – 10.50)	10.5(7.4- 11.3)	0.115
Pct (%) Median (IQR)	0.194(126-.206)	0.08(.05-.16)	<0.001
PLCR (%) Mean±SD	27.1±6.7	35.8±8.03	0.011
PLR Median (IQR)	83.6(71.22 – 112.22)	91.4(57.7- 135)	0.942

PLT - Platelet Count, PDW - Platelet Distribution Width, MPV - Mean Platelet Volume, Pct - Plateletcrit (percentage of blood volume occupied by platelets), PLCR - Platelet Large Cell Ratio, PLR - Platelet-to-Lymphocyte Ratio.

#### White blood cells and their indices for the studied groups

White blood cells and their indices for the control group (n=19) and the cirrhosis group (n=42). The cirrhosis group showed a significantly lower WBC count (P=0.006) and absolute lymphocyte count (P<0.001), along with a significantly higher neutrophil percentage (P<0.001) and NLR (P<0.001) relative to the controls. The lymphocyte percentage was significantly lower in the cirrhosis group (P<0.001). No statistically significant difference was observed for the absolute neutrophil count shared by the two categories (P=0.699) (Table.7).

Table (7) White blood cells and their indices for the studied groups.

Variable	Control group N= (19)	Cirrhosis group N= (42)	P - Value
WBC×10 <sup>3</sup> (cell/μL) Median (IQR)	5.7 (4.2-6.9)	4(2.9-5)	0.006
Lymph No×10 <sup>3</sup> (cell/μL) Median (IQR)	2.50 (1.90- 3.05)	0.85(0.67- 1.5)	<0.001
Neut No×10 <sup>3</sup> (cell/μL) Median (IQR)	2.16(1.70 – 3.10)	2.10(1.5-3.2)	0.099
Lymph% Mean ± SD	43.7±7.5	27.16±12.4	<0.001
Neut % Mean ± SD	43.7±8.4	57.7±14.4	<0.001
NLR Median (IQR)	0.96(0.80- 1.22)	2.3(1.3-3.6)	<0.001

WBC - White Blood Cell Count, Lymph no -

Lymphocyte Number, Neut no - Neutrophil Number, Lymph % - Lymphocyte Percentage, Neut % - Neutrophil Percentage, NLR - Neutrophil-to-Lymphocyte Ratio.

#### Area under curve (AUC), sensitivity, and specificity of some variables for Diagnosis of patients with cirrhosis versus control group.

The diagnostic performance of several biomarkers for distinguishing patients with cirrhosis from the control group, among these, RDW (AUC: 0.863, P < 0.001) and NLR (AUC: 0.829, P < 0.001) demonstrated the highest accuracy, combining strong sensitivity (81% and 82%, respectively) and specificity (78% and 73%, respectively). PLCR also performed well (AUC: 0.809, P = 0.006), with the highest sensitivity (84%) but moderate specificity (63%). GDNF achieving an AUC of 0.699 and balanced sensitivity (69%) and specificity (73.7%). Plateletcrit (Pct) provided good sensitivity (82%) with specificity of (56%), and an AUC of 0.789 (P < 0.001) (Table.8) (Fig.1 .2.3.4 and 5).

Table (8) Area under curve (AUC), sensitivity, and specificity of some variables for Diagnosis of patients with cirrhosis versus control group.

Variable	AUC	Cutoff	Sen%	Spe%	95% CI	P value
GDNF (ng/ml)	0.699	2.2	69%	73.7%	0.558-0.841	0.013
NLR	0.829	1.1	82%	73%	0.724-0.933	<0.001
RDW (%)	0.863	13	81%	78%	0.768-0.958	<0.001
PLCR (%)	0.809	30	84%	63%	0.646-0.971	0.006
Pct (%)	0.789	0.18	82%	56%	0.670-0.909	<0.001

GDNF - Glial Cell Line-Derived Neurotrophic Factor, NLR - Neutrophil-to-Lymphocyte Ratio, RDW - Red Cell Distribution Width, PLCR - Platelet Large Cell Ratio, Pct - Plateletcrit (percentage of blood volume occupied by platelets).

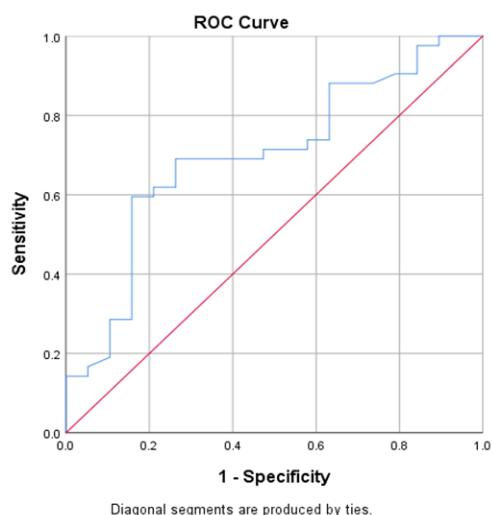


Figure (1): ROC curve of GDNF for Cirrhosis patients versus control group

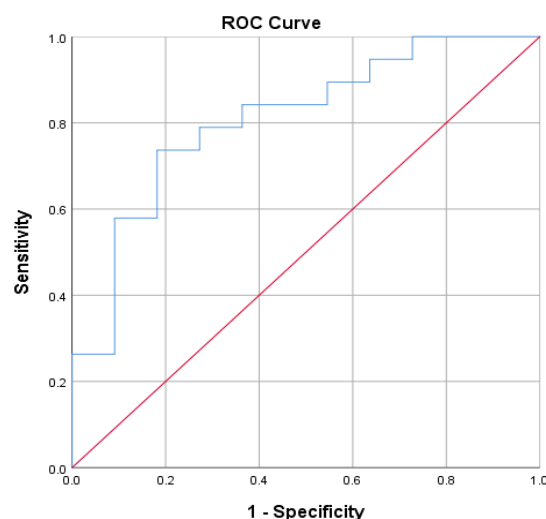


Figure (4): ROC curve of PLCR for Cirrhosis patients versus control group

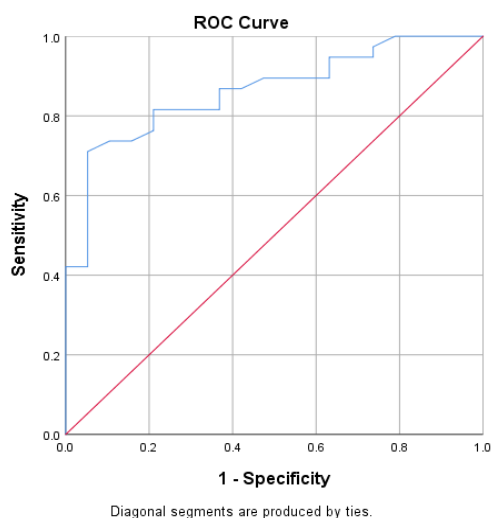


Figure (2): ROC curve of RDW for Cirrhosis patients versus control group

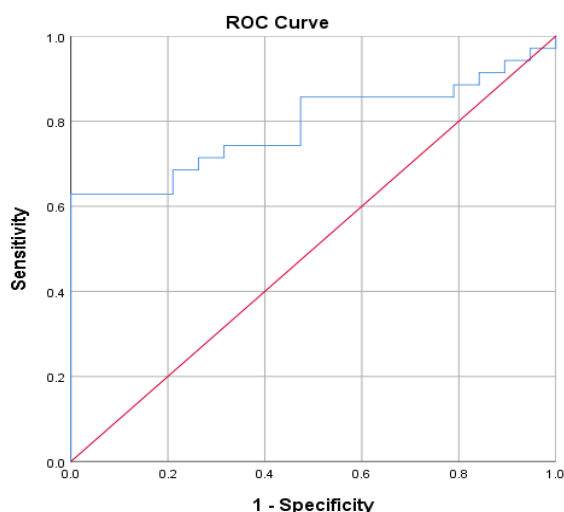


Figure (5): ROC curve of Pct for Cirrhosis patients versus control group

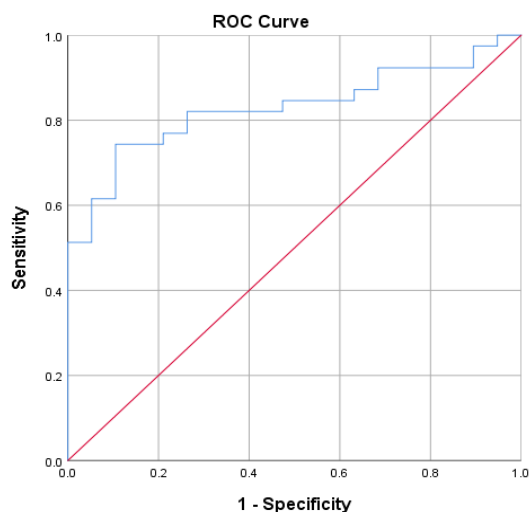


Figure (3): ROC curve of NLR for Cirrhosis patients versus control group

## Discussion:

Cirrhosis, the culmination of different liver injuries, originates from a process of necroinflammation followed by fibrogenesis. Histologically, it is defined by widespread nodular regeneration encased within thick fibrous bands, ultimately resulting in the loss of functional liver tissue and the breakdown of its structural framework (**Pampin et al., 2018**). This architectural disruption significantly impedes portal blood flow, leading to both portal hypertension and impaired hepatic synthetic function. Historically viewed as a terminal condition inevitably resulting in

mortality without liver transplantation. Cirrhosis is treatable but not curable. There are two targets when treating this illness, the first is to prevent the destruction of the liver while the second is to stop the complications (Zhou et al., 2014).

The significantly increased serum GDNF levels found in the cirrhosis group (2-3 ng/ml, IQR 1.6-2.0) versus the controls (1-7 ng/ml, 1-20-2-04) ( $P=0.001$ ) demonstrate a potential role of this marker in the context of liver cirrhosis. The chronic liver injury, fibrogenesis and inflammation may trigger an upregulation of GDNF production. Previous studies have suggested that GDNF can be expressed by several cell types within the liver, including hepatocytes and hepatic stellate cells (HSC) (Wang et al., 2018). Activated HSC have been shown to produce GDNF, and GDNF itself has been implicated in promoting HSC proliferation and activation, likely contributing to the progression of fibrosis (Wang et al., 2018). The observed elevation of circulating GDNF in cirrhosis patients might reflect a systemic response to the ongoing liver damage (Zhang et al., 2021).

One outcome from this study does not indicate major alterations in levels of potassium. Previous studies indicate that cirrhosis cases, particularly those on diuretics or with ascites, are prone to hypokalemia because of renal potassium wasting (Huang et al., 2021; Gurnani et al., 2021). In the context of uric acid, its levels were not significantly different in the studied groups. Previous studies suggested a possible correlation between elevated uric acid levels, increased oxidative stress and inflammation in cirrhosis cases, suggesting that uric acid is potentially implicated in the progression of liver disease. The uric acid levels are often elevated in metabolic disorders correlated with liver dysfunction, like cirrhosis and NAFLD (Sirota et al., 2013; Yang et al., 2022).

Results of serum liver profile indicated significant biochemical derangements in cirrhotic patients versus controls. The significantly decreased albumin levels in the cirrhotic patients ( $P<0.001$ ) align with the compromised synthetic function of the cirrhotic liver, a hallmark of the disease. Reduced albumin levels in patients with CLD may signal the onset of cirrhosis. A decline in plasma albumin is associated with cirrhosis, as these patients exhibit impaired albumin production

and compromised liver cell function. In advanced phases of cirrhosis, albumin levels can decrease by as much as 60–80% (Carvalho and Machado, 2018). Increased total and direct bilirubin ( $P<0.001$ ) are well-established characteristic of cirrhosis, hyperbilirubinemia works as an indicator of impaired liver function and often linked to the jaundice observed in cirrhotic patients (Lee et al., 2020).

Elevated ALP, AST, and GGT in the cirrhosis group ( $P<0.001$ ) are key indicators of cholestasis and hepatocellular injury. AST, a transaminase enzyme found in hepatocytes, is released into bloodstream upon liver cell damage its increased levels serve as a marker of hepatocellular damage (Lai et al., 2024). GGT is usually increased in different liver diseases, including cirrhosis, and can be sensitive to cholestasis and alcohol-related liver injury (Giannini et al., 2005). Levels of ALT ( $P < 0.001$ ) is often normal or mildly increased in advanced stages of cirrhosis, as the liver has limited functioning tissue left to release enzymes (Trapper and Lok, 2017).

Regarding RBC Indices, the cirrhosis patients demonstrated significantly Lower RBCs, HGB and HCT ( $P<0.001$ ), indicating the presence of anemia, a well-known outcome of chronic liver disease usually resulting from blood loss, hypersplenism and impaired erythropoietin Production (Xie et al., 2016). RDW was significantly higher in cirrhotic patients' group ( $<0.001$ ), reflecting increased Variation in red blood cells size.

This study demonstrated significant alteration in white blood cell and platelet indices. Patients with cirrhosis exhibited reduced total white blood cell and lymphocyte counts, accompanied by an elevated neutrophil percentage and NLR ratio, indicating systemic inflammation. Furthermore, NLR commonly identified as a useful biomarker for assessing prognosis in patients with cirrhosis (Peng et al., 2018; Wang et al., 2012). They also had significantly lower platelet counts and Pct, but higher PDW and PLCR, suggesting thrombocytopenia with altered platelet characteristics. These hematological alterations are consistent with the immune dysregulation and bone marrow suppression often associated with chronic liver disease (Peng et al., 2018).

The diagnostic evaluation of different biomarkers for distinguishing cirrhosis patients from control group reveals insightful differences in their performance metrics,

particularly sensitivity, specificity, and area under the curve (AUC). Among the studied parameters, GDNF achieved a moderate AUC of 0.699, with relatively balanced sensitivity (69%) and specificity (73.7%), indicating its potential as a supplementary marker. A study carried out by **Yang et al. (2022)** which employed both ELISA- based serum analysis and histological liver biopsy demonstrated the GDNF levels were significantly increased in liver fibrosis and cirrhotic patients, suggesting its role as non-invasive diagnostic biomarker. Furthermore, GDNF demonstrated good diagnostic value in identifying cirrhotic patients from healthy controls, with reported AUC of 0.84. This performance surpasses classical fibrosis indices such as APRI score, FIB-4 index, specifically in differentiating advanced fibrosis. The optimal cutoff for GDNF in predicting cirrhosis was 33.8 pg/mL, with significantly higher levels observed in cirrhotic patients compared to those without cirrhosis (33.8 versus 23.5 pg/mL,  $P < 0.001$ ). These results suggest that GDNF may serve as a non-invasive diagnostic marker for cirrhosis.

For diagnosis of cirrhotic patients versus controls, RDW exhibited the most promising diagnostic potential with an AUC of 0.863 ( $P < 0.001$ ), high sensitivity of 81%, and specificity of 78%, suggesting robust discriminative power. Similarly, NLR demonstrated comparable accuracy, with an AUC of 0.829 ( $P < 0.001$ ), sensitivity of 82%, and specificity of 73%, demonstrating its usefulness as a non-invasive inflammatory marker in liver pathology (**Zhao et al., 2019**). NLR exhibited comparable accuracy, with an AUC of 0.829 ( $P < 0.001$ ), sensitivity of 82%, and specificity of 73%, showing its value as a non-invasive inflammatory marker in liver pathology (**Zhao et al., 2019**). PLCR also showed favorable diagnostic ability, achieving high sensitivity (84%), although its specificity was moderate at 63%, with an AUC of 0.809 ( $P = 0.006$ ). Previous literature reported that PLCR level was significantly higher in cirrhotic patients and correlated with disease severity, proposing its possible role as non-invasive marker for liver fibrosis progression (**Zanetto, 2023**). Pct achieved an AUC of (0.789  $P < 0.001$ ), sensitivity of 82%, and specificity of 56%, suggesting moderate diagnostic utility (**Michalak et al., 2021**). Overall, these findings underscore the role of combining multiple biomarkers, particularly those introducing

hematological and inflammatory changes, to facilitate early diagnosis and monitoring of liver cirrhosis.

## References:

- Carvalho, J. R., & Machado, M. V. (2018). New insights about albumin and liver disease. *Annals of Hepatology*, 17(4), 547–560.
- Huang, J., Cai, M., & He, X. (2021, May 5). Serum potassium levels and prognosis in HBV-associated decompensated cirrhosis. *Journal of Clinical Laboratory Analysis*, 35(6).
- Lai, X., Chen, H., Dong, X., Zhou, G. (2024). AST to ALT ratio as a prospective risk predictor for liver cirrhosis in patients with chronic HBV infection. *European Journal of Gastroenterology & Hepatology*, 36(3), 305-313.
- Lee, H. A., Jung, J. Y., Lee, Y. S., Jung, Y. K., Kim, J. H., An, H., Jung, J. T., Byun, J. Y., Um, S. H., & Seo, Y. S. (2020). Direct Bilirubin Is More Valuable than Total Bilirubin for Predicting Prognosis in Patients with Liver Cirrhosis. *Gut and Liver*, 14(5), 599-605. <https://doi.org/10.5009/gnl20171>
- Peng, Y., Li, Y., He, Y., Chai, J., Zhang, Q., & Wang, Y. (2018). The role of neutrophil to lymphocyte ratio for the assessment of liver fibrosis and cirrhosis: A systematic review. *Expert Review of Gastroenterology & Hepatology*, 12(5), 503-513. <https://doi.org/10.1080/17474124.2018.1463158>
- Pimpin, L., Cortez-Pinto, H., Negro, F., Corbould, E., Lazarus, J. V., Webber, L., Sheron, N., & Committee, E.H.S (2018). Burden of liver disease in Europe: Epidemiology and analysis of risk factors to identify prevention policies. *Journal of Hepatology*, 69(3), 718-735. <https://doi.org/10.1016/j.jhep.2018.05.011>
- Sirota, J. C., Mcfann, K., Targher, G., Johnson, R. J., Chonchol, M., & Jalal, D. I. (2013). Elevated serum uric acid levels are associated with non-alcoholic fatty liver disease independently of metabolic syndrome features in the United States: Liver ultrasound data from the National Health and Nutrition Examination Survey. *Metabolism*, 62(3), 392–399.
- Sterling, R. K., Asrani, S. K., Levine, D., Duarte-Rojo, A., Patel, K., Fiel, M. I., Leung, D. H., Taouli, B., Alsawas, M., Murad, M. H., Dranoff, J. A., Taddei, T. H., & Rockey, D. C. (2025). AASLD practice guideline on noninvasive liver disease assessment of portal hypertension. *Hepatology*, 81(3), 1060–1085.
- Wang, J.-H., Chu, C.-J., Lin, Z.-Y., Lin, Y.-H., Chen, T.-M., & Kee, K.-M. (2012). Transient elastography and simple blood markers in the

- diagnosis of esophageal varices for compensated patients with hepatitis B virus-related cirrhosis. *Journal of Gastroenterology and Hepatology*, 27(7), 1113-1118.
- Wong, M. C. S., & Huang, J. (2018). The growing burden of liver cirrhosis: implications for preventive measures. *Hepatology International*, 12(2), 201-203. <https://doi.org/10.1007/s12072-018-9865-y>
- Xie, X., et al. (2016). [Correlation between red blood cell count and liver function status]. *Zhonghua Gan Zang Bing Za Zhi = Chinese Journal of Hepatology*, 24(2), 134-137.
- Xie, X.-Y., & Benmassaoud, A. (2025). Advances in the diagnosis and management of clinically significant portal hypertension in cirrhosis: A narrative review. *World Journal of Hepatology*, 17(6):104761.
- Yang, G., Zhuang, L., Sun, T., Yeo, Y. H., Tao, L., Zhang, W., Ma, W., Wu, L., Yang, Z., Yang, Y., Xue, D., Zhang, J., Feng, R., Matthias, P. E., Dooley, S., Seki, E., Liu, P., & Liu, C. (2022). Serum glial cell line-derived neurotrophic factor (GDNF) is a novel biomarker in predicting cirrhosis in patients with chronic hepatitis B. *Canadian Journal of Gastroenterology and Hepatology*, 2022, 9824009.
- Younossi, Z. M., Golabi, P., Price, J. K., Afendy, M., & Henry, L. (2024). The global epidemiology of NAFLD and NASH among patients with type 2 diabetes. *Clinical Gastroenterology and Hepatology*, 22(10), 1999–2010.
- Zanetto, A., Campello, E., Farinati, F., Shalaby, S., Turcato, G., Sciarrone, S., Rosi, S., Rodriguez-Castro, K. I., Galliazzo, S., Senzolo, M., Russo, F. P., Simioni, P., & Burra, P. (2023). Assessment of whole blood platelet aggregation in patients with cirrhosis: Challenges and opportunities. *Platelets*, 34(1), 2178823.
- Zhao, Y., Wu, W., Li, Y., Zhang, X., Wang, L., & Chen, H. (2022). Assessment of mean platelet volume and platelet distribution width in chronic liver disease. *Clinical Hemorheology and Microcirculation*, 81(3), 313–320. <https://doi.org/10.3233/CH-221443>
- Zhou, W. C., Zhang, Q. B., & Qiao, L. (2014). Pathogenesis of liver cirrhosis. *World Journal of Gastroenterology*, 20(23), 7312-7324. <https://doi.org/10.3748/wjg.v20.i23.7312>

## المخلص العربي

### عنوان البحث: تقييم العامل العصبي المغذي المشتق من الخلايا الدبقية في المصل كدلالة تشخيصية لمرضى تليف الكبد

محمد عبدالعزيز<sup>١</sup>، أمينة السيد<sup>١</sup>، لمياء ضيف<sup>٢</sup>، لطفي حبق<sup>٢</sup>، احسين فرج<sup>٢\*</sup>

<sup>١</sup>مركز جراحة الجهاز الهضمي، كلية الطب، جامعة المنصورة، المنصورة، مصر.

<sup>٢</sup>قسم علم الحيوان، كلية العلوم، جامعة دمياط، دمياط، مصر.

الخلفية: غالباً ما يكون تليف الكبد مرحلة غير قابلة للتراجع ومتقدمة من أمراض الكبد المزمن، تتميز بفقدان وظائف الكبد وإعادة التشكيل التليف. الهدف: تهدف هذه الدراسة إلى تقييم الفائدة التشخيصية للعامل العصبي المغذي المشتق من الخلايا الدبقية (GDNF) في التمييز بين مرضى التليف الكبدي والأفراد الأصحاء. الطرق: تم إشراك ما مجموعه ٦١ مشاركاً، منهم ٤٢ مريضاً بتليف الكبد و ١٩ شخصاً سليماً كضوابط. تم تقييم مستوى GDNF في المصل، وإنزيمات الكبد التقليدية، ومعايير وظائف الكلى، ومؤشرات تعداد الدم الكامل. النتائج: لوحظت تغيرات كبيرة في مؤشرات ملف الكبد مثل انخفاض الألبومين وارتفاع البيليروبين، وأنزيم أسبارتات أمينوترانسفيراز (AST)، وغاما جلوتاميل ترانسفيراز (GGT)، والنسبة المئوية الدولية (INR) لدى مرضى التليف الكبدي ( $P < 0.001$ ). كشف التحليل الدموي عن فقر الدم، ونقص الصفائح الدموية، وارتفاع عرض توزيع كريات الدم الحمراء (RDW)، بالإضافة إلى ارتفاع نسبة العدلات إلى اللبافويات (NLR)، مما يشير إلى التهاب جهاز. كانت مستويات GDNF مرتفعة بشكل ملحوظ في حالات التليف الكبدي، بمتوسط ٢,٣ نانوجرام/مل مقارنة بـ ١,٧٥ نانوجرام/مل في الضوابط ( $P < 0.001$ ). أظهر GDNF دقة تشخيصية متوسطة بمساحة تحت منحنى خصائص التشغيل المستقبلية (AUC) بلغت ٠,٦٩٩، وحساسية ٦٩%، وخصوصية ٧٣,٧%، مما يشير إلى قدرته كعلامة حيوية غير جراحية. أظهر مؤشرا RDW و NLR أعلى أداء تشخيصي، بقيم AUC بلغت ٠,٨٦٣ و ٠,٨٢٩ على التوالي. الاستنتاج: تدعم هذه النتيجة دمج GDNF والمؤشرات الحيوية الجديدة الأخرى لتحسين التشخيص المبكر والتقييم السريري لتليف الكبد.

## Prevalence Trends and Diagnostic Biomarkers in Chronic Liver Diseases

Mohamed M, Abdel-aziz<sup>1</sup>, Amina M. R. El-Sayed<sup>1</sup>, Lamiaa E. M. Deef<sup>2</sup>, Lotfy Z, Habbak<sup>2</sup> and Ihssin A. Faraj<sup>2</sup>

<sup>1</sup>Gastrointestinal Surgery Center, Faculty of Medicine, Mansoura University.

<sup>2</sup>Zoology, Department, Faculty of science, Damietta University, Damietta, Egypt.

Received: 11 June 2025 /Accepted: 25 July 2025

\*Corresponding author's E-mail: ihssin89@students.du.edu.eg

### Abstract

Chronic liver disease (CLD) significantly contributes to global morbidity and mortality, covering a spectrum of disorders with diverse etiologies. Hepatocellular damage in cirrhosis leads to hypoalbuminemia, increased bilirubin and extended prothrombin time. Accurate diagnosis, prognosis, and monitoring of chronic liver disease depend profoundly on the assessment of several biomarkers. This review provides a focused overview of key biochemical and hematological biomarkers utilized in the evaluation of major chronic liver disease types, covering viral hepatitis, non-alcoholic fatty liver disease (NAFLD). For each disease category, we discuss the clinical utility of traditional liver function tests (ALT, AST, bilirubin, albumin), markers of fibrosis (platelet count, APRI score, FIB-4 index), and other relevant hematological parameters. By synthesizing current evidence on the diagnostic and prognostic value of these biochemical and hematological indicators across different CLD etiologies, this review aims to provide a practical resource for clinicians and researchers in the field of hepatology.

**Keywords:** Chronic liver diseases (CLD), Biomarkers, Hepatitis B virus (HBV), Hepatitis C virus (HCV).

### Introduction

Chronic Liver Disease (CLD) presents a significant universal health challenge, a particularly high prevalence and impact in Egypt, where cirrhosis stands as a main reason of morbidity and mortality. Globally, CLD were the twelfth primary cause related to death in the United States in 2013, accounting for a substantial number of annual fatalities. While

compensated cirrhosis often presents asymptotically or with subtle signs in a considerable proportion of cases (30-40%), decompensated cirrhosis is typically characterized by severe clinical manifestations such as ascites, portal hypertension, variceal hemorrhage, and hepatic encephalopathy (Asrani et al.,2019).

CLD incorporates a comprehensive range of underlying etiologies, including viral infections, schistosomiasis, alcohol abuse, and



various genetic and metabolic disorders. These diverse insults ultimately converge on a common pathway leading to progressive hepatic dysfunction and cirrhosis (**Boon-Yasidhi & Karnsakul,2025**). The incidence of different reasons and the overall burden of cirrhosis and CLD exhibit geographical variations. Notably, the distribution of CLD etiologies within specific regions requires further investigation (**Younossi et al.,2017**).

Existing data regarding the prevalence, incidence, and natural history of CLD have largely been derived from retrospective studies (**Asrani et al.,2019**). Historically, CLD in Egypt has been strongly associated with schistosomiasis. Furthermore, a significant proportion of the Egyptian population (approximately 15%) is seropositive for Hepatitis C Virus (HCV), and a frequent association between schistosomiasis and HCV infection has been reported (**Abdelhamed and Elkassas,2024**). Given these factors and the potential for changing patterns of CLD etiology in Egypt, prospective studies are warranted to assess the etiological modes, clinical presentation, morbidity, and shifting patterns of CLD among Egyptian patients in this endemic area.

### Prevalence of Chronic liver disease:

Liver disorders are one of the main worldwide health problems, associated with two million deaths per year as a result of cases such as cirrhosis, viral hepatitis, and liver cancer, and accounting for approximately 4% of all global mortality—equivalent to one in every 25 deaths. Notably, one-third of these liver-related deaths occur in females. Liver cancer contributes to an estimated 600,000 to 900,000 deaths per year. Although currently ranked as the eleventh leading cause of death globally, the actual mortality of liver disease burden may be underestimated (**Asrani et al.,2019**).

Cirrhosis ranks among the top causes of death in several regions, it is the tenth leading cause in Africa, ninth in Europe and in both South East Asia. The global health impact of

cirrhosis is further emphasized by its substantial contribution to disability-adjusted life-years, where it ranks fifteenth overall. Among individuals aged 25 to 49, liver disease is the twelfth leading cause of disability -adjusted life-years, highlighting its disproportionate effect on younger demographics. Consequently, in Europe, the potential years of life lost due to cirrhosis are likely even higher (**WHO,2022**).

A comprehensive meta-analysis encompassing data from 38 countries estimated the global rate of NAFLD at 30.2%, with regional variations ranging from 16.1% in Australia to 34% in South America. The widespread presence of NAFLD is notably frequent in obese individuals, reaching 57.5%. Viral hepatitis, particularly hepatitis B and C, remains a significant contributor to CLD, with hepatitis B affecting approximately 254 million people globally (**WHO,2023**). In 2022, hepatitis B and C were responsible for 1.3 million deaths each, underscoring their impact on global mortality. Alcohol-related liver disease (ARLD) also contributes to the global CLD burden, with a worldwide prevalence of 4.8%. The increasing presence of metabolic risk factors, such as obesity, has led to a rise in metabolic-associated fatty liver disease (MAFLD), with global prevalence escalating from 25.3% between 1990–2006 to 38.0% between 2016–2019 (**Riazi et al.,2022**). These trends highlight the shifting etiology of CLD and emphasize the need for targeted public health response to handle the evolving risk factors associated with liver disease.

Economically, cirrhosis represents a considerable financial burden. In the United States alone, liver health services costs totaled \$32.5 billion in 2016, with the majority of expenditures linked to inpatient and emergency services. Over the past two decades, healthcare spending related to liver disease has grown at an annual rate of 4%, largely due to increased use of hospital-based care. The following sections will detail the burden associated with specific etiologies of liver disease, followed by an exploration of complications commonly arising across different liver conditions (**Ghamari et al.,2022**).

Table 1. Global epidemiological overview of hepatitis B and C.

	Viral hepatitis C 2019*	Viral hepatitis B 2019*	Viral hepatitis C 2015-2020**
Incidence	About 1.5 million (1.1-2.6 million) people newly infected with HBV	An estimated 1.5 million (1.3-1.8 million) people were newly infected with HCV	1.43 million
Prevalence	Around 296 million (228-423 million) people living with chronic HBV infection	58 million (46-76 million) people living with chronic HCV infection	56.8 million (UI 55.2-67.8)
Prevalence in the general population	3.8% (3-5%)	0.8% (0.6-1%)	0.7% (95% UI 0.7-0.9)
Prevalence in children	0.9% (0.7-1.6%) rate of HBV infection among children <5years		0.13% (UI 0.08-0.16)
Mortality (number)	820,000 (450,000-950,000) people dying from hepatitis B-related causes	290,000 (230,000-580,000) people dying from hepatitis C-related causes	257,816
Source, WHO - 2021	30.4 million (24.3-38 million) people with hepatitis B knew their hepatitis B status at the end of 2019	15.2 million (12.2-13 million) people with hepatitis C knew their hepatitis C status at the end of 2019	
Screening and diagnosis			
Treatment	6.6 million people (5.3-8.3 million) people diagnosed with hepatitis B received treatment in 2019	9.4 million (7.5-11.7 million) people diagnosed with hepatitis C received treatment from 2015 to 2019	10.1 million From 2015-2020

\*Data adjusted from WHO, 2021 (Global progress report on HIV, viral hepatitis, and sexually transmitted infections, 2021. Accountability for the global health sector strategies 2016-2021: actions for impact).

\*\*Adapted from Lancet Gastroenterol Hepatol 2022; 7: 396-415.

### Viral hepatitis

Viral hepatitis remains a major global health concern, with a significant mortality burden—contributes to roughly 1.34 million mortalities in 2015 alone. Several viruses, particularly hepatotropic types labeled A through E, are known to trigger liver inflammation. While many of these infections are acute, self-resolving hepatitis B (HBV), C (HCV), D (HDV), and E (HEV) have the potential to progress to chronic disease. Additionally, systemic infections caused by viruses such as Cytomegalovirus and Epstein-Barr virus can also lead to hepatic inflammation (Chen et al.,2019).

Hepatitis A and E are primarily spread via the fecal-oral route, frequently by oral intake of contaminated food or water (Blach et al.,2021). Conversely, hepatitis B, C, and D are transmitted through exposure to infected bodily fluids. Chronic hepatitis is characterized by a persistent inflammatory response in the liver, typically indicated by abnormal liver function tests and histological findings lasting at least six months. Chronic forms of hepatitis B, C, D, and E are diagnosed based on the detection of viral presence in the blood—or in stool for HEV—for more than six months following initial infection (Asrani et al.,2019).

### HBV

Approximately 30% of the global population has serological evidence of current or past hepatitis B virus (HBV) infection. The majority of transmissions occur through vertical (mother-to-child) or early years exposure, which remain the predominant routes of infection worldwide. Chronic HBV infection progresses through five distinct clinical phases, each with unique characteristics. The initial phase, previously termed the "immune-tolerant" stage, features high HBV-DNA levels exceeding  $10^6$  IU/mL, normal or mildly elevated alanine aminotransferase (ALT), and minimal hepatic inflammation. This is followed by an HBeAg-positive chronic hepatitis phase characterized by fluctuating viral loads, elevated ALT, and moderate to severe liver inflammation that may persist for extended periods (Zhai et al.,2021). The third phase represents an inactive carrier state with low HBV-DNA levels, normal ALT, and reduced inflammation of liver, though fibrosis severity depends on previous disease activity. Subsequently, some patients progress to HBeAg-negative chronic hepatitis, demonstrating variable viral replication, elevated ALT, and ongoing liver inflammation, with only about 1% achieving spontaneous clearance annually. The final phase involves

occult infection, where hepatitis B surface antigen becomes undetectable although there are core antibodies, often with very minimal or undetectable viral DNA and normal liver enzymes (Younossi et al., 2021). Clinical outcomes are significantly influenced by the timing of HBsAg clearance, with loss of surface antigen before cirrhosis development associated with favorable prognosis and reduced risk of complications. However, patients in any phase remain vulnerable to HBV reactivation under immunosuppressive conditions, necessitating careful monitoring in clinical practice. The typical pattern of HBV infection underscores the impact of early detection and appropriate management to prevent disease progression and improve long-term outcome (Cao et al., 2022).

### HCV

Hepatitis C virus (HCV) remains a critical international health burden, with nearly 1.75 million new infections reported in 2015. It is recognized as the most prevalent bloodborne infection in the United States and other Western nations. Approximately 90% of individuals infected with HCV develop chronic liver disease. Intravenous drug use constitutes the primary mode of transmission, responsible for around 80% of cases, while transfusion of blood products accounts for approximately 10.8%. Other, less frequent transmission pathways include organ transplantation, and non-sterile tattooing procedures (Younossi et al., 2019).

The World Health Organization reported that an estimated 71 million people were living with chronic HCV infection in 2015. However, this prevalence is not mirrored in diagnosis rates; in 2016, only 20% of infected individuals were diagnosed, and merely 13% of those diagnosed received treatment with direct-acting antivirals (Younossi et al., 2019).

A disproportionate burden of HCV infections—approximately 80%—is concentrated in just 31 of the 194 WHO member states, with the highest incidence rates reported in the Eastern Mediterranean and Eastern European regions. Despite a declining incidence of new infections, mortality associated with HCV continues to rise due to its progression to End-stage hepatic disorders, comprising fibrosis, cirrhosis, and hepatocellular carcinoma (HCC) (Cacoub et al., 2018).

### Non-alcoholic fatty liver disease (NAFLD)

NAFLD has a global prevalence of approximately 32.4%. The share of deaths attributable to NAFLD from all causes has risen from 0.1% to 0.17% (Devarbhavi et al., 2023). NAFLD is highly connected to metabolic comorbidities, and the increasing burden of these conditions has contributed to the rising prevalence of NAFLD, placing affected individuals at greater risk for progression to advanced liver disease. Lately, NAFLD has emerged as one of the leading causes of hepatocellular carcinoma (HCC) and has become a major indication for liver dysfunction in the United States (Younossi et al., 2019).

### Liver fibrosis

Hepatic fibrosis represents a dynamic and progressive pathological complications of chronic liver injury, recognized by the abnormal accumulation and remodeling of extracellular matrix (ECM) constituents, predominantly collagen. This fibrogenic response is a convergent pathway arising from diverse etiological insults, for example, viral hepatitis, chronic alcohol intake, non-alcoholic fatty liver disease (NAFLD), and autoimmune liver conditions. The main cellular mediator of this mechanism is the hepatic stellate cell (HSC), which undergoes activation into proliferative, contractile myofibroblast-like cells with a heightened capacity for ECM protein synthesis. Beyond HSCs, contributions to the fibrotic milieu originate from bone marrow-derived mesenchymal stem cells, portal fibroblasts, and the process of epithelial-to-mesenchymal transition (EMT) involving both hepatocytes and cholangiocytes. The perpetuation of hepatic insult and the attendant inflammatory signaling cascades sustain fibrogenesis, culminating in the potential development of cirrhosis, portal hypertension, hepatic insufficiency, and an elevated risk of hepatocellular carcinoma (Bataller & Brenner, 2005).

The clinical trajectory of liver fibrosis is critically dependent on its stage, with early fibrotic changes exhibiting potential for reversibility upon successful etiological treatment. However, unchecked progression to cirrhosis is accompanied by significant incidence and mortality, underscoring the

clinical imperative for timely diagnosis and therapeutic intervention. Histopathological assessment of liver biopsies, utilizing standardized scoring systems such as METAVIR and Ishak, remains a cornerstone in the staging of fibrosis and informing clinical management strategies. Complementary to invasive biopsy, non-invasive tools,

encompassing serum-based biomarkers (APRI, FIB-4) and advanced imaging techniques like transient elastography, are increasingly employed for the non-invasive fibrosis severity assessment (Castera et al., 2005). These advancements facilitate enhanced patient surveillance and risk stratification within both clinical and research paradigms.

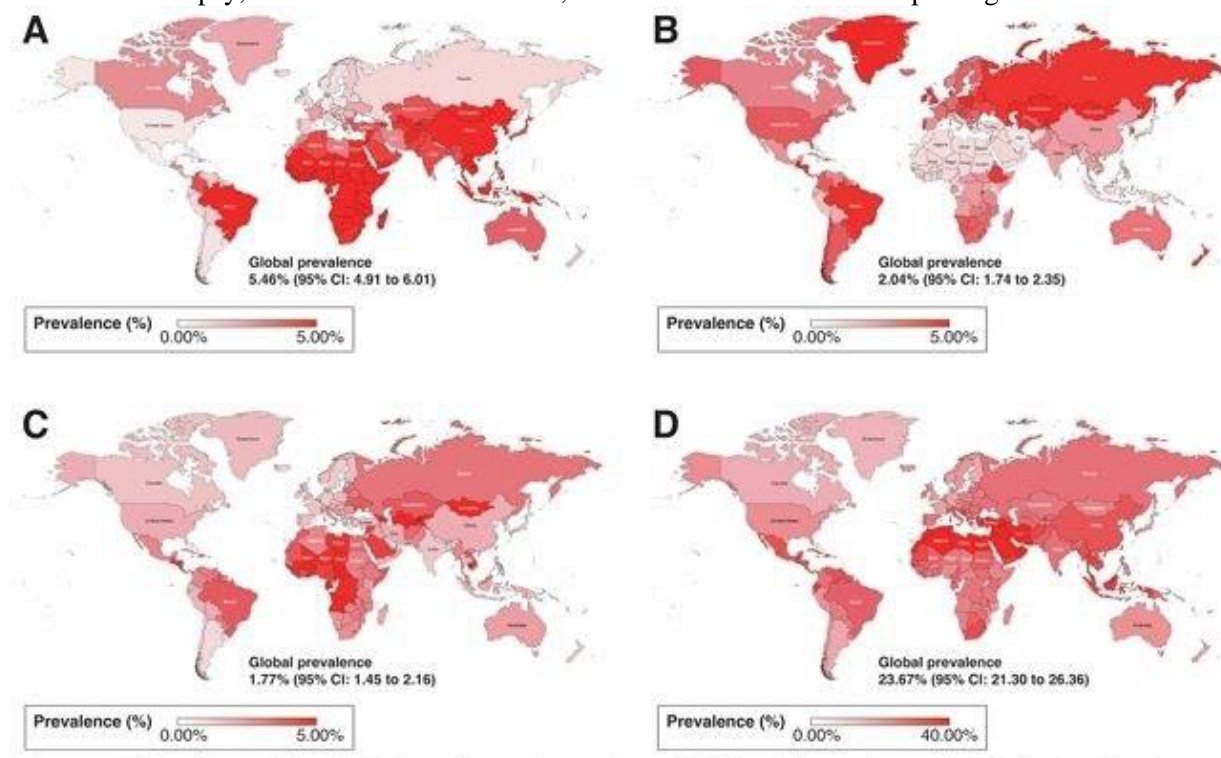


Figure 1. (A) Rate of hepatitis B virus, (B) Rate of hepatitis C virus, (C) Rate of alcohol-related liver disease, and (D) Rate of nonalcoholic fatty liver disease (in individuals age >20 years).

Several established clinical indices serve as adjuncts in the evaluation of hepatic physiology and the estimation of fibrosis burden. Child-Pugh score, a widely adopted clinical classification system, provides a prognostic assessment in chronic liver disease, specifically cirrhosis, by integrating five clinical and biochemical elements, serum bilirubin, serum albumin, prothrombin time, the occurrence and severity of ascites, and the presence and grade of hepatic encephalopathy, thereby categorizing patients from Class A (well-compensated) to Class C (decompensated) (Pugh et al., 1973). Furthermore, the APRI and FIB-4 indices represent readily applicable non-invasive models derived from routine hematological and biochemical analyses. APRI, estimated from aspartate aminotransferase (AST) levels and platelet count, with values exceeding 1.5 suggestive of significant fibrosis (Wai et al., 2003). FIB-4, which incorporates age, AST,

alanine aminotransferase (ALT), and platelet count, provides a stratified risk assessment for advanced fibrosis, with values above 3.25 indicating a higher probability and values below 1.45 generally excluding it (Sterling et al., 2006). These non-invasive tools contribute significantly to reducing reliance on invasive procedures and facilitating earlier detection and management of liver fibrosis.

Contemporary therapeutic methods are directed towards addressing the underlying etiological factors, mitigating hepatic inflammation, and inhibiting key signaling pathways involved in fibrogenesis. The growth of antifibrotic agents targeting pivotal molecules including transforming growth factor-beta (TGF- $\beta$ ) and platelet-derived growth factor (PDGF) continuous an active area of research, although no agents have yet received regulatory approval for liver fibrosis. Lifestyle modifications, targeted antiviral therapies for viral hepatitis, and meticulous

metabolic control in the context of NAFLD constitute essential components of current management. Experimental animal models, including chemically induced fibrosis using carbon tetrachloride (CCl<sub>4</sub>) and mechanical injury models like bile duct ligation (BDL) in rodent systems, continue to be indispensable for elucidating the intricate mechanisms of fibrogenesis and evaluating the efficacy of novel therapeutic interventions (**Kisseleva & Brenner, 2021**).

### *Liver Cirrhosis*

Liver diseases, primarily resulting from adverse outcomes including, cirrhosis, hepatocellular carcinoma (HCC), and viral hepatitis, account for approximately two million deaths annually. While cirrhosis remains the principal cause of liver-related mortality worldwide, liver cancer represents the principal contributor of death within this category. Globally, the predominant reasons of cirrhosis consist of hepatitis, alcohol abuse, and non-alcoholic fatty liver disorders (NAFLD). An estimated two billion individuals consume alcohol, many of whom are affected by alcohol-use disorders and are therefore at elevated risk for alcohol-related liver disease. Additionally, around two billion adults are classified as overweight or obese, and approximately 400 million have diabetes—both conditions that significantly promote the development of NAFLD and HCC. Acute liver diseases are commonly triggered by hepatitis, although a substantial proportion also result from drug-induced liver injury. This global overview reflects updated insights from the 2019 revised framework and emphasizes key areas of advancement in the understanding of liver disease, especially in terms of HCC, hepatitis, alcohol liver disease, and NAFLD (**Asrani et al., 2019; Devarbhavi et al., 2023**).

### *Hepatocellular Carcinoma (HCC)*

Liver tumor represents the fourth chief cause of tumor-related mortality globally and ranks second among men. The widespread occurrence of chronic HBV infection in places like Sub-Saharan Africa and Eastern Asia contributes to over 80% of hepatocellular carcinoma (HCC) cases worldwide. In recent decades, the epidemiological and etiological landscape of HCC has undergone significant

changes. Although HBV was responsible for more than 50% of HCC cases globally in 1990, this figure declined to 42% by 2019. In contrast, the occurrence of hepatitis C virus (HCV)-associated HCC has markedly decreased in regions like Japan and Europe, primarily stemming from the widespread adoption of direct-acting antiviral therapies. The share of HCC cases attributed to nonalcoholic steatohepatitis (NASH) and alcoholic steatohepatitis has escalated, with NASH rising from 5% to 6% and alcoholic steatohepatitis from 13% to 18% (**Kim, 2024**). Chronic HBV and HCV infections are major contributors to cirrhosis, which is frequently observed in HCC patients and forms a significant casual factor in HCC irrespective of its underlying etiology (**El-Serag, 2012**). In 2018, Egypt ranked as the country with the second-highest liver cancer risk globally, following Mongolia, where the incidence among men was approximately four times higher than that observed in China and South Korea. The age distribution of hepatocellular carcinoma cases worldwide is influenced by the dominant type of viral hepatitis and the age at which the infection is acquired. In regions with high HCC incidence, hepatitis B virus HBV, typically transmitted perinatally, is the top reason. Consequently, HCC tends to be diagnosed at a younger age in these areas compared to regions where hepatitis HCV often contracted later in life—is more prevalent (**Mittal and El-Serag, 2013**).

In Egypt, recent studies have shown a shift in the etiology of liver cancer, with HCV now contributing to approximately 40–50% of HCC cases. In contrast, the impact of HBV and combined HBV/HCV infections has declined, accounting for about 25% and 15% of cases, respectively (**El-Zayadi et al., 2005**). HCC is currently the most frequently diagnosed cancer among Egyptian men, the second most prevalent in women, and the leading cancer overall when considering both sexes combined (**Ferlay et al., 2018**). HCC share rose to 19.7% of all cancer cases in 2018, with 25,399 new cases reported. These figures were based on data from the Aswan, Damietta, and Minia cancer registries. Furthermore, HCC represents the primary cause of cancer-related mortality in Egypt, constituting 32.35% of all cancer deaths, as reported by the World Health Organization (WHO) (**Ferlay 2019**).

### *Aspartate aminotransferase (AST)*

Aspartate aminotransferase (AST) is an enzyme chiefly existing in the liver and heart, with lower concentrations found in the kidneys and muscles. It is released into the bloodstream following liver injury. The normal serum AST range is typically between 0 and 35 IU/L. Elevated levels of mitochondrial AST are observed in conditions such as myocardial infarction involving extensive tissue necrosis, as well as in chronic liver diseases marked by hepatic degeneration and necrosis. The diagnostic significance of the ratio of mitochondrial AST to total AST lies in its ability to distinguish between liver cell necrosis and alcoholic hepatitis. AST is commonly assessed in conjunction with alanine aminotransferase (ALT), another liver enzyme, as both tend to increase in response to hepatic damage. The AST/ALT ratio is a valuable tool for differentiating the basic origin of liver injury (**Anderson et al.,2000**).

### *Alanine aminotransferase ALT*

ALT is an enzyme primarily located in the liver, with lower concentrations present in the kidneys. It is fundamental to protein metabolism and energy production by aiding in the breakdown of food. The normal range for serum ALT levels fall between 7 and 56 IU/L. Hepatic cells injury leads to an increase in ALT levels in the bloodstream. ALT levels up to 300 IU/L are typically classified as indetermined, while elevations exceeding 500 IU/L are commonly associated with conditions that directly impact hepatocytes, such as viral hepatitis, ischemic liver failure, or toxic liver damage. Elevated aminotransferase levels are indicative of hepatitis infections. In hepatitis C, ALT elevation results from liver cell death due to both apoptosis and necrosis. Persistent ALT elevation lasting over six months in cases of acute hepatitis is a diagnostic marker for chronic hepatitis (**Anderson et al.,2000**).

### *Markers of liver synthetic function*

Albumin, a major serum protein constituting approximately 50%–60% of total plasma protein, is synthesized exclusively by the liver, making it a key indicator of hepatic synthetic capacity. While albumin levels are a useful reflection of liver function, they may also

be affected by extraneous factors such as systemic inflammation—given its nature as a negative acute-phase reactant—as well as inadequate protein intake, nephrotic syndrome, fluid retention, or protein-losing enteropathies. Albumin serves several functional roles, including the maintenance of plasma oncotic pressure and the transport of both endogenous substances (bilirubin) and external compounds (pharmaceutical agents). The normal serum albumin concentration typically ranges between 3.5 and 5 g/dL (**Tufoni et al.,2020**).

Prothrombin time (PT) and international normalized ratio (INR) perform as functional assessments of the extrinsic pathway of the coagulation cascade, for which the liver is responsible through the synthesis of several coagulation factors, as well as natural anticoagulants like protein C, protein S, and antithrombin. PT and INR are generally higher than activated partial thromboplastin time (aPTT) in liver disease due to compensatory production of factor VIII and von Willebrand factor in extrahepatic tissues, which can mask aPTT prolongation in vitro. However, due to concurrent deficiencies in both pro-coagulant and anticoagulant pathways, PT/INR and aPTT are not robust indicator of hemorrhage risk in individuals with cirrhosis. Furthermore, these parameters assess only pro-coagulant activity and do not account for disruptions in anticoagulant systems. In patients with CLD or cirrhosis, thrombocytopenia is frequently observed as a result of splenic sequestration and minimized synthesis of thrombopoietin, compounding the risk of hemorrhagic complications (**Harrison,2018**).

Although bilirubin is not a direct marker of hepatic synthetic function, its metabolism is closely associated with the liver's capacity for conjugation and excretion. Bilirubin is a terminal product of heme catabolism and circulates in the bloodstream bound to albumin. Hepatic processing involves conjugation and subsequent biliary excretion. Elevated serum levels of bilirubin are categorized as conjugated or unconjugated hyperbilirubinemia. Direct hyperbilirubinemia typically results from impaired hepatic excretion, such as in cholestatic conditions or inherited syndromes like Dubin-Johnson and Rotor. Conversely, indirect hyperbilirubinemia may arise from hepatocellular injury or increased hemolysis (**Ramirez-Mejia et al.,2024**).



### *Red blood cells indices*

Chronic liver disease (CLD) often leads to alterations in red blood cell (RBC) indices due to multifactorial mechanisms, including nutritional deficiencies, hypersplenism, and chronic inflammation. Common findings include decreased hemoglobin (HGB) levels, mean corpuscular volume (MCV), and mean corpuscular hemoglobin (MCH), reflecting microcytic or normocytic anemia, often associated with iron deficiency or anemia of chronic disease (ACD) (**Gonz-Casas et al., 2009**). Additionally, macrocytic anemia may occur because of folate or vitamin B12 deficiency, frequently observed in alcoholic liver disease (ALD) or advanced cirrhosis (**O'Leary & Friedman, 2017**). Hypersplenism, a consequence of portal hypertension (**Lata, 2012**).

The RBC distribution width (RDW) is often elevated in CLD, indicating increased variability in RBC size (anisocytosis), which correlates with disease severity and prognosis (**Li et al., 2015**). Furthermore, impaired hepatic synthesis of erythropoietin and hepcidin dysregulation contribute to anemia pathogenesis (**Girelli et al., 2016**). These hematological changes are critical markers for monitoring CLD progression and guiding therapeutic interventions, such as nutritional supplementation or splenectomy in select cases (**Verma et al., 2018**).

### *White blood cells indices*

Chronic liver disease (CLD) is frequently linked to alterations in white blood cell (WBC) parameters, driven by systemic inflammation, portal hypertension, and compromised immune function. Leukopenia, particularly neutropenia, is commonly observed in advanced stages of cirrhosis, largely attributed to hypersplenism-induced sequestration and destruction of leukocytes (**Giannini et al., 2003**). Moreover, diminished bone marrow activity and reduced synthesis of granulocyte colony-stimulating factor (G-CSF) further contribute to neutrophil depletion (**López-Karpovitch et al., 2016**). In contrast, leukocytosis may occur in response to acute bacterial infections or hepatic inflammation, with an elevated NLR serving like prognostic indicator for severity of disease and complications such as spontaneous bacterial

peritonitis (SBP) (**Kalra et al., 2018**).

Lymphopenia is also prevalent in CLD, often resulting from chronic immune dysfunction and malnutrition, thereby increasing vulnerability to infections (**Albillos et al., 2014**). In addition, monocyte dysfunction characterized by aberrant cytokine production contributes to the persistence of systemic inflammation (**Zimmermann et al., 2011**). Elevated NLR and PLR have been linked to adverse prognoses in hepatocellular carcinoma cases (HCC) and decompensated cirrhosis, underscoring their utility in risk stratification (**Chen et al., 2015**). Therefore, continuous monitoring of WBC indices is crucial for the early identification of infectious complications and the implementation of immunomodulatory interventions in CLD management.

### *Platelet indices:*

Platelet indices (PIs) are routinely obtained parameters included in automated complete blood count analyses. They serve as potential indicators of platelet morphology, activation status, and production dynamics. With advancements in hematology analyzers, the measurement of PIs has become efficient and standardized. In recent years, PIs have gained attention as emerging biomarkers with diagnostic and prognostic value across a range of acute and chronic diseases. Numerous studies have investigated their clinical relevance in conditions such as sepsis, thrombocytopenia, liver diseases, cardiovascular disorders, surgical trauma, and malignancies. Due to their noninvasive nature, low cost, and easy availability, PIs have become appealing for research on platelet biology over the past decade. Among these parameters, mean platelet volume (MPV) has been the most extensively studied. MPV reflects the average size of circulating platelets, typically ranging from 7.2 to 11.7 femtoliters (fL). Several factors, including ethnicity, age, physical activity, smoking, and alcohol consumption, can influence MPV values. Elevated MPV levels have been associated with poorer outcomes in cases such as pancreatic cancer and myocardial infarction. While reduced MPV has been linked to effective inflammation control in rheumatoid arthritis (**Gouda AM et al., 2024**).

Platelet distribution width (PDW) indicates platelet size variability. It increases upon platelet activation, reflecting platelet

anisocytosis. Plateletcrit (PCT), on the other hand, measures the volume percentage of platelets in the bloodstream, with normal values ranging from 0.22% to 0.24%. The platelet large cell ratio (P-LCR) represents the proportion of large platelets in circulation and normally falls within the 15–35% range. Studies have demonstrated a positive association among P-LCR, PDW, and MPV, and an inverse relationship between P-LCR and platelet count in thrombocytopenic patients. Furthermore, P-LCR has shown greater sensitivity to platelet size variation compared to MPV (Oral et al., 2019).

#### *Glial cell line-derived neurotrophic factor (GDNF)*

GDNF is a glycosylated homodimer stabilized by disulfide bonds and is considered a divergent member of the transforming growth factor-beta (TGF- $\beta$ ) protein family group. Clinical research has demonstrated elevated GDNF levels in both the parietal cortex and plasma of individuals with relapsing major depressive disorder. Furthermore, GDNF expression significantly increases following exposure to various cell-toxic agents (Lin et al., 1993). Elevated GDNF levels have also been observed in certain types of cancer cells. GDNF is increasingly recognized as a promising biomarker in the context of CLD. Evidence indicates that GDNF contributes to liver fibrogenesis by facilitating the hepatic stellate cells activation, a central mechanism in the development of fibrosis. Elevated GDNF expression has been reported in both liver tissue and serum of patients with advanced liver conditions, suggesting its practical use as a noninvasive marker of disease severity. Additionally, GDNF may participate in hepatocarcinogenesis by enhancing cellular survival and proliferation. These findings highlight GDNF's possible dual role as both a detective biomarker and a therapeutic target in CLD (Hu et al., 2021). Serum GDNF levels are significantly elevated versus healthy controls and those with chronic hepatitis B (CHB) without cirrhosis. Yang et al. (2022) have demonstrated that serum GDNF levels are higher in CHB patients with fibrosis (28.4 pg/ml vs. 11.6 pg/ml in non-fibrotic patients) and even more elevated in those with cirrhosis (33.8 pg/ml vs. 23.5 pg/ml in non-cirrhotic patients).

#### References:

- Albillos, A., Lario, M., & Álvarez-Mon, M. (2014). Cirrhosis-associated immune dysfunction: Distinctive features and clinical relevance. *Journal of Hepatology*, 61(6), 1385–1396. <https://doi.org/10.1016/j.jhep.2014.08.010>
- Anderson, F. H., Zeng, L., Rock, N. R., & Yoshida, E. M. (2000). An assessment of the clinical utility of serum ALT and AST in chronic hepatitis C. *Hepatology Research*, 18(1), 63–71.
- Asrani, S. K., Devarbhavi, H., Eaton, J., & Kamath, P. S. (2019). Burden of liver diseases in the world. *Journal of Hepatology*, 70(1), 151–171. <https://doi.org/10.1016/j.jhep.2018.09.014>
- Bataller, R., & Brenner, D. A. (2005). Liver fibrosis. *The Journal of Clinical Investigation*, 115(2), 209–218. <https://doi.org/10.1172/JCI24282>
- Boon-yasidhi, P., & Karnsakul, W. (2025). Non-invasive biomarkers and breath tests for diagnosis and monitoring of chronic liver diseases. *Diagnostics*, 15(1), Article 68. <https://doi.org/10.3390/diagnostics15010068>
- Cacoub, P., Bouri re, M., Asselah, T., et al. (2018). French patients with hepatitis C treated with direct-acting antiviral combinations: the effect on patient-reported outcomes. *Value in Health*, 21(10), 1218–1225.
- Cao, G., Jing, W., Lu, J., & Liu, Y. (2022). Countdown on global hepatitis B elimination by 2030: the global burden of liver disease related to hepatitis B and association with socioeconomic status. *Hepatology International*, 16(6), 1182–1296.
- Castera, L., Forns, X., & Alberti, A. (2005). Non-invasive evaluation of liver fibrosis using transient elastography. *Journal of Hepatology*, 43(3), 545–553. <https://doi.org/10.1016/j.jhep.2005.07.001>
- Chen, L., Zhang, Q., Chang, W., Du, Y., Zhang, H., & Cao, G. (2015). Viral and host inflammation-

- related factors that can predict the prognosis of hepatocellular carcinoma. *European Journal of Cancer*, 51(10), 1207–1221. <https://doi.org/10.1016/j.ejca.2015.02.019>
- Devarbhavi, H., Asrani, S. K., Arab, J. P., Nartey, Y. A., Pose, E., & Kamath, P. S. (2023). Global burden of liver disease: 2023 update. *Hepatology*, 79(2), 519–573. <https://doi.org/10.1002/hep.32303>
- El-Serag, H. B. (2012). Epidemiology of viral hepatitis and hepatocellular carcinoma. *Gastroenterology*, 142(6), 1264–1273. <https://doi.org/10.1053/j.gastro.2011.12.061>
- El-Zayadi, A. R., Badran, H. M., Barakat, E. M., Attia, M., Shawky, S., Omran, D., ... & Mohamed, M. K. (2005). Hepatocellular carcinoma in Egypt: A single center study over a decade. *World Journal of Gastroenterology*, 11(33), 5193–5198
- Ferlay, J., Ervik, M., Lam, F., Colombet, M., Mery, L., Pineros, M., ... & Bray, F. (2018). Global Cancer Observatory: Cancer Today. Lyon, France: International Agency for Research on Cancer. Retrieved May 31, 2019, from <https://gco.iarc.fr/today>
- Ferlay, J., Colombet, M., Soerjomataram, I., Mathers, C., Parkin, D. M., Piñeros, M., ... & Bray, F. (2019). Estimating the global cancer incidence and mortality in 2018: GLOBOCAN sources and methods. *International Journal of Cancer*, 144(8), 1941–1953. <https://doi.org/10.1002/ijc.31937>
- Giannini, E. G., Testa, R., & Savarino, V. (2003). Liver enzyme alteration: A guide for clinicians. *Canadian Medical Association Journal*, 168(3), 367–379. <https://www.ncbi.nlm.nih.gov/pmc/articles/PMC140456/>
- Girelli, D., Nemeth, E., & Swinkels, D. W. (2016). Hepcidin in the diagnosis of iron disorders. *Blood*, 127(23), 2809–2813. <https://doi.org/10.1182/blood-2015-12-639112>
- Gonz-Casas, R., Jones, E. A., & Moreno-Otero, R. (2009). Spectrum of anemia associated with chronic liver disease. *World Journal of Gastroenterology*, 15(37), 4653–4658. <https://doi.org/10.3748/wjg.15.4653>
- Gouda, A. M., Abdelaziz, M., Mousa, M. A., Saad, H. M., & Helaly, N. A. (2024). Evaluation of platelet indices in Egyptian cirrhotic patients. *AJGH*, 7(3), 163.
- Harrison, M. F. (2018). The misunderstood coagulopathy of liver disease: A review for the acute setting. *Western Journal of Emergency Medicine*, 19(5), 863–871. <https://doi.org/10.5811/westjem.2018.9.39160>
- Kalra, A., Wedd, J. P., & Bambha, K. M. (2018). Neutrophil-to-lymphocyte ratio correlates with prognosis in liver cirrhosis. *World Journal of Gastroenterology*, 24(45), 5128–5137. <https://doi.org/10.3748/wjg.v24.i45.5128>
- Kim, D. Y. (2024). Changing etiology and epidemiology of hepatocellular carcinoma: Asia and worldwide. *Journal of Liver Cancer*, 24(1), 62–70.
- Kisseleva, T., & Brenner, D. A. (2021). Mechanisms of fibrogenesis. *Experimental Biology and Medicine*, 246(13), 1429–1437. <https://doi.org/10.1177/15353702211018111>
- Lata, J. (2012). Hypersplenism in liver cirrhosis. *Hepatology International*, 6(1), 165–172. <https://doi.org/10.1007/s12072-011-9301-z>
- Li, J., Chen, Q., Luo, X., Hong, J., Pan, K., Lin, X., & Liu, X. (2015). Neutrophil-to-lymphocyte ratio positively correlates to age in healthy population. *Journal of Clinical Laboratory Analysis*, 29(6), 437–443. <https://doi.org/10.1002/jcla.21791>
- López-Karpovitch, X., Cárdenas, M. R., & Piedras, J. (2016). Hematologic manifestations of chronic liver disease. *Hematology*, 21(5), 295–303. <https://doi.org/10.1080/10245332.2015.1125081>
- Mittal, S., & El-Serag, H. B. (2013). Epidemiology of HCC: Consider the Population. *Journal of Clinical Gastroenterology*, 47(S2), S2–S6.
- O’Leary, J. G., & Friedman, L. S. (2017). Hematologic abnormalities in advanced liver disease. *Clinics in Liver Disease*, 21(3), 565–576.
- Oral, A., Şahin, T., Türker, F., & Koçak, E. (2019). Evaluation of Plateletcrit and Platelet Distribution Width in Patients with Non-Alcoholic Fatty Liver Disease: A Retrospective Chart Review Study. *Medical Science Monitor*, 25, 9882–9886.
- Pugh, R. N., Murray-Lyon, I. M., Dawson, J. L., Pietroni, M. C., & Williams, R. (1973). Transection of the oesophagus for bleeding oesophageal varices. *British Journal of Surgery*, 60(8), 646–649. <https://doi.org/10.1002/bjs.1800600817>
- Ramírez-Mejía, M. M., et al. (2024). The multifaceted role of bilirubin in liver disease: A literature review. *Journal of Clinical and Translational Hepatology*.
- Riazi, K., Azhari, H., Charette, J. H., Underwood, F. E., King, J. A., Afshar, E. E., ... & Kaplan, G. G. (2022). The prevalence and incidence of NAFLD worldwide: A systematic review and

- meta-analysis. The Lancet Gastroenterology & Hepatology*, 7(9), 851–861. [https://doi.org/10.1016/S2468-1253\(22\)00113-4](https://doi.org/10.1016/S2468-1253(22)00113-4)
- Sterling, R. K., Lissen, E., Clumeck, N., et al. (2006). Development of a simple noninvasive index to predict significant fibrosis in patients with HIV/HCV coinfection. *Hepatology*, 43(6), 1317–1325. <https://doi.org/10.1002/hep.21178>
- Tufoni, M., Zaccherini, G., Caraceni, P., & Bernardi, M. (2020). Albumin: Indications in chronic liver disease. *United European Gastroenterology Journal*, 8(5), 528–535. <https://doi.org/10.1177/2050640620921997>
- Verma, N., Singh, S., Taneja, S., & Duseja, A. (2018). Hematological disorders in chronic liver disease: An update. *Journal of Clinical and Experimental Hepatology*, 8(4), 397–403.
- Wai, C. T., Greenson, J. K., Fontana, R. J., Kalbfleisch, J. D., Marrero, J. A., Conjeevaram, H. S., & Lok, A. S. (2003). A simple noninvasive index can predict both significant fibrosis and cirrhosis in patients with chronic hepatitis C. *Hepatology*, 38(2), 518–526. <https://doi.org/10.1053/jhep.2003.50346>
- World Health Organization. (2017). *Global hepatitis report 2017*. Retrieved January 10, 2021, from <https://www.who.int/hepatitis/publications/global-hepatitis-report2017/en/>
- World Health Organization. (2023). Global health observatory: Chronic viral hepatitis. <https://www.who.int/data/gho/data/themes/chronic-viral-hepatitis>
- Younossi, Z. M., Wong, V. W., Anstee, Q. M., et al. (2020). Fatigue and pruritus in patients with advanced fibrosis due to nonalcoholic steatohepatitis: the impact on patient-reported outcomes. *Hepatology Communications*, 4(11), 1637–1650.
- Younossi, Z. M., Koenig, A. B., Abdelatif, D., Fazel, Y., Henry, L., & Wymer, M. (2019). Global epidemiology of nonalcoholic fatty liver disease—Meta-analytic assessment of prevalence, incidence, and outcomes. *Hepatology*, 64(1), 73–84. <https://doi.org/10.1002/hep.28431>
- Zimmermann, H. W., Seidler, S., Nattermann, J., Gassler, N., Hellerbrand, C., Zerneck, A., ... & Tacke, F. (2011). Functional contribution of elevated circulating and hepatic non-classical CD14+CD16+ monocytes to inflammation and human liver fibrosis. *PLoS One*, 6(4), e11049. <https://doi.org/10.1371/journal.pone.0011049>

## الملخص العربي

### عنوان البحث: الاتجاهات الوبائية والواسمات التشخيصية في أمراض الكبد المزمنة

محمد عبدالعزيز<sup>١</sup>، أمينة السيد<sup>١</sup>، لمياء ضيف<sup>٢</sup>، لطفي حيق<sup>٢</sup>، احسين فرج<sup>٢\*</sup>

<sup>١</sup>مركز جراحة الجهاز الهضمي، كلية الطب، جامعة المنصورة، المنصورة، مصر.  
<sup>٢</sup>قسم علم الحيوان، كلية العلوم، جامعة دمياط، دمياط، مصر.

تعد أمراض الكبد المزمنة سبباً رئيسياً للوفيات والاعتلال على الصعيد العالمي، وتشمل طيفاً واسعاً من الاضطرابات ذات المسببات المتنوعة. يعتمد التشخيص الدقيق والإنذار ومراقبة أمراض الكبد المزمنة بشكل كبير على تقييم العديد من المؤشرات الحيوية. يقدم هذا البحث لمحة مركزة عن المؤشرات الحيوية الكيميائية والدموية الرئيسية المستخدمة في تقييم الأنواع الأساسية لأمراض الكبد المزمنة، بما في ذلك التهاب الكبد الفيروسي ومرض الكبد الدهني غير الكحولي (NAFLD). لكل فئة مرضية، نناقش الفائدة السريرية لاختبارات وظائف الكبد التقليدية (مثل ALT، AST، البيليروبين، الألبومين)، ومؤشرات التليف (مثل عدد الصفائح الدموية، درجة APRI، ومؤشر FIB-4)، بالإضافة إلى المعايير الدموية الأخرى ذات الصلة. ومن خلال تجميع الأدلة الحالية حول القيمة التشخيصية والإنذارية لهذه المؤشرات الكيميائية والدموية عبر المسببات المختلفة لمرض الكبد المزمن، يهدف هذا البحث إلى توفير مرجع عملي للأطباء والباحثين في مجال أمراض الكبد.

## Studying the Clinical Value of Glial Cell Line-Derived Neurotrophic Factor and Other Biological Markers in Patients with Chronic Liver Diseases

Mohamed M, Abdel-aziz<sup>1</sup>, Amina M. R. El-Sayed<sup>1</sup>, Lamiaa E. M. Deef<sup>2</sup>, Lotfy Z, Habbak<sup>2</sup> and Ihssin A. Faraj<sup>2</sup>

<sup>1</sup>Gastrointestinal Surgery Center, Faculty of Medicine, Mansoura University.

<sup>2</sup>Zoology, Department, Faculty of science, Damietta University, Damietta, Egypt.

Received: 03 June 2025 /Accepted: 23 July 2025

\*Corresponding author's E-mail: ihssin89@students.du.edu.eg

### Abstract

**Background:** Chronic liver disease (CLD) is a degenerative process characterized by hepatic dysfunction and systemic alterations. Glial cell line-derived neurotrophic factor (GDNF), a member of the TGF- $\beta$  protein family group, has been implicated in cellular survival and tissue response to injury. The aim of this study is to assess the clinical value of selected biological markers, with a focus on glial cell line-derived neurotrophic factor (GDNF), in the diagnosis of patients with chronic liver diseases. **Methods:** The study included 82 participants: 63 patients with CLD and 19 healthy controls. Serum GDNF levels were measured, along with liver and kidney function tests and complete blood count. Statistical analyses were conducted to compare results across the two categories. **Results:** Levels of GDNF were markedly higher in the CLD group (median: 2.51 ng/mL) compared to the control group (median: 1.75 ng/mL,  $P = 0.001$ ). CLD patients showed significant variations in liver function tests, consisting of elevated bilirubin, AST, GGT, and INR, and decreased albumin. Hematological findings revealed lower hemoglobin, hematocrit, and RBC counts, alongside increased RDW and neutrophil-to-lymphocyte ratio. Platelet indices showed reduced counts and altered morphology. GDNF exhibited promising diagnostic ability in distinguishing patients with CLD from controls with an AUC of 0.743, sensitivity of 82.5% and specificity of 63.2%. **Conclusion:** The increased GDNF levels in CLD patients suggest a potential role as a non-invasive biomarker. Significant biochemical and hematological alterations further highlight the systemic impact of CLD. These findings support the need for further research into the diagnostic and prognostic utility of GDNF in liver disease.

**Keywords:** Chronic Liver disease (CLD), Platelets indices, Neutrophile to lymphocyte ratio (NLR), Glial cell line-derived neurotrophic factor (GDNF).

### Introduction

Chronic liver disease (CLD) is defined as a lasting damage to liver function. It often develops silently, with few or no symptoms in

the early phases. In the advanced stages, patients usually develop jaundice, fatigue and abdominal discomfort. Fibrosis and cirrhosis are the outcomes of the ongoing inflammation, liver tissue destruction, and regeneration that characterize CLD. Recent literature highlights metabolic dysfunction, viral hepatitis, and alcohol related liver injury as main factors driving to CLD around the world (**Mak et al., 2024**). An advanced stage of chronic liver disease is cirrhosis, which causes the liver's structure to be disrupted, extensive nodules to develop, vascular reorganization, neo angiogenesis, and extracellular matrix deposition. The mechanism of fibrosis and cirrhosis at a cellular level is the recruitment of stellate cells and fibroblasts, leading to fibrosis. Chronic liver disease is a prevalent clinical condition, with recent studies focusing on its etiological factors, management methods and clinical manifestations (**Sharma and Nagalli, 2023**).

Chronic liver diseases are a key factor of mortality and morbidity around the world with around 800,000 deaths per year resulting from liver cirrhosis (**Gitau and Menge, 2020**). CLD represents a rising global health concern, with an estimated 1.7 billion individuals affected worldwide as of 2021, driven primarily by non-alcoholic fatty liver disease (NAFLD), viral hepatitis, and alcohol-related liver injury (**Marcellin et al., 2023**). Among these, NAFLD—recently redefined as metabolic dysfunction-associated steatotic liver disease (MASLD)—has emerged as the most prevalent cause, affecting about 30.2% of the global adult population, with the highest rates observed in the Middle East and North Africa, reaching up to 42.6% (**Younossi et al., 2024**). In Egypt and similar regions, the burden of MASLD-related cirrhosis is steadily increasing, particularly among younger populations, reflecting both epidemiological transition and metabolic shifts. This rising prevalence highlights the urgent need for targeted screening strategies and public health interventions to reduce progression to cirrhosis and hepatocellular carcinoma (**Alshahrani et al., 2025**).

As reported by the National Vital Statistics Report 2017 from the Center for Disease Control and Prevention, about 4.5 million individuals had cirrhosis and CLD. Recent estimates report that more than 100 million Americans are affected by some types of liver disease. Furthermore, many individuals

remain undiagnosed, especially those with early phase cases like fatty liver disease (**Sharma and Nagalli, 2023**).

CLD early diagnosis is crucial for effective intervention. It progresses silently until advanced phases. Classic diagnostic tools like liver biopsy although considered the gold standard, are invasive and result in problems such as bleeding, pain and sampling error. This has led to growing demand for reliable, noninvasive markers that can accurately detect liver dysfunction and monitor progression of disease. Glial cell line-derived neurotrophic factor (GDNF) is a glycosylated, disulfide-linked homodimer that belongs to a distant subfamily within the transforming growth factor-beta (TGF- $\beta$ ) superfamily. Clinical investigations have demonstrated elevated GDNF levels in both the parietal cortex and plasma of individuals with recurrent major depressive disorder. Moreover, GDNF expression has been shown to increase markedly in response to cytotoxic stimuli, including exposure to ionizing radiation. Furthermore, GDNF levels are elevated in some cancer cell types (**Yang et al., 2022**). The present study aimed to evaluate the diagnostic potential of serum GDNF levels in chronic liver disease by comparing affected patients with healthy controls, while also assessing related clinical laboratory parameters.

#### *Patients and Methods*

##### **Ethical Approval:**

The Research and Ethical Committees of Al-Azhar Faculty of Medicine, Damietta, Egypt, approved this research. IRB00012367-25-02-006.

##### *Participants:*

The study included 82 participants, comprising 63 patients with CLD and 19 healthy controls. CLD diagnosis was based on clinical, biochemical, and imaging findings.

##### *Clinical diagnosis of CLD:*

The diagnosis of chronic liver disease (CLD) was based on a combination of clinical evaluation, laboratory testing, and imaging findings, in accordance with established hepatology guidelines (**EASL, 2021; AASLD,**



**2023).** Clinical criteria included a history of chronic hepatic symptoms or known liver disease lasting more than six months. Laboratory investigations comprised liver function tests, complete blood count, and viral hepatitis serology. Abdominal ultrasonography was performed to assess liver echotexture, surface nodularity, and signs of portal hypertension. Non-invasive fibrosis scores such as the FIB-4 index and APRI score were calculated. In selected cases, the diagnosis was made when clinical and paraclinical findings consistently indicated chronic hepatic injury or fibrosis.

#### *Blood Samples:*

The blood samples were collected without an anticoagulant in dry, clean test tubes. Blood was allowed to clot for 30 minutes at room temperature (25°C) for serum separation. The sera were then separated by centrifugation at 3000 rpm for 15 minutes at 25°C. The top yellow serum layer was carefully pipetted without disturbing the white buffy layer and transferred into Eppendorf tubes. Part of the serum samples was used to determine the levels of the other biochemical parameters. The remaining serum samples were aliquoted and stored at -80°C until used for the determination of glial cell line-derived neurotrophic factor (GDNF). Standard hematological techniques were employed for WBCs count, Neutrophils%, Lymphocytes%, RBCs count, HGB level and platelets count using hematology analyzer device Cell Tac MEK - 6510 - 6500. Japan. INR was determined using a thromboplastin-based prothrombin time assay performed on a semi-automated coagulation analyzer (Coatron M1, TECO GmbH, Germany), following the manufacturer's instructions.

#### *Biochemical Analysis:*

Serum samples were collected from all participants one day prior to any surgical intervention (if applicable). The following biochemical parameters were measured using standardized assays and methods at the Gastroenterology Surgery Center, Mansoura, Egypt: Creatinine (Cr), Uric Acid (UA), Potassium (K), alanine transaminase (ALT), aspartate transaminase (AST), alkaline phosphatase (ALP), gamma-glutamyl transferase (GGT), albumin, total bilirubin

(T.bili), direct bilirubin (D.bili), international normalized ratio (INR). All biochemical analyses were performed in a blinded manner. The individuals conducting the assays were unaware of the participants' clinical diagnosis to minimize potential bias.

Biochemical parameters were quantified using standardized, validated commercial assay kits in accordance with international laboratory protocols. Serum aspartate aminotransferase (AST) and alanine aminotransferase (ALT) activities were determined using commercially available kit (Biomatik, China; AST: Cat. #EKF57543, ALT: Cat. #EKF58248). Serum creatinine levels were measured using a colorimetric enzymatic assay (Cat. #EU3134; FineTest, China). Alkaline phosphatase (ALP) activity was assessed by a kinetic colorimetric method based on the recommendations of the International Federation of Clinical Chemistry (IFCC), using a kit from Spinreact S.A.U. Gamma-glutamyl transferase (GGT) activity was evaluated using a kinetic enzymatic colorimetric kit (Cat. #E-BC-K126-M; Elabscience, China.), while total and direct bilirubin concentrations were determined via the diazo method, also employing kits from Spinreact S.A.U. Serum albumin was measured using the bromocresol green (BCG) dye-binding method with a dedicated assay kit (Cat. #C035-2-1; NJ Bioengineering Institute, China) following the manufacturer instructions.

#### *Estimation of serum GDNF levels:*

The level of glial cell line-derived neurotrophic factor (GDNF) in serum samples was measured using a commercially available human GDNF ELISA kit (Cat. No. E0122Hu, BT-Laboratory, China), based on the sandwich enzyme-linked immunosorbent assay (ELISA) principle.

#### *Statistical Analysis:*

All statistical analyses were performed using of PASW Statistics software, version 26.0 (SPSS Inc., Chicago, IL, USA), for all analyses. Quantitative data were presented as mean  $\pm$  standard deviation when normally distributed, or as median (interquartile range) for non-normally distributed data. To evaluate significant differences in continuous variables between the control cohort and the chronic liver disease (CLD) group, an independent samples t-test was applied for normally distributed data,

while the Mann-Whitney U test was utilized for data that did not conform to a normal distribution.

## Results

### *Characteristic features of studied groups.*

CLD group had a significantly higher median age (57 years) compared to the control group (26 years) ( $P < 0.001$ ), while the gender distribution was comparable between groups ( $P = 0.954$ ). Hepatitis B surface antigen (HBsAg) positivity was negligible in both groups, whereas HCV antibody positivity was considerably higher in the CLD group (7.9%) compared to none in the control group ( $P = 0.001$ ). The CLD patients showed a range of Child-Pugh score, with only 31.9% in class A, while the control group was entirely score A ( $P = 0.001$ ). There was in the APRI and FIB4 scores, higher proportion of advanced class ( $\geq 1$  and  $\geq 3$ , respectively) with ( $P = 0.001$ ) for both (Table 1).

Table (1) Characteristic features of studied groups.

Variable	Control Group N=19	Chronic Liver Disease Group N=63	P-value
Age (yr)	26 (24-34)	57 (22,5-62)	0.001
Gender			
Male n (%)	14 (73.7)	46 (73)	0.954
Female n (%)	5 (26.3)	17 (27)	
HBs Ag n (%)			
+ve	0(0)	1(1.6)	0.377
-ve	19 (100)	57 (90.5)	
HCV Ab n (%)			
+ve	0(0)	5(7.9)	0.001
-ve	19 (100)	27 (42.9)	
Child n (%)			
A	19 (100)	23 (31.9)	0.001
B	0(0)	2 (33.3)	
C	0(0)	7(28.3)	
APRI n (%)			
1	18 (94.7)	27 (42.9)	0.001
2	1 (5.3)	15 (23.8)	
3	0(0)	21 (33.3)	
FIB4 n (%)			
1	19(100)	4(9.3)	0.001
2	0(0)	14(32.6)	
3	0(0)	25(58.1)	

HBsAg - Hepatitis B surface antigen, HCVAb - Hepatitis C virus antibody, Child - Child-Pugh score, APRI - Aspartate Aminotransferase to Platelet Ratio Index, FIB4 - Fibrosis-4 Index.

### *Serum level of glial cell line derived neurotrophic factor in the studied groups.*

The chronic liver disease (CLD) group

exhibited a significantly higher median GDNF level (2.51 ng/ml; IQR: 1.77–3.33) compared to the control group (1.75 ng/mL; IQR: 1.20–2.04) with a P-value of 0.001 (Table 2).

Table (2) Serum level of Glial Cell Line Derived Neurotrophic Factor in the studied groups.

Variable Median (IQR)	Control Group N=19	Chronic Liver Disease Group N=63	P-value
GDNF (ng/mL)	1.75 (1.20–2.04)	2.51 (1.77–3.33)	0.001

GDNF - Glial Cell Line-Derived Neurotrophic Factor

### *Serum levels of kidney profile in the studied group*

Creatinine (Cr) levels were comparable between the groups, with identical medians of 0.80 mg/dl ( $P = 0.744$ ). Potassium (K) and uric acid (UA) levels also showed no significant differences, with mean  $\pm$  SD values of  $4.30 \pm 0.449$  mEq/L and  $5.02 \pm 0.937$  mg/dl in the control group versus  $4.04 \pm 0.58$  and  $4.81 \pm 1.75$  in the CLD group ( $P = 0.136$  and  $0.644$ ). Sodium (Na) levels were slightly lower in the CLD group, with a median of 137 mEq/L compared to 141 mEq/L in controls, approaching statistical significance ( $P = 0.051$ ) (Table 3).

Table (3) Serum levels of kidney profile in the studied group.

Variable	Control Group N=19	Chronic Liver Disease Group N=63	P-value
Cr (mg/dl)	0.80 (0.70 – 0.90)	0.80 (0.70 – 0.90)	0.744
K(mEq/L)	4.30 $\pm$ 0.449	4.04 $\pm$ .58	0.136
UA (mg/dl)	5.02 $\pm$ 0.937	4.81 $\pm$ 1.75	0.644
Na(mEq/L)	141	137(132.5 – 140)	0.051

Cr - Creatinine, K – Potassium, UA - Uric Acid, Na- Sodium

### *Serum levels of different liver profile in studied groups.*

Albumin levels were significantly lower in the CLD group (median: 3.6 g/dL) compared to the control group (median: 4.5 g/dL,  $P < 0.001$ ). Total bilirubin (T. bili) and direct bilirubin (D. bili) levels were markedly elevated in the CLD group, with medians of 1.35 mg/dL and 0.70 mg/dL, respectively, compared to 0.60 mg/dL and 0.15 mg/dL in

controls ( $P < 0.001$ ). The CLD group also exhibited significantly higher levels of alkaline phosphatase (ALP), aspartate aminotransferase (AST), gamma-glutamyl transferase (GGT), and international normalized ratio (INR), with  $P < 0.001$  for all. Alanine aminotransferase (ALT) levels were slightly elevated in the CLD group, but this difference was not statistically significant ( $P = 0.147$ ) (Table 4).

Table (4) Serum levels of different liver profile in studied groups.

Variable Median (IQR)	Control Group N=19	Chronic Liver Disease Group N=63	P- value
Alb (g/dL)	4.50 (4.40-4.80)	3.6(3.0 – 3.9)	<0.001
T. bili(mg/dL)	0.60(.50 - .70)	1.35 (0.80 – 3.12)	<0.001
D.bili(mg/dL)	0.15(.10- .25)	0.70 (.300 – 1.50)	<0.001
ALP(IU/L)	5(5-5)	6 (5.0 – 8.0)	<0.001
AST(U/L)	21(20- 21)	41.5 (30.0 – 69.0)	<0.001
ALT(U/L)	23(21 - 27)	28.5 (21.0 – 48.0)	0.147
GGT(U/L)	17(12 - 27)	46 (30.50 – 89.50)	<0.001
INR`	1(1 – 1.10)	1.2 (1.0 – 1.5)	<0.001

Alb - Albumin, T.bili - Total Bilirubin, D.bili - Direct Bilirubin, ALP - Alkaline Phosphatase, AST - Aspartate Aminotransferase, ALT - Alanine Aminotransferase, GGT - Gamma-Glutamyl Transferase, INR - International Normalized Ratio.

#### *Red Blood Cells and Their indices in the studied groups.*

The CLD group exhibited significantly lower RBC counts (median:  $4.2 \times 10^6/\mu\text{L}$ ) compared to the control group (median:  $5.20 \times 10^6/\mu\text{L}$ ,  $P < 0.001$ ). Hemoglobin (HGB) and hematocrit (HCT) levels were also markedly reduced in the CLD group, with mean  $\pm$  SD values of  $11.31 \pm 2.34$  g/dL and  $34.06 \pm 6.96\%$ , respectively, compared to  $14.26 \pm 1.51$  g/dL and  $41.79 \pm 5.38\%$  in controls ( $P < 0.001$  for both). RDW level was significantly higher in the CLD group (median: 14.5%) versus the control group (median: 12.30%,  $P < 0.001$ ), improved interpretation of RDW. MCV, mean corpuscular hemoglobin (MCH), Mean corpuscular hemoglobin concentration (MCHC) showed no significant differences between the groups ( $P = 0.195$ , 0.814, and 0.358, respectively) (Table 5).

Table (5) Red Blood Cells and Their indices in the studied groups

Variable	Control Group N=19	Chronic Liver Disease Group N=63	P Value
RBCs $\times 10^6$ (cell/ $\mu\text{L}$ ) Median (IQR)	5.20(4.60 - 5.40)	4.2(3.42 – 4.60)	<0.001
HG (g/dL) Mean $\pm$ SD	14.26 $\pm$ 1.51	11.31 $\pm$ 2.34	<0.001
HCT (%) Mean $\pm$ SD	41.79 $\pm$ 5.38	34.06 $\pm$ 6.96	<0.001
MCV (fL) Median (IQR)	82.46(80.16 – 86.20)	85(80.63 – 90.0)	0.195
MCH(Pg) Median (IQR)	28.5(27.8 - 29.25)	28.7(26.80 – 30.60)	0.814
MCHC(g/dL) Mean $\pm$ SD	34.30 $\pm$ 1.72	33.28 $\pm$ 2.57	0.358
RDW (%) Median (IQR)	12.30(11.50 – 13.05)	14.5(12.95- 16.90)	<0.001

RBC - Red Blood Cell Count, HG – Hemoglobin, HCT – Hematocrit, MCV - Mean Corpuscular Volume, MCH - Mean Corpuscular Hemoglobin, MCHC - Mean Corpuscular Hemoglobin Concentration, RDW - Red Cell Distribution Width.

#### *White Blood Cells and Their indices in the studied groups.*

The CLD group exhibited a significantly lower median WBC count ( $4.3 \times 10^3/\mu\text{L}$ ) compared to the control group ( $5.7 \times 10^3/\mu\text{L}$ ,  $P = 0.039$ ). Lymphocyte count (Lymph No) was notably lower in the CLD group (median:  $1.02 \times 10^3/\mu\text{L}$ ) compared to the control group (median:  $2.50 \times 10^3/\mu\text{L}$ ,  $P < 0.001$ ), and lymphocyte percentage (Lymph %) was decreased in the CLD group (mean  $\pm$  SD:  $27.28 \pm 12.06\%$ ) compared to the controls (mean  $\pm$  SD:  $43.7 \pm 7.5\%$ ,  $P < 0.001$ ). On the other hand, neutrophil count (Neut No) and percentage (Neut %) were higher in the CLD group, but the difference in neutrophil count was not significant ( $P = 0.650$ ), while the neutrophil percentage was significantly increased (mean  $\pm$  SD:  $58.17 \pm 14.07\%$  in CLD vs.  $43.7 \pm 8.4\%$  in controls,  $P < 0.001$ ). The neutrophil-to-lymphocyte ratio (NLR) was significantly higher in the CLD group (median: 2.34) in contrast to the control group (median: 0.96,  $P < 0.001$ ) (Table 6).

Table (6) White Blood Cells and

Their indices in the studied groups.

Variable	Control Group N=19	Chronic Liver Disease Group N=63	P Value
WBC $\times 10^3$ (cell/ $\mu$ L) Median (IQR)	5.7(4.2 - 6.9)	4.3(3.22- 6.03)	0.039
Lymph No $\times 10^3$ (cell/ $\mu$ L) Median (IQR)	2.50(1.90- 3.05)	1.02(0.73 - 1.6)	<0.001
Neut No $\times 10^3$ (cell/ $\mu$ L) Median (IQR)	2.16(1.70 - 3.10)	2.68(1.55 - 3.50)	0.650
Lymph % Mean $\pm$ SD	43.7 $\pm$ 7.5	27.28 $\pm$ 12.06	<0.001
Neut % Mean $\pm$ SD	43.7 $\pm$ 8.4	58.17 $\pm$ 14.07	<0.001
NLR Median (IQR)	0.96(0.80- 1.22)	2.34(1.44 - 3.43)	<0.001

WBC - White Blood Cell Count, Lymph no - Lymphocyte Number, Neut no - Neutrophil Number, Lymph % - Lymphocyte Percentage, Neut % - Neutrophil Percentage, NLR - Neutrophil-to-Lymphocyte Ratio.

#### *Platelets and Their indices in the studied groups*

Platelet count (PLT) was significantly lower in the CLD group (median: 105  $\times 10^3/\mu$ L) compared to the control group (median: 209  $\times 10^3/\mu$ L,  $P < 0.001$ ), reflecting thrombocytopenia commonly associated with liver disease. PDW was considerably higher in the CLD group (median: 18.60%) than in controls (median: 13%,  $P = 0.043$ ), suggesting increased variability in platelet size. Pct was markedly decreased in the CLD patients (median: 0.089%) compared to controls (median: 0.149%,  $P < 0.001$ ). Conversely, platelet large cell ratio (PLCR) was higher in the CLD group (median: 33.9%) than in controls (median: 28.40%,  $P = 0.002$ ). MPV and PLR showed no significant differences between the groups ( $P = 0.116$  and 0.739, respectively) (Table 7).

Table (7) Platelets and Their indices in the studied groups

Variable Median (IQR)	Control Group N=19	Chronic Liver Disease Group N=63	P Value
PLT $\times 10^3$ (cell/ $\mu$ L)	209(191.9 - 252.9)	105(60.25- 166.77)	<0.001
PDW (%)	13(11.60 - 10.20)	18.60(13.35- 20.25)	0.043
MPV (fL)	9.30(6.50 - 10.50)	9.45(7.37 - 11.30)	0.116
Pct (%)	0.149(0.126- 0.206)	0.089(0.056- 0.144)	<0.001
PLCR (%)	28.40(21.60 - 30.60)	33.9(30.7- 41.1)	0.002
PLR	83.6(71.22 - 112.22)	90.9(60.28 - 134.4)	0.739

PLT - Platelet Count, PDW - Platelet Distribution Width, MPV - Mean Platelet Volume, Pct - Plateletcrit (percentage of blood volume occupied by platelets), PLCR - Platelet Large Cell Ratio, PLR - Platelet-to-Lymphocyte Ratio.

#### *Area under curve (AUC), sensitivity, and specificity of serum glial cell line-derived neurotrophic factor for diagnosis of patients with Chronic Liver disease*

The area under the curve (AUC), sensitivity (Sen%), specificity (Spe%), and 95% confidence intervals (CI) for GDNF in diagnosing chronic liver disease (CLD) patients was shown in (Table.8). Glial cell line-derived neurotrophic factor (GDNF) demonstrated a strong AUC of 0.743, with an 82.5% sensitivity and 63.2% specificity at cutoff of 1.62, and  $P$  value of ( $P < 0.001$ ) (Table 8) (Fig 1).

Table (8). Area under curve (AUC), sensitivity, and specificity of serum glial cell line-derived neurotrophic factor for diagnosis of patients with Chronic Liver disease

Variables	AUC	Cutoff	Sen%	Spe%	95% CI	P value
GDNF (ng/ml)	0.743	1.62	82.5%	63.2%	0.618- 0.868	<0.001

GDNF - Glial Cell Line-Derived Neurotrophic Factor, AUC- Area Under the curve, CI- Confidential Interval

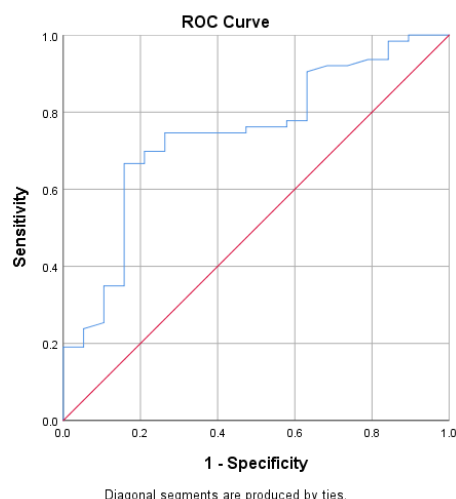


Fig 1. ROC curve for GDNF for diagnosis of patients with chronic liver disease

## Discussion

Chronic liver diseases (CLD) have a wide range of causes, including, long -term alcohol misuse, infections, autoimmune disease, and metabolic diseases. The last stage of chronic liver disease, cirrhosis, is recognized by vascular reorganization, neo-angiogenesis, the deposition of an extracellular matrix, disturbance of liver architecture and the development of extensive nodules. Liver cirrhosis may be classified into two phases, the compensated cirrhosis and the decompensated cirrhosis. There are no symptoms during the compensated cirrhosis, while in the decompensated one, portal pressure escalates above the normal range(>5mmHg). Worldwide epidemiological analysis underscores a growing burden of CLD driven primarily by metabolic dysfunction associated steatotic liver disease and alcohol related liver disease (Yu et al.,2024).

Glial cell line-derived neurotrophic factor (GDNF) is a robust protein that belongs to the transforming growth factor-beta (TGF- $\beta$ ) superfamily. It was basically introduced as a survival factor, but other research has revealed that GDNF has much broader biological functions. While historically studied in Parkinson disease context, current research suggests its dual upregulation in neural cell types during neurodegradation, highlighting significant value in inflammation and brain repair. It has fundamental role not only in the development and maintenance of the central

and peripheral nervous systems but also in organogenesis, spermatogenesis, and cellular responses in various tissues. GDNF is encoded by the GDNF gene, which is situated on chromosome 5p13.2 in humans (Sidorova and Saarma,2020).

The main signaling pathways activated by the GDNF-RET complex include the PI3K/AKT pathway, which promotes cell survival and has anti-apoptotic effects, and the MAPK/ERK pathway, which is associated with differentiation and cell proliferation. Src family kinases may also be involved in mediating downstream effects. These signaling mechanisms are critical not only in normal physiology but also in pathological conditions, such as cancer (Guo et al., 2024).

Beyond its neural roles, GDNF has been found to participate in tissue repair, neuroinflammation, and certain cancer processes. Elevated levels of GDNF have been implicated in tumor progression and resistance to therapy in some cancers, whereas in other contexts, GDNF may have protective effects. For instance, its neuroprotective properties have prompted investigation into its therapeutic potential in neurodegenerative diseases like Parkinson's disease. In liver disease, increasing evidence reported that GDNF may have diagnostic and prognostic ability. Furthermore, previous studies reported that GDNF levels are elevated in hepatic stellate cells and liver tissues of patients with advanced fibrosis(F4) (Zhuang et al.,2023).

In our study, gender distribution was similar between the categories ( $P=0.954$ ), indicating that female and male participants were equally represented in both study individuals. The percentage of HBV positivity was similar between the groups, while HCV was considerably higher in CLD group compared to none in the controls( $P=0.001$ ).

Level of GDNF was notably higher in the CLD group versus control group ( $P=0.001$ ). This is in line with studies suggesting that GDNF reduces hepatocytes apoptosis and oxidative stress while concurrently being involved in carcinogenesis. GDNF activates survival pathways, such as PI3K/Akt and ERK signaling, which counteract apoptosis signals. A study by Zhang et al. investigated serum GDNF levels in individuals with liver fibrosis. This study, which employed ELISA to quantify GDNF concentrations, demonstrated significantly increased serum GDNF in patients

with liver fibrosis versus controls. The study focused on circulating levels of GDNF and did not involve histological analysis of liver tissue (Zhang et al.,2019).

The serum kidney profile analysis revealed comparable creatinine, potassium, and uric acid levels between the control and chronic liver disease groups, suggesting that overall kidney function, as indicated by these markers, was not significantly compromised in the CLD cohort in this study. This finding aligns with some studies indicating that renal impairment is not always present in the early stages of CLD. Monitoring NA levels is essential for prognostication and CLD management. However, the slightly lower sodium levels in the CLD group, approaching statistical significance, warrant further consideration (Kiani & Zori,2023). Hyponatremia is a recognized complication of advanced liver disease, often associated with fluid retention and altered hormonal regulation (Ginès et al., 2018). While not statistically significant in this instance, this trend suggests the need for careful monitoring of electrolyte balance in CLD patients.

The current study demonstrated marked alterations in RBC indices among patients with CLD versus the controls, suggesting a high prevalence of anemia in CLD patients. Key erythrocyte parameters including RBC count, HGB, and HCT levels were considerably reduced in the CLD group ( $P < 0.001$  for all), consistent with prior findings in the literature (Hu et al., 2023; Mishra et al., 2021). These reductions are reflective of the multifactorial etiology of anemia in CLD, which may involve hypersplenism, gastrointestinal blood loss due to portal hypertension, nutritional deficiencies, impaired erythropoietin production, and direct bone marrow suppression.

The anemia observed in CLD is often of the normocytic normochromic type, suggesting preserved red cell morphology despite declined production or high destruction. This was reinforced by the findings in mean corpuscular volume (MCV) and mean corpuscular hemoglobin (MCH), which did not differ significantly between CLD patients and controls ( $P = 0.195$  and  $P = 0.814$ , respectively). Similarly, mean corpuscular hemoglobin concentration (MCHC) remained statistically unchanged ( $P = 0.358$ ). These results indicate that while anemia is prevalent, its features are typical of chronic inflammatory conditions,

which often present with normal RBC indices (Scheiner et al.,2020).

In contrast, RDW was considerably increased in CLD cases ( $P < 0.001$ ), indicating increased anisocytosis and suggesting a heterogeneous population of red cells. This finding may reflect ineffective erythropoiesis or a mixed anemia etiology, potentially involving both iron deficiency and vitamin B12 or folate deficiency. Elevated RDW has been associated with advanced fibrosis poor clinical outcome and portal hypertension (Haung et al.,2025).

Anemia in CLD tends to worsen with disease severity, as hemoglobin and hematocrit levels have been shown to correlate negatively with liver function scores such as the Child-Pugh score and MELD system. Both HGB and HCT tend to decrease as liver disease progresses, and their reduction has been significantly correlated with higher Child-Pugh classes (Abdel-Moneim & Mahmoud, 2023). Lower levels of hemoglobin have prognostic implications, being correlated with increased mortality and poorer clinical outcomes. These hematological parameters, therefore, work not only as evidence of anemia but also as important markers of disease progression and prognosis (Schettler et al., 2020).

Alterations in WBC indices further reflect the underlying pathophysiology of CLD. Leukopenia is frequently observed widely due to hypersplenism associated with portal hypertension, resulting in elevated sequestration of leukocytes in the enlarged spleen. Furthermore, different studies suggested that higher baseline WBC count independently predict the incidence of NAFLD. Additionally, bone marrow suppression from chronic inflammation, viral infections, and hepatotoxic insults can contribute to diminished leukocyte production. In contrast, leukocytosis may be observed in specific contexts such as alcoholic liver disease or systemic infections, reflecting acute inflammatory responses (Hu et al.,2024).

Elevated NLR has been linked to systemic inflammation, disease severity, complications, and poor survival in cirrhosis. Increased PLR has been associated with the degree of liver fibrosis, specifically in NALFD patients and chronic hepatitis C, suggesting its value as a non-invasive biomarker of liver dysfunction. These indices provide valuable insight into the immune-inflammatory dynamics in CLD and may enhance clinical assessment when integrated into routine



assessment (D'Amico et al.,2025).

The serum liver profile exhibited significant alterations in the CLD group. The observed lower albumin values are a well-established evidence of impaired hepatic synthesis capacity in CLD (Friedman et al., 2019). Similarly, the significantly elevated total and direct bilirubin levels reflect compromised bilirubin metabolism and excretion, characteristic of liver dysfunction (Sherlock & Dooley, 2018). Furthermore, the higher levels of alkaline phosphatase (ALP), aspartate aminotransferase (AST), gamma-glutamyl transferase (GGT), and international normalized ratio (INR) further corroborate the presence of liver damage and impaired synthetic function in the CLD group. These enzymes are commonly released into the bloodstream upon hepatocyte injury, and an elevated INR signifies impaired coagulation factor synthesis by the diseased liver. Other studies suggested that despite its prognostic value and inclusion in scoring systems such as MELD, INR does not reliably predict bleeding complications (Wang et al.,2023). While ALT levels were slightly elevated in the CLD cases, the lack of statistical significance might suggest that other enzymes, particularly AST, GGT, and ALP, were more sensitive indicators of the predominant type of liver injury in this specific CLD cohort. Overall, the distinct differences in the serum liver profile between the control and CLD groups strongly support the presence of significant hepatic dysfunction in the studied CLD population, consistent with established clinical and biochemical features of chronic liver disease.

Glial cell line-derived neurotrophic factor (GDNF) exhibited good diagnostic potential, with an AUC of 0.743, sensitivity of 82.5%, and specificity of 63.2% ( $P < 0.001$ ). GDNF, a neurotrophic factor, has been implicated in liver regeneration and fibrosis modulation, its moderate specificity suggests that while GDNF is sensitive to chronic liver disease, it may also be influenced by extrahepatic conditions, necessitating further validation in diverse cohorts (Yang et al.,2022).

One limitation of this study is the noticeable age difference between the control and CLD groups. The median age of the control group was 26 years, compared to 57 years in the CLD group. Since certain biological markers, including GDNF, may be influenced by age-

related physiological changes, this discrepancy could act as a confounding factor. Although the observed differences in GDNF levels were statistically significant, future studies should consider age-matched cohorts to more accurately isolate the effect of liver disease.

Additionally, no statistically significant correlation was observed between GDNF levels and Child–Pugh classification, suggesting that while GDNF may have diagnostic value, it may not reflect disease severity. This could be due to the limited sample size, heterogeneity in disease etiology, or the possibility that GDNF expression is altered early in liver disease but not progressively across severity stages. Future studies with larger, age-matched cohorts and stratification by liver disease stage are warranted.

## References

- Abdel-Moneim, A. E., & Mahmoud, A. M. (2023). Hematological alterations in cirrhosis and their association with Child–Pugh classification. *Egyptian Liver Journal*, 13(1), 45–52. <https://doi.org/10.1186/s43066-023-00213-1>.
- Alshahrani, A. M., & Bekheit, M. A. (2025). Epidemiological trends and burden of metabolic dysfunction-associated steatotic liver disease in the Middle East and North Africa region: A 32-year analysis of health impact. *Journal of Health, Population and Nutrition*, 44(1), Article 5.
- American Association for the Study of Liver Diseases (AASLD). (2023). Guidance on the clinical assessment of liver disease. *Hepatology*, Advance online publication. <https://doi.org/10.1002/hep.32900>.
- D'Amico, T., Miglionico, M., Cangemi, R., Romiti, G. F., De Fabrizio, B., Fasano, S., Recchia, F., Stefanini, L., Raparelli, V., Violi, F., Basili, S., & PRO-LIVER Collaborators. (2025). Neutrophil–lymphocyte ratio is associated with worse outcomes in patients with cirrhosis: Insights from the PRO-LIVER Registry. *Internal and Emergency Medicine*. Advance online publication. <https://doi.org/10.1007/s11739-025-03955-x>.
- European Association for the Study of the Liver (EASL). (2021). EASL Clinical Practice Guidelines on non-invasive tests for evaluation of liver disease severity and prognosis – 2021 update. *Journal of Hepatology*, 75(3), 659–689. <https://doi.org/10.1016/j.jhep.2021.05.025>
- Friedman, S. L., Gores, G. J., & Rojkind, M. (2019). Hepatic fibrosis. *Hepatology*, 70(1), 3–16.

- Ginès, P., Guevara, M., Arroyo, V., & Rodés, J. (2018). Hepatorenal syndrome. *The Lancet*, 362(9398), 1819–1827.
- Guo, X., Zhou, H., Liu, Y., Xu, W., Kanwore, K., & Zhang, L. (2024). Glial-cell-line-derived neurotrophic factor promotes glioblastoma cell migration and invasion via the SMAD2/3–SERPINE1–signaling axis. *International Journal of Molecular Sciences*, 25(18), 10229. <https://doi.org/10.3390/ijms251810229>.
- Hu, C., Zhang, L., & Li, X. (2023). Hematological abnormalities in chronic liver disease: Prevalence and clinical significance. *World Journal of Gastroenterology*, 29(14), 2151–2164. <https://doi.org/10.3748/wjg.v29.i14.2151>.
- Huang, Y., Ao, T., Wang, Y., Zhen, P., & Hu, M. (2025). The red cell distribution width is associated with all-cause and cardiovascular mortality among individuals with non-alcoholic fatty liver disease. *PLoS ONE*, 20(4), e0321789. <https://doi.org/10.1371/journal.pone.0321789>.
- Kiani, C., & Zori, A. G. (2023). Recent advances in pathophysiology, diagnosis and management of hepatorenal syndrome: A review. *World Journal of Hepatology*, 15(6), 741–754. <https://doi.org/10.4254/wjh.v15.i6.741>.
- Mak, L. Y., Liu, K., Chirapongsathorn, S., Kao, J. H., Kim, D. J., Sharma, B. C., Gani, R. A., Sollano, J., Lesmana, C. R. A., Jindal, A., Pham, V. H., Mohamed, R., Tsochatzis, E. A., & Chan, H. L. Y. (2024). Liver diseases and hepatocellular carcinoma in the Asia-Pacific region: Burden, trends, challenges and future directions. *Nature Reviews Gastroenterology & Hepatology*. Advance online publication. <https://doi.org/10.1038/s41575-024-00967-4>.
- Marcellin, P., Asselah, T., Buti, M., Chan, H. L. Y., Cornberg, M., Flisiak, R., ... & Wiegand, J. (2023). Global burden of liver disease: A rising challenge. *Journal of Hepatology*, 79(5), 1164–1178. <https://doi.org/10.1016/j.jhep.2023.04.012>.
- Mishra, P., Sen, S., & Dubey, A. (2021). Hematological abnormalities in chronic liver disease: A cross-sectional study. *Cureus*, 13(2), e13491. <https://doi.org/10.7759/cureus.13491>
- Scheiner, B., Semmler, G., Maurer, F., Schwab, P., Bucsics, T., & Traussnigg, R. (2020). Prevalence of and risk factors for anaemia in patients with advanced chronic liver disease. *Liver International*, 40(1), 194–204. <https://doi.org/10.1111/liv.14267>
- Schettler, A., Kreutz, R., & Schaefer, R. M. (2020). Hematologic changes in liver disease. *Hepatology International*, 14(5), 707–716. <https://doi.org/10.1007/s12072-020-10070-8>
- Sharma, A., & Nagalli, S. (2023). Chronic liver disease. In *StatPearls* [Internet]. StatPearls Publishing. <https://www.ncbi.nlm.nih.gov/books/NBK554597/>.
- Sherlock, S., & Dooley, J. (2018). Diseases of the liver and biliary system (12th ed.). Wiley-Blackwell.
- Sidorova, Y. A., & Saarma, M. (2020). Small molecules and peptides targeting glial cell line-derived neurotrophic factor receptors for the treatment of neurodegeneration. *International Journal of Molecular Sciences*, 21(18), 6575. <https://doi.org/10.3390/ijms21186575>
- Marcellin, P., Asselah, T., Buti, M., Chan, H. L. Y., Cornberg, M., Flisiak, R., ... & Wiegand, J. (2023). Global burden of liver disease: A rising challenge. *Journal of Hepatology*, 79(5), 1164–1178. <https://doi.org/10.1016/j.jhep.2023.04.012>.
- Wang, Q., Caldwell, S. H., Zhou, J., & Lisman, T. (2023). Bleeding and thrombotic complications in chronic liver disease: Rethinking the role of INR. *Clinical Gastroenterology and Hepatology*, 21(4), 456–466. <https://doi.org/10.1016/j.cgh.2023.04.016>.
- Yang, G.-Y., Zhuang, L.-P., Sun, T.-T., Ma, W.-T., Tao, L., Wu, L., Yeo, Y. H., Liu, C., Seki, E., & Liu, P. (2022). Serum glial cell line-derived neurotrophic factor (sGDNF) is a novel biomarker in predicting cirrhosis in patients with chronic hepatitis B. [Preprint]. <https://doi.org/10.21203/rs.3.rs-740620/v1>
- Younossi, Z. M., Stepanova, M., Ong, J. P., Jacobson, I. M., Bugianesi, E., Duseja, A., ... & Eguchi, Y. (2024). Global epidemiology of MASLD: A systematic review and meta-analysis. *The Lancet Gastroenterology & Hepatology*, 9(1), 24–36. [https://doi.org/10.1016/S2468-1253\(23\)00345-7](https://doi.org/10.1016/S2468-1253(23)00345-7).
- Yu, H., Wang, Z., & Zhao, G. (2024). Chronic liver disease and promising therapeutic strategy: A concise review. *Journals of Gastroenterology & Hepatology Research*, SAGE Advances. <https://journals.sagepub.com/doi/full/10.1177/09731296241228361>.
- Zhuang, L. P., Yang, G. Y., Sun, T. T., Ma, W. T., Tao, L., Wu, L., & Chen, W. (2023). Glial cell line-derived neurotrophic factor mediates hepatic stellate cell activation via ALK5/Smad signalling. *Cell Death & Disease*, 14, Article 102.
- Zhang, Y., Wang, X., Wang, L., Bai, M., Zhang, Y., Deng, H., Zhao, R., Zhang, Q., Wang, W., Tian, Z., & Zhang, H. (2019). Glial cell line-derived neurotrophic factor (GDNF) mediates hepatic stellate cell activation and liver fibrosis through ALK5/Smad signalling. *Gut*, 68(12), 2184–2196. <https://doi.org/10.1136/gutjnl-2018->

## الملخص العربي

## عنوان البحث: دراسة القيمة السريرية لعامل التغذية العصبية المشتق من الخلايا الدبقية ومؤشرات حيوية أخرى في المرضى المصابين بأمراض الكبد المزمنة

محمد عبدالعزيز<sup>١</sup>، أمينة السيد<sup>١</sup>، لمياء ضيف<sup>٢</sup>، لطفي حبق<sup>٢</sup>، احسين فرج<sup>٢</sup><sup>١</sup>مركز جراحة الجهاز الهضمي، كلية الطب، جامعة المنصورة، المنصورة، مصر.<sup>٢</sup>قسم علم الحيوان، كلية العلوم، جامعة دمياط، دمياط، مصر.

الخلفية: أمراض الكبد المزمنة (CLD) هي حالة تقدمية تتميز بخلل في وظائف الكبد وتغيرات جهازية. تم ربط عامل التغذية العصبي المشتق من الخلايا الدبقية (GDNF)، وهو أحد أعضاء عائلة  $TGF-\beta$  الفائقة، ببقاء الخلايا والاستجابة لإصابة الأنسجة. هدفت هذه الدراسة إلى تقييم مستويات GDNF في مصل الدم لدى مرضى مصابون بأمراض كبد مزمنة مقارنةً بالأشخاص الأصحاء، بالإضافة إلى تقييم المعلمات البيوكيميائية والدموية ذات الصلة. الطرق: شملت الدراسة ٨٢ مشاركاً: ٦٣ مريضاً بأمراض كبد مزمنة و ١٩ شخصاً سليماً. تم قياس مستويات GDNF في المصل، إلى جانب اختبارات وظائف الكبد والكلية وعدد الدم الكامل. أجريت التحليلات الإحصائية لمقارنة النتائج بين المجموعتين. النتائج: كانت مستويات GDNF أعلى بشكل ملحوظ في مجموعة CLD (الوسيط: ٢,٥١ نانو غرام/مل) مقارنةً بمجموعة الشواهد (الوسيط: ١,٧٥ نانو غرام/مل؛ القيمة الاحتمالية  $P = 0.001$ ). أظهر المرضى الذين يعانون من أمراض كبد مزمنة تغيرات ملحوظة في اختبارات وظائف الكبد، بما في ذلك ارتفاع البيليروبين، وإنزيمات AST، وGGT، وINR، وانخفاض الألبومين. وكشفت النتائج الدموية عن انخفاض في مستويات الهيموغلوبين، والهيماتوكريت، وعدد كريات الدم الحمراء، إلى جانب زيادة في RDW ونسبة العدلات إلى الخلايا اللمفاوية. كما أظهرت مؤشرات الصفائح الدموية انخفاضاً في العدد وتغيراً في الشكل. أظهر GDNF قدرة تشخيصية واعدة في التمييز بين الأشخاص المصابين بأمراض كبد مزمنة والأشخاص الأصحاء، حيث بلغت المساحة تحت المنحني ٠,٧٤٣، مع حساسية بلغت ٨٢,٥ % ونوعية بلغت ٦٣,٢ %. الاستنتاج: تشير المستويات المرتفعة من GDNF في مرضى CLD إلى دوره المحتمل كواسم حيوي غير جراحي. وتسلط التغيرات البيوكيميائية والدموية الهامة الضوء على التأثير الجهازي لأمراض الكبد المزمنة. وتدعم هذه النتائج الحاجة إلى إجراء المزيد من البحوث حول الفائدة التشخيصية والتنبؤية لـ GDNF في أمراض الكبد.

## Comparative Analysis of Seed Morphological Traits in Egyptian Cultivated Rice and Weedy Rice

Wesam MH. Abdallah<sup>\*1</sup>, Mamdouh S. Serag<sup>1</sup>, Reham M. Nada<sup>1</sup>, Gaber M. Abogadallah<sup>1</sup> and Sami H. Rabei<sup>1</sup>

<sup>1</sup> Department of Botany and Microbiology, Faculty of Science, Damietta University, New Damietta 34517, Egypt.

Received: 15 June 2025 /Accepted: 13 July 2025

\*Corresponding author's E-mail: Wesamhamdy @du.edu.eg

### Abstract

Weedy rice is a conspecific weed of cultivated rice that threatens the production of world rice. The present study aimed to differentiate Egyptian cultivated rice from weedy rice based on seed morphological traits. Seeds from eight cultivated rice varieties and twenty-five weedy rice plants were collected from different paddy fields. The morphological similarity between weedy and cultivated rice, coupled with weedy rice rapid growth, seed dormancy, and shattering, requires efforts to distinguish between them to effectively manage this problematic weed. The seed morphological traits were documented, such as hull, pericarp, and awn color; awn, palea, and lemma length, seed width and length; grain number; and grain weight. A cladistic analysis was performed using these traits. Notable variations in seed morphology were observed between cultivated and weedy rice. Cultivated rice seeds exhibit straw-colored hulls, white pericarps, and lack awns, whereas most weedy rice seeds have brown hulls, red-brown pericarps, and either short or long awns. The presence of awns and the high seed length-to-width ratio in most weedy rice can be considered adaptive mechanisms, facilitating seed dispersal. Cultivated rice generally has a higher grain weight than weedy rice, reflecting the better endosperm development, which results in greater grain mass. Understanding these morphological variations can be used by farmers for early identification and removal to prevent seed dispersal and control weedy rice. The analysis of the cladogram, which focused on seed morphology, demonstrated a significant relationship between cultivated and weedy rice, suggesting a shared genetic basis and possibly originating from a common ancestry.

**Keywords:** Awnless; cladogram analysis; morphological traits; pericarps; weedy rice.

### Introduction

Weedy rice (*Oryza spp.*), commonly referred to as red rice, is a member of the Poaceae family and the Oryzeae tribe. Weedy rice has appeared

as one of the major global threats to rice production in direct-seeded rice fields (Ziska et al., 2015). Weedy rice is an annual grass that resembles cultivated rice (*Oryza sativa*). Weedy rice has the same growth pattern as cultivated rice, such as the vegetative phase, reproductive phase, and ripening phase (Abd Hamid et al.,

2007). Weedy rice is classified as the same species as cultivated rice (*Oryza sativa*). Two scientific names are commonly used for weedy rice includes *Oryza sativa* L. and *Oryza sativa* f. *spontanea*. Genomic data have shown that *O. sativa* L. refers to weedy rice populations derived from cultivated *O. sativa*, while *O. sativa* f. *spontanea* refers only to specifically weedy types that derived from *O. rufipogon*. Neither of these names applies to African weedy rice, which is descended from African wild rice or *O. glaberrima* lineage. Therefore, when the lineage of the weedy population is unknown, the name for the weedy rice to use is the generalized name *Oryza spp* (Burgos et al., 2021). The studied weedy rice couldn't be wild rice because of the absence of wild rice in Egypt. Further genetic studies required to illustrate the origin of Egyptian weedy rice. Easy grain shattering, a lengthy seed dormancy period, and higher nitrogen efficiency for biomass production are the traits that differentiate weedy rice from cultivated rice (Rathore et al., 2017; Ghosh et al., 2017).

Compared to cultivated rice, weedy rice also has several of unfavorable characteristics, such as the ability to germinate more quickly and persist in the soil bed for up to ten years (Ferrero, 2003). In addition to some of the unfavorable traits of weedy rice, such as long shoots, strong tillering capacity, weak culms, pale leaf color, and red pericarp (Ziska et al., 2015; Tseng, 2017).

Seeds are vital reproductive units in higher plants, and the characteristics related to their germination and dispersal play a key role in determining plant performance, distribution, population establishment, and dynamics, ultimately guiding their evolutionary path. (Chen and Giladi, 2020; Huang et al., 2015; Razzaque et al., 2023).

Seed morphology is a key trait in plant biology. During the seedling stage, weedy plants are often difficult to differentiate from crops (Hoagland and Paul, 1978). However, after tillering, weeds can be identified based on several distinct morphological characteristics compared to rice varieties. These include a greater number of tillers that are longer and more slender, leaves that are often hispid on both surfaces, increased plant height, pigmentation in various plant parts, and a tendency for easy seed dispersal once seeds form in the panicle (Diarra et al., 1985; Coppo and Sarasso, 1990; Kwon et al., 1992; Suh et al.,

1997).

The seeds of most weed biotypes of *Oryza sativa* (Asian Rice) and *Oryza glaberrima* (African Rice) possess a pigmented pericarp, which is attributed to varying levels of anthocyanins, catechins, and catecholic tannins (Baldi, 1971). Weedy rice directly impacts farmers' income by reducing crop yields and diminishing the market value of the harvested rice (Olofsdotter et al., 2000).

Therefore, the main objective of the present study is to examine the morphological variation in seeds between weedy rice and cultivated rice to explore this weedy rice. This understanding may serve as a foundational step towards managing and controlling the presence of this destructive weed, thereby preserving the culinary and quality of Egyptian rice cultivars. The data obtained from this investigation could be valuable in clarifying the relationship between weedy rice and cultivated rice.

## Materials and methods

### Field study

This investigation was based on field surveys and greenhouse farming. The selected seven sites were indicated in Table 1. The seeds of Twenty-five samples of weedy rice were collected and dried well, then stored for the next growing season. From site I, WR1, WR2, WR4, WR5, and WR6 were collected. From site II, WR 8 and WR 10 were gathered. From site III, WR 11, WR 12, WR 13, WR 15, and WR 16 were collected. From site IV, WR 17 and WR 19 were gathered. From site V, WR 20, WR 21, WR 22, and WR 23 were gathered. From site VI, WR 24, WR 25, WR 26, WR 27, and WR 28 were gathered. From site VII, WR 29 and WR 30 were collected. Cultivated rice seeds such as Giza 178, Giza 179, Sakha 101, Sakha 102, Sakha 103, Sakha 104, and Egyptian Hybrid 1 were provided by the Agricultural Research Center, Egypt. IR64 seeds were kindly supplied by International Rice Research Institute (IRRI), Manila, Philippines. The stored seeds of the cultivated and weedy rice were germinated in 15 cm x 20 cm trays containing perlite under field conditions. Trays were irrigated with a full-strength Ruakura nutrient solution (Smith et al., 1983). When the rice samples were 120 days old, morphological seed traits were measured.

**Table 1:** Geographical sites of the weedy rice

Sites Numbers	Sites	Longitude (E)	Latitude (N)
I	Ezbet Zakareya Zaher RD	31.401028	31.662861
II	Al-Hawashim village	31.404250	31.662194
III	Nagaa Al Jabaylah	31.403611	31.646500
IV	Kafr Al Batekh	31.394639	31.732917
V	Ezbet Ibrahim Hammad	31.393778	31.606333
VI	Ezbet Om El Reda	31.401833	31.621139
VII	International coastal road	31.425167	31.634972

### *Determination of seed morphological traits*

The seed morphological traits of the rice cultivars and red rice were recorded according to (IRIR, 2007). The selected seed morphological traits with information on the methods for each attribute that was measured were shown in Table 2. The recorded morphological traits were hull color, pericarp (kernel) color, awn presence, awn length (cm), awn color, palea and lemma length (cm), seed width (cm), seed length (cm), seed length to width ratio, number of grains per panicle, and grain weight (g).

**Table 2.** Seed morphological traits of the cultivated and weedy Egyptian rice, containing details on how each attribute is measured (IRIR, 2007).

Seed traits	Description
Seed length (cm)	Distance from base to tip of the grain
Seed width (cm)	Maximum width perpendicular to the length
Length to width ratio	The percentage of seed length to seed width
Awn length (cm)	Length of the awn
Awn color	Pigmentation of the awn
grain weight	Mass of a grain
pericarp color	Pigmentation of pericarp
Hull color	Pigmentation of the hull
Grains number per panicle	Counting the number of grains per panicle

### *Determination of grain dry weight (g)*

The seeds of the rice cultivars and weedy rice were collected and stored in separate seed bags made of paper, dried in air, and then the dry weights of each seed were recorded individually using a precision analytical balance for all collected rice samples.

### *2.4 Cladistic analysis based on seed morphological traits*

The morphological characteristics of the seeds were detected for cultivated rice and weedy

rice, and the data were examined using Past Software V 3.23 (folk.uio.no/ohammer/past).

### *2.5 Statistical analysis*

All measurements were replicated as stated in each section. The morphological characteristics of the seeds for the cultivated and weedy rice were recorded, and the data were analyzed using Past Software V 3.23 to generate cladograms. A one-way ANOVA was performed using SigmaPlot v11.0 to assess differences in grain weight. Significance was defined at  $P \leq 0.05$ .

## **Results**

### *Morphological traits of the seed for cultivated and weedy rice*

Significant variation in seed morphology is observed between the cultivated rice and weedy rice, as illustrated in (Table 3) (Fig. 1). The hull color of all examined cultivated rice as well as WR 6, WR 10, WR 16, WR 20, WR 21, WR 23, and WR 30 is straw. The pericarp color is white in all studied cultivated rice and in WR 2, WR 6, WR 10, WR 11, WR 12, WR 13, WR 15, WR 17, WR 22, WR 23, WR 27, WR 29, and WR 30. In contrast it is light red-brown in WR 4, WR 5, WR 8, WR 20, WR 25, WR 26, and WR 28, and red-brown in WR 1, WR 16, WR 19, WR 21, and WR 24. All examined cultivated rice along with WR 16, WR 19, WR 20, WR 24, WR 25, WR 26, and WR 28 are awnless; whereas, the remaining weedy rice samples possess awns. The awn color among the studied weedy rice population varies with WR 1, WR 2, WR 4, WR 6, WR 11, WR 12, WR 13, WR 16, WR 17, and WR 23 exhibiting white awns; WR 5, WR 8, WR 10, WR 15, WR 21, WR 22, and WR 27 displaying straw-colored awns; and WR 29 and WR 30 having red awns. Awn length also varies among the weedy rice samples, specifically WR 1, WR 2, WR 5, WR 8, WR 13, WR 21, WR 23, WR 17, WR 27, and WR 29. Most weedy rice plants exceed cultivated rice in seed length-to-width ratio with the exception of IR64. Additionally, most weedy rice plants surpass cultivated rice in the number of grains per panicle, except for G 178.



**Table 3.** Seed morphological characters and character state of the studied cultivated and weedy rice.

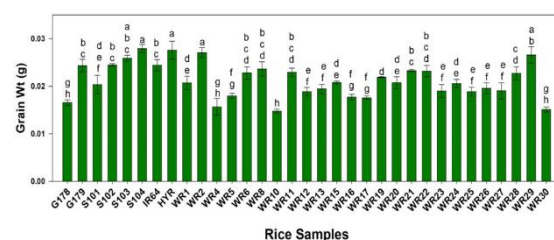
Seed traits		Rice samples																																		
characters	Character state	G 178	G 179	S 101	S 102	S 103	S 104	IR64	HYR	WR1	WR2	WR4	WR5	WR6	WR8	WR10	WR11	WR12	WR13	WR15	WR16	WR17	WR19	WR 20	WR 21	WR 22	WR 23	WR 24	WR 25	WR 26	WR 27	WR 28	WR 29	WR 30		
1. hull color	1.straw 2.brown	1	1	1	1	1	1	1	1	2	2	2	1	1	2	1	2	2	2	2	1	2	2	1	1	2	1	2	2	2	2	2	2	2	1	
2. pericarp color	1.white 2.light red brown 3.red brown	1	1	1	1	1	1	1	1	3	1	2	2	1	2	1	1	1	1	1	3	1	3	1	3	2	3	1	1	3	2	2	1	2	1	1
3. palea/lemma length(cm)	-	0.8	0.8	0.9	0.9	0.8	0.9	1	1	0.7-0.8	0.6	0.8	0.7-0.8	0.8	0.8	0.9-1	0.8	1	1	0.9	0.7	1	0.7	0.7-0.9	0.8-0.9	0.8	0.7	0.7	0.8	0.9	0.9	1	0.9	0.7		
4. seed length (cm)	-	0.7	0.7	0.8	0.8	0.7	0.8	0.9	0.8	0.6	0.5	0.7	0.6	0.7	0.8	0.8	0.7	0.9	0.9	0.8	0.9	0.9	0.6	0.7	0.7	0.7	0.6	0.7	0.8	0.8	0.9	0.6	0.8	0.9	0.9	
5. seed width (cm)	-	0.3	0.3	0.3	0.4	0.3	0.4	0.2	0.3	0.3	0.3	0.2	0.3	0.2	0.3	0.3	0.3	0.3	0.3	0.3	0.2	0.3	0.3	0.3	0.3	0.2	0.3	0.4	0.3	0.3	0.3	0.3	0.3	0.3		
6. seed length/width%	-	2.1	2.3	2.6	2	2.3	2	4.5	2.6	2	1.6	3.5	2	3.5	2.3	2.4	2.3	3	3	4	3	3	2	2.3	2.4	3.5	2	2	1.75	2.7	2	3	2.6	2		
7. Awn presence)	1.present 2.abscent	2	2	2	2	2	2	2	2	1	1	1	1	1	1	1	1	1	1	1	2	1	2	2	2	1	1	2	2	2	1	1	1	1		
8. Awn length(cm)	1.short 2.long 3.awnless	3	3	3	3	3	3	3	3	1	1	1	1	2	1	2	1	2	1	2	1	2	1	3	3	2	1	1	3	3	3	1	1	2		
9. awn color	1.white 2.straw 3.red 4.awnless	4	4	4	4	4	4	4	4	1	1	1	2	1	2	2	1	2	1	1	1	3	2	4	4	2	2	1	4	4	4	2	4	3	3	
10. no grains/panicle	of -	120-124	29-35	30-33	41-47	79-83	75-80	53-58	53-55	32-37	11-15	34-38	73-77	39	49-55	53-59	40-43	84-90	65-71	135-141	21-29	66	102-110	43-45	98-104	38-40	60-61	85-89	79-85	19-23	66-70	111-114	45-51	43-47		
11. grain weight (g)	-	0.02	0.024	0.02	0.024	0.03	0.03	0.024	0.03	0.021	0.03	0.02	0.018	0.023	0.024	0.013	0.023	0.018	0.019	0.02	0.017	0.017	0.022	0.02	0.02	0.023	0.019	0.02	0.018	0.02	0.019	0.02	0.03	0.015		

**Fig.1** Seed morphological traits of Egyptian cultivated and weedy rice.

#### Determination of grain weight of the cultivated and weedy rice

Grain weight was observed to be significantly higher in S 104, followed by HYR and WR 29, in comparison to other rice samples (Fig. 2). The maximum grain weight among cultivated rice was recorded in G 104, whereas the minimum grain weight was observed in G 178. In the case of weedy rice, WR 29 exhibited the highest grain weight, while WR 10 had the lowest grain weight. Generally,

most cultivated rice tends to exceed in terms of grain weight.

**Fig. 2** Changes of grain weight of the cultivated and weedy rice. Data are means  $\pm$  SE. Bars labeled with different letters are significantly different at  $P \leq 0.05$ .

#### Cladistics analysis of the cultivated rice and weedy rice according to seed morphological traits

Cladistic analysis categorized the 33 samples into three principal groups (GI–GIII) (Fig. 3), with distinct subgroups comprised both cultivated and weedy samples. The first group

(GI) was further divided into two subgroups (SGI-SGII); the first subgroup included WR 15, while the second subgroup comprised WR 19, WR 21, WR 28, and G 178. The second group (GII) was subdivided into four subgroups (SGI-SGIV); the first subgroup contained WR 8, WR 29, WR 10, IR64, and HYR; the second subgroup comprised WR 13, WR 27, WR 17, and WR 23; the third subgroup included WR 5, WR 25, S 103, and S 104; and the fourth subgroup involved WR 12 and WR 24. The third group (GIII) was subdivided into three subgroups (SGI-SGIII); the first subgroup comprised WR 6, WR 22, WR 11, WR 20, WR 30, and S 102; the second subgroup included WR 4, WR 1, G 179, and S 101; and the third subgroup comprised WR 16, WR 26, and WR 2.

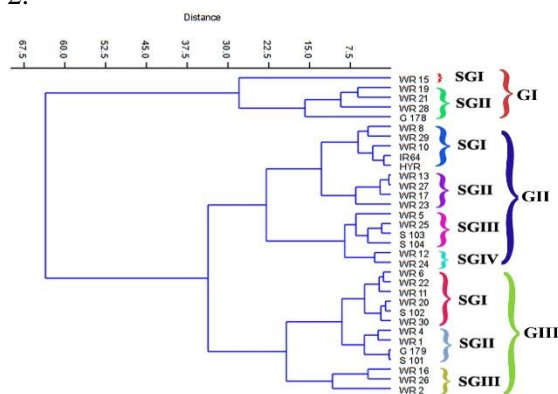


**Fig. 3.** Cladograms illustrate the relationship between cultivated rice and weedy rice based on seed morphological traits.

## Discussion

Egyptian weedy rice is an invasive paddy weed that infests rice paddies, leading to significant rice yield losses (Abdallah et al. 2025). Distinguishing cultivated rice from weedy rice is only feasible after the formation of panicles and seeds. Seed characteristics are believed to undergo strong environmental selection due to their substantial implications for fitness (Hierro et al., 2009; Chen and Giladi, 2020). Notable differences in seed morphological characteristics between the cultivated and weedy rice have been observed (Fig. 1). However, these seed traits have not been extensively studied in biogeographical research. Cultivated rice exhibits straw-colored hulls and white seed pericarps; whereas, more than half of the collected weedy rice samples exhibit brown hulls and reddish-brown pericarps, traits

associated with genes like Rc (Debeaujon et al., 2000). These pigments in weedy rice seeds may specify advantages such as protection from predators and environmental stresses; although they also reduce the quality of Egyptian milled rice.

The seed length-to-width ratio is generally higher in most weedy rice plants compared to cultivated rice, with the exception of IR64. Additionally, the presence of awns in most weedy rice indicates an adaptation for dispersal, either by attachment to animals or wind transport. The variation in the awn color and length among all the studied weedy rice populations reflects differing degrees of environmental adaptation and evolutionary advancement. Most weedy rice plants surpass cultivated rice in grain quantity per panicle, except for G 178, which may enhance their survival and proliferation under agricultural and natural selection pressures, thereby increasing their evolutionary fitness. This is indicative of their resilience in agroecosystems, fitness advantages, and reproductive strategy. The grain weight of most cultivated rice is higher than that of weedy rice (Fig. 2). Grain filling influences both grain weight and quality (Zhou et al., 2013), suggesting that grain filling is more efficient in cultivated rice than in weedy rice. This efficiency is attributed to the more complete endosperm development in cultivated rice than weedy rice resulting in higher grain mass. The lower grain weights of weedy rice may reflect trade-offs between seed quantity and investment per seed. The variations in seed traits of weedy rice confer an advantage over the crop, enabling it to withstand various abiotic stresses and adapt to diverse cropping techniques and changing environmental conditions (Fogliatto et al., 2012). Seed morphology is instrumental in the identification and classification of plants and weeds (Noda et al., 1985). Seed morphology has been shown to provide valuable characters for taxonomic relationships of plant families (Barthlott, 1981; Barthlott, 1984; Shetler, 1986). Understanding the variations in seed morphology between cultivated and weedy rice can aid in the management of weedy rice. These visible variations can be used by farmers for early identification and removal before complete heading to prevent seed dispersal. Additionally, they can guide the development of **selective herbicides** that allow control of targeted weedy rice.

According to seed morphology, cladogram analysis reveals a close relationship between cultivated rice and weedy rice (Fig. 3). Specifically, WR 15, WR 19, WR 21, and WR 28 are grouped with G 178, while WR 8, WR 29, and WR 10 are categorized in the same subgroup as IR64 and HYR. Additionally, WR 5 and WR 25 are clustered with S 103 and S 104; WR 6, WR 22, WR 11, WR 20, and WR 30 are grouped with S 102. Furthermore, WR 4 and WR 1 are clustered with G 179 and S 101, indicating the seed morphological similarities. These similarities suggest a common genetic background and a potentially shared origin. The accurate identification and differentiation of weedy rice from cultivated rice cannot depend on seed morphology alone due to the high seed morphological similarities between cultivated rice and some weedy rice. Therefore, it should be combined with physiological traits and genetic analysis.

## Conclusion

This study offers a comprehensive morphological assessment of Egyptian cultivated and weedy rice seeds, emphasizing significant differences that are useful for identification and management. Cladogram analysis supports the hypothesis of shared ancestry and evolutionary convergence. These findings are foundational for developing targeted weed control strategies and preserving rice grain quality in Egypt.

## Reference

- Abd Hamid AZ, Mansor M, Man A (2007) Life Cycle And Morphological Characteristics Of Weedy Rice (*Oryza Sativa* Complex, Locally Called Padi Angin), A Noxious Weed Of Rice fields In MALAYSIA. *Jurnal Biosains*. 18(1): 55–79
- Baldi G (1971) Presenza del carattere Pericarpo rosso in varietà di riso coltivate (*O. sativa*). *Il riso* 20: 299-302.
- Barthlott W (1981) Epidermal and seed surface characters of plants: systematic applicability and some evolutionary aspects. *Nordic Journal of Botany* 1: 345-355.
- Barthlott W (1984) Microstructural features of seed surface. In: V. H. Heywood and M. Moore (eds.), *Current Concepts in Plant Taxonomy*. Academic Press, London. pp.: 85-106.
- Burgos NR, Sudo MPS, Olsen KM, Werle I and Song BK (2021) Weedy rice (*Oryza* spp.): what's in a name? *Weed Science* 69(5):505 – 513.
- Chen SC, Giladi I (2020) Variation in morphological traits affects dispersal and seedling emergence in dispersive diaspores of *Geropogon hybridus*. *Am. J. Bot.* 107: 436–444. [CrossRef] [PubMed]
- Coppo B, Sarasso G (1990) Il riso crodo. In *Quaderno Agricolo, Istituto Federale di Credito Agrario, Piemonte, Liguria e Valle d'Aosta* 22: pp.15-29.
- Debeaujon I, Léon-Kloosterziel KM, Koornneef M (2000) Influence of the testa on seed dormancy, germination, and longevity in *Arabidopsis*. *Plant Physiol.* 122: 403–414.
- Diarra ARJ, Smith RJ, Talbert RE (1985) Red rice (*Oryza sativa*) control in drill-seeded rice (*Oryza sativa*). *Weed Sci.* 33: 703-707.
- Ferrero A (2003) Weedy rice, biological features and control. In Labrada, R. (ed.) *Weed management for developing countries*. FAO, Rome, Italy. p. 89-107.
- Fogliatto S, Vidotto F, Ferrero A (2012) Morphological characterisation of Italian weedy rice (*Oryza sativa*) populations. *Weed Res.* 52: 60–69.
- Ghosh D, Rathore M, Brahmachari K, Singh R, Kumar B (2017) Impact of burial and flooding depths on Indian weedy rice. *Crop Protection* 100: 106-110.
- Hierro JL, Eren Ö, Khetsuriani L, Diaconu A, Török K, Montesinos D, Andonian K, Kikodze D, Janoian L, Villarreal D et al. (2009) Germination responses of an invasive species in native and non-native ranges. *OIKOS*. 118: 529–538.
- Hoagland RE, Paul RN (1978) A comparative study of red rice and several commercial rice (*Oryza sativa*) varieties. *Weed Sci.* 6: 619-625.
- Huang FF, Peng SL, Chen BM, Liao HX, Huang QQ, Lin ZG, Liu G (2015) Rapid evolution of dispersal-related traits during range expansion of an invasive vine *Mikania micrantha*. *OIKOS*. 124: 1023–1030. [CrossRef].
- International Rice Research Institute (IRRI); The Africa Rice Center (WARDA) (2007) *Descriptors for wild and cultivated rice (Oryza spp.)*. Bioversity International.
- Kwon SL, Smith RJ, Talbert RE (1992) Comparative growth and development of red rice (*Oryza sativa*) and rice (*O. sativa*). *Weed Sci.* 40: 57-62.
- Noda K, Prakongvongs C, Chaiwiratnukul L (1985) Topography of the seeds and leaves of tropical weeds – with a scanning electron microscope. National Weed Science Research Institute Project, 158.
- Olofsdotter M, Valverde BE, Madsen KH (2000) Herbicide resistant rice (*Oryza sativa* L.): global

- implications for weedy rice and weed management. *Ann. Appl. Biol.* 137: 279–295.
- Rathore M, Singh R, Kumar B, Chauhan BS (2017) Characterization of functional trait diversity among Indian cultivated and weedy rice populations. *Scientific Reports*. 6:24176.
- Razzaque S, Heckman RW, Juenger TE (2023) Seed size variation impacts local adaptation and life-history strategies in a perennial grass. *Proc. R. Soc. B Biol. Sci.* 290: 20222460. [CrossRef] [PubMed].
- Shetler SJ (1986) Seed morphology in North American Campanulaceae. *Annals of the Missouri Botanical Garden*. 73: 653-688.
- Smith GS, Johnston CM, Cornforth IS (1983) Comparison of nutrient solutions for growth of plants in sand culture. *New Phytologist* 94: 537–548.
- Suh HS, Sato YI, Morishima H (1997) Genetic characterization of weedy rice (*Oryza sativa* L.) based on morpho-physiology, isozymes and RAPD markers. *Theoretical applied Genetics*. 94: 316-321.
- Tseng TM, Shivrain VK, LawtonRauh A, Burgos NR (2017) Dormancy linked population structure of weedy rice (*Oryza sativa*). *Weed Science*. 66:331-339. DOI: 10.1017/wsc.2017.86.
- Zhou B, Li S, Peng X, Kuang Q, Huang X, Yao J, Du B, Sun MX (2013) OsFIE2 plays an essential role in the regulation of rice vegetative and reproductive development. *New Phytol.* 201(1):66-79.doi: 10.1111/nph.12472.
- Ziska LH, Gealy DR, Burgos N, Caicedo AL, Gressel J, Lawton-Rauh AL et al. (2015) Weedy (red) rice: an emerging constraint to global rice production. *Adv. Agron.* 129: 181228.

## الملخص العربي

### عنوان البحث: التحليل المقارن للصفات الشكلية لبذور الأرز المصري المزروع والأرز العشبي

وسام محمد حمدي عبدالله<sup>1\*</sup>، ممدوح سالم سراج<sup>1</sup>، ريهام محمد ندا<sup>1</sup>، جابر مختار ابوجادالله<sup>1</sup>، سامي حسين ربيع<sup>1</sup>

<sup>1</sup> قسم النبات والميكروبيولوجي-كلية العلوم –جامعة دمياط – دمياط - مصر

الأرز العشبي هو حشيشة من نفس نوع الأرز المزروع، ويُشكل تهديداً لإنتاج الأرز العالمي. هدفت الدراسة الحالية إلى التمييز بين الأرز المصري المزروع والأرز العشبي استناداً إلى الصفات الشكلية للبذور. تم جمع بذور من ثمانية أصناف مزروعة من الأرز وخمسة وعشرين نباتاً من الأرز العشبي من حقول أرز مختلفة. إن التشابه المورفولوجي بين الأرز العشبي والمزروع، إلى جانب النمو السريع للأرز العشبي ووجود طور الكمون للبذور وسهولة تساقطها، يستدعي بذل الجهود للتمييز بينهما من أجل الإدارة الفعالة لهذه الحشيشة المزعجة.

تم توثيق الصفات الشكلية للبذور مثل لون الحبة، والطبقة الخارجية (الغلاف)، ولون السفا (الزوائد الشبيهة بالشعيرات)؛ وطول السفا، وطول وعرض الغمد والقنابة؛ وعرض وطول البذرة؛ وعدد الحبوب ووزن الحبوب. وأجري تحليل تفرعي (Cladistic analysis) باستخدام هذه الصفات. وقد لوحظت اختلافات واضحة في شكل البذور بين الأرز المزروع والعشبي. تظهر بذور الأرز المزروع غلافاً بلون قشي وحبّة لونها أبيض، وتفتقر إلى سفا. في حين أن معظم بذور الأرز العشبي تمتلك أغلفة بنية اللون، وحبّة لونها بني محمر، مع وجود سفا قصيرة أو طويلة. يمكن اعتبار أن وجود السفا والنسبة العالية لطول البذرة إلى عرضها في معظم الأرز العشبي آليات تكيفية تساعد في انتشار البذور. عموماً، يتميز الأرز المزروع بوزن حبة أعلى من الأرز العشبي، مما يعكس تطور الإندوسبيرم (السويداء) بشكل أفضل وبالتالي زيادة كتلة الحبة. إن فهم هذه الاختلافات الشكلية يمكن أن يساعد المزارعين في التعرف المبكر على الأرز العشبي وإزالته لمنع انتشار بذوره والسيطرة عليه..

## Comprehensive Evaluation of Morphological, Anatomical, and Palynological Characteristics of some Selected Taxa of Zygophyllaceae in Egypt.

Amal A. Draz<sup>\*1</sup>, Hasnaa A. Hosni<sup>2</sup>, Salwa A. Kawashty<sup>1</sup>, Sameh R. Hussein<sup>1</sup> and Eman M. Shamso<sup>2</sup>

<sup>1</sup> Phytochemistry and Plant Systematics Department, Pharmaceutical and Drug Industries Research Institute, National Research Centre, Cairo, Egypt, PO Box 12622.

<sup>2</sup> Botany and Microbiology Department, Faculty of Science, Cairo University, Giza, P.O. 12613, Egypt.

Received: 09 July 2025 /Accepted: 21 July 2025

\*Corresponding author's E-mail: [amal.draz@outlook.com](mailto:amal.draz@outlook.com)

### Abstract

This study presents a comprehensive comparative analysis of six Egyptian taxa from the family Zygophyllaceae, representing the genera *Fagonia*, *Zygophyllum*, and *Tribulus*. An integrative approach was employed, combining morphological, anatomical, and palynological investigations using both light microscopy (LM) and scanning electron microscopy (SEM). The main objective was to evaluate the taxonomic significance of these characters and enhance species identification and classification within the family. Morphological assessments included leaf structure, floral and fruit morphology, and seed characteristics. Anatomical studies focused on the tissue organization of stems, petioles, and leaf blades, with emphasis on epidermal features, vascular patterns, and crystal distribution. Palynological analysis revealed significant variation in pollen size, polarity, aperture types, and exine ornamentation. A total of 219 characters were scored and analyzed statistically using Minitab software. Cluster analysis and dendrogram construction revealed a clear separation of *Tribulus* species from *Fagonia* and *Zygophyllum* simplex, which conversely showed closer affinities. These findings highlight the diagnostic value of integrating morphological, anatomical, and palynological data, and support the recognition of *Tribulus* at a distinct taxonomic rank within Zygophyllaceae. Collectively, these characters provide valuable tools for the accurate delimitation and identification of taxa at both generic and specific levels.

**Keywords:** Anatomical characters, Cluster analysis, Macromorphological characters, Palynological characters, Zygophyllaceae.

### Introduction

Zygophyllaceae R.Br. (s.l.) is a large and

heterogenous family comprising approximately 285 species across 22 genera, mostly distributed in arid and semi-arid regions of the Old World, particularly in Africa, and extending into warm

temperate zones. Most species inhabit xerophytic and halophytic environments (Christenhusz and Byng, 2016). The delimitation of taxa within the family has changed multiple times due to the structural diversity and variable plasticity of its members. As a result, the family has long been a subject of taxonomic controversy. Additionally, some of its genera were even separated and treated as distinct families (Engler, 1931; Takhtajan 1969, 1986 & 2009; Cronquist 1988; Heywood et al., 2007; Shipaunov, 2012). In light of recent molecular phylogenetic analyses, integrated with morphological and anatomical data, the taxonomic position of Zygophyllaceae has been reassessed and redefined. Based on the recent molecular findings of Sheahan and Chase (1996, 2000), Beier et al. (2003), and APG III (2009), the family has been reclassified under the order Zygophyllales, alongside Krameriaceae. Currently, Zygophyllaceae is divided into five subfamilies viz.: Zygophylloideae, Morkillioideae, Tribuloideae, Seetzenioideae and Larreoideae; in which the Zygophylloideae recognized as the largest and strongly supported as a monophyletic group. This subfamily includes four genera: *Zygophyllum* L., *Fagonia* L., *Roepera* A. Juss., and *Tetraena* Maxim (Stevens 2001, onwards). From a palynological perspective, Zygophyllaceae is recognized as a eurypalynous family (Erdtman, 1952; Punt et al., 2007). Accordingly, the study of pollen morphology within this family plays a significant role in elucidating taxonomic relationships and affinities among its taxa. The pollen morphology of the Zygophyllaceae has been extensively studied by several authors. Early investigations were conducted by Erdtman (1952), Kuprianova and Alyoshina (1978), and Yunus and Nair (1988), with further contributions from more recent investigations by Perveen and Qaiser (2006), Bukhari et al. (2014), El-Atroush et al. (2015) and Taia et al. (2021). Perveen and Qaiser (2006) studied the pollen of 14 species representing five genera from Pakistan, recognizing four distinct pollen types and highlighting the diagnostic value of palynological characters at both generic and specific levels. Similarly, Bukhari et al. (2014) investigated selected species from Saudi Arabia, adding valuable insights to the regional palynological record. In a more focused study, Taia et al. (2021) examined 12 taxa of *Fagonia* from Libya and concluded that pollen

characteristics provide limited taxonomic delimitation within the genus.

Several studies have highlighted the significance of anatomical characters in the taxonomic classification of the family Zygophyllaceae. Metcalfe and Chalk (1957) established detailed anatomical characters of stems, petiole and leaves, while subsequent studies have highlighted the significance of internal vegetative features in distinguishing genera and species. Sheahan and Cutler (1993) examined 37 species across 19 genera, identifying diagnostic traits such as cuticle thickness, hypodermis, crystal types, pith structure, and venation patterns that distinguish subfamilies like Tribuloideae and Zygophylloideae. In *Tribulus* and *Fagonia*, various studies (e.g., Khalifa, 1968; Ahmed and Khafagi, 1997; Ahmed and Mohamed, 2005b) have investigated stem, leaf, petiole, and stipule anatomy, emphasizing their role in supporting generic boundaries and aiding reclassification. Additional investigations focusing on seed morphology, trichome types, and petiole vasculature (Ahmed, 1991; Khafagi, 2004; Abdel Khalik and Hassan, 2012) have further supported species-level distinctions. Regional anatomical studies from Saudi Arabia, Libya and Sudan (Waly et al., 2011; Elkamali et al., 2016; Taia et al., 2017; Gabr and Ragab, 2023) emphasized the taxonomic value of mesophyll structure, stele type, and crystal distribution in distinguishing *Tribulus*, *Fagonia*, *Zygophyllum*, and *Tetraena* species, further confirming the systematic significance of vegetative anatomy in Zygophyllaceae. Based on numerical analyses, Abdel Khalik (2012) investigated Egyptian species of Zygophyllaceae using morphological, palynological, and seed characteristics. The study revealed that, although the family is generally heterogeneous, the subfamilies Tribuloideae, Zygophylloideae, Seetzenioideae, and Tetradielidoideae are relatively homogeneous. It also suggested that traditional groupings within *Tribulus* and *Fagonia* seem to be artificial. Similarly, Shamso et al. (2013) analysed morphological data from eight genera and identified three distinct groups: one corresponding to Tribuloideae (*Tribulus*), a second to Zygophylloideae (*Zygophyllum* and *Fagonia*), and a third comprising *Seetzenia*, *Peganum*, and *Nitraria*, further supporting broader taxonomic distinctions within the family.



Furthermore, chemosystematic studies and DNA fingerprinting conducted by Draz et al. (2024; 2025) supported the taxonomic delimitation of species within the genera *Fagonia*, *Tribulus*, and *Zygophyllum*. Their study also investigated the genetic variability of *T. terrestris* across different populations, providing valuable insights into its genetic plasticity and adaptability.

In Egypt, the family Zygophyllaceae s.s. is represented by 33 species across five genera (Boulos, 2000, 2009). In the present study, six taxa belonging to three genera (*Fagonia*, *Tribulus*, and *Zygophyllum*) were investigated in detail. Morphological, palynological, and anatomical characteristics were examined using both light microscopy (LM) and scanning electron microscopy (SEM). The main objective of this study is to assess the taxonomic significance of these traits in selected species of Zygophyllaceae and to provide additional data to support species identification and classification within the family. Furthermore, the study aims to evaluate the degree of affinity and interrelationships among the investigated taxa through the application of numerical analysis.

## Materials and methods

### Plant materials

The present study was based on the examination of specimens kept in major Egyptian herbaria: Cairo University (CAI), the Agriculture Museum, Flora and Phytotaxonomy Researchs (CAIM), and National Research Centre (CAIRC), (Herbaria acronyms according to Thiers (2024); continuously updated). Additionally, fresh specimens were collected from various locations between March and April 2022 (Table 1). The identification of these specimens was confirmed by comparing them to collections located at the Herbarium of Cairo University and using several regional floras (Täckholm, 1974; Boulos, 2000; Zohary, 1972; Chaudary, 2001). The nomenclature of all taxa was updated according to several online databases, including *The Plant List* ([www.theplantlist.org](http://www.theplantlist.org)) and the *International Plant Names Index* ([www.ipni.org](http://www.ipni.org)). For taxa belonging to the genus *Fagonia*, the nomenclature followed additional sources such as *iNaturalist* ([www.inaturalist.org](http://www.inaturalist.org)), *Tropicos* ([www.tropicos.org](http://www.tropicos.org)), and the *Euro+Med PlantBase*.

**Table 1:** List of studied taxa, localities, and data of collection

Taxa	Locality, Date & collector	Voucher No.
<i>Tribulus pentandrus</i>	- Nasr City, Azhar Univ. for girls, 12/4/2022, Draz et al. s.n. (CAIRC)	- A313
	- Helwan, 31/1/1975, H. Hosni et al. s.n. (CAI)	- cai. 49.249.783.139
	- Wadi Angabiya, Suez Road 16/3/1956, El Hadidi & Batanouny s.n. (CAI)	- cai. 49.249.783.140
<i>Tribulus terrestris</i> var. <i>terrestris</i>	-Nasr City, Azhar Univ. for girls, 12/4/2022, Draz et al. s.n. (CAIRC)	- A307
	- N Qostul, Nubia, 29/12/1963, L. Boulos s.n. (CAI)	- cai. 49.249.784. 213
	-Gebel Catherine, Sinai, 21/8/1982, El Hadidi et al. s.n. (CAI)	- cai. 49.249.784. 214
<i>Tribulus terrestris</i> var. <i>orientalis</i>	-Oases Road, 6 <sup>th</sup> October City, Dream Park zone; 23/4/2022, Draz et al. s.n. (CAIRC)	- A308
	-80 Km Cairo-Fayoum desert road; 27/4/2022, Draz et al. s.n. (CAIRC)	- A309
	-Cairo University, 2/7/1976; Sisi s.n. (CAI)	- cai.49.249.784.02
	-Abu Zaabal, 31/8/1967, El Hadidi & Khattab s.n. (CAI)	- cai.49.249.784.02
<i>Fagonia glutinosa</i>	-Near Alameen desert, Matrouh governorate, 18/3/2022, Draz et al. s.n. (CAIRC)	- A311
	-Along Cairo-Alex desert road, South Tahrir province; 26/2/1968, Romee s.n. (CAI)	- cai.48.246.757.136
	-Wadi Natroun, 1/5/ 1976; Chertek s.n. (CAI)	- cai. 48.246.757.137
	-Burg El Arab, Maruit, 23 Apr 1929, Drar s.n. (CAIM)	- s.n.
<i>Fagonia scabra</i>	-Near Alameen desert, Matrouh governorate, 18/3/2022, Draz et al. s.n. (CAIRC)	- A312
	-Sinai, Mittla Pass; 7/4/1990; I. El Garf s.n. (CAI)	- cai. 48.246.764.87
	-Wadi Hof; 24/2/1956; M. Imam s.n. (CAI)	- cai. 48.246.764.88
	- Wadi Seyal, Red Sea, 4 Mar 1960, Hilaly & Khattab s.n. (CAIM)	- s.n.
<i>Zygophyllum simplex</i>	-Dabaa road, 72 km from Cairo, 18/3/2022, Draz et al. s.n. (CAIRC)	- A310
	-Alex-Cairo desert road, 85 Km from Cairo, 23/7/1970, Ibrahim & Mahdi s.n. (CAI)	- cai. 48.248.269.232
	- Siwa-Matruh road, 25/1/1987, A Fahmy, 39 (CAI)	- cai. 48.248.269.233

### *Morphological examination*

Morphological data were obtained from both fresh and herbarium specimens. For each taxon, at least 3–4 specimens (if available) were selected to reflect the morphological diversity observed within the species. The examined characters included habit, vegetative structures, as well as floral and fruit features (Table 2).

### *Pollen grains and seed examinations*

Pollen samples and seeds were obtained from the anthers of mature unopened flowering buds, while the seeds were collected from mature fruits. Pollen grains for light microscopy (LM) were produced following Erdtman's (1960) method and subsequently mounted in drops of glycerin jelly. Light microscopic examinations were performed using a Serico research microscope at (E 40, 0.65) with a 16x eyepiece, and the seeds were examined with a dissecting microscope. For SEM examination, Pollen and seeds were fixed onto stubs using double-sided tape. The stubs were subsequently coated with gold utilizing an Ion-sputter JFC-1100 apparatus. The samples were examined using a FE-SEM QUANTA FEG250Y at the Electron Microscopy Unit, National Research Centre, Dokki, with an accelerating voltage of 20 KV. A minimum of 15-20 pollen grains per specimen was measured. Pollen characteristics, such as shape, size, aperture type, and exine ornamentation, were evaluated (Table 3). Pollen terminology is followed Punt et al. (2007), Hesse et al. (2009), and Halbritter et al. (2018), whereas seed coat terminology is based on Barthlott (1981).

### *Anatomical examination*

For anatomical analysis, 3–5 specimens of the fourth internodes from the apex, mature blade, and petiole (if present) were selected and preserved in Formalin Acetic Alcohol (FAA) to preserve internal tissue structures. The samples were processed using the paraffin wax method following Johansen (1940) to prepare them for microtome sectioning at a thickness of 10–15 µm. Sections were mounted on glass slides using Haupt's adhesive, prepared by dissolving 1 g of gelatin in 50 ml of warm distilled water, followed by the addition of 7.5 ml of glycerol and a small phenol crystal, and refrigerating for

24 hours until solidified. After drying for 24 hours, the sections were stained using the standard Safranin-Fast Green double staining technique and mounted in Canada balsam (Sass, 1958). Sometimes, hand sectioning was also performed.

For epidermal studies, three pieces of lamina were treated with 5% KOH for 24 – 48 hr. to clear the tissues. Both the upper and lower epidermal layers were examined under a light microscope for stomatal and trichome characteristics. Terminology followed Metcalfe and Chalk (1957) and Evert 2006, and anatomical descriptions are summarized in Tables (4-6).

### *Statistical analysis*

A multivariate clustering analysis was performed on a data matrix comprising 219 morphological, palynological, and anatomical character states of six studied taxa using Minitab statistical software (version 2022). After the analysis, a dendrogram would be plotted, displaying the similarity and distance levels among the investigated taxa.

## **Results**

Using both light microscopy (LM) and scanning electron microscopy (SEM), six taxa representing three genera within the family Zygophyllaceae were investigated for their morphological, anatomical and palynological characteristics in order to identify the most important characters for taxonomic identification and differentiation. The diagnostic features observed are summarized in cumulative tables (2-6) and in Plates (1-6), with each character encoded in binary form (0/1) to facilitate comparative analysis. The studied taxa exhibited considerable variation in both macro- and micro-morphological traits, supporting their clear delimitation at both interspecific and intergeneric levels.

### *Macro-morphological variations*

The most informative and diagnostic morphological characters among the studied taxa were observed in both vegetative and reproductive structures, including growth habit, stem characteristics, leaf composition, and surface texture, as well as floral and fruit

morphology (Table 2). *Tribulus* taxa characterized by an herbaceous habit, paripinnate leaves with scarious stipules, and eglandular trichomes. In contrast, *Fagonia* species exhibit a suffrutescent growth form, unequal trifoliate leaves with spiny stipules, and glandular trichomes. *Zygophyllum simplex* is morphologically distinct from both genera, possessing sessile, unifoliate succulent leaves with scarious stipules, glabrous and a decumbent habit.

Floral morphological characters also showed significant variation among the studied taxa, particularly in flower size, sepal persistence, petal color, and structural traits at the stamen base. *Tribulus* taxa were distinguished by relatively large flowers (>10 mm in diameter), persistent sepals, yellow petals, and the presence of intrastaminal glands, while *Fagonia* species featured medium-sized flowers with mucronate, persistent sepals and violet petals. In contrast, *Zygophyllum simplex* exhibits the most distinct floral morphology, characterized

by the smallest flowers (<5 mm in diameter), caducous sepals, clawed yellow petals, and the presence of filament scales. At the generic level, *Tribulus* species distinguished by their schizocarpic fruits, with tuberculate, hairy surfaces and prominent features such as dentate wings or spines. In contrast, *Fagonia* and *Zygophyllum* produce capsular fruits with variable shapes and surface textures, ranging from smooth to moderately hairy. Seed morphology provided additional micro-level diagnostic features, with distinct differences in seed shape, hilum position, and surface sculpturing. *Tribulus* species exhibited a reticulate seed surface, with prolonged ellipsoid to obovoid shapes and a terminal hilum; while *Fagonia* showed puncticulate seed surfaces with globular projections, suborbicular seed shapes, and a subterminal hilum. In contrast, *Zygophyllum simplex* characterized by smooth, ellipsoid seeds and a terminal hilum, further emphasizing its unique taxonomic identity within the group (Plate 1).

**Table 2:** Data matrix of Morphological characters for six studied taxa of Zygophyllaceae. (0 = absent, 1 = present):

Organ	Character	Character state	<i>Tribulus pentandrus</i>	<i>T. terrestris</i> var. <i>terrestris</i>	<i>T. terrestris</i> var. <i>orientalis</i>	<i>Fagonia glutinosa</i>	<i>F. scabra</i>	<i>Zygophyllum Simplex</i>
Plant	Habit	Herb	1	1	1	0	0	1
		Shrub or Low shrub	0	0	0	1	1	0
	Duration	Annual	1	1	1	0	0	0
		Biennial	1	0	0	0	0	0
Stem	direction	Perennial	0	0	0	1	1	1
		Prostrate	1	1	0	1	0	0
		Ascending	0	0	1	0	0	0
		Procumbent	0	0	0	0	1	0
	Surface	Decumbent	0	0	0	0	0	1
		Pubescent	1	0	0	0	0	0
		Densely hairy	0	1	1	0	0	0
		Glandular hairs	0	0	0	1	1	0
		Glabrous	0	0	0	0	0	1
		Simple	0	0	0	0	0	1
Leaf or leaflet	Division of leaves	compound	1	1	1	1	1	0
		Size	Equal	1	1	0	0	1
	Number of leaflets	Unequal	0	0	0	1	1	0
		Many-foliolate	1	1	1	0	0	0
		Trifoliate	0	0	0	1	1	0
		Unifoliate	0	0	0	0	0	1
	Shape	Ovate-rhombical	0	0	0	1	0	0
		Elliptic-lanceolate	1	1	1	0	0	0
		Ovate-oblong	0	0	0	0	1	0
		Ellipsoidal	0	0	0	0	0	1
	Surface	Hairy on both sides	1	0	0	1	0	0
		Lower side hairy	0	1	1	0	1	0
		Glabrous	0	0	0	0	0	1
	Texture	Papery	1	1	1	1	1	0
		Succulent	0	0	0	0	0	1
	Type of hairs	Eglandular	1	1	1	0	0	0
		Glandular	0	0	0	1	1	0
	Apex	Obtuse	1	0	1	0	0	1

		Acute	0	1	1	0	0	0
		Mucronate	0	0	0	1	1	0
		Symmetric	0	0	0	1	1	1
		Asymmetric	1	1	1	0	0	0
Petiole	Presence	Present	1	1	1	1	1	0
		Absent	0	0	0	0	0	1
Stipule	Shape	Scarious	1	1	0	0	0	0
		Membranous	0	0	1	0	0	1
		Spiny	0	0	0	1	1	0
	Diameter	Less than 5 mm	0	0	0	0	0	1
		6-8 mm	0	0	0	1	0	0
		More than 10 mm	1	1	1	0	1	0
	Persistence	Persistent	1	1	1	1	1	0
		Caducous	0	0	0	0	0	1
	Shape	Lanceolate	1	1	1	0	0	0
		Ovate	0	0	0	1	1	1
	Surface	Eglandular	1	1	1	0	0	0
		Glandular	0	0	0	1	1	0
		Glabrous	0	0	0	0	0	1
	Apex	Acute	1	1	1	0	0	1
		Mucronate	0	0	0	1	1	0
Flower	Colour	Violet	0	0	0	1	1	0
		Yellow	1	1	1	0	0	1
		Spathulate	1	0	0	1	0	1
	Shape	Clavate	0	1	1	0	0	0
		Clawed	0	0	0	1	1	1
	Filament base	Without basal scales	1	1	1	1	1	0
		With basal scales	0	0	0	0	0	1
	Intrastaminal glands	Present	1	1	1	0	0	0
		Absent	0	0	0	1	1	1
	Shape	Globoid	1	0	0	0	0	0
		Oblong	0	1	1	0	0	1
		angular ovoid	0	0	0	1	0	0
		Winged conical	0	0	0	0	1	0
	Style	Present	0	0	0	1	1	1
		Absent	1	1	1	0	0	0
	Stigma	5-lobed	1	1	1	0	0	0
		Simple	0	0	0	1	1	1
	Surface	Hairy	1	1	1	1	1	0
		Glabrous	0	0	0	0	0	1
Fruit	Fruit stalk	Shorter or long as the fruit	0	0	0	1	0	1
		Much longer than fruit	1	1	1	0	1	0
	Size (diameter)	2-3 mm	0	0	0	1	0	1
		4-6 mm	0	0	0	0	1	0
		Over 6 mm	1	1	1	0	0	0
	Type	Schizocarp	1	1	1	0	0	0
		Capsule	0	0	0	1	1	1
	Surface	Pubescent	0	1	0	0	1	0
		Densely hairy	1	0	1	1	0	0
		Tuberculate	1	1	1	0	0	0
	Shape	Obovoid	0	0	0	0	0	1
		Obconical	0	0	0	0	1	0
		Spheroidal	0	0	0	1	0	0
	Appendage	Pyramidal	1	1	1	0	0	0
		5-lobed	0	0	0	1	1	0
		Narrowly winged	0	0	0	0	0	1
		2-4 spines	0	1	1	0	0	0
		Dentate triangular wings	1	0	0	0	0	0
Seeds	Colour	Brown	0	1	1	1	1	1
		Creamy	1	0	0	0	0	0
	Shape	prolonged ellipsoid	1	0	0	0	0	0
		Obovoid	0	1	1	0	0	0
		Suborbicular	0	0	0	1	1	0
		Ellipsoid	0	0	0	0	0	1
	Hilum position	Terminal	1	1	1	0	0	1
		Subterminal	0	0	0	1	1	0
	Sculpture	Reticulate	1	1	1	0	0	0
		puncticulate with globular particles	0	0	0	1	1	0
		Smooth	0	0	0	0	0	1

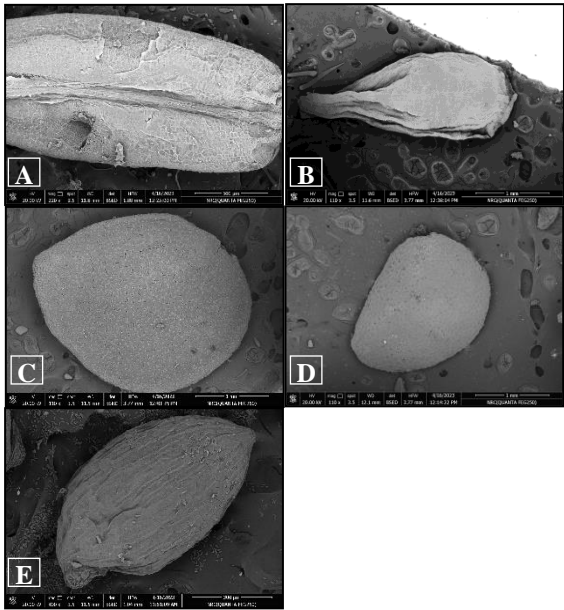


**Plate 1:** SEM photographs of the studied taxa seeds: (A) *Tribulus pentandrus*; (B) *Tribulus terrestris*; (C) *Fagonia glutinosa*; (D) *Fagonia scabra*; (E) *Zygophyllum simplex*

Micro-morphological variations

Palyno-morphological characters

Pollen characteristics of the studied taxa exhibited significant morphological variation, particularly in aperture type, pollen size, and exine sculpture, reflecting clear intergeneric differentiation. The findings are summarized in

**Table 3:** Data matrix of Palynological characters for studied taxa (0 = absent, 1 = present)

Character	Character state	<i>T. pentandrus</i>	<i>T. terrestris</i> var. <i>terrestris</i>	<i>T. terrestris</i> var. <i>orientalis</i>	<i>F. glutinosa</i>	<i>F. scabra</i>	<i>Z. simplex</i>
P/E ratio	1.00	1	1	1	0	0	0
	1.21-1.26	0	0	0	1	1	0
	1.12	0	0	0	0	0	1
Polarity	Isopolar	0	0	0	1	1	1
	Apolar	1	1	1	0	0	0
Pollen shape	Prolate-spheroidal	0	0	0	0	0	1
	Subprolate	0	0	0	1	1	0
	Spheroidal	1	1	1	0	0	0
Pollen size	Very small	0	0	0	0	0	1
	Small	0	0	0	0	1	0
	Medium	1	1	1	1	0	0
Aperture type	Poly-pantoporate	1	1	1	0	0	0
	Tricolporate	0	0	0	1	1	1
Exine sculpture	Coarsely Reticulate-cristate	0	1	1	0	0	0
	Coarsely reticulate	1	0	0	0	0	0
	microreticulate to faveolate	0	0	0	1	1	1

Table (3) and representative photographs of pollen grains are shown in Plates (2)

Among the studied genera, *Tribulus* exhibited the largest pollen grains (35–45 µm in diam.). the grains were apolar, poly-pantoporate, and spheroidal although some appeared cup-shaped due to the presence of a monocryptic pore, with a semitectate exine and coarsely reticulate to coarsely reticulate -cristate ornamentation pattern (Plate 2, A-D) In *T. pentandrus*, the tectum showed straight muri and regular hexagonal or pentagonal lumina, while *T. terrestris* featured winding muri with prominent pyramidal thickenings at the intersections and irregularly polygonal lumina. In contrast, *Fagonia* species displayed smaller to medium-sized pollen grains, with mean polar axes ranging from 22.36–26.65 µm and equatorial diameters from 18.46–21.13 µm. The grains were isopolar, tricolporate, and subprolate in shape, with slit-like to fusiform colpi and a tectate exine with microreticulate to foveolate sculpturing pattern (Plate 2, E & H). *Zygophyllum simplex* exhibited the smallest grains among all examined taxa, with a mean polar axis of 9.96 µm and a mean equatorial diameter of 8.88 µm. The grains were prolate-spheroidal, tricolporate, with slit-like colpi and a microreticulate–foveolate tectate exine (Plate 2, I & J).

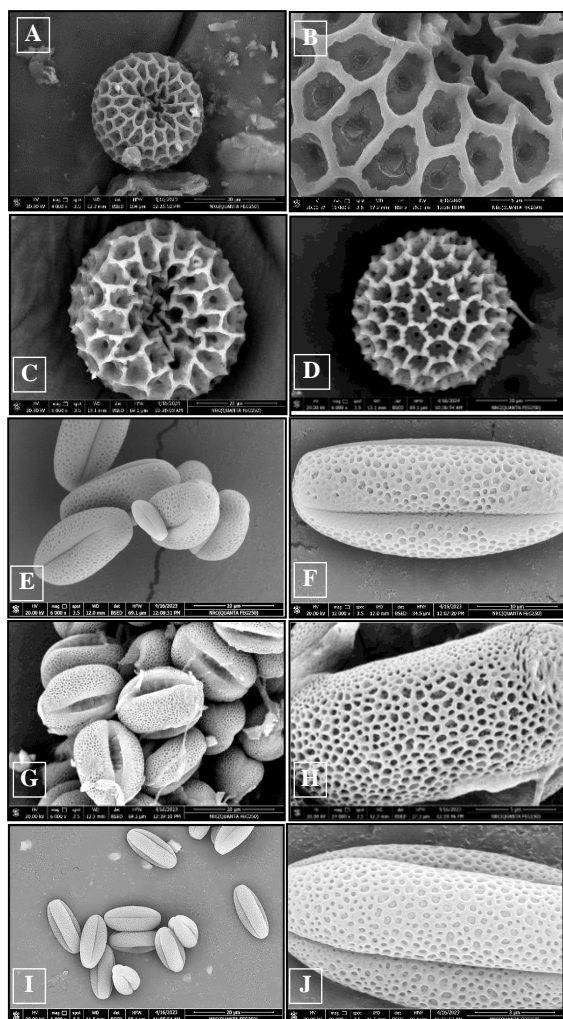


**Plate (2):** SEM photographs of the studied taxa pollen grains of: (A & B) *Tribulus pentandrus*; (C & D) *Tribulus terrestris*; (E & F) *Fagonia glutinosa*; (G & H) *Fagonia scabra*; (I & J) *Zygophyllum simplex*.

#### Anatomical characters

Comparative anatomical features, such as the presence or absence of petioles, stomatal positioning, trichome types, leaf outlines, mesophyll differentiation and vascular bundle arrangements, exhibit distinct patterns that are both taxonomically and adaptively significant, allowing clear differentiation among genera and species. Significant variation in anatomical characters was observed among the studied taxa, as presented in Table (4-6) and illustrated in Plates (3-6).

#### Stem Anatomy

The anatomical features of the stem of the present study showed significant variations in stem outline, cuticle thickness, cortex structure,

pith characteristics, and stele type (Table 4 & Plate 3). The outline of the stem cross section was useful for distinguishing between the studied taxa. It varies from terete in *Tribulus* and *Z. simplex* to terete with ridges and furrows in *Fagonia* species. A thick cuticle was observed in all studied taxa except *Z. simplex*, which uniquely possesses stem stomata. The cortex comprised parenchyma in *Tribulus* and *Zygophyllum*, while *Fagonia* exhibited both collenchyma and parenchyma with scattered patches of cortical fibers (Plate 3, D & E).

The vascular system differed significantly, was a eustele with 15-25 discrete vascular bundles in *Tribulus*, and an ectophloic siphonostele with continuous vascular rings in *Fagonia* and *Z. simplex* (Plate 3, D-F). The pith in all taxa composed of thin-walled parenchymatic cells, wide and centric in *Tribulus*, and narrow, excentric or crescent-shaped in the *Fagonia* and *Z. simplex*. Notably, lignified pith parenchyma was observed only in *Z. simplex* (Plate 3, F). Druses crystals were present in *Tribulus* and *Z. simplex*, but absent in *Fagonia* species. Within *Tribulus*, crystals were restricted to the pith of *T. terrestris* var. *terrestris* and were absent in var. *orientalis*. Additionally, crystals were observed in the vascular tissue only in *Z. simplex*.

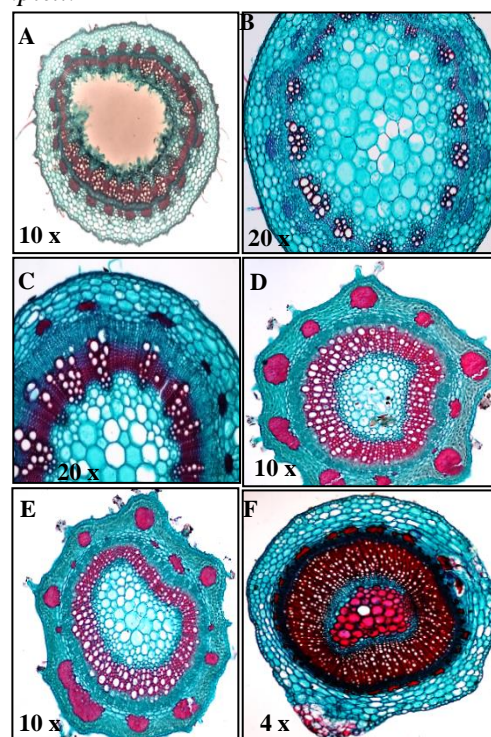


**Plate 3:** Photographs of transverse stem sections of: (A) *T. pentandrus*; (B) *T. terrestris* var. *terrestris*; (C) *T. terrestris* var. *orientalis*; (D) *F. glutinosa*; (E) *F. scabra*; (F) *Z. simplex*.



**Table 4:** Data matrix of stem anatomical characters for studied taxa (0 = absent, 1 = present)

Character		Character state	T. pentandrus	T. terrestris var. terrestris	T. terrestris var. orientalis	F. glutinosa	F. scabra	Z. simplex
Outline in T.S.		Terete	1	1	1	0	0	1
		±Terete with ridges & furrows	0	0	0	1	1	0
Dermal system	Cuticle	Thin	0	0	0	0	0	1
		Thick	1	1	1	1	1	0
	Presence	Present	1	1	1	1	1	0
		Absent	0	0	0	0	0	1
	Type	Eglandular unicellular	1	1	1	0	0	0
		Glandular	0	0	0	1	1	0
	Epidermal cells	Radial	1	0	0	0	1	1
		Tangential	0	1	1	1	0	0
	Stomata	Present	0	0	0	0	0	1
		Absent	1	1	1	1	1	0
	No. of tissues	One	1	1	1	0	0	1
		Two	0	0	0	1	1	0
Ground system	Cortex	Type of Polyhedral parenchyma	1	1	1	1	1	1
		Collenchyma	0	0	0	1	1	0
		Crystal presence	Present	1	1	0	0	0
			Absent	0	0	1	1	1
	Position	Centric	1	1	1	0	0	0
		Excentric	0	0	0	1	1	1
	Thickness	Hollow	1	0	0	0	0	0
		Solid	0	1	1	1	1	1
	Width	Narrow	0	0	0	1	1	1
		Wide	1	1	1	0	0	0
	Pith	Shape	Circular	1	1	0	0	0
			Crescent	0	0	1	1	1
	Types of parenchyma	Non-lignified	1	1	1	1	1	0
		Lignified (with pitted walls)	0	0	0	0	0	1
	Crystals presence	Present	1	1	0	0	0	0
		Absent	0	0	1	1	1	1
Vascular system	Type of stele	Siphonostele	0	0	0	1	1	1
		Eustele	1	1	1	0	0	0
	No. of V.B.	Cycle	0	0	0	1	1	1
		15-25	1	1	1	0	0	0
	2ry xylem components in interfascicular region	Fibers only	1	1	1	0	0	0
		Vessels & fibers	0	0	0	1	1	1
	2ry xylem components in fascicular region	Vessels	1	1	1	0	0	0
		Vessels & fibers	0	0	0	1	1	1
	Crystals	Present	0	0	0	0	0	1
		Absent	1	1	1	1	1	0

### Petiole anatomy

All examined taxa possessed well-developed petioles except *Zygophyllum simplex* which lacked a distinct petiole (Table 5, Plate 4). The diagnostic significance of petiole morphology is evident in their distinct outlines, which varied among the studied species from arc-shaped in

*Fagonia scabra*, circular in *F. glutinosa* and circular with ridges in *Tribulus* species (Plate 4, A-E). Notably, these ridges were divergent in *Tribulus pentandrus* and adjacent in *T. terrestris*. Cuticle thickness also varied, being relatively thick in *Fagonia* species and thinner in *Tribulus* species. Cortical tissue structure also varied among species; *F. glutinosa* having

multiple layers of polyhedral parenchyma, while the remaining taxa featured an outer layer of elongated chlorenchyma followed by parenchyma. In *Tribulus*, chlorenchyma confined to the ridges, whereas in *F. scabra* it formed a continuous ring. Vascular bundle arrangement further served as a reliable distinguishing feature; *Tribulus* species exhibited four main oval-shaped vascular

bundles with two smaller subsidiary bundles located at the ridges (Plate 4, A-C). Meanwhile, *Fagonia* species had a single arch-shaped vascular bundle, with *F. scabra* also showing distinctive scleridic patches beneath the vascular tissue (Plate 4, E). Additionally, druses crystals were observed in *Tribulus* taxa but were absent in *Fagonia* species.

**Table 5:** Data matrix of leaf petiole characters for studied taxa (0 = absent, 1 = present)

Character	Character state	<i>T. pentandrus</i>	<i>T. terrestris</i> var. <i>terrestris</i>	<i>T. terrestris</i> var. <i>orientalis</i>	<i>F. glutinosa</i>	<i>F. scabra</i>	<i>Z. simplex</i>
Occurrence	Present	1	1	1	1	1	0
	Absent	0	0	0	0	0	1
Outline in T.S.	Circular with 2- slightly ridges	0	1	0	0	0	0
	Circular with 2-adjacent ridges	0	0	1	0	0	0
	Circular with 2-divergent ridges	1	0	0	0	0	0
	± Circular	0	0	0	1	0	0
	Arc shaped	0	0	0	0	1	0
	Mixed	0	0	1	1	1	0
Dermal system	Cuticle thickness	Thin	1	1	0	0	0
	Trichomes	Glandular	0	0	1	1	0
		Eglandular	1	1	0	0	0
	Epidermis arrangement	Radially isodiametric	1	0	0	0	0
		Tangential	0	1	0	0	0
		Mixed	0	0	1	1	0
Ground system	No. of tissue	One	0	0	1	0	0
		Two	1	1	0	1	0
	Types of tissue	Elongated chlorenchyma (palisade)	1	1	1	0	1
		Polyhedral parenchyma	1	1	1	1	0
	Position of elongate chlorenchyma	In complete ring	0	0	0	1	0
Vascular system		Restricted at the ridges	1	1	1	0	0
	No. of V.B.	One	0	0	0	1	1
		Six (4-main V.B. & 2- subsidiary)	1	1	1	0	0
	Shape of main V.B.	Arch shaped	0	0	0	1	1
		Oval	1	1	1	0	0
	Druses	Present	1	1	1	0	0
		Absent	0	0	0	1	1
	Sclerieds	Present	0	0	0	0	1
		Absent	1	1	1	0	0

### Leaf Blade Anatomical Characters

The anatomical characters of the leaf blades of the studied taxa are summarized in Table (6) and illustrated in Plate (5). These features revealed distinct differences among the studied taxa.

The outline of the leaf blade in cross-section was found to be valuable for species differentiation, ranging from plano-convex to oblong in *Zygophyllum simplex*. Based on mesophyll structure, three main types were identified: dorsiventral (bifacial) leaves with a

subdermal hypodermis and Kranz anatomy, as observed in *Tribulus* species; isobilateral leaves, in *Fagonia* species; and radial or centric leaves, in *Z. simplex*. In *Tribulus* species, the palisade tissue was uniseriate and confined on the adaxial surface (Plate 5, A-F), whereas in *Fagonia* species it was biseriate on both adaxial and abaxial surfaces. Spongy mesophyll consisted of 2–3 layers in *Tribulus* species, and was reduced to 1–2 layers in *Fagonia* species (Plate 5, G-J). The blade anatomy of *Z. simplex* was unique, consisting of a uniseriate epidermis of isodiametric cells enclosing a centric

mesophyll. This mesophyll was further differentiated into an outer palisade layer and an inner water-storage parenchyma composed of 3–4 layers of large, thin-walled cells (Plate 5, K-L). The midrib anatomy also showed taxonomic significance. In *Tribulus* species and *Fagonia glutinosa*, the abaxial outline of the midrib was U-shaped; flattened-ribbon in *Fagonia scabra*; while in *Z. simplex*, the midrib was indistinct. A single central vascular bundle was present in all species except *F. scabra*, which exhibited two main vascular bundles

(Plate 5, I-J). The number of lateral vascular bundles ranged from 10–18 in most taxa, and reached up to 20–22 in *T. terrestris* I. In *Z. simplex*, several small peripheral bundles were embedded within the inner palisade layer, with the xylem oriented outward and the phloem inward. Druses crystals were observed in all *Tribulus* species and absent in *Fagonia* species and *Z. simplex*, further distinguishing these genera.

**Table 6:** Data matrix of lamina anatomical characters for studied taxa (0 = absent, 1 = present)

Character		Character state	<i>T. pentandrus</i>	<i>T. terrestris</i> var. <i>terrestris</i>	<i>T. terrestris</i> var. <i>orientalis</i>	<i>F. glutinosa</i>	<i>F. scabra</i>	<i>Z. simplex</i>
Dermal system	Stomata level	Raised	1	1	1	0	1	0
		Sunken	0	0	0	1	0	1
	Trichomes	Occurrence	Present	1	1	1	1	0
		Absent	0	0	0	0	0	1
	Types	Eglandular hairs	1	1	1	0	0	0
		Glandular hairs	0	0	0	1	1	0
	Cuticle thickness	Thick	0	0	0	1	1	1
		Thin	1	1	1	0	0	0
	Arrangement	Radial – tangential	1	1	1	1	1	0
		Radial	0	0	0	0	0	1
	Anticlinal walls	Recessed, ± straight	1	1	1	0	0	1
		Recessed, undulate	0	0	0	0	1	0
		Raised, straight	0	0	0	1	0	0
	Periclinal walls	Striated tabular to concave	0	1	1	0	0	0
		Smooth tabular to convex	1	0	0	1	1	0
		Papillate ± tabular	0	0	0	0	0	1
	Type	Dorsiventral	1	1	1	0	0	0
		Isobilateral	0	0	0	1	1	0
		Radial or centric	0	0	0	0	0	1
Mesophyll	palisade tissue	One row in one side	1	1	1	0	0	1
		2-rows in each side	0	0	0	1	1	0
	spongy tissue	1-2 rows	0	0	0	1	1	0
		2-3 rows	1	1	1	0	0	1
Water storage layer		Present	1	1	1	0	0	0
		Absent	0	0	0	1	1	1
Midrib	Abaxial outline	Flattened- ribbon	0	0	0	0	1	0
		U- shaped	1	1	1	1	0	0
		Not obvious	0	0	0	0	0	1
		Single	1	1	1	1	0	1
Vascular system	main vascular bundle	Two	0	0	0	0	1	0
		10 – 18	1	0	1	1	1	0
	No. of lateral vascular bundles	20 – 25	0	1	0	0	0	1
		Present	1	1	1	0	0	0
Crystals		Absent	0	0	0	1	1	1

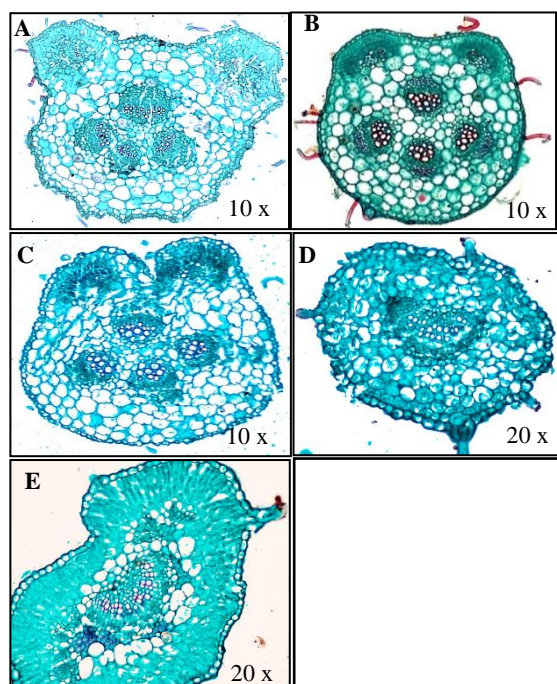


**Plate 4:** Photographs of transverse petiole sections of: (A) *Tribulus pentandrus*; (B) *Tribulus terrestris* var. *terrestris*; (C) *Tribulus terrestris* var. *orientalis*; (D) *Fagonia glutinosa*; (E) *Fagonia scabra*.

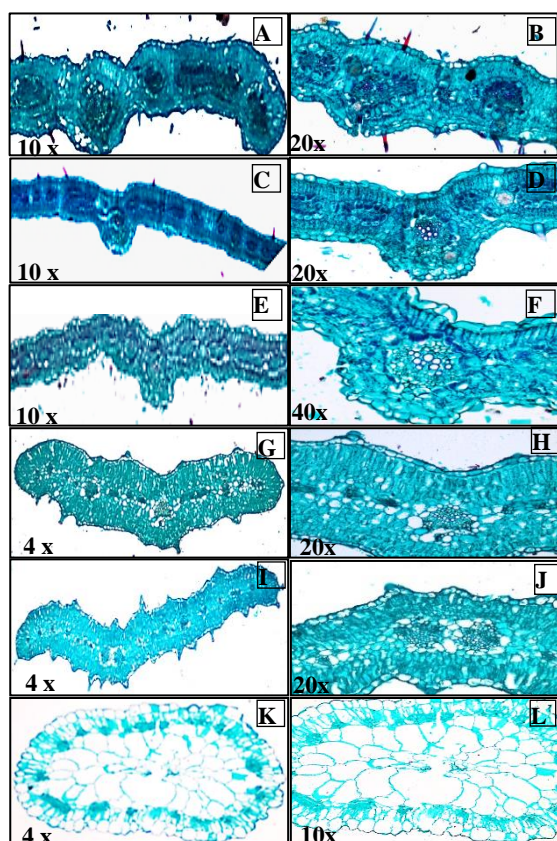


**Plate 5:** Photographs of transverse lamina sections of: (A-B) *Tribulus pentandrus*; (C-D) *Tribulus terrestris* var. *terrestris*; (E-F) *Tribulus terrestris* var. *orientalis*; (G-H) *Fagonia glutinosa*; (I-J) *Fagonia scabra*; (K-L) *Zygophyllum simplex*.

### Epidermal features and Indumentum

The current study focuses on micro-morphological features of trichomes, epidermal cells, and stomata. The data on the foliar epidermal characters of the taxa examined are presented in Table (6) and Plate (6).

Among the studied taxa, *Zygophyllum simplex* was the only completely glabrous species, while *Tribulus* and *Fagonia* species exhibited varying degrees of indumentum, from pubescent to densely hairy. Two distinct trichome types were observed: eglandular unicellular hairs in *Tribulus* taxa and glandular hairs in *Fagonia* species. The epidermal cells were polygonal in *Tribulus* taxa and *Z. simplex* (Plate 6, A-C & F), but irregular and indistinct in *Fagonia* species (Plate 6, D, E). Anticlinal wall patterns also varied, with *Tribulus* taxa and *Z. simplex* showing recessed,  $\pm$  straight walls, while *F. scabra* had recessed, undulate walls (Plate 6, E), and *F. glutinosa* displayed raised, straight walls. Regarding periclinal walls, *T. terrestris* had striated tabular to concave forms, *Fagonia* species had smooth tabular to convex surfaces, and *Z. simplex* exhibited papillate,  $\pm$  tabular walls. Stomatal position was another distinguishing feature; raised in *Tribulus* taxa and *F. scabra*, whereas *F. glutinosa* and *Z. simplex* exhibited sunken stomata (Plate 6, D & F).

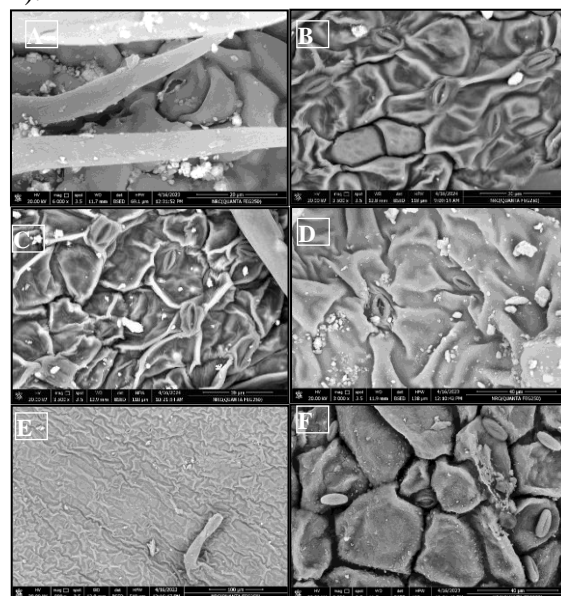


**Plate 6:** SEM Photograph of the lamina adaxial surface showing epidermal characteristics of: (A) *Tribulus pentandrus*; (B) *Tribulus terrestris* var. *terrestris*; (C) *Tribulus terrestris* var. *orientalis*; (D) *Fagonia glutinosa*; (E) *Fagonia scabra*; (F) *Zygophyllum simplex*.

### Cluster analysis

A multivariate statistical analysis was performed using 219 morphological, palynological, and anatomical character states, each represented by binary codes (0, 1), across the six studied taxa belonging to the family Zygophyllaceae. The analysis aimed to elucidate patterns of similarity and divergence among the studied taxa and to evaluate their taxonomic affinities. The cumulative data presented in Tables (2-6) and the resulting phenetic relationships are illustrated through a dendrogram (Fig. 1). The dendrogram shows that the studied taxa were separated into two main series (I, II), which included four clusters (I, II, III, and IV) at a similarity level of 32.08%. Series I comprised all representatives of the genus *Tribulus*, which characterized by many foliate leaves, schizocarpic fruits, pantoporate apolar pollen with coarse reticulate sculpturing, dorsiventral mesophyll with kranz anatomy and eglandular hairs. This series was further subdivided into two clusters at a higher similarity level of 84.32%. Cluster I included *T. pentandrus*, whereas Cluster II grouped the two varieties of *T. terrestris* (*T. terrestris* var. *terrestris* and *T. terrestris* var. *orientalis*) showing the highest degree of similarity (93.07%). Series II included taxa from the genera *Fagonia* and *Zygophyllum*, which were divided into two distinct clusters at a similarity level of 45.71%. This series is characterized by uni-or trifoliate leaves, capsule fruits, tri-colpate or colpate pollen, isobilateral or centric mesophyll without kranz anatomy and glandular hairs or glabrous. Cluster III comprised *Fagonia glutinosa* and *F. scabra*, exhibiting a high internal similarity of 81.93%, indicating close morphological and anatomical affinities. In contrast, Cluster IV was composed solely of *Zygophyllum simplex*, indicating its relative distinctiveness within this group.

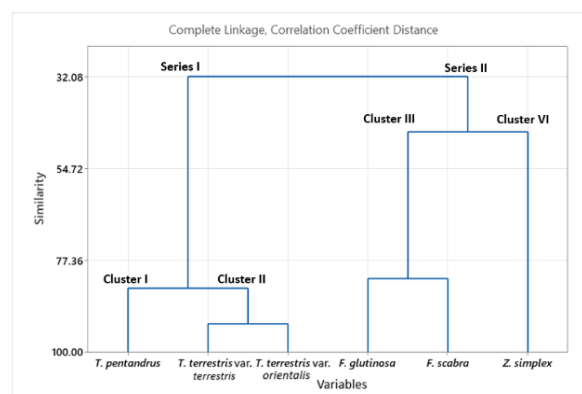


**Fig. 1** Dendrogram indicating the relationships among the six studied taxa of Zygophyllaceae based on combined morphological, palynological, and anatomical data analysis using Minitab statistical software

### Discussion

The present study provides a comprehensive comparative analysis of six taxa from three genera within the family Zygophyllaceae, focusing on a range of morphological, palynological, and anatomical traits. The diagnostic features examined include leaf architecture, floral morphology, fruit and seed characteristics, as well as palynological and anatomical variations. When considered collectively, these characters hold significant taxonomic value and contribute to the accurate identification and delimitation of taxa at both the genus and species levels.

A Comparative analysis of *Tribulus* species, *Fagonia* species, and *Zygophyllum simplex* revealed distinct morphological differences that support their generic separation within Zygophyllaceae. Vegetative traits, particularly leaf structure and trichome type, as well as floral morphology, fruit and seed characteristics, proved to be taxonomically informative. These findings are consistent with previous studies by El-Hadidi (1974, 1978), Hosni (1988), Beier (2005), and Abdel Khalik & Hassan (2012). This distinction is supported by the findings of Shamso et al. (2013), who conducted a numerical analysis of morphological characters across various species within Zygophyllaceae. Their study revealed the clear separation of *Tribulus* as a distinct phenon, apart from the cluster that encompassed both *Fagonia* and *Zygophyllum* species. Draz et al. (2024) documented two distinct forms of *Tribulus terrestris*, identified



as *T. terrestris* var. *terrestris* (Form I) and *T. terrestris* var. *orientalis* (Form II), highlighting the notable morphological plasticity of this species. Based on our findings, the morphological traits largely overlap between the two varieties, with the exception of differences in fruit surface characteristics, appendages, and the number of vascular bundles in the stem. Overall, the morphological diversity observed supports the current taxonomic delineation of these taxa and reflects ecological adaptations. These characters may serve as reliable diagnostic features for identification and classification.

Pollen grain characteristics have proven valuable for evaluating the taxonomy of Zygophyllaceae (Perveen & Qaiser, 2006; Bukhari et al., 2014). Significant variation was observed across the three studied genera *Tribulus*, *Fagonia*, and *Zygophyllum*, particularly in aperture type, pollen size, and exine sculpturing. In *Tribulus*, pollen grains exhibited a high degree of ultrastructural uniformity, especially regarding aperture type, exine ornamentation, and overall shape and size. These observations are in agreement with previous findings reported by Pragłowski (1987), Perveen & Qaiser (2006), Ben Nasri-Ayachi & Nabli (2009), Semerdjieva (2011), and El-Atrush et al. (2015). Tai et al. (2021) reported dimorphic pollen in Libyan accessions of *Fagonia*, characterized by the presence of two distinct aperture types within a single taxon. In contrast, the current study observed monomorphic pollen in Egyptian populations of *F. glandulosa*, exhibiting only a single aperture type. This variation may be attributed to geographic or environmental influences on pollen development and highlights the need for further molecular and biogeographic investigation. The two Egyptian *Fagonia* species examined in this study exhibited prolate pollen shapes, tricolporate apertures, and microreticulate-foveolate exine sculpturing, whereas *Zygophyllum simplex* displayed the smallest pollen grains among all taxa studied. These results are consistent with previous findings by El-Ghamery et al. (2002), Perveen & Qaiser, (2006); Abd El Khalik, (2012); Bukhari, (2014). Overall, the distinct palynological differences observed among *Tribulus*, *Fagonia*, and *Zygophyllum* validate their separation at the generic level within Zygophyllaceae. These results highlight diagnostic the value of pollen morphological

traits in resolving taxonomic relationships and underscore their potential as supplementary tools in future phylogenetic and ecological studies.

Anatomical characteristics are valuable taxonomic traits that play a significant role in resolving some taxonomic challenges at both the genera and species levels (Metcalf & Chalk 1957; Ganeva et al. 2009; Song & Hong 2018; Sathee & Jain, 2022; Gabr & Ragab 2023). They also reflect a plant adaptation to the extreme environmental conditions (Hameed et al. 2009; Ashraf & Harris, 2013; Elkhartbotly, 2016; Taia et al., 2017).

The outline of the stem cross section varied from terete in *Tribulus* taxa and *Zygophyllum simplex* to terete with ridges and furrows in *Fagonia* species, the same shape of the stem outline has been described by many authors: El Hadidi (1966); Taia et al. (2017). The vascular system showed notable variation among the studied taxa. *Tribulus* exhibited an eustele, while both *Fagonia* and *Zygophyllum simplex* possessed an ectophloic siphonostele characterized by continuous vascular rings. These findings are consistent with those reported by Ahmed & Mohamed (2005b) and Gabr & Ragab (2023). In the present study, the pith consisted of thin-walled parenchymatous cells in all taxa, being wide and centric in *Tribulus*, but narrow, excentric, or crescent-shaped in *Fagonia* species and *Z. simplex* (Elkamali et al., 2016). Notably, lignified pith parenchyma with pitted walls was observed only in *Z. simplex* (Sheahan & Cutler, 1993). This finding supports the explanation proposed by El Hadidi (1966), who stated that excentric pith formation may result from abnormal secondary xylem growth and lignification of pith cells, with pitted walls developing after the initiation of secondary growth.

The anatomical characteristics of the petiole also showed considerable variation among the studied taxa, providing valuable diagnostic features for species delimitation. Distinct petiole outlines, variations in cortical tissue structure, and the arrangement of vascular bundles served as reliable distinguishing features. These anatomical characteristics features are consistent with previous findings reported by Metcalf & Chalk (1957) and Gabr & Ragab (2023), highlighting the taxonomic significance of petiole morphology.

Leaf anatomical features provided a significant taxonomic distinction among the studied taxa.



A distinct abaxial layer of water storage cells (hypodermal layer) was observed only in *Tribulus* taxa, aligning with the findings of Metcalfe & Chalk (1957), Sheahan & Cutler (1993), and Nikolova & Vassilev (2011). The variability in mesophyll types ranging from dorsiventral and isobilateral to centric, along with differences in vascular tissue organization, has proven useful for both species and genus identification, and supporting its relevance in taxonomic studies. In *Tribulus*, the dorsiventral mesophyll comprises a single palisade layer and 2–3 compact spongy layers with reduced intercellular spaces, a structure associated with efficient CO<sub>2</sub> transfer in the C<sub>4</sub> pathway (Welkie & Caldwell, 1970). In contrast, *Zygophyllum simplex* exhibits a centric mesophyll, differentiated into an outer photosynthetic palisade layer and an inner water storage parenchyma composed of 3–4 rows of cells, consistent with the observations of Waly et al. (2011). These anatomical adaptations are characteristic of xerophytic environments, as supported by Zaman & Padmesh (2009), Abd Elhalim et al. (2016), and El Kharbotly (2016). The consistent presence of Kranz anatomy strongly indicates that C<sub>4</sub> photosynthesis is a defining feature of both *Tribulus* taxa and *Z. simplex*. In *Tribulus*, a complete Kranz sheath was observed encircling the vascular bundles, whereas in *Z. simplex*, the sheath appeared arc-shaped (Crookston & Moss, 1972; Sheahan & Cutler, 1993; Sheahan & Chase, 1996; Sage et al., 2011; Edwards & Voznesenskaya, 2011; Lauterbach et al., 2016). These findings are in accordance with Taia et al., (2017), who reported that the leaves of *Fagonia* species lack Kranz anatomy. In addition to the previous findings, druses crystals were absent in all *Fagonia* species but present in *Tribulus* and *Zygophyllum simplex*. In *Tribulus*, crystals were observed in the petiole, leaflets, and the stem pith of var. *terrestris*. In *Z. simplex*, druses were restricted to the vascular tissue of the stem. The complete absence of both Kranz anatomy and crystals in *Fagonia* further supports its anatomical distinction from *Tribulus* and *Zygophyllum*.

The present findings support the generic specificity of trichomes, as noted by Sheahan & Cutler (1993) and Gabr (2023). *Zygophyllum simplex* was completely glabrous, while *Tribulus* and *Fagonia* species showed varying degrees of indumentum. Eglandular unicellular hairs were observed in *Tribulus*, and glandular

hairs in *Fagonia*, both of which provide valuable taxonomic characters. These epidermal features, consistent with the observations of Abdel Khalik & Hassan (2012) and Gabr et al. (2013), support species and genus-level distinction within the family.

Cluster analysis of the combined characters revealed high intra-generic similarity, particularly between the two *Tribulus* varieties and between *Fagonia glutinosa* and *F. scabra*, and lower inter-generic similarity. *Tribulus* formed a distinct cluster, clearly separated from *Fagonia* and *Zygophyllum*, which grouped together. The separation of *Tribulus* from the other taxa supports its distinctiveness, characterized by several unique morphological (many foliate leaves and schizocarpic fruits), anatomical (dorsiventral mesophyll with Kranz anatomy and the presence of eglandular hairs), and palynological (pantoporate, apolar pollen with coarse reticulate sculpturing) characters. These findings align with traditional taxonomic classifications and previous numerical studies (Abdel Khalik, 2012; Shamsou et al., 2013; Gabr, 2023), supporting the placement of *Tribulus* in its own subfamily (*Tribuloideae*) or even a separate family (*Tribulaceae*), distinct from *Zygophylloideae*, which includes *Fagonia* and *Zygophyllum* (Sheahan & Cutler, 1993; El Hadidi, 1978; Saleh et al., 1982). Additionally, this statistical analysis is consistent with previous chemosystematic and fingerprinting studies by Draz et al. (2024, 2025), further supporting the distinct separation of *Tribulus* from other taxa. *Fagonia* species showed closer affinity to *Zygophyllum simplex*, suggesting a possible evolutionary relationship. Overall, these results confirm clear taxonomic distinctions among the studied genera.

## Conclusion

The combined morphological, palynological, and anatomical data of studied taxa of *Tribulus*, *Fagonia*, and *Zygophyllum* revealed clear intergeneric and interspecific distinctions within Zygophyllaceae s. l. Morphological traits such as leaf form, trichome type, floral and fruit structures, along with palynological features, particularly pollen aperture and exine patterns, provide valuable diagnostic characters for taxonomic delimitation. *Tribulus* is notably distinct in its pollen and fruit morphology, supporting its recognition at a higher taxonomic level. Anatomical characters, including stomatal position, leaf outline, mesophyll

differentiation, vascular arrangement, and crystal distribution, further reinforce these distinctions. By integrating morphological, palynological, and anatomical investigations with previously performed chemosystematic and fingerprinting analyses, this study provides strong evidence supporting the placement of *Tribulus* in a distinct subfamily (Tribuloideae) or even a separate family (Tribulaceae), apart from Zygophylloideae, which comprises *Fagonia* and *Zygophyllum*. These findings highlight the importance of integrative anatomical, palynological, and morphological studies in resolving taxonomic relationships and understanding ecological adaptations within the family Zygophyllaceae.

## References

- Abd Elhalim, M.E., Abo-Alatta, O.K., Habib, S.A., Abd Elbar, O.H. (2016). The anatomical features of the desert halophytes *Zygophyllum album* L. and *Nitraria retusa* (Forssk.) Asch. *Annal. Agric. Sci.* 61(1): 97-104.
- Abdel Khalik, K.N. (2012). A numerical taxonomic study of the family Zygophyllaceae from Egypt. *Acta Bot. Bras.* 26 (1): 165-180.
- Abdel Khalik, K., Hassan, N.M.S. (2012). Seed and trichome morphology of the Egyptian *Fagonia* (Zygophyllaceae) with emphasis on their systematic implications. *Nord. J. Bot.* 30(1): 116-126.
- Ahmed, K.A. (1991). Petiolar vasculature in *Fagonia* species and its taxonomic affinities. *Proc. Egypt, Acad. Sci.* 41:209-218.
- Ahmed, K.A., Khafagi, A.A.F. (1997). Numerical analysis of comparative data on leaf morphological and anatomical characters of *Fagonia*. *J. Fac. Educ.* 22: 277-286.
- Ahmed, K.A., Mohamed, A.H. (2005-b). A Taxonomic Study of The Genus *Tribulus* L. In Egypt II-Histological Features. *Arab Univ. J. Agric. Sci.* 13(2): 207-217.
- APG III. (2009). An update of the Angiosperm Phylogeny Group classification for the orders and families of flowering plants: APG III. *Bot. J. Linn. Soc.* 161: 105-121.
- Ashraf, M.H.P.J.C., Harris, P.J. (2013). Photosynthesis under stressful environments: An overview. *Photosynthetica*, 51: 163-190.
- Barthlott, W. (1981). Epidermal and seed surface characters of plants: systematic applicability and some evolutionary aspects. *Nordc. J. Bot.* 1(3): 345-355.
- Beier, B.A. (2005). A revision of the desert shrub *Fagonia* (Zygophyllaceae). *Syst. Biodivers.* 3(3): 221-263.
- Beier, B.A., Chase, M.W., Thulin, M. (2003). Phylogenetic relationships and taxonomy of subfamily Zygophylloideae (Zygophyllaceae) based on molecular and morphological data. *Plant Syst. Evol.* 240: 11-39.
- Ben Nasri-Ayachi, M., Nabli, A.M. (2009). Ultrastructure and ontogeny of the exine in *Tribulus terrestris* Linné (Zygophyllaceae). *Grana.* 48(2): 109-121.
- Boulos, L. (2000). "Flora of Egypt" (Geraniaceae-Boraginaceae) vol.2. Al Hadara publishing, Cairo, Egypt.
- Boulos, L. (2009). "Flora of Egypt Checklist", Revised Annotated Edition. Al Hadara Publishing, Cairo, Egypt.
- Bukhari, N.A., Al-arjany, K.M., Ibbrahim, M.M. (2014). The pollen morphology and its sharing in the taxonomy of some plant species in Saudi Arabia. *J. Pure. Appl. Microbiol.* 8 (5): 3897-3901.
- Chaudhary, S.A. (2001). Zygophyllaceae. "Flora of the Kingdom of Saudi Arabia". Illustrated. vol. 2, Part 1. Ministry of Agriculture and Water, Riyadh.
- Christenhusz, M.J., Byng, J.W. (2016). The number of known plants species in the world and its annual increase. *Phytotaxa.* 261(3): 201-217.
- Cronquist, A. (1988). "The evolution and classification of flowering plants". 2<sup>nd</sup> edition. Bronx, New York: New York Botanical Garden.
- Crookston, R.K., Moss, D.N. (1972). C-4 and C-3 carboxylation characteristics in the genus *Zygophyllum* (Zygophyllaceae). *Ann. Missouri Bot. Gard.* 59: 465-470.
- Draz, A.A., Farid, M.M., Shams, E.M., Hosni, H.A., Kawashty, S.A., Hussein, S.R. (2024). Metabolome mapping and DNA fingerprinting of *Tribulus terrestris* from three different Egyptian populations with the assessment of their morphological characters and antioxidant activity. *S. Afr. J. Bot.* 171: 454-472.
- Draz, A.A., Farid, M.M., Hosni, H.A., Shams, E.M., Kawashty, S.A., Hussein, S.R. (2025). Metabolite-Profiling and DNA-Fingerprinting of Some Selected Species of Family Zygophyllaceae with Assessment of Their Bioactive Potential. *Chem. Biodivers.* e202402695.
- Edwards, GE, Voznesenskaya EV. (2011). C4 photosynthesis: Kranz forms and single-cell C4 in terrestrial plants. In: Raghavendra AS, Sage RF, eds. C4 photosynthesis and related CO<sub>2</sub> concentrating mechanisms. Dordrecht, The Netherlands: Springer, pp. 29-61.
- El-Atroush, H., EL-Shabasy, A.E., Tantawy, M.A.,

- Barakat, H.M.S. (2015). Pollen morphology and protein pattern of *Nitraria retusa* and some selected taxa of Zygophyllaceae in Egypt. *Egypt. J. Bot.* 55(2): 207-230.
- El- Ghamery, A.A., Mansour, M.M., Abdel-Azeem, E.A., Kasem, A.M. (2002). Studies on seed coat and pollen grains morphology of some taxa of *Zygophyllum* (Zygophyllaceae) and their taxonomic implications. *Egypt. J. Biotechnol.* 12: 173-185.
- El Hadidi, M.N. (1966). The genus *Fagonia* in Egypt. *Candollea*. 21(1): 13-54.
- El Hadidi, M.N. (1974). Weitere Beobachtungen an der Gattung *Fagonia*. *Mitt. Bot. Staatssamml. München* 11: 387.
- El Hadidi, M.N. (1978). An introduction to the classification of *Tribulus* L. *Taeckholmia*. 9: 59-66.
- Elkamali, H.H., Eltahir, A.S., Yousif, I.S., Khalid, A.M.H., Elneel, E.A. (2016). Comparative Anatomical Study of the Stems and Leaflets of *Tribulus longipetalous*, *T. pentandrus* and *T. terrestris* (Zygophyllaceae). *O.A.Lib.J.* 3(8): 1-5.
- Elkharbotly, A.A. (2016). Studies on some anatomical features of selected plant species grown in sand dune areas of North Sinai, Egypt. *Acta Ecol. Sin.* 36(4): 246-251.
- Engler, A. (1931). Zygophyllaceae. In: Engler A, Prantl K (eds), *Die Natürlichen Pflanzenfamilien*, 2nd edition, Vol. 19a, Section 2: 144-184. Leipzig: Engelmann.
- Erdtman, G. (1952). Pollen morphology and plant taxonomy: angiosperms. Almqvist and Wiksell, Stockholm.
- Erdtman, G. (1960). The acetolysis method, a revised description. *Svensk Botanisk Tidskrift*, 54(4): 561-564.
- Evert, R.F. (2006). *Esau's Plant anatomy*, 3<sup>rd</sup> ed. A. John Wiley & sons Publ. doi: 10.1002/0470047380
- Euro+Med PlantBase. Available at: [www.emplantbase.org/home.html](http://www.emplantbase.org/home.html). (accessed May 2025)
- Gabr, D.G. (2023). Seed coat sculpture and epidermal study on some taxa of Zygophyllaceae from eastern region of Saudi Arabia. *Taeckholmia*. 43(1): 44-67.
- Gabr, D.G., Ragab, O.G. (2023). Morpho-anatomical Characters of Leaves and Stems as a Tool for the Identification of Some Taxa of Zygophyllaceae of Eastern Saudi Arabia. *Egypt. J. Bot.* 63(2): 389-402.
- Gabr, D.G., Mohamed, A.H., Khafagi, A.A. (2013). Study of the leaf epidermis in some Egyptian taxa of *Fagonia* L. by SEM. *Delta J. Sci.* 36(1): 20-33.
- Ganeva, T.S., Uzunova, K.R., Koleva, D. (2009). Comparative leaf epidermis investigation in species of genus *Crataegus* L. (Rosaceae) from Bulgaria. *Feddes Repert.* 120(3-4): 169-184.
- Halbritter, H., Ulrich, S., Grímsson, F., Weber, M., Zetter, R., Hesse, M., Buchner, R., Svojtka, M., Frosch-Radivo, A. (2018). "Illustrated pollen terminology". Springer Nature, 483pp.
- Hameed, M., Ashraf, M., Naz, N. (2009). Anatomical adaptations to salinity in cogon grass [*Imperata cylindrica* (L.) Raeuschel] from the Salt Range, Pakistan. *Plant soil.* 322: 229-238.
- Hesse, M., Halbritter, H., Zitter, R., Webber, M., Buchner, R., Frosch-Radivo, A., Ulrich, S. (2009). Pollen terminology, an illustrated handbook, Springer, 266pp.
- Heywood, V.H., Brummitt, R.K., Culham, A., Seberg, O. (2007). Flowering plant families of the world. Kew: Royal Botanic Gardens.
- Hosni, H.A. (1988). A conspectus of *Tribulus* in Arabia. *Taeckholmia*. 11: 1-18.
- IBNI (2023). The International Plant Names Index (2012). Published on the internet <http://www.ipni.org> [accessed May 2025].
- INaturalist. Available from <https://www.inaturalist.org>. (accessed May 2025).
- Johansen, D.A. (1940). *Plant Microtechnique*. McGraw-Hill Book Co., New York. 790 pp.
- Khafagi, A.A.F. (2004). The taxonomic significance of micro-and macro-morphological characters of spiny stipules in *Fagonia* species. *J. Fac. Educ.* 29: 167-177.
- Khalifa, S.F. (1968). *Taxonomic Studies on Some Plants Belonging to the Order Geraniales*. 324 pp. M.Sc. Thesis, Bot. Dept., Fac. Sci., Ain Shams Univ., Cairo, Egypt.
- Lauterbach, M., van der Merwe, P.D.W., Keßler, L., Pirie, M.D., Bellstedt, D.U., Kadereit, G. (2016). Evolution of leaf anatomy in arid environments—A case study in southern African *Tetraena* and *Roepera* (Zygophyllaceae). *Mol. Phylogenet. Evol.* 97: 129–144. <https://doi.org/10.1016/j.ympev.2016.01.002>.
- Kuprianova, L.A., Alyoshina, L.A. (1978). *Pollen and Spores of Plants from the Flora of European Part of the USSR*. Vol. II. Lamiaceae-Zygophyllaceae. Akad. Nauk S.S.S.R., Komarov Botanical Institute, Leningrad, 184 pp. (in Russian).
- Metcalf, C. R., Chalk, L. (1957). *Anatomy of Dicotyledons* II. Clarendon Press, Oxford. 557 pp.
- Minitab. (2022). Minitab statistical & data analysis software.
- Nikolova, A., Vassilev, A. (2011). A study on

- Tribulus terrestris* L. anatomy and ecological adaptation. *Biotechnol. Biotechnol. Equip.* 25(2): 2369-2372.
- Perveen, A, Qaiser, M. (2006). *Pollen flora of Pakistan*-XLIX. Zygophyllaceae. *Pak. J. Bot.* 38(2): 225-232.
- Pragłowski, J. (1987). Pollen morphology of Tribulaceae. *Grana.* 26(3): 193-211.
- Punt, W., Hoen, P.P., Blackmore, S., Nilsson, S., Le Thomas, A. (2007). Glossary of pollen and spore terminology. *Rev. Paleobot. Palynol.* 143(1-2):1- 81.
- Sage, R.F., Christin, P.A., Edwards, E.J. (2011). The C4 plant lineages of planet earth. *J. Exp. Bot.* 62: 3155–3169. <https://doi.org/10.1093/jxb/err048>.
- Saleh, N.A., El Hadidi, M.N., Ahmed, A.A. (1982). The chemosystematics of Tribulaceae. *Biochem. Sys. Ecol.* 10(4): 313-317.
- Sass, J.E. (1958). *Botanical microtechnique*. 3<sup>rd</sup> ed. Iowa State University, 228 pp.
- Sathee, L., Jain, V. (2022). Interaction of Elevated CO<sub>2</sub> and Form of Nitrogen Nutrition Alters Leaf Abaxial and Adaxial Epidermal and Stomatal Anatomy of Wheat Seedlings. *Protoplasma.* 259: 703–716.
- Semerdjieva, I. (2011). Studies on leaf anatomy of *Tribulus terrestris* L.(Zygophyllaceae) in populations from the Thracian floristic region. *Biotechnol. Biotechnol. Equip.* 25(2): 2373-2378.
- Shamso, E., Rabei, S., Hamdy, R. (2013). Identification keys and numerical studies of Zygophyllaceae (s. str) and allied families in Egypt. *Assiut Univ. J. Bot.* 42(2): 79-106.
- Sheahan, M.C., Cutler, D.F. (1993). Contribution of vegetative anatomy to the systematics of the Zygophyllaceae R. Br. *Bot. J. Linn. Soc.* 113(3): 227-262.
- Sheahan, M.C., Chase, M.W. (1996). A phylogenetic analysis of Zygophyllaceae R. Br. Based on morphological, anatomical & rbcL DNA sequence data. *Bot. J. Linn. Soc.* 122: 279–300.
- Sheahan, M.C., Chase, M.W. (2000). Phylogenetic relationships with Zygophyllaceae based on DNA sequences of three plastid regions, with special emphasis on Zygophylloideae. *Syst. Bot.* 25: 371–384.
- Shipaunov, A.B. (2012). *Systema angiospermarum*. Version 5.7. website <http://herba.msu.ru/shipunov/ang/current/syang.pdf> [Accessed May 2025].
- Song, J.H., Hong, S.P. (2018). Comparative petiole anatomy of the tribe Sorbarieae (Rosaceae) provide new taxonomically informative characters. *Nordic J. Bot.* 36(5): e01702 doi:10.1111/njb.01702.
- Stevens, P.F. (2001 onwards). Angiosperm phylogeny Website. Version 14, July 2017 [and more or less continuously updated since]." will do. <http://www.mobot.org/MOBOT/research/APweb/>.
- TPL, The Plant List. (2013). Version 1.1. Published on the Internet; <http://www.theplantlist.org/> (accessed on May 2025).
- Täckholm, V. (1974). *Students' Flora of Egypt* 2nd ed. Cairo University.
- Taia, W.K., Ibrahim, M.M., Riyad, S., Hassan, S.A. (2017). Anatomical study of the desert Fagonia L. species in Libya. *Egypt. J. Exp. Biol. (Botany).* 13(1): 135-144.
- Taia, W.K., Ibrahim, M.M., Hassan, S.A., Asker, A. (2021). Palynological study of the genus Fagonia L. (Zygophyllaceae, Zygophylloideae) in Libya. *LJST.* 13(1):29-37.
- Takhtajan, A.L. (1969). *Flowering plants: Origin and dispersal*. Edinburgh: Oliver & Boyd.
- Takhtajan A.L. (1986). *Floristic regions of the world*. Berkeley: University of California Press.
- Takhtajan A.L. (2009). *Flowering plants*. Berlin: Springer-Verlag.
- Thiers, B. (2024). *Index Herbariorum*. A Global Directory of Public Herbaria and Associated Staff. New York Botanical Garden's Virtual Herbarium. Available online <http://sweetgum.nybg.org/science/ih/> (accessed on March 2024).
- Tropicos.org. (2025). Missouri Botanical Garden. <http://tropicos.org>
- Waly, N.M., Al-Ghamdi, F.A., Al-Shamrani, R.I. (2011). Developing methods for anatomical identification of the genus Zygophyllum L. (Zygophyllaceae) in Saudi Arabia. *Life Sci. J.* 8(3):451-459.
- Welkie, G.W., Caldwell, M. (1970). Leaf anatomy of species in some dicotyledon families as related to the C3 and C4 pathways of carbon fixation. *Can. J. Bot.* 48(12): 2135-2146.
- Yunus, D., Nair, P.K.K. (1988). *Pollen morphology of Indian Geraniales*. V. XV-XVI.1-22. Today and Tomorrow's Printer. Publishers. New Dehli.
- Zaman, S., Padmesh, S. (2009). Leaf anatomical adaptations of selected Kuwait's native desert plants. *Eur. J. Sci. Res.* 37(2): 261-268.
- Zohary, M. (1972). *Flora Palaestina*. Vol.2: 244-258. Israel Academy of Sciences and Humanities, Jerusalem.

## الملخص العربي

### عنوان البحث: التقييم الشامل للصفات المورفولوجية و التشريحية و حبوب اللقاح لبعض الأنواع المختارة من الفصيلة الرطريبية في مصر

أمل عبدالصير دراز<sup>١\*</sup>، حسناء أحمد حسنى<sup>٢</sup>، سلوى على قوشتى<sup>١</sup>، سامح رضا حسين<sup>١</sup>، إيمان محمود شمسو<sup>٢</sup>

<sup>١</sup> قسم كيمياء و تصنيف النباتات – معهد بحوث الصناعات الصيدلانية و الدوائية – المركز القومي للبحوث – مصر

<sup>٢</sup> قسم النبات و الميكروبيولوجى – كلية العلوم – جامعة القاهرة - مصر

تقدّم هذه الدراسة تحليلاً مقارناً شاملاً لستة من الأنواع المصرية التابعة للعائلة الرطريبية ، و الممثلة للأجناس *Fagonia* و *Zygophyllum* و *Tribulus*. و قد تم عمل دراسة متكاملة تضم دراسات مورفولوجية، وتشريحية، وصفات حبوب اللقاح باستخدام كلا من المجهر الضوئي (LM) و المجهر الإلكتروني الماسح (SEM). و يعد الهدف الرئيسي للدراسة هو تقييم الأهمية التصنيفية لهذه الصفات المدروسة وتعزيز دقة تعريف وتصنيف هذه الأنواع داخل العائلة. وقد اشتملت الدراسات المورفولوجية صفات تركيب الأوراق ، والصفات المظهرية للأزهار والثمار، بالإضافة إلى خصائص البذور، و على الجانب الآخر ركزت الدراسات التشريحية على تنظيم و توزيع الأنسجة في السيقان والعناقيد الورقية وأنصال الأوراق ، مع التركيز على صفات البشرة الخارجية للأوراق، وأنماط الأنسجة الوعائية، وتوزيع البلورات. أما تحليل حبوب اللقاح فقد أظهر تباين واضح في حجم حبوب اللقاح، وقطبيتها، وأنواع الفتحات، وأنماط زخرفة السطح الخارجى لها. كما تم تسجيل وتحليل ٢١٩ صفة إحصائياً باستخدام برنامج Minitab ، و نتج عن هذا التحليل شجرة Dendrogram مبينة انفصال أنواع *Tribulus* عن باقي الأنواع المدروسة، في حين أظهرت تقارباً بين كلا من أنواع *Fagonia* و *Zygophyllum simplex*. كما أوضحت هذه الدراسة القيمة التصنيفية للتكامل بين النتائج المورفولوجية والتشريحية وحبوب اللقاح في اعتبار جنس *Tribulus* كوحدة تصنيفية متميزة داخل عائلة *Zygophyllaceae*. وعليه فإن هذه الصفات المجتمعة تعد قيم تصنيفية في تحديد الأنواع وتصنيفها بدقة على المستويين الجنسي والنوعي.

## Modelling Maritime Traffic at Damietta Port as M/M/c/N Queuing Model with Encouraged Arrivals

Ghadeer Alshreef<sup>\*1</sup> and Ahmed M K Tarabia<sup>1</sup>

<sup>1</sup>Department of Mathematics, Faculty of Science, Damietta University, Damietta, Egypt

Received: 03 July 2025 /Accepted: 12 July 2025

\*Corresponding author's E-mail: gh\_alshreef@du.edu.eg

### Abstract

Damietta Port is one of the most important ports in Egypt, with increased rates of ship arrival, loading and unloading during seasons and before holidays. We proposed an M/M/c/N queuing model which describes maritime traffic and ships handling. Numerical data were also discussed and plotted to investigate the attitude of the maritime traffic. The objective of the study is to improve the efficiency of logistical procedures and reduces truck waiting time and reduces ground congestion resulting from the transport, packing and unloading process.

**Keywords:** Queuing Model, M/M/c/N, Damietta port, Encouraged arrivals.

### Introduction

Queuing systems are widely applied and clearly observable in daily life. Our model in this paper is based on the nature of the author's surrounding environment and the place of life that is Damietta port is a vital authority in Damietta Governorate. The movement of loading and unloading ships in the docks of Damietta port represents a major and clear challenge, that is encouraged arrivals in this model represented by the increase in the number and rates of ships arriving at the port during seasonal or holiday periods, when the demand for food commodities and seasonal needs is at its highest levels. Rates also reach their highest levels during the harvest period of agricultural

crops that are exported to countries that lack these crops.

This model contributes to improving the efficiency of logistical procedures and determining appropriate times for trucks to enter the transport and unloading yards, which reduces truck waiting time and reduces ground congestion resulting from the transport, packing and unloading process.

### Model Description

Our model is a Markovian queuing model with multi-server, finite capacity and encouraged arrivals it subject to the following assumptions:

- Let  $P_i$  denotes the probability that the system has  $i$  customers (ships) in the



system, thus  $P_0$  means the probability that the system is empty and  $P_N$  express the probability that the system is full.

- The arrivals of the customers (ships) occur according to Poisson process with parameter  $\lambda(1+\alpha)$ , where  $\alpha$  is the percentage expresses the arrival rate of ships which calculated from observed and remarked data.
- In the case of decreases arrivals rate  $\alpha = 0.75$ , and in the case of increase arrivals rate we will take  $\alpha = 1.5$ .
- Service times are subjected to exponential distribution with parameter  $\mu$ .
- Ships are serviced in the order of their arrival (first come first served).
- The quay has maximum capacity  $c$  of ships, which can be served at the same time.
- The total capacity of the operation of loading and unloading ships is  $N$ .

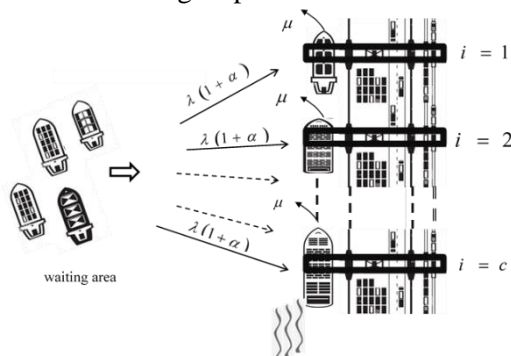


**Fig. 1** arrivals and serving the ships as M/M/c/N queuing model

This model is discussed in Gross and Harris (1998) and Sharma and Tarabia (2000) where the model is described in its simplest form. In Som and Seth (2017, 2018) evolve Markovian queuing model with a multi-server Feedback and encouraged arrivals also with a good addition which is customer impatience, and retention of impatient customers. They obtained the stationary system size probabilities. Also, they calculate some measures of efficiency and gave numerical discussions to illustrate attitude of the system. Some special cases are obtained and discussed. Recently in (2024) Cruz and Julia are analysis and discussed the queuing model of M/M/c with encouraged arrival, they assumed that the arrival rate is a function of the customer's number in the system. Their model was discussed by the technique of continuous time Markov chain, and the steady state probabilities are obtained too.

In this paper, we developed a M/M/c/N queuing

model to describe the maritime traffic and ship handling, and applied this model to the ship traffic in Damietta Port. The steady state probabilities of this model and the expected values of ship waiting times in the system and in the queue were calculated, and the numerical data of the model were discussed and plotted to investigate the maritime traffic situation.

### Mathematical Formulation of the Model

This applicable model can be described by the following balance equations:

$$\begin{aligned} \mu P_1 &= \lambda(1+\alpha) P_0, & i=0 \\ (i+1)\mu P_{i+1} &= (\lambda(1+\alpha) + i\mu) P_i - \lambda(1+\alpha) P_{i-1}, & 1 \leq i \leq c-1 \\ c\mu P_{i+1} &= (\lambda(1+\alpha) + c\mu) P_i - \lambda(1+\alpha) P_{i-1}, & c \leq i \leq N-1 \\ c\mu P_N &= \lambda(1+\alpha) P_{N-1}, & i=N \end{aligned}$$

Solving the system recurrently, then

$$P_i = \begin{cases} \frac{1}{i!} \left( \frac{\lambda(1+\alpha)}{\mu} \right)^i P_0, & 1 \leq i \leq c \\ \frac{1}{c^{i-c} c!} \left( \frac{\lambda(1+\alpha)}{\mu} \right)^i P_0 & c < i \leq N \end{cases}$$

where

$$P_0 = \Pr\{\text{system is empty}\}$$

$$P_N = \Pr\{\text{system is full}\},$$

Now, to calculate  $P_0$ , we will use the normality

condition  $\sum_{i=0}^N P_i = 1$ , then

$$P_0 = \left( \sum_{i=0}^c \frac{1}{i!} \left( \frac{\lambda(1+\alpha)}{\mu} \right)^i + \sum_{i=c+1}^N \frac{1}{c^{i-c} c!} \left( \frac{\lambda(1+\alpha)}{\mu} \right)^i \right)^{-1}$$

### Some Performance Measures

Here, we will introduce some useful performance measures, which can be calculated easily to Controlling the facilitating of Maritime Logistics:

- Expected system size  $L_s = \sum_{i=1}^N iP_i$
- Expected queue length  $L_q = \sum_{i=c}^N (i - c)P_i$
- Expected waiting time in the system  $W_s = \frac{L_s}{\lambda(1+\alpha)}$
- Expected waiting time in the queue  $W_q = \frac{L_q}{\lambda(1+\alpha)}$

### Numerical Illustrations

In this section we will introduce some numerical examples which illustrate the behavior of traffic flow in the port. In Table 1 and 2 we illustrate the case of un encouraged arrivals by assume  $\alpha=0.75$ , in Table 1, we assume  $N = 15, c = 4, \lambda = 5, 3 \leq \mu \leq 6$ , and

in Table 2 we assume  $N = 15, c = 4, \mu = 3, 3 \leq \lambda \leq 6$ . Table 3 and 4 are explaining the behavior in the encouraged arrivals case ( $\alpha = 1.5$ ). In Table 1 we can see that the predicted waiting time in the system and in the queue are decreasing while the service rate ( $\mu$ ) is increases with stable arrivals rate ( $\lambda$ ). Data in Table 2 provided that the expected waiting time in the system and in the queue are increasing while the arrivals rate ( $\lambda$ ) is increases with stable service rate ( $\mu$ ). In Table 3 once  $\mu \geq c$  the length of the queue will excessively get low as will as waiting time in the system and in the queue which give an approximated behavior for decreasing the expected waiting time in the system and in the queue when service rate ( $\mu$ ) is increases with stable arrivals rate ( $\lambda$ ) in the case of encouraged arrivals. Also Table 4 illustrate the case of encouraged arrivals that the predicted waiting time in the system and in the queue are increasing while the arrivals rate ( $\lambda$ ) is increases with stable service rate ( $\mu$ ).

**Table 1.** Relation between variant values of  $\mu$  at  $\alpha = 0.75, N = 15, c = 4, \lambda = 5$  and performance measures.

$\mu$	$P_0$	$L_s$	$L_q$	$W_s$	$W_q$
3	0.0646707	2.45420	0.09633140	0.280480	0.0110093
3.5	0.0919778	2.14252	0.01465560	0.244860	0.00167492
4	0.1207580	1.93880	0.00282091	0.221577	0.00032239
4.5	0.1502350	1.77124	0.00065603	0.202427	0.00007497
5	0.1796830	1.62734	0.00017807	0.185982	0.00002035
5.5	0.2085750	1.50241	0.000055019	0.171704	0.00000629
6	0.2365700	1.39334	0.000018997	0.159239	0.00000217

**Table 2.** Relation between variant values of  $\lambda$  at  $\alpha = 0.75, N = 15, c = 4, \mu = 3$  and performance measures.

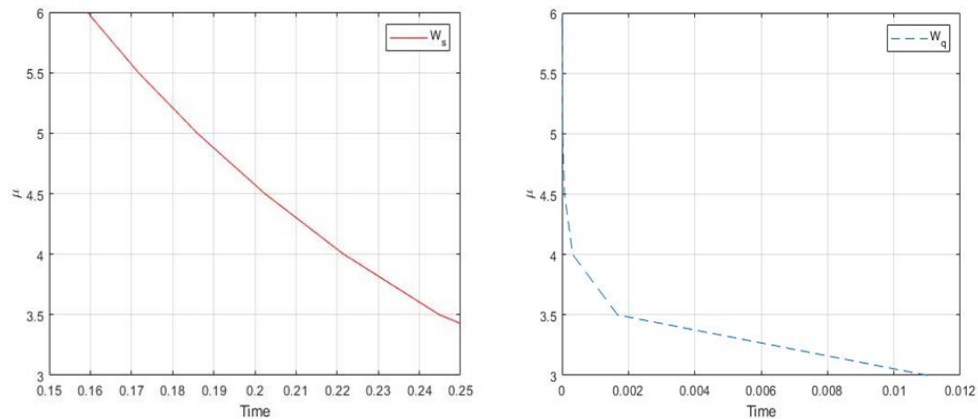
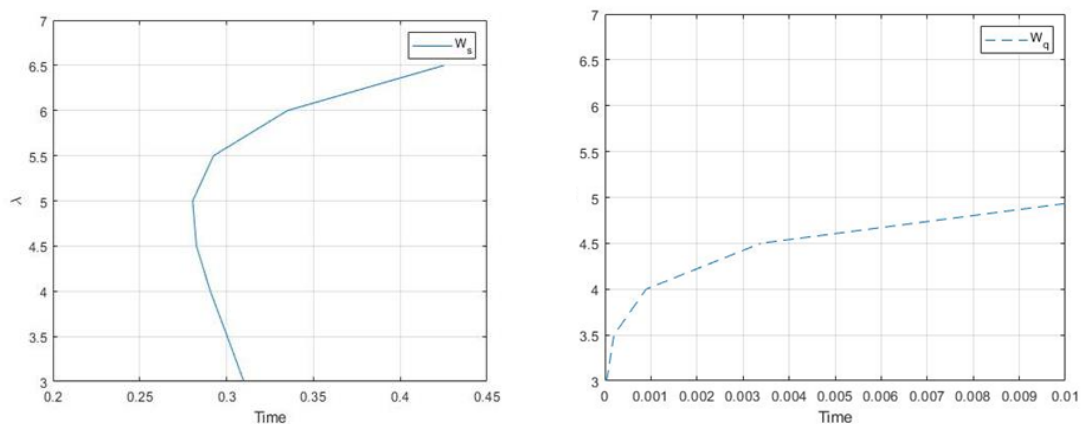
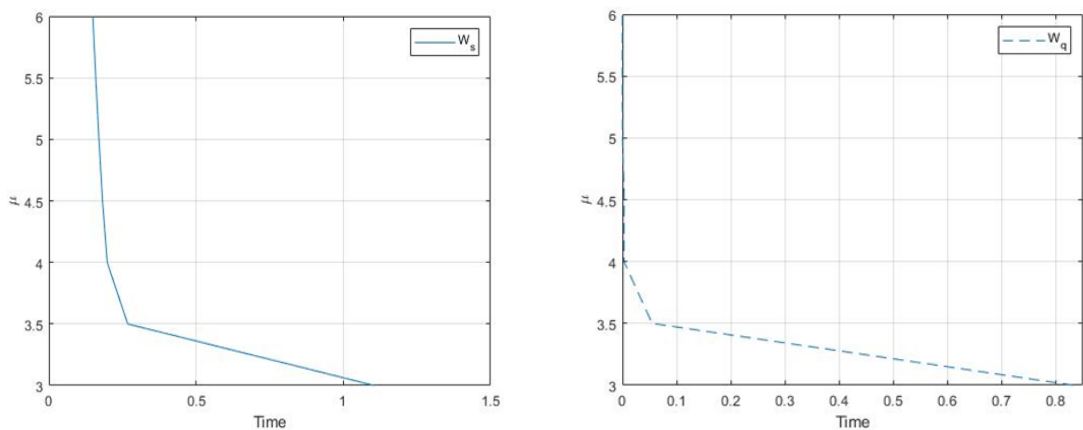
$\mu$	$P_0$	$L_s$	$L_q$	$W_s$	$W_q$
3	0.179683	1.62734	0.00017807	0.309969	0.000039177
3.5	0.137568	1.83976	0.00120067	0.300369	0.000196028
4	0.106228	2.03448	0.00626306	0.290640	0.000894722
4.5	0.0826829	2.22582	0.02667790	0.282644	0.003387670
5	0.064671	2.45420	0.09633140	0.280480	0.011009300
5.5	0.0504011	2.81845	0.30137800	0.292826	0.031312000
6	0.0384047	3.51853	0.82029200	0.335098	0.078123000
6.5	0.0276457	4.837701	1.91069000	0.425232	0.167973000

**Table 3.** Relation between variant values of  $\mu$  at  $\alpha = 1.5, N = 25, c = 4, \lambda = 5$  and performance measures.

$\mu$	$P_0$	$L_s$	$L_q$	$W_s$	$W_q$
3	0.0129190	13.8132	10.4064000	1.16506	0.832512000
3.5	0.0381802	3.34712	0.68578000	0.267769	0.054862400
4	0.0552472	2.47769	0.03714990	0.198216	0.002971990
4.5	0.0730428	2.27734	0.00273396	0.182188	0.000218717
5	0.0921072	2.12550	0.00026265	0.17004	0.00002101
5.5	0.1120620	1.98963	0.00003142	0.159171	0.00000250
6	0.1325310	1.86662	0.00000451	0.149329	0.00000036

**Table 4.** Relation between variant values of  $\lambda$  at  $\alpha = 1.5, N = 25, c = 4, \mu = 3$  and performance measures.

$\mu$	$P_0$	$L_s$	$L_q$	$W_s$	$W_q$
3	0.0921072	2.1255	0.0002627	0.283400	0.00003502
3.5	0.0652450	2.35135	0.0080701	0.268726	0.00092229
4	0.0468044	2.68957	0.1537980	0.268957	0.01537980
4.5	0.0315383	4.68408	1.8857400	0.416362	0.16762100
5	0.0129190	13.8132	10.406400	1.105060	0.83251200
5.5	0.0021707	22.3296	18.448600	1.623970	1.34171000
6	0.00027818	24.3546	20.372600	1.623640	1.35818000

**Fig 2, 3** The performance of waiting time at the system and waiting time at the queue in case  $\alpha = 0.75, N = 15, c = 4, \lambda = 5$ .**Fig. 4, 5** The performance of waiting time at the system and waiting time at the queue in case  $\alpha = 0.75, N = 15, c = 4, \mu = 3$ .**Fig. 6, 7** The performance of waiting time at the system and waiting time at the queue in case  $\alpha = 1.5, N = 25, c = 4, \lambda = 5$ .

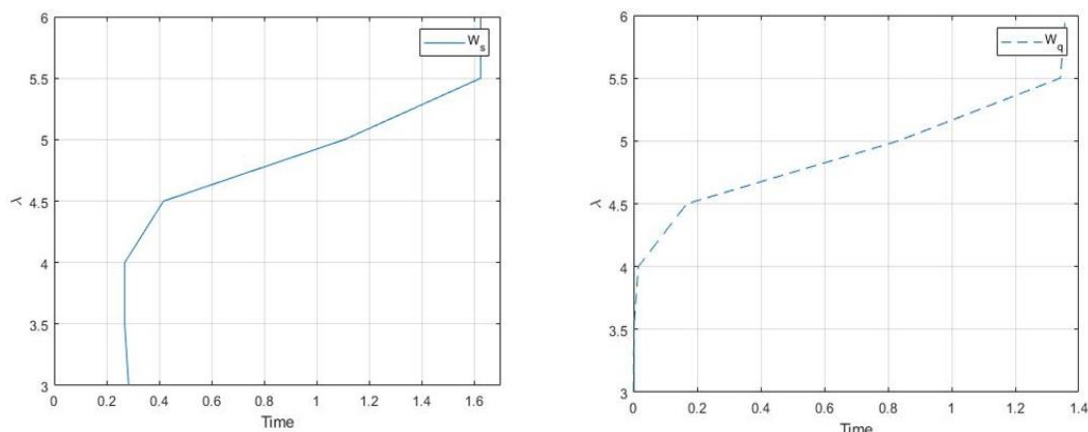


**Fig. 8, 9** The performance of waiting time at the system and waiting time at the queue in case  $\alpha = 1.5, N = 25, c = 4, \mu = 3$ .

## Conclusion

We describe the maritime traffic and ship handling in Damietta port as M/M/c/N Markovian queuing model. The steady state probabilities are calculated and some measures of fulfillment status like expected system size  $L_s$ , expected queue length  $L_q$ , expected waiting time in the system  $W_s$ , expected waiting time in the queue  $W_q$ . The numerical data of the model were discussed and plotted to investigate the maritime traffic situation which raising the efficiency of logistical procedures and optimizing the wasted waiting time in the future.

## Acknowledgment

Authors are grateful to Damietta Port Authority for facilities that gives to them while

preparing this paper.

## References

- Cruz A. and Julia Rose Mary J. (2024) Analysis of M/M/C Queuing Model with Encouraged Arrival. International journal of humanities and science, 1(2), 33-38.
- Gross, D. and Harris, C. (1998) Fundamentals of Queuing Theory. 3rd Edition, John Wiley, Chichester.
- Som, B.K., Seth.S. (2017) An M/M/1/N Queuing system with ncuraged Arrivals. Global Journal of Pure and Applied Mathematics, 17(3), 252-255.
- Som, B.K., Seth, S. (2018) M/M/C/N queuing systems with encouraged arrivals, reneging, retention and feedback customers. Yugoslav Journal of Operations Research, 28(3), 333-344.
- Sharma, O. and A. Tarabia (2000) A simple transient analysis of an M/M/1/N queue. Sankhyā: The Indian Journal of Statistics, Series A, 273-281.

## الملخص العربي

**عنوان البحث:** نمذجة حركة المرور البحرية في ميناء دمياط كنموذج لطابور M/M/c/N مع تشجيع الواصلين

غدير عبد الوهاب الشريف<sup>1\*</sup>، أحمد محمد كامل طرابية<sup>1</sup>

<sup>1</sup>قسم الرياضيات، كلية العلوم، جامعة دمياط، دمياط، مصر

في هذا البحث تم تقديم نموذج طابور متعدد الخادم كنموذج لحركة الملاحة البحرية للسفن في ميناء دمياط حيث تم وصف حركة الملاحة البحرية وفترة انتظار السفن للشحن والتفريغ على ارضية الميناء كنموذج رياضي يتمثل في طابور متعدد الخادم وتم حساب المدة المتوقعة للبقاء في النظام والمدة المتوقعة للبقاء على رصيف التفريغ كما تم القيام ببعض الحسابات الرقمية من واقع المعدلات الحقيقية لميناء دمياط.

## Chaotic Motion of an Electrodynamic Tethered Satellite System under Oblateness Effect in a Circular Orbit

A. Yousof<sup>\*1</sup>, A.M. Abdelaziz<sup>2</sup>, Abd El Hakeem Abd El Naby<sup>1</sup> and Yehia A. Abdel-Aziz<sup>2</sup>

<sup>1</sup>Damietta University, Mathematics Department, Damietta, Egypt.

<sup>2</sup>National Research Institute of Astronomy and Geophysics (NRIAG), Cairo, Egypt.

Received: 01 July 2025 /Accepted: 10 July 2025

\*Corresponding author's E-mail: A.usf@du.edu.eg

---

### Abstract

This paper investigates the chaotic behavior of an in-plane electrodynamic tethered satellite system (EDTSS) operating in a circular orbit under the influence of Earth's oblateness, represented by the  $J_2$  zonal harmonic. The system is modelled using the dumbbell model, consisting of two point masses connected by an inelastic tether. The equations of motion are derived through the Lagrangian formulation, incorporating the effects of the Lorentz force generated by the current interacting with Earth's magnetic field and the radial acceleration due to the oblateness of Earth. To analyze the conditions under which chaos may arise, the Melnikov method is applied, leading to the identification of a necessary condition for the occurrence of chaotic motion. Based on this condition, the parameter domains that are likely to result in chaotic behavior are determined. To confirm the analytical findings, numerical simulations are conducted and discussed. The results highlight the critical role of the oblateness effect and its interaction with electrodynamic forces in governing the nonlinear dynamics of tethered satellite systems.

**Keywords:** Chaos; Electromagnetic Force; Melnikov Analysis; Poincaré Section; Tethered Satellite System.

---

### Introduction

Space tether systems are a promising solution for enabling highly efficient and low-cost space operations, including debris removal (Ma X and Wen H, (2023) ; Razzaghi P et al., (2021) ; Svotina V and Cherkasova M, (2023) ), energy generation (Liu J et al., (2020) ; Liu J and McInnes CR, (2019) ; Hu W et al., (2018) ), and

asteroid exploration (Mashayekhi MJ and Misra AK, (2016) ; Zhong R and Wang Y, (2018) ). As space activities expand, these systems offer a sustainable and effective approach to future mission design. Thus, the tethered satellite system (TSS) has emerged as one of the most active areas of research in space sciences (Huang P et al., (2018) ; Sanmartin JR et al., (2010) ; Kumar K, (2006) ; Modi V et al., (1990) ; Sánchez-Arriaga G et al., (2024) ). A typical TSS consists of two or more satellites

connected by a tether element. Extensive studies have focused on these systems' modelling, dynamics, and control (Hong AaT et al., (2024) ; Andrievsky B et al., (2022) ). Both Newtonian and Lagrangian mechanics are commonly applied to derive the equations of motion, with either orbital elements or libration angles used to represent the system states. The tether itself is modelled in various ways, either as massless or massive, rigid or flexible, depending on the objectives and assumptions specific to each study ( Aslanov V and Ledkov A, (2012) ; Troger H et al., (2010) ).

The dynamics of a tethered satellite mission are significantly influenced by various environmental perturbations that must be carefully considered during modeling and control design. Among the most prominent perturbing forces are aerodynamic drag, which is particularly relevant in low Earth orbits; solar radiation pressure, which induces subtle but continuous force variations; and the oblateness of the Earth, represented by the  $J_2$  zonal harmonic, which alters the gravitational field and affects orbital stability. In addition to these, other perturbations such as third-body gravitational influences and magnetic torques may also impact the system depending on the mission profile. Accounting for these forces is essential to accurately predict system behaviour and ensure the success and longevity of tethered satellite operations.

Given the critical role of Earth's oblateness, represented by the  $J_2$  coefficient, many researchers have explored its influence on orbital and tethered system behaviour. Zheng P et al., (2008) developed a mathematical model using Lagrangian mechanics and numerical simulations to analyse the deployment of a tether-assisted deorbit system under Earth's  $J_2$  perturbation. Their results showed that  $J_2$  mainly affects in-plane motion during deployment, without inducing out-of-plane motion when the initial out-of-plane angle is zero. Yu B and Jin D, (2010) modelled a viscoelastic tethered satellite system and examined the effects of  $J_2$  and thermal perturbations. They found that  $J_2$  significantly affects deployment, especially with friction, while thermal effects mainly influence retrieval, resulting in distinct motion behaviours. Yu B et al., (2016) extended the analysis of a flexible tethered satellite system under additional perturbations, including air drag, solar radiation pressure, and orbital eccentricity. Using a

simplified two-degree-of-freedom model, they conducted numerical simulations that revealed bifurcations, quasi-periodic oscillations, and chaotic motions. They concluded that  $J_2$  perturbation and thermal effects strongly influence pitch dynamics and must be considered, while air drag and solar pressure have a lesser impact depending on orbital altitude. Yu B et al., (2020) applied Melnikov analysis to determine the conditions under which chaotic motion arises in a tethered satellite system operating in a circular orbit. Their study considered the combined effects of Earth's  $J_2$  perturbation and aerodynamic drag, showing that these perturbations can induce chaotic dynamics even when the tether is modelled as rigid. Yuan W et al., (2024) studied the chaotic motion of a tether-sail system in polar orbits, considering  $J_2$  perturbation and orbital eccentricity. Using Lagrangian modelling and Melnikov analysis, they showed that both  $J_2$  and eccentricity enhance chaotic behaviour.

Electrodynamic tethers (EDTs) provide key advantages over traditional tether systems by generating Lorentz forces without propellant, enabling efficient orbit control and power generation. Studies have examined the impact of Earth's  $J_2$  perturbation on EDT dynamics. Tikhonov A et al., (2017) showed that an electrodynamic control system can effectively counteract gravity gradient torque caused by  $J_2$  in near-Earth orbits.

To the best of our knowledge, no previous study has analytically examined the impact of Earth's oblateness ( $J_2$  perturbation) on the dynamics of electrodynamic tethered satellite systems. Therefore, this paper aims to fill this gap by focusing on the analytical characterization of such effects. The paper is organized as follows: In Section 2, the system is modelled as a dumbbell model with non-negligible tether mass, and the equations of motion are derived using the Lagrangian approach. In Section 3, the analytical Melnikov method is applied to identify conditions under which chaotic motion may occur. Section 4 presents numerical simulations that validate the analytical results. Finally, the conclusions are discussed in Section 5.



## Mathematical Model

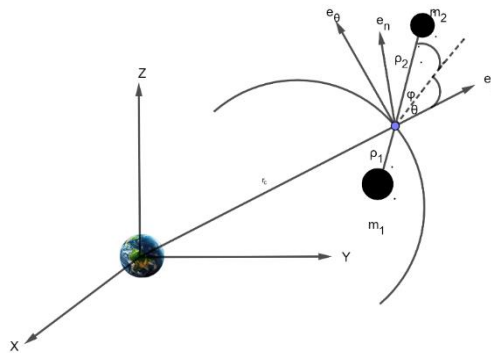


Fig. 1 Tethered Satellite System

Consider a tethered satellite system (TSS) orbiting Earth in a circular orbit, as shown in Fig. 1. A dumbbell model describes a TSS, which consists of a mother satellite connected to a subsatellite with a tether, where  $m_1$ ,  $m_2$ , and  $m_t$  are their masses, respectively.

An inertial frame,  $(X, Y, Z)$ , is considered, which is centered at Earth's center. The  $X$ -axis is oriented toward the vernal equinox, the  $Z$ -axis aligns with Earth's rotation axis, and the  $Y$ -axis lies within Earth's equatorial plane, maintaining a right-handed coordinate system. A rotating frame,  $(e_r, e_\theta, e_n)$ , centered at system's mass center, has a relative position vector to the inertial frame,  $r_c$ . The three unit vectors,  $(e_r, e_\theta, e_n)$ , points radially outward opposite to Earth's center of mass, oriented along the velocity direction, and completes the right-handed coordinate triad, respectively.

The mother satellite and subsatellite have position vectors relative to the system's mass center,  $\rho_1$  and  $\rho_2$ , respectively. The variable  $\theta$  represents the in-plane angle, while  $l$  denotes the tether length at any given time.

Suitable expressions for both kinetic and potential energies are essential for developing the system's Lagrangian. By integrating kinetic energy over the tether length and adding the kinetic energies of both the mother satellite and the subsatellite, one can obtain the total kinetic energy,  $T$ , as follows Aslanov V and Ledkov A, (2012)

$$T = \frac{1}{2} m \dot{r}_c^2 + \frac{1}{2} \mu_e (l^2 + l^2 (\dot{\theta} + \dot{\nu})^2), \quad (1)$$

where  $m = m_1 + m_2 + m_t$  is a total mass, the dot represents the derivative with respect to time,

$$\mu_e = \frac{(m_1 + m_t/2)(m_2 + m_t/2)}{(m_1 + m_2 + m_t) - m_t/6}$$

is a reduced mass, and  $\nu$  is the true anomaly.

By summing the potential energies of the system's elements, noting that the tether length is very small compared to the radius of the mass's center, the system's potential energy,  $W$ , can be written on the form

$$W = -\frac{\mu m}{r_c} - \frac{\mu \mu_e l^2}{2 r_c^3} (3 \cos^2 \theta - 1), \quad (2)$$

where  $\mu$  is Earth's gravitational strength constant.

Using Eqs. (1) and (2), Lagrangian,  $L$ , can be constructed as  $L = T - W$ . The system's Lagrangian equations of motion have the form

$$\frac{d}{dt} \frac{\partial L}{\partial \dot{q}_i} - \frac{\partial L}{\partial q_i} = Q_i, \quad (3)$$

where  $q_i = \theta, l$  are generalized coordinates, and  $Q_i$  are not potential generalized forces.

Using the following nondimensional transformation  $\frac{d}{dt} = \frac{d}{d\nu} \dot{\nu}$ ,  $L = \frac{l}{l_r}$ , equations of motion in nondimensional form can be written as

$$\theta'' + 2(\theta' + 1) \frac{L'}{L} + 3 \cos \theta \sin \theta = \frac{Q_\theta}{\mu_e l^2 \dot{\nu}^2}, \quad (4)$$

$$L'' - L[(\theta' + 1)^2 - 3 \cos^2 \theta + 1] = \frac{Q_l}{\mu_e \dot{\nu}^2}, \quad (5)$$

the accent means a derivative with respect to the variable  $\nu$  and  $\dot{\nu}^2 = \mu / r_c^3$ .

The system is under the influence of the Lorenz force resulting from the current flow through the tether interacting with the magnetic field and  $J_2$  perturbation since the oblateness of Earth is considered. A non-tilted dipole model of the magnetic field is considered; its components in orbital frame,  $B_r$ ,  $B_\theta$ , and  $B_n$ , are determined as follows Stevens RE, (2008) :

$$B_r = -2 \frac{\mu_m}{r_c^3} \sin \nu \sin i, \quad (6)$$

$$B_\theta = \frac{\mu_m}{r_c^3} \cos \nu \sin i, \quad (7)$$

$$B_n = \frac{\mu_m}{r_c^3} \cos i, \quad (8)$$

where  $i$  is an orbital inclination and  $\mu_m = 7.85 \cdot 10^{15} \text{ N / Am}^2$ , is the magnitude diploe

of Earth. It's assumed that a constant current,  $I$ , flows through the tether, and the magnetic field vector remains unchanged along the entire length. This constancy is attributed to the relatively small length of the tether compared to the system's mass radius. Following the principle of virtual work, the generalized electromagnetic torques  $Q_{\theta e}, Q_{\theta i}$ , can be written in the form:

$$Q_{\theta, e} = -\frac{Il^2(m_2 - m_1)}{2(m_1 + m_2 + m_t)}B_n, \quad (9)$$

$$Q_{\theta, i} = 0.$$

The effect of Earth's oblateness on the tethered satellite system can be evaluated using Earth's nonhomogeneous potential function,  $U$ , as mentioned in Kéchichian JA, (2021) as

$$U = \frac{\mu}{r_c} \left[ 1 - \sum_{n=2}^{\infty} J_n \left( \frac{R}{r_c} \right)^n P_n(\sin(\delta)) \right], \quad (10)$$

where  $J_n$  is a zonal harmonic of order  $n$ ,  $R$  is Earth's equatorial radius,  $\delta$  is the declination of the system's mass center to the equatorial plane, and  $P_n(\sin(\delta))$  is the Legendre polynomial of order  $n$  in  $\sin(\delta)$ . Neglecting the  $J_3$  and higher zonals, replacing  $\sin(\delta)$  by  $z/r_c$ , and using the transformation matrix to the rotating frame, one can obtain the radial perturbation acceleration as

$$a_{ob} = -\frac{3}{2} \frac{J_2 \mu R^2 r_c}{r_c^5} (1 - 3 \sin^2 i \sin^2 \nu). \quad (11)$$

Follows Zhong R and Zhu Z, (2013), the oblateness torque on the satellites caused by the acceleration is in the form

$$Q_{\theta, ob} = \gamma \sin(\theta) + \beta \sin(\theta) \cos(2\nu), \quad (12)$$

where

$$\gamma = \chi \cdot \left( 1 - \frac{3 \sin^2 i}{2} \right), \beta = \chi \cdot \left( \frac{3 \sin^2 i}{2} \right), \quad (13)$$

$$\chi = \left( \frac{3 J_2 \mu R^2 l^2 [m_2 M_m^2 - m_1 (1 - M_m)^2]}{2 r_c^5} \right),$$

where  $M_m = (m_1 + m_t / 2) / m$ .

In this paper, we delve into the nonlinear dynamics of the pitch motion during the station-keeping phase, where the tether length remains constant. Substituting Eqs. (9), (12) into Eq. (4) with  $L' = 0$ , noting that  $Q_{\theta} = Q_{\theta, e} + Q_{\theta, ob}$ , gives

$$\theta'' + 3 \cos \theta \sin \theta = \sigma_1 \sin \theta + \sigma_2 \sin \theta \cos 2\nu + \sigma_3, \quad (14)$$

where

$$\sigma_1 = \sigma^* \cdot \left( 1 - \frac{3 \sin^2 i}{2} \right), \sigma_2 = \sigma^* \cdot \left( \frac{3 \sin^2 i}{2} \right),$$

$$\sigma^* = \left( \frac{3 J_2 R^2 [m_2 M_m^2 - m_1 (1 - M_m)^2]}{2 \mu_e r_c^2} \right), \quad (15)$$

$$\sigma_3 = -\frac{I(m_2 - m_1) \mu_m \cos i}{2 m \mu_e \mu}.$$

One can see from Eq. (14) the electrodynamic tethered satellite system under Earth's oblateness is a nonlinear nonautonomous system.

### Analysis of Chaotic Motion

In this section, the Melnikov function is employed to derive the necessary condition under which the dynamical system may exhibit a chaotic behavior.

Using  $\theta = (\theta_1, \theta_2)^T = (\theta, \dot{\theta})^T$ , one can obtain the state equation of Eq. (14) as

$$\dot{\theta} = f(\theta) + g(\theta, \nu), \quad (16)$$

with

$$f(\theta) = \begin{bmatrix} f_1 \\ f_2 \end{bmatrix} = \begin{bmatrix} \theta_2 \\ -3 \sin \theta_1 \cos \theta_1 \end{bmatrix},$$

$$g(\theta, \nu) = \begin{bmatrix} g_1 \\ g_2 \end{bmatrix} = \begin{bmatrix} 0 \\ \sigma_1 \sin \theta_1 + \sigma_2 \sin \theta_1 \cos 2\nu + \sigma_3 \end{bmatrix}. \quad (17)$$

The perturbation vector,  $g(\theta, \nu) = g(\theta, \nu + p)$ , is periodic of period  $p = \pi$ .

When  $g(\theta, \nu) = 0$ , the system corresponds to the unperturbed Hamiltonian case, with the first integral given by

$$\frac{1}{2} \theta_2^2 + \frac{3}{2} \sin^2 \theta_1 = E, \quad (18)$$

where a constant,  $E$ , represents the total kinetic energy of the system.

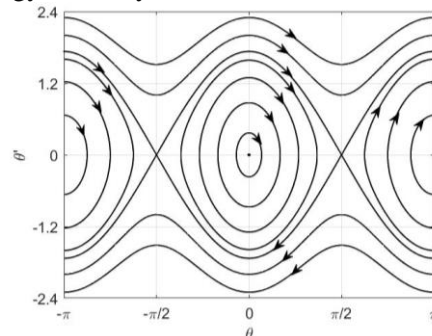


Fig. 2 Phase portrait of unperturbed system

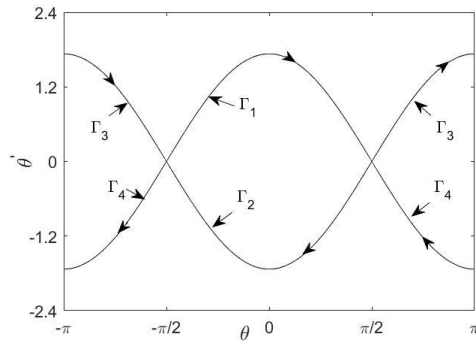


Fig. 3 Heteroclinic orbits

Figures (Fig. 2 and Fig. 3) present the phase portrait of the unperturbed system and the heteroclinic orbits that reach two different saddle points,  $p_i = (\mp\pi/2, 0)$ ,  $i = 1, 2$ . The heteroclinic orbits can be written in the form Yu B et al., (2020)

$$\begin{aligned} &(\theta_{10}^{\pm}(\nu), \theta_{20}^{\pm}(\nu)) \\ &= (\pm \sin^{-1}(\tanh(\sqrt{3}\nu)), \pm \sqrt{3} \operatorname{sech}(\sqrt{3}\nu)). \end{aligned} \quad (19)$$

In the case of the perturbed system when  $\mathbf{g}(\theta, \nu) \neq 0$ , near the equilibrium points, the heteroclinic orbits may split into unstable and stable manifolds. Chaos likely happens if these manifolds intersect transversally; according to Melnikov's analysis, the Melnikov function must have a simple zero (Yu B et al., (2022); Aslanov V, (2017)).

The Melnikov function is given by Aslanov VS, (2024)

$$M_{\pm}(\nu_0) = \int_{-\infty}^{+\infty} \mathbf{f}(\theta_0^{\pm}) \wedge \mathbf{g}(\theta_0^{\pm}, \nu + \nu_0) d\nu, \quad (20)$$

with  $\nu_0 \in [0, p]$ .

Substituting Eq. (17) into Eq. (20), using Eq. (19), yields

$$\begin{aligned} M_{\pm}(\nu_0) &= \int_{-\infty}^{+\infty} [\sigma_1 \sin \theta_{10}^{\pm}(\nu) + \sigma_2 \sin \theta_{20}^{\pm}(\nu) \\ &\quad \cdot \cos 2(\nu + \nu_0) + \sigma_3] \theta_{20}^{\pm}(\nu) d\nu \\ &= \pm \sqrt{3} \sigma_1 \int_{-\infty}^{+\infty} \operatorname{sech}(\sqrt{3}\nu) \tanh(\sqrt{3}\nu) d\nu \\ &\quad \pm \sqrt{3} \sigma_2 \int_{-\infty}^{+\infty} \operatorname{sech}(\sqrt{3}\nu) \tanh(\sqrt{3}\nu) \\ &\quad \cos(2\nu) d\nu \cdot \cos 2\nu_0 \\ &\quad \mp \sqrt{3} \sigma_2 \int_{-\infty}^{+\infty} \operatorname{sech}(\sqrt{3}\nu) \tanh(\sqrt{3}\nu) \\ &\quad \sin(2\nu) d\nu \cdot \sin 2\nu_0 \\ &\quad \pm \sqrt{3} \sigma_3 \int_{-\infty}^{+\infty} \operatorname{sech}(\sqrt{3}\nu) d\nu, \end{aligned}$$

(21)

calculating the integrals in Eq. (21), noting that when an odd function is integrated over a symmetrical interval gives zero. Under the mathematical condition,  $\sin 2\nu_0$  ranges in the interval  $[-1, 1]$ , the Melnikov function  $M_{\pm}(\nu_0)$  has simple zeros if

$$\left| \frac{\sigma_3}{\sigma_2} \right| < 0.2881. \quad (22)$$

Eq. (22) gives the necessary, but not sufficient, condition under which the system may exhibit a chaotic motion near the saddle points.

According to Eqs. (15) and (22), the following four cases can be concluded

- Case one: This is the case when both  $\sigma_2$  and  $\sigma_3$  vanish, the dynamical system equation represents the unperturbed case, which is plotted in Fig. 2 and Fig. 3.
- Case two: This is the case when the system is perturbed only by the effect of the Lorenz force, i.e.  $\sigma_3 \neq 0$  and  $\sigma_2 = 0$ , chaos doesn't occur since the condition, Eq. (22), is not satisfied.
- Case three: This is the case when the  $J_2$  effect constitutes the sole perturbation of the system, i.e.  $\sigma_3 = 0$  and  $\sigma_2 \neq 0$ , chaos might occur since Eq. (22) is satisfied.
- Case four: This is the case when the system is perturbed by both the Lorenz force and the oblateness acceleration, i.e.  $\sigma_3 \neq 0$  and  $\sigma_2 \neq 0$ , chaos may be estimated using Eq. (22).

## Numerical Results

This section presents a numerical simulation to verify the necessary condition, Eq. (22). The system's parameters are given as follows. The mother satellite mass,  $m_1 = 1020 \text{ Kg}$ , the subsatellite mass,  $m_2 = 70 \text{ Kg}$ , and the tether mass,  $m_t = 3.4 \text{ Kg}$ . The system orbits Earth in a circular orbit at an altitude of  $600 \text{ Km}$ , with an inclination of  $63^\circ$ .

One can note that  $\sigma_2$  and  $\sigma_3$  are dependent on the current passing through the tether,  $I$ , the inclination of the orbit,  $i$ , and the orbital altitude,  $H$ .

Firstly, at a specific altitude, using Eq. (22), the

chaotic zone in the parameter domain  $(I, i)$  is plotted in Fig. 4. The initial states of the system are  $(\theta, \theta') = (-\pi/2 + \pi/100, 0)$ , where  $\pi/100$  is a given perturbed angle, positioning the system near one of the unstable saddle points  $(\mp\pi/2, 0)$ . The point  $(0.001, \pi/6)$  lies in the chaotic zone, which corresponds to the system's orbit having an inclination of  $\pi/6$  with one mA current flowing through the tether. Fig. 5 presents a Poincaré section, indicating that the system is chaotic. Fig. 6 shows that the pitch motion angle is in irregular oscillation. If the orbit inclination is altered to  $\pi/60$ , the system is in a nonchaotic zone, which is described by Fig. 7 and Fig. 8, showing that the system is in a periodic motion.

Secondly, the chaotic zone in the parameter domain  $(i, H)$ , is plotted in Fig. 9 at  $I = 1\text{mA}$ . The point  $(\pi/6, 900)$  lies in the nonchaotic zone. Fig. 10 being a Poincaré section, demonstrates that the system exhibits a periodic solution. Fig. 11 confirms this observation, showing that the pitch angle maintains a regular periodic oscillation with respect to the variable  $\nu$ . When the inclination is adjusted to  $\pi/60$ , the system transitions into the chaotic zone. This transition is illustrated in Fig. 12. A Poincaré section corresponding to this state indicates that the system undergoes chaotic motion. Furthermore, Fig. 13 reveals that the pitch angle behaves as an irregular oscillator.

Finally, at an inclination of  $\pi/30$ , the chaotic region within the  $(I, H)$  parameter space is illustrated in Fig. 14. The point  $(0.3 \times 10^{-4}, 600)$ , lies within this chaotic region.

Fig. 15 and Fig. 16 confirm this result, demonstrating that the system exhibits chaotic behavior. However, when the current flowing through the tether is increased to  $0.3 \times 10^{-2}$  the system no longer displays chaotic motion. Fig. 17 and Fig. 18 illustrate the resulting tumbling periodic motion of the system.

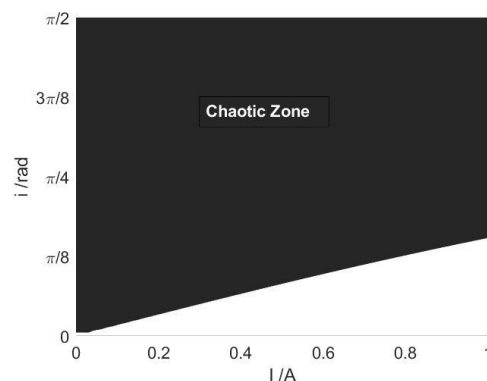


Fig. 4 Parameter domain for chaos

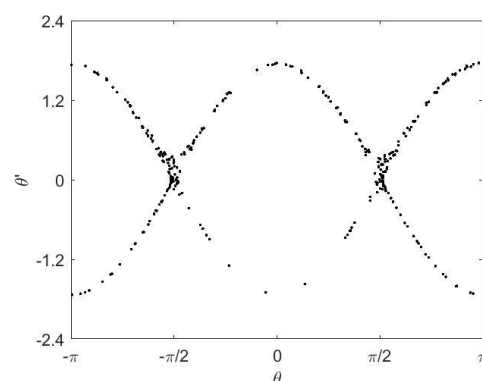


Fig. 5 Poincaré section

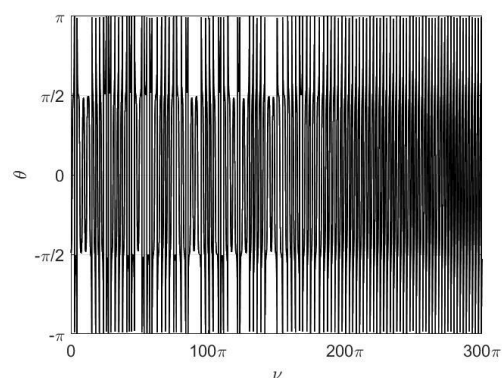


Fig. 6 Pitch angle versus  $\nu$

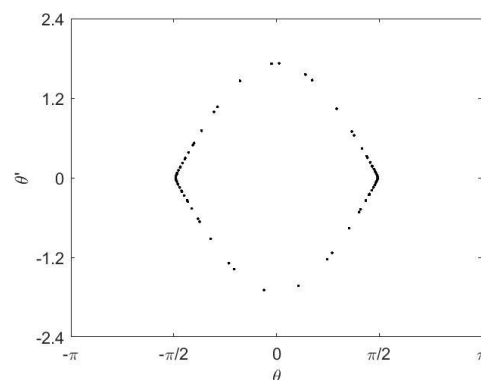


Fig. 7 Poincaré section

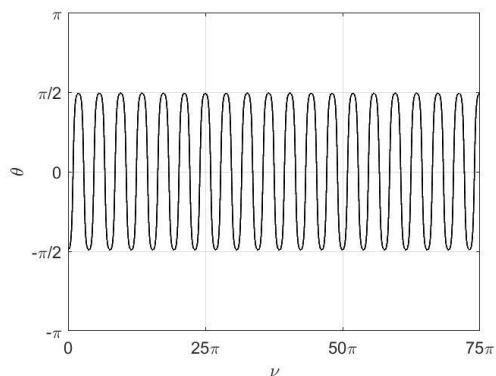


Fig. 8 Pitch angle versus  $\nu$

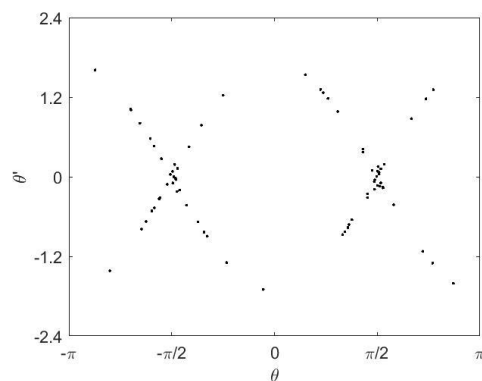


Fig. 12 Poincaré section

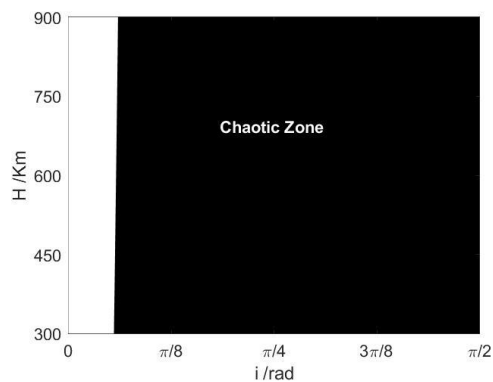


Fig. 9 Parameter domain for chaos

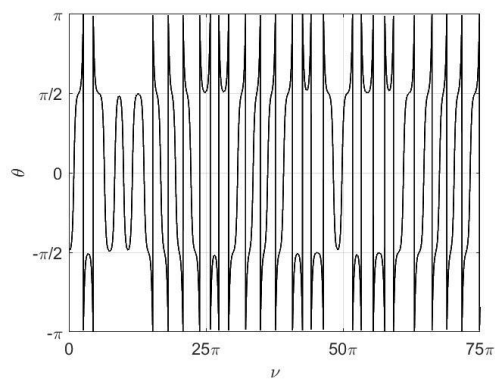


Fig. 13 Pitch angle versus  $\nu$

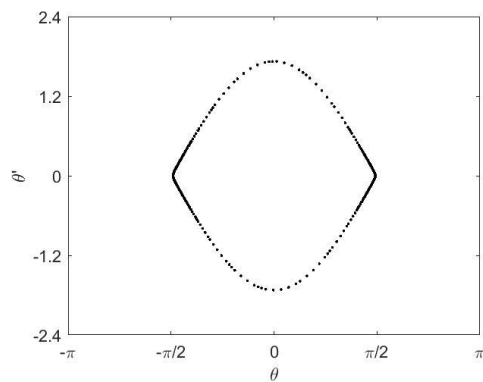


Fig. 10 Poincaré section

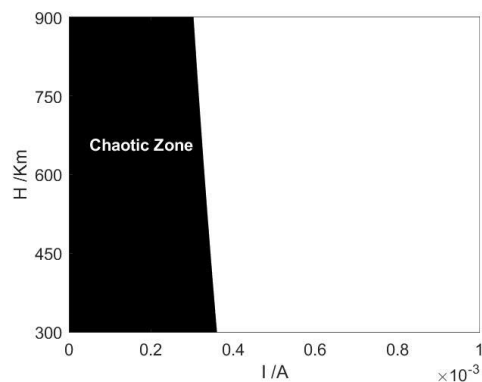


Fig. 14 Parameter domain for chaos

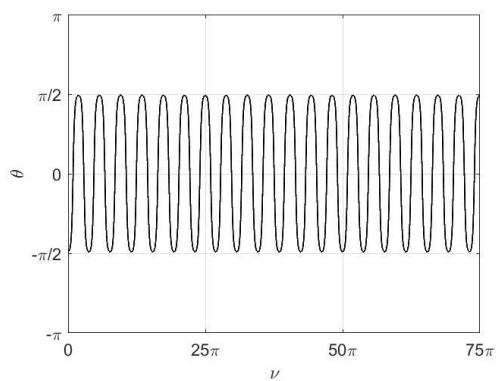


Fig. 11 Pitch angle versus  $\nu$

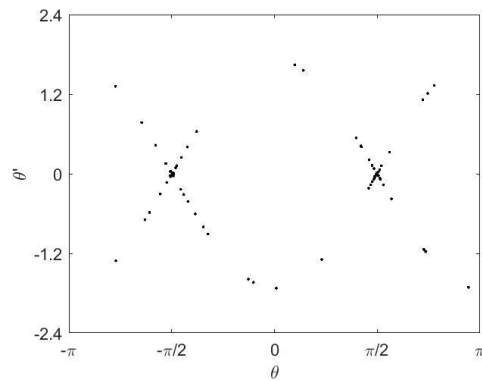


Fig. 15 Poincaré section

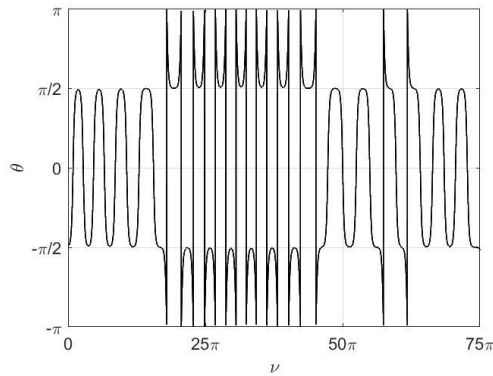


Fig. 16 Pitch angle versus  $\nu$

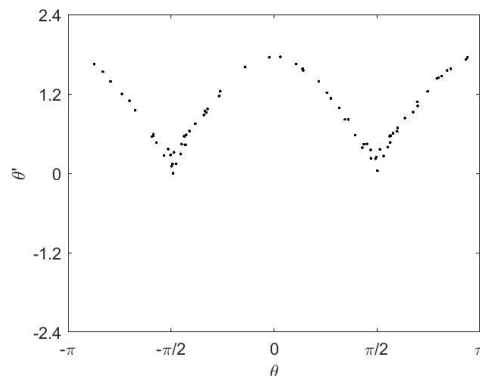


Fig. 17 Tumbling Poincaré section

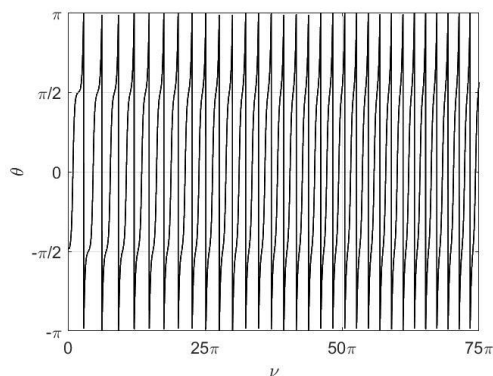


Fig. 18 Pitch angle versus  $\nu$

## Conclusions

In this work, the chaotic motion of an electrodynamic tethered satellite system in a circular orbit under the influence of Earth's oblateness ( $J_2$  effect) was analyzed. The system was modelled using a dumbbell configuration, representing two point masses connected by an inelastic tether. The equations of motion were derived via the Lagrangian approach, incorporating the effects of both the Lorentz force generated by the electrodynamic

interaction and the radial acceleration due to Earth's oblateness.

To assess the potential for chaotic behavior, the Melnikov method was applied to establish a necessary condition for the onset of chaos. This condition enabled the identification of parameter domains in which chaotic motion is likely to occur. Numerical simulations were then conducted to validate the analytical predictions.

From the Melnikov-based analysis, three key scenarios emerged:

1. When the system is perturbed solely by the Lorentz force, chaotic motion does not occur.
2. When the perturbation arises solely from the oblateness effect, chaotic motion may arise.
3. When both the Lorentz force and oblateness effect are present, chaos may occur depending on whether the system parameters satisfy the necessary condition.

These findings indicate that the presence of the Lorentz force alone is insufficient to induce chaos, even in combination with the  $J_2$  perturbation, unless the parameter values fall within the critical domain defined by the Melnikov analysis. This highlights the importance of carefully selecting system parameters to avoid unintended chaotic behavior in tethered satellite missions.

## References

- Ma X, and Wen H (2023) Deep learning for deorbiting control of an electrodynamic tether system. *Acta Astronautica*. 202: 26-33. <https://doi.org/10.1016/j.actaastro.2022.10.019>.
- Razzaghi P, Al Khatib E, Bakhtiari S, and Hurmuzlu Y (2021) Real time control of tethered satellite systems to de-orbit space debris. *Aerospace Science Technology*. 109: 106379. <https://doi.org/10.1016/j.ast.2020.106379>.
- Svotina V, and Cherkasova M (2023) Space debris removal—review of technologies and techniques. Flexible or virtual connection between space debris and service spacecraft. *Acta Astronautica*. 204: 840-853. <https://doi.org/10.1016/j.actaastro.2022.09.027>.
- Liu J, Liu B, Wu Z, Jiang J, and Tian L (2020) Dynamics and potential applications of a lunar space tethered system. *Acta Astronautica*. 169: 138-149. <https://doi.org/10.1016/j.actaastro.2020.01.021>.



- Liu J, and McInnes CR (2019) Resonant space tethered system for lunar orbital energy harvesting. *Acta Astronautica*. 156: 23-32. <https://doi.org/10.1016/j.actaastro.2018.08.037>.
- Hu W, Song M, and Deng Z (2018) Energy dissipation/transfer and stable attitude of spatial on-orbit tethered system. *Journal of Sound Vibration*. 412: 58-73. <https://doi.org/10.1016/j.jsv.2017.09.032>.
- Mashayekhi MJ, and Misra AK (2016) Effect of the finite size of an asteroid on its deflection using a tether-ballast system. *Celestial Mechanics and Dynamical Astronomy*. 125: 363-380. <https://doi.org/10.1007/s10569-016-9687-y>.
- Zhong R, and Wang Y (2018) Dynamics and control of a probe tethered to an asteroid. *Journal of Guidance, Control, and Dynamics*. 41: 1585-1590. <https://doi.org/10.2514/1.G003386>.
- Huang P, Zhang F, Chen L, Meng Z, Zhang Y, Liu Z, and Hu Y (2018) A review of space tether in new applications. *Nonlinear Dynamics*. 94: 1-19. <https://doi.org/10.1007/s11071-018-4389-5>.
- Sanmartin JR, Lorenzini EC, and Martinez-Sanchez M (2010) Electrodynamic tether applications and constraints. *Journal of Spacecraft and Rockets*. 47: 442-456. <https://doi.org/10.2514/1.45352>.
- Kumar K (2006) Review on dynamics and control of nonelectrodynamic tethered satellite systems. *Journal of Spacecraft and Rockets*. 43: 705-720. <https://doi.org/10.2514/1.5479>.
- Modi V, Lakshmanan P, and Misra A (1990) Dynamics and control of tethered spacecraft-a brief overview. Paper presented at the Dynamics Specialists Conference. <https://doi.org/10.2514/6.1990-1195>.
- Sánchez-Arriaga G, Lorenzini EC, and Bilén SG (2024) A review of electrodynamic tether missions: Historical trend, dimensionless parameters, and opportunities opening space markets. *Acta Astronautica*. <https://doi.org/10.1016/j.actaastro.2024.09.002>.
- Hong AaT, Varatharajoo R, and Chak Y-C (2024) Review of deployment controllers for space tethered system. *Advances in Space Research*. <https://doi.org/10.1016/j.asr.2024.11.061>.
- Andrievsky B, Popov AM, Kostin I, and Fadeeva J (2022) Modeling and control of satellite formations: A survey. *Automation*. 3: 511-544. <https://doi.org/10.3390/automation3030026>.
- Aslanov V, and Ledkov A. (2012). *Dynamics of tethered satellite systems*: Elsevier.
- Troger H, Alpatov A, Beletsky V, Dranovskii V, Khoroshilov V, Pirozhenko A, and Zakrzhevskii A. (2010). *Dynamics of tethered space systems*: CRC Press.
- Zheng P, Cao X, and Zhang S (2008)  $J_2$  perturbation effect on the deployment of tether-assisted deorbit system. Paper presented at the 2008 2nd International Symposium on Systems and Control in Aerospace and Astronautics. <https://doi.org/10.1109/ISSCAA.2008.4776269>.
- Yu B, and Jin D (2010) Deployment and retrieval of tethered satellite system under  $J_2$  perturbation and heating effect. *Acta Astronautica*. 67: 845-853. <https://doi.org/10.1016/j.actaastro.2010.05.013>.
- Yu B, Jin D, and Wen H (2016) Nonlinear dynamics of flexible tethered satellite system subject to space environment. *Applied Mathematics and Mechanics*. 37: 485-500. <https://doi.org/10.1007/s10483-016-2049-9>.
- Yu B, Xu S, and Jin D (2020) Chaos in a tethered satellite system induced by atmospheric drag and earth's oblateness. *Nonlinear Dynamics*. 101: 1233-1244. <https://doi.org/10.1007/s11071-020-05844-8>.
- Yuan W, Deng H, and Liu J (2024) Chaotic libration and control of a space tether-sail system in earth polar orbits with  $J_2$  perturbation. *Applied Mathematical Modelling*. 136: 115617. <https://doi.org/10.1016/j.apm.2024.07.024>.
- Tikhonov A, Antipov K, Korytnikov D, and Nikitin DY (2017) Electrodynamical compensation of disturbing torque and attitude stabilization of a satellite in  $J_2$  perturbed orbit. *Acta Astronautica*. 141: 219-227. <https://doi.org/10.1016/j.actaastro.2017.10.009>.
- Stevens RE. (2008). *Optimal control of electrodynamic tether satellites*. (Ph.D. Ph.D.), Air Force Institute of Technology,
- Kéchichian JA. (2021). *Orbital relative motion and terminal rendezvous*: Springer.
- Zhong R, and Zhu Z (2013) Libration dynamics and stability of electrodynamic tethers in satellite deorbit. *Celestial Mechanics and Dynamical Astronomy*. 116: 279-298. <https://doi.org/10.1007/s10569-013-9489-4>.
- Yu B, Tang Y, and Ji K (2022) Chaotic behaviors of an in-plane tethered satellite system with elasticity. *Acta Astronautica*. 193: 395-405. <https://doi.org/10.1016/j.actaastro.2022.01.024>.
- Aslanov V. (2017). *Rigid body dynamics for space applications*: Butterworth-Heinemann.
- Aslanov VS (2024) Suppressing chaotic oscillations of a tether anchored to the phobos surface under the 1:1 libration point. *Chaos, Solitons and Fractals*. 181: 114663. <https://doi.org/10.1016/j.chaos.2024.114663>.

## الملخص العربي

### عنوان البحث: الحركة الفوضوية لنظام قمر صناعي كهروديناميكي مربوط تحت تأثير تفلطح الأرض في مدار دائري

أحمد يوسف<sup>1\*</sup>، أحمد مجدي عبد العزيز<sup>2</sup>، عبد الحكيم أبو الفتوح عبد النبي<sup>1</sup>، يحيى أحمد عبد العزيز

<sup>1</sup>قسم الرياضيات، كلية العلوم، جامعة دمياط، دمياط، مصر.

<sup>2</sup>المركز القومي لبحوث الفلك والجيوفيزياء (NRIAG)، القاهرة، مصر.

يتناول هذا البحث دراسة السلوك الفوضوي لنظام قمر صناعي كهروديناميكي مربوط يتحرك في مستوى المدار تحت تأثير تفلطح الأرض (معامل  $J_2$ ) تم نمذجة النظام باستخدام نموذج الدمبل، والذي يمثل كتلتين نقطيتين متصلتين بواسطة حبل غير مرن. تم اشتقاق معادلات الحركة باستخدام منهج لاغرانج، بعد احتساب العزوم الناتجة عن قوة لورنتز والتسارع الشعاعي الناتج عن التفلطح الأرضي.

تم تطبيق تحليل ميلنيكوف لاشتقاق شرط ضروري لحدوث الحركة الفوضوية، مما أتاح تحديد مجالات القيم التي قد يظهر فيها هذا السلوك. كما تم دعم النتائج التحليلية بمحاكاة عددية تؤكد صحة هذا الشرط. أظهرت النتائج ثلاث حالات رئيسية:

1. عند وجود قوة لورنتز فقط، لا يحدث سلوك فوضوي.
2. عند وجود تأثير التفلطح فقط، قد يحدث سلوك فوضوي.
3. عند وجود كلا التأثيرين معاً، فإن حدوث الفوضى يعتمد على تحقيق الشرط الضروري الذي تم التوصل إليه باستخدام تحليل ميلنيكوف.

تشير هذه النتائج إلى أن وجود قوة لورنتز وحدها لا يكفي لإحداث الفوضى، حتى مع وجود تأثير  $J_2$ ، ما لم تكن المعلمات ضمن المجال الحرج الذي تم تحديده. وتبرز هذه الدراسة أهمية اختيار معلمات النظام بعناية لتجنب السلوك الفوضوي غير المرغوب فيه في تطبيقات الأقمار الصناعية المربوطة.

## Chaos Suppression in an Electrodynamic Tethered Satellite System via Sliding Mode Control under $J_2$ Perturbation

A. Yousof<sup>\*1</sup>, A.M. Abdelaziz<sup>2</sup>, Abd El Hakeem Abd El Naby<sup>1</sup> and Yehia A. Abdel-Aziz<sup>2</sup>

<sup>1</sup>Damietta University, Mathematics Department, Damietta, Egypt.

<sup>2</sup>National Research Institute of Astronomy and Geophysics (NRIAG), Cairo, Egypt.

Received: 09 July 2025 /Accepted: 20 July 2025

\*Corresponding author's E-mail: A.usf@du.edu.eg

### Abstract

This paper investigates the chaotic dynamics of an in-plane electrodynamic tethered satellite system (EDTSS) influenced by Earth's oblateness. The system is modelled using the dumbbell model, and the equations of motion are derived via the Lagrangian approach, accounting for the Lorentz force and the perturbation caused by the  $J_2$  zonal harmonic. The onset of chaos is analytically examined using Melnikov's method, which provides a necessary condition for the emergence of chaotic behavior in the system. To address this instability, a novel control strategy based on sliding mode control (SMC) is proposed, with the tether length serving as the control input. The controller is designed to suppress chaotic motion and guide the system toward either a desired oscillatory behavior or a predefined equilibrium point. Numerical simulations are carried out to verify the analytical condition for chaos and to evaluate the effectiveness of the proposed SMC-based tether length control. The results confirm the controller's capability to stabilize the system and eliminate undesired chaotic responses.

**Keywords:** Chaos, Earth's oblateness, Electromagnetic Force, Melnikov Analysis, Sliding Mode Control, Tethered Satellite System.

### Introduction

Space debris represents one of the most pressing challenges facing the global space community today. It is defined as all man-made objects in orbit or re-entering the Earth's atmosphere including defunct satellites, spent rocket stages, and fragments from disintegration, erosion, and collisions that no longer serve any useful

function, Unoosa (2010). As of 05 May 2025, the European Space Agency (ESA), using the MASTER-8 model, estimates that approximately 54,000 objects larger than 10 cm are currently orbiting Earth, including around 9,300 active payloads. In addition, nearly 1.2 million debris fragments range in size from 1 cm to 10 cm, while an estimated 140 million fragments measure between 1 mm and 1 cm. To address this growing threat, researchers and engineers have been actively developing

innovative technologies for debris mitigation and removal. Among these, electrodynamic tethered satellite systems have emerged as a promising solution for enabling highly efficient and cost-effective space operations. (Ma X and Wen H (2023); Razzaghi P et al. (2021); Svotina V and Cherkasova M (2023))

As a result, the tethered satellite system (TSS) has become one of the most prominent and actively explored topics in space science research (Modi V et al. (1990); Kumar K (2006); Sanmartin JR et al. (2010); Huang P et al. (2018); Sánchez-Arriaga G et al. (2024)).

A typical TSS consists of two or more satellites connected by a tether. Extensive research has been dedicated to the modelling, dynamic analysis, and control of such systems (Hong AaT et al. (2024); Andrievsky B et al. (2022)). To derive the equations of motion, both Newtonian and Lagrangian mechanics are commonly employed, and the system states are usually described using either orbital elements or libration angles. The tether itself is modelled in different forms either as massless or with mass, and either rigid or flexible depending on the specific objectives and assumptions of each study (Aslanov V and Ledkov A (2012); Troger H et al. (2010)).

The dynamics of tethered satellite missions are highly sensitive to various environmental disturbances, which must be carefully addressed during the modelling and control design phases. Key perturbative forces include aerodynamic drag, particularly significant in low Earth orbit, solar radiation pressure, which exerts continuous but subtle variations in force, and Earth's oblateness, characterized by the  $J_2$  zonal harmonic, which distorts the gravitational field and influences orbital stability. Additionally, other disturbances such as third-body gravitational effects and magnetic torques may also affect the system, depending on the specific mission parameters. Properly accounting for these perturbations is critical for accurately predicting system behavior and ensuring the effectiveness and long-term reliability of tethered satellite operations.

Due to the significant influence of Earth's oblateness which is represented by the  $J_2$  coefficient, numerous studies have investigated its effects on the dynamics of orbital and tethered satellite systems. Zheng P et al. (2008) developed a mathematical model using Lagrangian mechanics and performed numerical simulations to analyze the

deployment of a tether-assisted deorbit system under the influence of  $J_2$  perturbation. Their findings revealed that the  $J_2$  effect predominantly influences in-plane motion during deployment, without causing out-of-plane motion when the initial out-of-plane angle is zero. Yu B and Jin D (2010) examined a viscoelastic tethered satellite system, assessing the combined effects of  $J_2$  and thermal perturbations. Their results showed that  $J_2$  has a notable impact on deployment—especially in the presence of friction—while thermal perturbations mainly affect retrieval, leading to distinct motion profiles. In a subsequent study, Yu B et al. (2016) extended the analysis to a flexible tethered satellite system subjected to additional disturbances, including atmospheric drag, solar radiation pressure, and orbital eccentricity. Using a simplified two-degree-of-freedom model, their simulations revealed the emergence of bifurcations, quasi-periodic oscillations, and chaotic dynamics. They concluded that  $J_2$  and thermal effects significantly affect pitch motion and must be considered in system design, whereas the impact of drag and solar pressure depends on orbital altitude. Later, Yu B et al. (2020) employed Melnikov analysis to identify conditions under which chaos emerges in a tethered satellite system in a circular orbit. Their study showed that the combined influence of  $J_2$  and aerodynamic drag could trigger chaotic motion even in systems with rigid tethers. Yuan W et al. (2024) further investigated the chaotic dynamics of a tether-sail system in polar orbits, demonstrating through Lagrangian modelling and Melnikov analysis that both  $J_2$  perturbation and orbital eccentricity contribute to enhanced chaotic behavior.

Electrodynamic tethers (EDTs) offer significant advantages over traditional tether systems by enabling propellant-free generation of Lorentz forces, which can be harnessed for efficient orbit control and power generation. Several studies have explored the influence of Earth's  $J_2$  perturbation on the dynamics and control of EDT systems. Hallaj MaA and Assadian N (2016) modelled a tethered satellite formation as a massless rigid dumbbell system subjected to both electrodynamic forces and  $J_2$  perturbation. Their results demonstrated that precise and fuel-free formation control is achievable using electromagnetic actuation in combination with sliding mode control.

Tikhonov A et al. (2017) investigated an electrodynamic control system's ability to counteract gravity gradient torques induced by the  $J_2$  effect in near-Earth orbits, confirming its effectiveness in stabilizing satellite attitude. Razzaghi P et al. (2019) developed a viscoelastic tether model for space debris deorbiting, incorporating both  $J_2$  perturbation and atmospheric drag. They compared the performance of sliding mode control (SMC) and state-dependent Riccati equation (SDRE) controllers, finding that while both approaches stabilized librational motion and reduced orbital altitude, SMC achieved faster responses and exhibited greater robustness to system uncertainties. More recently, Liu J et al. (2021) proposed a fuzzy logic controller for managing continuous current flow in an EDT system under the influence of  $J_2$  and drag forces. Their approach outperformed traditional on-off control strategies by improving orbital boost efficiency and enhancing libration suppression across a range of orbital inclinations.

In this paper, a control strategy based on sliding mode control is proposed to suppress the chaotic motion of the system, either by guiding it toward a desired periodic trajectory or stabilizing it at a predefined equilibrium state. The structure of the paper is as follows: Section 2 presents the system modelling, where a dumbbell representation with a non-negligible tether mass is adopted, and the equations of motion are derived using the Lagrangian method. Section 3 applies the analytical Melnikov technique to determine the conditions under which chaotic motion may arise. In Section 4, a sliding mode controller is developed to mitigate chaotic behavior by adjusting the tether length. Section 5 provides numerical simulations that confirm the analytical findings and illustrate the performance of the proposed control scheme. Finally, Section 6 offers concluding remarks.

## Mathematical Model

A tethered satellite system (TSS) in a circular orbit around Earth is considered, as depicted in Fig. 1. The system is represented by a dumbbell model, comprising a mother satellite connected to a subsatellite through a tether. The corresponding masses of the mother satellite, subsatellite, and tether are denoted by  $m_1$ ,  $m_2$ ,

and  $m_t$ , respectively.

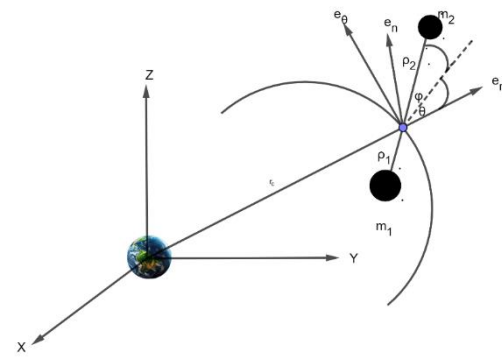


Fig. 1 Tethered Satellite System

An inertial coordinate frame  $(X, Y, Z)$ , is defined with its origin at the center of the Earth. The  $X$ -axis points toward the vernal equinox, the  $Z$ -axis is aligned with Earth's rotational axis, and the  $Y$ -axis lies in the equatorial plane, forming a right-handed coordinate system.

A rotating reference frame,  $(e_r, e_\theta, e_n)$ , centered at the system's center of mass, is defined with a relative position vector  $r_c$  with respect to the inertial frame. The three unit vectors  $(e_r, e_\theta, e_n)$  point radially outward away from Earth's center of mass, align with the direction of velocity, and complete a right-handed coordinate system, respectively.

The position vectors of the mother satellite and the subsatellite relative to the system's center of mass are denoted by  $\rho_1$  and  $\rho_2$ , respectively. The variable  $\theta$  represents the in-plane angle, while  $l$  indicates the tether length at any given time.

To construct the system's Lagrangian, appropriate expressions for both kinetic and potential energies are required. The total kinetic energy  $T$ , can be obtained by integrating the kinetic energy along the tether and summing it with the kinetic energies of the mother satellite and the subsatellite, as described by Aslanov V and Ledkov A (2012).

$$T = \frac{1}{2} m \dot{r}_c^2 + \frac{1}{2} \mu_e (\dot{l}^2 + l^2 (\dot{\theta} + \dot{\nu})^2), \quad (1)$$

where  $m = m_1 + m_2 + m_t$  is a total mass, the dot represents the derivative with respect to time,

$\mu_e = (m_1 + m_t / 2)(m_2 + m_t / 2) / (m_1 + m_2 + m_t) - m_t / 6$  is a reduced mass, and  $\nu$  is the true anomaly.

By summing the potential energies of all system components, and by considering that the tether length is negligible compared to the distance from the system's mass center to Earth, the total

potential energy of the system,  $W$ , can be expressed as follows:

$$W = -\frac{\mu m}{r_c} - \frac{\mu \mu_e l^2}{2r_c^3} (3\cos^2 \theta - 1), \quad (2)$$

where  $\mu$  is Earth's gravitational strength constant.

Based on Eqs. (1) and (2), the Lagrangian,  $\mathcal{L}$ , is formulated as the difference between the total kinetic and potential energies, i.e.,  $\mathcal{L} = T - W$ . The corresponding equations of motion derived from the Lagrangian take the following form:

$$\frac{d}{dt} \frac{\partial \mathcal{L}}{\partial \dot{q}_i} - \frac{\partial \mathcal{L}}{\partial q_i} = Q_i, \quad (3)$$

here, the generalized coordinates are  $q_i = \theta, l$  and  $Q_i$  represent non-conservative generalized forces.

By applying the following nondimensional transformation:

$$\frac{d(\cdot)}{dt} = \frac{d(\cdot)}{d\nu} \dot{\nu}, L = \frac{l}{r_c},$$

the equations of motion can be reformulated in nondimensional form as follows:

$$\theta'' + 2(\theta' + 1) \frac{L'}{L} + 3\cos \theta \sin \theta = \frac{Q_\theta}{\mu_e l^2 \dot{\nu}^2}, \quad (4)$$

$$L'' - L[(\theta' + 1)^2 - 3\cos^2 \theta + 1] = \frac{Q_l}{\mu_e \dot{\nu}^2}, \quad (5)$$

here, the prime symbol denotes differentiation with respect to the variable  $\nu$  and  $\dot{\nu}^2 = \mu / r_c^3$ .

The system is influenced by the Lorentz force generated from the interaction between the electric current flowing through the tether and the surrounding magnetic field, along with the  $J_2$  perturbation caused by Earth's oblateness. A non-tilted dipole model is used to represent the magnetic field, and its components in the orbital frame  $B_r, B_\theta$ , and  $B_n$ , are defined as follows Stevens RE (2008):

$$B_r = -2 \frac{\mu_m}{r_c^3} \sin \nu \sin i, \quad (6)$$

$$B_\theta = \frac{\mu_m}{r_c^3} \cos \nu \sin i, \quad (7)$$

$$B_n = \frac{\mu_m}{r_c^3} \cos i, \quad (8)$$

here,  $i$  represents the orbital inclination, and  $\mu_m = 7.85 \cdot 10^{15} \text{ N} / \text{Am}^2$ , denotes the magnetic dipole moment of Earth. It is assumed that a constant current  $I$ , flows along the tether, and the magnetic field remains uniform along its

length. This assumption is justified by the relatively short tether length compared to the characteristic radius of the system. According to the principle of virtual work, the generalized electromagnetic torques  $Q_{\theta e}$ , and  $Q_{le}$ , can be expressed as:

$$Q_{\theta, e} = -\frac{Il^2(m_2 - m_1)}{2(m_1 + m_2 + m_t)} B_n, \quad (9)$$

$$Q_{l, e} = 0.$$

The influence of Earth's oblateness on the dynamics of the tethered satellite system can be assessed through its non-uniform gravitational potential, denoted by  $U$ , as described by Kéchichian JA (2021). This potential is given by:

$$U = \frac{\mu}{r_c} \left[ 1 - \sum_{n=2}^{\infty} J_n \left( \frac{R}{r_c} \right)^n P_n(\sin(\delta)) \right], \quad (10)$$

where  $J_n$  represents the zonal harmonic coefficient of order  $n$ ,  $R$  is Earth's equatorial radius, and  $\delta$  is the declination of the system's center of mass relative to the equatorial plane. The term  $P_n(\sin(\delta))$  denotes the Legendre polynomial of degree  $n$  evaluated at  $\sin(\delta)$ . By disregarding higher-order terms such as  $J_3$  and above, substituting  $\sin(\delta)$  with  $z / r_c$ , and applying the transformation matrix to the rotating reference frame, the radial component of the perturbation acceleration can be derived as:

$$a_{ob} = -\frac{3}{2} \frac{J_2 \mu R^2 r_c}{r_c^5} (1 - 3\sin^2 i \sin^2 \nu). \quad (11)$$

According to Zhong R and Zhu Z (2013), the torque acting on the satellites due to Earth's oblateness-induced acceleration can be expressed as:

$$Q_{\theta, ob} = \gamma \sin(\theta) + \beta \sin(\theta) \cos(2\nu), \quad (12)$$

where

$$\gamma = \chi \cdot \left( 1 - \frac{3\sin^2 i}{2} \right), \beta = \chi \cdot \left( \frac{3\sin^2 i}{2} \right), \quad (13)$$

$$\chi = \left( \frac{3J_2 \mu R^2 l^2 [m_2 M_m^2 - m_1 (1 - M_m)^2]}{2r_c^5} \right),$$

where  $M_m = (m_1 + m_t) / m$ .

In this study, we focus on analysing the nonlinear behavior of pitch motion during the station-keeping phase, where the tether length is held constant. By substituting Eqs. (9), (12) into



Eq. (4), assuming  $L' = 0$ , and considering that the total torque  $Q_\theta$  is the sum of the electromagnetic and oblateness contributions, i.e.,  $Q_\theta = Q_{\theta,e} + Q_{\theta,ob}$ , we obtain:

$$\theta'' + 3\cos\theta\sin\theta = \sigma_1\sin\theta + \sigma_2\sin\theta\cos 2\nu + \sigma_3, \quad (14)$$

where

$$\sigma_1 = \sigma^* \cdot \left(1 - \frac{3\sin^2 i}{2}\right), \sigma_2 = \sigma^* \cdot \left(\frac{3\sin^2 i}{2}\right),$$

$$\sigma^* = \left( \frac{3J_2 R^2 [m_2 M_m^2 - m_1 (1 - M_m)^2]}{2\mu_e r_c^2} \right), \quad (15)$$

$$\sigma_3 = -\frac{I(m_2 - m_1)\mu_m \cos i}{2m\mu_e \mu}.$$

It is evident from Eq. (14) that the electrodynamic tethered satellite system, when influenced by Earth's oblateness, exhibits the characteristics of a nonlinear and nonautonomous system.

### 1 Analysis of Chaotic Motion

In this section, the Melnikov method is utilized to establish the necessary condition under which chaotic behaviour may appear in the dynamics of the system.

By defining the state vector as  $\theta = (\theta_1, \theta_2)^T = (\theta, \dot{\theta})^T$ , the state-space representation of Eq. (14) can be written as:

$$\dot{\theta} = \mathbf{f}(\theta) + \mathbf{g}(\theta, \nu), \quad (16)$$

where

$$\mathbf{f}(\theta) = \begin{bmatrix} f_1 \\ f_2 \end{bmatrix} = \begin{bmatrix} \theta_2 \\ -3\sin\theta_1 \cos\theta_1 \end{bmatrix}, \quad (17)$$

$$\mathbf{g}(\theta, \nu) = \begin{bmatrix} g_1 \\ g_2 \end{bmatrix} = \begin{bmatrix} 0 \\ \sigma_1 \sin\theta_1 + \sigma_2 \sin\theta_1 \cos 2\nu + \sigma_3 \end{bmatrix}. \quad (18)$$

The perturbation vector,  $\mathbf{g}(\theta, \nu) = \mathbf{g}(\theta, \nu + p)$ , is periodic of period  $p = \pi$ .

When  $\mathbf{g}(\theta, \nu) = 0$ , the system reduces to the unperturbed Hamiltonian form. In this case, the first integral of motion is expressed as:

$$\frac{1}{2}\dot{\theta}_2^2 + \frac{3}{2}\sin^2\theta_1 = E, \quad (19)$$

where  $E$  is a constant that denotes the total kinetic energy of the system.

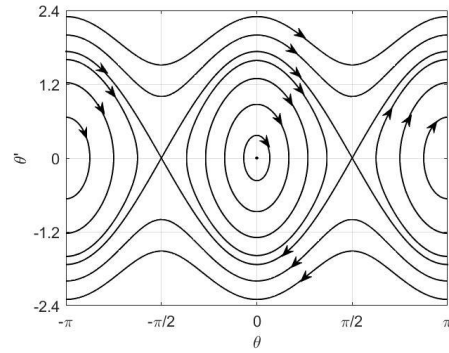


Fig. 2 Phase portrait of unperturbed system

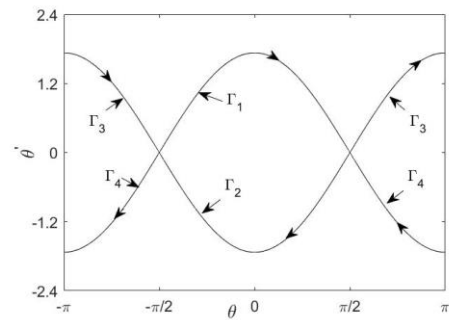


Fig. 3 Heteroclinic orbits

Fig. 2 and Fig. 3 illustrate the phase portrait of the unperturbed system, along with the heteroclinic orbits that connect two distinct saddle points given by  $p_i = (\mp\pi/2, 0)$ ,  $i = 1, 2$ . The analytical expressions for these heteroclinic orbits are provided in Yu B et al. (2020)

$$(\theta_{10}^\pm(\nu), \theta_{20}^\pm(\nu)) = (\pm \sin^{-1}(\tanh(\sqrt{3}\nu)), \pm \sqrt{3} \operatorname{sech}(\sqrt{3}\nu)). \quad (20)$$

For the perturbed system, when  $\mathbf{g}(\theta, \nu) \neq 0$ , near the equilibrium points, the heteroclinic orbits may divide into unstable and stable manifolds. Chaotic behavior is likely to occur if these manifolds intersect transversely. Based on Melnikov's theory, such a transverse intersection takes place when the Melnikov function has a simple zero (Yu B et al. (2022); Aslanov V (2017)).

The Melnikov function is defined as stated by Aslanov VS (2024)

$$M_\pm(\nu_0) = \int_{-\infty}^{+\infty} \mathbf{f}(\theta_0^\pm) \wedge \mathbf{g}(\theta_0^\pm, \nu + \nu_0) d\nu, \quad (21)$$

with  $\nu_0 \in [0, p]$ .

By substituting the expressions from Eq. (17) and Eq. (18) into Eq. (21) and performing the necessary integration steps, the resulting

expression for  $M_{\pm}(v_0)$  reveals terms involving products of even and odd functions over symmetric intervals. Notably, the integrals of odd functions over symmetric bounds cancel out, yielding zero. Based on this analysis and under the condition  $\sin 2v_0 \in [-1, 1]$ , the Melnikov function possesses simple zeros if the following inequality holds:

$$\left| \frac{\sigma_3}{\sigma_2} \right| < 0.2881. \quad (22)$$

This condition, though necessary, is not sufficient on its own to guarantee chaos. It indicates that the system may exhibit chaotic dynamics near the saddle points when satisfied.

### Tether Length Control

In this section, the sliding mode control method is applied to suppress the chaotic motion observed in the electrodynamic tethered satellite system by designing a controller that acts through tether length modulation.

With the state vector defined as  $\theta = (\theta_1, \theta_2)^T = (\theta, \theta')^T$ , using Eq. (9) and Eq. (12), Eq. (4) can be rewritten in the state-space form

$$\begin{aligned} \theta'_1 &= \theta_2, \\ \theta'_2 &= \sigma_1 \sin \theta + \sigma_2 \sin \theta \cos 2v + \sigma_3 \\ &\quad - 2(\theta_2 + 1)u - 3 \cos \theta \sin \theta, \end{aligned} \quad (23)$$

where  $u = L' / L$  represents the control input, which can be adjusted by actuating the reel mechanism on the mother satellite.

The sliding surface for the controlled system is defined by

$$s = A e_{err}^T \quad (24)$$

where  $A = [a_1, a_2]$  is a constant vector with  $a_2 = 1$  and  $a_1 > 0$ , (Hurwitz condition).

The tracking error state vector is defined as:

$$e_{err}^T = \begin{bmatrix} e_{err} \\ e'_{err} \end{bmatrix} = \begin{bmatrix} e_1 \\ e_2 \end{bmatrix} = \begin{bmatrix} \theta_1 - \theta_{1d} \\ \theta_2 - \theta_{2d} \end{bmatrix} \quad (25)$$

where  $\theta_{1d}$  and  $\theta_{2d}$  denote the desired states or trajectories, depending on the control objective. To proceed with controller design, the derivative of the sliding surface is computed as follows

$$\begin{aligned} s' &= a_1 e'_1 + e'_2 \\ &= a_1 (\theta'_1 - \theta'_{1d}) + (\theta'_2 - \theta'_{2d}) \\ &= a_1 (\theta'_1 - \theta'_{1d}) + F(\theta, v) - 2(\theta_2 + 1)u - \theta'_{2d}, \end{aligned}$$

(26)

where

$$F(\theta, v) = \sigma_1 \sin \theta + \sigma_2 \sin \theta \cos 2v + \sigma_3 - 3 \cos \theta \sin \theta.$$

By using the constant rate reaching law  $s' = -k \text{sign}(s)$ ,  $k > 0$ , and substituting into Eq. (26), the control input  $u$  can be obtained as

$$u = \frac{1}{2(\theta_2 + 1)} [a_1 (\theta'_1 - \theta'_{1d}) + F(\theta, v) - \theta'_{2d} + k \text{sign}(s)]. \quad (27)$$

The selection of the gain  $k$  is a critical aspect of controller design. As noted in Liu J (2017), a small value of  $k$  can result in an excessively long reaching time, thereby diminishing the controller's effectiveness. Conversely, a large value may induce chattering, which is undesirable in practical implementations.

To verify the stability of the controlled system, a positive definite Lyapunov function is

selected as  $V = \frac{1}{2} s^2$ . Taking its derivative

yields:

$$\begin{aligned} V' &= s s' \\ &= s(-k \text{sign}(s)) = -k |s| < 0. \end{aligned} \quad (28)$$

From Eq. (28), it is evident that the Lyapunov function is negative definite. Hence, the controlled system described in Eq. (23) is asymptotically stable.

### Numerical Results

This section presents numerical simulations to verify the necessary condition for the onset of chaotic motion, as given by Eq. (22). This condition indicates that for certain values of  $\sigma_3$  (representing the Lorentz effect) and  $\sigma_2$  (representing the oblateness effect), the system may exhibit chaotic behavior if the condition is satisfied. In addition to validating this analytical condition, the effectiveness of the proposed sliding mode controller based on tether length control is also evaluated for its ability to guide the system toward either a desired state or a desired trajectory.

The system parameters used in the simulation are as follows. The mother satellite mass,  $m_1 = 1020 \text{ Kg}$ , the subsatellite mass,  $m_2 = 70 \text{ Kg}$ , and the tether mass,  $m_t = 3.4 \text{ Kg}$ . The system is assumed to orbit the Earth in a circular orbit at an altitude of  $600 \text{ Km}$ , and an inclination of  $63^\circ$ .

The initial conditions of the system are given by  $(\theta, \theta') = (-\pi/2 + \pi/100, 0)$ , where  $\pi/100$  represents a small perturbation angle that places the system close to the unstable saddle point at  $(\mp\pi/2, 0)$ .

It can be observed that  $\sigma_2$  and  $\sigma_3$  are functions of the electric current  $I$  flowing through the tether, the orbital inclination  $i$ , and the orbital altitude  $H$ .

For a system orbit with an inclination of  $\pi/6$ , a current of 1 mA flowing through the tether, and an altitude of 600 km, the necessary condition provided by Eq. (22) is satisfied, indicating that the system may exhibit chaotic behavior.

Fig. 4 confirms the presence of chaotic behavior in the system, as the Poincaré section displays discrete points clustered near the saddle point. Fig. 5 illustrates that the pitch angle exhibits irregular oscillations, further confirming the chaotic behavior of the system.

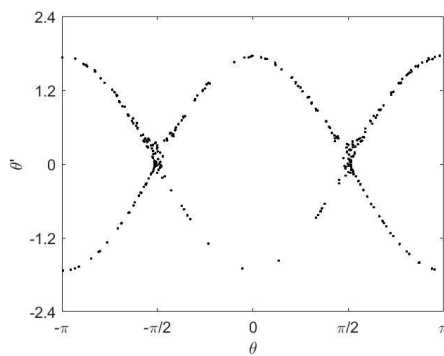


Fig. 4 Poincaré section

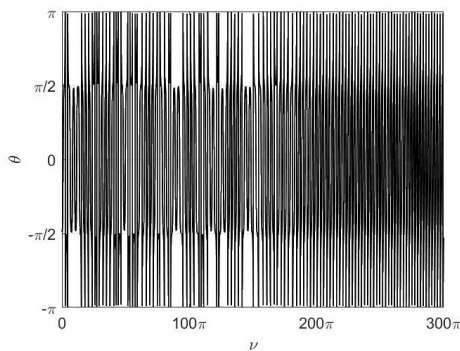


Fig. 5 Pitch angle versus  $\nu$

When the system's inclination is  $\pi/60$ , and a current of 1 mA flows through the tether at an altitude of 900 km, the necessary condition given by Eq. (22) is satisfied. The Poincaré section shown in Fig. 6, corresponding to this state, indicates that the system exhibits chaotic motion. Additionally, Fig. 7 shows that the pitch angle behaves as an irregular oscillator,

further confirming the presence of chaos.

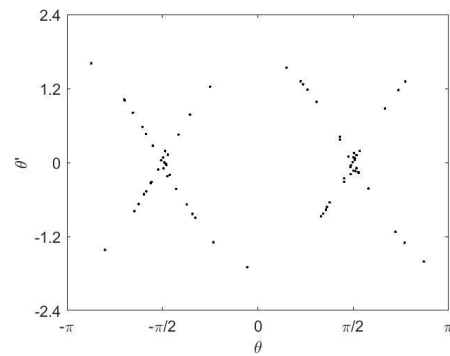


Fig. 6 Poincaré section

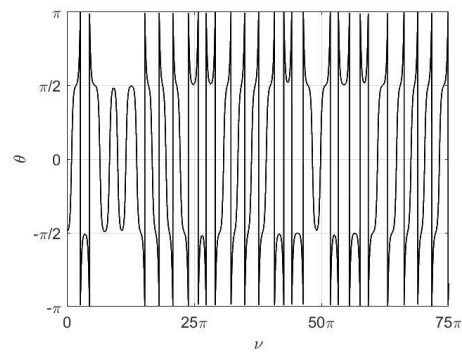


Fig. 7 Pitch angle versus  $\nu$

Another case is considered when the system has an inclination of  $\pi/30$ , with a current of  $0.3 \times 10^{-4}$  (A) flowing through the tether at an altitude of 600 km. In this scenario, the necessary condition given by Eq. (22) is also satisfied. Fig. 8 and Fig. 9 confirm this result, demonstrating that the system exhibits chaotic behavior.

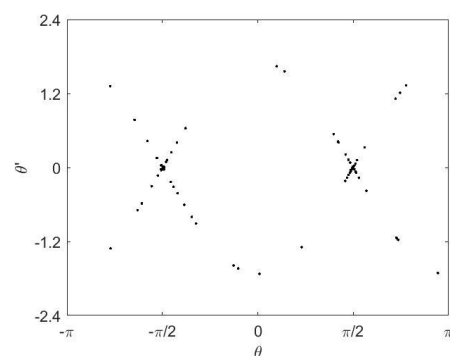


Fig. 8 Poincaré section

The following numerical simulations evaluate the effectiveness of tether length control using a sliding mode controller. This controller is designed to suppress the chaotic motion illustrated in Fig. 4 and Fig. 5, allowing the system to either follow a desired oscillatory behavior or steer the chaotic motion toward a predefined pitch angle through the proposed

control law.

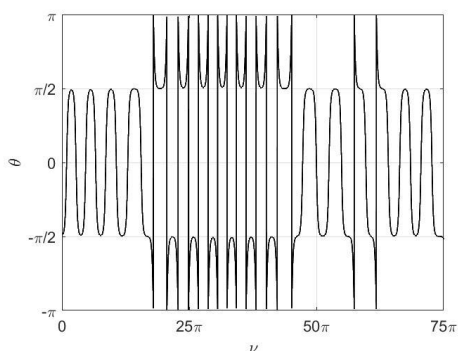


Fig. 9 Pitch angle versus  $\nu$

Fig. 10 and **Error! Reference source not found.** demonstrate the controller's ability to stabilize the system into a desired oscillatory state. As illustrated, the controlled system exhibits periodic behavior similar to that of the unperturbed system, with a period of 11.2155. Fig. 12 and

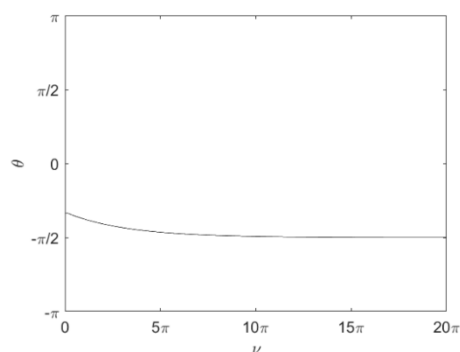


Fig. 13 demonstrate that the controller effectively drives the chaotic motion toward the desired equilibrium point from the initial condition  $(-\pi/3, 0)$ .

Fig. 12 presents the Poincaré section, which clearly illustrates the system's convergence toward the desired equilibrium point. This is further supported by

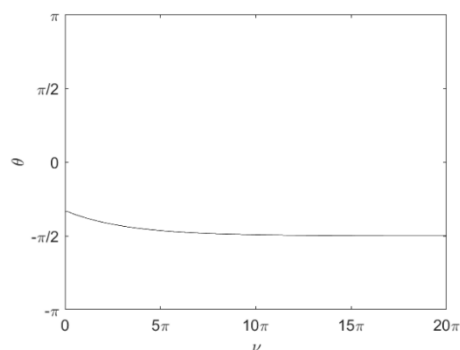


Fig. 13, which shows the variation of the pitch angle with respect to the true anomaly, confirming the system's tendency to settle at the target equilibrium.

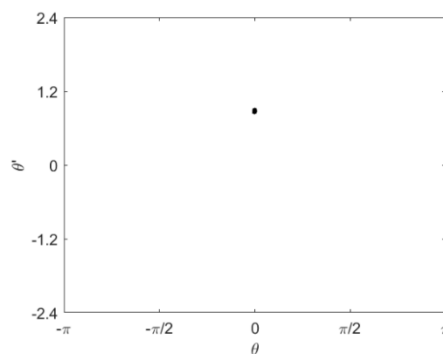


Fig. 10 Poincaré section

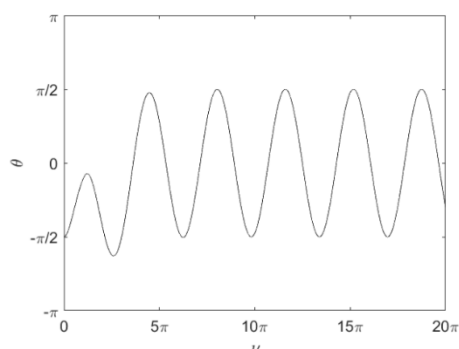


Fig. 11 Pitch angle versus  $\nu$

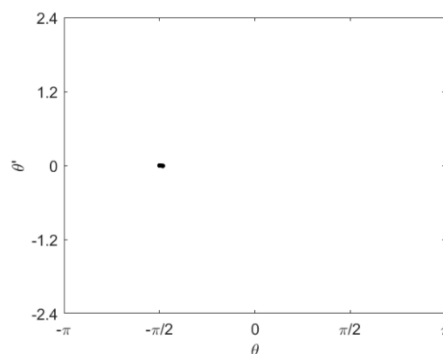


Fig. 12 Poincaré section

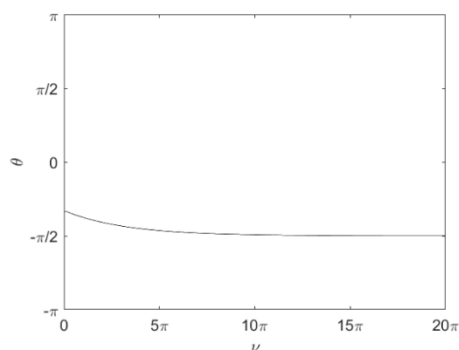


Fig. 13 Pitch angle versus  $\nu$

## Conclusions

This study presented a control strategy based on sliding mode control (SMC) to regulate the pitch motion of an electrodynamic tethered satellite system (EDTSS) in a circular orbit around Earth. The system was modelled using a dumbbell configuration, taking into account perturbations from both the Lorentz force, generated by the interaction between the current flowing through the tether and Earth's magnetic field, and the Earth's oblateness ( $J_2$  effect). The equations of motion were derived using the Lagrangian approach.

Melnikov analysis was applied to determine the necessary condition under which the system may exhibit chaotic behavior. Numerical simulations were conducted to validate the analytical findings and to demonstrate the existence of chaos under certain conditions. Furthermore, the effectiveness of the proposed SMC-based controller, which utilizes tether length as the control input, was verified. The controller successfully suppressed chaotic motion and steered the system either toward a desired periodic trajectory or a predefined equilibrium point.

The results confirm the robustness and efficiency of the proposed control strategy in stabilizing the chaotic behavior of the EDTSS. However, further experimental validation is recommended to support the theoretical and numerical findings. This research offers valuable insights into the dynamic behavior and control of tethered satellite systems and contributes to the development of reliable methods for their real-world implementation

## References

- Unoosa. (2010). Space debris mitigation guidelines of the committee on the peaceful uses of outer space.
- Ma X, and Wen H (2023) Deep learning for deorbiting control of an electrodynamic tether system. *Acta Astronautica*. 202: 26-33. <https://doi.org/10.1016/j.actaastro.2022.10.019>.
- Razzaghi P, Al Khatib E, Bakhtiari S, and Hurmuzlu Y (2021) Real time control of tethered satellite systems to de-orbit space debris. *Aerospace Science Technology*. 109: 106379. <https://doi.org/10.1016/j.ast.2020.106379>.
- Svotina V, and Cherkasova M (2023) Space debris removal-review of technologies and techniques. Flexible or virtual connection between space debris and service spacecraft. *Acta Astronautica*. 204: 840-853. <https://doi.org/10.1016/j.actaastro.2022.09.027>.
- Modi V, Lakshmanan P, and Misra A (1990) Dynamics and control of tethered spacecraft-a brief overview. Paper presented at the Dynamics Specialists Conference. <https://doi.org/10.2514/6.1990-1195>.
- Kumar K (2006) Review on dynamics and control of nonelectrodynamic tethered satellite systems. *Journal of Spacecraft and Rockets*. 43: 705-720. <https://doi.org/10.2514/1.5479>.
- Sanmartin JR, Lorenzini EC, and Martinez-Sanchez M (2010) Electrodynamic tether applications and constraints. *Journal of Spacecraft and Rockets*. 47: 442-456. <https://doi.org/10.2514/1.45352>.
- Huang P, Zhang F, Chen L, Meng Z, Zhang Y, Liu Z, and Hu Y (2018) A review of space tether in new applications. *Nonlinear Dynamics*. 94: 1-19. <https://doi.org/10.1007/s11071-018-4389-5>.
- Sánchez-Arriaga G, Lorenzini EC, and Bilén SG (2024) A review of electrodynamic tether missions: Historical trend, dimensionless parameters, and opportunities opening space markets. *Acta Astronautica*. <https://doi.org/10.1016/j.actaastro.2024.09.002>.
- Zheng P, Cao X, and Zhang S (2008)  $J_2$  perturbation effect on the deployment of tether-assisted deorbit system. Paper presented at the 2008 2nd International Symposium on Systems and Control in Aerospace and Astronautics. <https://doi.org/10.1109/ISSCAA.2008.4776269>.
- Yu B, and Jin D (2010) Deployment and retrieval of tethered satellite system under  $J_2$  perturbation and heating effect. *Acta Astronautica*. 67: 845-853. <https://doi.org/10.1016/j.actaastro.2010.05.013>.
- Yu B, Jin D, and Wen H (2016) Nonlinear dynamics of flexible tethered satellite system subject to space environment. *Applied Mathematics and Mechanics*. 37: 485-500. <https://doi.org/10.1007/s10483-016-2049-9>.
- Yu B, Xu S, and Jin D (2020) Chaos in a tethered satellite system induced by atmospheric drag and earth's oblateness. *Nonlinear Dynamics*. 101: 1233-1244. <https://doi.org/10.1007/s11071-020-05844-8>.
- Yuan W, Deng H, and Liu J (2024) Chaotic libration and control of a space tether-sail system in earth polar orbits with  $J_2$  perturbation. *Applied Mathematical Modelling*. 136: 115617. <https://doi.org/10.1016/j.apm.2024.07.024>.
- Hallaj MaA, and Assadian N (2016) Sliding mode control of electromagnetic tethered satellite formation. *Advances in Space Research*. 58: 619-634. <http://dx.doi.org/10.1016/j.asr.2016.05.019>.
- Tikhonov A, Antipov K, Korytnikov D, and Nikitin DY (2017) Electrodynamical compensation of

- disturbing torque and attitude stabilization of a satellite in J2 perturbed orbit. *Acta Astronautica*. 141: 219-227. <https://doi.org/10.1016/j.actaastro.2017.10.009>.
- Razzaghi P, Al Khatib E, and Bakhtiari S (2019) Sliding mode and sdre control laws on a tethered satellite system to de-orbit space debris. *Advances in Space Research*. 64: 18-27. <https://doi.org/10.1016/j.asr.2019.03.024>.
- Liu J, Zhu ZH, Li G, and Zhan X (2021) Fuzzy-based continuous current control of electrodynamic tethers for stable and efficient orbital boost. *Aerospace Science Technology*. 118: 106999. <https://doi.org/10.1016/j.ast.2021.106999>.
- Aslanov V, and Ledkov A. (2012). *Dynamics of tethered satellite systems*: Elsevier.
- Stevens RE. (2008). *Optimal control of electrodynamic tether satellites*. (Ph.D. Ph.D.), Air Force Institute of Technology,
- Kéchichian JA. (2021). *Orbital relative motion and terminal rendezvous*: Springer.
- Zhong R, and Zhu Z (2013) Libration dynamics and stability of electrodynamic tethers in satellite deorbit. *Celestial Mechanics and Dynamical Astronomy*. 116: 279-298. <https://doi.org/10.1007/s10569-013-9489-4>.
- Aslanov VS (2024) Suppressing chaotic oscillations of a tether anchored to the phobos surface under the 11 libration point. *Chaos, Solitons and Fractals*. 181: 114663. <https://doi.org/10.1016/j.chaos.2024.114663>.
- Liu J. (2017). *Sliding mode control using matlab*: Academic Press.

## الملخص العربي

**عنوان البحث:** قمع الفوضى في نظام قمر صناعي كهروديناميكي مربوط باستخدام التحكم بأسلوب الانزلاق تحت تأثير اضطراب معامل  $J_2$

أحمد يوسف<sup>1\*</sup>، أحمد مجدي عبد العزيز<sup>2</sup>، عبد الحكيم أبو الفتوح عبد النبي<sup>1</sup>، يحيى أحمد عبد العزيز<sup>2</sup>

<sup>1</sup>قسم الرياضيات، كلية العلوم، جامعة دمياط، دمياط، مصر.  
<sup>2</sup>المركز القومي لبحوث الفلك والجيوفيزياء (NRIAG)، القاهرة، مصر.

يتناول هذا البحث دراسة السلوك الفوضوي لنظام قمر صناعي كهروديناميكي مربوط يتحرك داخل مستوى مداري دائري حول الأرض تحت تأثير تفلطح الأرض المُمثل بمعامل  $J_2$ . تم نمذجة النظام باستخدام نموذج الدمبل، حيث تم اشتقاق معادلات الحركة باستخدام منهج لاغرانج مع أخذ تأثير كل من القوة الكهرومغناطيسية الناتجة عن تفاعل التيار المار في الحبل مع المجال المغناطيسي الأرضي، بالإضافة إلى تأثير التفلطح الأرضي في الحسابات. تم استخدام تحليل ميلنيكوف لاشتقاق شرط ضروري لظهور السلوك الفوضوي في النظام. ولمعالجة هذه الفوضى، تم اقتراح استراتيجية تحكم جديدة تعتمد على التحكم بأسلوب الانزلاق (SMC)، حيث يُستخدم طول الحبل كإشارة تحكم. يهدف المتحكم إلى كبح السلوك الفوضوي وتوجيه النظام إما نحو حالة تنذبب منتظمة أو نحو نقطة توازن محددة مسبقاً. أظهرت النتائج قدرة المتحكم على تثبيت النظام والقضاء على السلوك الفوضوي غير المرغوب فيه، مما يدل على قوة وفعالية الطريقة المقترحة. ومع ذلك، توصي الدراسة بإجراء تجارب عملية مستقبلاً للتحقق من فعالية هذا المتحكم على أرض الواقع. وتُعد هذه الدراسة مساهمة مهمة في فهم ديناميكا أنظمة الأقمار الصناعية المربوطة وتطوير طرق تحكم موثوقة لتطبيقات الفضاء الفعلية.



## Berwald and Chern Connections under Anisotropic Conformal Transformations on Conic Pseudo-Finsler Surfaces

Nabil L. Youssef <sup>1</sup>, S. G. Elgendi <sup>2,3</sup>, A. A. Kotb <sup>\*4</sup>, Ebtsam H. Taha<sup>1</sup> and A. M. Tarabia<sup>4</sup>

<sup>1</sup>Department of Mathematics, Faculty of Science, Cairo University, Giza, Egypt

<sup>2</sup>Department of Mathematics, Faculty of Science, Islamic University of Madinah, Madinah, Kingdom of Saudia Arabia

<sup>3</sup>Department of Mathematics, Faculty of Science, Benha University, Benha, Egypt

<sup>4</sup>Department of Mathematics, Faculty of Science, Damietta University, Damietta , Egypt

Received: 11 July 2025 /Accepted: 21 July 2025

\*Corresponding author's E-mail: [alikutb@du.edu.eg](mailto:alikutb@du.edu.eg)

### Abstract

This paper extends our previous research on anisotropic conformal changes  $F(x, y) \mapsto \bar{F}(x, y) = e^{\phi(x, y)} F(x, y)$ . The study focuses on the behavior of the Berwald connection, which measures the deviation of a Finsler structure from a Riemannian one, and the Chern-Rund connection on conic pseudo-Finsler surfaces under this anisotropic conformal transformation, along with the dynamical covariant derivative. In particular, we express the Landsberg tensor of the transformed Finsler metric  $\bar{F}$  in terms of the difference between the horizontal coefficients of the Berwald and Chern-Rund connections. Consequently, we find the necessary and sufficient conditions under which the Landsbergian property is preserved under the anisotropic conformal transformation. Our findings shed light on the relationship between anisotropic conformal transformations and the intrinsic geometry of Finsler surfaces. Additionally, we provide explicit formulas for the anisotropic conformal transformation of the dynamical covariant derivatives in the context of conic pseudo-Finsler surfaces.

**Keywords:** anisotropic conformal change; conic pseudo-Finsler surface; modified Berwald frame; dynamical covariant derivative; Berwald connection.

### Introduction

Anisotropic conformal transformations generalize classical (isotropic) conformal changes by allowing the conformal factor to depend not only on the position but also on the

direction. In the Finsler geometry, this transformation takes the form  $F(x, y) \mapsto \bar{F}(x, y) = e^{\phi(x, y)} F(x, y)$ , where the function  $\phi(x, y)$  encodes the directional anisotropy. This anisotropy is important in various physical scenarios such as enables richer models of describing the universe, new solutions to gravitational field equations, light propagation

in anisotropic materials and potential explanations for phenomena not addressed by isotropic theories [Friedl-Sz'asz et al., 2025; Heefer et al., 2023; Hohmann et al., 2020; Pfeifer and Wohlfarth, 2012; Savvopoulos and Stavrinou, 2023; Voicu et al., 2023; Youssef et al., 2024; Youssef et al., 2025b].

The anisotropic conformal transformation of a conic pseudo-Finsler surface has been introduced and thoroughly investigated in [Youssef et al., 2024; Youssef et al., 2025a; Youssef et al., 2025b]. Unlike isotropic conformal changes, anisotropic conformal changes do not necessarily yield a pseudo-Finsler metric. Consequently, we have determined the necessary and sufficient conditions for  $(M, \bar{F})$  to remain a conic pseudo-Finsler surface under such transformations. Notably, there exist non-homothetic conformal factors  $\phi(x, y)$  that preserve the geodesic spray. Moreover, it is possible to transform a pseudo-Finsler metric into a pseudo-Riemannian one, and vice versa. These results highlight the greater geometric flexibility and significance of anisotropic conformal transformations. We have further investigated the relationships between key geometric objects of  $F$  and their counterparts for  $\bar{F}$ , including the Berwald, Landsberg, and Douglas tensors, as well as the  $T$ -tensor. In particular, we have determined the conditions under which the geodesic spray of a two-dimensional pseudo-Berwald metric  $\bar{F}$  is metrizable by a two-dimensional pseudo-Riemannian metric  $F$ . Furthermore, we study the Cartan connection and derive several identities satisfied under the anisotropic conformal transformation.

In Finsler geometry, the Berwald and Chern-Rund connections are canonical linear connections defined on the pullback bundle or the tangent bundle of a Finsler manifold [Miron and Anastasiei 2012; YOUSSEF, 2008; Youssef et al., 2009]. The Berwald connection generalizes the Levi-Civita connection of Riemannian geometry and measures how far a Finsler structure departs from being Riemannian. A Finsler space is called a Berwald space if its Berwald curvature vanishes [Antonelli et al., 2013; Bao et al., 2012; Bidabad and Tayebi, 2011; Youssef et al., 2010; Shen and Shen, 2016; Bucataru and Miron, 2007]. Both Berwald and Chern connections are torsion-free and only slightly fail to be fully metric-compatible, an expected feature in the

Finsler setting. These connections coincide when the underlying Finsler structure is Landsbergian and when the structure is of Berwald type, they reduce to a linear connection on the manifold  $M$  that acts directly on the tangent bundle  $TM$ .

In this paper, we explore specific properties of the Berwald connection on conic pseudo-Finsler surfaces  $(M, F)$ . We express the connection coefficients in terms of the modified Berwald frame. The transformation of the horizontal coefficients under anisotropic conformal changes has already been studied in our previous work [Youssef et al., 2024]. Here, we further examine the dynamical covariant derivative and provide an alternative proof that the dynamical covariant derivative of the modified Berwald frame vanishes. Additionally, we analyze how the dynamical covariant derivative transforms under anisotropic conformal changes. Furthermore, we study the Chern-Rund connection, express its horizontal coefficients using the modified Berwald frame and derive their transformation under anisotropic conformal changes.

It is known that the difference between the Berwald and Chern-Rund connections is the Landsberg tensor. Therefore, we drive the anisotropic conformal transformation of the Landsberg tensor. As a result, we determine the necessary and sufficient conditions under which the Landsbergian property is preserved under the anisotropic conformal transformation Proposition 4.7.

## Notation and preliminaries

Let  $M$  be a smooth manifold of dimension  $n$ . The tangent bundle of  $M$  is denoted by  $(TM, \pi_M, M)$ , where  $TM$  is the disjoint union of all tangent spaces at each point of  $M$ , and  $\pi_M: TM \rightarrow M$  is the canonical projection onto the base manifold. The slit tangent bundle is defined as  $\mathcal{T}M = TM \setminus \{0\}$ , which is the tangent bundle with the zero section removed. A local coordinate system on  $M$  is denoted by  $(x^i)$ , which induces local coordinates  $(x^i, y^i)$  on  $TM$ , where  $x^i$  are coordinates on the base and  $y^i$  are the components of tangent vectors in each fiber.

A smooth function  $f \in C^\infty(\mathcal{T}M)$  is considered to be positively homogeneous of degree  $r$  in the fiber coordinates  $y$ , denoted  $f \in h(r)$ , if it satisfies

$$f(x, \lambda y) = \lambda^r f(x, y), \quad \forall \lambda > 0.$$

A conic sub-bundle of  $TM$  is a non-empty open subset  $\mathcal{A} \subseteq TM$  such that  $\pi_M(\mathcal{A}) = M$  and  $\mathcal{A}$  is invariant under positive scaling of the fiber coordinates; that is, for any  $(x, y) \in \mathcal{A}$  and any  $\lambda > 0$ , one has  $(x, \lambda y) \in \mathcal{A}$ .

**Definition 2.1** A conic pseudo-Finsler metric on  $M$  is a smooth function  $F: \mathcal{A} \rightarrow \mathbb{R}$ , with  $F \in h(1)$ , defined on a conic sub-bundle  $\mathcal{A} \subseteq TM$ . For each point  $(x, y) \in \mathcal{A}$ , the Hessian matrix

$$g_{ij}(x, y) := \frac{1}{2} \partial_i \partial_j F^2(x, y),$$

$$\text{where } \partial_i := \frac{\partial}{\partial y^i},$$

must be nondegenerate. The pair  $(M, F)$  is called a conic pseudo-Finsler manifold.

In terms of the Finsler metric  $F$ , there exists a unique nonlinear Cartan (Ehresmann) connection in the conic sub-bundle  $\mathcal{A} \subset TM$  with coefficients determined by

$$G_i^j = \frac{1}{4} \partial_i [g^{jk} (y^m \partial_m \partial_k F^2 - \partial_k F^2)].$$

This nonlinear connection defines the horizontal derivatives  $\delta_i := \partial_i - G_i^j \partial_j$ . The coefficients of the geodesic spray coefficients of  $F$  can be expressed as

$$G^i = \frac{1}{4} g^{ik} (y^m \partial_m \partial_k F^2 - \partial_k F^2).$$

It is evident that  $G^i$  are smooth and positively homogeneous of degree 2 in  $\mathcal{A}$ ; furthermore, the geodesic spray can be defined globally on  $TM$  as  $S = y^i \partial_i - 2G^i \partial_i$ .

We are concerned with a two-dimensional Finsler space  $(M, F)$  with coordinates  $x = (x^i)$ ,  $y = (y^i)$ , where  $i = 1, 2$ . Then we have

$$\ell^i = \frac{1}{F} y^i, \quad \ell_i = \partial_i F, \quad h_{ij} = F \partial_i \partial_j F, \quad (2.1)$$

The angular metric tensor  $h_{ij}$  of an  $n$ -dimensional Finsler space has the matrix  $(h_{ij})$  of rank  $n - 1$ . In a two-dimensional space, the angular metric has a matrix of rank one and we have

$$\det(h_{ij}) = h_{11} h_{22} - (h_{12})^2 = 0. \quad (2.2)$$

If  $h_{11} = h_{22} = 0$ , then (2.2) implies  $h_{12} = 0$ , leading to a contradiction  $h_{ij} = 0$ . Therefore, we assume  $h_{ij} \neq 0$  and choose the sign  $\varepsilon = \pm 1$  for  $h_{11}$ . We find that  $\varepsilon h_{11} = (m_1)^2$  uniquely determines a non-zero  $m_1$  up to the sign of  $h_{11}$ . Subsequently,  $\varepsilon h_{12} = m_1 m_2$  determines  $m_2$ , and (2.2) gives  $\varepsilon h_{22} = (m_2)^2$ . Consequently, we have  $(m_1, m_2)$  and the sign  $\varepsilon$ , satisfying

$$h_{ij} = \varepsilon m_i m_j. \quad (2.3)$$

Henceforward, we work in a two-dimensional conic pseudo-Finsler space equipped with a modified Berwald frame  $(\ell_i, m_i)$ . The components  $g_{ij}$  of the metric tensor are given by

$$g_{ij} = \ell_i \ell_j + \varepsilon m_i m_j \quad (2.4)$$

and its inverse as

$$g^{ij} = \ell^i \ell^j + \varepsilon m^i m^j. \quad (2.5)$$

Consequently, the Kronecker delta takes the form

$$\delta_j^i = \ell^i \ell_j + \varepsilon m^i m_j, \quad (2.6)$$

where  $\varepsilon$  is called the signature of  $F$ . The two vector fields  $\ell = (\ell^1, \ell^2)$  and  $m = (m^1, m^2)$  have been chosen in such a way that they satisfy  $g(\ell, \ell) = 1$ ,  $g(\ell, m) = 0$ ,  $g(m, m) = \varepsilon$ .

The main scalar  $\mathcal{I}(x, y)$  is a  $h(0)$ -smooth function that is derived from the Cartan tensor [Antonelli et al., 2013] and defined by

$$FC_{ijk} = \mathcal{I} m_i m_j m_k. \quad (2.7)$$

For a smooth function  $f \in C^\infty(TM)$ , the vertical and horizontal scalar derivatives  $(f_{;1}, f_{;2})$  and  $(f_{,1}, f_{,2})$  in a Finsler surface  $(M, F)$  are given by

$$\begin{aligned} F \partial_i f &= f_{;1} \ell_i + f_{;2} m_i, \\ \delta_i f &= f_{,1} \ell_i + f_{,2} m_i \end{aligned} \quad (2.8)$$

where

$$f_{;1} = y^i \partial_i f, \quad f_{;2} = \varepsilon F (\partial_i f) m^i,$$

$$f_{,1} = (\delta_i f) \ell^i, \quad f_{,2} = \varepsilon (\delta_i f) m^i.$$

In particular, if  $f$  is  $h(r)$ , then  $f_{,1} = rf$ .

**Lemma 2.2** [Matsumoto, 2003] Let  $(M, F)$  be a conic pseudo-Finsler surface equipped with modified Berwald frames. Then, we have the following:

$$(i) \quad \ell^i m_i = \ell_i m^i = 0, \quad m^i m_i = \varepsilon, \quad \ell^i \ell_i = 1,$$

$$(ii) \quad F \partial_j \ell_i = \varepsilon m_i m_j = h_{ij}, \quad F \partial_j \ell^i = \varepsilon m^i m_j,$$

$$(iii) \quad F \partial_j m_i = -(\ell_i - \varepsilon \mathcal{I} m_i) m_j, \quad F \partial_j m^i = -(\ell^i + \varepsilon \mathcal{I} m^i) m_j.$$

**Definition 2.3** [Youssef et al., 2024] An anisotropic conformal change of a conic pseudo-Finsler metric  $F$  is defined by

$$F \mapsto \bar{F}(x, y) = e^{\phi(x, y)} F(x, y), \quad (2.9)$$

where the conformal factor  $\phi(x, y)$  is a smooth  $h(0)$ -function on  $\mathcal{A}$ . Under this transformation, the following condition holds:

$$\begin{aligned} F^2 (\partial_i \partial_j \phi + (\partial_i \phi) (\partial_j \phi)) m^i m^j + \varepsilon \\ = \sigma - (\phi_{;2})^2 + \varepsilon \neq 0, \end{aligned}$$

$$\text{with } \sigma = \phi_{;2;2} + \varepsilon \mathcal{I} \phi_{;2} + 2(\phi_{;2})^2.$$

In this case, we say that  $F$  is anisotropically conformally changed to  $\bar{F}$ . The transformation (2.9) is called proper if the conformal factor  $\phi(x, y)$  is neither isotropic nor homothetic, i.e.,  $\phi_{;2} \neq 0$ .

Now, we define the v-scalar derivatives  $(f_{;a}, f_{;b})$  and h-scalar derivatives  $(f_{,a}, f_{,b})$  in  $(M, \bar{F})$  for  $f$  by:

$$\bar{F}\partial_i f = f_{;a}\bar{\ell}_i + f_{;b}\bar{m}_i,$$

$$\bar{\delta}_i f = f_{,a}\bar{\ell}_i + f_{,b}\bar{m}_i,$$

where

$$f_{;a} = y^i \partial_i f, \quad f_{;b} = \varepsilon \bar{F}(\partial_i f) \bar{m}^i,$$

$$f_{,a} = (\bar{\delta}_i f) \bar{\ell}^i, \quad f_{,b} = \varepsilon (\bar{\delta}_i f) \bar{m}^i.$$

In [Youssef et al., 2024], we studied the anisotropic conformal change of a conic pseudo-Finsler surface  $(M, F)$  equipped with a modified Berwald frame and determined how this change affects the components of the Berwald frame  $(\ell, m)$  of  $F$ , that is,

$$\bar{\ell}_i = e^\phi [\ell_i + \phi_{;2} m_i], \quad \bar{\ell}^i = e^{-\phi} \ell^i, \quad (2.10)$$

$$\left. \begin{aligned} \bar{m}_i &= e^\phi \sqrt{\frac{\varepsilon}{\rho}} m_i, \\ \bar{m}^i &= e^{-\phi} \sqrt{\varepsilon \rho} [m^i - \varepsilon \phi_{;2} \ell^i]. \end{aligned} \right\} \quad (2.11)$$

$$\rho = \frac{1}{\sigma + \varepsilon - (\phi_{;2})^2} \quad (2.12)$$

Furthermore, the anisotropic conformal change of the geodesic spray coefficients, geodesic spray, Barthel connection coefficients and Berwald connection coefficients are given, respectively, by

$$\bar{G}^i = G^i + Q m^i + P \ell^i, \quad (2.13)$$

$$\bar{S} = S - 2(Q m^i + P \ell^i) \partial_i, \quad (2.14)$$

$$\begin{aligned} \bar{G}_j^i &= G_j^i + \frac{1}{F} \{ 2P \ell^i \ell_j + (P_{;2} - Q) \ell^i m_j \\ &+ 2Q \ell_j m^i + (\varepsilon P + Q_{;2} - \varepsilon J Q) m^i m_j \}, \end{aligned} \quad (2.15)$$

$$\begin{aligned} \bar{G}_{jk}^i &= G_{jk}^i + \frac{1}{F^2} [(2P \ell^i + 2Q m^i) \ell_j \ell_k \\ &+ \{(P_{;2} - Q) \ell^i + (\varepsilon P + Q_{;2} - \varepsilon J Q) m^i\} \\ &(\ell_j m_k + \ell_k m_j) + \{(\varepsilon P + P_{;2;2} - 2Q_{;2} \\ &+ \varepsilon J P_{;2}) \ell^i + (2\varepsilon P_{;2} + \varepsilon Q + Q_{;2;2} \\ &- \varepsilon J_{;2} Q - \varepsilon J Q_{;2}) m^i\} m_j m_k], \end{aligned} \quad (2.16)$$

where

$$2Q = \varepsilon \rho F^2 (\phi_{;2} \phi_{,1} + \phi_{,1;2} - 2\phi_{;2}), \quad (2.17)$$

$$\begin{aligned} 2P &= -\rho F^2 \phi_{;2} (\phi_{;2} \phi_{,1} + \phi_{,1;2} - 2\phi_{;2}) \\ &+ F^2 \phi_{,1}, \end{aligned} \quad (2.18)$$

$$2\varepsilon \phi_{;2} Q + 2P = F^2 \phi_{,1}. \quad (2.19)$$

Also, we have the following identities [Youssef et al., 2025a]:

$$\begin{aligned} \frac{\phi_{;2}}{2\rho} (F^2 \rho_{,1} - 2\varepsilon \rho_{;2} Q) &= P_{;2} + 2\varepsilon \phi_{;2;2} Q \\ &- F^2 \phi_{;2,1} + Q, \end{aligned} \quad (2.20)$$

$$\begin{aligned} \frac{\phi_{;2}}{2\rho} (F^2 \rho_{,1} - 2\varepsilon \rho_{;2} Q) &= -P_{;2} - 2\varepsilon \phi_{;2} Q_{;2} + \\ &F^2 \phi_{,2} + Q. \end{aligned} \quad (2.21)$$

$$\frac{1}{2\rho} (F^2 \rho_{,1} - 2\varepsilon \rho_{;2} Q) = P - \varepsilon Q_{;2} - J Q. \quad (2.22)$$

$$\begin{aligned} \phi_{;2} P + P_{;2} + \varepsilon \phi_{;2} Q_{;2} - J \phi_{;2} Q \\ - F^2 \phi_{;2} - Q = 0. \end{aligned} \quad (2.23)$$

## Berwald connection and dynamical covariant derivative

**Definition 3.1** [Antonelli et al., 2013] For a conic pseudo-Finsler surface  $(M, F)$  there exists a unique linear connection  $\mathcal{B}\Gamma = (G_{jk}^i, G_j^i, 0)$ , that satisfies the following:

**B1:**  $y^i_{|j} = 0$  i.e.  $G_j^i = G_{jk}^i y^k$ ,

**B2:**  $\mathcal{B}\Gamma$  is h-metric:  $F_{|i} = 0$ ,

**B3:**  $\mathcal{B}\Gamma$  is h-symmetric:  $T_{jk}^i = 0$ , i.e.  $G_{jk}^i = G_{kj}^i$ ,

**B4:** the  $(v)hv$ -torsion tensor:  $P_{jk}^i = 0$ , i.e.  $\partial_k G_j^i = G_{jk}^i$ ,

**B5:**  $(h)hv$ -torsion vanishes, i.e.  $C_{jk}^i = 0$ .

This connection  $\mathcal{B}\Gamma = (G_{jk}^i, G_j^i, 0)$ , is called Berwald connection. The horizontal and vertical covariant derivatives of  $X_j^i$  with respect to Berwald connection are given respectively by:

$$\nabla_{\delta_k}^B X_j^i = X_{j|k}^i = \delta_k X_j^i + X_j^r G_{rk}^i - X_r^i G_{jk}^r,$$

$$\nabla_{\partial_k}^B X_j^i = X_j^i|_k = \partial_k X_j^i.$$

**Proposition 3.2** Let  $(M, F)$  be a pseudo-Finsler surface. Then, for the Berwald connection  $\mathcal{B}\Gamma = (G_{jk}^i, G_j^i, 0)$ , the following relations hold:

(i)  $\ell^i_{|j} = 0, \quad \ell_{i|j} = 0, \quad m^i_{|j} =$

$$\varepsilon J_{,1} m^i m_j, \quad m_{i|j} = -\varepsilon J_{,1} m_i m_j,$$

(ii)  $F m^i|_j = -\ell^i m_j - \varepsilon J m^i m_j, \quad F m_i|_j =$   
 $-\ell_i m_j + \varepsilon J m_i m_j,$

(iii)  $F \ell^i|_j = \varepsilon m^i m_j, \quad F \ell_i|_j = \varepsilon m_i m_j,$

(iv)  $(\ell_i m_j + \ell_j m_i)|_k = -\varepsilon J_{,1} (\ell_i m_j +$   
 $\ell_j m_i) m_k.$

(v)  $G_j^i = -F \delta_j \ell^i.$

*Proof.*

- (i) Since  $y^i = F \ell^i$ , take the horizontal covariant derivative of both sides and using **B1** and **B2**, we obtain  $\ell^i_{|j} = 0$ . The Berwald

connection is not h-metrical, then

$$g_{ij|k} = -2\mathcal{I}_{,1}m_i m_j m_k \quad (3.1)$$

Moreover, since  $\ell_i = g_{ij}\ell^j$ , then from (3.1) and Lemma 2.2 (i) along with  $\ell^i_{|j} = 0$ , we have

$$\begin{aligned} \ell_{i|r} &= g_{ij|r}\ell^j + g_{ij}\ell^j_{|r} \\ &= -2\mathcal{I}_{,1}m_i m_j m_r \ell^j = 0. \end{aligned}$$

Next, differentiating  $\ell_i m^i = 0$  and  $g_{ij}m^i m^j = \varepsilon$  horizontally, leads to  $\ell_i m^i_{|j} = 0$  and  $m_i m^i_{|j} = \mathcal{I}_{,1}m_j$ . Thus we get

$$m^i_{|j} = \varepsilon\mathcal{I}_{,1}m^i m_j.$$

From  $m_i = g_{ir}m^r$  and (3.1), we get

$$\begin{aligned} m_{i|j} &= g_{ir|j}m^r + g_{ir}m^r_{|j} \\ &= -2\mathcal{I}_{,1}m_i m_r m_j m^r + \varepsilon\mathcal{I}_{,1}g_{ir}m^r m_j \\ &= -\varepsilon\mathcal{I}_{,1}m_i m_j. \end{aligned}$$

Consequently, we obtain

$$\begin{aligned} \ell^i_{|j} &= 0, \quad \ell_{i|j} = 0, \\ m^i_{|j} &= \varepsilon\mathcal{I}_{,1}m^i m_j, \quad m_{i|j} = -\varepsilon\mathcal{I}_{,1}m_i m_j. \end{aligned}$$

(ii) From Lemma 2.2 (iii) and the vertical covariant derivative of  $\mathcal{B}\Gamma$ , we obtain

$$\begin{aligned} Fm^i_{|j} &= F\partial_j m^i = -\ell^i m_j - \varepsilon\mathcal{I}m^i m_j. \\ Fm_{i|j} &= F\partial_j m_i = -\ell_i m_j + \varepsilon\mathcal{I}m_i m_j. \end{aligned}$$

(iii) Similarly to (ii), from Lemma 2.2 (i) and the vertical covariant derivative of  $\mathcal{B}\Gamma$ , we have

$$\begin{aligned} F\ell^i_{|j} &= F\partial_j \ell^i = \varepsilon m^i m_j. \\ F\ell_{i|j} &= F\partial_j \ell_i = \varepsilon m_i m_j. \end{aligned}$$

(iv) Follows directly from (i).

(v) From (i), we have, then

$$\ell^i_{|j} = 0, \quad \text{so} \quad \delta_j \ell^i + \ell^k G^i_{jk} = 0.$$

By B1,

$$0 = F\delta_j \ell^i + y^k G^i_{jk} = F\delta_j \ell^i + G^i_j.$$

Therefore,

$$G^i_j = -F\delta_j \ell^i.$$

**Definition 3.3** A nonlinear connection induces a dynamical covariant derivative  $\nabla_D$  that acts on functions  $f \in C^\infty(\mathcal{A})$  and Finsler vector fields  $X \in \Gamma(\pi^*TM)$  as follows:

$$\nabla_D f = y^i \delta_i f = S(f), \quad (3.2)$$

$$\nabla_D X = (\nabla X^i) \partial_i, \quad \nabla X^i = y^j \delta_j X^i + G^i_j X^j, \quad (3.3)$$

where  $X = X^i \partial_i$  in local coordinates. This definition allows  $\nabla_D$  to map functions and Finsler vector fields to their corresponding counterparts.

Let  $T^{r_1 r_2 \dots r_p}_{s_1 s_2 \dots s_q}(x, y)$  be the components of an  $(p, q)$ -d-tensor field  $T$ . Then the dynamical covariant derivative  $\nabla_D$  maps  $T$  to a tensor field with components:

$$\begin{aligned} \nabla_D T^{r_1 r_2 \dots r_p}_{s_1 s_2 \dots s_q} &= y^k \delta_k T^{r_1 r_2 \dots r_p}_{s_1 s_2 \dots s_q} + G^r_1 T^{mr_2 \dots r_p}_{s_1 s_2 \dots s_q} | \\ &\quad + \dots + G^r_p T^{r_1 r_2 \dots m}_{s_1 s_2 \dots s_q} \\ &\quad - G^m_{s_1} T^{r_1 r_2 \dots r_p}_{ms_2 \dots s_q} - \dots - G^m_{s_q} T^{r_1 r_2 \dots r_p}_{s_1 s_2 \dots m}. \end{aligned} \quad (3.4)$$

A scalar function with vanishing dynamical covariant derivative is constant along geodesics, and therefore is a first integral of the geodesic spray  $S$ .

**Lemma 3.4** In Finsler surfaces, a scalar function  $f \in C^\infty(\mathcal{A})$  is constant along the geodesic, that is, it is a first integral of the geodesic spray if and only if  $f_{,1} = 0$ .

*Proof.* A function  $f$  is constant along geodesics if its total derivative along the spray vector field vanishes:

$$\frac{df}{dt} = \nabla_D f = S(f) = 0.$$

From (2.8), we have

$$0 = y^i \delta_i f = y^i (f_{,1} \ell_i + f_{,2} m_i).$$

The conclusion follows from Lemma 2.2 (i), which implies that this holds if and only if  $f_{,1} = 0$ .

**Lemma 3.5** The dynamical covariant derivative  $\nabla_D$ , the Berwald connection  $\nabla^B$  are related by

$$y^k \nabla^B_{\delta_k} = \nabla_D.$$

We present an alternative proof of the well-known result that the dynamical covariant derivative of the Berwald frame of a conic pseudo-Finsler surface vanishes [Bucataru and Miron, 2007].

**Lemma 3.6** Let  $(M, f)$  be a conic pseudo-Finsler surface equipped with a Berwald frame  $(\ell, m)$ . Then the dynamical covariant derivatives of  $(\ell, m)$  vanish.

*Proof.* From Proposition 3.2 (i), we have

$$\begin{aligned} \ell^i_{|j} &= 0, \quad \ell_{i|j} = 0, \\ m^i_{|j} &= \varepsilon\mathcal{I}_{,1}m^i m_j, \quad m_{i|j} = -\varepsilon\mathcal{I}_{,1}m_i m_j \end{aligned}$$

Along with Lemma 3.5, we get

$$\begin{aligned} \nabla_D \ell^i &= y^j \delta^i_j \ell^i = 0, \\ \nabla_D \ell_i &= y^j \delta_{ij} \ell_i = 0, \\ \nabla_D m^i &= y^j \delta^i_j m^i = \varepsilon F\mathcal{I}_{,1}m^i m_j \ell^j = 0, \\ \nabla_D m_i &= y^j \delta_{ij} m_i = -\varepsilon F\mathcal{I}_{,1}m_i m_j \ell^j = 0. \end{aligned}$$

Hence, the dynamical covariant derivative of the Berwald frame vanishes.

Under the anisotropic conformal transformation  $F \rightarrow \bar{F} = e^\phi F$ , we define the dynamical covariant derivatives in  $(M, \bar{F})$  as

$$\bar{\nabla}_D f = y^i \bar{\delta}_i f = \bar{S}(f), \quad (3.5)$$

$$\bar{\nabla}_D X_j^i = y^k \bar{\delta}_k X_j^i + \bar{G}_k^i X_j^k - \bar{G}_j^k X_k^i, \quad (3.6)$$

where  $\bar{S}$  and  $\bar{G}_j^i$  are given by equations (2.14) and (2.15), respectively, and the horizontal derivative  $\bar{\delta}_j$  is defined by

$$F\bar{\delta}_j = F\delta_j - (2P\ell^i\ell_j + (P_{;2} - Q)\ell^i m_j + 2Q\ell_j m^i + (\varepsilon P + Q_{;2} - \varepsilon JQ)m^i m_j)\delta_i. \quad (3.7)$$

**Proposition 3.7** Let the conic pseudo-Finsler metric  $F$  be anisotropically conformal to  $\bar{F} = e^\phi F$ . Then we have:

$$\bar{\nabla}_D f = \nabla_D f - \frac{2}{F}(f_{;1}P + \varepsilon f_{;2}Q). \quad (3.8)$$

$$\begin{aligned} \bar{\nabla}_D X^i &= \nabla_D X^i + \frac{1}{F}[(-2P A_{;1} - 2\varepsilon Q A_{;2} \\ &\quad + \varepsilon QB + 2P A + \varepsilon P_{;2}B)\ell^i \\ &\quad + (-2P B_{;2} - 2\varepsilon Q B_{;2} + PB + \varepsilon Q_{;2}B \\ &\quad + QJB)m^i]. \end{aligned} \quad (3.9)$$

*Proof.* Firstly, from (3.5), (2.14) and (2.8) for a scalar function  $f \in C^\infty(M)$ , we have

$$\begin{aligned} \bar{\nabla}_D f &= (S - 2(P\ell^i + Qm^i)\delta_i)(f) \\ &= S(f) - 2(P\ell^i + Qm^i)(f_{;1}\ell_i + f_{;2}m_i) \end{aligned}$$

By using Lemma 2.2 (i), we obtain

$$\bar{\nabla}_D f = \nabla_D f - \frac{2}{F}(f_{;1}P + \varepsilon f_{;2}Q)$$

Secondly, on a Finsler surface, any tangent vector can be expressed in the form

$$X^i = A(x, y)\ell^i + B(x, y)m^i, \quad \text{with } A, B \in C^\infty(TM).$$

Consequently, From (2.8) and Lemma 2.2 (ii) and (iii), we get

$$\begin{aligned} F\hat{\partial}_j X^i &= F\hat{\partial}_j(A\ell^i + Bm^i) \\ &= A_{;1}\ell^i\ell_j + (A_{;2} - B)\ell^i m_j + B_{;1}m^i\ell_j + \\ &\quad (B_{;2} + \varepsilon A - \varepsilon JB)m^i m_j. \end{aligned} \quad (3.10)$$

According to (3.6), we get

$$\begin{aligned} \bar{\nabla}_D X^i &= y^k \bar{\delta}_k X^i + \bar{G}_k^i X^k - \bar{G}_j^i X^j \\ &= S(X^i) - 2(P\ell^j + Qm^j)\delta_j(X^i) \\ &\quad + G_k^i X^k + \frac{1}{F}(2P\ell^i\ell_k + (P_{;2} \\ &\quad - Q)\ell^i m_k + 2Q\ell_k m^i + (\varepsilon P + Q_{;2} \\ &\quad - \varepsilon JQ)m^i m_k)(A\ell^k + Bm^k) \end{aligned}$$

From (3.10) and Lemma 2.2 (i), we obtain

$$\begin{aligned} \bar{\nabla}_D X^i &= \nabla_D X^i + \frac{1}{F}[(-2P A_{;1} - 2\varepsilon Q A_{;2} \\ &\quad + \varepsilon QB + 2P A + \varepsilon P_{;2}B)\ell^i \\ &\quad + (-2P B_{;2} - 2\varepsilon Q B_{;2} + PB + \varepsilon Q_{;2}B \\ &\quad + QJB)m^i]. \end{aligned}$$

### Chern-Rund connection and anisotropic change

**Definition 4.1** [Antonelli et al., 2013] For a

conic pseudo-Finsler surface  $(M, F)$  there exists a unique linear connection  $\mathcal{R}\Gamma = (\Gamma_{jk}^i, G_j^i, 0)$ , that satisfies the following:

**R1:**  $y_{|j}^i = 0$ , i.e.  $G_j^i = \Gamma_{jk}^i y^k$ ,

**R2:**  $\mathcal{R}\Gamma$  is  $h$ -metric:  $g_{ij|k}^* = 0$ ,

**R3:**  $\mathcal{R}\Gamma$  is  $h$ -symmetric:  $T_{jk}^i = 0$ , i.e.  $\Gamma_{jk}^i = \Gamma_{kj}^i$ ,

**R4:** (h) hv-torsion vanishes, i.e.  $C_{jk}^i = 0$ ,

This linear connection is called Chern (Rund) connection. The geometric objects associated with Chern connection will be marked by a star.

The horizontal and vertical covariant derivatives of  $X_j^i$  w.r.t. Chern connection are given respectively by:

$$X_{j|k}^i := \delta_k X_j^i + X_j^r \Gamma_{rk}^i - X_r^i \Gamma_{jk}^r, \quad X_j^i|_k := \partial_k X_j^i.$$

**Lemma 4.2** Let  $(M, F)$  be a conic pseudo-Finsler surface. Then the modified Berwald frame satisfies

$$\begin{aligned} \ell^i(\delta_k \ell_j) + \varepsilon m^i(\delta_k m_j) \\ = -\ell_j(\delta_k \ell^i) - \varepsilon m_j(\delta_k m^i) \end{aligned}$$

*Proof.* Since we have

$$\delta_j^i = \ell^i \ell_j + \varepsilon m^i m_j.$$

taking the horizontal derivative yields

$$\begin{aligned} 0 &= \delta_k(\delta_j^i) = \delta_k(\ell^i \ell_j + \varepsilon m^i m_j) \\ &= \ell_j(\delta_k \ell^i) + \ell^i(\delta_k \ell_j) + \varepsilon m_j(\delta_k m^i) \\ &\quad + \varepsilon m^i(\delta_k m_j) \end{aligned}$$

Consequently, we have

$$\begin{aligned} \ell^i(\delta_k \ell_j) + \varepsilon m^i(\delta_k m_j) \\ = -\ell_j(\delta_k \ell^i) - \varepsilon m_j(\delta_k m^i) \end{aligned}$$

**Proposition 4.3** Let  $(M, F)$  be a pseudo-Finsler surface. Then, for the Chern-Rund connection  $\mathcal{R}\Gamma = (\Gamma_{jk}^i, G_j^i, 0)$ , the following relations hold:

(i)  $\ell_j^* = 0$ ,  $\ell_{i|j}^* = 0$ ,  $m_{i|j}^* = 0$ ,  $m_{i|j}^* = 0$ ,

(ii)  $Fm^i|_j = -\ell^i m_j - \varepsilon Jm^i m_j$ ,

$$Fm_i|_j = -\ell_i m_j + \varepsilon Jm_i m_j,$$

(iii)  $F\ell^i|_j = \varepsilon m^i m_j$ ,  $F\ell_i|_j = \varepsilon m_i m_j$ ,

(iv)  $F(\ell_i m_j - \ell_j m_i)|_k = \varepsilon J(\ell_i m_j - \ell_j m_i)m_k$ .

(v)  $\Gamma_{kj}^i = \ell^i \delta_k \ell_j + \varepsilon m^i \delta_k m_j$ .

*Proof.*

(i) Since the Finsler metric satisfies  $F^2 = g_{ij}y^i y^j$ , it follows from **R1** and **R2** that



$$F^*_{|i} = 0. \quad (4.1)$$

Since  $y^i = F \ell^i$ , differentiating horizontally gives

$$0 = y^i_{|j} = F^*_{|j} \ell^i + F \ell^i_{|j}.$$

By (4.1), we have  $\ell^i_{|j} = 0$ .

Next, taking the horizontal covariant derivative of the covector  $\ell_i = g_{ij} \ell^j$ , we obtain

$$\ell^*_{i|r} = g^*_{ij|r} \ell^j + g_{ij} \ell^j_{|r}.$$

By **R2** and  $\ell^j_{|r} = 0$ , we have  $\ell^*_{i|r} = 0$ .

Moreover, differentiating  $\ell_i m^i = 0$  and  $g_{ij} m^i m^j = \varepsilon$  horizontally, we get  $\ell_i m^i_{|j} = 0$  and  $m_i m^i_{|j} = 0$ . Thus we get  $m^i_{|j} = 0$ .

Finally, from  $m_i = g_{ir} m^r$  and **R2**, we get  $m^*_{i|j} = g^*_{ir|j} m^r + g_{ir} m^r_{|j} = 0$ , where  $m^i_{|j} = 0$ .

(ii) From Lemma 2.2 (iii) and the vertical covariant derivative of  $\mathcal{R}\Gamma$ , we obtain

$$F m^i_{|j} = F \partial_j m^i = -\ell^i m_j - \varepsilon \mathcal{I} m^i m_j.$$

$$F m_i_{|j} = F \partial_j m_i = -\ell_i m_j + \varepsilon \mathcal{I} m_i m_j.$$

(iii) Similarly to (ii), from Lemma 2.2 (i) and the vertical covariant derivative of  $\mathcal{R}\Gamma$ , we have

$$F \ell^i_{|j} = F \partial_j \ell^i = \varepsilon m^i m_j.$$

$$F \ell_i_{|j} = F \partial_j \ell_i = \varepsilon m_i m_j.$$

(iv) Follows directly from (ii) and (iii).

(v) From (i), we have  $\ell^*_{j|k} = 0$  and  $m^*_{j|k} = 0$ , then

$$\delta_k \ell_j - \ell_r \Gamma^r_{kj} = 0. \quad (4.2)$$

$$\delta_k m_j - m_r \Gamma^r_{kj} = 0. \quad (4.3)$$

Multiply (4.2) by  $\ell^i$  and (4.3) by  $\varepsilon m^i$ , then solve these equations to find  $\Gamma^i_{jk}$  (taking into account  $\delta_j^i = \ell^i \ell_j + \varepsilon m^i m_j$ ), we get

$$\Gamma^i_{kj} = \ell^i \delta_k \ell_j + \varepsilon m^i \delta_k m_j$$

#### Remark 4.4

(a) From Proposition 4.3 (i), we have  $\ell^i_{|j} = 0$

and  $m^i_{|j} = 0$ . Therefore, we obtain the following equations:

$$\delta_j \ell^i + \ell^k \Gamma^i_{jk} = 0, \quad (4.4)$$

$$\delta_j m^i + m^k \Gamma^i_{jk} = 0. \quad (4.5)$$

By multiplying (4.4) by  $\ell_r$  and (4.5) by  $\varepsilon m_r$ , and solving these equations to find  $\Gamma^i_{jk}$  (taking into account  $\delta_j^i = \ell^i \ell_j + \varepsilon m^i m_j$ ), we get

$$\Gamma^i_{jk} = -\ell_j \delta_k \ell^i - \varepsilon m_j \delta_k m^i.$$

(b) The symmetry of  $\Gamma^i_{jk}$  (i.e.,  $\Gamma^i_{jk} = \Gamma^i_{kj}$ ) is obtained from (a), Lemma 4.2, and Proposition 4.3 (v).

**Proposition 4.5** Let  $(M, F)$  be conic pseudo-Finsler surface and (2.9) be the anisotropic conformal transformation. The transformation of the horizontal coefficients of Chern connection are given by

$$\begin{aligned} F^2 \bar{\Gamma}^i_{jk} = & F^2 \Gamma^i_{jk} + 2P \ell^i \ell_j \ell_k + 2Q m^i \ell_j \ell_k \\ & + (P_{;2} - Q)(\ell^i m_j \ell_k + \ell^i \ell_j m_k) \\ & + \left( F^2 \phi_{;2} \frac{\rho_{;2}}{2\rho} + F^2 \phi_{;2,2} - (1 + \varepsilon \phi_{;2,2} \right. \\ & + \varepsilon \phi_{;2} \frac{\rho_{;2}}{2\rho})(\varepsilon P + Q_{;2} - \varepsilon \mathcal{I} Q) \Big) \ell^i m_j m_k \\ & + (\varepsilon P + Q_{;2} - \varepsilon \mathcal{I} Q)(m^i \ell_j m_k + m^i m_j \ell_k) \\ & + \left( \varepsilon F^2 \phi_{;2} - \varepsilon F^2 \frac{\rho_{;2}}{2\rho} - \left( \varepsilon \mathcal{I} + \phi_{;2} - \frac{\rho_{;2}}{2\rho} \right) \right. \\ & \left. \left. (\varepsilon P + Q_{;2} - \varepsilon \mathcal{I} Q) \right) m^i m_j m_k. \end{aligned}$$

*Proof.* The anisotropic transformation of  $\Gamma^i_{jk}$ , in view of Proposition 4.3 (v), is given by

$$F^2 \bar{\Gamma}^i_{jk} = -F^2 \bar{\ell}_j \bar{\delta}_k \bar{\ell}^i - \varepsilon F^2 \bar{m}_j \bar{\delta}_k \bar{m}^i \quad (4.6)$$

Firstly, using (2.10), (2.1) and (3.7), we can find the anisotropic transformation of the first term of (4.6).

$$\begin{aligned} F^2 \bar{\ell}^i \bar{\delta}_k \bar{\ell}_j = & e^{-\phi} \ell^i (F^2 \delta_k - [2P \ell^r \ell_k + (P_{;2} \\ & - Q) \ell^r m_k + 2Q \ell_k m^r + (\varepsilon P + Q_{;2} \\ & - \varepsilon \mathcal{I} Q) m^r m_k] F \partial_r) (e^\phi (\ell_j + \phi_{;2} m_j)) \end{aligned}$$

From (2.8), we get

$$\begin{aligned} F^2 \bar{\ell}^i \bar{\delta}_k \bar{\ell}_j = & e^{-\phi} \ell^i (e^\phi F^2 [\delta_k \ell_j + (\phi_{;1} \ell_k \\ & + \phi_{;2} m_k)(\ell_j + \phi_{;2} m_j) + \phi_{;2} \delta_k m_j \\ & + (\phi_{;2,1} \ell_k + \phi_{;2,2} m_k) m_j] \\ & - e^\phi [2P \ell^r \ell_k + (P_{;2} - Q) \ell^r m_k \\ & + 2Q \ell_k m^r + (\varepsilon P + Q_{;2} \\ & - \varepsilon \mathcal{I} Q) m^r m_k] [\phi_{;2} m_r (\ell_j + \phi_{;2} m_j) \\ & + \varepsilon m_j m_r + \phi_{;2,2} m_j m_r + \phi_{;2} (-\ell_j m_r \\ & + \varepsilon \mathcal{I} m_j m_r)]) \end{aligned}$$

By using Lemma 2.2 (i), we obtain

$$\begin{aligned} F^2 \bar{\ell}^i \bar{\delta}_k \bar{\ell}_j = & F^2 \ell^i \delta_k \ell_j + F^2 \phi_{;2} \ell^i \delta_k m_j \\ & + F^2 \ell^i [(\phi_{;1} \ell_k + \phi_{;2} m_k)(\ell_j + \phi_{;2} m_j) \\ & + (\phi_{;2,1} \ell_k + \phi_{;2,2} m_k) m_j] - \ell^i [2\varepsilon Q \ell_k \end{aligned}$$

$$\begin{aligned}
 & + (P + \varepsilon Q_{;2} - \mathcal{I}Q)m_k][\phi_{;2}(\ell_j + \phi_{;2}m_j) \\
 & + \varepsilon m_j + \phi_{;2;2}m_j + \phi_{;2}(-\ell_j + \varepsilon \mathcal{I}m_j)] \\
 \text{From the formula of } \rho \text{ (2.12), we get} \\
 & F^2 \bar{\ell}^i \bar{\delta}_k \bar{\ell}_j = F^2 \ell^i \delta_k \ell_j + F^2 \phi_{;2} \ell^i \delta_k m_j \\
 & + F^2 \ell^i [(\phi_{;1} \ell_k + \phi_{;2} m_k)(\ell_j + \phi_{;2} m_j) \\
 & + (\phi_{;2;1} \ell_k + \phi_{;2;2} m_k)m_j] - \ell^i [2\varepsilon Q \ell_k + (P \\
 & + \varepsilon Q_{;2} - \mathcal{I}Q)m_k] \frac{1}{\rho} m_j \\
 & = F^2 \ell^i \delta_k \ell_j + F^2 \phi_{;2} \ell^i \delta_k m_j \\
 & + F^2 (\phi_{;1} \ell_k + \phi_{;2} m_k) \ell^i \ell_j \\
 & + [F^2 \phi_{;2} \phi_{;1} + F^2 \phi_{;2;1} - \frac{2\varepsilon}{\rho} Q] \ell^i m_j \ell_k \\
 & + [F^2 \phi_{;2} \phi_{;2} + F^2 \phi_{;2;2} - \frac{1}{\rho} (P + \varepsilon Q_{;2} \\
 & - \mathcal{I}Q)] \ell^i m_j m_k \quad (4.7)
 \end{aligned}$$

Secondly, we find the second term of (4.6), by (2.10) and (2.11) along with (3.7), we have

$$\begin{aligned}
 \varepsilon F^2 \bar{m}^i \bar{\delta}_k \bar{m}_j & = \varepsilon (e^{-\phi} \sqrt{\varepsilon \rho} (m^i \\
 & - \varepsilon \phi_{;2} \ell^i)) (F^2 \delta_k - [2P \ell^r \ell_k + (P_{;2} \\
 & - Q) \ell^r m_k + 2Q \ell_k m^r + (\varepsilon P + Q_{;2} \\
 & - \varepsilon \mathcal{I}Q) m^r m_k] F \dot{\partial}_r) e^{\phi} \sqrt{\frac{\varepsilon}{\rho}} m_j.
 \end{aligned}$$

From (2.8), we get

$$\begin{aligned}
 \varepsilon F^2 \bar{m}^i \bar{\delta}_k \bar{m}_j & = \varepsilon \sqrt{\varepsilon \rho} (m^i - \varepsilon \phi_{;2} \ell^i) \\
 & \left( F^2 \sqrt{\frac{\varepsilon}{\rho}} m_j (\phi_{;1} \ell_k + \phi_{;2} m_k) \right. \\
 & - \varepsilon F^2 \sqrt{\varepsilon \rho} m_j \frac{(\rho_{;1} \ell_k + \rho_{;2} m_k)}{2\rho^2} \\
 & + F^2 \sqrt{\frac{\varepsilon}{\rho}} \delta_k m_j - [2P \ell^r \ell_k + (P_{;2} \\
 & - Q) \ell^r m_k + 2Q \ell_k m^r + (\varepsilon P + Q_{;2} \\
 & - \varepsilon \mathcal{I}Q) m^r m_k] \left[ \sqrt{\frac{\varepsilon}{\rho}} \phi_{;2} m_j m_r \right. \\
 & - \varepsilon \sqrt{\varepsilon \rho} m_j \frac{\rho_{;2} m_r}{2\rho^2} + \sqrt{\frac{\varepsilon}{\rho}} (-\ell_j m_r \\
 & \left. \left. + \varepsilon \mathcal{I} m_j m_r) \right] \right)
 \end{aligned}$$

By applying Lemma 2.2 (i), we can rewrite the expression as follows:

$$\begin{aligned}
 \varepsilon F^2 \bar{m}^i \bar{\delta}_k \bar{m}_j & = \varepsilon F^2 m^i \delta_k m_j - F^2 \phi_{;2} \ell^i \delta_k m_j \\
 & - 2\varepsilon \phi_{;2} Q \ell^i \ell_j \ell_k - \phi_{;2} (P + \varepsilon Q_{;2} \\
 & - \mathcal{I}Q) \ell^i \ell_j m_k + 2Q m^i \ell_j \ell_k + (\varepsilon P + Q_{;2} \\
 & - \varepsilon \mathcal{I}Q) m^i \ell_j m_k + (\varepsilon F^2 \phi_{;2} - \varepsilon F^2 \frac{\rho_{;2}}{2\rho}
 \end{aligned}$$

$$\begin{aligned}
 & - (\varepsilon P + Q_{;2} - \varepsilon \mathcal{I}Q) (\phi_{;2} - \frac{\rho_{;2}}{2\rho} \\
 & + \varepsilon \mathcal{I}) m^i m_j m_k + (\varepsilon F^2 \phi_{;1} - \varepsilon F^2 \frac{\rho_{;1}}{2\rho} \\
 & - 2Q (\phi_{;2} - \frac{\rho_{;2}}{2\rho} + \varepsilon \mathcal{I})) m^i m_j \ell_k \\
 & + (-F^2 \phi_{;2} \phi_{;1} + F^2 \phi_{;2} \frac{\rho_{;1}}{2\rho} + 2\varepsilon \phi_{;2} Q (\phi_{;2} \\
 & - \frac{\rho_{;2}}{2\rho} + \varepsilon \mathcal{I})) \ell^i m_j \ell_k + (-F^2 \phi_{;2} \phi_{;2} \\
 & + F^2 \phi_{;2} \frac{\rho_{;2}}{2\rho} + \phi_{;2} (P + \varepsilon Q_{;2} - \mathcal{I}Q) (\phi_{;2} - \\
 & \frac{\rho_{;2}}{2\rho} + \varepsilon \mathcal{I})) \ell^i m_j m_k \quad (4.8)
 \end{aligned}$$

From (4.7) and (4.8), we determine the anisotropic conformal transformation of the horizontal coefficients of Cartan connection

$$\begin{aligned}
 F^2 \bar{\Gamma}_{jk}^{\star i} & = F^2 \Gamma_{jk}^{\star i} + (F^2 \phi_{;1} - 2\varepsilon Q \phi_{;2}) \ell^i \ell_j \ell_k \\
 & + (F^2 \phi_{;2} - \varepsilon \phi_{;2} (\varepsilon P + Q_{;2} - \varepsilon \mathcal{I}Q)) \ell^i \ell_j m_k \\
 & + (F^2 \phi_{;2} \frac{\rho_{;1}}{2\rho} - \varepsilon \phi_{;2} \frac{\rho_{;2}}{\rho} Q + F^2 \phi_{;2;1} - 2Q \\
 & - 2\varepsilon Q \phi_{;2;2}) \ell^i m_j \ell_k + (F^2 \phi_{;2} \frac{\rho_{;2}}{2\rho} + F^2 \phi_{;2;2} \\
 & - (1 + \varepsilon \phi_{;2;2} + \varepsilon \phi_{;2} \frac{\rho_{;2}}{2\rho}) (\varepsilon P + Q_{;2} \\
 & - \varepsilon \mathcal{I}Q)) \ell^i m_j m_k + 2Q m^i \ell_j \ell_k + (\varepsilon F^2 \phi_{;1} \\
 & - \varepsilon F^2 \frac{\rho_{;1}}{2\rho} + \frac{\rho_{;2}}{\rho} Q - 2\varepsilon \mathcal{I}Q - 2\phi_{;2} Q) m^i m_j \ell_k \\
 & + (\varepsilon F^2 \phi_{;2} - \varepsilon F^2 \frac{\rho_{;2}}{2\rho} - (\varepsilon \mathcal{I} + \phi_{;2} - \frac{\rho_{;2}}{2\rho}) (\varepsilon P \\
 & + Q_{;2} - \varepsilon \mathcal{I}Q)) m^i m_j m_k + (\varepsilon P + Q_{;2} \\
 & - \varepsilon \mathcal{I}Q) m^i \ell_j m_k.
 \end{aligned}$$

From (2.19) and (2.20)- (2.22) the formula of  $\bar{\Gamma}_{jk}^{\star i}$  can be obtained.

**Proposition 4.6** Let the conic pseudo-Finsler metric  $F$  be anisotropically conformal to  $\bar{F} = e^{\phi} F$ . Then the Landsberg tensor of  $\bar{F}$  is given by

$$\begin{aligned}
 \bar{L}_{jk}^i & = L_{jk}^i + \frac{1}{F^2} [((\varepsilon P + P_{;2;2} - 2Q_{;2} \\
 & + \varepsilon \mathcal{I} P_{;2}) \ell^i + (2\varepsilon P_{;2} + \varepsilon Q + Q_{;2;2} - \varepsilon \mathcal{I}_{;2} Q \\
 & - \varepsilon \mathcal{I} Q_{;2}) m^i) m_j m_k - (F^2 \phi_{;2} \frac{\rho_{;2}}{2\rho} \\
 & + F^2 \phi_{;2;2} - (1 + \varepsilon \phi_{;2;2} + \varepsilon \phi_{;2} \frac{\rho_{;2}}{2\rho}) (\varepsilon P \\
 & + Q_{;2} - \varepsilon \mathcal{I}Q)) \ell^i m_j m_k - (\varepsilon F^2 \phi_{;2} \\
 & - \varepsilon F^2 \frac{\rho_{;2}}{2\rho} - (\varepsilon \mathcal{I} + \phi_{;2} - \frac{\rho_{;2}}{2\rho}) (\varepsilon P + Q_{;2} \\
 & - \varepsilon \mathcal{I}Q)) m^i m_j m_k].
 \end{aligned}$$

*Proof.* Let  $(M, F)$  be a conic pseudo-Finsler surface equipped with the Chern connection

$\mathcal{R}\Gamma = (\Gamma_{jk}^i, G_j^i, 0)$  and the Berwald connection  $\mathcal{B}\Gamma = (G_{jk}^i, G_j^i, 0)$ . The Landsberg tensor is defined as the difference between the horizontal coefficient of the two connections, consequently,

$$L_{jk}^i := G_{jk}^i - \Gamma_{jk}^i.$$

Under the given anisotropic transformation, the transformed Landsberg tensor is given by

$$\bar{L}_{jk}^i = \bar{G}_{jk}^i - \bar{\Gamma}_{jk}^i.$$

From (2.16) and Proposition 4.5 we get

$$\begin{aligned} \bar{L}_{jk}^i &= L_{jk}^i + \frac{1}{F^2} [(\varepsilon P + P_{;2;2} - 2Q_{;2} \\ &\quad + \varepsilon \mathcal{I}P_{;2}) \ell^i + (2\varepsilon P_{;2} + \varepsilon Q + Q_{;2;2} \\ &\quad - \varepsilon \mathcal{I}_{;2}Q - \varepsilon \mathcal{I}Q_{;2}) m^i] m_j m_k \\ &\quad - (F^2 \phi_{;2} \frac{\rho_{;2}}{2\rho} + F^2 \phi_{;2;2} - (1 + \varepsilon \phi_{;2;2} \\ &\quad + \varepsilon \phi_{;2} \frac{\rho_{;2}}{2\rho})(\varepsilon P + Q_{;2} - \varepsilon \mathcal{I}Q)) \ell^i m_j m_k \\ &\quad - (\varepsilon F^2 \phi_{;2} - \varepsilon F^2 \frac{\rho_{;2}}{2\rho} - (\varepsilon \mathcal{I} + \phi_{;2} \\ &\quad - \frac{\rho_{;2}}{2\rho})(\varepsilon P + Q_{;2} - \varepsilon \mathcal{I}Q)) m^i m_j m_k]. \end{aligned}$$

**Proposition 4.7** *Let  $(M, F)$  be a conic pseudo-Finsler metric and (2.9) be the proper anisotropic conformal transformation, provided that the conformal factor is horizontally constant. Then the property of being Landsbergian is preserved if and only if  $\phi_{;2;2} = 0$ .*

*Proof.* As, if the conformal factor is horizontally constant ( $\phi_{;1} = \phi_{;2} = 0$ ), that is  $P = Q = 0$  [Youssef et al., 2024, Theorem 4.11]. From Proposition 4.6, we have

$$\begin{aligned} \bar{L}_{jk}^i &= L_{jk}^i + \frac{1}{F^2} [-(F^2 \phi_{;2} \frac{\rho_{;2}}{2\rho} \\ &\quad + F^2 \phi_{;2;2}) \ell^i m_j m_k + \varepsilon F^2 \frac{\rho_{;2}}{2\rho} m^i m_j m_k]. \end{aligned}$$

Consequently the Landsbergian property is preserved under the anisotropic conformal transformation if and only if

$$\phi_{;2} \frac{\rho_{;2}}{2\rho} + \phi_{;2;2} = 0, \quad \frac{\rho_{;2}}{2\rho} = 0.$$

Since (2.9) is proper i.e.  $\phi_{;2} \neq 0$ , then the Landsbergian property is preserved if and only if  $\phi_{;2;2} = 0$ .

## References

Antonelli, P. L., Ingarden, R. S., and Matsumoto, M. (2013). The theory of sprays and Finsler spaces with applications in physics and biology, volume

58. Springer Science & Business Media.

Bao, D., Chern, S.-S., and Shen, Z. (2012). An introduction to Riemann-Finsler geometry, volume 200. Springer Science & Business Media.

Bidabad, B. and Tayebi, A. (2011). Properties of generalized berwald connections. Bulletin of the Iranian Mathematical Society, 35(1):235–252.

Bucataru, I. and Miron, R. (2007). Finsler-Lagrange geometry: Applications to dynamical systems. Editura Academiei Romane Bucharest.

Friedl-Sz asz, A., Popovici-Popescu, E., Voicu, N., Pfeifer, C., and Heefer, S. (2025). Cosmological landsberg-finsler spacetimes. Physical Review D, 111(4):044058.

Heefer, S., Pfeifer, C., Reggio, A., and Fuster, A. (2023). A cosmological unicorn solution to finsler gravity. Physical Review D, 108(6):064051.

Hohmann, M., Pfeifer, C., and Voicu, N. (2020). Cosmological finsler spacetimes. Universe, 6(5):65.

Matsumoto, M. (2003). Finsler geometry in the 20th-century. handbook of finsler geometry. vol. 1, 2, 557-966.

R. Miron and M. Anastasiei, *The geometry of Lagrange spaces: theory and applications*, Springer Science & Business Media **59** (2012).

Pfeifer, C. and Wohlfarth, M. N. (2012). Finsler geometric extension of einstein gravity. Physical Review D—Particles, Fields, Gravitation, and Cosmology, 85(6):064009.

Savvopoulos, C. and Stavrinou, P. (2023). Anisotropic conformal dark gravity on the lorentz tangent bundle spacetime. Physical Review D, 108(4):044048. 1

Shen, Y.-B. and Shen, Z. (2016). Introduction to modern Finsler geometry. World Scientific Publishing Company.

Voicu, N., Cheraghchi, S., and Pfeifer, C. (2023). Birkhoff theorem for berwaldfinsler spacetimes. Physical Review D, 108(10):104060.

Youssef, N. L., Abed, S., and Soleiman, A. (2010). Geometric objects associated with the fundamental connections in finsler geometry. J. Egyptian Math. Soc., 18:67–90 (arXiv: 0805.2489).

N.L. Youssef, *Cartan and Berwald connections in the pullback formalism*, Algebras, Groups and Geometries **25** (2008), 363–386.

N.L. Youssef, S.H. Abed and A. Soleiman, *A global approach to the theory of connections in Finsler geometry*, Tensor (Japan) **71** (2009), 187–208, arXiv:0801.3220.

Youssef, N. L., Elgendi, S., Kotb, A., and Taha, E. H. (2024). Anisotropic conformal change of

conic pseudo-finsler surfaces, I. Classical and Quantum Gravity, 41(17):175005.  
Youssef, N. L., Elgendi, S., Kotb, A., and Taha, E. H. (2025a). Anisotropic conformal change of cartan connection of a conic pseudo-finsler

surface. Submitted.

Youssef, N. L., Elgendi, S., Kotb, A., and Taha, E. H. (2025b). Anisotropic conformal change of conic pseudo-finsler surfaces, II. submitted.

## الملخص العربي

**عنوان البحث:** إتصالات بيرفلد وتشيرن تحت التحويلات التشاكلية الاتجاهية على الأسطح الفينسلرية

نبيل يوسف<sup>٢</sup>، صلاح الجندي<sup>٣</sup>، علي قطب<sup>١\*</sup>، ابتسام طه<sup>٢</sup>، أحمد طرابية<sup>١</sup>

<sup>١</sup>قسم الرياضيات-كلية العلوم-جامعة دمياط- مصر

<sup>٢</sup>قسم الرياضيات-كلية العلوم-جامعة القاهرة- مصر.

<sup>٣</sup>قسم الرياضيات-كلية العلوم-الجامعة الإسلامية- السعودية

<sup>٤</sup>قسم الرياضيات-كلية العلوم-جامعة بنها – مصر.

تعتمد هذه الورقة على استكمال عملنا السابق حول التحويلات التشاكلية الاتجاهية

$$F(x, y) \rightarrow \bar{F}(x, y) = e^{\varphi(x, y)} F(x, y)$$

الهدف الأساسي من هذه الدراسة هو دراسة سلوك اتصال بيرفلد، الذي يحدد مدى انحراف هندسة فينسلر عن الهندسة الريمانية، وكذلك تم دراسة اتصال تشيرن-رونند على أسطح فينسلر. وتم دراسة تأثير التحويل التشاكلي الاتجاهي على هذين الاتصالين بوجه الخصوص، ومن ثم نستنتج ممتد لاندسبيرج لدالة فنسلر  $\bar{F}$  المحولة من خلال التعبير عنه من حيث الفرق بين المعاملات الأفقية لاتصالات بيرفلد وتشيرن-رونند. وبالتالي، أوجدنا الشروط الضرورية والكافية التي يتم بموجبها الحفاظ على خاصية لاندسبيرجيان في ظل هذا التحول الاتجاهي حيث ان هذا الشرط يعتمد على عامل التحويل الاتجاهي. يوفر هذا النهج رؤية جديدة للتفاعل بين التحول الاتجاهي والهندسة الجوهرية لأسطح فينسلر.

## On the Spectra of some Infinite Band Matrices as Operators on the Cesàro Sequence Space $\sigma_0$

Rabha M. El-Ashwah<sup>1</sup>, Hassan A. El-Morshedy<sup>1</sup>, Asmaa M. Shindy<sup>\*1</sup> and Saad. R. El-Shabrawy<sup>1</sup>

<sup>1</sup>Department of Mathematics, Faculty of Science, Damietta University, Damietta 34517, Egypt.

Received: 20 July 2025 /Accepted: 30 July 2025

<sup>\*</sup>Corresponding author's E-mail: asmaashindy15@gmail.com

### Abstract

In this paper, spectral analysis of infinite triangular double-band matrices acting as operators on the Cesàro space  $\sigma_0$  is given. The study includes a detailed analysis of the spectrum, distinguishing between different types of the spectrum (e.g., point spectrum, residual spectrum, continuous spectrum, defect spectrum, compression spectrum and approximate point spectrum). Besides, a finer subdivision of the spectrum is given. A generalization of the study to symmetric and non-symmetric tridiagonal matrices is also derived. The technique used in this study is flexible enough to address the spectral problem of the underlying operators in various sequence spaces.

**Keywords:** Spectrum, Sequence spaces, Infinite matrices.

### Introduction

Several authors have analyzed the spectra of various infinite matrix structures, such as band matrices (matrices with non-zero elements confined to diagonal band, which includes lower and upper triangular double-band matrices), Jacobi matrices (tridiagonal matrices with specific properties), and more general matrix forms. Such matrices can usually be identified with linear operators on sequence spaces. Also, several operators, like the difference operators, which are defined by difference equations, often involve infinite band matrices. It should be noted that, no general method exists for finding the spectrum of an

arbitrary infinite matrix. In fact, in the case of infinite matrices, the methods used are often tailored to the specific matrix operator and the type of sequence space being considered.

In this paper, we concern ourselves with obtaining the spectra of infinite double-band matrices, in both lower and upper forms. Furthermore, tridiagonal matrices are also of our concern. Our results, in the current paper, substantially complement recent results on the difference operators and their adjoints from [Altay and Başar 2004, Altay and Başar 2005, Akhmedov and Başar 2006, Akhmedov and Başar 2007, Karakaya and Altun 2010, Dutta and Tripathy 2013, Tripathy and Das 2015, El-Shabrawy and Abu-Janah 2018, El-Shabrawy and Sawano 2021], the Jacobi operators from [El-Shabrawy and Shindy 2020], the tridiagonal

non-symmetric matrices as operators from [El-Shabrawy and Shindy 2025] and other related results.

Before giving a complete description of the spectral problem we want to address, we recall some notations used in this paper.

By  $\ell^\infty$ ,  $c$  and  $c_0$ , we denote the Banach spaces of bounded, convergent and null sequences of complex numbers with the supremum norm, respectively. We use  $\ell^p$  ( $1 \leq p < \infty$ ) to denote the Banach space of  $p$ -absolutely summable sequences with the well-known  $\ell^p$ -norm. The symbol  $bv$  stands for the Banach space of all sequences  $x = (x_k)_{k=0}^\infty$  for which the following norm

$$\|x\|_{bv} = \left| \lim_{k \rightarrow \infty} x_k \right| + |x_0| + \sum_{k=1}^\infty |x_k - x_{k-1}|$$

is finite. Furthermore, the space  $bv_0 = bv \cap c_0$  is a Banach space with the  $bv$ -norm, whose dual space is norm isomorphic to the Banach space  $bs$  (cf. [Wilansky 1984, Theorems 7.2.9 and 7.3.5(ii)]), where

$$bs = \left\{ x = (x_k)_{k=0}^\infty : \|x\|_{bs} = \sup_{N \geq 0} \left| \sum_{k=0}^N x_k \right| < \infty \right\}.$$

The space of  $p$ -bounded variation sequences, denoted by  $bv_p$  ( $1 < p < \infty$ ), is the Banach space of all sequences  $x = (x_k)_{k=0}^\infty$  for which  $(x_k - x_{k-1})_{k=0}^\infty \in \ell^p$ , where  $x_{-1} = 0$ . The space  $cs$  is the Banach space of all sequences  $x = (x_k)_{k=0}^\infty$  such that  $\sum_{k=0}^\infty x_k$  is convergent, with the norm

$$\|x\|_{cs} = \sup_n \left| \sum_{k=0}^n x_k \right|.$$

The Hahn sequence space  $h$  [Rao 1990] is defined by

$$h = \{x = (x_k)_{k=0}^\infty \in c_0 : \|x\|_h = \sum_{k=0}^\infty (k+1)|x_{k+1} - x_k| < \infty\},$$

which is a Banach space. Also, we consider the Cesàro sequence space  $\sigma_\infty$ , defined by

$$\sigma_\infty = \left\{ x = (x_k)_{k=0}^\infty : \|x\|_{\sigma_\infty} = \sup_N \frac{1}{N+1} \left| \sum_{k=0}^N x_k \right| < \infty \right\}.$$

In this paper, we give attention to the Cesàro-type space  $\sigma_0$ , which is the Banach space defined by

$$\sigma_0 = \left\{ x = (x_k)_{k=0}^\infty : \lim_{N \rightarrow \infty} \frac{1}{N+1} \sum_{k=0}^N x_k = 0 \right\}$$

with the  $\sigma_\infty$ -norm. Moreover, it is known that  $\sigma_0^* \simeq h$  (cf. [Goes and Goes 1970, Theorem 3.7 (ii)]).

Throughout the paper, we adopt the following conventions:

- Suppose  $\mathbb{N} = \{1, 2, 3, \dots\}$  and  $\mathbb{N}_0 = \{0, 1, 2, \dots\}$ .
- The set of real numbers and the set of complex numbers are denoted by  $\mathbb{R}$  and  $\mathbb{C}$ , respectively.
- Let  $X$  be an infinite-dimensional Banach space and write  $\mathcal{B}(X)$  for the space of all bounded linear operators from  $X$  into itself. For an operator  $T \in \mathcal{B}(X)$ , its adjoint operator  $T^* \in \mathcal{B}(X^*)$ , where  $X^*$  is the dual space of  $X$ .
- In a sequence space, we typically represent the zero element as  $\mathbf{0} = (0, 0, 0, \dots)$ .
- The symbol  $\emptyset$  denotes the empty set.
- For a nonzero real number  $r$ , define the closed disc  $\bar{\Delta}_r$ , circumference  $\partial\Delta_r$  and open disc  $\Delta_r$  as follows:  
 $\bar{\Delta}_r := \{\lambda \in \mathbb{C} : |\lambda| \leq |r|\},$   
 $\partial\Delta_r := \{\lambda \in \mathbb{C} : |\lambda| = |r|\}$   
 and  
 $\Delta_r := \{\lambda \in \mathbb{C} : |\lambda| < |r|\}.$

When  $r = 1$ , the index is omitted.

To introduce our problem, consider the infinite-dimensional lower triangular double-band matrix  $B(r, s) = (b_{nk})$  [Altay and Başar 2005];

$$b_{nk} = \begin{cases} r, & \text{if } k = n, \\ s, & \text{if } k = n - 1, \\ 0, & \text{otherwise,} \end{cases}$$

where  $r, s \in \mathbb{R}$  and  $s \neq 0$ . On a Banach sequence space  $\mu$ , this matrix can be identified with a linear operator  $B(r, s): \mu \rightarrow \mu$ ;

$$(B(r, s)x)_n = rx_n + sx_{n-1},$$

where  $x = (x_n)_{n=0}^\infty \in \mu$ ,  $n \in \mathbb{N}_0$ .

The operator  $B(r, s)$  is called the generalized difference operator. In fact, if  $r = 1$  and  $s = -1$ , the operator  $B(r, s)$  is reduced to the difference operator  $\Delta$  [Altay and Başar 2004]. Also, for the case  $s = 1 - r$ , the operator  $B(r, s)$  coincides with the Zweier operator  $Z^r$  [Altay and Karakuş 2005]. The spectral problem of the operator  $B(r, s)$  has been extensively studied in various sequence spaces. Notable investigations include  $c_0, c$  [Altay and



Başar 2005],  $\ell^p$  ( $1 \leq p < \infty$ ),  $bv_p$  ( $1 \leq p < \infty$ ) [Furkan and Bilgiç 2006, Bilgiç and Furkan 2008],  $cs$  [Dutta and Tripathy 2013],  $bv_0$ ,  $h$  [El-Shabrawy and Abu-Janah 2018] and  $\ell^\infty$ ,  $bv$  [El-Shabrawy and Sawano 2021].

The transpose of the matrix  $B(r, s)$  is denoted by  $U(r, s)$ , which can be identified with a linear operator in many sequence spaces [Karakaya and Altun 2010]. If  $r = 1$  and  $s = -1$ , the operator  $U(r, s)$  coincides with the operator  $\Delta^+$  [Dündar and Başar 2013]. In many investigations [Karakaya and Altun 2010, Tripathy and Das 2015], the spectra of the operator  $U(r, s)$  have been studied in the Banach spaces  $c_0$ ,  $c$  and  $cs$ .

Furthermore, for  $r, s, q \in \mathbb{R}$  and  $n, k \in \mathbb{N}_0$ , we consider the tridiagonal matrix

$$T = T(r, q, s) = (t_{nk});$$

$$t_{nk} = \begin{cases} q, & \text{if } k = n, \\ s, & \text{if } k = n - 1, \\ r, & \text{if } k = n + 1, \\ 0, & \text{otherwise.} \end{cases}$$

This infinite matrix can be identified with a linear operator on a Banach sequence space  $\mu$  as  $T: \mu \rightarrow \mu$ ;

$$(T(r, q, s)x)_n = (Tx)_n$$

$$= sx_{n-1} + qx_n + rx_{n+1}, \quad (1)$$

where  $x = (x_n)_{n=0}^\infty \in \mu$ ,  $n \in \mathbb{N}_0$ .

If  $s = r$ , then  $T(r, q, s)$  is reduced to the Jacobi matrix  $J(q, r) = T(r, q, r)$  [Altun 2011, Berezanskii 1968, El-Shabrawy and Shindy 2020]. Furthermore,  $B(r, s) = T(0, r, s)$  and  $U(r, s) = T(s, r, 0)$  are included in the class of  $T(r, q, s)$ ; see [Altay and Başar 2005, Karakaya and Altun 2010]. So, it seems natural to firstly assume that  $r, s \neq 0$ . However, for either the case  $r = 0$ ; or the case  $s = 0$ , see the conclusion in the last section. The spectra of  $T(r, q, s)$  were determined in the spaces  $c_0$ ,  $c$ ,  $\ell^1$  and  $\ell^\infty$  in [Bilgiç and Altun 2019]. More recently, this problem was studied in the Banach spaces  $h$  and  $bv_0$  [El-Shabrawy and Shindy 2025].

To the authors' knowledge, the spectral problem has still not received enough attention in the Cesàro sequence space  $\sigma_0$ . So, in the current paper, we address the study of the spectra of the operators  $B(r, s)$ ,  $U(r, s)$  and  $T(r, q, s)$  on  $\sigma_0$ . This investigation represents a natural continuation of the studies by Akhmedov and Başar (2006, 2007), Altay and

Başar (2004, 2005), Karakaya and Altun 2010, Dutta and Tripathy 2013, Tripathy and Das 2015, El-Shabrawy and Abu-Janah 2018, Sawano and El-Shabrawy 2021, and El-Shabrawy and Shindy (2020, 2025).

Our work in the current paper is outlined in the following way: Section 2 provides a brief overview of basic definitions and facts related to the spectrum and various types of the spectrum. Section 3 focuses on the study of the spectra of the operators  $B(r, s)$  and  $U(r, s)$  acting on the sequence space  $\sigma_0$ . A generalization of the study to tridiagonal matrices has been obtained in Section 4. Finally, in the last section, a conclusion and future research are provided.

## Preliminaries

To ensure the paper is self-contained, we briefly gather some basic definitions and preliminary facts which will be useful throughout the paper.

For any given  $\lambda \in \mathbb{C}$  and  $T \in \mathcal{B}(X)$ , we write  $T_\lambda = T - \lambda I$ , where  $I$  is the identity operator on  $X$ . The *spectrum* of  $T$ , denoted by  $\sigma(T, X)$ , is the set of all scalars  $\lambda \in \mathbb{C}$  for which  $T_\lambda$  is not bijective. Its complement in  $\mathbb{C}$  is known as the *resolvent set* of  $T$ , denoted by  $\rho(T, X)$ . The spectrum  $\sigma(T, X)$  can be partitioned into various subsets, classified according to the properties of  $\mathcal{R}(T_\lambda)$  and the bounded invertibility of the operator  $T_\lambda$ . The *point spectrum*  $\sigma_p(T, X)$  of  $T$  is defined by

$\sigma_p(T, X) = \{\lambda \in \mathbb{C} : T_\lambda \text{ is not injective}\};$   
the *residual spectrum*  $\sigma_r(T, X)$  of  $T$  is defined by

$\sigma_r(T, X) = \{\lambda \in \mathbb{C} : T_\lambda \text{ is injective, but } \mathcal{R}(T_\lambda) \text{ is not dense}\};$

the *continuous spectrum*  $\sigma_c(T, X)$  of  $T$  is defined by

$\sigma_c(T, X) = \{\lambda \in \mathbb{C} : T_\lambda \text{ is injective and } \mathcal{R}(T_\lambda) \text{ is dense, but } T_\lambda^{-1} \text{ is unbounded}\}.$

Following [Appell et al. 2004] three more subsets of the spectrum can be defined as follows:

$\sigma_\delta(T, X) = \{\lambda \in \mathbb{C} : T_\lambda \text{ is not surjective}\};$   
 $\sigma_{co}(T, X) = \{\lambda \in \mathbb{C} : \mathcal{R}(T_\lambda) \text{ is not dense}\};$   
 $\sigma_{ap}(T, X) = \{\lambda \in \mathbb{C} : \exists (x_k) \text{ in } X \text{ such that}$

$\|x_k\| = 1 \forall k \in \mathbb{N}, \lim_{k \rightarrow \infty} \|T_\lambda x_k\| = 0\}$ ,  
which are called the *defect spectrum*,  
*compression spectrum* and *approximate point spectrum*, respectively. Note that these subsets of the spectrum overlap and

$$\begin{aligned}\sigma(T, X) &= \sigma_{\text{ap}}(T, X) \cup \sigma_\delta(T, X) \\ &= \sigma_{\text{ap}}(T, X) \cup \sigma_{\text{co}}(T, X).\end{aligned}$$

Another important classification of the spectrum, which is due to [Taylor and Halberg 1957], is also considered. To be more precise, let  $T$  be a linear operator on a Banach space  $X$  into itself. The operator  $T_\lambda$  is classified I, II or III, according as  $\mathcal{R}(T_\lambda) = X$ ;  $\overline{\mathcal{R}(T_\lambda)} = X$ , but  $\mathcal{R}(T_\lambda) \neq X$ ; or  $\overline{\mathcal{R}(T_\lambda)} \neq X$ . Furthermore,  $T_\lambda$  is classified 1, 2 or 3 according as  $T_\lambda^{-1}$  exists and is bounded; exists, but is not bounded; or does not exist. By combining these possibilities, we obtain different states of the operator. If  $T \in \mathcal{B}(X)$ , the complex plane is subdivided into parts corresponding to the states of the operator  $T_\lambda$ :  $I_1\sigma(T, X)$ ,  $I_2\sigma(T, X)$ ,  $I_3\sigma(T, X)$ ,  $II_1\sigma(T, X)$ ,  $II_2\sigma(T, X)$ ,  $II_3\sigma(T, X)$ ,  $III_1\sigma(T, X)$ ,  $III_2\sigma(T, X)$  and  $III_3\sigma(T, X)$ . Consequently, we obtain a complete disjoint subdivision of the spectrum. Precisely, the following relations hold:

$$\begin{aligned}\sigma(T, X) &= I_3\sigma(T, X) \cup II_2\sigma(T, X) \cup II_3\sigma(T, X) \\ &\quad \cup III_1\sigma(T, X) \cup III_2\sigma(T, X) \\ &\quad \cup III_3\sigma(T, X);\end{aligned}$$

$$\begin{aligned}\sigma_p(T, X) &= I_3\sigma(T, X) \cup II_3\sigma(T, X) \\ &\quad \cup III_3\sigma(T, X);\end{aligned}$$

$$\sigma_r(T, X) = III_1\sigma(T, X) \cup III_2\sigma(T, X);$$

$$\sigma_c(T, X) = II_2\sigma(T, X).$$

It should be noted that  $II_1\sigma(T, X) = \emptyset$  since any boundedly invertible operator on a Banach space into itself should have a closed range (cf. [Taylor and Halberg 1957, Theorem 10]). Furthermore,  $I_2\sigma(T, X) = \emptyset$  as a consequence of the closed graph theorem. We observe that  $\lambda \in \rho(T, X)$  if and only if  $T_\lambda \in I_1\sigma(T, X)$ ; otherwise  $\lambda \in \sigma(T, X)$ .

From the definition, we notice that

$$\sigma_\delta(T, X) = \sigma(T, X) \setminus I_3\sigma(T, X).$$

Also, we have

$$\sigma_{\text{ap}}(T, X) = \sigma(T, X) \setminus III_1\sigma(T, X)$$

(cf. [Taylor and Lay 1986, p. 282]).

It is worthwhile to assert that, if  $T \in \mathcal{B}(\sigma_0)$  is represented by a matrix  $A$ , then its adjoint  $T^*$

$\in \mathcal{B}(\sigma_0^*)$  is represented by the transpose matrix  $A^t$ ; see [Taylor and Lay 1986, Problem 7, P.233].

For the sake of simplicity for the reader, we recall the following theorems which are concerned with the spectra of the operators  $U(r, s)$  and  $B(r, s)$  on the Hahn sequence space  $h$ . In fact, these results are crucial in the sequel.

**Theorem 2.1.** [El-Shabrawy and Shindy 2025, Theorem 3.4] We have  $U(r, s) \in \mathcal{B}(h)$ . Moreover, the following results are satisfied:

- (1):  $\sigma(U(r, s), h) = \{\lambda \in \mathbb{C} : |\lambda - r| \leq |s|\}$ .
- (2):  $\sigma_p(U(r, s), h) = \{\lambda \in \mathbb{C} : |\lambda - r| < |s|\}$ .
- (3):  $\sigma_p(U(r, s)^*, h^*) = \emptyset$ .
- (4):  $\sigma_r(U(r, s), h) = \emptyset$ .
- (5):  $\sigma_c(U(r, s), h) = \{\lambda \in \mathbb{C} : |\lambda - r| = |s|\}$ .

**Theorem 2.2.** [EL-Shabrawy and Abu-Janah 2018] We have  $B(r, s) \in \mathcal{B}(h)$ . Moreover, the following results are satisfied:

- (1):  $\sigma(B(r, s), h) = \{\lambda \in \mathbb{C} : |\lambda - r| \leq |s|\}$ .
- (2):  $\sigma_p(B(r, s), h) = \emptyset$ .
- (3):  $\sigma_p(B(r, s)^*, h^*) = \{\lambda \in \mathbb{C} : |\lambda - r| \leq |s|\}$ .
- (4):  $\sigma_r(B(r, s), h) = \{\lambda \in \mathbb{C} : |\lambda - r| \leq |s|\}$ .
- (5):  $\sigma_c(B(r, s), h) = \emptyset$ .
- (6):  $\sigma_{\text{ap}}(B(r, s), h) = \{\lambda \in \mathbb{C} : |\lambda - r| = |s|\}$ .
- (7):  $\sigma_\delta(B(r, s), h) = \{\lambda \in \mathbb{C} : |\lambda - r| \leq |s|\}$ .
- (8):  $\sigma_{\text{co}}(B(r, s), h) = \{\lambda \in \mathbb{C} : |\lambda - r| \leq |s|\}$ .

Furthermore, we report on some recent results concerning the spectra of the operator  $T$  acting on the Hahn space  $h$ .

**Theorem 2.3.** [El-Shabrawy and Shindy 2025] For  $|r| < |s|$ , we have  $T \in \mathcal{B}(h)$ . Moreover, the following results are satisfied:

- (1):  $\sigma(T, h) = Q\left(\overline{\Delta} \setminus \Delta_{\frac{r}{s}}\right)$ .
- (2):  $\sigma_p(T, h) = \emptyset$ .
- (3):  $\sigma_p(T^*, h^*) = Q\left(\overline{\Delta} \setminus \Delta_{\frac{r}{s}}\right)$ .
- (4):  $\sigma_r(T, h) = Q\left(\overline{\Delta} \setminus \Delta_{\frac{r}{s}}\right)$ .
- (5):  $\sigma_c(T, h) = \emptyset$ .

**Theorem 2.4.** [El-Shabrawy and Shindy 2025] For  $|r| > |s|$ , we have  $T \in \mathcal{B}(h)$ . Moreover, the following results are satisfied:

- (1):  $\sigma(T, h) = Q\left(\overline{\Delta}_{\frac{r}{s}} \setminus \Delta\right)$ .
- (2):  $\sigma_p(T, h) = Q\left(\Delta_{\frac{r}{s}} \setminus \overline{\Delta}\right)$ .
- (3):  $\sigma_p(T^*, h^*) = \emptyset$ .

$$(4): \sigma_r(T, h) = \emptyset.$$

$$(5): \sigma_c(T, h) = Q\left(\partial\Delta \cup \partial\Delta_{\frac{r}{s}}\right).$$

**Theorem 2.5.** [El-Shabrawy and Shindy 2025]  
For  $|r| = |s|$ , we have  $T \in \mathcal{B}(h)$ . Moreover, the following results are satisfied:

$$(1): \sigma(T, h) = Q(\partial\Delta).$$

$$(2): \sigma_p(T, h) = \emptyset.$$

$$(3): \sigma_p(T^*, h^*) = \begin{cases} Q(\partial\Delta \setminus \{1\}), & \text{if } r = s, \\ Q(\partial\Delta), & \text{if } r = -s. \end{cases}$$

$$(4): \sigma_r(T, h) = \begin{cases} Q(\partial\Delta \setminus \{1\}), & \text{if } r = s, \\ Q(\partial\Delta), & \text{if } r = -s. \end{cases}$$

$$(5): \sigma_c(T, h) = \begin{cases} Q(\{1\}), & \text{if } r = s, \\ \emptyset, & \text{if } r = -s. \end{cases}$$

### Spectra of the operators $B(r, s)$ and $U(r, s)$ on $\sigma_0$

In this section, we completely determine the spectrum and various parts of the spectrum of the operators  $B(r, s)$  and  $U(r, s)$  on the Cesàro space  $\sigma_0$ . Firstly, the following theorem, which completes the results in Theorem 2.1 is given. It is necessary for our proofs in the current section.

**Theorem 3.1.** We have the following results:

$$(1): \sigma_{ap}(U(r, s), h) = \{\lambda \in \mathbb{C} : |\lambda - r| \leq |s|\}.$$

$$(2): \sigma_\delta(U(r, s), h) = \{\lambda \in \mathbb{C} : |\lambda - r| = |s|\}.$$

$$(3): \sigma_{co}(U(r, s), h) = \emptyset.$$

*Proof.*

$$(1): \text{By utilizing Theorem 2.1(4), we obtain that } III_1\sigma(U(r, s), h) = \emptyset. \text{ Combined this with the fact that } \sigma_{ap}(U(r, s), h)$$

$$= \sigma(U(r, s), h) \setminus III_1\sigma(U(r, s), h),$$

implies

$$\sigma_{ap}(U(r, s), h) = \{\lambda \in \mathbb{C} : |\lambda - r| \leq |s|\},$$

where we have used the result in Theorem 2.1(1).

$$(2): \text{In fact, we have}$$

$$I_3\sigma(U(r, s), h) \subseteq \sigma_p(U(r, s), h) = \{\lambda \in \mathbb{C} : |\lambda - r| < |s|\}.$$

Conversely, let  $\lambda \in \mathbb{C}$  such that  $|\lambda - r| < |s|$ . Then,  $U(r, s) - \lambda I$  is not injective. Furthermore, from [El-Shabrawy and Shindy 2025, Proposition 3.2(3)],  $U(r, s) - \lambda I$  is surjective. Then  $\lambda \in I_3\sigma(U(r, s), h)$ . This concludes that,  $I_3\sigma(U(r, s), h) = \{\lambda \in \mathbb{C} : |\lambda - r| < |s|\}$ . Thus,

$$\sigma_\delta(U(r, s), h)$$

$$= \sigma(U(r, s), h) \setminus I_3\sigma(U(r, s), h) = \{\lambda \in \mathbb{C} : |\lambda - r| = |s|\},$$

where we have used the result in Theorem 2.1(1).

$$(3): \text{Follows immediately from the relation } \sigma_{co}(U(r, s), h) = \sigma_p(U(r, s)^*, h^*) \text{ and using Theorem 2.1(3).}$$

The next is our first main theorem.

**Theorem 3.2.** We have  $B(r, s) \in \mathcal{B}(\sigma_0)$ . Furthermore, the following statements are satisfied:

$$(1): \sigma(B(r, s), \sigma_0) = \{\lambda \in \mathbb{C} : |\lambda - r| \leq |s|\}.$$

$$(2): \sigma_p(B(r, s), \sigma_0) = \emptyset.$$

$$(3): \sigma_p(B(r, s)^*, \sigma_0^*) = \{\lambda \in \mathbb{C} : |\lambda - r| < |s|\}.$$

$$(4): \sigma_r(B(r, s), \sigma_0) = \{\lambda \in \mathbb{C} : |\lambda - r| < |s|\}.$$

$$(5): \sigma_c(B(r, s), \sigma_0) = \{\lambda \in \mathbb{C} : |\lambda - r| = |s|\}.$$

$$(6): \sigma_{ap}(B(r, s), \sigma_0) = \{\lambda \in \mathbb{C} : |\lambda - r| = |s|\}.$$

$$(7): \sigma_\delta(B(r, s), \sigma_0) = \{\lambda \in \mathbb{C} : |\lambda - r| \leq |s|\}.$$

$$(8): \sigma_{co}(B(r, s), \sigma_0) = \{\lambda \in \mathbb{C} : |\lambda - r| < |s|\}.$$

$$(9): I_3\sigma(B(r, s), \sigma_0) = II_3\sigma(B(r, s), \sigma_0) = III_3\sigma(B(r, s), \sigma_0) = \emptyset.$$

$$(10): II_2\sigma(B(r, s), \sigma_0) = \{\lambda \in \mathbb{C} : |\lambda - r| = |s|\}.$$

$$(11): III_1\sigma(B(r, s), \sigma_0) = \{\lambda \in \mathbb{C} : |\lambda - r| < |s|\}.$$

$$(12): III_2\sigma(B(r, s), \sigma_0) = \emptyset.$$

*Proof.*

$$(1): \text{The result follows from [Appell et al. 2004, Proposition 1.3] and Theorem 2.1(1). In fact, we have}$$

$$\begin{aligned} \sigma(B(r, s), \sigma_0) &= \sigma(B(r, s)^*, \sigma_0^*) \\ &= \sigma(U(r, s), h) \\ &= \{\lambda \in \mathbb{C} : |\lambda - r| \leq |s|\}. \end{aligned}$$

$$(2): \text{It can be shown that, for all } \lambda \in \mathbb{C}, (B(r, s) - \lambda)x = \mathbf{0} \text{ has only the zero solution for } x.$$

$$(3): \text{Since}$$

$$\begin{aligned} \sigma_p(B(r, s)^*, \sigma_0^*) &= \sigma_p(U(r, s), h), \\ \text{then applying Theorem 2.1(2) yields the desired result.} \end{aligned}$$

$$(4): \text{Follows immediately from the relation } \sigma_r(B(r, s), \sigma_0)$$

$$= \sigma_p(B(r, s)^*, \sigma_0^*) \setminus \sigma_p(B(r, s), \sigma_0)$$

and then applying Statements (2) and (3).

$$(5): \text{Since } \sigma_p(B(r, s), \sigma_0), \sigma_r(B(r, s), \sigma_0) \text{ and } \sigma_c(B(r, s), \sigma_0) \text{ form a disjoint subdivision of } \sigma(B(r, s), \sigma_0), \text{ then, by applying Statements (1), (2) and (4), we obtain that } \sigma_c(B(r, s), \sigma_0) = \{\lambda \in \mathbb{C} : |\lambda - r| = |s|\}.$$

$$(6) - (7): \text{Follow immediately from [Appell et al. 2004, Proposition 1.3] and using Theorem 3.1(1)-(2). Indeed, we have}$$

$$\begin{aligned} \sigma_{ap}(B(r, s), \sigma_0) &= \sigma_\delta(B(r, s)^*, \sigma_0^*) \\ &= \sigma_\delta(U(r, s), h) \end{aligned}$$

- $= \{\lambda \in \mathbb{C} : |\lambda - r| = |s|\}$   
 and  
 $\sigma_\delta(B(r, s), \sigma_0) = \sigma_{ap}(B(r, s)^*, \sigma_0^*)$   
 $= \sigma_{ap}(U(r, s), h)$   
 $= \{\lambda \in \mathbb{C} : |\lambda - r| \leq |s|\}.$
- (8): Follows immediately from [Appell et al. 2004, Proposition 1.3] and Statement (3). Indeed, we have  
 $\sigma_{co}(B(r, s), \sigma_0) = \sigma_p(B(r, s)^*, \sigma_0^*)$   
 $= \{\lambda \in \mathbb{C} : |\lambda - r| < |s|\}.$
- (9): The result follows from Statement (2) and the fact that  
 $\sigma_p(B(r, s), \sigma_0) = I_3 \sigma(B(r, s), \sigma_0)$   
 $\cup II_3 \sigma(B(r, s), \sigma_0) \cup III_3 \sigma(B(r, s), \sigma_0).$
- (10): Simply observe that  
 $II_2 \sigma(B(r, s), \sigma_0) = \sigma_c(B(r, s), \sigma_0)$   
 and then apply Statement (5).
- (11): Let  $\lambda \in \{\lambda \in \mathbb{C} : |\lambda - r| < |s|\}$ . Since  
 $\sigma_r(B(r, s), \sigma_0)$   
 $= III_1 \sigma(B(r, s), \sigma_0) \cup III_2 \sigma(B(r, s), \sigma_0),$   
 then, to show  $\lambda \in III_1 \sigma(B(r, s), \sigma_0)$ , it suffices to show that  $B(r, s)^* - \lambda I$  is surjective [Taylor and Halberg 1957, Theorem 4]. This follows from the fact that  
 $\sigma_\delta(B(r, s)^*, \sigma_0^*) = \sigma_\delta(U(r, s), h)$   
 $= \{\lambda \in \mathbb{C} : |\lambda - r| = |s|\},$   
 where we have used Theorem 3.1(2). Thus, we conclude that  
 $\{\lambda \in \mathbb{C} : |\lambda - r| < |s|\}$   
 $\subseteq III_1 \sigma(B(r, s), \sigma_0).$   
 The second inclusion follows by using [Gindler and Taylor 1962, Theorem 3.3]. In fact, we have  
 $III_1 \sigma(B(r, s), \sigma_0)$   
 $\subseteq \text{int}(\{\lambda \in \mathbb{C} : |\lambda - r| < |s|\})$   
 $= \{\lambda \in \mathbb{C} : |\lambda - r| < |s|\}.$
- (12): Follows immediately.
- Next, we give our second main theorem, which is concerned with the spectra of the operator  $U(r, s)$  on the Cesàro space  $\sigma_0$ .
- Theorem 3.3.** *We have  $U(r, s) \in \mathcal{B}(\sigma_0)$ . Furthermore, the following statements are satisfied:*
- (1):  $\sigma(U(r, s), \sigma_0) = \{\lambda \in \mathbb{C} : |\lambda - r| \leq |s|\}.$   
 (2):  $\sigma_p(U(r, s), \sigma_0) = \{\lambda \in \mathbb{C} : |\lambda - r| \leq |s|\} \setminus \{r + s\}.$   
 (3):  $\sigma_p(U(r, s)^*, \sigma_0^*) = \emptyset.$   
 (4):  $\sigma_r(U(r, s), \sigma_0) = \emptyset.$   
 (5):  $\sigma_c(U(r, s), \sigma_0) = \{r + s\}.$   
 (6):  $\sigma_{ap}(U(r, s), \sigma_0) = \{\lambda \in \mathbb{C} : |\lambda - r| \leq |s|\}.$   
 (7):  $\sigma_\delta(U(r, s), \sigma_0) = \{\lambda \in \mathbb{C} : |\lambda - r| = |s|\}.$   
 (8):  $\sigma_{co}(U(r, s), \sigma_0) = \emptyset.$

- (9):  $I_3 \sigma(U(r, s), \sigma_0) = \{\lambda \in \mathbb{C} : |\lambda - r| < |s|\}.$   
 (10):  $III_3 \sigma(U(r, s), \sigma_0) = \emptyset.$   
 (11):  $II_3 \sigma(U(r, s), \sigma_0) = \{\lambda \in \mathbb{C} : |\lambda - r| = |s|\} \setminus \{r + s\}.$   
 (12):  $II_2 \sigma(U(r, s), \sigma_0) = \{r + s\}.$   
 (13):  $III_1 \sigma(U(r, s), \sigma_0) = III_2 \sigma(U(r, s), \sigma_0) = \emptyset.$

*Proof.*

- (1): The required result follows from [Appell et al. 2004, Proposition 1.3] and Theorem 2.2(1). In fact, we have

$$\begin{aligned} \sigma(U(r, s), \sigma_0) &= \sigma(U(r, s)^*, \sigma_0^*) \\ &= \sigma(B(r, s), h) \\ &= \{\lambda \in \mathbb{C} : |\lambda - r| \leq |s|\}. \end{aligned}$$

- (2): Firstly, we recall that,  
 $\sigma_p(U(r, s), \sigma_0) \subseteq \sigma(U(r, s), \sigma_0)$   
 $= \{\lambda \in \mathbb{C} : |\lambda - r| \leq |s|\}.$

Furthermore, suppose that

$(U(r, s) - \lambda I)x = \mathbf{0}$  for  $x \neq \mathbf{0}$ . Thus,

$$x_n = \left(\frac{\lambda - r}{s}\right)^n x_0, \quad n \in \mathbb{N}.$$

Then, we should assume that  $x_0 \neq 0$  and  $\frac{\lambda - r}{s} \neq 1$  since otherwise we would obtain either  $x = \mathbf{0}$  or  $x \notin \sigma_0$ . With this, if  $|\lambda - r| \leq |s|$ ,

$$\begin{aligned} \sum_{k=0}^n x_k &= x_0 \sum_{k=0}^n \left(\frac{\lambda - r}{s}\right)^k \\ &= x_0 \frac{1 - \left(\frac{\lambda - r}{s}\right)^{n+1}}{1 - \left(\frac{\lambda - r}{s}\right)}. \end{aligned}$$

Then,  $\frac{1}{n+1} \sum_{k=0}^n x_k \rightarrow 0$  as  $n \rightarrow \infty$ . That is,  $x = (x_k) \in \sigma_0$  and so,  
 $\lambda \in \sigma_p(U(r, s), \sigma_0).$

- (3): The result follows immediately from the fact that

$$\sigma_p(U(r, s)^*, \sigma_0^*) = \sigma_p(B(r, s), h)$$

and then applying Theorem 2.2(2).

- (4): Using the relation

$$\begin{aligned} \sigma_r(U(r, s), \sigma_0) \\ &= \sigma_p(U(r, s)^*, \sigma_0^*) \setminus \sigma_p(U(r, s), \sigma_0) \end{aligned}$$

along with Statements (2) and (3), the required result follows.

- (5): The result follows based on the fact that  $\sigma_p(U(r, s), \sigma_0)$ ,  $\sigma_r(U(r, s), \sigma_0)$  and  $\sigma_c(U(r, s), \sigma_0)$  form a disjoint partition of  $\sigma(U(r, s), \sigma_0)$ , and then applying the results in Statements (1), (2) and (4).

- (6) - (7): Follow immediately from [Appell et al. 2004, Proposition 1.3] and then using Theorem 2.2 (6)-(7). Indeed, we have

$$\begin{aligned} \sigma_{ap}(U(r, s), \sigma_0) &= \sigma_\delta(U(r, s)^*, \sigma_0^*) \\ &= \sigma_\delta(B(r, s), h) \\ &= \{\lambda \in \mathbb{C} : |\lambda - r| \leq |s|\} \end{aligned}$$

and

$$\begin{aligned}\sigma_\delta(U(r, s), \sigma_0) &= \sigma_{ap}(U(r, s)^*, \sigma_0^*) \\ &= \sigma_{ap}(B(r, s), h) \\ &= \{\lambda \in \mathbb{C} : |\lambda - r| = |s|\}.\end{aligned}$$

- (8): It follows from [Appell et al. 2004, Proposition 1.3] and Statement (3) that  $\sigma_{co}(U(r, s), \sigma_0) = \sigma_p(U(r, s)^*, \sigma_0^*) = \emptyset$ .

- (9): It is known that  $I_3\sigma(U(r, s), \sigma_0) \subseteq \sigma_p(U(r, s), \sigma_0)$ . Then, applying [Gindler and Taylor 1962, Theorem 4.2], we obtain  $I_3\sigma(U(r, s), \sigma_0) \subseteq \{\lambda \in \mathbb{C} : |\lambda - r| < |s|\}$ . Conversely, let  $\lambda \in \mathbb{C}$  such that  $|\lambda - r| < |s|$ . Then  $\lambda \notin \sigma_\delta(U(r, s), \sigma_0)$  and  $\lambda \in \sigma_p(U(r, s), \sigma_0)$ . This implies that  $U(r, s) - \lambda I$  is surjective and not injective. Consequently  $\lambda \in I_3\sigma(U(r, s), \sigma_0)$ . This completes the proof of the statement.

- (10): Clearly,  $III_3\sigma(U(r, s), \sigma_0) \subseteq \sigma_p(U(r, s), \sigma_0)$   
 $= \{\lambda \in \mathbb{C} : |\lambda - r| \leq |s|\} \setminus \{r + s\}$ .  
 Conversely, for all  $\lambda \in \mathbb{C}$  such that  $|\lambda - r| \leq |s|$  and  $\lambda \neq r + s$ , we have  $\lambda \in \sigma_p(U(r, s), \sigma_0)$  and  $\lambda \notin \sigma_p(U(r, s)^*, \sigma_0^*)$ . This implies that  $U(r, s) - \lambda I$  is not injective and  $U(r, s) - \lambda I$  has a dense range (cf. [Taylor and Halberg 1957, Theorem 1]). Consequently,  $\lambda \notin III_3\sigma(U(r, s), \sigma_0)$ . Thus,  $III_3\sigma(U(r, s), \sigma_0) = \emptyset$ .

- (11): From the definition of  $II_3\sigma(U(r, s), \sigma_0)$  and using Statements (2), (9) and (10), we obtain

$$\begin{aligned}II_3\sigma(U(r, s), \sigma_0) &= \sigma_p(U(r, s), \sigma_0) \setminus \\ &\quad [I_3\sigma(U(r, s), \sigma_0) \cup III_3\sigma(U(r, s), \sigma_0)] \\ &= \{\lambda \in \mathbb{C} : |\lambda - r| = |s|\} \setminus \{r + s\}.\end{aligned}$$

- (12): Follows from the fact that  $II_2\sigma(U(r, s), \sigma_0) = \sigma_c(U(r, s), \sigma_0)$  and use Statement (5).

- (13): It is known that  $\sigma_r(U(r, s), \sigma_0) = III_1\sigma(U(r, s), \sigma_0) \cup III_2\sigma(U(r, s), \sigma_0)$ . With this and the result in Statement (4), we obtain the required result.

### Spectra of the operator $T(r, q, s)$ on $\sigma_0$

For the sake of brevity, if there is no confusion, we sometimes use  $T$  instead of  $T(r, q, s)$ , especially when combined with another symbol. Now, the method on which we

proceed in order to find the spectra of  $T$  depends on examining the injectivity and surjectivity of the complex functions;

$$Q(z) = sz + q + rz^{-1} \quad \text{and}$$

$$P(z) = rz + q + sz^{-1},$$

where  $r, q$  and  $s$  are fixed real numbers with  $r, s \neq 0$ . Observe that, if  $\alpha_1$  and  $\alpha_2$  are the roots of  $Q$ , they are nonzero, and  $\alpha_1^{-1}$  and  $\alpha_2^{-1}$  are the roots of  $P$ . Furthermore, the following relations are satisfied:

$$\alpha_1 + \alpha_2 = \frac{-q}{s} \quad \text{and} \quad \alpha_1\alpha_2 = \frac{r}{s}. \quad (2)$$

The right-shift operator and the left-shift operator are defined by  $(Rx)_n = x_{n-1}$  and  $(Lx)_n = x_{n+1}$ , respectively: they yield a factorization of the operator  $T$ ;

$$T = s(I - \alpha_1 L) \circ (R - \alpha_2 I), \quad (3)$$

where  $\alpha_1$  and  $\alpha_2$  are the roots of the function  $Q$  and interchangeably. As an immediate consequence, the boundedness of  $T$  on  $\sigma_0$  follows from the boundedness of  $R$  and  $L$ .

We need the following proposition.

**Proposition 4.1.**  $T \in (\sigma_0; \sigma_0)$  is injective if and only if one of the following conditions holds:

- (i): the function  $Q$  has a root inside  $\Delta$ ,
- (ii): either 1 or  $-1$  is a double root of  $Q$ .

*Proof.*

The operator  $T$  is not injective if and only if there exists  $x = (x_n) \neq \mathbf{0}$  in  $\sigma_0$  with  $Tx = \mathbf{0}$ . From [Bilgiç and Altun 2019, Lemma 1.1], the solution of  $Tx = \mathbf{0}$  is given by

$$x_n = \begin{cases} c \left( \frac{\alpha_2}{\alpha_1^n} - \frac{\alpha_1}{\alpha_2^n} \right), & \text{if } \alpha_1 \neq \alpha_2, \\ c \frac{1+n}{\alpha^n}, & \text{if } \alpha_1 = \alpha_2 = \alpha, \end{cases}$$

where  $\alpha_1$  and  $\alpha_2$  are the roots of the function  $Q$ . So, in the forthcoming, we will validate the result by considering three cases for the possibilities of  $\alpha_1$  and  $\alpha_2$ .

- (i): Suppose  $\alpha_1 \neq \alpha_2$  and  $|\alpha_1| = |\alpha_2| = |\alpha|$ . We may assume that  $\alpha_1 = |\alpha|(\cos\theta + isin\theta)$  and  $\alpha_2 = |\alpha|(\cos\theta - isin\theta)$  for some  $0 < \theta < \pi$ . Then

$$\begin{aligned}\lim_{n \rightarrow \infty} \frac{1}{n+1} \sum_{k=0}^n x_k &= \\ \lim_{n \rightarrow \infty} \frac{1}{n+1} \sum_{k=0}^n c \left( \frac{|\alpha|(\cos\theta - isin\theta)}{|\alpha|^k(\cos\theta + isin\theta)^k} - \frac{|\alpha|(\cos\theta + isin\theta)}{|\alpha|^k(\cos\theta - isin\theta)^k} \right) &= \\ \lim_{n \rightarrow \infty} \frac{1}{n+1} \sum_{k=0}^n c \left( \frac{|\alpha|(\cos\theta - isin\theta)}{|\alpha|^k(\cos\theta + isin\theta)^k} - \frac{|\alpha|(\cos\theta + isin\theta)}{|\alpha|^k(\cos\theta - isin\theta)^k} \right) &= \end{aligned}$$

$$= -2ic \lim_{n \rightarrow \infty} \frac{1}{n+1} \sum_{k=0}^n \frac{1}{|\alpha|^{k-1}} \sin((k+1)\theta) = 0$$

for  $|\alpha_1| = |\alpha_2| = |\alpha| \geq 1$ . However, for  $|\alpha_1| = |\alpha_2| = |\alpha| < 1$ , we have  $x = (x_n) \notin \sigma_0$  [El-Shabrawy and Shindy 2025, Proposition 2.2(1)]. Thus,  $T$  is not injective in  $\sigma_0$  if and only if  $|\alpha_1| = |\alpha_2| = |\alpha| \geq 1$ .

(ii): Suppose  $\alpha_1 \neq \alpha_2$  and  $|\alpha_1| \neq |\alpha_2|$ . We have

$$\begin{aligned} \sum_{k=0}^n x_k &= c \sum_{k=0}^n \left( \frac{\alpha_2}{\alpha_1^k} - \frac{\alpha_1}{\alpha_2^k} \right) \\ &= c \left[ \sum_{k=0}^n \frac{\alpha_2}{\alpha_1^k} - \sum_{k=0}^n \frac{\alpha_1}{\alpha_2^k} \right]. \end{aligned}$$

Hence, we have the following two cases:

- (a): If  $|\alpha_1| > |\alpha_2| \geq 1$  or  $|\alpha_2| > |\alpha_1| \geq 1$ , then  $\lim_{n \rightarrow \infty} \frac{1}{n+1} \sum_{k=0}^n x_k = 0$ .
- (b): If  $|\alpha_1| < |\alpha_2| \leq 1$ ,  $|\alpha_2| < |\alpha_1| \leq 1$ ,  $|\alpha_1| < 1 < |\alpha_2|$  or  $|\alpha_2| < 1 < |\alpha_1|$ , then  $x = (x_n) \notin \sigma_\infty$ . So,  $x = (x_n) \notin \sigma_0$ .

Thus, in Case (ii),  $T$  is not injective in  $\sigma_0$  if and only if  $|\alpha_1| \geq 1$  and  $|\alpha_2| \geq 1$ .

(iii): Suppose  $\alpha_1 = \alpha_2 = \alpha$ . Then,  $\alpha_1$  and  $\alpha_2$  are real. So, we study three cases:

(a): If  $|\alpha| > 1$ , then

$$\begin{aligned} \lim_{n \rightarrow \infty} \frac{1}{n+1} \sum_{k=0}^n x_k \\ = c \lim_{n \rightarrow \infty} \frac{1}{n+1} \sum_{k=0}^n \frac{1+k}{\alpha^k} = 0. \end{aligned}$$

(b): If  $|\alpha| < 1$ , then  $x = (x_n) \notin \sigma_\infty$ . So,  $x = (x_n) \notin \sigma_0$ .

(c): If  $|\alpha| = 1$ , then  $\alpha = -1$  or  $\alpha = 1$ . For  $\alpha = -1$ , we have

$$\begin{aligned} \lim_{n \rightarrow \infty} \frac{1}{n+1} \sum_{k=0}^n x_k \\ = c \lim_{n \rightarrow \infty} \frac{1}{n+1} \begin{cases} \frac{n+2}{2}, & \text{if } n \text{ is even,} \\ -\frac{n+1}{2}, & \text{if } n \text{ is odd.} \end{cases} \end{aligned}$$

So,

$$\lim_{n \rightarrow \infty} \frac{1}{n+1} \sum_{k=0}^n x_k \neq 0.$$

However, for  $\alpha = 1$ , we have

$$\lim_{n \rightarrow \infty} \frac{1}{n+1} \sum_{k=0}^n x_k = \frac{c}{2} \lim_{n \rightarrow \infty} (n+2).$$

From Cases (a), (b) and (c), we conclude that, in the case where  $\alpha_1 = \alpha_2$ ,  $T$  is not injective in  $\sigma_0$  if and only if  $|\alpha_1| = |\alpha_2| > 1$ .

As an immediate result of Proposition 4.1, we have the following:

**Corollary 4.1.**  $T - \lambda I \in (\sigma_0: \sigma_0)$  is injective if and only if one of the following conditions holds:

- (i): the function  $Q - \lambda$  has a root inside  $\Delta$ ,
- (ii): either 1 or  $-1$  is a double root of  $Q - \lambda$ .

Now, we consider the following lemma for the right-shift operator  $R$ :

**Lemma 4.2.** Let  $\alpha \in \mathbb{C}$ . Then,  $R - \alpha I \in (\sigma_0: \sigma_0)$  is surjective if and only if  $\alpha \notin \bar{\Delta}$ .

*Proof.* The result follows directly from Theorem 3.2(7).

As a consequence of Theorem 3.3(7), we establish the following lemma.

**Lemma 4.3.** Let  $\alpha \in \mathbb{C}$ . Then,  $I - \alpha L \in (\sigma_0: \sigma_0)$  is surjective if and only if  $\alpha \notin \partial \Delta$ .

With the help of Lemmas 4.2 and 4.3, we can introduce the following analogy to [El-Shabrawy and Shindy 2025, Proposition 2.3], whose proof can be derived in a similar manner.

**Proposition 4.2.**  $T \in (\sigma_0: \sigma_0)$  is surjective if and only if the roots of the function  $Q$  do not lie on  $\partial \Delta$  and at least one root of  $Q$  is outside  $\bar{\Delta}$ .

Consequently, from Proposition 4.2, we have the following corollary.

**Corollary 4.2.**  $T - \lambda I \in (\sigma_0: \sigma_0)$  is surjective if and only if the roots of  $Q - \lambda$  do not lie on  $\partial \Delta$  and at least one root of  $Q - \lambda$  is outside  $\bar{\Delta}$ .

Next, we give our first main theorem on the spectra of the operator  $T$ .

**Theorem 4.1** For  $|r| < |s|$ , we have  $T \in \mathcal{B}(\sigma_0)$ . Furthermore, the following statements hold:

- (1):  $\sigma(T, \sigma_0) = Q \left( \bar{\Delta} \setminus \Delta_{\frac{r}{s}} \right)$ .
- (2):  $\sigma_p(T, \sigma_0) = \emptyset$ .
- (3):  $\sigma_p(T^*, \sigma_0^*) = Q \left( \Delta \setminus \bar{\Delta}_{\frac{r}{s}} \right)$ .
- (4):  $\sigma_r(T, \sigma_0) = Q \left( \Delta \setminus \bar{\Delta}_{\frac{r}{s}} \right)$ .
- (5):  $\sigma_c(T, \sigma_0) = Q \left( \partial \Delta_{\frac{r}{s}} \cup \partial \Delta \right)$ .
- (6):  $I_3 \sigma(T, \sigma_0) = \Pi_3 \sigma(T, \sigma_0) = \text{III}_3 \sigma(T, \sigma_0) = \emptyset$ .
- (7):  $\Pi_2 \sigma(T, \sigma_0) = Q \left( \partial \Delta_{\frac{r}{s}} \cup \partial \Delta \right)$ .
- (8):  $\text{III}_1 \sigma(T, \sigma_0) = Q \left( \Delta \setminus \bar{\Delta}_{\frac{r}{s}} \right)$ .
- (9):  $\text{III}_2 \sigma(T, \sigma_0) = \emptyset$ .
- (10):  $\sigma_{\text{ap}}(T, \sigma_0) = Q \left( \partial \Delta_{\frac{r}{s}} \cup \partial \Delta \right)$ .



$$(11): \sigma_{\delta}(T, \sigma_0) = Q\left(\bar{\Delta} \setminus \Delta_{\frac{r}{s}}\right).$$

$$(12): \sigma_{co}(T, \sigma_0) = Q\left(\Delta \setminus \bar{\Delta}_{\frac{r}{s}}\right).$$

*Proof.*

(1): From [Appell et al. 2004, Proposition 1.3], we have

$$\sigma(T, \sigma_0) = \sigma(T^*, \sigma_0^*) = \sigma(T^*, h),$$

where  $T^*$  is the transpose of  $T$ . Now, by applying Theorem 2.4(1), with swapping  $r$  and  $s$ , we thereby obtain

$$\sigma(T, \sigma_0) = P\left(\bar{\Delta}_{\frac{s}{r}} \setminus \Delta\right) = Q\left(\bar{\Delta} \setminus \Delta_{\frac{r}{s}}\right),$$

where swapping  $r$  and  $s$  implies replacing  $Q$  by  $P$ .

(2): Since the product of the two roots of  $Q - \lambda$  equals  $\frac{r}{s}$ , then,  $Q - \lambda$  has a root inside  $\Delta$ . By Corollary 4.1,  $T - \lambda I$  is injective. Therefore,  $T$  has no eigenvalues in  $\sigma_0$ , so that

$$\sigma_p(T, \sigma_0) = \emptyset.$$

(3): Follows immediately from Theorem 2.4(2). Indeed, we have

$$\sigma_p(T^*, \sigma_0^*) = \sigma_p(T^*, h) = Q\left(\Delta \setminus \bar{\Delta}_{\frac{r}{s}}\right).$$

(4): By using the relation  $\sigma_r(T, \sigma_0) = \sigma_p(T^*, \sigma_0^*) \setminus \sigma_p(T, \sigma_0)$  and applying Statements (2) and (3), the result follows directly.

(5): It is known that

$$\begin{aligned} \sigma_c(T, \sigma_0) &= \sigma(T, \sigma_0) \setminus [\sigma_p(T, \sigma_0) \cup \sigma_r(T, \sigma_0)] \\ &= Q\left(\bar{\Delta} \setminus \Delta_{\frac{r}{s}}\right) \setminus Q\left(\Delta \setminus \bar{\Delta}_{\frac{r}{s}}\right) \\ &\subseteq Q\left(\partial \Delta_{\frac{r}{s}} \cup \partial \Delta\right). \end{aligned}$$

Conversely, let  $\lambda \in Q\left(\partial \Delta_{\frac{r}{s}} \cup \partial \Delta\right)$ .

Then,  $\lambda \in P\left(\partial \Delta_{\frac{s}{r}} \cup \partial \Delta\right)$ . Therefore, there exists a root  $\gamma$  of  $P - \lambda$  such that  $\gamma \in \partial \Delta_{\frac{s}{r}} \cup \partial \Delta$ . That is  $|\gamma| = \left|\frac{s}{r}\right|$  or  $|\gamma| = 1$ . Therefore, there exists a root of  $P - \lambda$ , which lies on  $\partial \Delta$ . Hence, by [El-Shabrawy and Shindy 2025, Proposition 2.1],  $T^* - \lambda I$  is injective, and then,  $\lambda \notin \sigma_p(T^*, \sigma_0^*)$ . So,  $\lambda \notin \sigma_r(T, \sigma_0)$ . This implies that  $\lambda \in \sigma_c(T, \sigma_0)$ .

Consequently,

$$Q\left(\partial \Delta_{\frac{r}{s}} \cup \partial \Delta\right) \subseteq \sigma_c(T, \sigma_0).$$

Thus, we conclude that

$$\sigma_c(T, \sigma_0) = Q\left(\partial \Delta_{\frac{r}{s}} \cup \partial \Delta\right).$$

(6): The result follows immediately from Statement (2) and the fact that  $\sigma_p(T, \sigma_0) = I_3 \sigma(T, \sigma_0) \cup II_3 \sigma(T, \sigma_0) \cup III_3 \sigma(T, \sigma_0)$ .

(7): Simply observe that  $II_2 \sigma(T, \sigma_0) = \sigma_c(T, \sigma_0)$ . It remains to apply Statement (5).

(8): We have

$$III_1 \sigma(T, \sigma_0) \subseteq \sigma_r(T, \sigma_0) = Q\left(\Delta \setminus \bar{\Delta}_{\frac{r}{s}}\right).$$

Conversely, let

$\lambda \in Q\left(\Delta \setminus \bar{\Delta}_{\frac{r}{s}}\right) = P\left(\Delta_{\frac{s}{r}} \setminus \bar{\Delta}\right)$ . In this case, there exists a root  $\gamma$  of  $P - \lambda$  such that  $\gamma \in \Delta_{\frac{s}{r}} \setminus \bar{\Delta}$ . From [El-Shabrawy and Shindy 2025, Proposition 2.3],  $T^* - \lambda I$  is surjective. That is  $T - \lambda I$  has a bounded inverse (cf. [Taylor and Halberg 1957, Theorem 4]). Additionally, we have  $\lambda \in \sigma_p(T^*, \sigma_0^*)$ , which implies that  $T^* - \lambda I$  is not injective. Then,  $T - \lambda I$  does not have a dense range (cf. [Taylor and Halberg 1957, Theorem 1]). That is we have  $\lambda \in III_1 \sigma(T, \sigma_0)$ . Thus,

$$III_1 \sigma(T, \sigma_0) = Q\left(\Delta \setminus \bar{\Delta}_{\frac{r}{s}}\right).$$

(9): Based on the fact that  $III_2 \sigma(T, \sigma_0) = \sigma_r(T, \sigma_0) \setminus III_1 \sigma(T, \sigma_0)$  and then applying Statements (4) and (8), the result follows immediately.

(10): We have

$$\begin{aligned} \sigma_{\delta}(T^*, \sigma_0^*) &= \sigma_{ap}(T, \sigma_0) \\ &= \sigma(T, \sigma_0) \setminus III_1 \sigma(T, \sigma_0) \\ &= Q\left(\bar{\Delta} \setminus \Delta_{\frac{r}{s}}\right) \setminus Q\left(\Delta \setminus \bar{\Delta}_{\frac{r}{s}}\right) \\ &\subseteq Q\left(\partial \Delta \cup \partial \Delta_{\frac{r}{s}}\right). \end{aligned}$$

Conversely, let

$$\lambda \in Q\left(\partial \Delta \cup \partial \Delta_{\frac{r}{s}}\right) = P\left(\partial \Delta \cup \partial \Delta_{\frac{s}{r}}\right).$$

Then, there exists a root  $\gamma$  of  $P - \lambda$  such that  $\gamma \in \partial \Delta \cup \partial \Delta_{\frac{s}{r}}$ . Therefore,  $P - \lambda$  should have a root on  $\partial \Delta$ . By [El-Shabrawy and Shindy 2025, Proposition 2.3],  $T^* - \lambda I$  is not surjective. So,  $\lambda \in \sigma_{\delta}(T^*, \sigma_0^*)$ .

Therefore,

$$\begin{aligned} Q\left(\partial \Delta \cup \partial \Delta_{\frac{r}{s}}\right) &\subseteq \sigma_{\delta}(T^*, \sigma_0^*) \\ &= \sigma_{ap}(T, \sigma_0). \end{aligned}$$

As a result

$$\sigma_{ap}(T, \sigma_0) = \sigma_{\delta}(T^*, \sigma_0^*)$$

$$= Q\left(\partial\Delta \cup \partial\Delta_{\frac{r}{s}}\right).$$

(11): The result follows directly from the fact that

$$\begin{aligned}\sigma_{\delta}(T, \sigma_0) &= \sigma(T, \sigma_0) \setminus I_3\sigma(T, \sigma_0) \\ &= Q\left(\bar{\Delta} \setminus \Delta_{\frac{r}{s}}\right).\end{aligned}$$

(12): It is a direct consequence of Statement (3) and the fact that

$$\sigma_{co}(T, \sigma_0) = \sigma_p(T^*, \sigma_0^*).$$

**Theorem 4.2.** For  $|r| > |s|$ , we have  $T \in \mathcal{B}(\sigma_0)$ . Furthermore, the following statements hold:

- (1):  $\sigma(T, \sigma_0) = Q\left(\bar{\Delta}_{\frac{r}{s}} \setminus \Delta\right).$
- (2):  $\sigma_p(T, \sigma_0) = Q\left(\bar{\Delta}_{\frac{r}{s}} \setminus \Delta\right).$
- (3):  $\sigma_p(T^*, \sigma_0^*) = \emptyset.$
- (4):  $\sigma_r(T, \sigma_0) = \emptyset.$
- (5):  $\sigma_c(T, \sigma_0) = \emptyset.$
- (6):  $I_3\sigma(T, \sigma_0) = Q\left(\Delta_{\frac{r}{s}} \setminus \bar{\Delta}\right).$
- (7):  $\Pi_3\sigma(T, \sigma_0) = Q\left(\partial\Delta_{\frac{r}{s}} \cup \partial\Delta\right).$
- (8):  $\text{III}_3\sigma(T, \sigma_0) = \emptyset.$
- (9):  $\Pi_2\sigma(T, \sigma_0) = \emptyset.$
- (10):  $\text{III}_1\sigma(T, \sigma_0) = \text{III}_2\sigma(T, \sigma_0) = \emptyset.$
- (11):  $\sigma_{ap}(T, \sigma_0) = Q\left(\bar{\Delta}_{\frac{r}{s}} \setminus \Delta\right).$
- (12):  $\sigma_{\delta}(T, \sigma_0) = Q\left(\partial\Delta_{\frac{r}{s}} \cup \partial\Delta\right).$
- (13):  $\sigma_{co}(T, \sigma_0) = \emptyset.$

*Proof.*

(1): From Theorem 2.3(1), we have

$$\begin{aligned}\sigma(T, \sigma_0) &= \sigma(T^*, \sigma_0^*) \\ &= \sigma(T^*, h) \\ &= P\left(\bar{\Delta} \setminus \Delta_{\frac{r}{s}}\right) \\ &= Q\left(\bar{\Delta}_{\frac{r}{s}} \setminus \Delta\right).\end{aligned}$$

(2): Firstly, we have

$$\sigma_p(T, \sigma_0) \subseteq \sigma(T, \sigma_0) = Q\left(\bar{\Delta}_{\frac{r}{s}} \setminus \Delta\right).$$

Conversely, suppose that

$\lambda \in Q\left(\bar{\Delta}_{\frac{r}{s}} \setminus \Delta\right)$ . Then, there exists a root  $\beta$  of  $Q - \lambda$  such that  $\beta \in \bar{\Delta}_{\frac{r}{s}} \setminus \Delta$ . So,  $1 \leq |\beta| \leq \left|\frac{r}{s}\right|$ . Therefore, the two roots of  $Q - \lambda$  lie outside  $\Delta$ . Since it can never happen that 1 or  $-1$  is a double root of  $Q - \lambda$ , then, by Corollary 4.1,  $T - \lambda I$  is not injective, and then,  $\lambda \in \sigma_p(T, \sigma_0)$ . Thus, we conclude that

$$\sigma_p(T, \sigma_0) = Q\left(\bar{\Delta}_{\frac{r}{s}} \setminus \Delta\right).$$

(3): Follows immediately from Theorem 2.3(2). Indeed, we have

$$\sigma_p(T^*, \sigma_0^*) = \sigma_p(T^*, h) = \emptyset.$$

(4): By using the relation

$$\sigma_r(T, \sigma_0) = \sigma_p(T^*, \sigma_0^*) \setminus \sigma_p(T, \sigma_0)$$

and applying Statement (3), the result follows immediately.

(5): Follows immediately.

(6): Let  $\lambda \in I_3\sigma(T, \sigma_0)$ . Then,  $T - \lambda I$  is surjective and not injective. By, Corollaries 4.1 and 4.2, it follows that both roots of  $Q$  must be outside  $\bar{\Delta}$ . This implies that  $Q - \lambda$  has a root  $\beta$  satisfying  $1 < |\beta| < \left|\frac{r}{s}\right|$ . Hence,  $\beta \in \Delta_{\frac{r}{s}} \setminus \bar{\Delta}$ , and so,  $\lambda = Q(\beta) \in Q\left(\Delta_{\frac{r}{s}} \setminus \bar{\Delta}\right)$ . Thus, we conclude that

$$I_3\sigma(T, \sigma_0) \subseteq Q\left(\Delta_{\frac{r}{s}} \setminus \bar{\Delta}\right).$$

Conversely, let  $\lambda \in Q\left(\Delta_{\frac{r}{s}} \setminus \bar{\Delta}\right)$ . Then, there exists a root  $\beta$  of  $Q - \lambda$  such that  $1 < |\beta| < \left|\frac{r}{s}\right|$ . So, by Corollaries 4.1 and 4.2,  $T - \lambda I$  is surjective and not injective. Thus  $\lambda \in I_3\sigma(T, \sigma_0)$ . So,  $Q\left(\Delta_{\frac{r}{s}} \setminus \bar{\Delta}\right) \subseteq I_3\sigma(T, \sigma_0)$ .

This ends the proof of Statement (6).

(7)- (8): Simply observe

$$\begin{aligned}\Pi_3\sigma(T, \sigma_0) \cup \text{III}_3\sigma(T, \sigma_0) &= \sigma_p(T, \sigma_0) \setminus I_3\sigma(T, \sigma_0) \\ &= Q\left(\bar{\Delta}_{\frac{r}{s}} \setminus \Delta\right) \setminus Q\left(\Delta_{\frac{r}{s}} \setminus \bar{\Delta}\right) \\ &\subseteq Q\left(\partial\Delta_{\frac{r}{s}} \cup \partial\Delta\right).\end{aligned}$$

Conversely, let  $\lambda \in Q\left(\partial\Delta_{\frac{r}{s}} \cup \partial\Delta\right)$ .

Then,  $\lambda \in P\left(\partial\Delta_{\frac{r}{s}} \cup \partial\Delta\right)$ . Therefore, there exists a root  $\gamma$  of  $P - \lambda$  such that  $\gamma \in \partial\Delta_{\frac{r}{s}} \cup \partial\Delta$ . This implies that,  $P - \lambda$

has the two roots inside  $\bar{\Delta}$ . So, by [El-Shabrawy and Shindy 2025, Proposition 2.1],  $T^* - \lambda I$  is injective. From [Taylor and Halberg 1957, Theorem 1],  $T - \lambda I$  has a dense range.

On the other hand,  $\lambda \in Q\left(\partial\Delta_{\frac{r}{s}} \cup \partial\Delta\right)$  implies that there exists a root  $\beta$  of  $Q - \lambda$  such that  $|\beta| = 1$  or  $|\beta| = \left|\frac{r}{s}\right|$ . Therefore, one of the roots of  $Q - \lambda$

lies on  $\partial\Delta$  and the other one is not inside  $\Delta$ . So, by Corollaries 4.1 and 4.2,  $T - \lambda I$  is neither surjective nor injective.

Consequently,  $\lambda \in \Pi_3\sigma(T, \sigma_0)$ . Thus,

$$Q\left(\partial\Delta_{\frac{r}{s}} \cup \partial\Delta\right) = \Pi_3\sigma(T, \sigma_0)$$

$$\text{and } \text{III}_3\sigma(T, \sigma_0) = \emptyset.$$

(9): Simply observe that

$$\Pi_2\sigma(T, \sigma_0) = \sigma_c(T, \sigma_0).$$

It remains to apply Statement (5).

(10): Since

$$\sigma_r(T, \sigma_0) = \text{III}_1\sigma(T, \sigma_0) \cup \text{III}_2\sigma(T, \sigma_0),$$

then the desired result follows by applying Statement (4).

(11): Indeed, we have

$$\begin{aligned}\sigma_{\text{ap}}(T, \sigma_0) &= \sigma(T, \sigma_0) \setminus \text{III}_1(T, \sigma_0) \\ &= Q\left(\overline{\Delta}_r \setminus \Delta\right).\end{aligned}$$

(12): We have

$$\begin{aligned}\sigma_\delta(T, \sigma_0) &= \sigma(T, \sigma_0) \setminus I_3(T, \sigma_0) \\ &= Q\left(\overline{\Delta}_r \setminus \Delta\right) \setminus Q\left(\Delta_r \setminus \overline{\Delta}\right) \\ &\subseteq Q\left(\partial\Delta_{\frac{r}{s}} \cup \partial\Delta\right).\end{aligned}$$

Conversely, let  $\lambda \in Q\left(\partial\Delta_{\frac{r}{s}} \cup \partial\Delta\right)$ . One can show that  $T - \lambda I$  is not surjective, and then,  $\lambda \in \sigma_\delta(T, \sigma_0)$ . Thus, we conclude that

$$\sigma_\delta(T, \sigma_0) = Q\left(\partial\Delta_{\frac{r}{s}} \cup \partial\Delta\right).$$

(13): It is a direct consequence of Statement (3) and the fact that

$$\sigma_{\text{co}}(T, \sigma_0) = \sigma_p(T^*, \sigma_0^*).$$

**Theorem 4.3.** For  $|r| = |s|$ , we have  $T \in \mathcal{B}(\sigma_0)$ . Furthermore, the following statements hold:

- (1):  $\sigma(T, \sigma_0) = Q(\partial\Delta)$ .
- (2):  $\sigma_p(T, \sigma_0) = \begin{cases} Q(\partial\Delta \setminus \{-1, 1\}), & \text{if } r = s, \\ Q(\partial\Delta), & \text{if } r = -s. \end{cases}$
- (3):  $\sigma_p(T^*, \sigma_0^*) = \emptyset$ .
- (4):  $\sigma_r(T, \sigma_0) = \emptyset$ .
- (5):  $\sigma_c(T, \sigma_0) = \begin{cases} Q(\{-1, 1\}), & \text{if } r = s, \\ \emptyset, & \text{if } r = -s. \end{cases}$
- (6):  $I_3\sigma(T, \sigma_0) = \emptyset$ .
- (7):  $\Pi_3\sigma(T, \sigma_0) = \begin{cases} Q(\partial\Delta \setminus \{-1, 1\}), & \text{if } r = s, \\ Q(\partial\Delta), & \text{if } r = -s. \end{cases}$
- (8):  $\text{III}_3\sigma(T, \sigma_0) = \emptyset$ .
- (9):  $\Pi_2\sigma(T, \sigma_0) = \begin{cases} Q(\{-1, 1\}), & \text{if } r = s, \\ \emptyset, & \text{if } r = -s. \end{cases}$
- (10):  $\text{III}_1\sigma(T, \sigma_0) = \text{III}_2\sigma(T, \sigma_0) = \emptyset$ .
- (11):  $\sigma_{\text{ap}}(T, \sigma_0) = Q(\partial\Delta)$ .
- (12):  $\sigma_\delta(T, \sigma_0) = Q(\partial\Delta)$ .

$$(13): \sigma_{\text{co}}(T, \sigma_0) = \emptyset.$$

*Proof.*

(1): From Theorem 2.5(1), we have

$$\begin{aligned}\sigma(T, \sigma_0) &= \sigma(T^*, \sigma_0^*) \\ &= \sigma(T^*, h) \\ &= P(\partial\Delta) \\ &= Q(\partial\Delta).\end{aligned}$$

(2): Let  $r = s$ . Suppose that  $\lambda \in \sigma_p(T, \sigma_0)$ .

Then,  $T - \lambda I$  is not injective. Since the product of the two roots of  $Q - \lambda$  equals 1, therefore, by Corollary 4.1, the two roots lie on  $\partial\Delta$  and that neither  $-1$  nor  $1$  is a double root of  $Q - \lambda$ . Let  $\beta$  be a root of  $Q - \lambda$ . Then,  $\beta \in \partial\Delta \setminus \{-1, 1\}$ . That is, we have

$$\lambda = Q(\beta) \in Q(\partial\Delta \setminus \{-1, 1\}).$$

$$\sigma_p(T, \sigma_0) \subseteq Q(\partial\Delta \setminus \{-1, 1\}).$$

Conversely, let  $\lambda \in Q(\partial\Delta \setminus \{-1, 1\})$ .

Then, there exists  $\beta \in \partial\Delta \setminus \{-1, 1\}$  such that  $\lambda = Q(\beta)$ . Therefore,  $\beta$  is a root of  $Q - \lambda$  that satisfies  $|\beta| = 1$  and  $\beta \notin \{-1, 1\}$ . By Corollary 4.1,  $T - \lambda I$  is not injective, and so,  $\lambda \in \sigma_p(T, \sigma_0)$ .

Hence,

$$Q(\partial\Delta \setminus \{-1, 1\}) \subseteq \sigma_p(T, \sigma_0).$$

This concludes that

$$\sigma_p(T, \sigma_0) = Q(\partial\Delta \setminus \{-1, 1\}).$$

Let  $r = -s$ . The proof is similar to case  $r = s$ .

(3): This result follows directly from Theorem 2.5(2). Indeed, we have  $\sigma_p(T^*, \sigma_0^*) = \sigma_p(T^*, h) = \emptyset$ .

(4): Based on the relation

$$\sigma_r(T, \sigma_0) = \sigma_p(T^*, \sigma_0^*) \setminus \sigma_p(T, \sigma_0)$$

and using Statement (3), the result follows immediately.

(5): If  $r = -s$ , the proof follows immediately from the relation

$$\begin{aligned}\sigma_c(T, \sigma_0) &= \sigma(T, \sigma_0) \setminus [\sigma_p(T, \sigma_0) \cup \sigma_r(T, \sigma_0)], \\ &\text{and then applying Statements (1), (2) and (4). Now, let } r = s. \text{ In fact, we have} \\ \sigma_c(T, \sigma_0) &= Q(\partial\Delta) \setminus Q(\partial\Delta \setminus \{-1, 1\}) \\ &\subseteq Q(\{-1, 1\}).\end{aligned}$$

On the other hand, let  $\lambda \in Q(\{-1, 1\})$ . Then,  $-1$  and  $1$  are the double roots of  $Q - \lambda$ . This implies that  $T - \lambda I$  is injective. Therefore,  $\lambda \notin \sigma_p(T, \sigma_0)$ .

Consequently,  $\lambda \in \sigma_c(T, \sigma_0)$ .

We conclude that

$$Q(\{-1, 1\}) \subseteq \sigma_c(T, \sigma_0).$$

This concludes the result.

(6): Let  $r = s$ . From the fact that

$$I_3\sigma(T, \sigma_0) \subseteq \sigma_p(T, \sigma_0).$$

We have

$$I_3\sigma(T, \sigma_0) \subseteq Q(\partial\Delta \setminus \{-1, 1\}).$$

Conversely, let  $\lambda \in Q(\partial\Delta \setminus \{-1, 1\})$ .

Therefore, there exists a root  $\beta$  of  $Q - \lambda$  such that  $\beta \in \partial\Delta \setminus \{-1, 1\}$ . So, by Corollaries 4.1 and 4.2,  $T - \lambda I$  is neither injective nor surjective. So,  $\lambda \notin I_3\sigma(T, \sigma_0)$ . This concludes that  $I_3\sigma(T, \sigma_0) = \emptyset$ .

Let  $r = -s$ . The proof is similar to case  $r = s$ .

- (7)-(8): Let  $r = s$ . Simply observe that
- $$\begin{aligned} \Pi_3\sigma(T, \sigma_0) \cup \text{III}_3\sigma(T, \sigma_0) \\ \subseteq \sigma_p(T, \sigma_0) \setminus I_3\sigma(T, \sigma_0) \\ = Q(\partial\Delta \setminus \{-1, 1\}). \end{aligned}$$

Now, let  $\lambda \in Q(\partial\Delta \setminus \{-1, 1\})$ . Then,  $\lambda \in P(\partial\Delta \setminus \{-1, 1\})$ . Therefore, there exists a root  $\gamma$  of  $P - \lambda$  such that  $\gamma \in \partial\Delta \setminus \{-1, 1\}$ . This implies that the two roots of  $P - \lambda$  are inside  $\bar{\Delta}$ . So, by [El-Shabrawy and Shindy 2025, Proposition 2.1],  $T^* - \lambda I$  is injective. Also, from [Taylor and Halberg 1957, Theorem 1],  $T - \lambda I$  has a dense range, and consequently,  $\lambda \in \Pi_3\sigma(T, \sigma_0)$ .

Therefore,

$$\Pi_3\sigma(T, \sigma_0) = Q(\partial\Delta \setminus \{-1, 1\}).$$

and

$$\text{III}_3\sigma(T, \sigma_0) = \emptyset.$$

The case  $r = -s$  follows by a similar argument.

- (9): Simply observe that  $\Pi_2\sigma(T, \sigma_0) = \sigma_c(T, \sigma_0)$ . It remains to use Statement (5).
- (10): Since  $\sigma_r(T, \sigma_0) = \text{III}_1\sigma(T, \sigma_0) \cup \text{III}_2\sigma(T, \sigma_0)$ , then the desired result follows by applying Statement (4).
- (11): Indeed, from Statements (1) and (10), we have  $\sigma_{\text{ap}}(T, \sigma_0) = \sigma(T, \sigma_0) \setminus \text{III}_1(T, \sigma_0) = Q(\partial\Delta)$ .
- (12): Follows directly from Statements (1) and (6) that  $\sigma_\delta(T, \sigma_0) = \sigma(T, \sigma_0) \setminus I_3(T, \sigma_0) = Q(\partial\Delta)$ .
- (13): It is a direct consequence of Statement (3) and the fact that  $\sigma_{\text{co}}(T, \sigma_0) = \sigma_p(T^*, \sigma_0^*)$ .

An important result is in order before ending this section. Consider the special case

where  $r = s > 0$ . Then, the operator  $T(r, q, s)$  is reduced to the Jacobi operator  $J(q, r)$ . If this is the case, we observe that

$$Q(\partial\Delta) = [q - 2r, q + 2r],$$

$$Q(\partial\Delta \setminus \{-1, 1\}) = (q - 2r, q + 2r),$$

$$Q(\{-1, 1\}) = \{q - 2r, q + 2r\}.$$

Consequently, we have the following important corollary:

**Corollary 4.5.** *Let  $r$  and  $q$  be fixed real numbers with  $r > 0$ . We have  $J(q, r) \in \mathcal{B}(\sigma_0)$ . Furthermore, the following statements hold:*

- (1):  $\sigma(J(q, r), \sigma_0) = [q - 2r, q + 2r]$ .
- (2):  $\sigma_p(J(q, r), \sigma_0) = (q - 2r, q + 2r)$ .
- (3):  $\sigma_p(J(q, r)^*, \sigma_0^*) = \emptyset$ .
- (4):  $\sigma_r(J(q, r), \sigma_0) = \emptyset$ .
- (5):  $\sigma_c(J(q, r), \sigma_0) = \{q - 2r, q + 2r\}$ .
- (6):  $I_3\sigma(J(q, r), \sigma_0) = \emptyset$ .
- (7):  $\Pi_3\sigma(J(q, r), \sigma_0) = (q - 2r, q + 2r)$ .
- (8):  $\text{III}_3\sigma(J(q, r), \sigma_0) = \emptyset$ .
- (9):  $\Pi_2\sigma(J(q, r), \sigma_0) = \{q - 2r, q + 2r\}$ .
- (10):  $\text{III}_1\sigma(J(q, r), \sigma_0) = \emptyset$ .
- (11):  $\sigma_{\text{ap}}(J(q, r), \sigma_0) = [q - 2r, q + 2r]$ .
- (12):  $\sigma_\delta(J(q, r), \sigma_0) = [q - 2r, q + 2r]$ .
- (13):  $\sigma_{\text{co}}(J(q, r), \sigma_0) = \emptyset$ .

In Corollary 4.5, the results established in Statements (1)-(5) agree with the results in [El-Shabrawy and Shindy 2020, Theorem 4.1]. While, the remaining results are new contributions.

## Conclusion and work in progress

In this paper, a detailed study on the spectra of the infinite matrices  $B(r, s)$ ,  $U(r, s)$  and  $T(r, q, s)$  as operators on the Cesàro sequence space  $\sigma_0$  has been given. In fact, the class of the operators  $T(r, q, s)$  includes  $B(r, s) = T(0, r, s)$  and  $U(r, s) = T(s, r, 0)$ . We assert that the technique presented in Section 4 is flexible to be adapted to study the spectral problem of the operators  $B(r, s)$  and  $U(r, s)$ . In fact, analogous to Corollaries 4.1, 4.2, 4.3 and 4.4, the reader can easily verify the following proposition.

**Proposition 5.1.** *The following statements are satisfied:*

- (1):  $B(r, s) - \lambda I \in (\sigma_0: \sigma_0)$  is injective.
- (2):  $B(r, s)^* - \lambda I \in (\text{h: h})$  is injective if and only if  $|\lambda - r| \geq |s|$ .
- (3):  $B(r, s) - \lambda I \in (\sigma_0: \sigma_0)$  is surjective if

and only if  $|\lambda - r| > |s|$ .

- (4):  $B(r, s)^* - \lambda I \in (h: h)$  is surjective if and only if  $|\lambda - r| \neq |s|$ .  
 (5):  $U(r, s) - \lambda I \in (\sigma_0: \sigma_0)$  is injective if either  $|\lambda - r| > |s|$  or  $\lambda = r + s$ .  
 (6):  $U(r, s)^* - \lambda I \in (h: h)$  is injective.  
 (7):  $U(r, s) - \lambda I \in (\sigma_0: \sigma_0)$  is surjective if and only if  $|\lambda - r| \neq |s|$ .  
 (8):  $U(r, s)^* - \lambda I \in (h: h)$  is surjective if and only if  $|\lambda - r| > |s|$ .

Then, by similar calculations like in the preceding section, we can obtain results that agree with those in Section 3. This gives a new technique for determining the spectra of the operators  $B(r, s)$  and  $U(r, s)$ .

Further study on the spectra of the operator  $T(r, q, s)$  on sequence spaces, like  $\sigma_\infty$  and  $bs$ , is required. However, some difficulties caused some problems in characterizing the residual and the continuous spectra of  $T(r, q, s)$  on  $\sigma_\infty$  and  $bs$ . The problem is in progress and we hope to have advances regarding these results in future publication.

## References

- A. M. Akhmedov, F. Başar, The fine spectra of the difference operator  $\Delta$  over the sequence space  $\ell_p$  ( $1 \leq p < \infty$ ), *Demonst. Math.* 39 (3) (2006), 585–595.
- A. M. Akhmedov, F. Başar, The fine spectra of the difference operator  $\Delta$  over the sequence space  $bv_p$  ( $1 \leq p < \infty$ ), *Acta Math. Sin. (Engl. Ser.)* 23 (10) (2007), 1757–1768.
- B. Altay, F. Başar, On the fine spectrum of the difference operator  $\Delta$  on  $c_0$  and  $c$ , *Inform. Sci.* 168 (2004), 217–224.
- B. Altay, F. Başar, On the fine spectrum of the generalized difference operator  $B(r, s)$  over the sequence spaces  $c_0$  and  $c$ , *Int. J. Math. Math. Sci.* 18 (2005), 3005–3013.
- M. Altun, Fine spectra of tridiagonal symmetric matrices, *Int. J. Math. Math. Sci.*, 2011, Art. ID 161209, 10 pp.
- B. Altay, M. Karakuş, On the spectrum and the fine spectrum of the Zweier matrix as an operator on some sequence spaces, *Thai J. Math.* 3 (2005), 153–162.
- J. Appell, E. De Pascale, A. Vignoli, *Nonlinear Spectral Theory*. De Gruyter series in nonlinear analysis and applications 10. Berlin:Walter de Gruyter; 2004.
- Ju. M. Berezanskii, *Expansions in Eigenfunctions of Selfadjoint Operators*, Amer. Math. Soc., Providence, 1968.
- H. Bilgiç, M. Altun, Fine spectra of tridiagonal Toeplitz matrices, *Ukrainian Math. J.* 71(6) (2019), 853–868.
- H. Bilgiç, H. Furkan, On the fine spectrum of the generalized difference operator  $B(r, s)$  over the sequence spaces  $\ell_p$  and  $bv_p$ , ( $1 < p < \infty$ ), *Nonlinear Anal.* 68 (2008), 499–506.
- A. J. Dutta, B. C. Tripathy, Fine spectrum of the generalized difference operator  $B(r, s)$  over the class of convergent series, *Int. J. Anal.*, 2013, Art. ID 630436, 4 pp.
- E. Dündar, F. F. Başar, On the fine spectrum of the upper triangle double band matrix  $\Delta^+$  on the sequence space  $c_0$ , *Math. Commun.* 18 (2013), 337–348.
- S. R. EL-Shabrawy, S. H. Abu-Janah, Spectra of the generalized difference operator on the sequence spaces  $bv_0$  and  $h$ , *Linear Multilinear Algebra* 66(8) (2018), 1691–1708.
- S. R. El-Shabrawy, Y. Sawano, On the compactness and spectra of the generalized difference operator on the spaces  $\ell^\infty$  and  $bv$ , *Oper. Matrices* 15(3) (2021), 959–983.
- S. R. El-Shabrawy, A. M. Shindy, Spectra of the constant Jacobi matrices on Banach sequence spaces, *Rev. R. Acad. Cienc. Exactas Fís. Nat. Ser. A Mat. RACSAM* 114(4) (2020), Art. No.182, 23 pp.
- S. R. El-Shabrawy, A. M. Shindy, On the spectra of tridiagonal non-symmetric matrices, *J. Math. Anal. Appl.* 548(2) (2025), 129421.
- H. Furkan, H. Bilgiç, K. Kayaduman, On the fine spectrum of the generalized difference operator  $B(r, s)$  over the sequence spaces  $\ell_1$  and  $bv$ , *Hokkaido Math. J.* 35 (2006), 893–904.
- H. A. Gindler, A. E. Taylor, The minimum modulus of a linear operator and its use in spectral theory, *Studia Math.* 22 (1962), 15–41.
- G. Goes, S. Goes, Sequences of bounded variation and sequences of Fourier coefficients. I, *Math. Z.* 118 (1970), 93–102.
- V. Karakaya, M. Altun, Fine spectra of upper triangular double-band matrices, *J. Comput. Appl. Math.* 234 (2010), 1387–1394.
- Y. Sawano, S. R. El-Shabrawy, The spectra of the generalized difference operators on the spaces of convergent series, *Linear Multilinear Algebra* 69(4) (2021) 732–751.
- K. C. Rao, The Hahn sequence space, *Bull. Calcutta Math. Soc.* 82 (1990), 72–78.
- A. E. Taylor, CJA Jr. Halberg, General theorems about a bounded linear operator and its conjugate, *J. Reine Angew. Math.* 198 (1957), 93–111.
- A. E. Taylor, D. C. Lay, *Introduction to Functional*

- Analysis, 2nd ed. Robert E. Krieger Publishing Co., Malabar, Florida, 1986.
- B. C. Tripathy, R. Das, Spectrum and fine spectrum of the upper triangular matrix  $U(r, s)$  over the sequence space  $cs$ , *Proyecciones* 34(2) (2015), 107–125.
- A. Wilansky, *Summability Through Functional Analysis*, North-Holland Mathematics Studies, Vol. 85, North-Holland, Amsterdam, 1984.

## الملخص العربي

### عنوان البحث: حول أطيف بعض المصفوفات ذات النطاق لانهاية البعد كمؤثرات على فراغ المتتابعات لشيزارو $\sigma_0$

رابحة محمد الأشوح<sup>١</sup>، حسن أحمد المرشدي<sup>١</sup>، أسماء محمد شندي<sup>١</sup>، سعد رشاد الشبراوي<sup>١</sup>

<sup>١</sup>قسم الرياضيات، كلية العلوم، جامعة دمياط، دمياط، مصر.

قدّم هذا العمل دراسة طيفية لبعض المصفوفات المعروفة، وهي المصفوفات المثلثية السفلية والعلوية ثنائية النطاق، كمؤثرات على فراغ المتتابعات لشيزارو  $\sigma_0$ . تتضمن الدراسة تحليلاً دقيقاً لطيف هذه المؤثرات، مع التمييز بين أنواع الطيف المختلفة مثل: الطيف النقطي، الطيف المتبقي، الطيف المتصل، طيف العيب، طيف الضغط، والطيف التقريبي النقطي. كما يُقدّم تقسيماً أدق للطيف. وتمتد الدراسة لتشمل تعميماً على المصفوفات ثلاثية الأقطار المتماثلة وغير المتماثلة. ويتميز الأسلوب المُتَّبَع في البحث بمرونة تسمح بتطبيقه لدراسة المسألة الطيفية للمؤثرات موضع الدراسة في فراغات متتابعات أخرى.



## Comparative Analysis of Spectral Indices to Assess Coastal Salinization in Northeastern Nile Delta, Egypt

Reem A. ElNaggar<sup>\*1</sup>, Ayman I. Taha<sup>2</sup>, Hany M. Shaaban<sup>2</sup>, Eman R. Nofal<sup>3</sup> and Hatem M. Aboelkhair<sup>1</sup>

<sup>1</sup>Faculty of Science Damietta University, 34517, Damietta, Egypt.

<sup>2</sup>National Research Institution for astronomy and geophysics, 11722, Helwan, Cairo, Egypt.

<sup>3</sup>Research Institute for Groundwater, National Water Research Center, 13621, El-Kanater El-Khairiya, Egypt.

Received: 14 June 2025 /Accepted: 22 June 2025

\*Corresponding author's E-mail: reem.elnaggar@du.edu.eg

### Abstract

Soil salinization driven by seawater intrusion poses a growing threat to agriculture in the northeastern Nile Delta, where shallow groundwater tables and intensive irrigation facilitate salt accumulation at the surface. This study mapped surface salinity and its impact on vegetation along a 50 km area from New Mansoura City to Mansoura using a Landsat 8 OLI. Unsupervised K-means clustering identified five land-use/land-cover classes (water, vegetation, barren land, urban, and sabkha), allowing for the computation of eight spectral indices per class: Normalized Difference Vegetation Index (NDVI), Soil-Adjusted Vegetation Index (SAVI), Salinity Indices S1–S4, Normalized Difference Salinity Index (NDSI), and Vegetation Soil Salinity Index (VSSI). Zonal statistics quantified index distributions, and linear regression of index values against distance from the shoreline assessed spatial trends. Vegetation indices (NDVI, SAVI) effectively highlighted canopy stress but showed minimal coastal gradients ( $\beta_1 \approx -1.8 \times 10^{-6} \text{ m}^{-1}$ ;  $R^2 \approx 0$ ), reflecting the mitigating effect of local irrigation. Brightness-based indices and NDSI captured salt-crust signatures, with mean S1–S3 values increasing from agricultural fields (13 222–14 972) to sabkha (19 122–20 080) and positive but low-magnitude coastal slopes (e.g., S1  $\beta_1 = 0.1255 \text{ m}^{-1}$ ;  $R^2 < 0.003$ ). The hybrid VSSI provided the strongest separation between vegetated and salt-stressed zones (mean VSSI:  $-79\ 163$  vs.  $-125\ 610$ ). These results demonstrate differential sensitivity of spectral indices to salinity and vegetation stress, which can be used to monitor soil salinity with minimum cost and allow further analysis and surveys only when necessary.

**Keywords:** Soil salinity, Seawater intrusion, Landsat 8, Remote sensing, salinity monitoring

### Introduction

Soil salinization from seawater intrusion is a growing threat to coastal agriculture worldwide.

Rising sea levels and reduced river flows are allowing saltwater to penetrate farther inland, increasing soil salt content and harming crops (Bear, 1999). In Egypt's Nile Delta – one of the world's most vulnerable deltas – sea levels have been rising, pushing saltwater into soils and

aquifers and leading to higher soil salinity. Persistent irrigation practices combined with seasonal fluctuations in the water table have led to widespread salt accumulation, compromising soil structure, reducing agricultural productivity, and degrading ecosystem health (Armanuos et al., 2022; Nofal et al., 2015).

Human activity in this region is intensive. The Dakahlia governorate is a major agricultural area where farms grow rice, cotton, wheat and high-value vegetables and fruits, many of which are irrigated from the Nile's Damietta Branch and local aquifers (Alshrabsy et al., 2024; Mansour & Mark, 2025). New Mansoura is a planned coastal city developed for housing and industry. The local economy also includes agro-industry and export-oriented horticulture. This heavy water use, combined with low elevation and rising sea levels, has worsened waterlogging and salt intrusion. Sea-level rise and reduced flow in the Damietta branch are causing brackish water to invade croplands and aquifers, leading to soil degradation and deteriorated vegetation. Protecting this fertile delta requires reliable monitoring of salinity levels.

Remote sensing techniques offer a cost-effective and spatially comprehensive approach for monitoring surface salinity over large areas, overcoming the limitations of sparse in-situ measurements (Nguyen et al., 2020). Researchers have developed numerous spectral indices that correlate with soil salt content or with vegetation stress resulting from salinity (Table 1). Common indices include the Normalized Difference Vegetation Index (NDVI) and Soil-Adjusted Vegetation Index (SAVI), which drops as salt stress reduces plant greenness; Normalized Difference Salinity Index (NDSI) and various Salinity Indices (S1–S4) that are designed to highlight bare soils with high salt reflectance; and specialized indices like the Vegetation Soil Salinity Index (VSSI), which combines visible/infrared bands to detect salt under partial vegetation cover. Many studies have shown strong correlations between these indices and measured soil electrical conductivity (EC) in field surveys (Dehni &

Lounis, 2012).

These spectral indices have been successfully applied in coastal and delta regions worldwide. In Vietnam's Mekong Delta (Tra Vinh Province), (Nguyen et al., 2020) used Landsat 8 to compute NDVI, SAVI, VSSI and other indices and found that the near-infrared band and the VSSI had the strongest correlation with measured soil salinity ( $R^2 \approx 0.80$  and  $0.70$ , respectively). Their Landsat-derived salinity maps (for the topsoil) agreed closely with in-situ EC measurements, demonstrating that satellite data can reliably track coastal salinity intrusion. In Pakistan's Indus Delta, (Aeman et al., 2023) linked saltwater-driven changes in vegetation to electrical conductivity using the VSSI: areas undergoing erosion and intrusion showed high VSSI values ( $0.7$ – $1.2$ ) and elevated EC, whereas accreting regions had lower VSSI and more mangrove growth. Other studies in arid and semi-arid deltas have reported similar results using multi-temporal Landsat analyses (using NDSI, BI, SI, NDVI, SAVI, etc.) and have mapped salinity variations in Turkish coastal plains (Azabdaftari & Sunar, 2016).

The main objective of this study is to assess the effectiveness of spectral indices derived from Landsat-8 in detecting and mapping surface soil salinity along a 50 km stretch between New Mansoura and Mansoura. By evaluating how well these indices reflect actual salinity patterns in a region undergoing rapid environmental and anthropogenic changes, we aim to identify reliable remote sensing indicators for monitoring salinity intrusion.

We hypothesize that vegetation- and soil-based spectral indices, particularly VSSI and NDSI, will show strong spatial correspondence with observed salinity gradients in this part of the Nile Delta, due to their sensitivity to both bare soil reflectance and vegetation stress. The findings could guide improved land management, crop planning, and salinity mitigation efforts to sustain agriculture and the local economy in the face of environmental stress.

Table 1 Spectral indices employed for evaluating vegetation condition and soil salinity in the study area. Each index is defined by its mathematical expression and associated reference, with formulations designed to enhance sensitivity to either vegetation vigor or surface salt accumulation

Index	Equation	Reference
SAVI	$SAVI = ((1 + L) * NIR - Red) / (Red + NIR + L)$	(Huete, 1988)
NDVI	$NDVI = \frac{NIR - Red}{NIR + Red}$	(Khan et al., 2001)
NDSI	$NDSI = \frac{(NIR - Red)}{(NIR + Red)}$	(Khan et al., 2001)
S1	$S1 = \sqrt{Green^2 + Red^2}$	(Douaoui et al., 2006)
S2	$S2 = \sqrt{Red * Green}$	(Douaoui et al., 2006)
S3	$S3 = \sqrt{Blue * Red}$	(Khan et al., 2001)
S4	$S4 = \sqrt{Green^2 + Red^2 + NIR^2}$	(Douaoui et al., 2006)
VSSI	$VSSI = 2 * Green - 5 * (Red + NIR)$	(Dehni & Lounis, 2012)

## Study area

The study area is situated along a 50 km southeastward profile in the northeastern Nile Delta, extending from the northwestern margin of New Mansoura City to Mansoura (Figure 1). It is a flat, low-lying coastal plain formed by Nile sediments and shaped by Mediterranean marine influences. Geomorphologically, the area comprises a narrow coastal belt of dunes and sand flats, backed by a fluvio-marine plain

and an inland floodplain (Pennington et al., 2017). Near the coast, the soil is predominantly sandy (fine sand) with low organic matter, while the soil on the former river delta platforms is medium- to fine-textured loams and clays (El Nahry et al., 2015). In the Mansoura area, recent studies have recorded extreme salinization (soil EC up to ~190 dS/m) in some fields, attributed to shallow saline groundwater and seawater intrusion (Youssef et al., 2024).

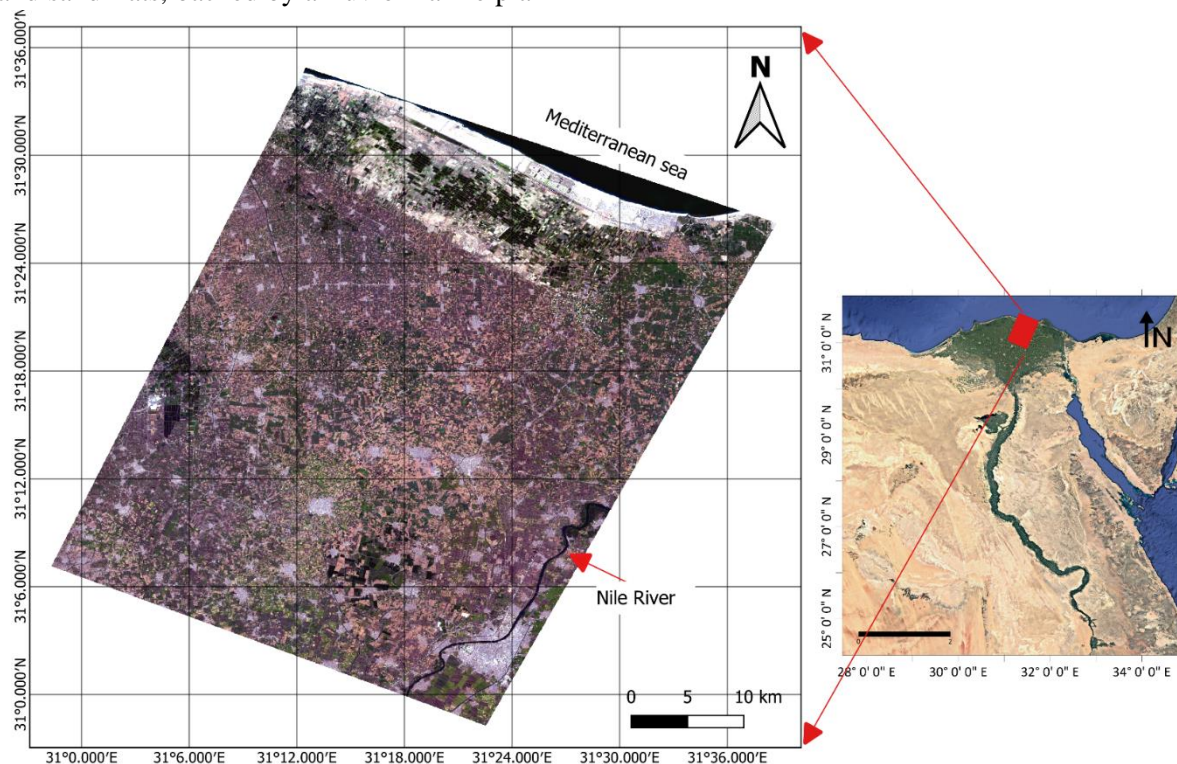


Figure 1: True Color satellite image showing the study area located in the northern part of the east and middle delta within the jurisdiction of Damietta and Dakahlia Governates.

## Methodology

This study combined geospatial processing in QGIS 3.28 with quantitative analysis in Python to characterize surface salinity and its impact on vegetation in a coastal zone subject to seawater intrusion. A Level-2T Landsat 8 OLI image (September 2022) was selected for salinity assessment based on local climatic conditions. As shown in the climate (Figure 2), September corresponds to a period of minimal precipitation and moderate temperatures. This combination is ideal for analyzing salinity using spectral indices, as it minimizes surface moisture interference that could obscure the spectral signature of salt crusts and stressed vegetation. Indices such as NDSI, SI, and VSSI are more effective under drier conditions, where reflectance from salt-affected soils and stressed vegetation is clearer and more distinguishable. Additionally, avoiding months of peak summer temperatures (e.g., July and August) helps reduce the confounding effects of thermal stress on vegetation, which could mimic or mask salinity symptoms. Therefore, the September image offers an optimal balance, with low moisture and moderate temperature conditions that enhance the reliability of salinity index detection in coastal environments prone to seawater intrusion.

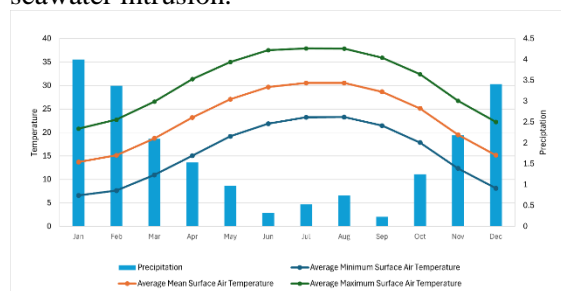


Figure 2 : Monthly Climatology of Average of Minimum Surface Air Temperature, Average Mean Surface Air Temperature, Average Maximum Surface Air, Temperature & Precipitation 1991-2020; Arab Republic of Egypt

Eight spectral indices (NDVI, SAVI, NDSI, S1–S4, VSSI) were calculated via the Raster Calculator tool in QGIS software (Table 1). Employing the unsupervised K-means LULC classification, we obtained 5 classes: water, vegetation, barren, urban, and sabkha classes (Figure 3). In Python, a Pearson correlation matrix was calculated with pandas to assess interrelationships among indices (Abdi, 2007). Subsequently, ordinary least squares (OLS)

linear regression models were used to evaluate how each index varied with coastal distance, yielding slope, intercept,  $R^2$ , and p-values for each LULC class. This integrated workflow ensured reproducible spatial and statistical analysis of salinity trends and vegetation stress.

## Spectral indices

Landsat 8's Operational Land Imager (OLI) provides multispectral data at 30 m resolution across visible, near-infrared (NIR), and shortwave-infrared (SWIR) bands, enabling the computation of spectral indices that exploit contrasts in soil brightness and vegetation stress associated with salinization (Cao et al., 2022). A Level-2 T Landsat 8 OLI image processed for atmospheric and geometric correction by Landsat, acquired on 09 September 2022, was obtained from the USGS Earth Explorer archive, including bands 2 (Blue) through 7 (SWIR). No additional temporal images or in situ salinity measurements were available; instead, index performance was validated through comparison with established results from the literature.

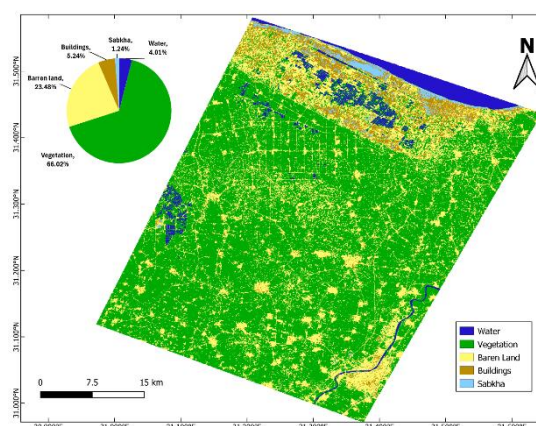


Figure 3 LULC map of the study area with class proportions. Vegetation is dominant, while sabkha and water cover minimal areas, derived from K-mean classification of Landsat 9 image

## Normalized Difference Vegetation Index (NDVI).

Although originally developed for crop-health assessment, NDVI serves as an indirect salinity indicator in semi-arid and arid environments (Table 1), since high soil salinity induces plant stress and canopy thinning, which lowers NIR reflectance relative to red. Thus, declines in NDVI can signal zones of elevated surface



salinity where vegetation is adversely affected (Figure 4).

#### Soil-Adjusted Vegetation Index (SAVI).

To correct for soil-background brightness in sparse vegetation, SAVI modifies NDVI by introducing a canopy-density factor (L) (Table 1). This adjustment reduces soil-line influence, particularly important in semi-arid sabkha fringes, yielding improved detection of vegetation stress due to salinity. Compared to NDVI, SAVI offers greater sensitivity to salinity-induced canopy changes in areas of low to moderate vegetation cover (Huete, 1988) (Figure 4).

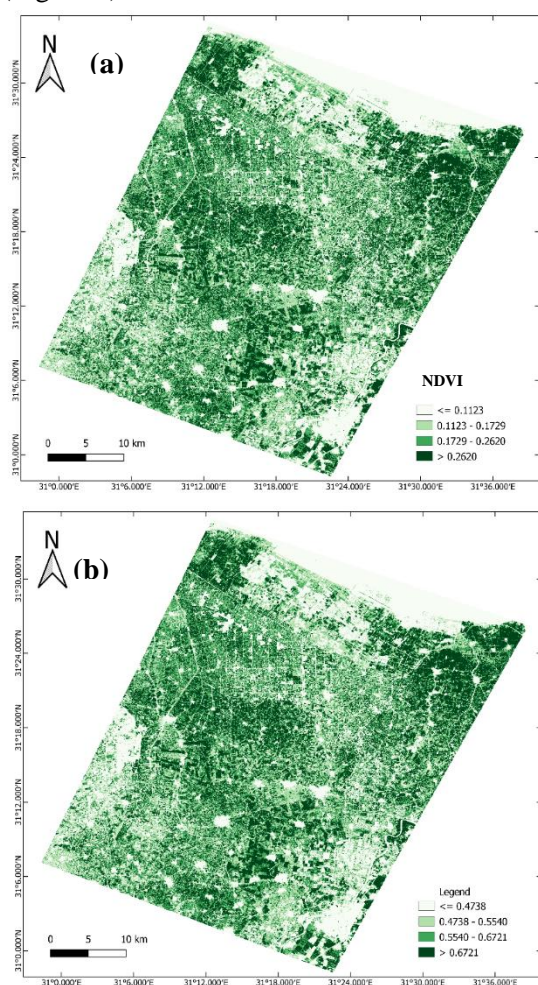


Figure 4 (a) Normalized Difference Vegetation Index (NDVI) map highlighting vegetation density; lower values indicate stressed or sparse vegetation. (b) Soil-Adjusted Vegetation Index (SAVI) map showing no difference in detection in sparsely vegetated areas through soil brightness correction.

#### Normalized Difference Salinity Index (NDSI).

Saline soil often exhibits higher reflectance in the red region (due to salt crusts and soil brightness) and lower reflectance in the NIR. By inverting the NDVI formulation (Table 1), NDSI directly targets salt-encrusted surfaces, producing high values in sabkha and salt-affected zones. Its simplicity and sensitivity to surface salts make it a widely used index in deltaic salinity studies (Figure 5).

#### Brightness-Based Indices (S1, S2, S3, S4).

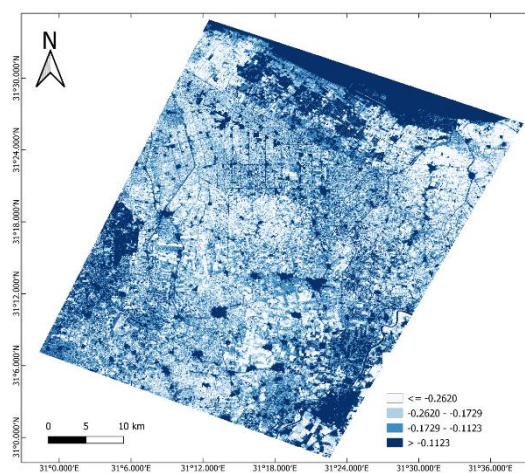


Figure 5 Normalized Difference Salinity Index (NDSI) map identifying salt-affected zones; higher values correspond to increased salinity presence.

Salt-affected soils typically exhibit high reflectance across visible bands, producing elevated S1–S4 values (Table 1). The S1–S4 indices were employed to quantify soil brightness and surface reflectance characteristics associated with salinity. S1 captures overall soil brightness by combining the red and green bands using a Euclidean norm, assigning higher values to bright or salt-encrusted soils and lower values to darker, organic-rich surfaces. Although it may face limitations in sandy terrain, S1 is particularly effective in the silty, dark soils typical of the Nile Delta. S2 quantifies brightness as a geometric mean of red and green reflectance, offering a more balanced sensitivity to vegetated and non-vegetated areas, though it may be influenced by mixed land covers. S3 emphasizes reflectance in the blue and red bands, enhancing detection of salt crusts that strongly reflect in these wavelengths. S4 integrates green, red, and NIR reflectance into a composite brightness index. However, its

reliance on the NIR band can reduce its effectiveness in areas with minimal vegetation,

especially where salinity obscures spectral vegetation signals (Figure 6).

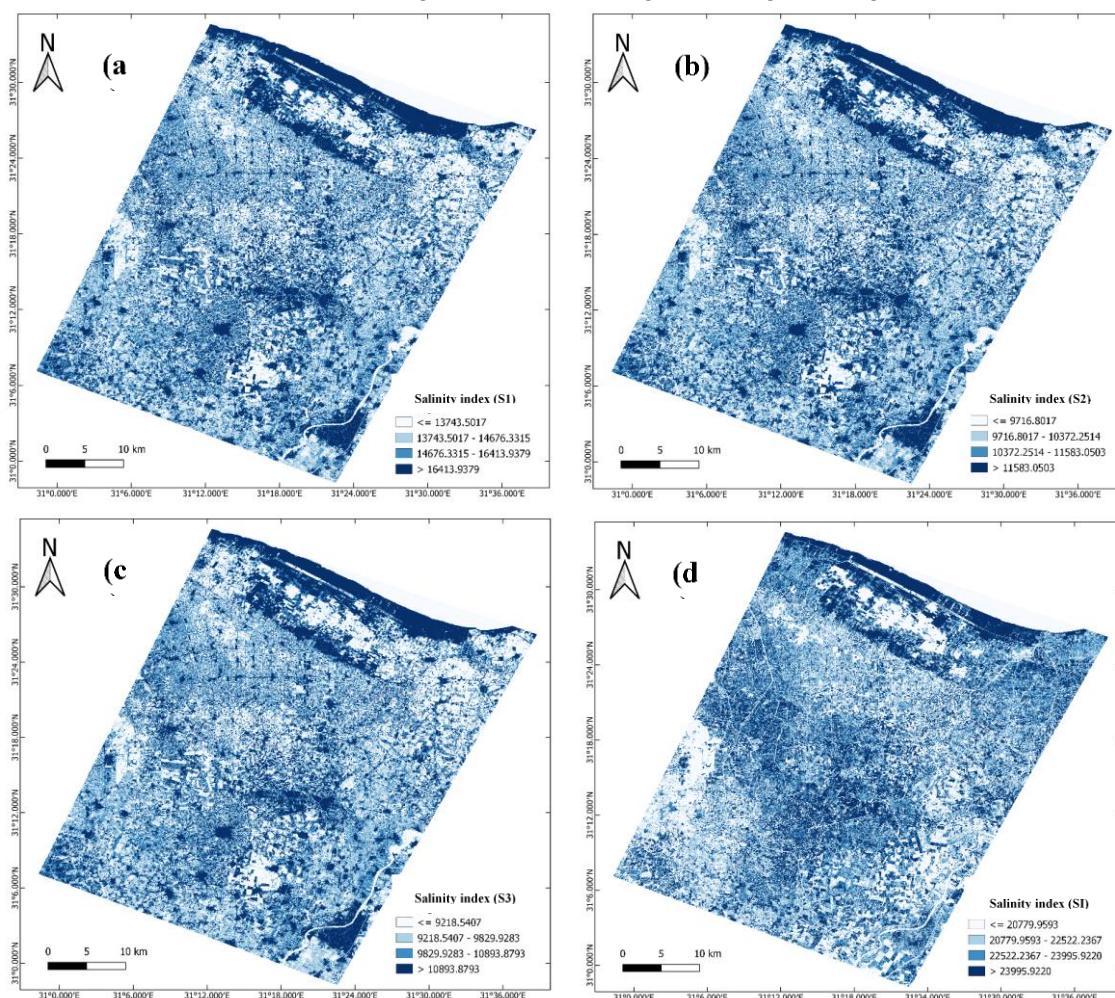


Figure 6 (a) S1 index map capturing soil brightness variations linked to salt crust formation, with lighter areas indicating higher salinity. (b) S2 index map showing enhanced spectral sensitivity to saline soils, useful in detecting sabkha and salt flats. (c) S3 index map highlighting subtle salt-induced brightness changes in coastal soils, aiding in delineation of salinized zones. (d) Salinity Index (S4) map reflecting soil salinity levels based on visible and near-infrared reflectance, with brighter regions suggesting salt accumulation.

#### *Vegetation–Soil Salinity Index (VSSI).*

Proposed by (Dehni & Lounis, 2012), the VSSI integrates spectral responses from both vegetation and bare-soil bands to discriminate between vegetation stress and pure soil brightness Table (1). High negative VSSI values correspond to stressed vegetation over saline soils, whereas less negative values mark healthy vegetation or non-saline soils. In practice, VSSI enhances separation of sabkha from vegetated areas under mixed-cover conditions, improving mapping accuracy along ecotonal transitions Figure (7).

All spectral indices—namely NDVI, NDSI, SI, S1, S2, S3, VSSI, and SAVI—were computed from a single Landsat 8 Operational Land

Imager (OLI) scene acquired in September 2022. Each index was calculated according to its specific spectral formula and saved as a separate raster layer for subsequent analysis. To analyze the spatial trends of salinity indicators, zonal statistics were extracted based on land use/land cover (LULC) classifications derived via unsupervised K-means clustering. This step enabled the computation of mean, minimum, maximum, and standard deviation values for each index within each classified LULC zone. These zonal summaries provided the basis for understanding how salinity-related reflectance patterns varied across different surface types and their spatial relationship to coastal proximity.

The statistical component of the analysis was



conducted in Python (version 3.10), leveraging the libraries pandas, numpy, and rasterio and linregress linear regression from SciPy library for data manipulation and linear regression modeling. For each spectral index, a simple linear regression model was constructed to examine the trend of reflectance values as a function of distance from the coast. This approach was applied independently to each LULC class to account for land cover variability.

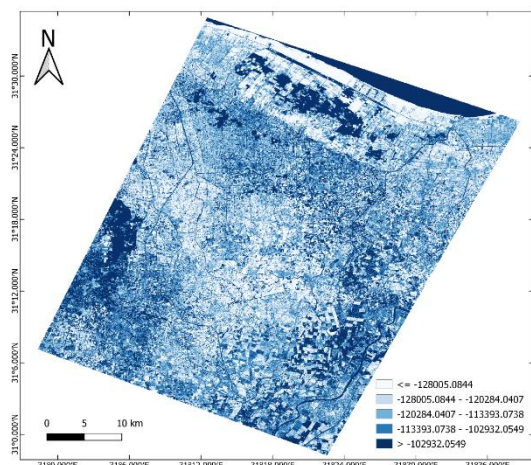


Figure 7 Vegetation–Soil Salinity Index (VSSI) map integrating vegetation and soil responses to effectively distinguish salinity-affected ecotones.

The coefficient of determination ( $R^2$ ) was used for model performance and to determine the significance of the regression slope (p-value). A statistically significant negative or positive slope was interpreted as a potential indicator of increasing or decreasing salinity gradients, respectively, which may be linked to seawater intrusion. The use of linear regression in this context provides a quantifiable measure of spatial salinity trends, building upon its established application in environmental remote sensing (Montgomery, 2013). By integrating QGIS-based spatial processing with Python's robust statistical framework, the methodology ensured a reproducible, transparent, and scalable workflow for coastal salinity assessment.

## Results

This study evaluated the performance of multiple spectral indices in detecting coastal salinization and differentiating saline-affected surfaces, particularly sabkhas, from vegetated areas. Emphasis was placed on the ability of

brightness- and salinity-related indices to capture both absolute salinity and spatial gradients from the shoreline inland.

### Land-Use/Land-Cover Distribution

The unsupervised K-means clustering produced a clear delineation of five land-use/land-cover (LULC) classes across the 50 km profile (Table 2). Vegetation dominates the study area, covering 66.05 % (1,618 km<sup>2</sup>), followed by barren land at 23.70 % (575 km<sup>2</sup>). Water bodies, urban areas, and sabkha account for the remaining 4 % (98 km<sup>2</sup>), 5 % (129 km<sup>2</sup>), and 1 % (30 km<sup>2</sup>), respectively. This distribution reflects the intensive agricultural use of the Nile Delta's fluvial plains, interspersed with salt-flat (sabkha) patches near the coast and expanding urban development in the study area.

Table 2: LULC class area statistics along the study area.

Class	Pixel Count	Area (km <sup>2</sup> )	Percentage (%)
Water	109 309	98.38	4.00
Vegetation	1 798 179	1 618.36	66.05
Barren land	639 383	575.44	23.70
Urban	142 816	128.53	5.32
Sabkha	33 794	30.41	1.19

### Vegetation-Based Indices: NDVI and SAVI

The Normalized Difference Vegetation Index (NDVI) and Soil-Adjusted Vegetation Index (SAVI) both decline markedly in areas affected by salinity stress, yet their sensitivity differs by land cover. In the vegetation class, NDVI values range from −0.105 to 0.530 (mean = 0.200, SD = 0.087), whereas barren land exhibits slightly lower vegetation signals (mean = 0.185, SD = 0.098). Sabkha areas show near-zero NDVI (mean = 0.067, SD = 0.066), reflecting minimal healthy vegetation (Table 3). SAVI amplifies these differences by compensating for low canopy cover: vegetation areas yield a mean SAVI of 0.330 (SD = 0.143), barren land 0.306 (SD = 0.161), and sabkha only 0.111 (SD = 0.109).

Linear regression of NDVI against distance from the shoreline produced a slight negative slope ( $\beta_1 = -1.83 \times 10^{-6} \text{ m}^{-1}$ ;  $p < 0.001$ ), though  $R^2$  was effectively zero, indicating that coastal proximity exerts only a weak influence on canopy greenness across the transect. SAVI regression mirrored this trend ( $\beta_1 = -1.83 \times 10^{-6}$



$m^{-1}$ ;  $p < 0.001$ ), confirming that soil-adjustment does not substantially alter the spatial gradient in vegetation stress under these conditions. These results suggest that while NDVI and SAVI effectively distinguish salinity-impacted vegetation in mixed-cover zones, their spatial trends are muted by irrigation and crop management practices that mitigate coastal salinity effects.

Table 3: NDVI and SAVI statistics by LULC class.

Index	Class	Mean	SD	Min	Max
NDVI	Vegetation	0.2000	0.0869	-0.1051	0.5299
	Barren	0.1852	0.0976	-0.1268	0.5541
	Sabkha	0.0673	0.0662	-0.1168	0.4331
SAVI	Vegetation	0.3300	0.1434	-0.1733	0.8743
	Barren	0.3056	0.1610	-0.2092	0.9142
	Sabkha	0.1110	0.1093	-0.1928	0.7147

### Salinity-Specific Indices: NDSI and Brightness Metrics

The Normalized Difference Salinity Index (NDSI) and brightness-based indices (S1, S2, S3, S4, and SI) exhibited stronger sensitivity to soil salinity than vegetation-based indices. Mean NDSI values were consistently negative, reflecting higher SWIR reflectance relative to NIR—a pattern indicative of salinity presence. Among the land cover classes, sabkha areas recorded the highest (least negative) NDSI values (mean =  $-0.067$ ), followed by water ( $-0.042$ ) and vegetation ( $-0.200$ ), consistent with surface salt accumulation. However, linear regression of NDSI against distance from the shoreline produced negligible slopes ( $\beta_1 \approx 0$ ;  $R^2 < 0.01$ ) (Table 4), suggesting limited capability to capture subtle salinity gradients across mixed land cover and moisture conditions.

Brightness-based indices displayed clearer differentiation among land cover classes. The S1 index showed the strongest contrast, with mean values increasing from 13,222 in vegetated areas to 19,122 in sabkha, accompanied by a moderate standard deviation. This suggests good class separation with limited internal variation, making S1 the most effective indicator of surface salinity under the study area conditions. S2 and S3 indices exhibited similar spatial trends, although S2 may be more sensitive to mixed land covers or transition zones. All three indices showed positive but low-magnitude regression slopes (e.g., S1:  $\beta_1 = 0.1255 \text{ m}^{-1}$ ,  $p < 0.001$ ;  $R^2 < 0.003$ ) (Table 4), suggesting slightly increased soil brightness near the coast.

In contrast, the S4 index displayed high

standard deviation across all classes, indicating substantial internal variability and potential class overlap. Its reliance on the near-infrared (NIR) band may reduce its reliability in highly reflective or mixed-cover environments, consistent with (Douaoui et al., 2006) findings. These results collectively highlight the superiority of the S1 index in detecting surface salinity and differentiating between stressed sabkha and vegetated lands. While indices like NDSI and S2 remain informative, their performance is more susceptible to land cover complexity and soil moisture variability.

Table 4 NDSI and brightness-based index statistics by LULC class.

Index	Class	Mean	SD	Min	Max
NDSI	Vegetation	-0.2000	0.0869	-0.5299	0.1051
	Sabkha	-0.0673	0.0662	-0.4331	0.1168
S1	Sabkha	19 122.40	4 131.03	11 351.48	34 287.72
	Vegetation	13 222.02	2 549.09	9 528.08	30 010.39
S2	Sabkha	13 488.49	2 904.09	8 013.29	24 152.97
	Vegetation	9 334.83	1 799.21	6 737.05	21 188.67
S3	Sabkha	12 509.92	2 503.71	7 666.96	22 256.57
	Vegetation	8 841.66	1 596.32	3 103.01	19 020.99
S4	Sabkha	25 157.34	5 633.83	13 596.55	45 909.51
	Vegetation	16 929.69	4 266.71	13 115.99	37 970.43

### Vegetation–Soil Salinity Index (VSSI)

The Vegetation–Soil Salinity Index (VSSI) exhibits strong class discrimination, with mean values ranging from  $-79 \text{ } 163$  in vegetation to  $-125 \text{ } 610$  in sabkha. More negative VSSI indicates greater vegetation stress over saline soils (Table 5). Despite this clear separation, VSSI's regression slope is effectively zero across all classes, reflecting uniform salinity stress within each LULC category rather than a linear coastal gradient. Nevertheless, VSSI's ability to integrate vegetation and soil reflectance makes it a powerful tool for mapping mixed-cover salinity impacts, especially in ecotonal zones where pure soil or vegetation indices may fail.

Table 5: VSSI statistics by LULC class

Class	Mean	SD	Min	Max
Water	-79163.38	26226.418	-195647	0.5299
Vegetation	-115531.06	14321.255	-215576.25	0.5541
Barren land	-116886.53	14902.781	-242398.83	0.4331
Urban	-122518.195	18939.1	-228510.69	
Sabkha	-125609.83	31828.773	-235678.62	

### Correlation matrix

The correlation matrix of the spectral indices revealed distinct interrelationships that underscore their utility in monitoring soil

salinity and vegetation status (Figure 8). Strong positive correlations were observed between vegetation-based indices, particularly the Normalized Difference Vegetation Index (NDVI) and Soil-Adjusted Vegetation Index (SAVI), which showed a perfect correlation ( $r = 1.00$ ). This reflects their similar mathematical structure and consistent response to green biomass, further confirming that soil brightness is not a major issue in the study area and that both indices can be used interchangeably.



Figure 8 Correlation matrix showing relationships between vegetation, brightness, and composite salinity indices used to assess coastal salinization. Strong contrasts highlight complementary index behavior.

Salinity indices (S1, S2, S3) were also strongly intercorrelated ( $r = 1.00$ ), demonstrating their coherence in capturing salt-affected bare soil across the landscape. S1 in particular exhibited the best class separation with moderate internal variation, supporting its utility as the most effective salinity index under local conditions. The composite salinity index S4, while positively correlated with S1 and S2 ( $r \approx 0.72$ ), showed a high internal standard deviation across land cover classes, indicating substantial within-class variability and reduced discriminatory power—likely due to its dependency on the NIR band, which introduces noise in low-vegetation areas.

The Vegetation–Soil Salinity Index (VSSI) exhibited a strong negative correlation with S4 ( $r = -0.99$ ), further reinforcing its ability to distinguish between vegetated zones and salt-encrusted surfaces. Moderate to strong negative correlations between VSSI and the brightness-based indices (S1–S3,  $r \approx -0.60$ ) further highlight its effectiveness in detecting stressed vegetation under salinity pressure. Overall, the

matrix emphasizes the complementary nature of vegetation and salinity indices and identifies S1 and VSSI as particularly effective for characterizing salinity impacts within the coastal Nile Delta setting.

## Discussion

This study demonstrates that soil salinity from seawater intrusion measurably affects vegetation health and surface reflectance patterns across the Mansoura transect. While vegetation indices (NDVI, SAVI) successfully indicated areas of plant stress, their spatial coherence was limited, likely due to the confounding effects of irrigation and land management. In contrast, brightness-based indices (S1–S3) captured more consistent patterns of increasing soil salinity toward the coastal sabkha. Among these, S1 emerged as the most reliable indicator, offering strong mean separation between sabkha and vegetated zones and moderate internal variability, making it particularly effective under the local soil and moisture conditions. This is due to the dependence on the red and green bands which concentrate on soil brightness and identify the salt patches. Although the area has high moisture content, which was expected to hinder measurement using brightness-based indices, this index performed well due to the dark nature of the soil which allowed for more visibility and contrast of salt. S4, however, showed high standard deviation within each land cover class and poor class discrimination, in line with its known sensitivity to NIR noise.

The Vegetation–Soil Salinity Index (VSSI), by integrating both vegetation and brightness cues, revealed a strong inverse relationship with salinity indices, reinforcing its value in highlighting areas of vegetation loss due to salinity. While VSSI is not a direct salinity proxy, its high negative correlation with salinity indices makes it a powerful complementary tool in mixed-cover landscapes. Although these findings were based on a single Landsat image, they underscore that no single index suffices for brightness indices, especially S1, map salt accumulation in bare areas, while VSSI helps detect vegetative responses to salinity stress. This model is based solely on remotely sensed data without field validation due to lack of funding and equipment at the time of the study. We used previous work and previously

validated indices, some of which were used in the study area to validate our findings.

## Conclusion and Recommendations

Soil salinity induced by seawater intrusion in the northeastern Nile Delta significantly reduces vegetation vigor and alters surface reflectance. Among the tested indicators, S1 provided the clearest separation between sabkha and vegetated zones, demonstrating its effectiveness in identifying salt-encrusted soils. The VSSI proved especially useful in mixed-cover areas, where it helped delineate zones of vegetation stress in response to underlying salinity. While NDVI and SAVI remain valid for vegetation monitoring, they are less reliable in areas affected by variable irrigation or sparse crop cover.

We recommend adopting a complementary index approach: using S1 for soil salinity detection and VSSI for early warning of salinity stress in crops. Routine monitoring with these indices, supported by targeted field surveys and conductivity data, can inform improved drainage, adaptive irrigation, and salt-tolerant crop strategies to sustain productivity in the face of rising salinization. For future work we suggest analyzing the salinity mapping in the area using different satellites imagery (e.g., Sentinel-2) to define the most efficient satellite and indices these results should be compared to field samples or geophysical studies to increase model certainty.

## References:

- Aeman, H., Shu, H., Abbas, S., Aisha, H., & Usman, M. (2023). Sinking delta: Quantifying the impacts of saltwater intrusion in the Indus Delta of Pakistan. *Science of the Total Environment*, 880. <https://doi.org/10.1016/j.scitotenv.2023.163356>
- ALSHRABSY, A. N., Kenawy, A. M., & Mohamed, E. F. (2024). Assessment of Irrigation Water Quality in the Reclaimed Lands in the North of Dakahlia Governorate. *Journal of Soil Sciences and Agricultural Engineering*, 15(3), 51–65. <https://doi.org/10.21608/JSSAE.2024.270005.1217>
- Armanuos, A. M., Gamal, M., Ibrahim, E., Negm, A., Takemura, J., Yoshimura, C., & Mahmod, W. E. (2022). Investigation of Seawater Intrusion in the Nile Delta Aquifer, Egypt. In *Journal of Engineering Research* (Vol. 6, Issue 1). ERJ.
- Azabdaftari, A., & Sunar, F. (2016). SOIL SALINITY MAPPING USING MULTITEMPORAL LANDSAT DATA. The International Archives of the Photogrammetry, Remote Sensing and Spatial Information Sciences, XLI-B7, 3–9. <https://doi.org/10.5194/ISPRS-ARCHIVES-XLI-B7-3-2016>
- Bear, J. (1999). Seawater Intrusion in Coastal Aquifers — Concepts, Methods and Practices - Seawater intrusion in coastal aquifers : concepts, methods, and practices. In *Theory and Applications of Transport in Porous Media: Vol. NA* (Issue NA). <https://doi.org/10.1007/978-94-017-2969-7>
- Cao, X., Chen, W., Ge, X., Chen, X., Wang, J., & Ding, J. (2022). Multidimensional soil salinity data mining and evaluation from different satellites. *Science of the Total Environment*, 846. <https://doi.org/10.1016/j.scitotenv.2022.157416>
- Dehni, A., & Lounis, M. (2012). Remote sensing techniques for salt affected soil mapping: Application to the Oran region of Algeria. *Procedia Engineering*, 33, 188–198. <https://doi.org/10.1016/j.proeng.2012.01.1193>
- Douaoui, A. E. K., Nicolas, H., & Walter, C. (2006). Detecting salinity hazards within a semiarid context by means of combining soil and remote-sensing data. *Geoderma*, 134(1–2), 217–230. <https://doi.org/10.1016/j.geoderma.2005.10.009>
- El Nahry, A. H., Ibraheim, M. M., & El Baroudy, A. A. (2015). ASSESSMENT OF SOIL DEGRADATION IN THE NORTHERN PART OF NILE DELTA, EGYPT USING REMOTE SENSING AND GIS TECHNIQUES. *Remote Sensing and Spatial Information Sciences*. <https://doi.org/10.5194/isprsarchives-XL-7-W3-1461-2015>
- Huete, A. R. (1988). A Soil-Adjusted Vegetation Index (SAVI) 295. In *REMOTE SENSING OF ENVIRONMENT* (Vol. 25).
- Khan, N. M., Rastoskuev, V. V., Shalina, E. V., & Sato, Y. (2001). Mapping Salt-affected Soils Using Remote Sensing Indicators-A Simple Approach With the Use of GIS IDRISI.
- Mansour, M. M. A., & Mark, C. (2025). Land Productivity and Fertility Nexus Study in Dakahlia Governorate Using Gis and Remote Sensing. *Journal of Soil Sciences and Agricultural Engineering*, 16(3), 39–46. <https://doi.org/10.21608/JSSAE.2025.367377.1276>
- Montgomery, D. C. . (2013). Introduction to linear regression analysis. 163. [https://books.google.com/books/about/Introduction\\_to\\_Linear\\_Regression\\_Analysis.html?Id=lsyirzh09oec](https://books.google.com/books/about/Introduction_to_Linear_Regression_Analysis.html?Id=lsyirzh09oec)

- Nguyen, K. A., Liou, Y. A., Tran, H. P., Hoang, P. P., & Nguyen, T. H. (2020). Soil salinity assessment by using near-infrared channel and Vegetation Soil Salinity Index derived from Landsat 8 OLI data: a case study in the Tra Vinh Province, Mekong Delta, Vietnam. *Progress in Earth and Planetary Science*, 7(1), 1–16. <https://doi.org/10.1186/S40645-019-0311-0/FIGURES/11>
- Nofal, E. R., Amer, M. A., El-Didy, S. M., & Fekry, A. M. (2015). Delineation and modeling of seawater intrusion into the Nile Delta Aquifer: A new perspective. *Water Science*, 29(2), 156–166. <https://doi.org/10.1016/j.wsj.2015.11.003>
- Pennington, B. T., Sturt, F., Wilson, P., Rowland, J., & Brown, A. G. (2017). The fluvial evolution of the Holocene Nile Delta. *Quaternary Science Reviews*, 170, 212–231. <https://doi.org/10.1016/j.quascirev.2017.06.017>
- Youssef, Y. M., Gemail, K. S., Atia, H. M., & Mahdy, M. (2024). Insight into land cover dynamics and water challenges under anthropogenic and climatic changes in the eastern Nile Delta: Inference from remote sensing and GIS data. *Science of the Total Environment*, 913. <https://doi.org/10.1016/j.scitotenv.2023.169690>

## الملخص العربي

**عنوان البحث:** تحليل مقارن للمؤشرات الطيفية لتقييم تملح السواحل في شمال شرق دلتا النيل، مصر

ريم علي النجار<sup>١\*</sup>، أيمن طه<sup>٢</sup>، هاني شعبان<sup>٢</sup>، إيمان نوفل<sup>٣</sup>، حاتم أبو الخير<sup>١</sup>

<sup>١</sup>كلية العلوم، جامعة دمياط، ٣٤٥١٧، دمياط، مصر

<sup>٢</sup>المعهد القومي للبحوث الفلكية والجيوفيزيقية، ١١٧٢٢، حلوان، القاهرة، مصر

<sup>٣</sup>معهد بحوث المياه الجوفية، المركز القومي لبحوث المياه، ١٣٦٢١، القناطر الخيرية، مصر

يشكل تملح التربة الناتج عن تغلغل مياه البحر تهديداً متزايداً للزراعة في شمال شرق دلتا النيل، حيث تسهم المياه الجوفية الضحلة وتُظلم الري المكثف في تراكم الأملاح على سطح التربة. تهدف هذه الدراسة إلى رسم خرائط لتوزيع الملوحة السطحية وتأثيرها على الغطاء النباتي على امتداد ٥٠ كيلومتراً من مدينة المنصورة الجديدة حتى مدينة المنصورة، باستخدام بيانات القمر الصناعي Landsat 8 OLI. تم تطبيق تصنيف غير موجه باستخدام خوارزمية K-means لتحديد خمسة أنواع من استخدامات/أغطية الأرض (مياه، نباتات، أراضي جرداء، عمران، سبخة)، ما أتاح حساب ثمانية مؤشرات طيفية لكل فئة: NDVI، SAVI، NDSI، S1-S3، VSSI. استُخدمت الإحصاءات النطاقية لتحليل توزيعات المؤشرات، بينما استخدم الانحدار الخطي لتقييم الاتجاهات المكانية للمؤشرات وفقاً للمسافة من الخط الساحلي. أظهرت مؤشرات الغطاء النباتي NDVI، SAVI قدرة على تمييز الإجهاد النباتي، لكنها لم تُظهر تدرجات ساحلية واضحة ( $\beta_1 \approx -1.8 \times 10^{-6}$ ؛  $R^2 \approx 0$ )، مما يعكس فعالية الري المحلي في التخفيف من آثار الملوحة. أما المؤشرات المعتمدة على السطوح ومؤشر NDSI، فقد رصدت تراكم القشور الملحية بوضوح، حيث ازدادت القيم المتوسطة لمؤشرات S1-S3 من الأراضي الزراعية (١٣,٢٢٢-١٤,٩٧٢) إلى مناطق السبخة (١٩,١٢٢-٢٠,٠٨٠) مع وجود ميل إيجابي طفيف نحو الساحل مثلاً:  $\beta_1$  لمؤشر  $S1 = 0.1255$ ؛  $R^2 < 0.003$ ). وقد أظهر المؤشر الهجين VSSI أعلى قدرة على التمييز بين المناطق النباتية والمناطق المتضررة من التملح (متوسط (٧٩,١٦٣-) مقابل (١٢٥,٦١-) تُظهر هذه النتائج تفاوت حساسية المؤشرات الطيفية تجاه الملوحة والإجهاد النباتي، مما يتيح مراقبة ملوحة التربة بكفاءة وتكلفة منخفضة، وتوجيه التحاليل والمسوح التفصيلية فقط عند الضرورة.

## Structural, Thermal and Transport Properties of 1,2,9-trimethyl-7H-furo[3,2-f]chromen-7-one]

A. M. Melad<sup>\*1,2</sup>, N. A. El- Ghamaz<sup>1</sup> and M. M. El-Shabaan<sup>1</sup>

<sup>1</sup>Department of Physics, Faculty of Science, Damietta University, Damietta 34517, Egypt.

<sup>2</sup>Department of Physics, Faculty of Education, Alzintan University, AL zintan, Libya.

Received: 27 May 2025 /Accepted: 01 July 2025

\*Corresponding author's E-mail: 00afaf.ali00@gmail.com

### Abstract

A coumarine derivative namely 1,2,9-trimethyl-7H-furo[3,2-f]chromen-7-one (TFC) is subjected to investigate thermal, structural, and AC conduction properties. The XRD investigation showed that TFC in powder form is polycrystalline and demonstrates monoclinic crystal system. Thermogravimetric analyses proved that TFC has a good thermal stability from room temperature up to approximately 460 K. furthermore, it undergoes decomposition in one major step in the temperature range 460 – 583 K. Ac and dc electrical conductivity measurements revealed that TFC showed a semiconductor behavior. The thermal activation energy for DC conductivity  $\Delta E_{dc}$  are found to be 0.0576 and 0.617 eV in the low and high temperature regions, respectively. The analyses of AC conductivity as a function of temperature and frequency revealed that the correlated barriers hopping (CBH) conduction mechanism is the dominant mechanism for conduction of charge carriers in TFC. The related parameters for the CBH are calculated.

**Keywords:** Coumarine, XRD, thermal properties, AC conductivity, electrical modulus, Correlated barrier hopping (CBH)

### Introduction

Among organic materials is Coumarin family which is naturally occurring organic compound. Coumarin derivatives are utilized in various fields like medicine, dyes, and fluorescence (P n.d.; Sontisiri et al. 2025; Sun et al. 2020). Coumarin was first isolated in 1820 (Sarker and Nahar 2017). Coumarin and its derivatives have gained considerable attention for decades

because of their wide range of applications in Pharmacology (Barot et al. 2015; Kadhum et al. 2011; Xu et al. 2021) and biological activity (Mohammed and Ahamed 2022).

Researches continue to produce new coumarin derivatives and providing insights into how modifications can enhance their functionality and effectiveness in biological systems (Detsi, Kontogiorgis, and Hadjipavlou-Litina 2017). Also, the change of substituent group certainly will affect thermal properties of coumarins. This effect appeared obviously in the

derivatives of 2-[(4-Methyl-2-oxo-2H-chromen-7-yl)oxy]-N'-(substitutedmethylene) where the melting point is varied from 252°C to 298°C (Satyanarayana et al. 2009). Many coumarin derivatives showed photoluminescence and electroluminescence properties (Kotchapadist et al. 2015; Pramod, Renuka, and Nadaf 2019). The presence of these properties strongly recommend coumarin derivatives in optoelectronic application such as OLEDs (Goel et al. 2012; Kumar, Puttaraju, and Patil 2016). Also, some coumarin derivatives have been investigated as temperature thermometer in polymer-supported materials (Pedro et al. 2023).

Kotchapadist et al. reported that, N-Coumarin derivatives demonstrated thermal stability up to a temperature of about 400 °C and recommended these derivatives for OLED due to the precast of emission spectra in the visible region of spectra. The emission properties of these N-Coumarin derivatives have been tuned by varying thiophene units in the conjugated backbone or changing the type of substituent (Kotchapadist et al. 2015).

To our knowledge, there is no direct investigation concerning the ac conductivity properties of natural or synthetic Coumarins. In this study we aimed to extract information about the thermal stability of new synthesized coumarine derivative as well as its structural and electrical properties arriving to the possible conduction mechanisms, which can help in propose these compounds under investigation for the suitable technological applications.

## Experimental

### Materials

In the present study, one of the coumarine derivatives which is 1,2,9-trimethyl-7H-furo[3,2-f]chromen-7-one (TFC) (Elgogary, Hashem, and Khodeir 2015) is subjected to investigation without any further treatment. The chemical structure of TFC shown in Fig.1.

### Thermal Analysis

Thermo gravimetric analysis (TGA) and differential scanning calorimetric (DSC) measurements are recorded by (Simultaneous Thermal Analyzers DSC/TGA, TA Instruments STD Q600) in the temperature range 300 - 650

K. °

### X-ray Diffraction Analysis

The crystal structure of TFC in powder form is investigated by using X-Ray diffraction (XRD) technique and recorded by "D2 phaser company bruker, Germany" X-ray diffractometer having Cu as a target. The Ni-filtered CuK<sub>α</sub> radiation of wavelength ( $\lambda = 1.5406 \text{ \AA}$ ) is used. The X-ray tube's voltage and current were 30 kV and 10 mA, respectively. The experimental results are analyses using fullprof software (Dinnebier n.d.; Lin et al. 2008), and optimized by Chekcell software (Tan and Shaari 2008).

### Alternating current (AC) measurements

The AC measurements are carried out by the programmable automatic RLC bridge model Hioki 3532-50 LCR Hi Tester, in the frequency range from 100 Hz to 1 MHz and temperature range 300 - 443 K. The powder of TFC is compressed to form pellets under a pressure of 5 tons/cm<sup>2</sup>. The resulting pellets have a diameter of 1.2 cm and a thickness of about 1 mm. The samples are placed in a holder specially designed to minimize stray capacitance. The temperature of the sample is monitored during the measurements by using a NiCr-NiAl thermocouple. All measurements are done in dark and in air.

## Results and Discussion

### Thermal

The TGA and DTG curves for TFC, in the temperature range 300 – 650 K are presented in Figs.2 and 3. The curves prove a good thermal stability from room temperature up to approximately 460 K. It is noticed that TFC is undergo decomposition in one major step in the temperature range 460 – 583 K with a maxima transition temperature of 581 K (see Fig.3). Fig.4 presents the DSC charts of TFC in the temperature range 300 – 650 K. It is found that, the first endothermic peaks for TFC is in the range 473 – 492 K. Taking into account that, there is no loss of mass occurs up to this temperatures range, it can be confirmed that all these endothermic peaks can be attributed to the melting process at melting temperature ( $T_m$ ). The values of  $T_m$  can be extracted from DSC

curve and found to be about 500K. This result is confirmed by visual observation by melting apparatus. The last endothermic peaks in the DSC curves for TFC is positioned at the same temperature of this maximum transition temperature which extracted from DTG (see Fig 3). Taking this observation into account, the phase transition process at temperature 585 TFC can be attributed to boiling process at boiling temperature ( $T_b$ ). As a conclusion, and TFC is thermally stable up to the 500 K. This result recommend the suitable temperature range of studying the dielectric properties and conductivity to be in the range from room temperature to temperature below the melting temperature ( $T_m$ ). At this point, it is worth to replace the expiration “decomposition” in TGA analyses at the temperature range 555-581 K with the term “loss of mass by evaporation due to boiling process”.

#### X-ray diffraction (XRD)

The XRD patterns of TFC in the diffraction angle range  $2\theta = 4 - 70^\circ$  is illustrated in Fig.5. The XRD pattern is characterized by many sharp peaks which confirm the polycrystalline nature of TFC in the powder form. Crystal structure system, lattice parameters and Miller indices ( $hkl$ ) of the investigated compounds are obtained by fullprof software (Dinnebier n.d.; Lin et al. 2008), and optimized by Chekcell software (Tan and Shaari 2008). It is found that the TFC has monoclinic crystal system with optimized space group  $P1_2/m$ . All mentioned parameters are computed and summarized in Tables 1 and 2.

The average crystallite size  $D$  can be calculated using the following well known Scherre's equation(El-Ghamaz, Moqbel, and El-Shabaan 2020):

$$D = \frac{m\lambda}{\beta_{hkl} \cos\theta_{hk}}, \quad (1)$$

where  $\beta_{hkl}$ . Is the full width at half maximum in radians,  $\lambda$  is the wavelength of the incident x-ray ( $\lambda=1.5406 \text{ \AA}$ ) and  $\theta_{hkl}$  the diffraction angle of the peak with miller indices  $hkl$ . Also the dislocation density  $\delta$  and the micro strain  $\mu$  can be calculated using the following relations (Correlation between ionic radii of metal azodye complexes and electrical conductivity n.d.; El-Nahass et al. 2008)

$$\delta = \frac{1}{D^2} \quad (2)$$

$$\mu = \frac{\beta_{hkl} \cos\theta_{hkl}}{4} \quad (3)$$

The values of  $D$ ,  $\delta$  and  $\mu$  is calculated and listed in Table 3.

#### Dielectric properties

##### Electrical Modulus

The dielectric modulus  $\tilde{M}$  defined as the inverse of the complex permittivity  $\tilde{\epsilon}$  and is a concept used in the study of dielectric materials practically in analyzing relaxation processes and conductivity. The complex dielectric constant  $\tilde{\epsilon}$  can be expressed by the following relation (Conducting Polymers. VII. Effect of Doping with Iodine on the Dielectrical and Electrical Conduction Properties of Polyaniline n.d.):

$$\tilde{\epsilon} = \epsilon_1 - i\epsilon_2 \quad (4)$$

where  $\epsilon_1$  is the real part and  $\epsilon_2$  is the imaginary part of the dielectric constant.  $\epsilon_1$  and  $\epsilon_2$  are calculated by using the following relations (Dielectrical properties and conduction mechanism of quinoline Schiff base and its complexes n.d.; El-Nahass and Ali 2012):

$$\epsilon_1 = C \frac{d}{\epsilon_0 A} \quad (5)$$

$$\epsilon_2 = \epsilon_1 \tan\delta \quad (6)$$

where  $\epsilon_0$  is the permittivity of the free space,  $C$  is the measured capacitance and  $\tan\delta$  is the measured dissipation factor of the three compound in the tablet form. Also, the complex electric modulus,  $\tilde{M}$  given by the following relation (Jung 2013):

$$\tilde{M} = M_1 + i M_2 \quad (7)$$

where  $M_1$  and  $M_2$  are the real and imaginary parts of the electric modulus respectively, and can be calculated from the dielectric constant using the following relations (El-Nahass and Ali 2012):

$$M_1 = \frac{\epsilon_1}{\epsilon_1^2 + \epsilon_2^2} \quad (8)$$

$$M_2 = \frac{\epsilon_2}{\epsilon_1^2 + \epsilon_2^2} \quad (9)$$

The obtained values of  $M_1$  and  $M_2$  for TFC as a function of frequency are depicted in Figs. 6 and 7, respectively. In the low frequency region, the values of  $M_1$  tends to zero. This behavior suggests that the compound TFC exhibit minimal polarization or motion at these frequencies. This behavior is typical in materials that may not have yet reached their



characteristic response times which are needed to effectively transition through energy states (Barsoukov and Macdonald 2005). The more increase of test frequency, the more increase of  $M_1$  as seen in Fig. 6. This behavior could be due to the enhancement of polarization of the TFC, as higher frequencies enable more active molecular dynamics and dipole orientations contributing to the overall dielectric response (Liu, Cole, and Low 2013). The spectra of  $M_1$  demonstrate a peak around 1000 Hz which is shifted toward higher frequency with increasing temperature. It is often attributed to thermal activation of charge carriers (Bose and Sarma n.d.). As temperature rises, molecular motion increases, allowing the materials to respond to oscillating electric fields with higher frequency, thus shifting the peak to higher frequencies (Jonscher 1999).

Fig. 7 shows the variation of  $M_2$  with frequency for TFC. It is noticed that, a typical relaxation peak that moves towards higher frequencies by increasing temperature. The presence of a typical relaxation peak indicates that the materials exhibit a relaxation process that is sensitive to frequency. As temperature increases, this peak shifts towards higher frequencies, suggesting that the molecular dynamics become faster at elevated temperatures (El-Ghamaz, Moqbel, and El-Shabaan 2020; Yu et al. 2017). The characteristic relaxation time is calculated by inverse of frequency of the maximum position, i.e.,  $\tau = 1/f_{max}$ . The variation of  $\tau$  with temperature of TFC is calculated and depicted in Fig. 7. It is clear that the behavior of relaxation time is affected by the temperature and shows decreasing trend in general and has a peak value at about 348 K (El-Nahass, El-Barry, and Abdel Rahman 2006; Jung 2013; Yu et al. 2017).

### Electrical conductivity

The AC (alternating current) electrical conductivity is critically important in material science. It provides insight into the behavior and properties of material especially under alternating electric field and give information about how charge carriers move through a material. The AC electrical conductivity ( $\sigma_{ac}$ ) can be calculated using the following relation (Dielectrical properties and conduction mechanism of quinoline Schiff base and its complexes n.d.):

$$\sigma_{ac} = \epsilon_0 \omega \epsilon_2 \quad (10)$$

where  $\omega$  is the angular frequency ( $\omega = 2\pi f$ ,  $f$  is the frequency). The temperature dependence of conductivity can be discrepant by the following archaic relation (Effect of Doping with Nickel Ions on the Electrical Properties of Poly(aniline-co-oanthranilic acid) and Doped Copolymer as Precursor of NiO Nanoparticles. In: Foxit. <https://www.foxit.com/pdf-to-word/n.d.>).

$$\sigma_{ac} = \sigma_0 \exp\left(\frac{-\Delta E_{ac}}{k_B T}\right) \quad (11)$$

where  $\sigma_0$  is the pre-exponential factor and  $\Delta E$  is the activation energy for AC conductivity,  $k_B$  is Boltzmann's constant, and  $T$  is the absolute temperature. The relation between  $\sigma_{ac}$  and  $1000/T$  for different test frequency is presented in Fig. 8. It is noticed that  $\sigma_{ac}$  demonstrate semiconductor behavior. The thermal activation  $\Delta E_{ac}$  can be obtained from the slope of the straight line segments in the low and high temperature regions respectively. Fig. 9 (a,b) presents the relation of frequency dependence of  $\Delta E_{ac(1)}$  and  $\Delta E_{ac(2)}$  for TFC in the temperature rang 303 – 385 K and 385 – 440 K, respectively. The value of  $\Delta E_{dc}$  can be determined from the relation between  $\ln \sigma_{ac}$  versus  $1000/T$  for  $f = 0$  Hz (see Fig. 8). The values of  $\Delta E_{dc(1)}$  and  $\Delta E_{dc(2)}$  are found to be 0.0576 and 0.617 eV, respectively. The relatively low values of  $\Delta E_{ac(1)}$ , suggests that the conduction process of charge carries can be described by hopping mechanism (Effect of Doping with Nickel Ions on the Electrical Properties of Poly(aniline-co-oanthranilic acid) and Doped Copolymer as Precursor of NiO Nanoparticles. In: Foxit. <https://www.foxit.com/pdf-to-word/n.d.>). Furthermore, in the higher temperature range, the obtained values of  $\Delta E_{ac(2)}$  suggest that the conduction of charge carries can be described by thermal activation process.

The AC conductivity ( $\sigma_{ac}$ ) can be described as a function of frequency according to the following relation (Elliott 1987).

$$\sigma_{ac} = A \omega^S \quad (12)$$

where,  $A$  is a constant depending on temperature and  $S$  is the frequency exponent that its behavior with temperature indicates give information about the most probably conduction mechanism (Dielectrical properties and conduction mechanism of quinoline Schiff base and its complexes n.d.). Fig 10. Presents,  $\ln \sigma_{ac}$  as a function of  $\ln \omega$  in the temperature range 303 - 443 K for TFC. It is observed that

$\sigma_{ac}$  increases with the increase of frequency in all the frequency range under test. Also, it is observed that, all curves show two different slopes in the low and high regions of frequency. The value of  $S$  is directly the slope at the higher frequency region. The value of  $S$  is obtained and presented as a function of temperature in Fig 11. The value of  $S$  show a continuous decrease with the increase of temperature. This behavior confirms that the correlated barrier hopping (CBH) mechanism to be the operating condition mechanism. Similar behavior has been recorded for many organic compounds in which the CBH conduction mechanism were proposed as the operating conduction mechanism (N. A. El-Ghamazl and E. n.d.; Yu et al. 2017). In CBH model,  $\sigma_{ac}$  is given by the following relation (Bose and Sarma n.d.; Effect of Doping with Nickel Ions on the Electrical Properties of Poly(aniline-co-oanthranilic acid) and Doped Copolymer as Precursor of NiO Nanoparticles. In: Foxit. <https://www.foxit.com/pdf-to-word/n.d.>):

$$\sigma_{ac} = \frac{1}{24} \pi^3 N^2 \varepsilon_1 \varepsilon_0 \omega R_{\omega}^6 \quad (13)$$

where  $N$  is the density of pairs of sites, and  $R_{\omega}$  is the hopping distance which can be deduced at angular frequency  $\omega$ .  $R_{\omega}$  is evaluated as follows (El-Nahass, El-Barry, and Abd el Rahman 2006; Geometrical structures, thermal, optical and electrical properties of azo quinoline derivatives n.d.):

$$R_{\omega} = \frac{e^2}{\pi \varepsilon_1 \varepsilon_0 [W_m + kT \ln(\omega \tau_0)]} \quad (14)$$

where  $W_m$  is the maximum barrier height (the energy required moving the electron from a site to infinity and  $\tau_0$  is the relaxation time with frequency, the  $\omega R_{\omega}^6$  component in the CBH model represents frequency dependency and may be represented in terms of the frequency exponent  $S$  as shown below:

$$S = 1 - \frac{6k_B T}{W_m - kT \ln(1/\omega \tau_0)} \quad (15)$$

Which can be approached to the following relation:

$$S = 1 - \frac{6k_B T}{W_m} \quad (16)$$

As a consequence, the CBH expects a temperature-dependent exponent,  $S$ , to reduce when the temperature rises and escalates to unity when the temperature declines to zero kelvin.

The maximum barrier height  $W_m$  is determined as 2.49 eV. The values of  $\tau_0$ ,  $r_m$ ,  $N$ , For TFC are

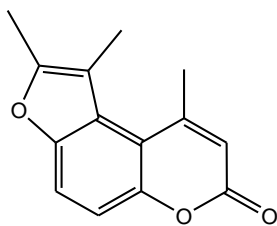
determined in different temperature and listed in Table 4.

## Conclusion

1,2,9-trimethyl-7*H*-furo[3,2-*f*]chromen-7-one] (TFC) is one of coumarin derivatives that showed good thermal stability from room temperature up to approximately 460 K. It decomposed in one major step with maximum decomposition rate at 581 K. The powder of TFC is polycrystalline and has a monoclinic crystal structure with lattice parameters 13.446 Å, 4.566 Å, 10.557 Å, 90°, 90.62° and 90° for  $a$ ,  $b$ ,  $c$ ,  $\alpha$ ,  $\beta$  and  $\gamma$ , respectively. The average crystallite size was estimated to be 506 nm. The study of the dielectric modulus proved that TFC exhibits minimum polarization at low frequency. The polarization is enhanced with the more increase of applied test frequency which enables more active molecular dynamics and dipole orientation contributing to the overall dielectric response. In general TFC showed semiconductor behavior in the temperature range 303- 440 K. the investigation of conduction mechanism confirmed that the correlated barrier hopping (CBH) mechanism is the operating conduction mechanism for AC conductivity.

## Objectives

Computational methods can be employed to provide valuable molecular information for these coumarin derivatives. Therefore, the principal objective of this work was to investigate the structure, electronic and optical properties of these same derivatives (Lin et al. 2008) in order to establish the relationship between the chemical substitutions and computed molecular properties to aid in the design of materials with potential optoelectronic applications.



1,2,9-trimethyl-7H-furo[3,2-f]chromen-7-one(TFC)  
Fig.1 The molecular structural for TFC.

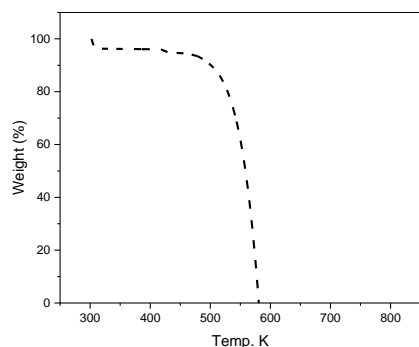


Fig. 2: The TGA curves for TFC.

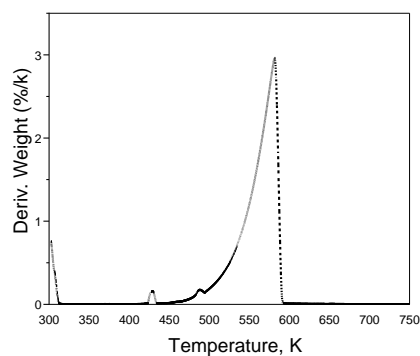


Fig. 3. The DTG curve for TFC.

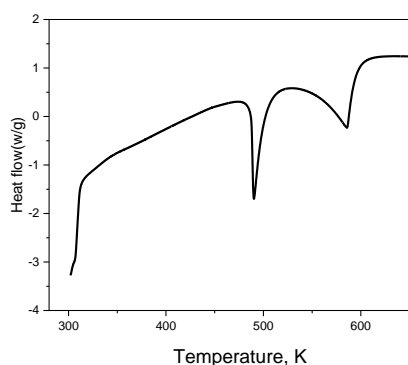


Fig. 4 .The DSC curve for TFC.

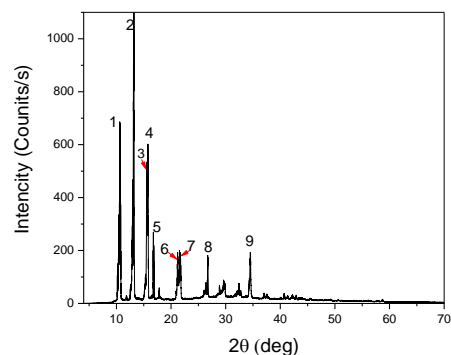


Fig. 5. The XRD patterns for TFC.

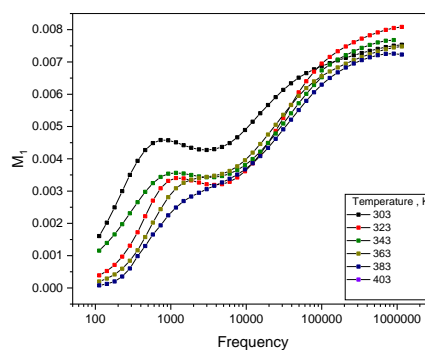


Fig. 6. Frequency dependence of the electric modulus,  $M_1$ , for TFC at different temperatures.

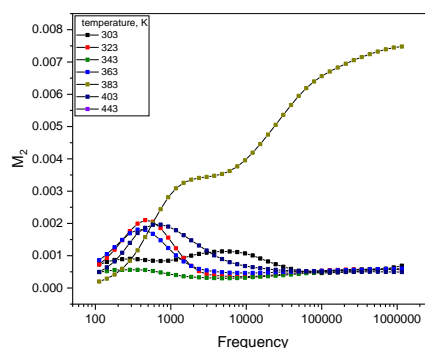


Fig. 7. Frequency dependence of the electric modulus,  $M_2$ , for TFC at different temperatures.

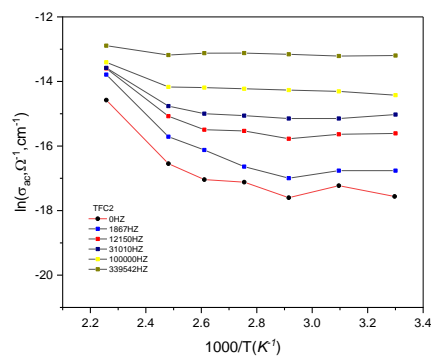


Fig.8.  $\text{Ln}\sigma_{ac}$  as a function of  $1000/T$  for TFC.

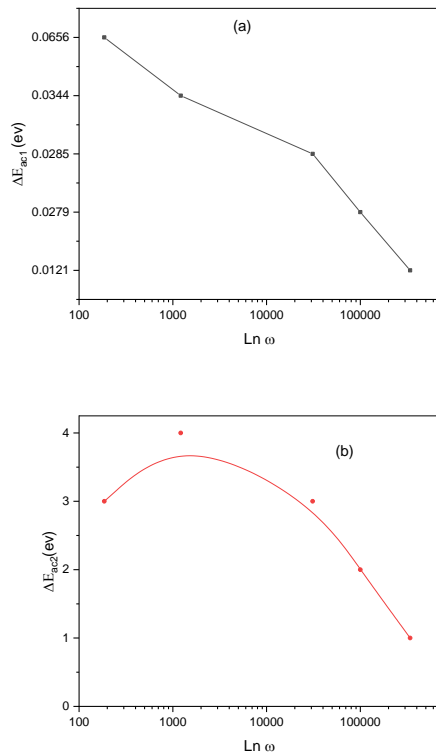


Fig. 9. (a) Temperature dependence of  $\Delta E_{ac1}$  and  $\Delta E_{ac2}$  respectively for FTC at different frequencies.

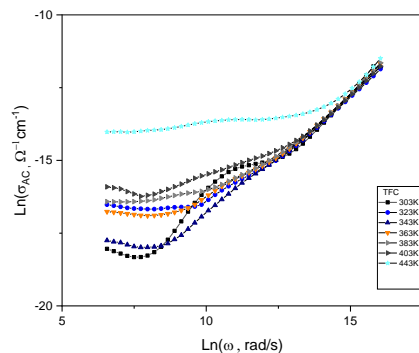


Fig 10.  $\ln \sigma_{ac}$ . Versus  $\ln \omega$  for TFC.

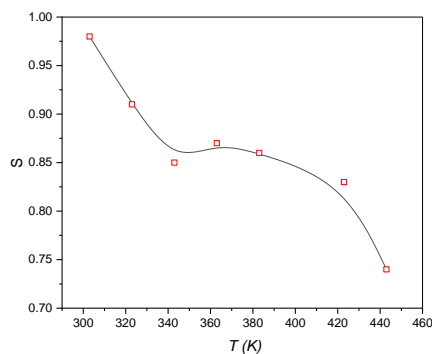


Fig.11. the temperature dependence of  $S$  for TFC.

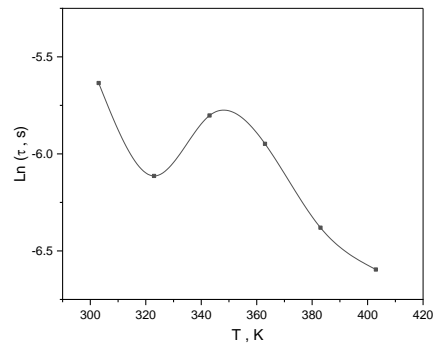


Fig.12  $\ln(\tau, s)$  as a function of  $T$  for TFC.

Table1.The indexed Miller indices ( $h k l$ ) and in inter-planer spacing ( $d_{hkl}$ ) for TFC.

Selected reflections						
Peak No.	$h k l$	$d_{hkl}$	$2\theta_{obs}$	$2\theta_{cal}$	$\Delta(2\theta)$	
1	1 0 1	8.2590	10.6470	10.7024	-0.0554	
2	2 0 0	6.7083	13.1591	13.1592	-0.0001	
3	2 0 1	5.6894	15.5783	15.5378	0.0405	
4	2 0 1	5.6370	15.7396	15.6919	0.0477	
5	0 0 2	5.2820	16.7894	16.7835	0.0059	
6	0 1 1	4.1837	21.2021	21.1833	0.0188	
7	3 0 1	4.1034	21.6428	21.6079	0.0349	
8	1 1 2	3.3360	26.7225	26.6766	0.0459	
9	$\bar{1}$ 0 4	2.5963	34.5080	34.5359	-0.0279	

Table 2. The lattice parameters ( $a, b, c, \alpha, \beta$  and  $\gamma$ ) and crystal system for TFC.

parameters	TFC
Crystal system	Monclinc
$a$ (Å)	13.4460
$b$ (Å)	4.5660
$c$ (Å)	10.5570
$\alpha$ (deg)	90.000
$\beta$ (deg)	90.62
$\gamma$ (deg)	90.000
Space group	$P1_2/m$
$D$ (nm)	506.21
$\delta$ (m) $^{-2} \times 10^{12}$	3.9
$\mu \times 10^{-3}$	0.68

Table 3. The value of  $D, \delta$  and  $\mu$  for TFC.

parameters	TFC
$D(nm)$	506.21
$\delta(m)^{-2} \times 10^{12}$	3.9
$\mu \times 10^{-3}$	0.68

Table 4. The  $W_m$  is the maximum barrier height, the  $\tau_o$  is characteristic relaxation time,  $N$  expects a temperature-dependent exponent,  $r_m$  represents frequency, for TFC.

Compound	TFC	$W_m(eV) = 2.49 \text{ eV}$		
T K	F HZ	$\tau_o \times 10^{-3}$	$r_m \times 10^{-11} m$	$N \times 10^{31} \text{ ev/m}^3$
303	280	3.5714	1.5675	6.3237
323	452	2.2123	1.6648	5.1750
343	331	3.0211	1.5907	6.0459
363	383	2.6109	1.5568	6.5111
383	590	1.6949	1.5139	6.9906
403	732	1.3661	1.4804	7.1834

## References

- Barot, Kuldipsinh P., Shailesh V. Jain, Laurent Kremer, Shubhra Singh, and Manjunath D. Ghatge. 2015. "Recent Advances and Therapeutic Journey of Coumarins: Current Status and Perspectives." *Medicinal Chemistry Research* 24(7): 2771–98. doi:10.1007/s00044-015-1350-8.
- Barsoukov, Evgenij, and J. Ross Macdonald. 2005. *Impedance Spectroscopy Theory, Experiment, and Applications*. Hoboken, N.J: Wiley-Interscience.
- Bose, K. S., and R. H. Sarma. "Dielectrical Properties and Conduction Mechanism of Quinoline Schiff Base and Its Complexes." *N. A. El-Ghamaz1 • A. A. El-Bindary2 • M. A. Diab2 • A. Z. El-Sonbati2 • S. G. Nozha2* 66(4). doi:10.1007/s11164-015-2164-5.
- "Conducting Polymers. VII. Effect of Doping with Iodine on the Dielectrical and Electrical Conduction Properties of Polyaniline." *Foxit*. www.tandfonline.com/lrst. (September 2, 2024).
- "Correlation between Ionic Radii of Metal Azodye Complexes and Electrical Conductivity." *Foxit*. m.adiab@yahoo.com (M.A. Diab).
- Detsi, Anastasia, Christos Kontogiorgis, and Dimitra Hadjipavlou-Litina. 2017. "Coumarin Derivatives: An Updated Patent Review (2015-2016)." *Expert Opinion on Therapeutic Patents* 27(11): 1201–26. doi:10.1080/13543776.2017.1360284.
- "Dielectrical Properties and Conduction Mechanism of Quinoline Schiff Base and Its Complexes." *Foxit*. A. Z. El-Sonbati elsonbatisch@yahoo.com (September 2, 2024).
- Dinnebier, R. "From the Editor of Newsletter 32." Effect of Doping with Nickel Ions on the Electrical Properties of Poly(aniline-co-oanthranilic acid) and Doped Copolymer as Precursor of NiO Nanoparticles. In: *Foxit*. https://www.foxit.com/pdf-to-word/. "Effect of Doping with Nickel Ions on the Electrical Properties of Poly(Aniline-Co-Oanthranilic Acid) and Doped Copolymer as Precursor of NiO Nanoparticles. In: *Foxit*. https://www.foxit.com/pdf-to-word/." Effect of Doping with Nickel Ions on the Electrical Properties of Poly(aniline-co-oanthranilic acid) and Doped Copolymer as Precursor of NiO Nanoparticles. In: *Foxit*. https://www.foxit.com/pdf-to-word/.
- El-Ghamaz, N. A., M. S. Moqbel, and M. M. El-Shabaan. 2020. "Theoretical and Experimental Studies on Structural and Optical Properties of Two Quinoxaline 1,4dioxide Derivatives." *Journal of Materials Science: Materials in Electronics* 31(24): 22012–27. doi:10.1007/s10854-020-04703-x.
- Elgogary, Sameh Ramadan, Neveen Mohamed Hashem, and Mohamed Nabeel Khodeir. 2015. "Synthesis and Photooxygenation of Linear and Angular Furocoumarin Derivatives as a Hydroxyl Radical Source: Psoralen, Pseudopsoralen, Isopseudopsoralen, and Allopsoralen." *Journal of Heterocyclic Chemistry* 52(2): 506–12. doi:10.1002/jhet.2084.
- Elliott, S.R. 1987. "STUDY THE ELECTRICAL PROPERTIES AND AC CONDUCTIVITY OF OURE PMMA AND PMMA DOPED WITH AZO DYE." *International Journal of Physics* 36(2): 135–217. doi:editor@tjprc.org.
- El-Nahass, M. M., A. A. Atta, H. E. A. El-Sayed, and E. F. M. El-Zaidia. 2008. "Investigations on Growth, XRD, Strain, FTIR, UV–Vis NIR, Photoluminescence, SHG, and Z-Scan Analyses of L-Cysteine Picrate Single Crystal for NLO and Optical Limiting Applications." *Applied Surface Science* 254(8): 2458–65.
- El-Nahass, M. M., A. M. A. El-Barry, and S. Abd el Rahman. 2006. "Ac Conductivity and Dielectric Properties of TlIn 0.975 Y 0.025 S 2 Single Crystal." *physica status solidi (a)* 203(2): 317–26. doi:10.1002/pssa.200521304.
- El-Nahass, M.M., and H.A.M. Ali. 2012. "AC Conductivity and Dielectric Behavior of Bulk Furfurylidenemalononitrile." *Solid State Communications* 152(12): 1084–88. doi:10.1016/j.ssc.2012.03.002.
- "Geometrical Structures, Thermal, Optical and Electrical Properties of Azo Quinoline Derivatives." *Foxit*. www.elsevier.com/locate/molliq.
- Goel, Atul, Vijay Kumar, Salil P. Singh, Ashutosh Sharma, Sattey Prakash, Charan Singh, and R. S. Anand. 2012. "Non-Aggregating Solvatochromic Bipolar Benzo[f]Quinolines and Benzo[a]Acridines for Organic Electronics." *Journal of Materials Chemistry* 22(30): 14880–88. doi:10.1039/C2JM31052J.
- Jonscher, Andrew K. 1999. "Dielectric Relaxation in Solids." *Journal of Physics D: Applied Physics* 32(14): R57–70. doi:10.1088/0022-3727/32/14/201.
- Jung, Woo-Hwan. 2013. "Dielectric Relaxation and Hopping Conduction in La 2 NiO 4+ δ." *Journal of Materials* 2013: 1–6. doi:10.1155/2013/169528.
- Kadhum, Abdul Amir H., Ahmed A. Al-Amiery, Ahmed Y. Musa, and Abu Bakar Mohamad. 2011. "The Antioxidant Activity of New Coumarin Derivatives." *International Journal of Molecular Sciences* 12(9): 5747–61. doi:10.3390/ijms12095747.
- Kotchapadist, Palita, Narid Prachumrak, Thitiya Sunonnam, Supawadee Namuangruk, Taweesak

- Sudyoadsuk, Tinnagon Keawin, Siriporn Jungsuttiwong, and Vinich Promarak. 2015. "Synthesis, Characterisation, and Electroluminescence Properties of N-Coumarin Derivatives Containing Peripheral Triphenylamine." *European Journal of Organic Chemistry* 2015(3): 496–505. doi:10.1002/ejoc.201402680.
- Kumar, Shiv, Boregowda Puttaraju, and Satish Patil. 2016. "A Deep-Blue Electroluminescent Device Based on a Coumarin Derivative." *ChemPlusChem* 81(4): 384–90. doi:10.1002/cplu.201500572.
- Lin, Hsiu-Chen, Shin-Hui Tsai, Chien-Shu Chen, Yuan-Ching Chang, Chi-Ming Lee, Zhi-Yang Lai, and Chun-Mao Lin. 2008. "Powder3D: An Easy to Use Program for Data Reduction and Graphical Presentation of Large Numbers of Powder Diffraction Patterns." *Biochemical Pharmacology* 75(6): 1416–25. doi:10.1016/j.bcp.2007.11.023.
- Liu, Xiaogang, Jacqueline M. Cole, and Kian Sing Low. 2013. "Conducting Polymers. VI. Effect of Doping with Iodine on the Dielectrical and Electrical Conduction Properties of Polyacrylonitrile." *The Journal of Physical Chemistry C* 117(28): 14731–41. doi:10.1021/jp310397z.
- Mohammed, Ali Y., and Luma S. Ahamed. 2022. "Synthesis and Characterization of New Substituted Coumarin Derivatives and Study Their Biological Activity." *Chemical Methodologies* (Online First). doi:10.22034/CHEMM.2022.349124.1569.
- N. A. El-Ghamazl and E., Hajer Abusnina. *AC Electrical Properties, Thermal Analysis and Emission Spectrum of Chitosan Polymer*.
- P, Jigar L. *The Introduction of Coumarin*. Blue Rose Publishers.
- Pedro, Gonçalo, Frederico Duarte, Dmitrii A. Cheptsov, Nikita Yu Volodin, Ivan V. Ivanov, Hugo M. Santos, Jose Luis Capelo-Martinez, et al. 2023. "Exploring Coumarin-Based Boron Emissive Complexes as Temperature Thermometers in Polymer-Supported Materials." *Sensors* 23(3): 1689. doi:10.3390/s23031689.
- Pramod, A. G., C. G. Renuka, and Y. F. Nadaf. 2019. "Electronic Structure, Optical Properties and Quantum Chemical Investigation on Synthesized Coumarin Derivative in Liquid Media for Optoelectronic Devices." *Journal of Fluorescence* 29(4): 953–68. doi:10.1007/s10895-019-02409-w.
- Sarker, Satyajit D., and Lutfun Nahar. 2017. "Progress in the Chemistry of Naturally Occurring Coumarins." In *Progress in the Chemistry of Organic Natural Products 106*, eds. A. Douglas Kinghorn, Heinz Falk, Simon Gibbons, and Jun'ichi Kobayashi. Cham: Springer International Publishing, 241–304. doi:10.1007/978-3-319-59542-9\_3.
- Satyanarayana, V. S. V., P. Sreevani, Amaravadi Sivakumar, and V. Vijayakumar. 2009. "Synthesis and Antimicrobial Activity of New Schiff Bases Containing Coumarin Moiety and Their Spectral Characterization." *Arkivoc* 2008(17): 221–33. doi:10.3998/ark.5550190.0009.h21.
- Sontisiri, Pakornsiri, Dusit Promrug, Dumrongkiet Arthan, Nathawut Choengchan, and Panumart Thongyoo. 2025. "A New Coumarin-Based 'OFF-ON' Fluorescent Sensor for H<sub>2</sub>S Detection in HeLa Cells." *Spectrochimica Acta Part A: Molecular and Biomolecular Spectroscopy* 326: 125170. doi:10.1016/j.saa.2024.125170.
- Sun, Xiao-ya, Teng Liu, Jie Sun, and Xiao-jing Wang. 2020. "Synthesis and Application of Coumarin Fluorescence Probes." *RSC Advances* 10(18): 10826–47. doi:10.1039/C9RA10290F.
- Tan, K B, and H Shaari. 2008. "Reaction Study and Phase Formation in Bi 2O<sub>3</sub>-ZnO-Nb 2O<sub>5</sub> Ternary System." *Number* 9(2).
- Xu, Zhi, Qingtai Chen, Yan Zhang, and Changli Liang. 2021. "Electronic Conduction Mechanism and Optical Spectroscopy of Indigo Carmine as Novel Organic Semiconductors." *Fitoterapia* 150: 104863. doi:10.1016/j.fitote.2021.104863.
- Yu, Tianzhi, Zeyang Zhu, Yanjun Bao, Yuling Zhao, Xiaoxiao Liu, and Hui Zhang. 2017. "AC Conductivity and Dielectric Behavior of Bulk Furfurylidenemalononitrile." *Dyes and Pigments* 147: 260–69. doi:10.1016/j.dyepig.2017.08.017.

## الملخص العربي

## عنوان البحث: دراسة الخصائص التركيبية و الحرارية و خواص العزل الكهربى لمشتق الكومارين (CFT) -1,2,9-trimethyl-7H-furo[3,2-f]chromen-7-one]

عفاف ميلاد على<sup>١</sup>، ناصر عبده عبد الرزاق الغماز<sup>١</sup>، مي محمود محمد الشبعان<sup>١</sup><sup>١</sup> قسم الفيزياء - كلية العلوم - جامعة دمياط - دمياط - مصر

فى الدراسة الحالية تمت دراسة الخواص التركيبية و الحرارية و خواص العزل الكهربى لأحد مشتقات الكومارين (CFT) . أظهرت الدراسة أن CFT ذات طبيعة عديدة التبلور حيث أن بلوراته لها شكل أحادى الميل وتم قياس متوسط حجم البلورة فكان ٥٠٦ نانومتر . أظهرت دراسة معامل العزل الكهربى (suludom cirtceleid) أن مشتقة الكومارين CFT لها معامل استقطاب صغير جدا عند الترددات المنخفضة و مع زيادة التردد يتحسن معامل الاستقطاب مما يسهل ديناميكية الجزيئات و تحسن الاستجابة للمجال الكهربى المتردد. وجد أن CFT يظهر سلوك أشباه الموصلات ووجد أن آلية التوصيل للتيار المتردد هى آلية القفز المترابط عبر حواجز الطاقة (HBC).